Ultrahigh-pressure metamorphism: Deep continental subduction

edited by

Bradley R. Hacker
Geological Sciences
Institute for Crustal Studies
University of California
Santa Barbara, California 93106
USA

William C. McClelland
Department of Geological Sciences
University of Idaho
Moscow, Idaho 83844
USA

Juhn G. Liou
Department of Geological and Environmental Sciences
Stanford University
Stanford, California 94305-2115
USA

THE
GEOLOGICAL
SOCIETY
OF AMERICA

Special Paper 403

3300 Penrose Place, P.O. Box 9140 ▪ Boulder, Colorado 80301-9140 USA

2006

Published by The Geological Society of America, Inc.
3300 Penrose Place, P.O. Box 9140, Boulder, Colorado 80301-9140, USA
www.geosociety.org

Printed in U.S.A.

GSA Books Science Editor: Abhijit Basu

Cataloging-in-Publication Data is available from the Library of Congress

ISBN-10 0-8137-2403-9
ISBN-13 978-0-8137-2403-4

Cover: Spectacular ultrahigh-pressure garnet peridotite from Otrøy, Norway: Cr-pyrope megacryst fragments from a 2-m-long garnet lens; close-up view (8.5 × 10 cm image) of 30 × 60 × 90 cm orthopyroxene megacryst with exsolved clinopyroxene and garnet; and 2 cm "holly-leaf" majoritic garnet megacrysts in peridotite. Photographs by Herman van Roermund and Bradley Hacker. For more details, see Van Roermund, H.L.M., Drury, M.J., Barnhoorn, A., and de Ronde, A.A., 2000, Super-silicic garnet microstructures from an orogenic garnet peridotite, evidence for an ultra-deep (>6 GPa) origin: Journal of Metamorphic Geology, v. 18, p. 135–147, and references therein.

10 9 8 7 6 5 4 3 2 1

Contents

Preface v

1. ***Diachronous histories for the Dabie-Sulu orogen from high-temperature geochronology*** 1
   M.L. Leech, L.E. Webb, and T.N. Yang

2. ***U-Pb SHRIMP geochronology and trace-element geochemistry of coesite-bearing zircons, North-East Greenland Caledonides***. 23
   W.C. McClelland, S.E. Power, J.A. Gilotti, F.K. Mazdab, and B. Wopenka

3. ***The Sino-Korean–Yangtze suture, the Huwan detachment, and the Paleozoic–Tertiary exhumation of (ultra)high-pressure rocks along the Tongbai–Xinxian–Dabie Mountains*** 45
   L. Ratschbacher, L. Franz, E. Enkelmann, R. Jonckheere, A. Pörschke, B.R. Hacker, S. Dong, and Y. Zhang

4. ***$^{40}Ar/^{39}Ar$ thermochronology of the Sulu terrane: Late Triassic exhumation of high- and ultrahigh-pressure rocks and implications for Mesozoic tectonics in East Asia*** 77
   L.E. Webb, M.L. Leech, and T.N. Yang

5. ***Polyphase subduction and exhumation of the Sulu high-pressure–ultrahigh-pressure metamorphic terrane*** 93
   Z. Xu, , L. Zeng, F. Liu, J. Yang, Z. Zhang, M. McWilliams, and J.G. Liou

6. ***SHRIMP U-Pb zircon dating of the Rongcheng eclogite and associated peridotite: New constraints for ultrahigh-pressure metamorphism of mantle-derived mafic-ultramafic bodies from the Sulu terrane***. 115
   R. Zhao, J.G. Liou, R.Y. Zhang, and T. Li

7. ***Late chloritoid-staurolite assemblage in a garnet-kyanite–bearing metapelite from the ultrahigh-pressure Brossasco-Isasca unit (Dora-Maira Massif, Western Alps): New petrological constraints for a portion of the decompressional path***. 127
   C. Groppo, D. Castelli, and R. Compagnoni

8. ***Hydroxyl in diopside of diamond-free ultrahigh-pressure dolomitic marble from the Kokchetav Massif, Kazakhstan*** 139
   M. Kikuchi and Y. Ogasawara

9. ***Petrologic characterization of Guatemalan lawsonite eclogite: Eclogitization of subducted oceanic crust in a cold subduction zone*** 147
   T. Tsujimori, V.B. Sisson, J.G. Liou, G.E. Harlow, and S.S. Sorensen

10. ***Non-ultrahigh-pressure unit neighboring the Sulu ultrahigh-pressure terrane, eastern China: Transformation of Proterozoic granulite and gabbro to garnet amphibolite*** 169
    R.Y. Zhang, J.G. Liou, T. Tsujimori, and S. Maruyama

Preface

The most provocative recent plate-tectonic revelation is that continental crust was subducted to depths of >100 km and exhumed at numerous locations worldwide throughout the Phanerozoic. It is now recognized that the formation and exhumation of these "ultrahigh-pressure"—or UHP—rocks is an inherent and fundamental dynamic aspect of collisional orogenesis that affects a panoply of earth processes, including, but not limited to, exchange of material between the crust and mantle, the generation and collapse of mountain belts, the formation of continental crust, and the influence of UHP rock formation and exhumation on tectonic plate motions.

This volume is a collection of papers highlighting recent discoveries, stemming from a series of sessions on ultrahigh-pressure tectonics at the 2004 International Geological Congress in Florence, Italy. Constructive reviews were provided by W.G. Ernst, Leander Franz, John Goodge, Jeremy Hourigan, Trevor Ireland, Scott Johnston, Ikuo Katayama, Andrew Kylander-Clark, Helen Lang, Christopher Mattinson, Jed Mosenfelder, Lothar Ratschbacher, Franco Rolfo, David Root, Hans-Peter Schertl, Michael Terry, Simon Wallis, Emily Walsh, Martin Wong, and Thomas Zack.

Bradley R. Hacker
William C. McClelland
Juhn G. Liou

Geological Society of America
Special Paper 403
2006

Diachronous histories for the Dabie-Sulu orogen from high-temperature geochronology

M.L. Leech*
Geological and Environmental Sciences, Stanford University, Stanford, California 94305, USA
L.E. Webb
Department of Earth Sciences, Syracuse University, Syracuse, New York 13244, USA
T.N. Yang
Institute of Geology, Chinese Academy of Geological Sciences, Beijing, 100037, China

ABSTRACT

New U-Pb sensitive high-resolution ion microprobe (SHRIMP) dating of zircon from the ultrahigh-pressure Sulu terrane, eastern China, records three events in the evolution of the orogen. Peak ultrahigh-pressure and retrograde metamorphism in the Middle to Late Triassic (ca. 230–200 Ma) is recorded in zircon mantles and rims; cathodoluminescence imaging, grain morphology, and U-Th-Pb and rare earth element chemistry cannot distinguish between ultrahigh-pressure and retrograde zircon growth. Comparison of high-temperature thermochronology for the Sulu and Dabie–Hong'an areas suggests that peak ultrahigh-pressure metamorphism in Sulu took place at ca. 230 Ma, postdating Dabie–Hong'an by 10 m.y.; this age disparity has implications for collision-subduction-exhumation models for the entire Qinling–Hong'an–Dabie–Sulu orogen and suggests that Sulu was a separate ultrahigh-pressure slab that was never adjacent to Dabie. Relict zircon cores and mantles preserve protolith ages between 700 and 790 Ma, reflecting the Yangtze craton affinity of the Sulu terrane and supporting other evidence indicating that the suture between the Yangtze and Sino-Korean cratons lies along the Yantai-Qingdao-Wulian fault zone. Late Jurassic to Early Cretaceous ages from a pegmatite vein near the suture probably reflect early melting related to a widespread magmatic event that affected the northern margin of the Dabie-Sulu belt.

Keywords: U-Pb zircon SHRIMP dating, Qinling–Hong'an–Dabie–Sulu orogen, eastern China, Triassic ultrahigh-pressure (UHP) metamorphism, Yangtze craton.

*Present address: Department of Geosciences, San Francisco State University, San Francisco, California 94132, USA.

Leech, M.L., Webb, L.E., and Yang, T.N., 2006, Diachronous histories for the Dabie-Sulu orogen from high-temperature geochronology, *in* Hacker, B.R., McClelland, W.C., and Liou, J.G., eds., Ultrahigh-pressure metamorphism: Deep continental subduction: Geological Society of America Special Paper 403, p. 1–22, doi: 10.1130/2006.2403(01).

INTRODUCTION TO THE QINLING–HONG'AN–DABIE–SULU OROGEN

The Sulu terrane (Fig. 1), the eastern extension of the larger Qinling–Hong'an–Dabie–Sulu orogen, was the one of the first ultrahigh-pressure (UHP) subduction zone complexes shown to contain microdiamond, requiring UHP metamorphism at pressures in excess of 3.2 GPa at >130 km depth (Sobolev and Shatsky, 1990; Xu et al., 1992). Ultrahigh-pressure metamorphism occurred during the Triassic northward subduction of the Yangtze craton beneath the Sino-Korean craton (e.g., Liou et al., 1996; Hacker et al., 2000, 2004; Chen et al., 2003). Mineralogical evidence for Early to Middle Triassic UHP metamorphism is found in minor eclogite and garnet peridotites, and their host quartzofeldspathic gneisses, that all followed the same pressure-temperature-time (*P-T-t*) path during subduction

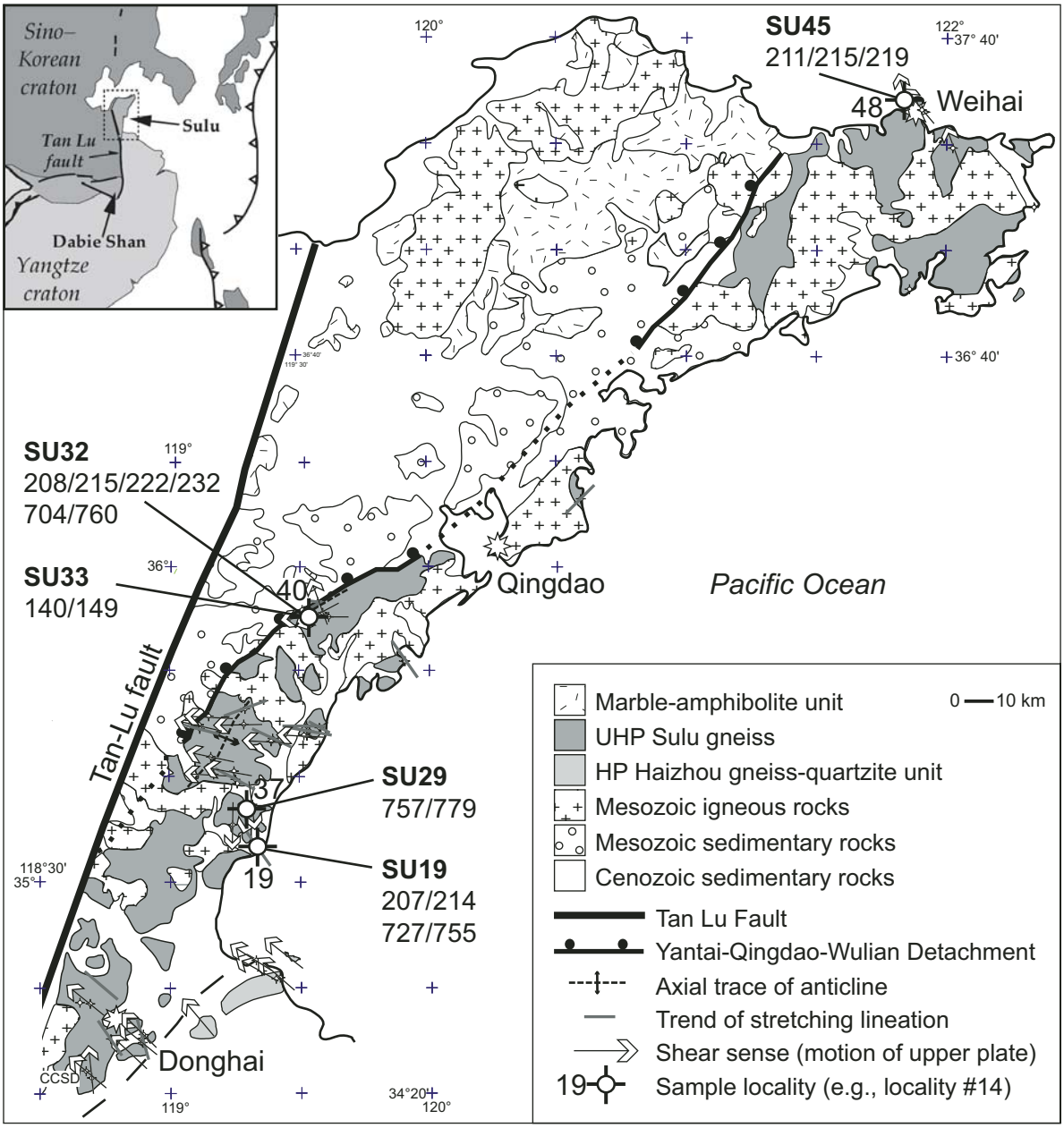

Figure 1. General geologic map of the Sulu terrane, part of the Shandong Peninsula, eastern China (after Wallis et al., 1999; Webb et al., this volume). Sample numbers for U-Pb sensitive high-resolution ion microprobe (SHRIMP) dating are shown in bold (Appendix 1 contains complete U-Th-Pb data). Weighted mean ages (in Ma) summarize age data for each sample. The Qinling–Hong'an–Dabie blocks are shown on the inset map in medium gray (Dabie is labeled, the Qinling and Hong'an blocks are further west). UHP—ultrahigh pressure.

and exhumation (e.g., Xu et al., 1992; Liou et al., 1996, and references therein; Tabata et al., 1998). Conditions for UHP metamorphism in the Dabie and Sulu areas were ~600–800 °C and from to 3.0–4.0 GPa (W.G. Ernst, 2005, personal commun.). Exhumation of these UHP rocks to middle- to upper-crustal levels was complete by the latest Triassic to Early Jurassic (e.g., Hacker et al., 2000; Ratschbacher et al., 2000; Webb et al., 1999, this volume), and likely proceeded during coeval detachment faulting/shearing and gneiss dome formation (Webb et al., 2002, this volume; Leech et al., 2003). The northern part of the orogen experienced extensive magmatism in the Early Cretaceous (Hacker et al., 1998; Ratschbacher et al., 2000; Grimmer et al., 2002) and later oblique sinistral offset along the Tan-Lu fault (Fig. 1).

An extensive collection of $^{40}Ar/^{39}Ar$ ages for the Hong'an, Dabie, and Sulu areas (e.g., Hacker et al., 2000, and references therein; Webb et al., 1999) documents synexhumation cooling of the UHP rocks to the middle to upper crust, but the precise timing of UHP metamorphism across the orogen remains elusive. Various workers have used high-temperature thermochronometry (U-Th-Pb, Sm-Nd, and Rb-Sr) to address this issue, but many individual attempts are plagued by large analytical errors, a lack of sufficient data, age ranges spanning both peak and retrograde metamorphism, and assumptions about the ~2000 km orogen having a uniform subduction-exhumation history. Here we present new U-Pb SHRIMP (sensitive high resolution ion microprobe) dating of zircon for the Sulu terrane, compare this new data to the existing body of dating for the UHP metamorphic event, and discuss the implications for an orogenic model with UHP metamorphism taking place in the Sulu area ~10 m.y. after UHP metamorphism in the Dabie–Hong'an area.

NEW U-Pb SHRIMP DATING FOR SULU

Samples of UHP quartzofeldspathic gneiss (host rocks to eclogite) from three different areas in the Sulu terrane, and a mylonitized gneiss and pegmatite vein from near the Yantai-Qingdao-Wulian fault were collected to establish the timing of UHP metamorphism, retrograde metamorphism and exhumation-related deformation, and later magmatism, respectively. Quartzofeldspathic lithologies were chosen for the relative abundance of zircon that could be extracted for U-Pb SHRIMP dating; zircon can record a long history of growth recorded in relict internal parts of zircon grains, can record higher-temperature events (~1000 °C) than other thermochronometers (Cherniak and Watson, 2003), making dating peak metamorphic conditions more likely, and can record lower-temperature events during recrystallization. Three of these samples (SU29, SU33, and SU45) are the same samples from which other mineral phases were extracted for dating by the $^{40}Ar/^{39}Ar$ method in Webb et al. (this volume), the results of which are summarized in the following section.

Sample Preparation and Analytical Technique

A total of 143 zircon U-Pb SHRIMP analyses were completed for five samples (Fig. 2; see Appendix 1 for U-Th-Pb data for all analyses). Zircons were separated and mounted using standard sample-preparation methods for ion microprobe analysis (Williams, 1998), and U-Pb SHRIMP analyses, data reduction using *Squid*, and plotting using *Isoplot* followed standard techniques (Williams, 1998; Ludwig, 1999, 2001). No morphologic or color differentiation was made during handpicking for the sample mount. Separated zircons include euhedral, subrounded, and irregularly shaped grains that display clear core-mantle-rim zoning relationships under cathodoluminescence (CL) imaging (Fig. 3). SHRIMP analyses targeted rims that appeared to be metamorphic based on CL imaging (i.e., lack of zoning, rounded grain morphology); analysis of zircon mantles and cores was done for age comparison with metamorphic rims and to establish different growth domains within the zircons. Pb/U ratios were calibrated with reference standard R33 (419 Ma; Black et al., 2004), which was analyzed after about every fourth unknown analysis. Zircons were analyzed using the SHRIMP-RG (reverse geometry) at the Stanford–U.S. Geological Survey Microanalysis Center. U-Th-Pb data for each ~30 μm spot were collected in five scans.

Descriptions of Dated Samples

All five samples dated in this study came from the UHP Sulu gneiss unit (Fig. 1). Figure 2 shows Tera-Wasserburg concordia diagrams for all analyses from all five samples; these concordia plots include some discordant data and display mixing trends and discordance due to common Pb (all concordia plots [Figs. 2, 4, and 5] show data uncorrected for common Pb). All ages (single-grain or weighted mean ages [95% confidence level]) described for dating in this study are ^{207}Pb-corrected $^{206}Pb/^{238}U$ ages from concordant data or data within 1%–2% of concordance (see ages listed with concordia plots in Figs. 4 and 5); high U, high common Pb, and discordant analyses were excluded from age calculations.

Sample SU19

Sample SU19 is a quartzofeldspathic gneiss from the central part of the UHP Sulu terrane within the core of the large gneiss dome structure (locality 19: 35°10′N, 119°14′E; Fig. 1). Relict Proterozoic zircon domains in sample SU19 yield ages between 702 and 767 Ma; two distinct populations within that range give weighted mean ages of 727 ± 15 Ma (3 grains) and 755 ± 12 Ma (5 grains) from concordant analyses. These Proterozoic domains are generally bright cores and mantles with oscillatory zoning in cathodoluminescence (CL) imaging and have relatively high Th/U ratios between 0.6 and 1.7 (Figs. 2A, 3, and 4). Concordant Late Triassic analyses yield weighted mean ages for two age groups at 207 ± 3 Ma (5 grains) and 214 ± 4 Ma (4 grains); these ages result from uniformly nonluminescent, rounded metamorphic rims and have very low Th/U ratios (<<0.1) (Figs. 5 and 6; Appendix 1).

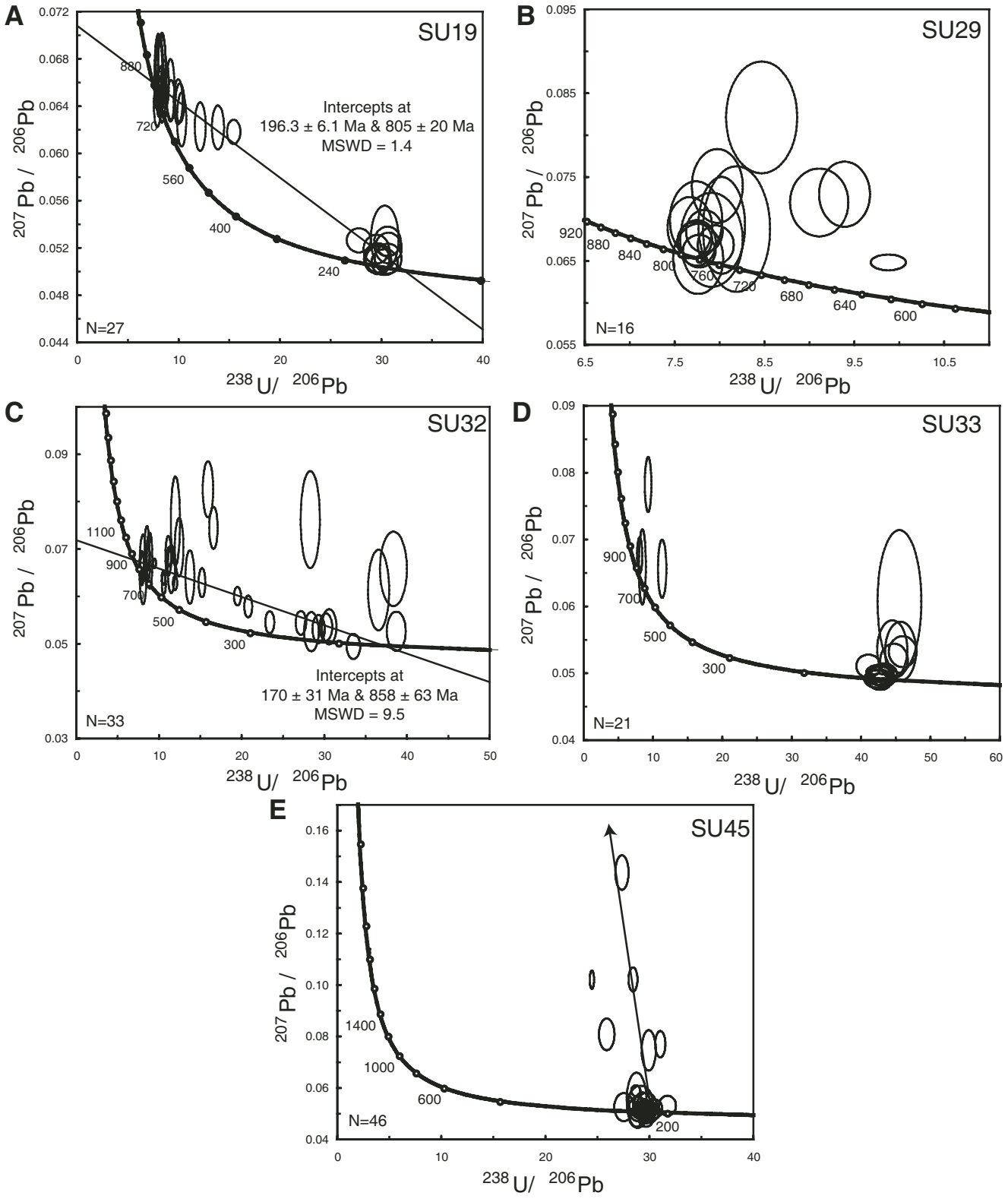

Figure 2. Tera-Wasserburg concordia diagrams for all zircon analyses from all samples (data uncorrected for common Pb; error ellipses are 2σ). A and C include intercept lines that show mixing for discordant data between Proterozoic and Mesozoic analyses for samples SU19 and SU32 (intercept ages are not used for interpretation—see weighted mean ages in Figs. 4 and 5). E shows a projection to common Pb ratio ($^{207}Pb/^{206}Pb$ = 0.86 based on Cumming and Richards, 1975) for six discordant analyses from sample SU45. *N* is the number of zircons analyzed for each sample. MSWD—mean square of weighted deviates.

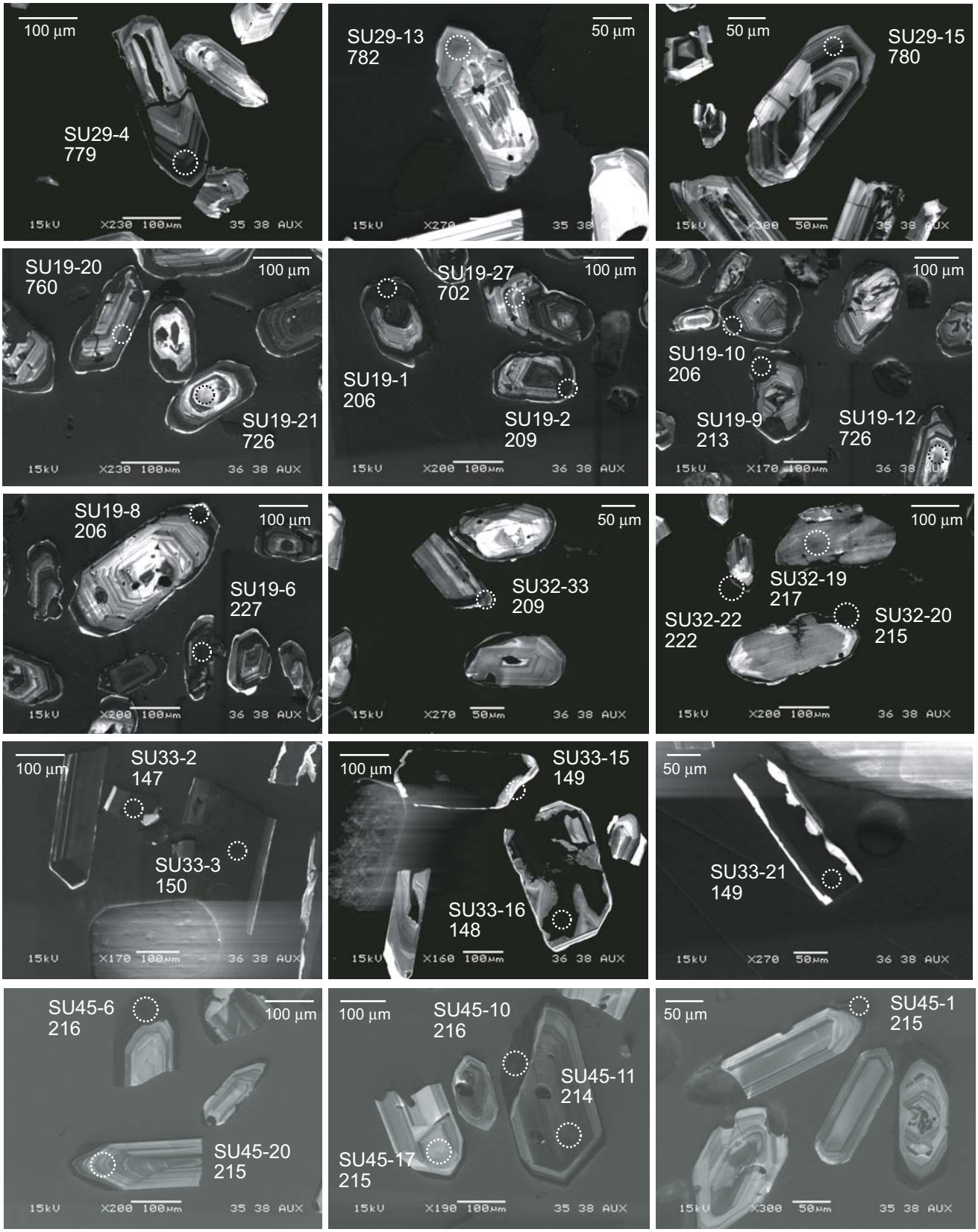

Figure 3. Cathodoluminescence (CL) images of representative analyzed zircons from each sample. Analysis number with corrected $^{206}Pb/^{238}U$ age and spot locations (dashed circles) correspond to those listed in Appendix 1. Streaking is due to charging on nonzircon grains.

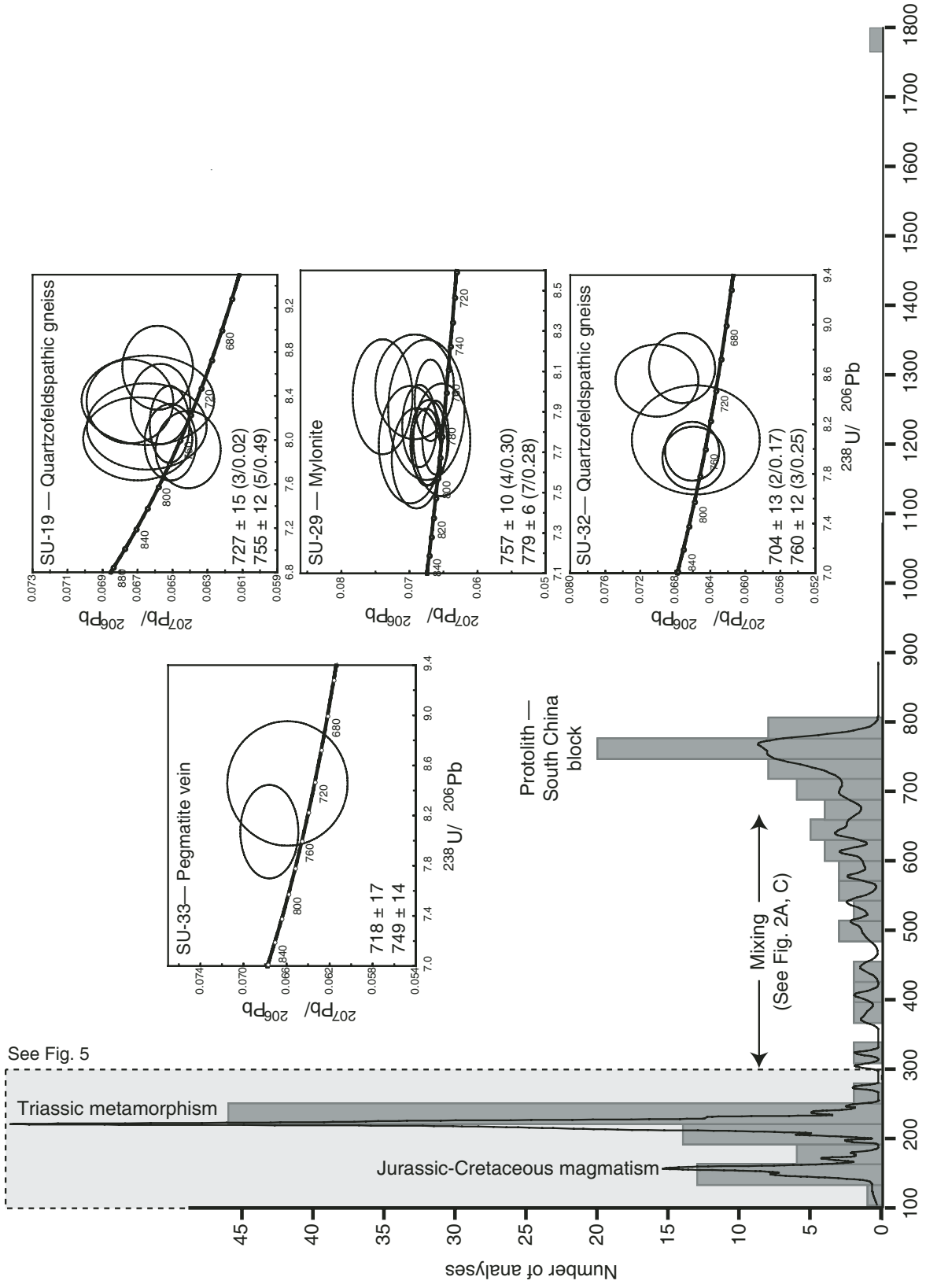

Figure 4. Histogram and probability density curve for all $^{238}U/^{206}Pb$ ages (^{207}Pb corrected) from all samples. Three main events are recorded: relict protolith ages from zircon cores (ca. 780–700 Ma), Triassic metamorphism (220–210 Ma), and Late Jurassic–Early Cretaceous magmatism (150–140 Ma); data between 700 Ma and 300 Ma represent mixing in samples SU19 and SU32. Tera-Wasserburg concordia diagrams show concordant and near-concordant Proterozoic analyses for samples SU19, SU29, SU32, and SU33 (data uncorrected for common Pb; error ellipses are 2σ); single-grain ages and weighted mean ages for multiple age groups in each sample are listed, with the number of analyses and mean square of weighted deviates (MSWD) included for those averages (in parentheses). Age groups delineated by weighted mean ages were determined based on weighted mean age plots of concordant data (data weighted by 2σ data-point errors; analyses high in common Pb were excluded).

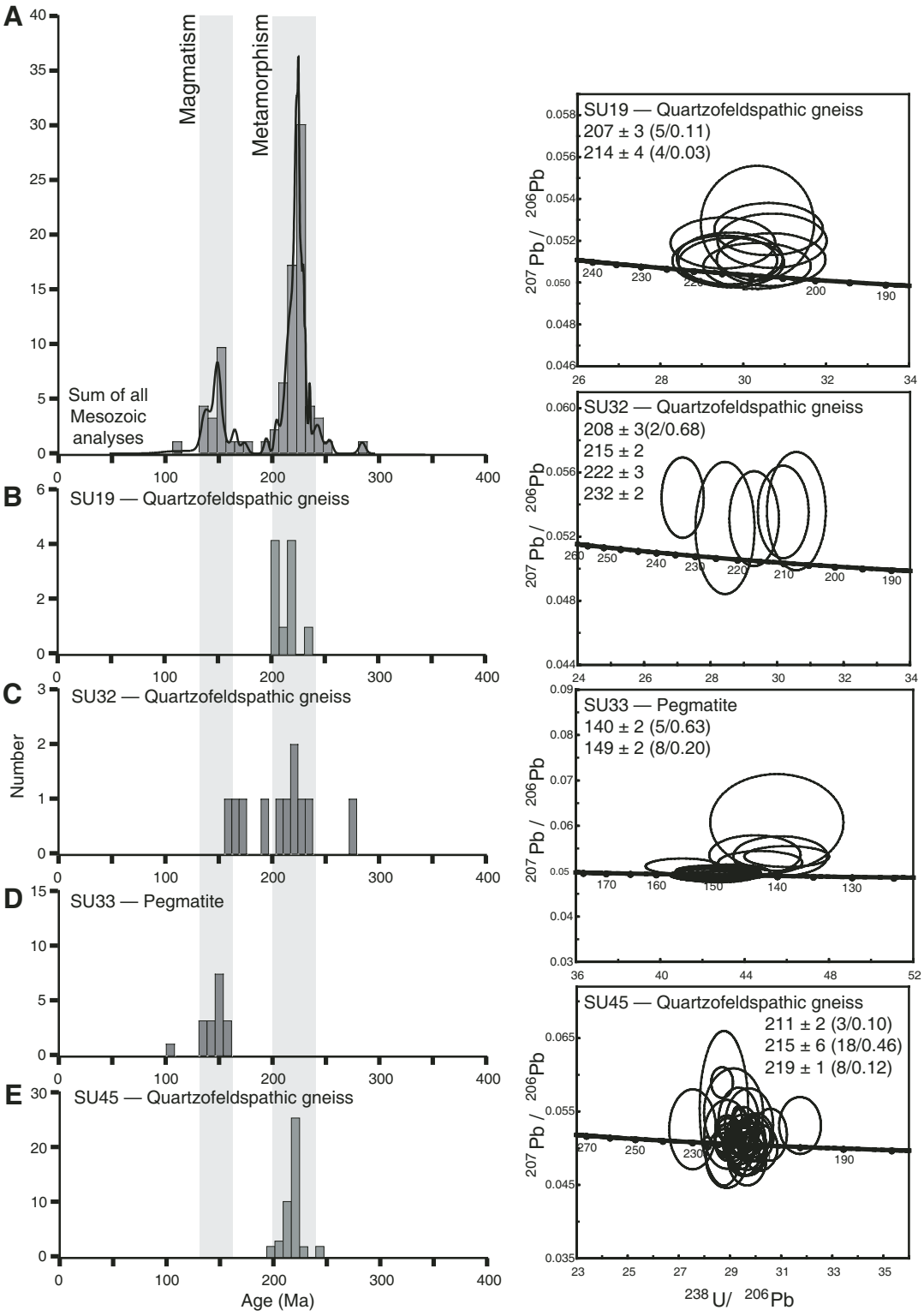

Figure 5. Histogram and probability density curves for (A) summary of Late Permian to Early Cretaceous age data; and (B–E) individual samples SU19, SU32, SU33, and SU45. Samples SU19, SU32, and SU45 record $^{238}U/^{206}Pb$ ages corresponding to ultrahigh-pressure (UHP) and retrograde metamorphism; sample SU33 records melting associated with a later magmatic event. Tera-Wasserburg concordia diagrams show only concordant and near-concordant analyses (data uncorrected for common Pb; error ellipses are 2σ); weighted mean ages for multiple age groups in each sample are listed, with the number of analyses and mean square of weighted deviates (MSWD) included for those averages (in parentheses). Age groups delineated by weighted mean ages were determined based on weighted mean age plots of concordant data (data weighted by 2σ data-point errors; analyses high in common Pb were excluded).

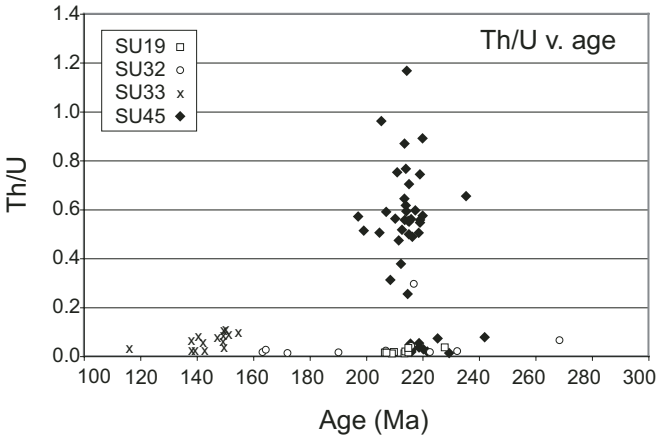

Figure 6. Th-U data for all zircons yielding Mesozoic ages (samples SU19, SU32, SU33, and SU45). This plot shows U-Th data for all Mesozoic data points and includes analyses excluded in weighted mean ages (see discussion in text).

Sample SU29

Sample SU29 is a mylonitized quartzofeldspathic biotite gneiss also from near the central part of the Sulu terrane (locality 37: 35°31′N, 119°08′E; Fig. 1). All U-Pb analyses from sample SU29 yield Late Proterozoic ages between 738 and 786 Ma (concordant analyses only); two subpopulations yield weighted mean ages of 757 ± 10 Ma (4 grains) and 779 ± 6 Ma (7 grains) (Figs. 2B, 3, and 4). The zircon grains are bright with oscillatory zoning under CL, and have Th/U ratios between 0.6 and 2.5 (Appendix 1); later metamorphic zircon growth appears to be absent in this sample. Biotite from SU29 yielded a $^{40}Ar/^{39}Ar$ weighted mean age of 136 ± 1 Ma (Webb et al., this volume).

Samples SU32 and SU33

Quartzofeldspathic gneiss (SU32) and granitic pegmatite vein (SU33) samples are from the Haohung-Taolin area (locality 40: 35°50′N, 119°32′E) near the Yantai-Qingdao-Wulian fault zone along the NW flank of the central dome structure in Sulu (Fig. 1). Samples SU32 and SU33 both record Proterozoic and Mesozoic histories (Figs. 2C–D, 3, and 4). Five concordant Proterozoic analyses from SU32 fall between 701 and 764 Ma, comprising two age groups with weighted mean ages of 704 ± 13 Ma (2 grains) and 760 ± 12 Ma (3 grains). These relict domains are composed of luminescent cores and mantles with oscillatory zoning in CL, and have Th/U ratios between 0.7 and 1.2 (Appendix 1). SU32 gives five concordant analyses with a weighted mean age of 208 ± 3 Ma (2 analyses) and single-grain analyses at 215 ± 2 Ma, 222 ± 3 Ma, and 232 ± 2 Ma (Fig. 2C, 3, and 5). Th/U ratios for the Triassic data fall between 0.01 and 0.04, and come from dark, rounded zircon rims (Fig. 6; Appendix 1).

Sample SU33 yields two concordant ages at 718 ± 17 Ma and 749 ± 14 Ma; these analyses are from a luminescent core and mantle (external to an irregular core) with oscillatory zoning and have Th/U ratios between 0.7 and 1.8 (Figs. 2D and 4; Appendix 1). Late Jurassic to Early Cretaceous spot ages from SU33 yield weighted mean ages of 140 ± 2 Ma (5 grains) and 149 ± 2 (8 grains); these data have Th/U ratios <<0.01 and come from both luminescent rims and nonluminescent cores with oscillatory zoning (Figs. 3, 5, and 6; Appendix 1). White mica from SU33 yields a $^{40}Ar/^{39}Ar$ weighted mean age of 128 ± 1 Ma (Webb et al., this volume).

Sample SU45

Sample SU45 is a quartzofeldspathic biotite gneiss from an island outcrop near Weihai on the Shandong Peninsula (locality 48: 37°31′N, 122°01′E; Fig. 1). Apart from one Early Proterozoic age, this sample yields only Mesozoic data for both luminescent oscillatory-zoned cores and mantles, as well as uniformly nonluminescent, rounded rims (Figs. 2E, 3, and 5). These Mesozoic data have weighted mean ages of 211 ± 2 Ma (3 grains), 215 ± 6 Ma (18 grains), and 219 ± 1 Ma (8 grains) and unusually high Th ratios (0.01–1.2) compared to other metamorphic zircons in this study (Fig. 6; Appendix 1). Biotite from sample SU45 produced a $^{40}Ar/^{39}Ar$ weighted mean age of 70 ± 2 Ma (Webb et al., this volume).

RARE EARTH ELEMENT ANALYSES OF TRIASSIC ZIRCON DOMAINS

Rare earth element (REE) data were collected using the SHRIMP-RG in the same analysis spots for which U-Pb dating was done in an attempt to distinguish between eclogite-facies zircon growth and lower-grade metamorphic zircon growth.

Analytical Technique

The lack of well-characterized zircon crystals for REE calibration standards requires calibration to other REE and zircon standards. For our analyses, we calibrated to NIST SRM 611 and NIST SRM 613 (REE-spiked) glasses; SL13 standard zircon (REE concentrations based on SL13-LA-CH in Hoskin, 1998); and CZ3 (U-concentration standard). NIST glasses and SL13 zircon were analyzed at the beginning and end of the SHRIMP session. Rare earth data were collected in three scans, with the CZ3 standard repeated after every twelfth analysis; multiple CZ3 and SL13 standards were run before and after each sample. Details of data reduction were as described by Hoskin (1998); data were normalized to the chondrite values of McDonough and Sun (1995).

Summary and Interpretation of REE Data

Three samples analyzed for REEs (SU19, SU32, SU45) show consistent patterns of depleted light (L) REEs, with pronounced positive Ce anomalies and enriched heavy (H) REEs with respect to middle (M) REEs (Fig. 7). Figure 7 shows REE patterns for zircons yielding Triassic ages in core-mantle and

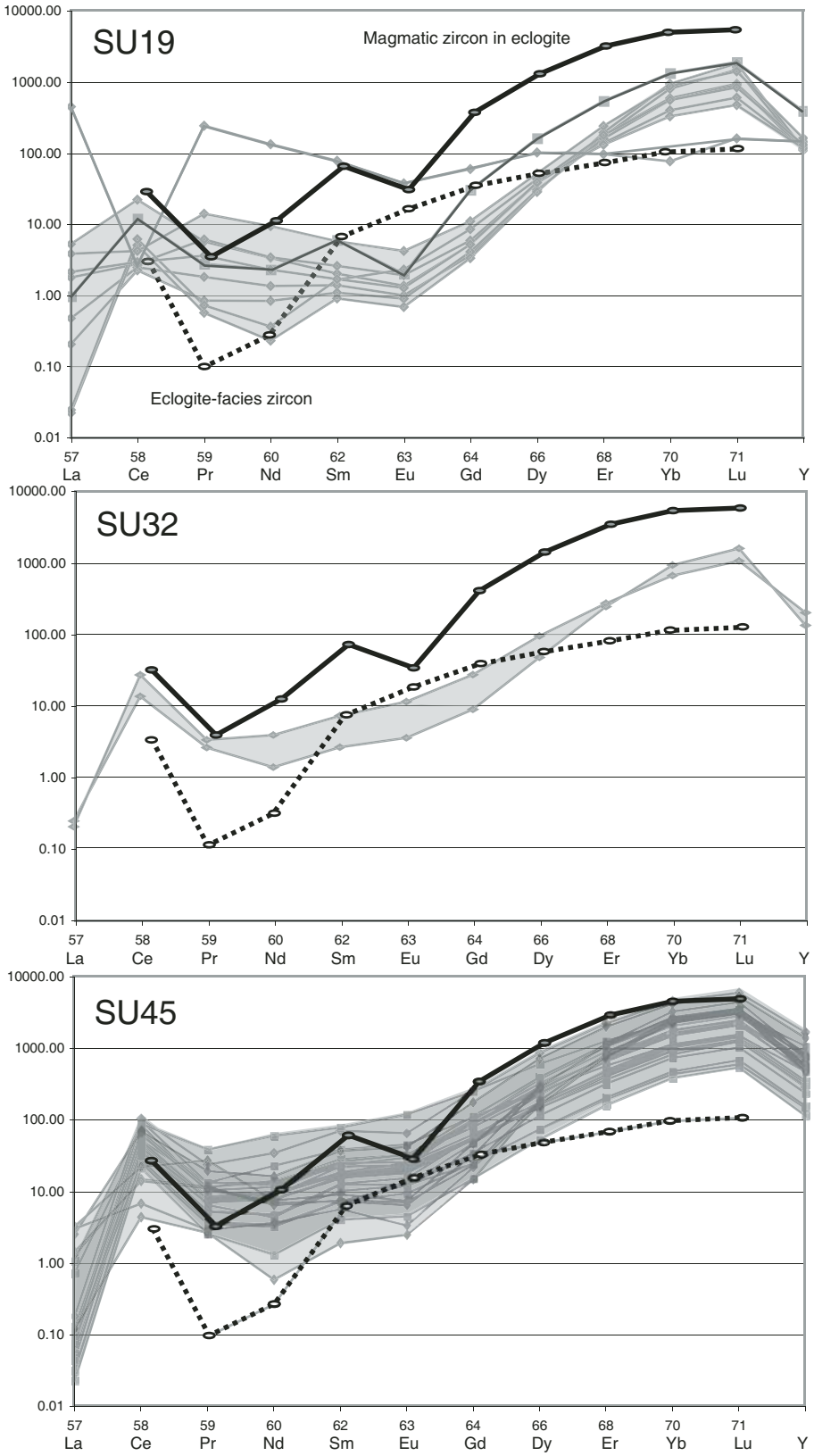

Figure 7. Chondrite-normalized (McDonough and Sun, 1995) rare earth element (REE) patterns of zircons yielding Mesozoic U-Pb ages for cores-mantles (dark-gray lines and fields) and rims (light-gray lines and fields) for samples SU19, SU32, and SU45. Heavy solid black and dashed black lines show typical patterns for magmatic zircon and eclogite-facies zircon, respectively (from Rubatto and Hermann, 2003).

rim growth domains (see also Fig. 3). In general, core-mantle analyses give a broader range of LREE values and a smaller range of HREE values, whereas rim analyses show a smaller range of LREEs and a broader range of HREE values.

A single-rim analysis for sample SU19 shows a pronounced Eu anomaly, whereas core-mantle analyses show only a slight Eu anomaly; both core-mantle and rim analyses have an enriched HREE signature compared to the MREEs (two analyses with negative Ce anomalies and very different REE patterns were ignored because these analyses may have sampled inclusions within zircon). Rim analyses for SU32 lack a Eu anomaly and show enrichment in HREEs. Despite the relatively high Th/U ratios for SU45 (resulting from relatively high Th concentrations; Fig. 6 and Appendix 1), the REE patterns for this sample are comparable to SU19 and SU32. In sample SU45, the core-mantle analyses lack a negative Eu anomaly, while rim analyses show only a slight negative Eu anomaly. Ages corresponding to these zircon core-mantle and rim domains span the entire period of metamorphism from ca. 230 to 200 Ma; i.e., rim ages are not systematically younger than mantle ages and have no apparent correlation to any particular age group (see following).

Zircon growing in the presence of garnet should show a depleted HREE pattern, because garnet preferentially incorporates HREEs (see example from Rubatto and Hermann [2003] in Fig. 7). In contrast, magmatic zircon grown in the presence of plagioclase should have elevated HREEs and a negative Eu anomaly (example in Fig. 7; Hermann et al., 2001; Rubatto, 2002; Rubatto and Hermann, 2003).

Our age and REE data for zircons are from quartzofeldspathic gneisses that have abundant feldspar and only rare to minor garnet, consequently, the REE patterns are generally consistent with zircon growing in association with feldspar. These REE patterns do not rule out zircon crystallization at eclogite-facies conditions in a largely garnet-free rock, but may in fact reflect zircon growth at amphibolite-facies conditions based on our interpretation of the age data for these samples.

DISCUSSION OF NEW U-Pb SHRIMP DATING

Zircon records a long history of events during the evolution of the Sulu terrane. Relict zircon domains preserve protolith ages (Fig. 4), and newer zircon growth and recrystallization record metamorphism from UHP conditions during retrogression (Figs. 5 and 8), and mark the early stages of melting (Fig. 5) during a widespread magmatic event.

Proterozoic Protolith Ages and Yangtze Craton Affinity

The location of the suture between the Yangtze and Sino-Korean cratons has been a matter of significant debate, and U-Pb dating of zircon is helping to piece together the Precambrian history of this region (e.g., Hacker et al., 1998; B.R. Hacker, 2005, personal commun.); Faure et al., 2001, 2003; Grimmer et al., 2003; Wu et al., 2004; Zheng et al., 2004a; Ratschbacher et al., this volume; B.R. Hacker (2005, personal commun.). The predominance of ages between 650 and 850 Ma is used to identify the Yangtze craton, and the absence of these ages (locally the presence of 400–480 Ma ages) signifies a Sino-Korean craton affinity (Hacker et al., 1998). Zircon cores and mantles from four different samples in this study produced ages between 700 and 790 Ma (Fig. 4; Appendix 1), strengthening earlier interpretations that the Sulu gneiss belongs to the Yangtze craton. In the Sulu area, the location of the suture has conventionally been placed along the Yantai-Qingdao-Wulian fault, based on the differences in the geology to the southeast and northwest of the fault, where the UHP Sulu gneiss marks the northern extent of the Yangtze craton (Fig. 1). Faure et al. (2001, 2003) more recently suggested that the suture lies northwest of the Yantai-Qingdao-Wulian fault, based on similarities in deformational style, the presence of migmatites, and a granulite-facies overprint across the fault. New dating (Wu et al., 2004; B.R. Hacker (2005, personal commun.) supports this by showing that some high-grade rocks northwest of the Yantai-Qingdao-Wulian fault do have ca. 750 Ma ages. B.R. Hacker (2005, personal commun.) interpreted this to mean that the Sulu area northwest of the Yantai-Qingdao-Wulian fault is part of the Qinling microcontinent, which rifted from the Yangtze craton (Ratschbacher et al., this volume) during the breakup of Rodinia and was not subducted during the Triassic UHP orogeny.

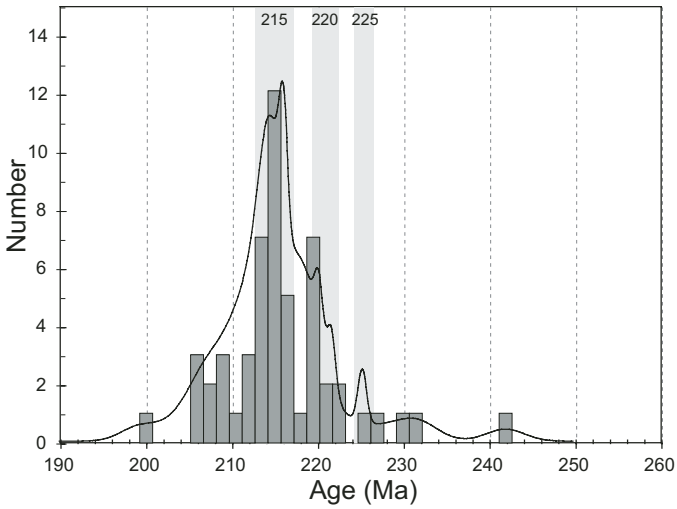

Figure 8. Histogram and probability density curve for all concordant single-grain ages between 250 and 200 Ma from samples SU19, SU32, and SU45. Major age groups recorded in zircon fall around 220 Ma and 215 Ma.

Cretaceous Magmatism

Dating of a pegmatite vein (sample SU33) near the Yantai-Qingdao-Wulian fault zone yields weighted mean ages between ca. 140 and 150 Ma using concordant single-grain ages from

138 ± 2 Ma to 155 ± 3 Ma (Fig. 5). These ages slightly overlap the 137–126 Ma ages of undeformed igneous rocks in northern Dabie (Ratschbacher et al., 2000), and may reflect an early stage of related melting.

Triassic UHP and Retrograde Metamorphism

Concordant single-grain ages for this study range from ca. 240 Ma to 200 Ma, with probability density curve peaks at ca. 225 Ma, 220 Ma, and 215 Ma (Fig. 8); there were an insufficient number of spot analyses older than 220 Ma (Appendix 1) to define distinct age groups apart from what is seen in the probability density curve in Figure 8. These age groups are indistinguishable on the basis of their U-Th-Pb concentrations, Th/U ratios, grain morphology, CL images, or REE patterns. The age of UHP metamorphism in the Sulu terrane has been estimated between ca. 220 and 230 Ma, based on dating of coesite-bearing domains in zircon (Yang et al., 2003; Liu et al., 2004b), a disparity of 10 m.y.; combining all the individual attempts to date UHP metamorphism (Fig. 9), instead of relying on a single "best" study, may reveal a more reliable date. Based on the distribution of all Sulu ages shown in Figure 9, the ages in this study all date synexhumation retrograde metamorphism—apart from a few single-grain ages ca. 230 Ma that may record UHP metamorphism. This interpretation is further supported by the $^{40}Ar/^{39}Ar$ dating presented in Webb et al. (this volume), suggesting amphibolite- to upper greenschist–facies metamorphism at ca. 213 Ma in some of the same samples. Many of the ages reported from high-temperature thermochronometry for the Hong'an–Dabie and Sulu areas span both peak and retrograde metamorphism (Fig. 9; Appendices 2 and 3). In fact, the distribution of ages seen in Figure 9 suggests that it is perhaps more accurate to describe these ages as recording a period of metamorphism beginning with peak *P-T* conditions and continuing through the initial exhumation.

There are many examples of low- to intermediate-temperature zircon crystallization, including amphibolite-facies zircon growth in UHP rocks from the Kokchetav Massif (Hermann et al., 2001). Hermann et al. (2001) showed that UHP eclogite-facies zircon (identified by the presence of coesite and diamond) have U-Th-Pb concentrations and cathodoluminescence that are identical to upper amphibolite– to granulite-facies zircon. Metamorphic recrystallization of zircon rims at post-peak amphibolite-facies conditions may result from dehydration reaction–derived fluids during exhumation (Hermann et al., 2001; Leech, 2001); the intermittent presence of these fluids could allow zircon (re)crystallization during exhumation during changing *P-T* conditions.

Yang et al. (2003) and Liu et al. (2004b) produced weighted mean ages for coesite-bearing domains in zircon (mantles) of 221 ± 12 Ma for eclogite in peridotites and 231 ± 4 Ma for host gneisses, respectively, and interpreted these ages as the time of UHP metamorphism. Liu et al. (2004b) compared those ages with ages from quartz-bearing zircon rims and calculated a weighted mean age of 211 ± 4 Ma for the amphibolite-facies overprint. We have not identified coesite and/or diamond within our dated zircon that would enable interpretations like Yang et al. (2003) and Liu et al. (2004b), but the Th/U ratios for our zircons are on par with metamorphic zircons from other Sulu gneiss samples (e.g., 0.01–0.8 from Liu et al. [2004b] compared to <<0.01–1.2 from this study). While this is an excellent approach, the data of Yang et al. (2003) and Liu et al. (2004b) suffer from some problems that we discuss in the following; a better approach is to look at all dates for Sulu as a whole (Fig. 9).

Timing of UHP Metamorphism in the Dabie-Sulu Orogen

Results of U-Pb SHRIMP dating of zircon from the Sulu gneiss in this study are representative of all the high-temperature thermochronology for Sulu (compare Figs. 8 and 9A). Figure 9 compares all published high-temperature geochronology (U-Pb, Pb-Pb, Pb-Th, Sm-Nd, and Rb-Sr) for both the Sulu (including this study) and Hong'an–Dabie areas that attempt to date UHP metamorphism (details of the data included in Figure 9 are in Appendices 2 and 3); $^{40}Ar/^{39}Ar$ analyses have been specifically excluded, because these dates record cooling through temperatures well below UHP conditions (e.g., ~350 °C for muscovite and ~450 °C for phengite; MacDougall and Harrison, 1988). Histograms of these ages in Figures 9A (Sulu) and 9E (Dabie–Hong'an) span similar ranges (broadly 260–200 Ma), but the probability density curves for each data set define different age populations. The dominant age groups for analyses from Sulu fall around 229 Ma, 219 Ma, and 207 Ma, while they are ~10 m.y. older in the Dabie–Hong'an areas (240 Ma, 228 Ma, and 216 Ma).

Outliers in the data displayed in the histograms in Figure 9 may be explained in several ways: A few of the older ages come from analyses of zircons from ultramafic rocks or eclogite within ultramafic rocks that may not have experienced the same *P-T-t* history as the UHP rocks within the Sulu gneiss (e.g., 242 ± 8 Ma from zircons in dunite from Sulu; Zhao et al., this volume); several are concordia intercept ages with large uncertainties (e.g., 258 ± 25 Ma; Zheng et al., 2004b); several are lower intercept ages from very discordant data (e.g., the 228 ± 29 Ma date of Yang et al., 2003); and some are weighted mean ages with high mean square of weighted deviates (MSWD) values (e.g., 2.2 for a 208 ± 4 Ma age for a paragneiss from Liu et al., 2004b).

Based on the summary of the dating for both the Sulu and Hong'an–Dabie areas shown in Figure 9, and taking into account the problems described above, we suggest that UHP metamorphism took place at ca. 230 Ma in Sulu and at ca. 240 Ma in Hong'an–Dabie area, and that all younger dates represent retrograde metamorphism during exhumation.

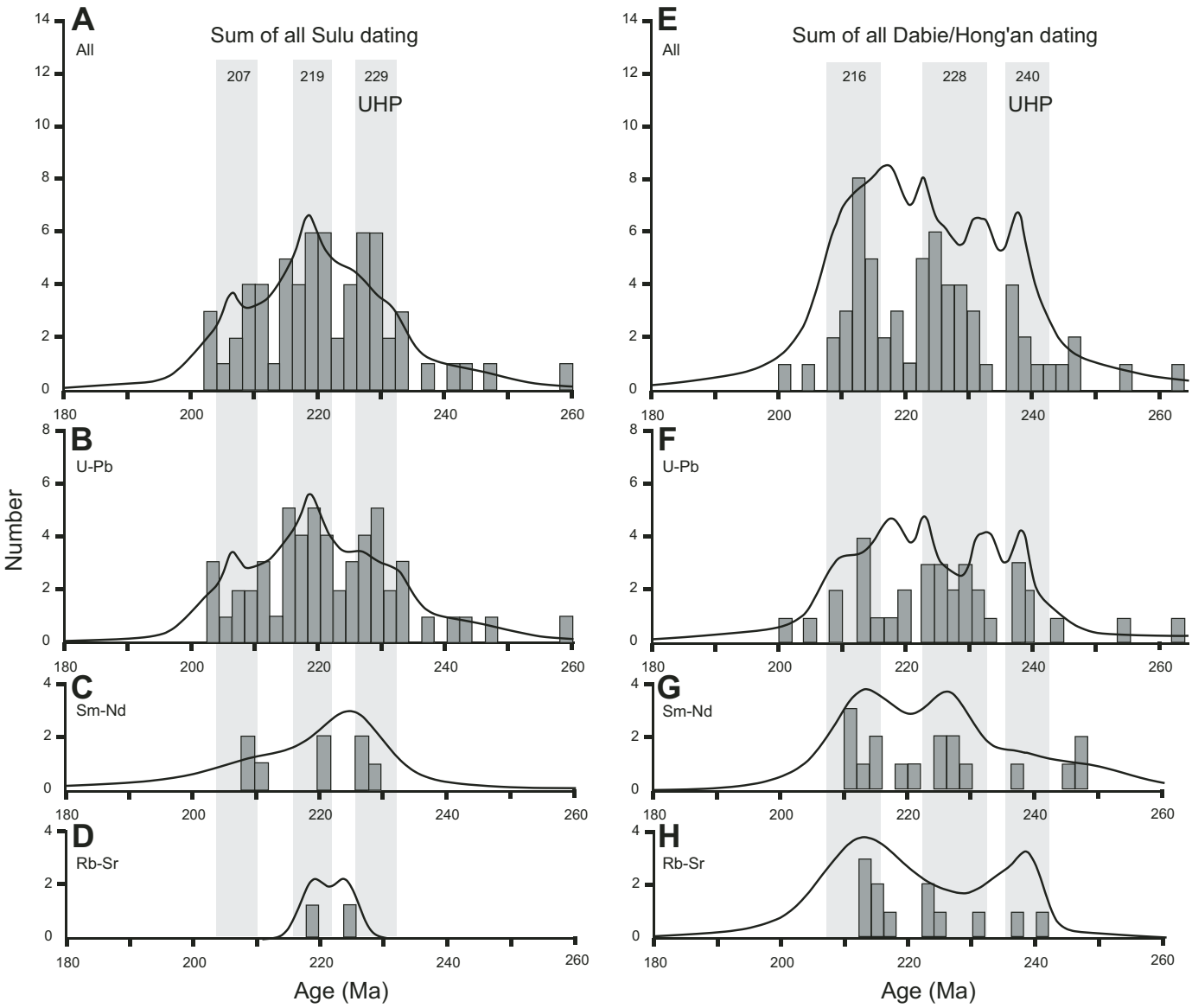

Figure 9. Histograms and probability density curves for all high-temperature thermochronometry for the Sulu and Dabie–Hong'an areas representing Triassic ultrahigh-pressure (UHP) to Early Jurassic retrograde metamorphism. A and E summarize all ages for Sulu and Dabie, respectively; B and F show only U-Pb ages (with a few Pb-Pb and Th-Pb dates); C and G show only Sm-Nd data; and D and H contain Rb-Sr data. Age groups from multiple chronometers marked with gray bands show that the Dabie–Hong'an area experienced UHP metamorphism at ca. 240 Ma, as much as 15 m.y. earlier than the Sulu area. Ages that have error estimates <±30 m.y. from all published high-temperature geochronology for the Hong'an, Dabie, and Sulu areas between 260 and 200 Ma are included (the likely age range for peak and retrograde metamorphism). Data include published weighted mean ages, lower intercept ages on concordia plots, and single-grain ages where the weighted mean ages or intercept ages were not available; weighted mean ages were calculated when possible for large numbers of published single-grain ages (e.g., Wallis et al., 2005) to avoid weighting single-grain ages too heavily. *Isoplot* was used to produce the histograms and probability density curves from the data presented in Appendices 2 and 3. Data for Sulu are from Li et al. (1993, 1999); Ames et al. (1996); Rumble et al. (2002); Zheng et al. (2002, 2004b); Yang et al. (2003); Liu et al. (2004a, 2004b); Wallis et al. (2005); Yang et al. (2005); Zhao et al. (2005); B.R. Hacker (2005, personal commun.); Zhao et al. (this volume); and this study. Data from the Dabie–Hong'an areas are from Ames et al. (1993, 1996); Li et al. (1993, 1999); Okay et al. (1993); Chavagnac and Jahn (1996); Bruguier et al. (1997); Rowley et al. (1997); Hacker et al. (1998, 2000); Maruyama et al. (1998) cit. in Hacker and Wang (1995); Ayers et al. (2002); Chen et al. (2003); Grimmer et al. (2003); Zheng et al. (2003, 2004b); Li et al. (2004); and Liu et al. (2004c).

REVISED MODEL FOR COLLISION, SUBDUCTION, AND UHP METAMORPHISM

There are significant implications for orogen-scale development if UHP metamorphism occurred in the Dabie–Hong'an area 10 m.y. before Sulu reached UHP conditions. Models like B.R. Hacker (2005, personal commun.) that assume uniform timing of UHP metamorphism in the Dabie and Sulu areas are potentially flawed in light of evidence from this study, which suggests that they may have had separate, though related, orogenic histories.

Traditionally, it has been assumed that reversing strike-slip motion along the Tan-Lu fault would restore Sulu to its original orogenic position adjacent to Dabie and that UHP metamorphism took place simultaneously east and west of the Tan-Lu fault. Assuming therefore that structures in both the Hong'an–Dabie and Sulu areas would be parallel if they had a common history, Webb et al. (2002) described a model whereby Sulu must have rotated ~25° counterclockwise during offset along the Tan-Lu fault. These simplified views contrast with more complex models: Hacker et al. (2000, 2004) described a detailed model for subduction and exhumation of the Dabie–Hong'an area based on paleomagnetic data, which suggest 60° of clockwise rotation during exhumation of a subducted wedge-shaped or Florida-like promontory. But this model did not account for differences in the timing of UHP metamorphism and exhumation in the Sulu area.

The tectonic evolution of the Dabie-Sulu belt is greatly simplified if we use a model that does not require contiguity between Sulu with Dabie and allows a 10 m.y. time difference for UHP metamorphism in Sulu and Dabie; both are more consistent with the rotational exhumation model of Hacker et al. (2000, 2004). Dabie–Hong'an and Sulu were certainly part of the same deeply subducted leading edge of the Yangtze craton, but perhaps they were not adjacent parts of the Yangtze craton (see Figure 5 in Hacker et al., 2004). The summary of the dating from the two areas shown in Figure 9 suggests that the Dabie area was the first to be subducted to UHP depths; this may have resulted from the irregular shape of either or both of the Sino-Korean or Yangtze cratons. In order to honor the rotational exhumation model suggested by paleomagnetic data, Dabie may have resided at UHP depths until ca. 230 Ma, when a crustal delamination/slab breakoff event (Leech, 2001; Leech et al., 2005) or a buoyancy-induced tear between oceanic and continental crust (Hacker et al., 2000, 2004) beginning in the east in Sulu triggered exhumation. Alternatively, rotational exhumation of Dabie–Hong'an began first, entirely separate from Sulu, and different exhumation processes for the two areas were not linked (i.e., Sulu did not participate in the clockwise rotational exhumation and was a separate UHP slab returned to the surface). Some of the ~25° of rotation required to restore structures in Sulu parallel to Dabie may not be due to rotation during translation along the Tan-Lu fault, but rather can be explained by a separate collision-exhumation history.

ACKNOWLEDGMENTS

We thank Joe Wooden, Frank Mazdab, Chris Mattinson, and Bob Jones for help with sample preparation, data analysis and reduction. This research is supported by a grant to J.G. Liou at Stanford University (National Science Foundation grant EAR-0003355). Many thanks are due to Bill McClelland, Brad Hacker, Trevor Ireland, Jeremy Hourigan, and one anonymous reviewer for helpful suggestions that improved an earlier version of this manuscript.

APPENDIX 1. U-Th-Pb DATA FOR ALL SHRIMP ANALYSES OF ZIRCON

Analysis spot	U (ppm)	Th (ppm)	Th/U	$^{204}Pb/^{206}Pb^{*}$	$^{206}Pb^{\dagger}$ (%)	$^{238}U/^{206}Pb^{*}$		$^{207}Pb/^{206}Pb^{*}$		$^{207}Pb/^{235}U^{\#}$		$^{206}Pb/^{238}U$ Age† (Ma)	
SU19-1	1898	15	0.01	0.0000	0.2	30.6735	1.7469	0.0511	1.0079	0.2282	2.0663	206.5	3.6
SU19-2	2460	22	0.01	0.0001	0.1	30.3359	1.7423	0.0508	0.8809	0.2261	2.1018	208.9	3.6
SU19-3	587	3	0.01	0.0001	0.4	30.3410	1.8384	0.0528	2.1187	0.2330	3.1582	208.3	3.8
SU19-4	1885	47	0.03	0.0000	0.2	29.5095	1.7472	0.0519	0.9584	0.2395	2.0869	214.3	3.7
SU19-5	2137	20	0.01	0.0001	0.1	29.7114	1.7461	0.0510	0.9457	0.2312	2.1537	213.2	3.7
SU19-6	2671	78	0.03	0.0000	0.3	27.7805	1.7385	0.0526	0.7900	0.2604	1.9299	227.3	3.9
SU19-7	467	393	0.87	0.0001	0.6	10.1257	1.7811	0.0643	1.0424	0.8636	2.1536	603.8	10.5
SU19-8	1872	20	0.01	0.0002	0.3	30.6140	1.7451	0.0526	0.9680	0.2260	2.4470	206.5	3.6
SU19-9	1861	24	0.01	0.0001	0.1	29.6783	1.7557	0.0512	0.9868	0.2336	2.1437	213.3	3.7
SU19-10	2153	21	0.01	0.0001	0.3	30.6956	1.7512	0.0520	1.0178	0.2275	2.3186	206.1	3.6
SU19-11	335	95	0.29	0.0001	0.6	12.1349	1.8084	0.0623	1.3455	0.6923	2.3567	507.3	9.0
SU19-12	180	127	0.73	0.0003	0.5	8.3492	1.8647	0.0674	1.4999	1.0304	3.5042	725.6	13.2
SU19-13	2156	20	0.01	0.0000	0.1	29.5558	1.7469	0.0511	0.9524	0.2347	2.0277	214.2	3.7
SU19-14	345	237	0.71	0.0000	0.6	9.9626	1.7980	0.0644	1.1980	0.8862	2.3322	613.3	10.8
SU19-15	601	336	0.58	0.0002	0.8	13.8890	1.7728	0.0622	1.2212	0.5843	2.7136	444.6	7.7
SU19-16	241	158	0.68	0.0001	0.4	10.3046	1.8321	0.0629	1.4749	0.8248	2.5429	594.6	10.6
SU19-17	124	83	0.69	0.0000	0.4	8.0100	1.9221	0.0670	1.9022	1.1415	2.7917	755.8	14.1
SU19-18	241	211	0.90	0.0001	0.5	9.1980	1.8392	0.0653	1.6477	0.9464	2.9336	662.1	11.9
SU19-19	392	266	0.70	0.0001	0.4	9.2606	1.7865	0.0645	1.0657	0.9438	2.1854	658.4	11.4
SU19-20	533	411	0.80	0.0000	0.1	7.9790	1.7764	0.0651	0.9250	1.1212	2.0202	760.3	13.1
SU19-21	104	119	1.18	0.0002	0.4	8.3599	1.9849	0.0664	2.3313	1.0508	3.6901	725.6	14.0
SU19-22	1871	680	0.38	0.0002	0.9	15.4351	1.7466	0.0618	0.6670	0.5255	2.1908	401.0	6.9
SU19-23	96	131	1.40	0.0000	0.3	8.1229	1.9694	0.0665	2.1051	1.1273	3.2234	746.0	14.3
SU19-24	285	182	0.66	0.0001	0.0	7.9127	1.8107	0.0641	1.1848	1.1018	2.2670	767.4	13.5
SU19-25	793	1335	1.74	0.0000	0.2	8.1420	1.7525	0.0652	0.7134	1.0988	1.8996	745.5	12.7
SU19-26	472	344	0.75	0.0001	0.3	8.3258	1.7884	0.0657	1.0586	1.0550	2.3334	729.1	12.7
SU19-27	317	201	0.66	0.0001	0.4	8.6553	1.7999	0.0659	1.2512	1.0119	2.5349	702.0	12.3
SU29-1	192	475	2.55	0.0000	0.3	7.9574	1.0348	0.0669	1.4183	1.1625	1.7608	760.7	7.7
SU29-2	79	131	1.71	0.0003	0.5	7.6702	1.3222	0.0690	2.1586	1.1594	3.1251	786.3	10.2
SU29-3	85	82	1.00	0.0002	1.3	9.1091	1.4564	0.0720	2.2929	1.0415	3.5682	663.1	9.5
SU29-4	271	238	0.91	0.0000	0.2	7.7728	0.9592	0.0662	1.1993	1.1762	1.5390	778.8	7.3
SU29-5	52	82	1.63	0.0002	0.6	7.7379	1.5354	0.0699	2.6912	1.1889	3.7664	778.8	11.7
SU29-6	34	42	1.28	–0.0001	0.7	8.1884	1.8617	0.0688	4.4423	1.1759	4.8471	738.2	13.6
SU29-7	61	99	1.67	0.0006	1.2	7.9744	1.4567	0.0739	2.4241	1.1194	5.8958	752.8	10.8
SU29-8	34	44	1.33	0.0005	0.4	7.9100	1.7938	0.0675	3.3885	1.0292	7.5977	764.5	13.5
SU29-9	1415	2050	1.50	0.0001	0.6	9.8775	0.8051	0.0648	0.5919	0.8892	1.1007	618.1	4.9
SU29-10	58	88	1.57	0.0000	0.1	7.7614	1.4669	0.0653	2.6126	1.1601	2.9947	780.8	11.2
SU29-11	76	107	1.46	–0.0001	0.7	8.0239	1.3188	0.0692	3.4033	1.2178	3.5886	752.5	9.9
SU29-12	122	121	1.03	0.0009	1.5	9.3908	1.2302	0.0730	2.1728	0.8654	7.1115	643.0	7.9
SU29-13	225	207	0.95	0.0001	0.3	7.7250	1.0102	0.0675	1.2984	1.1735	1.7369	782.3	7.7
SU29-14	174	222	1.32	0.0000	0.5	7.8299	1.0625	0.0685	1.5027	1.2195	1.8323	771.2	8.0
SU29-15	142	138	1.01	0.0002	0.3	7.7478	1.1123	0.0672	1.6485	1.1364	2.8222	780.4	8.5
SU29-16	33	21	0.66	0.0015	2.4	8.4680	1.9098	0.0821	3.3147	0.9533	13.6165	703.2	13.4
SU32-1	55	44	0.83	0.0002	1.1	13.7353	1.6217	0.0641	3.5605	0.6177	4.4902	448.4	7.3
SU32-2	65	57	0.91	0.0001	0.9	8.5516	1.3864	0.0701	2.7590	1.1171	3.1589	706.7	9.7
SU32-3	59	39	0.69	0.0002	1.0	11.4911	1.5387	0.0658	3.1408	0.7580	3.7360	532.8	8.1
SU32-4	55	82	1.55	0.0001	0.7	8.8687	1.5481	0.0676	3.5438	1.0176	4.1282	684.2	10.5
SU32-5	108	60	0.57	0.0013	2.6	16.5861	1.2486	0.0745	2.4257	0.4485	11.0030	367.9	4.7
SU32-6	283	6	0.02	0.0002	0.5	38.7042	1.2058	0.0526	3.1989	0.1779	4.2483	163.7	2.0

(continued)

APPENDIX 1. U-Th-Pb DATA FOR ALL SHRIMP ANALYSES OF ZIRCON *(continued)*

Analysis spot	U (ppm)	Th (ppm)	Th/U	$^{204}Pb/^{206}Pb^{*}$	$^{206}Pb^{\dagger}$ (%)	$^{238}U/^{206}Pb^{*}$		$^{207}Pb/^{206}Pb^{*}$		$^{207}Pb/^{235}U^{\#}$		$^{206}Pb/^{238}U$ Age† (Ma)	
SU32-7	91	102	1.15	0.0002	0.2	7.9823	1.2150	0.0661	1.9054	1.0971	2.5113	759.1	9.0
SU32-8	28	21	0.79	0.0013	2.3	11.9807	1.8616	0.0759	5.0588	0.6393	12.6867	505.2	9.6
SU32-9	17	13	0.80	–0.0005	0.2	8.0738	2.2241	0.0657	4.5446	1.2488	4.8177	751.1	16.4
SU32-10	375	5	0.01	0.0001	0.0	33.5185	0.9925	0.0494	2.1737	0.1994	2.4749	189.5	1.9
SU32-11	484	16	0.03	0.0001	1.0	19.4926	0.8984	0.0600	1.3216	0.4150	1.8145	319.5	2.9
SU32-12	867	314	0.37	0.0001	0.6	10.5356	0.8256	0.0638	0.8952	0.8194	1.5299	581.2	4.7
SU32-13	67	71	1.10	–0.0001	0.2	7.9266	1.3067	0.0659	2.1967	1.1782	2.5277	764.4	9.8
SU32-14	431	27	0.06	0.0005	0.4	23.4001	0.9477	0.0545	1.7145	0.2799	5.1917	268.7	2.5
SU32-15	437	17	0.04	0.0003	0.7	20.8003	0.9490	0.0579	1.6091	0.3485	3.5527	300.5	2.8
SU32-16	1078	992	0.95	0.0002	0.8	9.4441	0.8077	0.0670	0.6001	0.9265	1.4495	644.1	5.1
SU32-17	428	8	0.02	0.0006	0.5	30.5808	1.1790	0.0536	2.8053	0.2008	9.0147	206.5	2.4
SU32-18	301	213	0.73	0.0000	0.5	10.5877	0.9469	0.0627	1.3719	0.8247	31.8449	579.2	5.4
SU32-19	116	34	0.30	0.0014	3.3	28.2986	1.6846	0.0762	5.4794	0.2619	19.2006	216.7	3.9
SU32-20	324	13	0.04	0.0002	0.4	29.3074	1.0377	0.0531	2.2773	0.2387	2.8531	215.5	2.2
SU32-21	64	52	0.83	0.0023	3.6	15.9276	1.6211	0.0826	2.9260	0.4003	29.1435	378.9	6.4
SU32-22	488	7	0.01	0.0003	0.3	28.4342	1.2765	0.0525	3.2036	0.2352	6.7931	222.2	2.8
SU32-24	60	49	0.85	0.0000	0.6	8.6519	1.3299	0.0672	2.2918	1.0713	2.6499	701.1	9.2
SU32-25	159	67	0.44	0.0002	1.0	15.2005	1.0803	0.0629	1.9786	0.5366	3.3422	406.6	4.4
SU32-26	35	26	0.77	–0.0009	1.7	12.4316	1.7073	0.0704	3.5655	0.9380	9.3153	490.6	8.4
SU32-27	73	22	0.32	0.0004	1.3	11.1336	1.3126	0.0686	2.4665	0.7695	4.2075	547.6	7.2
SU32-28	284	78	0.28	0.0002	1.3	11.2416	0.9337	0.0684	1.1871	0.7983	2.3174	542.6	5.0
SU32-29	221	3	0.01	0.0018	2.1	38.3570	1.7368	0.0658	4.8652	0.1360	28.0786	162.4	2.9
SU32-30	869	55	0.06	0.0000	0.7	11.9410	0.8684	0.0628	0.9124	0.7169	1.3920	515.0	4.4
SU32-31	129	1	0.01	0.0006	1.5	36.5541	1.4229	0.0613	5.6690	0.1951	7.8256	171.4	2.6
SU32-32	455	7	0.02	0.0002	0.5	27.1594	0.9553	0.0544	1.8810	0.2625	3.5521	231.9	2.2
SU32-33	414	5	0.01	0.0003	0.4	30.1851	1.0351	0.0535	2.1987	0.2248	5.1057	209.2	2.2
SU33-1	1097	42	0.04	0.0005	0.6	46.0014	1.7861	0.0532	1.7686	0.1372	5.0837	137.8	2.5
SU33-2	1506	81	0.06	0.0001	0.1	43.3190	1.7664	0.0498	1.4061	0.1550	2.4065	146.9	2.6
SU33-3	3383	288	0.09	0.0000	0.0	42.5381	1.7400	0.0488	0.9143	0.1575	1.9775	149.8	2.6
SU33-4	2460	167	0.07	0.0000	0.1	42.2755	1.7473	0.0492	1.0679	0.1589	2.0995	150.6	2.6
SU33-5	15	1	0.06	0.0200	25.9	33.7215	4.4753	0.2545	7.4224	N/A	N/A	140.1	9.8
SU33-6	3736	261	0.07	0.0002	0.3	41.0529	1.7381	0.0511	1.3694	0.1636	2.5904	154.7	2.7
SU33-7	1442	56	0.04	0.0001	0.1	42.7582	1.7701	0.0493	1.4467	0.1545	2.5282	148.9	2.6
SU33-8	3148	256	0.08	0.0000	0.2	42.5688	1.7421	0.0501	0.9463	0.1605	2.0697	149.4	2.6
SU33-9	5	0	0.00	0.0313	19.9	44.3753	7.0797	0.2059	23.2853	N/A	N/A	115.3	12.4
SU33-10	692	20	0.03	0.0000	0.4	44.7452	1.8176	0.0519	2.0012	0.1599	2.7031	141.9	2.6
SU33-11	226	0	0.00	0.0003	0.6	45.7001	1.9959	0.0533	3.3664	0.1479	5.7895	138.7	2.8
SU33-12	35	27	0.80	0.0002	0.4	8.4564	2.3971	0.0659	3.4622	1.0162	4.9377	717.9	16.8
SU33-13	3136	218	0.07	0.0000	0.1	42.4252	1.7422	0.0494	0.9621	0.1593	2.1065	150.0	2.6
SU33-14	247	0	0.00	0.0003	0.6	44.4930	1.9899	0.0536	3.3171	0.1533	5.6095	142.4	2.8
SU33-15	35	0	0.01	0.0087	6.8	39.7503	3.2795	0.1026	11.2161	N/A	N/A	149.4	5.5
SU33-16	1909	87	0.05	0.0000	0.1	42.9270	1.7562	0.0496	1.2079	0.1573	2.1637	148.3	2.6
SU33-17	81	74	0.94	–0.0001	1.0	11.3090	2.1816	0.0656	2.7010	0.8145	3.4424	541.2	11.6
SU33-18	54	0	0.00	0.0024	1.5	45.5307	2.8384	0.0608	7.1638	0.0683	74.8228	137.9	4.0
SU33-19	143	247	1.78	0.0001	0.5	8.0722	1.8849	0.0676	1.6278	1.1182	2.7048	749.6	13.7
SU33-20	89	124	1.44	0.0008	2.1	9.2895	2.1001	0.0782	2.1392	0.9745	5.5329	645.7	13.4
SU33-21	2564	145	0.06	0.0000	0.2	42.7889	1.7472	0.0499	1.0405	0.1604	2.0494	148.7	2.6
SU45-1	1938	492	0.26	0.0002	0.5	29.3958	0.3141	0.0542	1.0063	0.2374	2.1336	214.7	0.7
SU45-2	3411	264	0.08	0.0041	6.4	24.4791	0.3403	0.1021	1.3962	0.2104	24.3976	242.0	2.2

(continued)

APPENDIX 1. U-Th-Pb DATA FOR ALL SHRIMP ANALYSES OF ZIRCON *(continued)*

Analysis spot	U (ppm)	Th (ppm)	Th/U	$^{204}Pb/^{206}Pb^{*}$	$^{206}Pb^{\dagger}$ (%)	$^{238}U/^{206}Pb^{*}$		$^{207}Pb/^{206}Pb^{*}$		$^{207}Pb/^{235}U^{\#}$		$^{206}Pb/^{238}U$ Age† (Ma)	
SU45-3	3985	290	0.08	0.0000	0.0	28.1146	0.2214	0.0507	0.6822	0.2471	0.8139	225.3	0.5
SU45-4	4083	112	0.03	0.0001	0.2	28.7107	0.2194	0.0523	0.6874	0.2441	1.0380	220.2	0.5
SU45-5	129	84	0.67	0.0023	3.7	25.8993	1.1830	0.0808	3.0923	0.2404	22.5308	235.2	3.1
SU45-6	4809	116	0.02	0.0000	0.1	29.2980	0.1992	0.0509	0.6322	0.2373	0.7670	216.2	0.4
SU45-7	999	642	0.66	0.0000	0.0	29.6796	0.4336	0.0505	1.4089	0.2316	1.6216	213.6	0.9
SU45-8	4117	90	0.02	0.0000	0.1	28.5615	0.2152	0.0511	0.6885	0.2441	0.8147	221.7	0.5
SU45-9	606	362	0.62	0.0000	0.0	29.1516	0.5580	0.0505	1.7997	0.2397	1.8778	217.4	1.2
SU45-10	2688	134	0.05	0.0002	0.4	29.2797	0.2691	0.0538	1.3731	0.2417	2.0753	215.6	0.6
SU45-11	1267	969	0.79	0.0001	0.1	29.5724	0.3852	0.0515	1.2452	0.2321	1.9062	214.1	0.8
SU45-12	3682	60	0.02	0.0000	0.1	29.3036	0.2251	0.0515	0.7279	0.2389	0.8483	216.0	0.5
SU45-13	92	45	0.50	0.0003	0.5	29.1417	1.6212	0.0548	4.5003	0.2379	6.2502	216.3	3.5
SU45-14	197	99	0.52	0.0059	11.7	27.3632	0.9516	0.1437	1.9052	0.2576	33.8395	204.7	4.0
SU45-15	1004	148	0.15	0.0000	0.4	3.1232	0.2829	0.1124	0.5904	4.9646	0.6546	1784.7	5.2
SU45-16	246	145	0.61	–0.0001	0.2	30.5844	0.8592	0.0519	2.7879	0.2381	2.8786	207.0	1.8
SU45-17	150	106	0.73	0.0002	0.4	29.3429	1.1051	0.0537	3.4904	0.2391	4.3890	215.2	2.4
SU45-18	372	230	0.64	0.0001	0.3	29.5458	0.7028	0.0527	2.2698	0.2391	2.5060	214.0	1.5
SU45-19	99	1	0.01	0.0001	0.2	27.5429	1.3629	0.0526	4.2326	0.2535	5.2180	229.4	3.2
SU45-20	351	193	0.57	–0.0002	0.0	29.4515	0.7414	0.0505	2.6482	0.2482	3.5235	215.2	1.6
SU45-21	105	57	0.57	0.0004	0.6	28.7652	1.3487	0.0554	7.7548	0.2381	9.0780	219.0	3.2
SU45-22	370	274	0.77	–0.0001	0.1	28.9095	0.7229	0.0512	2.3122	0.2546	2.3910	219.0	1.6
SU45-23	188	111	0.61	–0.0001	–0.2	29.6738	1.0206	0.0484	2.9539	0.2317	3.0507	214.2	2.2
SU45-24	208	107	0.53	0.0003	0.4	31.7412	1.0520	0.0531	2.9758	0.2077	6.3035	199.2	2.1
SU45-25	343	162	0.49	0.0001	0.2	29.9469	0.8597	0.0516	2.2263	0.2285	2.6617	211.4	1.8
SU45-26	328	163	0.52	0.0000	–0.2	29.5244	0.8498	0.0489	2.2362	0.2316	2.5184	215.1	1.8
SU45-27	1465	455	0.32	0.0036	6.5	28.4295	0.6105	0.1022	1.8652	0.2253	10.4938	208.6	1.6
SU45-28	1339	1192	0.92	0.0000	0.0	28.8101	0.6171	0.0507	1.0554	0.2457	1.3244	219.9	1.3
SU45-29	1027	587	0.59	0.0018	3.4	31.0524	0.6438	0.0770	2.7107	0.2190	10.6003	197.5	1.4
SU45-30	137	79	0.59	0.0008	–0.2	28.8704	1.1424	0.0486	3.3954	0.1747	12.9462	220.0	2.5
SU45-31	625	731	1.21	0.0000	0.1	29.5753	0.7081	0.0508	1.5604	0.2386	1.7556	214.3	1.5
SU45-32	253	142	0.58	–0.0003	0.0	30.1747	0.9268	0.0501	2.5394	0.2481	4.4630	210.2	2.0
SU45-33	349	194	0.57	–0.0001	0.2	29.4484	0.8328	0.0518	2.0986	0.2497	2.2091	214.9	1.8
SU45-34	178	109	0.64	–0.0003	0.0	29.6160	1.0515	0.0500	3.0456	0.2515	3.0429	214.2	2.3
SU45-35	274	264	1.00	0.0023	3.1	29.9381	0.9288	0.0746	4.2793	0.1759	19.2427	205.4	2.1
SU45-36	220	192	0.90	0.0002	0.0	29.6579	0.9518	0.0503	2.6522	0.2161	3.7292	213.8	2.0
SU45-37	115	64	0.57	–0.0002	0.2	28.8775	1.2498	0.0519	3.6830	0.2607	5.2219	219.1	2.8
SU45-38	2026	71	0.04	0.0006	1.1	28.6915	0.6094	0.0589	1.4408	0.2374	4.8091	218.6	1.3
SU45-39	374	193	0.53	0.0001	0.2	29.7667	0.8253	0.0516	2.0542	0.2325	2.3163	212.7	1.8
SU45-40	247	186	0.78	0.0002	0.1	30.0089	0.9442	0.0515	2.5975	0.2241	3.2198	211.0	2.0
SU45-41	107	41	0.39	0.0000	0.3	29.7491	1.2938	0.0532	3.8129	0.2464	4.0264	212.4	2.8
SU45-42	186	104	0.58	0.0001	–0.1	29.7065	1.0256	0.0499	2.9138	0.2245	3.7188	213.6	2.2
SU45-43	1132	60	0.05	0.0001	0.3	28.9065	0.6598	0.0528	1.2801	0.2479	1.8985	218.6	1.4
SU45-44	31	11	0.37	0.0624	91.5	40.8379	2.4156	0.7695	2.8710	N/A	N/A	13.4	10.1
SU45-45	347	194	0.58	0.0000	0.0	29.3477	0.8522	0.0505	2.1898	0.2372	2.3498	216.0	1.8
SU45-46	443	223	0.52	0.0001	0.1	28.9805	0.7901	0.0510	1.9097	0.2334	3.2635	218.6	1.7

Note: 1σ error unless noted otherwise.
*Uncorrected; error given as percentage.
†Corrected for ^{207}Pb.
#Corrected for ^{204}Pb; error given as percentage.

APPENDIX 2. SUMMARY OF ALL HIGH-TEMPERATURE GEOCHRONOMETRY FOR THE SULU AREA

Age (Ma)	Error (±Ma)	Dating method	Type of age	# of analyses	MSWD	Rock type	Reference
U-Pb							
217	9	U-Pb	Intercept	6	N/A	Eclogite	Ames et al., 1996
202	13	U-Pb	Intercept	N/A	N/A	Unknown	Li et al., 1999
223	2	U-Pb IMP	Single-grain	1	N/A	Gneiss	Rumble et al., 2002
220	1	U-Pb IMP	Weighted mean	2	0.6	Garnet peridotite	Rumble et al., 2002
233	2	U-Pb IMP	Single-grain	1	N/A	Garnet peridotite	Rumble et al., 2002
221	12	U-Pb IMP	Probability curve	9	47	Peridotite	Yang et al., 2003
228	29	U-Pb IMP	Intercept	24	1.3	Eclogite	Yang et al., 2003
231	4	U-Pb IMP	Weighted mean	16	1.8	Gneiss	Liu et al., 2004b
208	4	U-Pb IMP	Weighted mean	6	2.2	Gneiss	Liu et al., 2004b
213	5	U-Pb IMP	Weighted mean	6	1.7	Gneiss	Liu et al., 2004b
228	5	U-Pb IMP	Weighted mean	14	1.1	Gneiss	Liu et al., 2004b
247	5	U-Pb IMP	Single-grain	1	N/A	Eclogite	Zheng et al., 2004b
219	8	U-Pb IMP	Single-grain	1	N/A	Eclogite	Zheng et al., 2004b
241	5	U-Pb IMP	Single-grain	1	N/A	Eclogite	Zheng et al., 2004b
217	3	U-Pb IMP	Single-grain	1	N/A	Eclogite	Zheng et al., 2004b
215	6	U-Pb IMP	Single-grain	1	N/A	Eclogite	Zheng et al., 2004b
231	7	U-Pb IMP	Single-grain	1	N/A	Eclogite	Zheng et al., 2004b
229	7	U-Pb IMP	Single-grain	1	N/A	Eclogite	Zheng et al., 2004b
226	7	U-Pb IMP	Single-grain	1	N/A	Eclogite	Zheng et al., 2004b
227	3	U-Pb IMP	Single-grain	1	N/A	Granitic gneiss	Zheng et al., 2004b
258	25	U-Pb IMP	Single-grain	1	N.A	Eclogite	Zheng et al., 2004b
224	14	U-Pb	Intercept	5	4.0	Granitic gneiss	Zheng et al., 2004b
218	16	U-Pb	Intercept	5	6.5	Granitic gneiss	Zheng et al., 2004b
224	27	U-Pb	Intercept	6	7.9	Granitic gneiss	Zheng et al., 2004b
207	1	U-Pb IMP	Weighted mean[#]	11	0.8	Dike	Wallis et al., 2005
222	2	U-Pb IMP	Weighted mean[#]	14	1.3	Dike	Wallis et al., 2005
215	5	U-Pb IMP	Weighted mean	13	N/A	Quartz syenite	Yang et al., 2005
237	8	U-Pb IMP	Weighted mean	30	N/A	Eclogite	Zhao et al., 2005
217	4	U-Pb*	Weighted mean	9	0.4	Granitic gneiss	B.R. Hacker, 2005, pers. comm.
228	2	U-Pb*	Weighted mean	14	0.6	Granitic gneiss	B.R. Hacker, 2005, pers. comm.
224	5	U-Pb*	Weighted mean	3	0.1	Augen gneiss	B.R. Hacker, 2005, pers. comm.
216	2	U-Pb*	Weighted mean	5	0.2	Granitic gneiss	B.R. Hacker, 2005, pers. comm.
202	3	U-Pb*	Weighted mean	6	0.2	Granitic gneiss	B.R. Hacker, 2005, pers. comm.
226	5	U-Pb*	Weighted mean	2	2.3	Granitic gneiss	B.R. Hacker, 2005, pers. comm.
205	3	U-Pb*	Weighted mean	6	N/A	Granitic gneiss	B.R. Hacker, 2005, pers. comm.
219	2	U-Pb*	Weighted mean	7	0.7	Granitic gneiss	B.R. Hacker, 2005, pers. comm.
220	2	U-Pb*	Weighted mean	N/A	0.8	Granitic gneiss	B.R. Hacker, 2005, pers. comm.
226	2	U-Pb*	Weighted mean	N/A	0.6	Granitic gneiss	B.R. Hacker, 2005, pers. comm.
203	3	U-Pb*	Weighted mean	7	N/A	Granitic gneiss	B.R. Hacker, 2005, pers. comm.

(continued)

APPENDIX 2. SUMMARY OF ALL HIGH-TEMPERATURE GEOCHRONOMETRY FOR THE SULU AREA *(continued)*

Age (Ma)	Error (±Ma)	Dating method	Type of age	# of analyses	MSWD	Rock type	Reference
U-Pb							
218	2	U-Pb*	Weighted mean	8	0.0	Granitic gneiss	B.R. Hacker, 2005, pers. comm.
210	8	U-Pb*	Intercept	N/A	1.1	Granitic gneiss	B.R. Hacker, 2005, pers. comm.
210	5	U-Pb IMP	Weighted mean	12	1.7	Granitic gneiss	Liu et al., 2004a
228	5	U-Pb IMP	Weighted mean	17	1.8	Granitic gneiss	Liu et al., 2004a
242	8	U-Pb IMP	Single-grain	1	N/A	Dunite	Zhao et al., this volume.
232	7	U-Pb IMP	Single-grain	1	N/A	Eclogite	Zhao et al., this volume
208	3	U-Pb IMP	Weighted mean	2	0.7	Granitic gneiss	This paper
222	3	U-Pb IMP	Single-grain	1	N/A	Granitic gneiss	This paper
215	2	U-Pb IMP	Single-grain	1	N/A	Granitic gneiss	This paper
232	2	U-Pb IMP	Single-grain	1	N/A	Granitic gneiss	This paper
207	3	U-Pb IMP	Weighted mean	5	0.1	Granitic gneiss	This paper
211	2	U-Pb IMP	Weighted mean	3	0.1	Granitic gneiss	This paper
214	4	U-Pb IMP	Weighted mean	4	0.0	Granitic gneiss	This paper
215	6	U-Pb IMP	Weighted mean	18	0.5	Granitic gneiss	This paper
219	1	U-Pb IMP	Weighted mean	8	0.1	Granitic gneiss	This paper
Sm-Nd							
221	6	Sm-Nd	Isochron - min	2	N/A	Eclogite	Li et al., 1993
209	31	Sm-Nd	Isochron - min	4	N/A	Eclogite	Li et al., 1993
228	6	Sm-Nd	Isochron	N/A	N/A	Unknown	Li et al., 1999
226	4	Sm-Nd	Isochron - min/WR	4	0.9	Eclogite	Li et al., 1999
226	5	Sm-Nd	Isochron - min/WR	4	N/A	Eclogite	Zheng et al., 2002
221	18	Sm-Nd	Isochron - min	2	N/A	Eclogite	Zheng et al., 2002
211	6	Sm-Nd	Isochron - min	2	N/A	Eclogite	Zheng et al., 2002
208	15	Sm-Nd	Isochron - min	2	N/A	Eclogite	Zheng et al., 2002
Rb-Sr							
219	2	Rb-Sr	Isochron - min/WR	3	N/A	Eclogite	Li et al., 1999
224	2	Rb-Sr	Isochron - min/WR	3	N/A	Eclogite	Li et al., 1999

Note: Notation for type of ages: Intercept, lower intercept age on concordia diagram; probability curve, peak on cumulative probability curve; weighted mean, weighted mean age of multiple analyses; single-grain, either age from a single grain or single spot age from ion microprobe analysis; isochron, isochron age for either Sm-Nd or Rb-Sr dating (min, mineral; WR, whole-rock). IMP, ion microprobe analysis; U-Pb, may be age from various methods, including ICP-MS, conventional isotope dilution, etc. N/A, not available in original publication or not applicable. When omitted from original publications and possible from data presented, MSWD was calculated from original data; the number of analyses were calculated or estimated from original data when not explicitly stated in original publications. Errors reported are 1σ. MSWD, mean square of weighted deviates.

*Combination of ion microprobe and ICP-MS U-Pb analyses.

#Weighted mean age calculated for individual analyses reported in Wallis et al. (2005).

APPENDIX 3. SUMMARY OF ALL HIGH-TEMPERATURE GEOCHRONOMETRY FOR THE DABIE–HONG'AN AREA

Age (Ma)	Error (±Ma)	Dating method	Type of age	# of analyses	MSWD	Rock type	Reference
U-Pb/Pb-Pb/Pb-Th							
209	2	U-Pb	Intercept	3	N/A	Eclogite	Ames et al., 1993
212	11	U-Pb	Intercept	4	N/A	Eclogite	Ames et al., 1993
218	2	U-Pb	Intercept	3	N/A	Eclogite	Ames et al., 1996
218	2	U-Pb	Intercept	3	N/A	Eclogite	Ames et al., 1996
214	10	U-Pb	Intercept	3	N/A	Eclogite	Ames et al., 1996
227	22	U-Pb	Intercept	4	N/A	Gneiss	Ames et al., 1996
233	1	U-Pb	Single-grain	N/A	N/A	Sandstone	Bruguier et al., 1997
231	1	U-Pb	Single-grain	N/A	N/A	Sandstone	Bruguier et al., 1997
225	4	U-Pb	Intercept	6	N/A	Eclogite	Rowley et al., 1997
218	2	U-Pb	Intercept	15	N/A	Gneiss	Rowley et al., 1997
225	4	U-Pb IMP	Probability curve	8	N/A	Gneiss	Hacker et al., 1998
236	3	U-Pb IMP	Probability curve	12	N/A	Gneiss	Hacker et al., 1998
224	9	U-Pb	Unknown	N/A	N/A	Unknown	Maruyama et al., 1998, cit. in Hacker and Wang, 1995
236	2	U-Pb	Single-grain	N/A	N/A	Unknown	Li et al., 1999
238	1	U-Pb	Single-grain	N/A	N/A	Unknown	Li et al., 1999
215	5	U-Pb IMP	Weighted mean	8	N/A	Granitic gneiss	Hacker et al., 2000
230	3	U-Pb IMP	Weighted mean	26	0.7	Eclogite	Ayers et al., 2002
236	32	U-Pb IMP	Intercept	11	7.0	Quartzite	Ayers et al., 2002
238	3	U-Pb IMP	Weighted mean	6	0.7	Quartzite	Ayers et al., 2002
223	1	Pb-Th IMP	Intercept	6	N/A	Quartzite	Ayers et al., 2002
209	4	Pb-Th IMP	Isochron	25	0.7	Clinopyroxenite	Ayers et al., 2002
213	3	U-Pb	Intercept	N/A	2.7	Quartzite	Chen et al., 2003
205	12	U-Pb	Intercept	N/A	1.1	Granitic gneiss	Chen et al., 2003
217	4	Pb-Pb	Single-grain	N/A	N/A	Sandstone	Grimmer et al., 2003
226	10	Pb-Pb	Single-grain	N/A	N/A	Sandstone	Grimmer et al., 2003
228	12	U-Pb	Intercept	4	N/A	Granitic gneiss	Zheng et al., 2003
226	8	U-Pb	Intercept	6	N/A	Granitic gneiss	Zheng et al., 2003
222	4	U-Pb IMP	Weighted mean	3	0.1	Eclogite	Li et al., 2004
242	3	U-Pb IMP	Weighted mean	8	2.1	Eclogite	Li et al., 2004
254	30	U-Pb IMP	Intercept	7	2.9	Eclogite	Li et al., 2004
229	12	U-Pb IMP	Weighted mean	8	N/A	Eclogite	Liu et al., 2004c
213	5	U-Pb IMP	Weighted mean	13	N/A	Eclogite	Liu et al., 2004c
229	22	U-Pb IMP	Intercept	5	0.7	Granitic gneiss	Liu et al., 2004c
213	4	U-Pb*	Intercept	5	1.1	Gneiss	Zheng et al., 2004b
222	6	U-Pb*	Intercept	5	0.4	Granitic gneiss	Zheng et al., 2004b
201	14	U-Pb*	Intercept	5	2.9	Granitic gneiss	Zheng et al., 2004b
262	28	U-Pb*	Intercept	5	7.4	Granitic gneiss	Zheng et al., 2004b

(continued)

APPENDIX 3. SUMMARY OF ALL HIGH-TEMPERATURE GEOCHRONOMETRY FOR THE DABIE–HONG'AN AREA *(continued)*

Age (Ma)	Error (±Ma)	Dating method	Type of age	# of analyses	MSWD	Rock type	Reference
Sm-Nd							
229	3	Sm-Nd	Isochron - min/WR	4	N/A	Grt-Bt gneiss	Li et al., 1993
244	11	Sm-Nd	Isochron - min/WR	3	N/A	Eclogite	Li et al., 1993
224	20	Sm-Nd	Isochron - min	3	N/A	Eclogite	Li et al., 1993
221	5	Sm-Nd	Isochron - min	4	N/A	Eclogite	Li et al., 1993
246	8	Sm-Nd	Isochron - min/WR	2	N/A	Eclogite	Okay et al., 1993
246	8	Sm-Nd	Isochron	N/A	N/A	Unknown	Li et al., 1999
226	3	Sm-Nd	Isochron - min/WR	4	0.3	Eclogite	Li et al., 1999
226	3	Sm-Nd	Isochron - min/WR	6	0.1	Gneiss	Li et al., 1999
210	9	Sm-Nd	Isochron - min/WR	3	0.3	Eclogite	Chavagnac and Jahn, 1996
214	7	Sm-Nd	Isochron - min/WR	3	0.4	Eclogite	Chavagnac and Jahn, 1996
211	4	Sm-Nd	Isochron - min/WR	3	0.6	Eclogite	Chavagnac and Jahn, 1996
213	3	Sm-Nd	Isochron - min/WR	2	N/A	Eclogite	Chavagnac and Jahn, 1996
215	5	Sm-Nd	Isochron - min/WR	3	0.5	Eclogite	Chavagnac and Jahn, 1996
218	4	Sm-Nd	Isochron - min	2	N/A	Eclogite	Chavagnac and Jahn, 1996
210	7	Sm-Nd	Isochron - min/WR	3	0.0	Peridotite	Chavagnac and Jahn, 1996
225	7	Sm-Nd	Isochron - min	7	0.7	Garnets	Chavagnac and Jahn, 1996
236	4	Sm-Nd	Isochron - min	4	1.4	Eclogite	Li et al., 2004
Rb-Sr							
240	2	Rb-Sr	Isochron - min/WR	2	N/A	Eclogite	Okay et al., 1993
236	3	Rb-Sr	Isochron - min/WR	2	N/A	Eclogite	Okay et al., 1993
212	5	Rb-Sr	Isochron - min/WR	2	N/A	Eclogite	Chavagnac and Jahn, 1996
223	13	Rb-Sr	Isochron - min/WR	3	7.4	Eclogite	Chavagnac and Jahn, 1996
214	6	Rb-Sr	Isochron - min/WR	3	2.0	Eclogite	Chavagnac and Jahn, 1996
212	19	Rb-Sr	Isochron - min	4	2.5	Phengites	Chavagnac and Jahn, 1996
214	6	Rb-Sr	Isochron - min/WR	4	N/A	Eclogite	Li et al., 1999
223	13	Rb-Sr	Isochron - min/WR	3	N/A	Eclogite	Li et al., 1999
230	7	Rb-Sr	Isochron - min	3	1.9	Eclogite	Li et al., 2004
225	34	Rb-Sr	Isochron - min/WR	3	24	Eclogite	Liu et al., 2004
212	7	Rb-Sr	Isochron - min/WR	5	16	Eclogite	Liu et al., 2004
216	10	Rb-Sr	Isochron - min/WR	4	27	Blueschist	Liu et al., 2004

Note: Notation for type of ages: Intercept, lower or upper intercept age on concordia diagram; Probability curve, peak on probability density curve; Weighted mean, weighted mean age of multiple analyses; Single-grain, either age from a single grain or single spot age from ion microprobe analysis; Isochron, isochron age for either Sm-Nd or Rb-Sr dating (min, mineral; WR, whole-rock). IMP, ion microprobe analysis; U-Pb, may be age from various methods including ICP-MS, conventional isotope dilution, etc. N/A, not available in original publication or not applicable. When omitted from original publications and when possible from data presented, MSWD was calculated from original data; the number of analyses were calculated or estimated from original data when not explicitly stated in original publications. Errors reported are 1σ. MSWD, mean square of weighted deviates.

*Combination of ion microprobe and ICP-MS U-Pb analyses.

#Weighted mean age calculated for individual analyses reported in Wallis et al. (2005).

REFERENCES CITED

Ames, L., Tilton, G.R., and Zhou, G., 1993, Timing of collision of the Sino-Korean and Yangtse cratons: U-Pb zircon dating of coesite-bearing eclogites: Geology, v. 21, p. 339–342, doi: 10.1130/0091-7613(1993)021<0339:TOCOTS>2.3.CO;2.

Ames, L., Zhou, G., and Xiong, B., 1996, Geochronology and isotopic character of ultrahigh-pressure metamorphism with implications for collision of the Sino-Korean and Yangtze cratons, central China: Tectonics, v. 15, p. 472–489, doi: 10.1029/95TC02552.

Ayers, J.C., Dunkle, S., Gao, S., and Miller, C., 2002, Constraints on timing of peak and retrograde metamorphism in the Dabie Shan ultrahigh-pressure metamorphic belt, east-central China, using U-Th-Pb dating of zircon and monazite: Chemical Geology, v. 186, p. 315–331, doi: 10.1016/S0009-2541(02)00008-6.

Black, L.P., Kamo, S.L., Allen, C.M., Davis, D.W., Aleinikoff, J.N., Valley, J.W., Mundil, R., Campbell, I.H., Korsch, R.J., Williams, I.S., and Foudoulis, C., 2004, Improved $^{206}Pb/^{208}U$ microprobe geochronology by the monitoring of a trace-element–related matrix effect: SHRIMP ID-TIMS, ELA-ICP-MS, and oxygen isotope documentation for a series of zircon standards: Chemical geology, v. 205, p. 115–140.

Bruguier, O., Lancelot, J.R., and Malavieille, J., 1997, U-Pb dating on single detrital zircon grains from the Triassic Songpan-Ganze flysch (central China): Provenance and tectonic correlations: Earth and Planetary Science Letters, v. 152, p. 217–231, doi: 10.1016/S0012-821X(97)00138-6.

Chavagnac, V., and Jahn, B.-M., 1996, Coesite-bearing eclogites from the Bixiling Complex, Dabie Mountains, China: Sm-Nd ages, geochemical characteristics and tectonic implications: Chemical Geology, v. 133, p. 29–51, doi: 10.1016/S0009-2541(96)00068-X.

Chen, F., Siebel, W., Guo, J., Cong, B., and Satir, M., 2003, Late Proterozoic magmatism and metamorphism recorded in gneisses from the Dabie high-pressure metamorphic zone, eastern China: Evidence from zircon U-Pb geochronology: Precambrian Research, v. 120, p. 131–148, doi: 10.1016/S0301-9268(02)00162-6.

Cherniak, D.J., and Watson, E.B., 2003, Diffusion in zircon: Reviews in Mineralogy and Geochemistry, v. 53, p. 113–143, doi: 10.2113/0530113.

Cumming, G.L., and Richards, J.R., 1975, Ore lead isotope ratios in a continuously changing earth: Earth and Planetary Science Letters, v. 28, p. 155–171, doi: 10.1016/0012-821X(75)90223-X.

Faure, M., Lin, W., and Le Breton, N., 2001, Where is the North China–South China block boundary in eastern China?: Geology, v. 29, p. 119–122, doi: 10.1130/0091-7613(2001)029<0119:WITNCS>2.0.CO;2.

Faure, M., Lin, W., Monié, P., Le Breton, N., Poussineau, S., Panis, D., and Deloule, E., 2003, Exhumation tectonics of the ultrahigh-pressure metamorphic rocks in the Qinling orogen in east China: New petrological-structural-radiometric insights from the Shandong Peninsula: Tectonics, v. 22, p. 1018, doi: 10.1029/2002TC001450.

Grimmer, J.C., Jonckheere, R., Enkelmann, E., Ratschbacher, L., Hacker, B.R., Blythe, A.E., Wagner, G.A., Wu, Q., Liu, S., and Dong, S., 2002, Late Cretaceous–Cenozoic history of the southern Tan-Lu fault zone: Apatite fission-track and structural constraints from the Dabie Shan (eastern China): Tectonophysics, v. 359, p. 225–253, doi: 10.1016/S0040-1951(02)00513-9.

Grimmer, J.C., Ratschbacher, L., McWilliams, M., Franz, L., Gaitzsch, I., Tichomirowa, M., Hacker, B.R., and Zhang, Y., 2003, When did the ultrahigh-pressure rocks reach the surface? A $^{207}Pb/^{206}Pb$ zircon $^{40}Ar/^{39}Ar$ white mica, Si-in-white mica, single-grain provenance study of Dabie Shan synorogenic foreland sediments: Chemical Geology, v. 197, p. 87–110, doi: 10.1016/S0009-2541(02)00321-2.

Hacker, B.R., and Wang, Q., 1995, Ar/Ar geochronology of ultrahigh-pressure metamorphism in central China: Tectonics, v. 14, p. 994–1006, doi: 10.1029/95TC00932.

Hacker, B.R., Ratschbacher, L., Webb, L.E., Ireland, T., Walker, D., and Dong, S., 1998, U/Pb zircon ages constrain the architecture of the ultrahigh-pressure Qinling-Dabie orogen, China: Earth and Planetary Science Letters, v. 161, p. 215–230, doi: 10.1016/S0012-821X(98)00152-6.

Hacker, B.R., Ratschbacher, L., Webb, L.E., McWilliams, M.O., Ireland, T., Calvert, A., Dong, S., and Wenk, H.-R., 2000, Exhumation of ultrahigh-pressure continental crust in east central China: Late Triassic–Early Jurassic tectonic unroofing: Journal of Geophysical Research, v. 105, p. 13,339–13,364, doi: 10.1029/2000JB900039.

Hacker, B.R., Ratschbacher, L., and Liou, J.G., 2004, Subduction, collision and exhumation in the ultrahigh-pressure Qinling-Dabie orogen, *in* Malpas, J., et al., eds., Aspects of the Tectonic evolution of China: Geological Society of London Special Publication 226, p. 157–175.

Hermann, J., Rubatto, D., Korsakov, A., and Shatsky, V.S., 2001, Multiple zircon growth during fast exhumation of diamondiferous, deeply subducted continental crust (Kokchetav Massif, Kazakhstan): Contributions to Mineralogy and Petrology, v. 141, p. 66–82.

Hoskin, P.W.O., 1998, Minor and trace element analysis of natural zircon ($ZrSiO_4$) by SIMS and laser ablation ICPMS: A consideration and comparison of two broadly competitive techniques: Journal of Trace and Microprobe Techniques, v. 16, p. 301–326.

Leech, M.L., 2001, Arrested orogenic development: Eclogitization, delamination, and tectonic collapse: Earth and Planetary Science Letters, v. 185, p. 149–159, doi: 10.1016/S0012-821X(00)00374-5.

Leech, M.L., Webb, L.E., Yang, T., and Xu, Z., 2003, Microstructural analysis of the ultrahigh-pressure Sulu terrane, eastern China: Eos (Transactions, American Geophysical Union), v. 84, p. F1391.

Leech, M.L., Singh, S., Jain, A.K., Klemperer, S.L., and Manickavasagam, R.M., 2005, The onset of India-Asia continental collision: Early, steep subduction required by the timing of UHP metamorphism in the western Himalaya: Earth and Planetary Science Letters, v. 234, p. 83–97, doi: 10.1016/j.epsl.2005.02.038.

Li, S., Xiao, Y., Liou, D., Chen, Y., Ge, N., Zhang, Z., Sun, S., Cong, B., Zhang, R., Hart, S.R., and Wang, S., 1993, Collision of the North China and Yangtze and formation of coesite-bearing eclogites: Timing and processes: Chemical Geology, v. 109, p. 89–111, doi: 10.1016/0009-2541(93)90063-O.

Li, S., Jagoutz, E., Lo, C.-H., Chen, Y., Li, Q., and Xiao, Y., 1999, Sm/Nd, Rb/Sr, and $^{40}Ar/^{39}Ar$ isotopic systematics of the ultrahigh-pressure metamorphic rocks in the Dabie-Sulu belt, central China: A retrospective view: International Geology Review, v. 41, p. 1114–1124.

Li, X.-P., Zheng, Y.-F., Wu, Y.-B., Chen, F., Gong, B., and Li, Y.-L., 2004, Low-*T* eclogite in the Dabie terrane of China: Petrological and isotopic constraints on fluid activity and radiometric dating: Contributions to Mineralogy and Petrology, v. 148, p. 443–470.

Liou, J.G., Zhang, R.Y., Eide, E.A., Maruyama, S., Wang, X., and Ernst, W.G., 1996, Metamorphism and tectonics of high-*P* and ultrahigh-*P* belts in Dabie-Sulu regions, eastern central China, *in* Yin, A., and Harrison, T.M., eds., The tectonic evolution of Asia: New York, Cambridge University Press, p. 300–343.

Liu, F., Xu, Z., and Xue, H., 2004a, Tracing the protolith, UHP metamorphism, and exhumation ages of orthogneiss from the SW Sulu terrane (eastern China): SHRIMP U-Pb dating of mineral inclusion-bearing zircons: Lithos, v. 78, p. 411–429, doi: 10.1016/j.lithos.2004.08.001.

Liu, F., Xu, Z., Liou, J.G., and Song, B., 2004b, SHRIMP U-Pb ages of ultrahigh-pressure and retrograde metamorphism of gneisses, south-western Sulu terrane, eastern China: Journal of Metamorphic Geology, v. 22, p. 315–326, doi: 10.1111/j.1525-1314.2004.00516.x.

Liu, X., Jahn, B.-M., Liu, D., Dong, S., and Li, S., 2004c, SHRIMP U-Pb zircon dating of metagabbro and eclogites from western Dabieshan (Hong'an block), China, and its tectonic implications: Tectonophysics, v. 394, p. 171–192, doi: 10.1016/j.tecto.2004.08.004.

Ludwig, K.R., 1999, Using Isoplot/Ex, Version 2.01: A geochronological toolkit for Microsoft Excel: Berkeley Geochronology Center Special Publication no. 1a, 47 p.

Ludwig, K.R., 2001, Eliminating mass-fractionation effects on U-Pb isochron ages without doubles-spiking of Pb: Geochimica et Cosmochimica Acta, v. 65, p. 3139–3145, doi: 10.1016/S0016-7037(01)00637-8.

MacDougall, I., and Harrison, T.M., 1988, Geochronology and thermochronology by the $^{40}Ar/^{39}Ar$ method: Oxford Monographs on Geology and Geophysics Volume 9: Oxford, Oxford University Press, 212 p.

McDonough, W.F., and Sun, S.-S., 1995, The composition of the Earth: Chemical Geology, v. 120, p. 223–253, doi: 10.1016/0009-2541(94)00140-4.

Okay, A.I., Sengor, A.M.C., and Satir, M., 1993, Tectonics of an ultrahigh-pressure metamorphic terrane: Dabie Shan, China: Tectonics, v. 12, p. 1320–1334.

Ratschbacher, L., Hacker, B.R., Webb, L.E., McWilliams, M., Ireland, T., Dong, S., Calvert, A., Chateigner, D., and Wenk, H.-R., 2000, Exhumation of the ultrahigh-pressure continental crust in east central China: Cretaceous and Cenozoic unroofing and the Tan-Lu fault: Journal of Geophysical Research, v. 105, p. 13,303–13,338, doi: 10.1029/2000JB900040.

Rowley, D.B., Xue, F., Tucker, R.D., Peng, X., Baker, J., and Davis, A., 1997, Ages of ultrahigh pressure metamorphism and protolith orthogneisses from eastern Dabie Shan: U/Pb zircon geochronology: Earth and Planetary Science Letters, v. 151, p. 191–203, doi: 10.1016/S0012-821X(97)81848-1.

Rubatto, D., 2002, Zircon trace element geochemistry: Partitioning with garnet and the link between U-Pb ages and metamorphism: Chemical Geology, v. 184, p. 123–138, doi: 10.1016/S0009-2541(01)00355-2.

Rubatto, D., and Hermann, J., 2003, Zircon formation during fluid circulation in eclogites (Monviso, western Alps): Implications for Zr and Hf budget in subduction zones: Geochimica et Cosmochimica Acta, v. 67, p. 2173–2187, doi: 10.1016/S0016-7037(02)01321-2.

Rumble, D., Giorgis, D., Ireland, T., Zhang, Z., Xu, H., Yui, T.F., Yang, J., Xu, Z., and Liou, J.G., 2002, Low $\delta^{18}O$ zircons, U-Pb dating, and the age of the Qinglongshan oxygen and hydrogen isotope anomaly near Donghai in Jiangsu Province, China: Geochimica et Cosmochimica Acta, v. 66, p. 2299–2306, doi: 10.1016/S0016-7037(02)00844-X.

Sobolev, N.V., and Shatsky, V.S., 1990, Diamond inclusions in garnets from metamorphic rocks: A new environment for diamond formation: Nature, v. 343, p. 742–746, doi: 10.1038/343742a0.

Tabata, H., Maruyama, S., and Liou, J.G., 1998, Coesite inclusions of zircon from the ultrahigh-pressure Dabie metamorphic terrane, central China: American Geophysical Union, Western Pacific Geophysics Meeting Abstracts, v. 79, p. 152.

Wallis, S., Enami, M., and Banno, S., 1999, The Sulu UHP terrane: A review of the petrology and structural geology: International Geology Review, v. 41, p. 906–920.

Wallis, S., Tsuboi, M., Suzuki, K., Fanning, M., Jiang, L., and Tanaka, T., 2005, Role of partial melting in the evolution of the Sulu (eastern China) ultrahigh-pressure terrane: Geology, v. 33, p. 129–132, doi: 10.1130/G20991.1.

Webb, L.E., Hacker, B.R., Ratschbacher, L., McWilliams, M.O., and Dong, S., 1999, Thermochronologic constraints on deformation and cooling history of high- and ultrahigh-pressure rocks in the Qinling-Dabie orogen, eastern China: Tectonics, v. 18, p. 621–638, doi: 10.1029/1999TC900012.

Webb, L.E., Leech, M.L., Yang, T., and Xu, Z., 2002, Kinematics of structures of the ultrahigh-pressure Sulu terrane, eastern China: Eos (Transactions, American Geophysical Union), v. 83, p. F1245.

Williams, I.S., 1998, U-Th-Pb geochronology by ion microprobe, *in* McKibben, M.A., Shanks, W.C., III, and Ridley, W.I., eds., Applications of microanalytical techniques to understanding mineralizing processes: Reviews in Economic Geology, v. 7, p. 1–35.

Wu, Y.-B., Zheng, Y.-F., and Zhou, J.-B., 2004, Neoproterozoic granitoids in northwest Sulu and its bearing on the North China–South China blocks boundary in east China: Geophysical Research Letters, v. 31, p. L07616, doi: 10.1029/2004GL019785.

Xu, S., Okay, A.I., Shouyuan, J., Sengor, A.M.C., Wen, S., Liu, Y., and Jiang, L., 1992, Diamond from the Dabie Shan metamorphic rocks and its implication for tectonic setting: Science, v. 256, p. 80–82.

Yang, J.-H., Chung, S.-L., Wilde, S.A., Wu, F.-Y., Chu, M.-F., Lo, C.-H., and Fan, H.R., 2005, Petrogenesis of post-orogenic syenites in the Sulu orogenic belt, east China: Geochronological, geochemical and Nd-Sr isotopic evidence: Chemical Geology, v. 214, p. 99–125, doi: 10.1016/j.chemgeo.2004.08.053.

Yang, J.S., Wooden, J.L., Wu, C.L., Liu, F.L., Xu, Z.Q., Shi, R.D., Katayama, I., Liou, J.G., and Maruyama, S., 2003, SHRIMP U-Pb dating of coesite-bearing zircon from the ultra-high-pressure metamorphic rocks, Sulu terrane, east China: Journal of Metamorphic Geology, v. 21, p. 551–560, doi: 10.1046/j.1525-1314.2003.00463.x.

Zhao, R., Liou, J.G., Zhang, R.Y., and Wooden, J.L., 2005, SHRIMP U-Pb dating of zircon from the Xugou UHP eclogite, Sulu terrane, eastern China: International Geology Review, v. 47, p. 805–814.

Zheng, J., Griffin, W.L., O'Reilly, S.Y., Lu, F., Wang, C., Zhang, M., Wang, F., and Li, H., 2004a, 3.6 Ga lower crust in central China: New evidence on the assembly of the North China craton: Geology, v. 32, p. 229–232, doi: 10.1130/G20133.1.

Zheng, Y.-F., Wang, Z.-R., Li, S.-G., and Zhao, Z.-F., 2002, Oxygen isotope equilibrium between eclogite minerals and its constraints on mineral Sm-Nd chronometer: Geochimica et Cosmochimica Acta, v. 66, p. 625–634, doi: 10.1016/S0016-7037(01)00801-8.

Zheng, Y.-F., Gong, B., Zhao, Z.-F., Fu, B., and Li, Y.-L., 2003, Two types of gneisses associated with eclogite at Shuanghe in the Dabie terrane: Carbon isotope, zircon U-Pb dating and oxygen isotope: Lithos, v. 70, p. 321–343, doi: 10.1016/S0024-4937(03)00104-X.

Zheng, Y.-F., Wu, Y.-B., Chen, F.-K., Gong, B., Li, L., and Zhao, Z.-F., 2004b, Zircon U-Pb and oxygen isotope evidence for a large-scale ^{18}O depletion event in igneous rocks during the Neoproterozoic: Geochimica et Cosmochimica Acta, v. 68, p. 4145–4165, doi: 10.1016/j.gca.2004.01.007.

MANUSCRIPT ACCEPTED BY THE SOCIETY 21 SEPTEMBER 2005

Geological Society of America
Special Paper 403
2006

U-Pb SHRIMP geochronology and trace-element geochemistry of coesite-bearing zircons, North-East Greenland Caledonides

William C. McClelland*
Department of Geological Sciences, University of Idaho, Moscow, Idaho 83844, USA
Siobhán E. Power
Jane A. Gilotti
Department of Geoscience, University of Iowa, Iowa City, Iowa 52242, USA
Frank K. Mazdab
U.S Geological Survey–Stanford Ion Probe Laboratory, 367 Panama Mall, Stanford, California 94305, USA
Brigitte Wopenka
Department of Earth and Planetary Sciences, Washington University, St. Louis, Missouri 63130, USA

ABSTRACT

Obtaining reliable estimates for the timing of eclogite-facies metamorphism is critical to establishing models for the formation and exhumation of high-pressure and ultrahigh-pressure (UHP) metamorphic terranes in collisional orogens. The presence of pressure-dependent phases, such as coesite, included in metamorphic zircon is generally regarded as evidence that zircon growth occurred at UHP conditions and, if dated, should provide the necessary timing information. We report U-Pb sensitive high-resolution ion microprobe (SHRIMP) ages and trace-element SHRIMP data from coesite-bearing zircon suites formed during UHP metamorphism in the North-East Greenland Caledonides. Kyanite eclogite and quartzofeldspathic host gneiss samples from an island in Jøkelbugt (78°00′N, 18°04′W) contained subspherical zircons with well-defined domains in cathodoluminescence (CL) images. The presence of coesite is confirmed by Raman spectroscopy in six zircons from four samples. Additional components of the eclogite-facies inclusion suite include kyanite, omphacite, garnet, and rutile. The trace-element signatures in core domains reflect modification of igneous protolith zircon. Rim signatures show flat heavy rare earth element (HREE) patterns that are characteristic of eclogite-facies zircon. The kyanite eclogites generally lack a Eu anomaly, whereas a negative Eu anomaly persists in all domains of the host gneiss. The ^{207}Pb-corrected $^{206}Pb/^{238}U$ ages range from 330 to 390 Ma for the host gneiss and 330–370 Ma for the kyanite eclogite. Weighted mean $^{206}Pb/^{238}U$ ages for coesite-bearing domains vary from 364 ± 8 Ma for the host gneiss to 350 ± 4 Ma for kyanite eclogite. The combined U-Pb and REE data interpreted in conjunction with observed CL domains and inclusion suites suggest that (1) Caledonian metamorphic zircon formed by both new zircon growth and recrystallization, (2) UHP metamorphism occurred near the end of the Caledonian collision, and (3) the 30–50

*Corresponding author e-mail: wmcclell@uidaho.edu.

McClelland, W.C., Power, S.E., Gilotti, J.A., Mazdab, F.K., and Wopenka, B., 2006, U-Pb SHRIMP geochronology and trace-element geochemistry of coesite-bearing zircons, North-East Greenland Caledonides, *in* Hacker, B.R., McClelland, W.C., and Liou, J.G., eds., Ultrahigh-pressure metamorphism: Deep continental subduction: Geological Society of America Special Paper 403, p. 23–43, doi: 10.1130/2006.2403(02).

m.y. span of ages records long residence times at eclogite-facies conditions for the UHP rocks of North-East Greenland. This spread in observed ages is interpreted to be characteristic of metamorphic rocks that have experienced relatively long (longer than 10 m.y.) residence times at UHP conditions.

Keywords: ultrahigh-pressure, coesite, U-Pb SHRIMP, Caledonides, Greenland.

INTRODUCTION

Subduction of continental material to depths of 100–120 km within collisional orogenic belts is widely accepted, based on the preservation of coesite and microdiamonds as inclusions in eclogite-facies minerals (Chopin, 2003, and references therein). Most ultrahigh-pressure (UHP) terranes lie in the footwall or subducted slab of the orogen (Michard et al., 1995; Hacker et al., 2000; Avigad et al., 2003). This geometry permits models based on buoyancy principles, in which dense mantle or oceanic material drags attached continental material to anomalous depths during subduction. Upon break off of the entire slab or delamination of the crust from the lithospheric mantle, the more buoyant continental material can be exhumed to normal crustal levels (Chemenda et al., 1996; Burov et al., 2001; Doin and Henry, 2001; Gerya et al., 2002; Roselle and Engi, 2002). In contrast, UHP metamorphic terranes in the overriding plate of collisional orogens, such as the Greenland Caledonides, carry significant implications for geodynamic models of collisional orogens and require alternatives to the popular continental subduction model (e.g., Ryan, 2001). The age of metamorphism is one of the most important parameters in defining models for formation and exhumation of UHP terranes in these different settings. Comparison of the ages of UHP metamorphism in the Western Gneiss Region of the Scandinavian Caledonides at 410–400 Ma (Carswell et al., 2003; Root et al., 2004) with the Greenland Caledonides at ca. 360 Ma (Gilotti et al., 2004) clearly suggests that the timing and duration of UHP metamorphism varies in different settings within an orogen.

The North-East Greenland eclogite province (Gilotti, 1993) contains widespread evidence for high-pressure metamorphism at 410–390 Ma (Brueckner et al., 1998; Elvevold and Gilotti, 2000). Evidence for UHP metamorphism in the North-East Greenland eclogite province was recognized by the presence of polycrystalline quartz pseudomorphs after coesite preserved in garnet and omphacite (Gilotti and Ravna, 2002). This paper documents the presence of coesite as inclusions in zircon from the same eclogites and host gneisses. The age of UHP metamorphism was reported as 360 ± 5 Ma, ~40 m.y. younger than high-pressure metamorphism observed elsewhere in the North-East Greenland eclogite province (Gilotti et al., 2004). This paper provides additional definitive evidence for the timing of UHP metamorphism in North-East Greenland.

Recent studies have demonstrated the importance of conducting in situ U-Pb analyses in conjunction with cathodoluminescence (CL) imaging and analysis of inclusion suites to link age information with UHP metamorphism (e.g., Hermann et al., 2001; Katayama et al., 2001; Liu et al., 2002, 2005; Kaneko et al., 2003; Yang et al., 2003). Three analytical techniques were employed to link zircon ages with UHP metamorphic conditions in this study: (1) Coesite was identified in zircons with laser Raman spectroscopy; (2) U-Pb ages were established by ion microprobe for domains defined by variation in CL intensities; and (3) rare earth element (REE) geochemistry of the CL-defined domains was obtained in an effort to tie the age determinations to UHP metamorphism by using flat heavy (H) REE patterns and the lack of a negative Eu anomaly in metamorphic zircon as a proxy for zircon growth at eclogite-facies conditions (Rubatto and Hermann, 2003).

GEOLOGICAL SETTING

The North-East Greenland eclogite province is preserved as the structurally highest sheet in a west-directed thrust belt developed along the Laurentian margin during the Caledonian collision with Baltica (Fig. 1; Higgins and Leslie, 2000; Higgins et al., 2004). The province is part of the Laurentian continental basement and is largely composed of quartzofeldspathic gneisses derived from 2.0 to 1.8 Ga deformed, calc-alkaline batholiths and crosscutting 1.74 Ga granitoids (Kalsbeek et al., 1993; Hull et al., 1994; Kalsbeek, 1995). Mafic rocks form meter- to kilometer-scale lenses and layers within the quartzofeldspathic gneisses, and many of them preserve a high-pressure mineralogy. Common lithologies include: eclogite sensu stricto, garnet clinopyroxenite, garnet websterite, websterite, and coronitic metagabbro (Gilotti, 1993, 1994; Gilotti and Elvevold, 1998; Lang and Gilotti, 2001). Protoliths of the eclogite-facies rocks were pre-Caledonian mafic dikes, mafic to ultramafic intrusions, and mafic xenoliths in the Paleoproterozoic calc-alkaline batholiths (Gilotti, 1993, 1994; Brueckner et al., 1998).

Two strike-slip shear zones divide the North-East Greenland eclogite province into western, central, and eastern blocks (Fig. 1). The vast majority of the high-pressure rocks in the eclogite province record medium-temperature (600–750 °C), high-pressure (1.5–2.3 GPa) metamorphic conditions (Brueckner et al., 1998; Elvevold and Gilotti, 2000) typical of a continental eclogite terrane. Spatial variation in pressure and temperature across the North-East Greenland eclogite province has yet to be discerned, in part due to the paucity of assemblages that are amenable to robust thermobarometry. In contrast, the Western Gneiss Region of Norway, a similar terrane on the Baltica margin, shows a steady increase in temperature

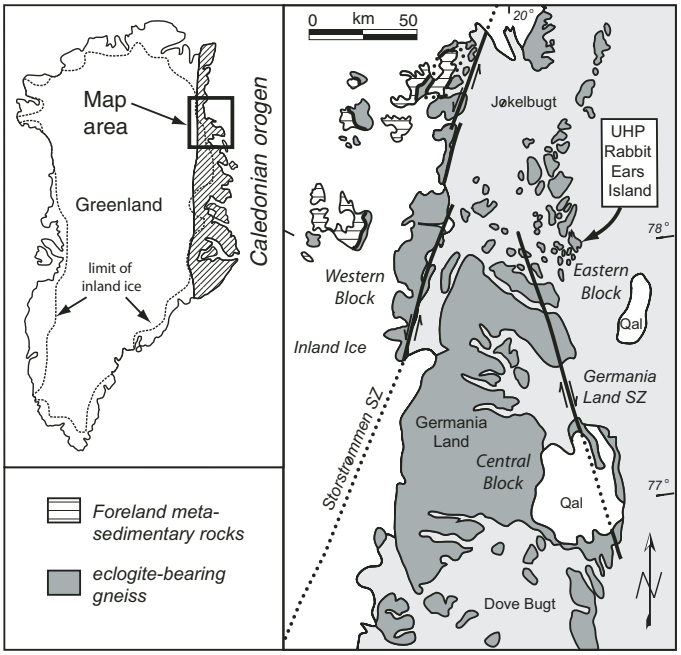

Figure 1. Simplified geologic map of the North-East Greenland eclogite province showing the ultrahigh-pressure (UHP) locality on an island in Jøkelbugt informally known as Rabbit Ears Island. SZ—subduction zone.

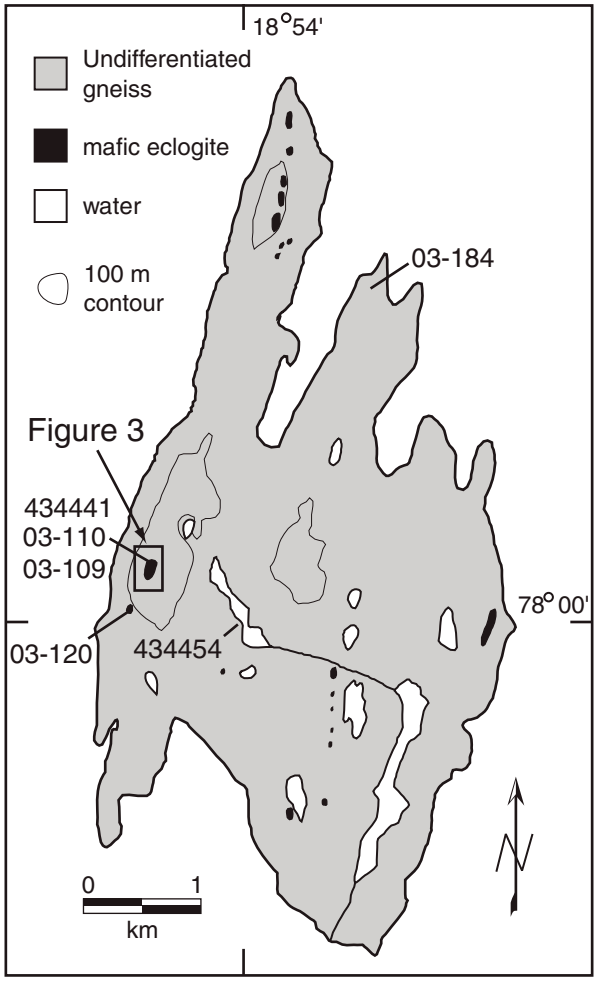

Figure 2. Geological map of Rabbit Ears Island showing location of samples mentioned in text.

toward the west (Griffin et al., 1985). The age of eclogite-facies metamorphism in the central and western blocks ranges from ca. 410–390 Ma (Gilotti et al., 2004).

Ultrahigh-pressure metamorphism is currently known from a small island in the eastern block, informally referred to as Rabbit Ears Island (Figs. 1 and 2; Gilotti and Ravna, 2002). Eclogite pods range from 1 to 50 m in width and 1 to >100 m in length, and are located in relatively narrow zones that can be traced for several kilometers along strike (Fig. 2). The eclogite-rich zones are parallel to the dominant NNW-striking gneissosity in the host rocks, and are interpreted as boudinaged, layered mafic intrusions. Many of the boudins have a blocky shape with pegmatites and leucogranites filling boudin necks and boudin-normal fractures (Fig. 3). The majority of the mafic boudins on Rabbit Ears Island consists of decimeter-scale, interlayered kyanite eclogite, bimineralic eclogite, and garnet-rich quartzite. The layering is interpreted to be a primary feature inherited from a layered mafic intrusive protolith. The eclogitic layers contain a foliation defined by kyanite, garnet, and omphacite that is parallel to that in the surrounding host gneisses; the layering and the foliation are isoclinally folded. The host rocks contain minor metapelite, but are mainly quartzofeldspathic orthogneisses that vary from mafic to more felsic compositions at the decimeter to 100 m scales. In contrast to the amphibole-bearing gneisses that dominate most other areas of the North-East Greenland eclogite province, abundant clinopyroxene is found in the host gneisses, indicating better preservation of the eclogite-facies history on Rabbit Ears Island.

Gilotti and Ravna (2002) identified microstructural and geothermobarometric features indicative of UHP metamorphism in the kyanite eclogites and their host gneisses. The microstructures include polycrystalline quartz inclusions with radial fractures in garnet, omphacite, and kyanite. Palisade quartz forms an outer rim around very finely recrystallized quartz in a number of inclusions, which is a diagnostic feature of pseudomorphs after coesite (Chopin and Sobolev, 1995; Hacker and Peacock, 1995). Polycrystalline quartz rods and single-quartz crystals with radial fractures are more abundant. Geothermobarometry on the garnet + omphacite + kyanite + quartz/coesite + phengite assemblage, using the Ravna and Terry (2004) calibration, returned temperatures in excess of 950 °C and pressures well into the coesite stability field (Gilotti and Ravna, 2002). The temperature may be overestimated and the pressure underestimated because of the difficulty in finding pristine phengite. The garnet-clinopyroxene equilibria line (calculated using Ravna, 2000) intersects the garnet + clinopyroxene

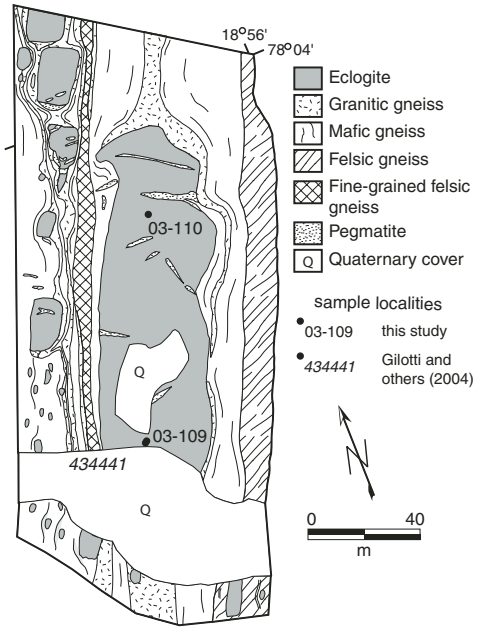

Figure 3. Detailed geological map of blocky, layered eclogite boudins surrounded by different gneissic lithologies, with two of the coesite-bearing kyanite eclogite sample locations shown. Pegmatites, emplaced during boudinage, cut the eclogite blocks at high angles, and granitic gneiss fills the boudin necks.

+ phengite equilibria at even higher temperatures, and is considered unreliable due to the assumption that all Fe is ferrous. Coesite, a major index mineral for UHP metamorphism, has now been identified in these rocks, leaving no doubt about their UHP provenance (see following).

Sample Description

Four samples from Rabbit Ears Island are now known to contain coesite. Three of the samples are from kyanite eclogite layers in mafic eclogite boudins, and the fourth sample is from the quartzofeldspathic host gneiss. The samples were collected during field work in 2003; their locations are shown on Figures 2 and 3. Minerals in thin section were identified using a petrographic microscope aided by energy dispersive analysis (EDS) on the JEOL 5600 scanning electron microscope (SEM) housed at Stanford University, Stanford, California.

Kyanite Eclogite

Samples 03-109 and 03-110 are from different kyanite eclogite layers within a 40 × 140 m blocky boudin (Fig. 3). Sample 03-109 is from the same exact location as 434441, the kyanite eclogite described by Gilotti and Ravna (2002) and dated by Gilotti et al. (2004; see their Figure 2f for a photomicrograph of the mineral assemblage). Kyanite eclogite sample 03-120 was collected from a similar banded eclogite boudin ~500 m south of 03-109. All three samples are medium grained, and contain the eclogite-facies assemblage garnet + omphacite + kyanite + quartz/coesite + phengite + rutile + zircon. The high-pressure assemblage is best preserved as inclusions in garnet and zircon. Polycrystalline and single-crystal quartz inclusions with radial fractures are abundant in garnet, but also occur in omphacite and kyanite. Millimeter-scale, elongate garnets lie parallel to the foliation defined by compositional layering and aligned omphacite, kyanite, and amphibole. Zircons occur enclosed in kyanite or along grain boundaries of other high-pressure phases (Fig. 4A). The samples have experienced variable amounts of retrogression, with 03-120 being the best preserved. Characteristic retrograde features include: diopside + plagioclase symplectites after omphacite; plagioclase ± amphibole halos around kyanite, garnet, and omphacite; biotite + plagioclase symplectites after phengite; and green amphibole directly replacing omphacite and as isolated poikioblastic crystals in the matrix.

Host Gneiss

The eclogite blocks are surrounded by interlayered mafic to felsic quartzofeldspathic gneisses (e.g., Fig. 3). Sample 03-184 was collected from quartzofeldspathic gneiss in an area that lacks boudinaged eclogite blocks (Fig. 2) but consists of decimeter-scale garnet-clinopyroxene–rich layers isoclinally folded with garnet-bearing felsic gneiss. The main high-pressure minerals—garnet + clinopyroxene + kyanite—are preserved throughout, but modal quartz + plagioclase vary considerably from layer to layer. The diopsidic clinopyroxene has a ragged, skeletal texture. Garnet and zircon preserve inclusions of the high-pressure mineral assemblage. As in the mafic rocks, zircon generally is enclosed in kyanite (Fig. 4C) but also occurs at grain boundaries of other high-pressure phases. Very fine-grained symplectites of amphibole + plagioclase surround kyanite and garnet; retrograde green amphibole is also abundant. Gilotti and Ravna (2002) calculated P = 2.5 GPa and T = 826 °C from kyanite + omphacite + quartz + phengite inclusions preserved in a single garnet from a sample collected at another host gneiss locality (434454; Fig. 2) that is much more strongly retrogressed than 03-184; they considered this to record a point on the retrograde path.

SAMPLE PREPARATION AND RAMAN SPECTROSCOPY

Analytical Methods

Zircons were separated from samples of kyanite eclogite, quartzofeldspathic orthogneiss, and one paragneiss by standard crushing and gravimetric techniques. The zircon separates were placed in alcohol and examined under a binocular microscope for handpicking of inclusion-bearing grains. The selected zircons from both the eclogites and the gneisses were clear, subspherical grains, ranging from 50 to 400 μm in diameter. Approximately 220 grains with 1–5 inclusions per grain from each of eight samples were mounted on double-sided adhesive tape on glass plates. All visible inclusions were analyzed by in situ laser Raman spectroscopy at the Department of Earth and

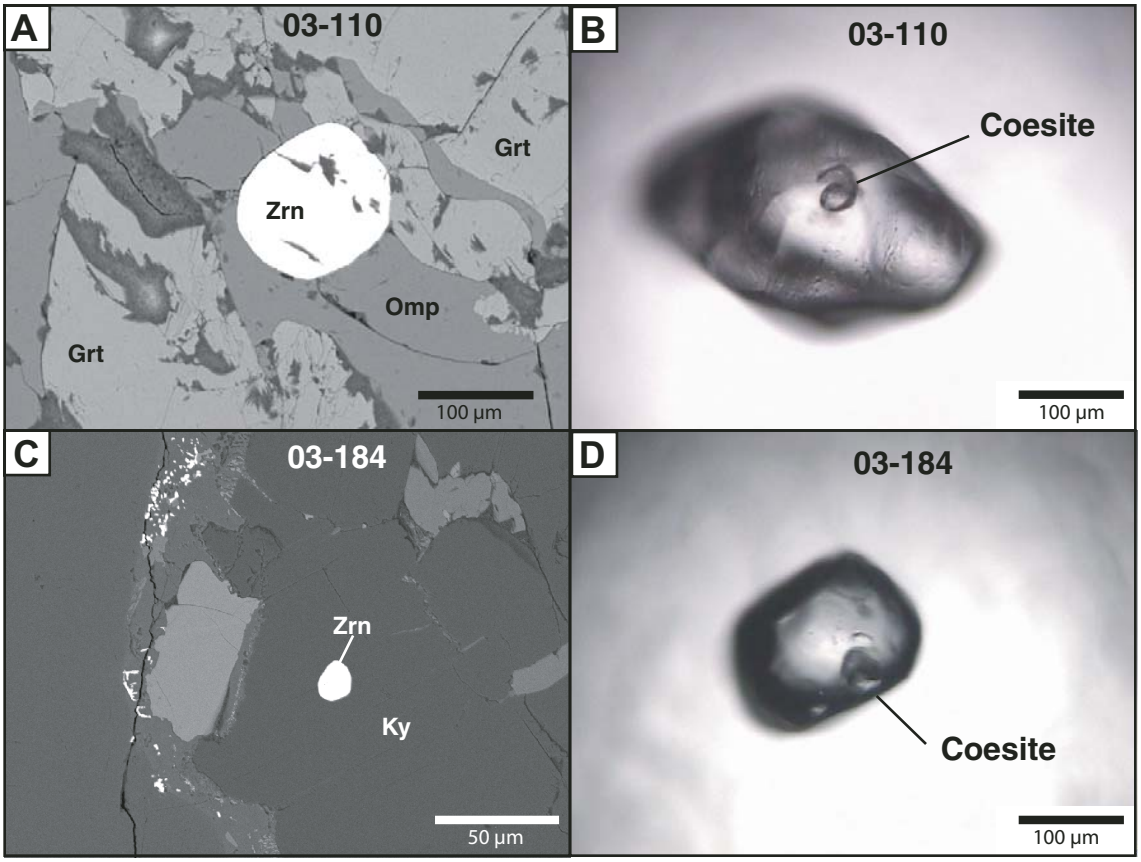

Figure 4. Backscattered-electron (A, C) and transmitted-light (B, D) images of zircon grains from eclogite and host gneiss. Eclogite sample 03-110: (A) Large, spherical zircon (Zrn) within garnet (Grt) and omphacite (Omp). (B) Subhedral, ovoid zircon with coesite inclusion (grain 56, Fig. 6). Host gneiss sample 03-184: (C) Small zircon in kyanite (Ky). (D) Spherical zircon with coesite inclusion (grain 48, Fig. 6). Coesite inclusions were identified via Raman microprobe analysis (see Fig. 5). Mineral abbreviations are after Kretz (1983).

Planetary Sciences, Washington University, St. Louis, Missouri. The instrument used was an integrated, fiber-optically coupled microscope-spectrometer-detector Raman microprobe system (see van Zuilen et al., 2005, for instrumental details). The 532 nm laser beam used to excite the Raman scattering was focused to ~1 µm, which allowed pinpoint analysis of individual phases within an inclusion.

Results

Zircons from all samples are morphologically ovoid to soccer-ball shaped, consistent with their origin in high-grade metamorphic rocks (Vavra et al., 1999; Schaltegger et al., 1999). Inclusion suites in over 1700 zircons were analyzed, and six coesite grains were identified in four different samples. Four coesite inclusions were found in zircon from the kyanite eclogites: one from 03-109, two from 03-110 (Fig. 4B), and one in 03-120. The coesites are round, 17–45 µm in diameter, and darker than the surrounding zircon matrix. We identified two coesite inclusions in the quartzofeldspathic host gneiss sample 03-184 (Fig. 4D). Zircons in the gneiss are on average larger than those found in the eclogites, and the coesite inclusions have diameters of 45 and 60 µm. After polishing, one coesite was seen in backscattered-electron (BSE) images to be a composite inclusion with the presence of omphacite confirmed by EDS.

Coesite can be unambiguously identified via Raman spectroscopy, because its Raman spectrum is distinctly different from any of the other SiO_2 polymorphs. Of specific relevance for the present study is that the Raman spectra of quartz and coesite are very different. Whereas the two most prominent peaks for quartz are at 464 and 204 Δcm^{-1}, the strongest peaks for coesite are at 524, 474, 428, 328, 270, and 207 Δcm^{-1}. The six coesite inclusions identified in the present study showed all the peaks for coesite and none of the quartz peaks (Fig. 5). Because the Raman scattering efficiency of zircon is much stronger compared to that of coesite, the peaks of the overlying zircon matrix are always detected (see Fig. 5), despite the fact that the method is close to confocal, and the laser beam is focused into the coesite inclusion below the sample surface. The strongest Raman peak for zircon is at 1005 Δcm^{-1} (not

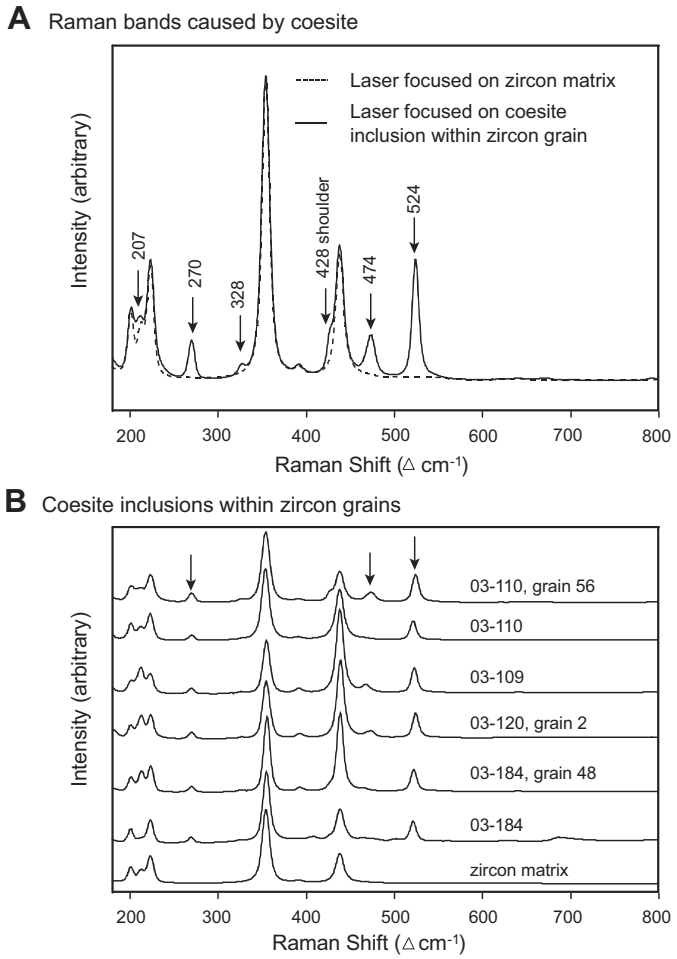

Figure 5. Raman spectra of coesite inclusions in zircon from eclogite and host gneiss from North-East Greenland. (A) Detailed spectrum generated with the laser focused on a coesite inclusion within zircon (solid line) compared to spectrum generated with laser focused on clean zircon matrix of grain from kyanite eclogite 03-110 shown in Figure 4B. The peaks caused by coesite are marked with arrows. (B) Spectra from six different coesite inclusions in zircon compared to the spectrum of the zircon host mineral. The most prominent peaks due to coesite are at 270, 474, and 524 Δcm^{-1} and are indicated with arrows. Grain numbers correspond to grains shown in Figure 6.

shown in Fig. 5), and characteristic weaker peaks occur at 438, 391, 354, 223, and 201 Δcm^{-1}. Figure 5B shows the spectra from six of the coesite grains found in the eclogites and gneiss, along with the spectrum for the zircon matrix. The Raman identification of the coesite inclusions within the isolated zircon grains of the North-East Greenland eclogite province region was straightforward for two reasons: (1) as mentioned already, none of the peaks for well-crystalline zircon overlap with the peaks for coesite, and (2) the zircons have low-U and low-Th concentrations, and thus their Raman spectra do not show any effects of metamictization. This means that the zircon peaks are very intense with narrow peak widths, which makes it easy to spectrally resolve them from the coesite peaks (see Fig. 5A).

U-Pb SHRIMP ANALYSIS

Analytical Methods

Zircons, including three of the coesite-bearing zircons, one each from samples 03-110, 03-120, and 03-184, were removed from glass slides used for Raman analysis, mounted in epoxy resin, and polished specifically to expose previously identified coesite inclusions and generally expose the interiors of all zircon grains. A coesite inclusion was successfully exposed in samples 03-110 and 03-184. CL images were collected for each sample using consistent settings to allow qualitative comparison between grains. Domains were defined within individual grains on the basis of variation in CL intensity. Although reasons for variation in luminescence in zircon are varied and poorly documented (see discussion in Nasdala et al., 2003), the CL domains generally coincide with variation in U concentration; low luminescent zones generally correspond with higher-U concentrations (e.g., Rubatto and Gebauer, 2000). Assuming that the CL domains may reflect different growth or recrystallization zones and therefore record age variations, the CL images were used to select spots for U-Pb analysis (Fig. 6). Zircons were analyzed for U-Pb isotopes on the SHRIMP-RG (sensitive high-resolution ion microprobe–reverse geometry) instrument at the U.S. Geological Survey–Stanford University Ion Probe Laboratory, Stanford, California. A 25–30-μm-diameter spot size was used for all analyses. The analytical routine followed Williams (1998), and data reduction utilized the SQUID program of Ludwig (2001a). The concentration of U was calibrated using zircon standard CZ3 (U = 550 ppm). Isotopic compositions were calibrated by replicate analyses of zircon standard R33 (419 Ma; Black et al., 2003). Zircons from the samples were analyzed during three sessions and from two different mounts. Calibration errors for $^{206}Pb/^{238}U$ ratios of R33 for the different analytical sessions were 0.81%, 0.39%, and 1.13% (2σ). The calculated external errors were incorporated when data from all sessions and mounts were compiled and compared. Most ages are younger than 1 Ga, so discussion and interpretation of analyses are based on $^{206}Pb/^{238}U$ ages calculated from ratios corrected for common Pb using the ^{207}Pb method. Ages older than 1 Ga are based on $^{207}Pb/^{206}Pb$ ages calculated from ratios corrected for common Pb using the measured ^{204}Pb. Common Pb compositions were estimated from Stacey and Kramers (1975).

Analyses were grouped according to domains determined by CL imaging, and ages were calculated as inverse-variance weighted mean $^{206}Pb/^{238}U$ ages with errors reported at the 95% confidence level. Age calculations and Tera-Wasserburg diagrams were generated with the Isoplot/Ex program of Ludwig (2001b). Analytical results are presented in Table 1 and plotted in Figures 7 and 8. The Caledonian $^{206}Pb/^{238}U$ ages calculated for each sample are plotted in order of decreasing age in Figure 8 to compare the age variation as a function of CL domain and the range of all analyses regardless of CL domain.

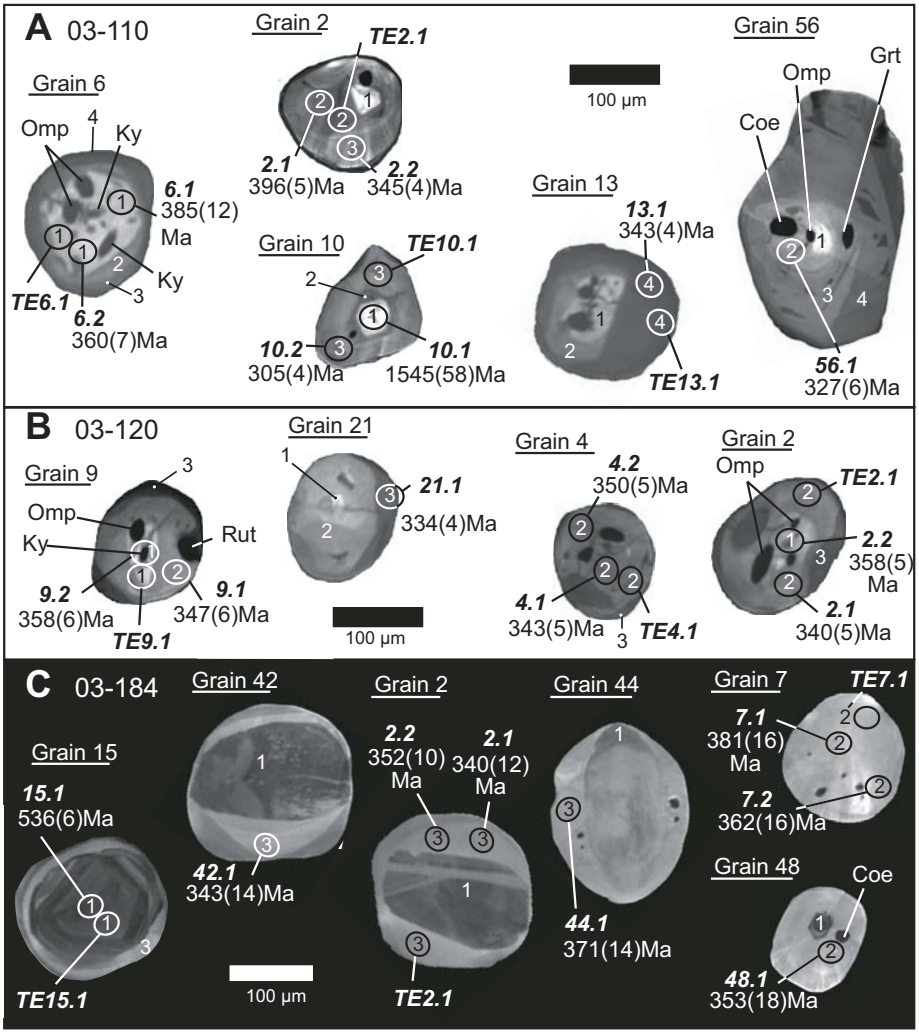

Figure 6. Representative cathodoluminescence (CL) images of subhedral to rounded zircon in dated coesite-bearing samples. Ellipses indicate sensitive high-resolution ion microprobe–reverse geometry (SHRIMP-RG) analysis spots labeled by grain number, spot number, and the corresponding U-Pb ages (±1σ Ma). Ellipses labeled TE indicate trace-element analysis spots. Numbers within the ellipses and on grains note assigned CL domain. Dark spots within the grains are generally inclusions. Where identified, inclusions are labeled with mineral abbreviations after Kretz (1983). (A) Zircons from kyanite eclogite 03-110 were divided into four CL domains. Coesite (Coe) occurs in domain 2 of grain 56. High-pressure/ultrahigh-pressure (HP/UHP) inclusions of kyanite (Ky), omphacite (Omp), and garnet (Grt) are also found in domains 1 and 2. (B) Zircons from kyanite eclogite 03-120 have three discernible CL domains. HP/UHP inclusions are abundant in domains 1 and 2. Coesite occurs in grain 2, but is not exposed at the polished surface. Rut—rutile. (C) Zircons from host gneiss 01-184 contain three CL domains. Grains 15, 42, 2, and 44 show a progression of recrystallization within and growth around older zircon. Grains 7 and 48, consisting almost entirely of low-U zircon, are assigned to domain 2. Grain 48 contains coesite.

Results

Zircons from UHP kyanite eclogite, sample 03-110, are subspherical, equant grains that exhibit four CL domains: (1) luminescent cores, (2) less luminescent cores and mantles, (3) less luminescent rims, and (4) low luminescent rims (e.g., grains 6 and 56; Fig. 6A). Not all domains are present in all grains (e.g., grains 2, 10, and 13; Fig. 6A) The CL domains generally correspond to variations in U concentration, although there is overlap. Domain 1 is characterized as low U (1–83 ppm), whereas both domains 2 and 3 have intermediate-U concentrations (10–243 ppm and 39–156 ppm, respectively). Domain 4 is high U (93–333 ppm) with respect to the other domains. Domain 1 contains inclusions of kyanite and omphacite and gives $^{206}Pb/^{238}U$ ages ranging from 328 to 1545 Ma. Th/U ratios range from 0.004 to 0.77, with the higher ratios associated with older ages. The three Proterozoic ages are interpreted to record the presence of igneous zircon from the mafic protolith, however, the inclusions of high-pressure eclogite-facies minerals point to new zircon growth in this domain during Caledonian metamorphism as well. Excluding the five oldest analyses and the youngest analysis, domain 1 gives a weighted mean

TABLE 1. U-Pb GEOCHRONOLOGIC DATA AND APPARENT AGES

Spot[a]	inclusions[a]	U (ppm)	Th (ppm)	Th/U	$^{206}Pb^{*b}$ (ppm)	$f^{206}Pb_c$ [b c]	$^{238}U/^{206}Pb$ [c]		$^{207}Pb/^{206}Pb$		$^{206}Pb/^{238}U$[d](Ma)		$^{207}Pb/^{206}Pb$[d] (Ma)	
Sample GL03-110 Kyanite eclogite														
Domain 1														
6.1	k,o	8	0.1	0.02	0.4	1.2	16.2549	(3)	0.05440	(15)	385	(12)		
6.2	k,o TE	12	0.1	0.01	1.4	<0.01	17.4189	(2)	0.05358	(6)	360	(7)		
8.1		23	0.2	0.01	1.1	0.7	18.0141	(2)	0.05927	(6)	346	(7)		
10.1		28	20.8	0.77	6.7	1.8	3.6257	(4)	0.11137	(3)	1545	(58)	1777	(68)
12.1		24	0.1	0.004	1.2	0.5	17.3172	(2)	0.05768	(6)	360	(7)		
14.1	TE	28	0.6	0.02	1.4	0.7	16.8373	(2)	0.05970	(5)	369	(7)		
15.1	TE	81	46.0	0.59	10.7	4.2	6.4857	(2)	0.10382	(2)	888	(15)		
32.1	TE	35	0.7	0.02	4.6	0.3	15.1380	(2)	0.05711	(3)	411	(9)		
38.1		1	0.0	0.02	0.1	7.2	12.3794	(7)	0.11489	(17)	466	(34)		
41.1		55	1.9	0.36	2.6	0.5	18.4198	(2)	0.05746	(5)	339	(8)		
44.1		83	4.5	0.06	4.0	0.4	17.9496	(2)	0.05665	(3)	348	(7)		
46.1		41	0.9	0.02	2.1	<0.01	16.8986	(2)	0.05399	(5)	371	(9)		
49.1	o	37	0.4	0.01	3.2	0.1	9.9016	(4)	0.06116	(4)	620	(22)		
52.1		50	1.1	0.02	2.6	0.4	16.9024	(2)	0.05743	(4)	369	(8)		
53.1	k	81	3.9	0.05	3.7	0.9	18.9771	(2)	0.06019	(3)	328	(7)		
55.1		56	0.6	0.01	2.7	0.4	17.7373	(2)	0.05633	(4)	352	(8)		
Domain 2														
2.1	TE	127	0.4	0.003	6.9	<0.01	15.8447	(1)	0.05214	(3)	396	(5)		
3.1	TE	243	6.5	0.03	11.4	<0.01	18.2427	(1)	0.05330	(2)	344	(4)		
4.2	TE	35	0.1	0.004	4.0	0.5	17.6347	(1)	0.05741	(3)	354	(5)		
5.1		111	1.3	0.01	5.4	0.1	17.7011	(1)	0.05447	(3)	354	(5)		
5.2	TE	46	0.5	0.01	5.3	0.3	17.6140	(1)	0.05625	(3)	355	(5)		
9.1		235	13.0	0.06	11.5	<0.01	17.5660	(1)	0.05346	(2)	357	(5)		
9.2	TE	160	5.3	0.03	22.6	<0.01	14.2697	(2)	0.05334	(3)	438	(7)		
15.2		143	13.1	0.10	16.4	0.06	17.5035	(1)	0.05419	(2)	358	(4)		
16.1	TE	39	0.3	0.01	4.5	0.2	17.4394	(1)	0.05547	(3)	359	(5)		
20.1		27	0.3	0.01	2.9	0.5	18.5601	(2)	0.05727	(4)	337	(5)		
23.1		16	0.2	0.01	1.8	1.2	18.6515	(2)	0.06311	(5)	333	(6)		
27.1		19	0.2	0.01	2.2	0.2	17.3043	(2)	0.05571	(5)	361	(6)		
31.1		39	0.3	0.01	4.4	0.1	18.1876	(1)	0.05414	(3)	345	(5)		
33.1	TE	10	0.1	0.01	1.3	17.5	15.2433	(2)	0.19391	(6)	340	(10)		
35.1	TE	48	0.6	0.01	5.5	0.1	17.6307	(1)	0.05442	(3)	355	(5)		
36.1	o	101	1.7	0.02	4.3	<0.01	20.2729	(2)	0.05232	(3)	310	(6)		
40.1	k,r	87	1.1	0.01	3.8	0.05	19.6490	(2)	0.05316	(4)	320	(7)		
42.1		151	4.2	0.03	7.1	0.3	18.1292	(2)	0.05565	(3)	345	(7)		
43.1	o,g	116	1.7	0.02	5.6	<0.01	17.9717	(2)	0.05185	(3)	350	(7)		
47.1	o,g	115	0.9	0.01	5.5	0.4	18.0250	(2)	0.05696	(3)	347	(7)		
48.1		106	1.6	0.02	4.9	0.4	18.6003	(2)	0.05621	(3)	336	(7)		
50.1	o	142	1.9	0.01	6.8	<0.01	17.7810	(2)	0.05213	(3)	353	(7)		
51.1		93	1.5	0.02	4.6	0.1	17.4962	(2)	0.05439	(3)	358	(8)		
54.1	g,r	163	2.6	0.02	7. 5	<0.01	18.7929	(2)	0.05262	(3)	334	(7)		
56.1	c,o,g	162	2.4	0.02	7.3	0.4	19.1412	(2)	0.05633	(3)	327	(6)		
Domain 3														
1.1		73	0.4	0.016	3.5	0.3	18.1377	(1)	0.05536	(3)	345	(5)		
2.2		47	0.6	0.01	5.2	0.3	18.1151	(1)	0.05561	(3)	345	(5)		
7.1	TE	152	1.5	0.01	7.1	0.1	18.3497	(1)	0.05386	(2)	342	(4)		
10.2	TE	40	0.3	0.01	4.0	0.4	20.5736	(1)	0.05553	(3)	305	(4)		
17.1		44	0.6	0.01	4.7	0.5	18.5805	(1)	0.05744	(3)	336	(5)		
18.1		42	0.6	0.01	4.7	0.01	18.1148	(2)	0.05354	(4)	346	(6)		
19.1	TE	63	0.4	0.01	6.4	0.3	19.6381	(1)	0.05552	(3)	319	(4)		
22.1	TE	51	0.4	0.01	5.7	<0.01	18.2873	(1)	0.05278	(3)	343	(4)		
24.1		55	0.8	0.01	6.1	<0.01	18.2472	(1)	0.05169	(3)	345	(4)		
25.1		64	1.1	0.02	6.8	<0.01	18.9904	(1)	0.05248	(3)	331	(4)		
26.1		53	0.7	0.01	5.8	0.3	18.5007	(1)	0.05552	(3)	338	(4)		
28.1	TE	70	0.8	0.01	7.9	0.02	18.0255	(1)	0.05368	(2)	348	(4)		
29.1		156	7.8	0.05	17.1	<0.01	18.3346	(1)	0.05128	(2)	343	(4)		
30.1		119	5.5	0.05	13.3	0.3	18.0051	(1)	0.05572	(2)	347	(4)		
39.1	o	131	2.4	0.02	6.1	0.2	18.4613	(2)	0.05447	(3)	340	(7)		

(*continued*)

TABLE 1. U-Pb GEOCHRONOLOGIC DATA AND APPARENT AGES (*continued*)

Spot[a]	inclusions[a]	U (ppm)	Th (ppm)	Th/U	$^{206}Pb^{*b}$ (ppm)	$f^{206}Pb_c$ [b c]	$^{238}U/^{206}Pb$ [c]		$^{207}Pb/^{206}Pb$		$^{206}Pb/^{238}U$[d] (Ma)		$^{207}Pb/^{206}Pb$[d] (Ma)	
Sample GL03-110 Kyanite eclogite (*continued*)														
Domain 4														
3.2		136	11.2	0.09	14.5	0.2	18.8303	(1)	0.05500	(2)	333	(4)		
4.1		280	17.6	0.07	13.5	0.3	17.8518	(1)	0.05602	(2)	350	(4)		
8.2		127	7.2	0.06	14.0	0.04	18.1764	(1)	0.05371	(2)	345	(4)		
11.1	TE	333	20.5	0.06	15.6	<0.01	18.3431	(1)	0.05206	(2)	343	(4)		
13.1	TE	292	14.3	0.05	13.7	0.2	18.2430	(1)	0.05491	(2)	343	(5)		
21.1		93	3.4	0.04	9.9	0.08	18.7613	(1)	0.05377	(2)	334	(4)		
34.1	TE	115	6.5	0.06	12.8	<0.01	17.9997	(1)	0.05304	(3)	349	(4)		
37.1		245	17.4	0.07	11.3	0.3	18.5986	(2)	0.05524	(2)	337	(6)		
45.1	o	276	79.9	0.30	11.9	<0.01	20.0455	(2)	0.05225	(2)	314	(6)		
Sample GL03-120 Kyanite eclogite														
Domain 1														
1.1	TE	3	0.2	0.06	0.17	1.98	17.2526	(4)	0.06956	(19)	356	(15)		
1.2		1	0.1	0.09	0.30	3.84	8.9651	(4)	0.09306	(10)	657	(27)		
2.2	c?	21	1.5	0.07	2.48	0.77	17.3577	(1)	0.05990	(4)	358	(5)		
3.2	k,o TE	11	0.5	0.05	1.61	4.60	14.0252	(2)	0.09256	(5)	424	(8)		
5.2		1	0.0	0.04	0.17	2.64	9.61130	(6)	0.08223	(14)	622	(36)		
6.2		8	0.3	0.03	0.86	0.81	18.0991	(2)	0.05988	(7)	344	(7)		
7.2	TE	9	0.1	0.01	1.08	0.45	16.7351	(3)	0.05772	(6)	372	(11)		
8.2		19	0.4	0.02	2.38	0.13	16.3188	(2)	0.05540	(5)	383	(6)		
9.2	k,o	18	0.9	0.05	2.30	9.16	15.9279	(2)	0.12754	(3)	358	(6)		
10.1	o	27	11.8	0.46	1.63	5.41	13.9766	(2)	0.09903	(4)	422	(10)		
12.1		24	0.6	0.03	1.15	1.59	17.9075	(2)	0.06615	(4)	345	(7)		
20.1	o	20	0.4	0.02	2.30	0.33	17.3365	(2)	0.05645	(4)	360	(6)		
Domain 2														
2.1	c? TE	42	0.5	0.01	1.94	0.33	18.4192	(2)	0.05591	(4)	340	(5)		
4.1	TE	61	0.9	0.02	2.87	0.19	18.2682	(1)	0.05484	(4)	343	(5)		
4.2	TE	29	1.0	0.03	3.29	0.46	17.8343	(1)	0.05724	(4)	350	(5)		
5.1		67	0.7	0.01	3.23	0.22	17.7068	(1)	0.05535	(3)	353	(5)		
6.1	TE	104	1.9	0.02	4.90	0.08	18.1742	(1)	0.05402	(3)	345	(5)		
8.1	TE	88	1.4	0.02	4.19	0.24	18.1015	(1)	0.05535	(3)	346	(5)		
9.1	r TE	35	0.2	0.01	1.64	<0.01	18.0992	(2)	0.05225	(5)	347	(6)		
10.2		56	3.6	0.07	5.41	0.89	20.9611	(2)	0.05947	(4)	298	(6)		
12.2		25	0.2	0.01	2.90	0.09	17.4055	(1)	0.05452	(8)	360	(5)		
14.1		96	2.4	0.03	4.49	0.31	18.3603	(1)	0.05580	(3)	341	(5)		
15.1	g	118	2.8	0.02	5.72	0.04	17.7597	(1)	0.05391	(3)	353	(5)		
16.1	o	76	1.7	0.02	3.66	0.61	17.8975	(1)	0.05838	(3)	348	(5)		
17.1		114	2.6	0.02	5.46	0.20	17.9681	(1)	0.05510	(3)	348	(5)		
18.1		7	0.3	0.04	0.84	7.77	16.1292	(2)	0.11633	(5)	358	(9)		
19.1	TE	24	1.0	0.04	2.79	0.23	17.4684	(1)	0.05562	(4)	358	(5)		
Domain 3														
3.1		170	12.3	0.08	8.10	0.04	17.9844	(1)	0.05381	(2)	349	(4)		
7.1		194	25.3	0.14	9.36	<0.01	17.7917	(1)	0.05243	(2)	353	(4)		
11.1		174	16.2	0.10	8.37	0.00	17.9124	(1)	0.05347	(2)	350	(4)		
13.1	TE	264	18.8	0.07	12.21	0.09	18.5511	(1)	0.05395	(2)	338	(4)		
13.2		111	7.9	0.07	12.24	0.37	18.2874	(1)	0.05633	(2)	342	(4)		
21.1		73	10.6	0.15	7.85	0.43	18.6957	(1)	0.05665	(3)	334	(4)		
Sample GL03-184 Quartzofeldpsathic orthogneiss														
Domain 1														
1.1	TE	324	92.8	0.30	16.1	0.5	17.3238	(1)	0.05758	(2)	360	(4)		
5.1	TE	202	64.5	0.33	28.0	4.0	6.1996	(1)	0.10319	(1)	928	(13)		
13.1	TE	233	60.9	0.27	13.1	1.7	15.2980	(1)	0.06868	(2)	401	(6)		
13.2		286	89.4	0.32	27.0	3.4	9.1126	(1)	0.08917	(2)	650	(10)		
14.1	TE	162	43.5	0.28	9.2	0.8	15.1282	(1)	0.06118	(5)	410	(5)		
14.2		200	52.4	0.27	13.8	2.0	12.4985	(2)	0.07328	(3)	487	(8)		
15.1	TE	159	21.2	0.14	12.2	2.4	11.2600	(1)	0.07787	(1)	536	(6)		
19.1		280	63.3	0.23	28.1	3.6	8.5442	(2)	0.09214	(1)	689	(14)		
47.1		244	71.2	0.30	53.0	3.0	3.9549	(2)	0.11506	(1)	1414	(25)	1888	(13)

(*continued*)

TABLE 1. U-Pb GEOCHRONOLOGIC DATA AND APPARENT AGES (*continued*)

Spot[a]	inclusions[a]	U (ppm)	Th (ppm)	Th/U	$^{206}Pb^{*}$[b] (ppm)	$f^{206}Pb_c$[b c]	$^{238}U/^{206}Pb$[c]		$^{207}Pb/^{206}Pb$		$^{206}Pb/^{238}U$[d](Ma)		$^{207}Pb/^{206}Pb$[d] (Ma)
Sample GL03-184 Quartzofeldpsathic orthogneiss (*continued*)													
Domain 2													
6.1	TE	124	46.2	0.39	6.2	0.4	17.0305	(2)	0.05751	(2)	366	(6)	
7.1	TE	3	0.04	0.01	0.2	1.4	16.2067	(4)	0.06551	(14)	381	(16)	
7.2		4	0.03	0.01	0.2	9.8	15.6155	(4)	0.13306	(10)	362	(16)	
12.2	o,g	3	0.25	0.08	0.2	3.5	17.2523	(5)	0.08173	(14)	351	(17)	
29.1	g	4	0.13	0.03	0.2	11.3	16.2505	(5)	0.14455	(11)	342	(19)	
35.1		10	0.41	0.04	0.5	0.3	16.4840	(4)	0.05649	(11)	379	(13)	
37.1		6	0.17	0.03	0.3	<0.01	16.4580	(4)	0.05130	(15)	382	(16)	
43.1	o	8	0.28	0.04	0.4	1.4	18.3248	(4)	0.06439	(11)	338	(14)	
48.1	c	4	0.07	0.02	0.2	1.4	17.5268	(5)	0.06456	(16)	353	(18)	
Domain 3													
1.2		13	1.5	0.11	0.6	0.8	19.1802	(3)	0.05945	(9)	325	(9)	
2.1	TE	8	0.12	0.02	0.4	2.9	17.9329	(4)	0.07625	(9)	340	(13)	
2.2		13	0.21	0.02	0.6	2.0	17.4480	(3)	0.06915	(8)	352	(10)	
3.1		11	0.14	0.01	0.6	2.1	16.9297	(2)	0.07069	(8)	362	(9)	
3.2	TE	4	0.05	0.01	0.2	0.9	15.4718	(4)	0.06194	(19)	400	(18)	
4.1	TE	5	0.04	0.01	0.2	1.5	16.9509	(4)	0.06607	(12)	364	(14)	
4.2		4	0.03	0.01	0.2	4.1	15.8982	(4)	0.08726	(13)	378	(17)	
6.2		55	10.1	0.19	2.7	<0.01	17.2571	(2)	0.05207	(4)	364	(7)	
8.1	k,o TE	12	0.81	0.07	0.6	<0.01	17.9200	(2)	0.04963	(8)	352	(8)	
8.2		16	2.2	0.14	0.8	2.3	17.8174	(3)	0.07194	(7)	344	(9)	
9.1	TE	6	0.02	0.00	0.3	1.9	18.1714	(3)	0.06851	(11)	339	(11)	
9.2		4	0.02	0.01	0.2	4.7	16.4092	(4)	0.09171	(11)	364	(16)	
10.1		8	0.12	0.01	0.4	<0.01	16.9760	(3)	0.05264	(10)	370	(10)	
10.2		6	0.06	0.01	0.3	3.2	16.4499	(4)	0.07946	(11)	369	(14)	
11.1		4	0.04	0.01	0.2	0.4	16.4500	(4)	0.05733	(15)	379	(14)	
11.2		3	0.02	0.01	0.2	3.7	16.0642	(5)	0.08410	(13)	375	(18)	
12.1	o,g TE	3	0.21	0.07	0.2	2.9	17.8303	(4)	0.07670	(15)	342	(15)	
16.1		23	0.30	0.01	1.2	0.7	16.6155	(2)	0.05966	(7)	374	(8)	
17.1		61	0.74	0.01	3.0	0.6	17.3918	(2)	0.05830	(4)	358	(7)	
18.1	TE	9	0.19	0.02	0.4	4.7	17.2758	(3)	0.09125	(8)	346	(11)	
20.1	g	3	0.13	0.05	0.1	6.4	16.1649	(5)	0.10516	(15)	363	(20)	
21.1		4	0.04	0.01	0.2	4.0	15.9107	(4)	0.08609	(12)	378	(17)	
22.1		7	0.23	0.03	0.4	2.3	15.7130	(3)	0.07256	(9)	389	(13)	
23.1	TE	13	0.68	0.06	0.6	0.6	18.3922	(3)	0.05804	(9)	339	(9)	
24.1		14	1.6	0.11	0.7	2.3	18.0829	(3)	0.07161	(8)	339	(10)	
25.1		14	0.23	0.02	0.7	0.5	16.9423	(3)	0.05766	(9)	368	(12)	
26.1		12	0.26	0.02	0.6	0.2	17.7569	(3)	0.05551	(11)	352	(12)	
27.1		73	33.4	0.47	5.9	3.1	10.5927	(2)	0.08422	(3)	564	(11)	
28.1		9	0.66	0.08	0.4	1.0	17.6688	(4)	0.06181	(10)	351	(13)	
30.1		8	0.35	0.05	0.4	1.1	16.0044	(4)	0.06345	(12)	386	(16)	
32.1		19	0.29	0.02	0.9	1.7	17.4747	(3)	0.06738	(8)	353	(11)	
33.1		67	3.9	0.06	3.2	0.4	17.6772	(2)	0.05662	(4)	353	(7)	
34.1	o	6	0.47	0.08	0.3	3.4	17.0636	(4)	0.08133	(10)	355	(15)	
36.1		6	0.62	0.10	0.3	1.1	15.9388	(4)	0.06301	(12)	388	(17)	
38.1		5	0.46	0.11	0.2	0.6	15.7824	(5)	0.05976	(14)	394	(19)	
39.1	g	2	0.15	0.07	0.2	5.6	12.1027	(6)	0.10208	(14)	484	(31)	
40.1		8	0.73	0.10	0.4	<0.01	17.4619	(4)	0.05054	(13)	360	(14)	
41.1		14	1.67	0.13	0.9	4.4	12.4698	(4)	0.09220	(6)	476	(18)	
42.1		7	0.32	0.05	0.3	0.7	18.1535	(4)	0.05930	(12)	343	(14)	
44.1		9	0.14	0.02	0.4	0.2	16.8239	(4)	0.05579	(12)	371	(14)	
45.1		17	2.1	0.13	0.8	0.0	17.8632	(3)	0.05352	(8)	351	(11)	
46.1		6	0.24	0.04	0.3	4.5	16.6088	(4)	0.09007	(11)	360	(16)	

Note: Zircon analyses were performed on the SHRIMP-RG ion microprobe at the USGS-Stanford Ion Probe Laboratory at Stanford University. Calibration concentrations and isotopic compositions were based on replicate analyses of CZ3 (550 ppm U), and R33 (419 Ma; Black and others, 2003). Analytical routine followed Williams (1998). Data reduction utilized Ludwig (2001a).

[a] See text for discussion of domains. Spots labeled as grain number-analysis number. Abbreviations: k = kyanite, o = omphacite; c = coesite; g = garnet; r = rutile; TE = trace element analysis in same domain; see Table 2. Coesite is queried for grain 2 of sample 03-120 because the inclusion is not exposed at the mount surface.

[b] Pb^{*} denotes radiogenic Pb; Pb_c denotes common Pb; $f^{206}Pb_c = 100*(^{206}Pb_c/^{206}Pb_{total})$.

[c] Reported ratios are not corrected for common Pb. Errors are reported in parentheses as percent at the 1 σ level.

[d] $^{206}Pb/^{238}U$ ages calculated from ratios corrected for common Pb using ^{207}Pb. $^{207}Pb/^{206}Pb$ ages calculated from ratios corrected for common Pb using ^{204}Pb. Uncertainties in millions of years reported as 1σ.

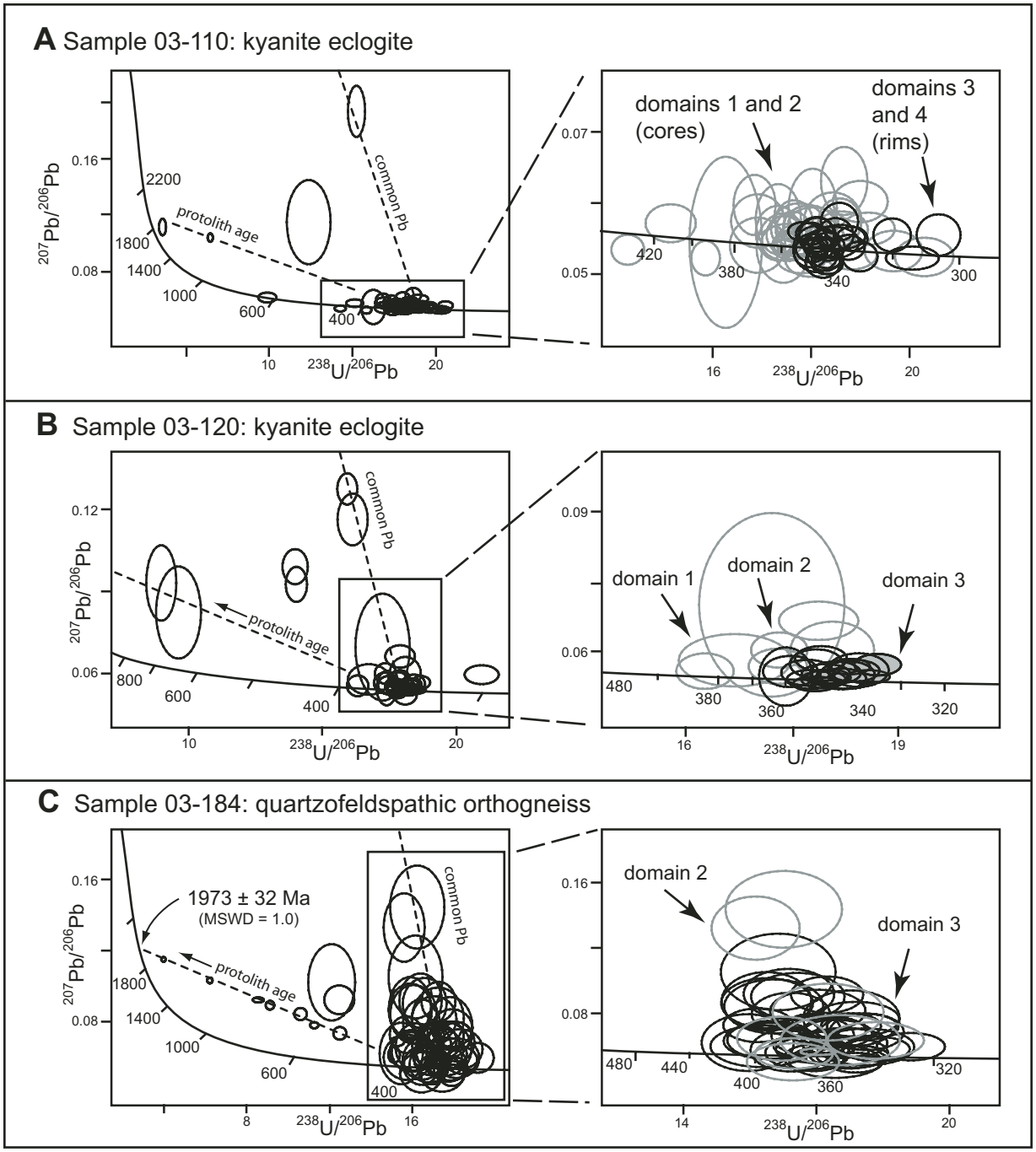

Figure 7. Tera-Wasserburg plots of sensitive high-resolution ion microprobe (SHRIMP) U-Pb data of zircon from kyanite eclogites (A) 03-110 and (B) 03-120, and (C) quartzofeldspathic host gneiss 03-184. Data are 1σ error ellipses uncorrected for common Pb. See text and Figure 8 for age interpretations. MSWD—mean square of weighted deviates.

$^{206}Pb/^{238}U$ age of 358 ± 9 Ma, with a mean square of weighted deviates (MSWD) of 2.7 (Fig. 8A). This age is within error of the 360 ± 5 Ma $^{206}Pb/^{238}U$ age reported from similarly low-U cores in zircon from a sample of kyanite eclogite, 434441, collected from the same pod at locality 03-109 (Fig. 3; Gilotti et al., 2004). Domain 2 contains inclusions of coesite, kyanite, omphacite, garnet, and rutile, has Th/U ratios of 0.003–0.10, and gives ages ranging from 310 to 438 Ma. The weighted mean $^{206}Pb/^{238}U$ age of domain 2 is 350 ± 4 Ma (MSWD = 2.5), after rejecting the two oldest and three youngest analyses on the basis of inheritance and Pb loss, respectively. Domains 3 and 4 distinguished in CL as having intermediate- and high-U con-

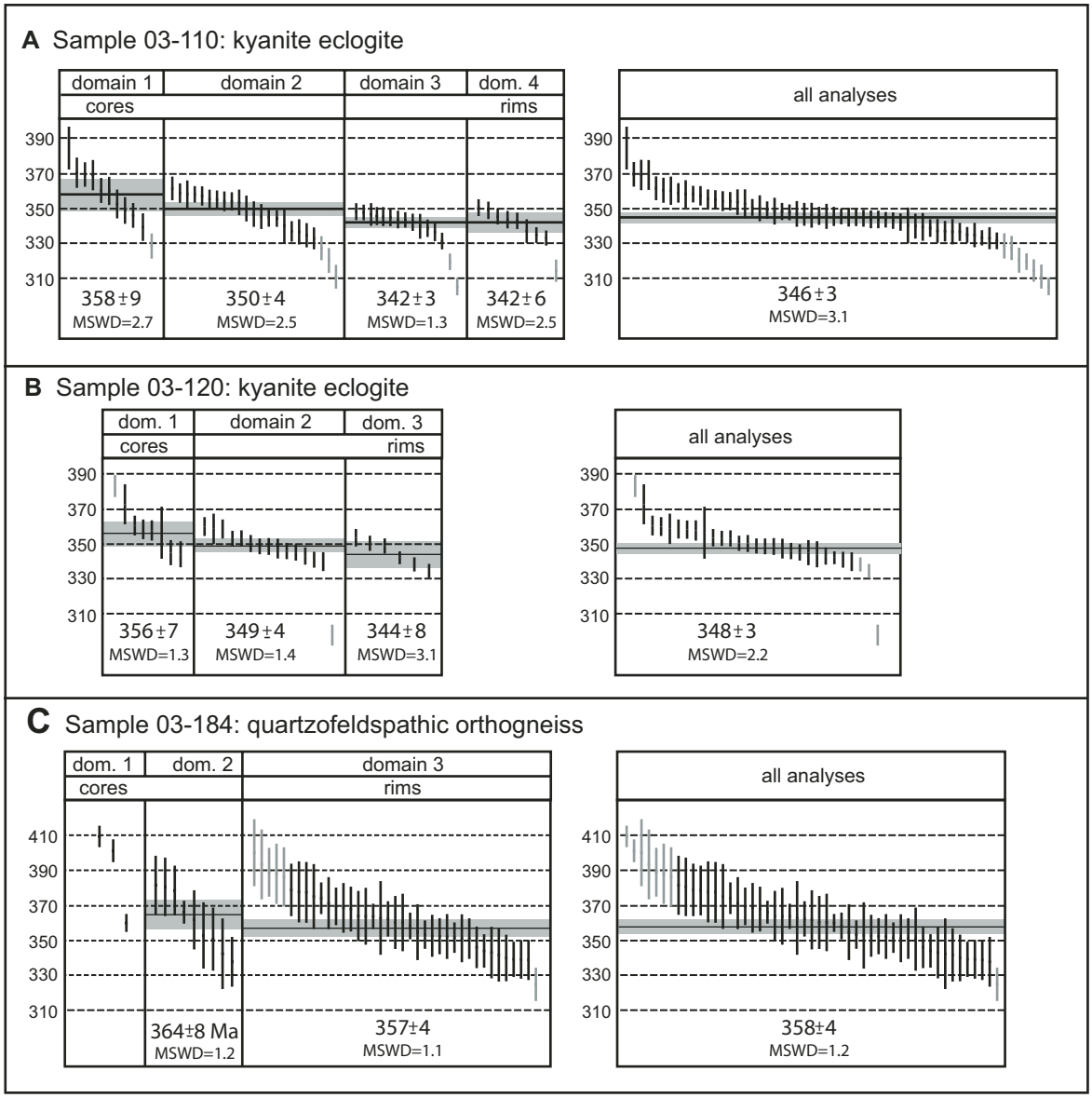

Figure 8. $^{206}Pb/^{238}U$ ages (in Ma) for kyanite eclogites (A) 03-110 and (B) 03-120, and (C) quartzofeldspathic host gneiss 03-184. Data are ^{207}Pb corrected, plotted with 1σ error bars, and sorted by age. Plots to the left show data separated according to cathodoluminescence (CL) domain and cite the weighted mean $^{206}Pb/^{238}U$ ages (95%confidence level), calculated with analyses shown in pale gray excluded. Plots on the right show the entire range of Caledonian ages within each sample. MSWD—mean square of weighted deviates.

centrations collectively give ages ranging from 305 to 350 Ma, with no significant difference in weighted mean age (342 ± 3 versus 342 ± 6 Ma; Fig. 8A) or Th/U ratio between the two domains. Assuming that the three youngest ages reflect Pb loss or younger rim growth during retrogression, the remaining 20 analyses from both domains 3 and 4 give a weighted mean $^{206}Pb/^{238}U$ age of 342 ± 3 Ma (MSWD = 1.6). Comparison of core domains 1 and 2 with rim domains 3 and 4 shows a systematic shift from older to younger ages (Figs. 7A and 8A). All analyses yield a weighted mean $^{206}Pb/^{238}U$ age of 346 ± 3 Ma (MSWD = 3.1).

Subspherical zircons separated from kyanite eclogite sample 03-120 are similar in character to those from 03-110, but have only three discernible CL domains (Fig. 6B). Domain 1 consists of low-U cores (1–27 ppm) that are not preserved in all grains (e.g., grain 4, Fig. 6B). The cores are mantled by zircon of intermediate-U concentration (7–118 ppm) assigned to domain 2. This domain is in turn overgrown by higher-U rims (73–264 ppm) of domain 3. The general core-to-rim increase in U concentration is matched by a general increase in Th concentration from 0.03 to 20 ppm, such that Th/U ratios of 0.005–0.46 are relatively constant throughout. Domain 1 contains kyanite and omphacite

inclusions, while the intermediate-U domain 2 encloses kyanite, omphacite, and garnet. The coesite inclusion in sample 03-120 (grain 2, Fig. 6B) was not exposed during polishing, so the coesite-bearing domain is not definitively known. Calculated $^{206}Pb/^{238}U$ ages from all domains range from 298 to 657 Ma (Figs. 7B and 8B). Excluding the five oldest core ages, which are interpreted to record mixing of protolith and metamorphic zircon signatures, domain 1 gives a weighted mean $^{206}Pb/^{238}U$ age of 356 ± 7 Ma (MSWD = 1.3). With the exclusion of the one anomalously young age, analyses from domain 2 provide a weighted mean age of 349 ± 4 Ma (MSWD = 1.4). The high-U rims of domain 3 yield a similar weighted mean age of 344 ± 8 Ma (MSWD = 3.1). Although there is a core-to-rim decrease in observed mean age, the significance cannot be assessed due to the overlapping errors for each domain (Fig. 8B). All analyses give a weighted mean $^{206}Pb/^{238}U$ age of 348 ± 3 Ma (MSWD = 2.2). The presence of similar inclusions in domains 1 and 2 indicates little change in metamorphic conditions during zircon growth or recrystallization, perhaps indicating that this sample remained at eclogite-facies conditions at least until 349 ± 4 Ma.

The quartzofeldspathic host gneiss sample, 03-184, yields subspherical grains with multiple CL domains (Fig. 6C), which are subdivided into high-U cores (domain 1; 159–324 ppm), low-U cores and mantles (domain 2; 3–124 ppm), and low-U rims (domain 3; 2–73 ppm). Some grains have oscillatory zoned higher-U domain 1 cores overgrown by distinct low-U rims of varying thickness, which are assigned to domain 3 (grain 15; Fig. 6C). Others show a gradation from well-defined cores, to cores with a network of lower-U veins and patchy, cloudy zones, which are attributed to recrystallization (grains 2, 42, and 44; Fig. 6C). Grains that appear as homogeneous lower-U grains are assigned to domain 2 (grains 7 and 48; Fig. 6C). The homogeneous low-U grains may represent either total recrystallization of igneous zircon, growth of metamorphic zircon, or both. Distinction between low-U grains of domain 2 and low-U rims of domain 3 becomes somewhat arbitrary as the rims thicken. The high-U cores have Th/U ratios of 0.14–0.33 characteristic of igneous zircon and $^{206}Pb/^{238}U$ ages ranging from 401 to 1414 Ma—excepting one younger age of 360 Ma (Figs. 7C and 8C). Regression of the six oldest data yields concordia intercept ages of 1973 ± 32 and 395 ± 19 Ma (MSWD = 1.0), respectively (Fig. 7C). The upper intercept age is interpreted as the emplacement age of the igneous protolith. Low-U grains assigned to domain 2 have Th/U ratios of 0.01–0.39, give $^{206}Pb/^{238}U$ ages ranging from 338 to 382 Ma and a weighted mean age of 364 ± 8 Ma (MSWD = 1.2). Coesite, omphacite, and garnet inclusions are observed in domain 2. Distinct low-U zircon rims of domain 3 contain inclusions of kyanite, omphacite, and garnet. Forty-three analyses of the domain 3 rims yield Th/U ratios of 0.004–0.47 and $^{206}Pb/^{238}U$ ages of 325–400 Ma, plus three older ages between 476 and 564 Ma. Inferring that the eight oldest rim ages represent mixtures of protolith and Caledonian zircon and the youngest age reflects Pb loss, the remaining 33 analyses give a weighted mean $^{206}Pb/^{238}U$ age of 357 ± 4 Ma (MSWD = 1.1) (Fig. 8C). The combined weighted mean $^{206}Pb/^{238}U$ age calculated for domains 2 and 3 is 358 ± 4 Ma (MSWD = 1.2).

SHRIMP-RG TRACE-ELEMENT ANALYSIS

Analytical Methods

Trace-element analyses for P, Y, REEs, Hf, Th, and U in zircon were carried out with the SHRIMP-RG using similar primary current and spot size to that used for U-Pb age determinations. In addition, by closing the Yα and collector slits, mass resolution was increased from M/ΔM = 6500–9500 to resolve the REE element peaks from interfering oxides (e.g., $^{141}Pr^{16}O$ from ^{157}Gd, and all comparable pairs).

The elemental peaks for ^{30}Si, P, Y, ^{96}Zr, ^{139}La, ^{140}Ce, ^{146}Nd, ^{147}Sm, ^{153}Eu, ^{157}Gd, Th, and ^{238}U were measured; for Pr, ^{163}Dy, ^{166}Er, ^{172}Yb, ^{175}Lu, and ^{180}Hf, the larger oxide peaks were measured. For each element, the average raw count rate for three measurement cycles was normalized to the average Si count rate and corrected for natural isotopic abundance. Periodic measurements of standard zircon from the Mud Tank carbonatite, Australia (Hoskin and Ireland, 2000), were compared to general calibration curves derived from analyses of NIST 611 glass (Pearce et al., 1997) to derive specific calibration factors for each element and to eliminate any matrix effect differences between the glass and zircon standards. Chondrite-normalized REE plots presented in Figure 9 use the chrondrite REE abundances of Anders and Grevesse (1989) multiplied by a factor of 1.36 (Korotev, 1996).

Results

Trace-element data from the three samples (Table 2) were collected from the same CL domains used in collection and interpretation of the U-Pb data; i.e., spot analyses for trace elements were made adjacent to but within the same domains as spots used for U-Pb analysis, as noted in Table 1. Chondrite-normalized REE values are plotted by domain in Figure 9. The trace-element patterns and variations discussed in the following are consistent with, but expand upon, earlier results reported from laser ablation–inductively coupled plasma–mass spectrometry (LA-ICP-MS) analyses of zircon from a kyanite eclogite on Rabbit Ears Island (Gilotti et al., 2004). SHRIMP-RG was used for this study due to its ability to analyze a smaller volume of material, and thus allow for better spatial resolution among CL domains than LA-ICP-MS. In general, all the samples have trace-element abundances and patterns characteristic of eclogite-facies metamorphic zircon (Rubatto, 2002; Hoskin and Schaltegger, 2003).

Three analyses of the low-U domain 1 cores in sample 03-110 show slightly negative to no Eu anomaly (Eu/Eu* = 0.4–0.9) and HREE patterns with $Lu_{(N)}/Gd_{(N)}$, calculated with chondrite-normalized values, ranging from 24 to 43 and $Lu_{(N)}$ = 25–43 (Fig. 9A). Domain 2, with intermediate-U concentra-

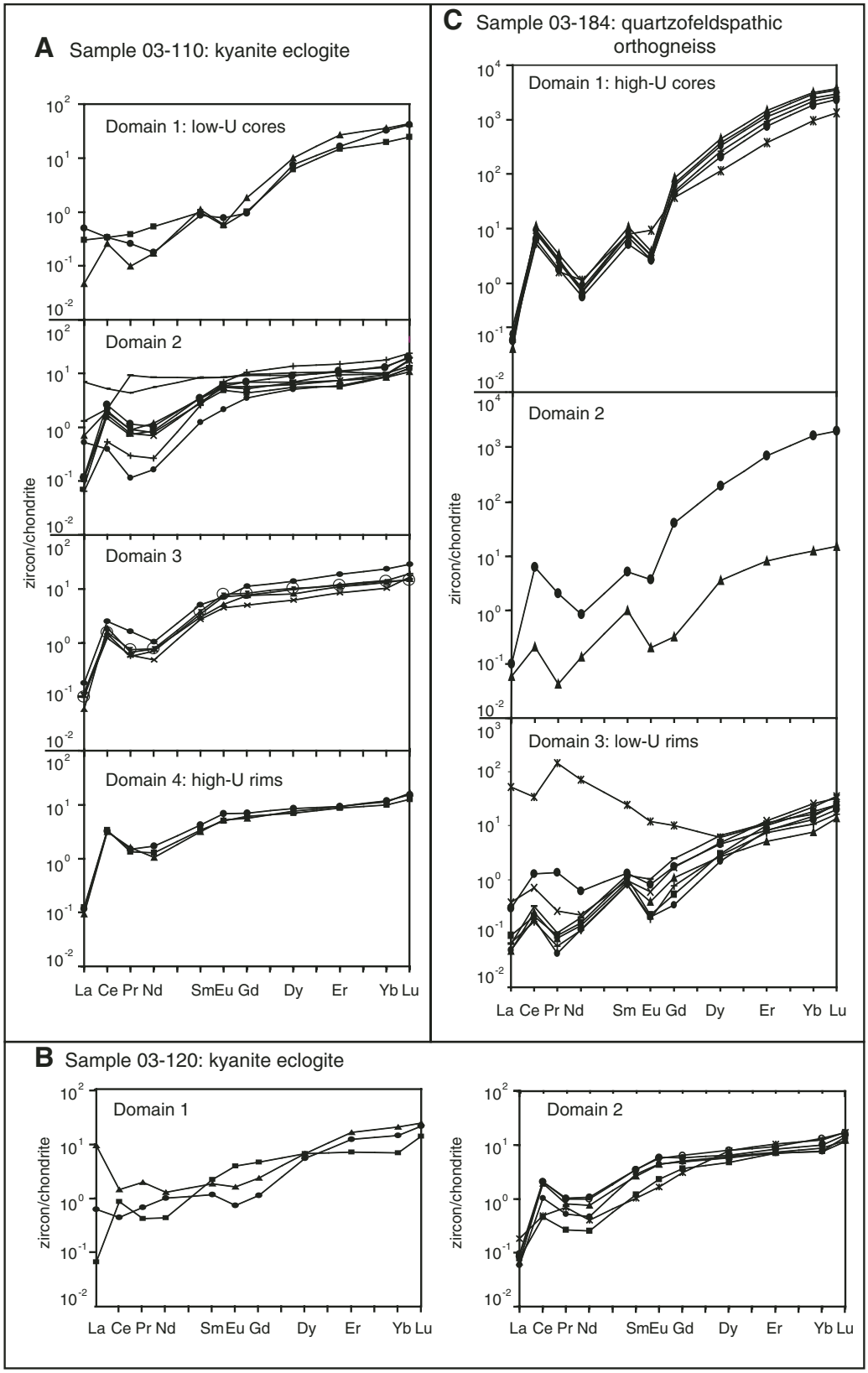

Figure 9. Chondrite-normalized rare earth element (REE) patterns for the different cathodoluminescence (CL) domains of zircons in the three U-Pb dated samples. Note the trend toward more consistent and flatter heavy (H) REE patterns toward the rims, as well as the absence of a Eu anomaly in the rims of the eclogites (03-110 and 03-120).

TABLE 2. ZIRCON TRACE ELEMENT DATA

Spot[a]	La	Ce	Nd	Sm	Eu	Pr	Gd	Dy	Er	Yb	Lu	Eu/Eu*	$Lu_{(N)}$[b]	$\frac{Lu_{(N)}}{Gd_{(N)}}$	P	Y	Hf	Th	U	U[c]
Sample GL03-110	Kyanite eclogite																			
Domain 1																				
6.1	0.10	0.28	0.33	0.20	0.04	0.05	0.27	2.00	3.20	4.32	0.81	0.6	25	24	32.5	12.3	19800	0.28	14	360
14.1	0.16	0.27	0.11	0.18	0.06	0.03	0.25	2.48	3.57	7.19	1.35	0.9	41	43	34.2	13.0	20500	0.55	9	28
32.1	0.01	0.21	0.11	0.22	0.04	0.01	0.48	3.28	5.80	7.85	1.42	0.4	43	24	19.2	19.7	15520	0.21	16	35
Domain 2																				
2.1	0.02	0.44	0.16	0.52	0.53	0.04	2.82	4.55	3.22	3.94	0.79	1.3	24	2	31.0	13.9	21100	0.18	100	127
3.1	0.04	2.16	0.64	0.69	0.44	0.14	1.83	2.95	2.33	2.80	0.64	1.2	19	3	26.6	10.0	19340	1.95	133	344
4.1	0.17	0.32	0.10	0.25	0.17	0.01	0.94	1.70	1.29	1.97	0.40	1.0	12	3	22.2	6.2	17400	0.09	40	35
5.1	0.04	1.55	0.49	0.57	0.37	0.11	1.16	1.85	1.23	1.92	0.41	1.4	13	3	24.4	6.2	20180	0.55	80	46
9.1	2.22	4.24	3.43	1.68	0.65	0.53	2.56	3.38	2.31	3.01	0.65	0.9	20	2	21.7	10.5	16650	7.72	287	160
15.1	0.04	1.40	0.44	0.58	0.42	0.09	1.41	2.27	1.59	2.11	0.58	1.4	18	3	26.6	7.4	20230	0.48	69	81
16.1	0.02	1.17	0.49	0.66	0.46	0.08	1.77	2.18	1.95	2.04	0.56	1.3	17	3	27.5	7.9	19750	0.32	64	39
33.1	0.42	1.82	5.22	1.67	0.65	1.13	2.45	3.04	2.31	2.21	0.46	1.0	14	2	22.1	9.6	18,570	0.25	53	10
35.1	0.23	1.65	0.73	0.69	0.43	0.11	1.53	2.06	1.59	1.88	0.36	1.3	11	2	25.4	7.3	19,210	0.67	84	48
Domain 3																				
7.1	0.05	1.99	0.62	0.99	0.53	0.19	2.93	4.47	3.99	5.13	0.93	0.9	28	3	26.8	17.2	16470	0.87	112	152
10.1	0.03	1.28	0.47	0.76	0.59	0.09	2.24	3.33	2.51	3.07	0.48	1.4	15	2	26.8	11.6	19450	0.42	80	40
19.1	0.03	0.97	0.28	0.53	0.33	0.07	1.31	2.00	1.80	2.23	0.54	1.2	16	3	24.5	7.5	18600	0.29	71	63
22.1	0.04	1.15	0.42	0.67	0.53	0.06	1.99	3.16	2.55	3.11	0.63	1.4	19	3	24.8	9.3	21540	0.63	116	51
28.1	0.02	1.50	0.45	0.58	0.38	0.08	1.98	2.61	2.34	2.86	0.49	1.1	15	2	27.6	9.2	18220	0.42	92	70
Domain 4																				
11.1	0.03	2.61	0.65	0.63	0.40	0.19	1.49	2.50	2.00	2.52	0.55	1.2	17	3	26.4	8.1	18340	5.66	178	333
13.1	0.04	2.66	1.04	0.84	0.52	0.18	1.89	2.79	2.01	2.65	0.51	1.2	15	2	26.7	9.2	19980	6.01	219	292
34.1	0.04	2.79	0.79	0.67	0.39	0.16	1.64	2.28	1.90	2.19	0.42	1.1	13	2	24.9	7.6	17440	7.31	179	115
Sample GL03-120	Kyanite eclogite																			
Domain 1																				
1.1	2.90	1.16	0.77	0.36	0.12	0.23	0.62	2.13	3.47	4.42	0.78	0.8	24	10	30.8	12.7	19660	0.30	5	3
3.1	0.20	0.35	0.60	0.23	0.05	0.08	0.30	1.77	2.55	3.08	0.69	0.6	21	19	24.5	9.0	19840	0.17	7	11
7.1	0.02	0.69	0.26	0.43	0.29	0.05	1.20	2.15	1.48	1.48	0.45	1.2	14	3	21.4	6.5	22110	0.28	32	9

(continued)

TABLE 2. ZIRCON TRACE ELEMENT DATA *(continued)*

Spot[a]	La	Ce	Nd	Sm	Eu	Pr	Gd	Dy	Er	Yb	Lu	Eu/Eu*	$Lu_{(N)}$[b]	$\frac{Lu_{(N)}}{Gd_{(N)}}$	P	Y	Hf	Th	U	U[c]
Sample GL03-120	Kyanite eclogite *(continued)*																			
Domain 2																				
2.1	0.02	0.84	0.29	0.58	0.34	0.06	1.31	1.91	1.54	1.66	0.39	1.2	12	2	20.6	6.0	22220	0.25	27	42
4.1	0.03	1.72	0.67	0.70	0.45	0.13	1.57	2.16	1.84	2.22	0.52	1.3	16	3	25.7	7.3	22450	0.55	52	61
6.1	0.02	1.61	0.47	0.53	0.34	0.10	1.35	2.03	1.60	1.95	0.40	1.2	12	2	21.8	6.8	20340	0.48	58	104
8.1	0.03	1.66	0.59	0.67	0.43	0.12	1.70	2.60	1.98	2.94	0.56	1.2	17	3	27.5	9.0	20400	0.61	63	88
9.1	0.02	0.38	0.16	0.24	0.18	0.03	0.99	1.59	1.52	1.73	0.47	1.1	14	4	24.0	6.9	21360	0.30	22	35
19.1	0.06	0.41	0.25	0.21	0.13	0.08	0.82	2.63	2.29	2.74	0.57	0.9	17	6	23.9	10.6	21350	0.3	6	24
Domain 3																				
13.1	0.05	2.68	0.96	0.73	0.40	0.17	1.56	1.98	1.81	1.89	0.37	1.1	11	2	19.6	7.9	12840	7.5	132	264
Sample GL03-184	Quartzofeldspathic orthogneiss																			
Domain 1																				
1.1	0.03	5.10	0.34	1.04	0.20	0.22	11.71	70	167	408	77	0.2	2320	53	256	597	13040	22	123	324
5.1	0.02	9.00	0.64	2.15	0.29	0.41	22.68	146	319	701	124	0.1	3750	44	282	841	20960	35	190	202
13.1	0.03	7.22	0.51	1.67	0.24	0.31	18.23	123	282	642	114	0.1	3460	51	267	754	20020	28	167	233
14.1	0.04	7.63	0.44	1.62	0.24	0.33	16.52	111	248	548	98	0.1	2980	48	231	669	20670	25	165	162
15.1	0.03	4.38	0.69	1.59	0.71	0.20	9.91	38	82	207	44	0.5	1330	36	101	231	12630	8.7	116	159
16.1	0.05	6.81	0.42	1.37	0.20	0.30	13.15	88	203	483	89	0.1	2680	54	188	545	20880	24	145	nd
Domain 2																				
6.1	0.03	4.93	0.51	0.99	0.27	0.24	10.61	63	150	359	67	0.3	2020	51	150	387	17140	15	76	55
7.1	0.02	0.17	0.08	0.20	0.02	0.01	0.08	1.15	1.73	2.72	0.49	0.4	15	47	28.0	7.0	23000	0.01	2	4
Domain 3																				
2.1	0.09	1.04	0.38	0.26	0.06	0.16	0.47	1.49	1.78	2.88	0.66	0.5	20	11	26.5	7.3	22900	0.11	6	8
3.1	0.02	0.20	0.09	0.18	0.03	0.01	0.29	0.88	1.11	1.67	0.46	0.4	14	13	19.3	4.2	23540	0.06	4	4
4.1	0.03	0.17	0.09	0.21	0.02	0.01	0.14	0.99	2.21	4.07	0.81	0.3	25	47	24.3	6.6	22680	0.03	3	4
8.1	16.80	28.11	44.54	4.90	0.90	17.40	2.67	2.02	2.34	5.01	1.15	0.8	35	3	28.7	7.5	24830	1.2	9	12
9.1	0.02	0.14	0.07	0.16	0.01	0.01	0.20	0.93	1.60	2.38	0.54	0.2	16	22	25.8	5.4	24080	0.04	3	4
12.1	0.02	0.15	0.07	0.16	0.02	0.01	0.09	0.72	1.74	3.35	0.83	0.4	25	75	26.6	5.2	25910	0.01	2	3
18.1	0.12	0.58	0.14	0.19	0.05	0.03	0.45	1.59	2.63	5.68	1.07	0.5	32	19	28.5	9.1	24460	0.36	5	9
23.1	0.02	0.26	0.12	0.24	0.08	0.01	0.65	2.16	2.44	3.66	0.79	0.6	24	10	27.1	8.7	28130	0.35	9	13

Note: All analyses were performed on the SHRIMP-RG ion microprobe at the USGS-Stanford Ion Probe Laboratory at Stanford University. All abundances expressed in ppm.

[a]Grain numbers and domains are the same as in Table 1.

[b]$Lu_{(N)}$ and $Gd_{(N)}$ values are chondrite-normalized.

[c]U concentration determined from domain by CZ3 during U/Pb analysis.

tions, is characterized by higher and more variable light (L) REE values, slightly positive to no Eu anomalies (Eu/Eu* = 0.9–1.4), generally positive Ce anomalies, and flat HREE patterns ($Lu_{(N)}/Gd_{(N)}$ = 2–4; $Lu_{(N)}$ = 11–24). Patterns observed for domains 3 and 4 are more systematic (Fig. 9A). The domains lack a negative Eu anomaly (Eu/Eu* = 0.9–1.4), have well-defined positive Ce anomalies, and flat HREE patterns ($Lu_{(N)}/Gd_{(N)}$ = 2–3; $Lu_{(N)}$ = 13–28). The variation observed in the REE patterns coincides reasonably well with the different CL domains.

Domain 1 zircon cores from kyanite eclogite 03-120 have characteristics similar to those observed in the previous sample: variable REE abundances, negative to no Eu anomaly (Eu/Eu* = 0.6–1.4), and flat HREE patterns ($Lu_{(N)}/Gd_{(N)}$ = 3–19; $Lu_{(N)}$ = 14–24). Patterns in domain 2 are more systematic, and are characterized by the absence of a Eu anomaly (Eu/Eu* = 0.9–1.3), positive Ce anomalies, and flat HREE patterns ($Lu_{(N)}/Gd_{(N)}$ = 2–6; $Lu_{(N)}$ = 11–17). No trace-element analyses were obtained from high-U rims of domain 3.

The REE signatures from zircons within the quartzofeldspathic gneiss are markedly different than those from the kyanite eclogites. The high-U cores of domain 1 have enriched HREE ($Lu_{(N)}/Gd_{(N)}$ = 36–54; $Lu_{(N)}$ = 1332–3751) and well-developed positive Ce anomalies and negative Eu anomalies (Eu/Eu* = 0.1–0.5). Domain 2 analyses are transitional between domains 1 and 3. Domain 3 has markedly depleted HREE ($Lu_{(N)}/Gd_{(N)}$ = 3–75; $Lu_{(N)}$ = 14–35) and smaller positive Ce anomalies and negative Eu anomalies (Eu/Eu* = 0.2–0.8). Domain 1 patterns are attributed to an igneous protolith signature, whereas domains 2 and 3 record growth and recrystallization during metamorphism.

DISCUSSION

The results of both the U-Pb and trace-element analyses on coesite-bearing zircon suites examined in this study generally vary as a function of CL domains, which in turn reflect a general variation in U concentration. In addition to establishing the timing of UHP metamorphism in North-East Greenland, interpretation of the results addresses several issues concerning the significance of U-Pb ages obtained for UHP rocks in other settings. These include: (1) to what extent do the metamorphic zircons represent recrystallization of existing zircons versus new zircon growth by precipitation, and (2) does the considerable spread in U-Pb ages observed from some UHP metamorphic zircons represent analytical scatter or geologically meaningful variation in age?

Recrystallization versus New Growth

Metamorphic zircon forms either by growth of new zircon or recrystallization of pre-existing zircon (Hoskin and Schaltegger, 2003, and references therein). In this study, growth of zircon as new grains and rims on xenocrystic cores is clearly established from inclusions of coesite, as well as kyanite, garnet, and omphacite, within the grains. New zircon must trap coesite during UHP metamorphism, because the coesite-to-quartz transition is thought to be extremely rapid. Experimental and theoretical considerations (Mosenfelder and Bohlen, 1997; Perrillat et al., 2003) predict that 100-μm-sized coesite crystals will transform to quartz in less than 1 m.y. at temperatures below 400 °C. Lenze et al. (2005) considered the transformation to be quasi-instantaneous on geologic time scales, based on experiments where coesite reverts to quartz within hours after rapid decompression from 3 GPa to 2.7 GPa at 800 °C. Once grown, zircon protects coesite inclusions from fluid infiltration that would have led to its transformation during high-temperature decompression (Mosenfelder et al., 2005). Complications may arise when quartz inclusions within igneous zircon are present (e.g., Gebauer et al., 1997), but in all cases, the timing of UHP metamorphism will be same or younger than the age of zircon that encloses the coesite. For the North-East Greenland samples, we unequivocally equate the presence of coesite inclusions with zircon growth at UHP conditions. New zircon formed through precipitation from anatectic melts, metamorphic fluids, or through subsolidus net-transfer reactions is not expected to contain inherited components. Therefore, the age of coesite-bearing zircon is interpreted to record the timing of zircon growth at UHP conditions.

Recrystallization of protolith zircon is signified by the retention of older isotopic or trace-element signatures (e.g., Rubatto, 2002; Puga et al., 2005). All of the samples in this study contain zircon grains with remnants of xenocrystic cores that record a Paleoproterozoic protolith age (Fig. 7). Inherited cores are best preserved in the host gneiss 03-184. CL textures, U-Pb ages, and REE analyses clearly record variable recrystallization of pre-existing zircon with new rim overgrowths (Fig. 6C). The core-to-rim variation in REE patterns in the host gneiss sample exemplifies the depletion of HREE, slightly negative to absent Eu anomaly, and persistent positive Ce anomaly that is characteristic of zircon recrystallized at subsolidus, high-grade metamorphic conditions (Hoskin and Black, 2000; Rubatto, 2002). In addition to the older ages obtained from the core region, five low-U rim analyses give older U-Pb ages (older than 390 Ma) and are interpreted to reflect an inheritance signature due to incomplete recrystallization. Similarly, a small number of low-U domain 1 cores in the kyanite eclogite samples yield older U-Pb ages thought to be a memory effect. Zircon suites from all three of the samples are interpreted to record both processes: recrystallization and new growth.

Spread in U-Pb Ages

The U-Pb ages vary smoothly from 370 to 330 Ma for kyanite eclogite and 390–330 Ma for the host gneiss (Fig. 8). The observed variation may be explained by analytical scatter, combined effects of inheritance and Pb loss, or a true variation in age. The 40–60 m.y. range in ages is not attributed to analytical

scatter, since the variation is similar in all samples, regardless of U concentration. There is a distinct break at the upper end of the range to older ages that clearly represent inheritance signatures. Similarly, younger ages that clearly reflect Pb loss or new growth during amphibolite-facies retrograde metamorphism are recognized as outliers in all of the samples (Fig. 8). For the remaining analyses, the mean ages of the various domains do decrease from core to rim as expected, although the domain ages generally overlap within analytical uncertainty. The REE patterns and inclusion suites indicate that the domains are unique as well. Data from kyanite eclogite sample 03-110 indicate that the low-U domain 1 cores record recrystallization and zircon growth during prograde eclogite-facies metamorphism at ca. 360 Ma. The disappearance of the slightly negative Eu anomaly between domains 1 and 2 may reflect complete removal of plagioclase during eclogitization. The appearance of coesite in the domain 2 zircon that mantles the low-U cores (Fig. 6A) establishes that the UHP metamorphism was ongoing at 350 ± 4 Ma. Subsequent rim growth occurred at 342 ± 4 Ma, perhaps in part during amphibolite-facies retrograde metamorphism. This progression of ages combined with the REE data is interpreted to record a true variation in zircon growth and recrystallization at eclogite-facies conditions at least to 350 Ma. The coesite-bearing domain from the host gneiss gives an older age of 364 ± 8 Ma. The difference in ages over relatively short distances as a function of lithology suggests that the timing of zircon recrystallization and growth varied according to fluid availability and zircon-forming net-transfer reactions. Assuming the range in ages is geologically meaningful, UHP metamorphism in North-East Greenland was ongoing by 370 Ma and continued through 350 Ma.

Geochronologic Implications

The inclusion suites in conjunction with the U-Pb and REE data indicate that the CL domains observed in the UHP zircons resulted from both new growth and recrystallization. Recrystallized zircon can give a mixed protolith plus metamorphic U-Pb signature, but this is much less likely for newly grown domains that contain eclogite-facies inclusions. Using this study as an example, this distinction generally cannot be made on the basis of U concentration or Th/U ratio. Nevertheless, ion microprobe techniques provide the spatial resolution to isolate domains of new growth from xenocrystic cores, as well as to recognize zones that record memory effects of the protolith due to incomplete recrystallization. The observed range in U-Pb ages in the Greenland eclogite-facies zircons is interpreted to reflect long-lived zircon crystallization and growth. The weighted mean of the entire range in this case masks the geological significance of the age spread.

The general differences between secondary ion mass spectrometry (SIMS) and isotope-dilution thermal-ionization mass spectrometry (ID-TIMS) analytical techniques are well documented and generally accepted (e.g., Davis et al., 2003; Parrish and Noble, 2003). In essence, there is a tradeoff between spatial resolution and precision. ID-TIMS analyses can establish a high-precision mean age for the timing of zircon recrystallization and growth, but it is difficult to avoid or isolate inheritance signatures that result from dissolution of xenocrystic material or partially recrystallized domains. SIMS analyses can spatially isolate different domains but have difficulty in establishing high-precision ages necessary to resolve slight variations in age. As an example, Root et al. (2004) argued that the observed 40 m.y. spread in SHRIMP ages on zircon from the Western Gneiss Region in Norway reflects inheritance. The inferred age for UHP metamorphism of 405–400 Ma is based on interpretation of slightly discordant chemical abrasion ID-TIMS data (see Mattinson, 2005, for analytical method). As illustrated by this study, the age variability defined by SHRIMP analyses may in fact record continuous zircon growth and recrystallization over a long time span. In this case, the ID-TIMS data would record the mean age of the zircon, with the slight discordance reflecting the memory effects of incompletely recrystallized protolith zircon.

Tectonic Implications

The long residence time at eclogite-facies conditions proposed for UHP rocks in the Greenland Caledonides differs substantially from the rapid subduction (Kaneko et al., 2003) and exhumation demonstrated for other UHP terranes (e.g., Hacker et al., 2003; Rubatto and Hermann, 2001; Lapen et al., 2003). The fast rates fit models incorporating return-flow concepts in a subduction channel to explain rapid exhumation (e.g., Chemenda et al., 1996). The long residence time at eclogite-facies conditions in the North-East Greenland eclogite province suggests that UHP terranes in the overriding plates of collisional orogens may be formed and exhumed by different mechanisms than those in the downgoing plate. Gilotti et al. (2004) showed that the North-East Greenland eclogite province experienced high-pressure metamorphism at ca. 410–390 Ma, but only the oldest ages observed in the host gneiss zircons in this study are consistent with this age. In this study, it was not possible to distinguish between recrystallized zones with slight retention of older components and new growth as early as 400 Ma in the UHP zircons. This may, however, be the case for the host gneiss sample (Fig. 8). If the 385–410 Ma ages that were rejected in calculation of the weighted mean ages in fact do not contain inheritance, the age range over which the UHP terrane experienced eclogite-facies conditions would be extended to ca. 400–350 Ma. Nevertheless, our interpretation of the combined U-Pb, REE, and inclusion suite data is that the UHP rocks in the North-East Greenland eclogite province stayed at eclogite-facies high-pressure to UHP conditions for 10–20 m.y.

CONCLUSIONS

The combined results of the SHRIMP U-Pb and REE analyses, and inclusion suite analysis on kyanite eclogite and host gneiss samples suggest that UHP metamorphic zircon

forms due to both recrystallization of protolith zircons and new growth. Although a few older ages represent incomplete resetting during recrystallization, the span of 370–350 Ma ages from kyanite eclogite is inferred to record continuous growth and thus residence time at eclogite-facies to UHP conditions. The older age span observed for the host gneiss indicates that new zircon growth initiated at least 10 m.y. earlier in the host gneisses than in kyanite eclogites. Variations in ages observed in UHP terranes may, therefore, reflect differences in bulk composition rather than differences in timing of metamorphism. The long residence times indicated for the North-East Greenland eclogites are interpreted to be indicative of UHP metamorphism within the overriding plate of a collisional orogen.

ACKNOWLEDGMENTS

National Science Foundation grants to Gilotti (EAR-0208236) and McClelland (EAR-0208158) supported the field work and analytical work, respectively. We are grateful to the Danish Polar Center for coordinating the logistics for the field work, and to the staff at the Danmarkshavn weather station for their generous help and hospitality. We thank Ben Hallett for his help with the detailed mapping and sampling. Helpful reviews were provided by Brad Hacker, Andrew Kylander-Clark, Chris Mattinson, and Dave Root.

REFERENCES CITED

Anders, E., and Grevesse, N., 1989, Abundances of the elements: Meteoritic and solar: Geochimica et Cosmochimica Acta, v. 53, p. 197–214, doi: 10.1016/0016-7037(89)90286-X.

Avigad, D., Chopin, C., and Le Bayon, R., 2003, Thrusting and extension in the southern Dora-Maira ultra-high-pressure massif (Western Alps): View from below the coesite-bearing unit: The Journal of Geology, v. 111, p. 57–70, doi: 10.1086/344664.

Black, L.P., Kamo, S.L., Williams, I.S., Mundil, R., Davis, D.W., Korsch, R.J., and Foudoulis, C., 2003, The application of SHRIMP to Phanerozoic geochronology; a critical appraisal of four zircon standards: Chemical Geology, v. 200, p. 171–188, doi: 10.1016/S0009-2541(03)00166-9.

Brueckner, H.K., Gilotti, J.A., and Nutman, A., 1998, Caledonian eclogite facies metamorphism of Early Proterozoic protoliths from the North-East Greenland eclogite province: Contributions to Mineralogy and Petrology, v. 130, p. 103–120, doi: 10.1007/s004100050353.

Burov, E., Jolivet, L., Le Pourhiet, L., and Poliakov, A., 2001, A thermomechanical model of exhumation of high pressure (HP) and ultra-high pressure (UHP) metamorphic rocks in Alpine-type collision belts: Tectonophysics, v. 342, p. 113–136, doi: 10.1016/S0040-1951(01)00158-5.

Carswell, D.A., Brueckner, H.K., Cuthbert, S.J., Mehta, K., and O'Brien, P.J., 2003, The timing of stabilisation and the exhumation rate for ultra-high pressure rocks in the Western Gneiss Region of Norway: Journal of Metamorphic Geology, v. 21, p. 601–612, doi: 10.1046/j.1525-1314.2003.00467.x.

Chemenda, A.I., Mattauer, M., and Bokun, A.N., 1996, Continental subduction and a mechanism for exhumation of high pressure metamorphic rocks: New modeling, field data from Oman: Earth and Planetary Science Letters, v. 143, p. 173–182, doi: 10.1016/0012-821X(96)00123-9.

Chopin, C., 2003, Ultrahigh-pressure metamorphism: Tracing continental crust into the mantle: Earth and Planetary Sciences Letters, v. 212, p. 1–14, doi: 10.1016/S0012-821X(03)00261-9.

Chopin, C., and Sobolev, N.V., 1995, Principal mineralogic indicators of UHP in crustal rocks, *in* Coleman, R.G., and Wang, X., eds., Ultrahigh-pressure metamorphism: Cambridge, Cambridge University Press, p. 96–131.

Davis, D.W., Williams, I.S., and Krogh, T.E., 2003, Historical development of zircon geochronology, *in* Hanchar, J.M., and Hoskin, P.W.O., eds., Zircon: Reviews in Mineralogy and Geochemistry, v. 53, p. 145–181.

Doin, M.P., and Henry, P., 2001, Subduction initiation and continental crust recycling: The roles of rheology and eclogitization: Tectonophysics, v. 342, p. 163–191, doi: 10.1016/S0040-1951(01)00161-5.

Elvevold, S., and Gilotti, J.A., 2000, Pressure-temperature evolution of retrogressed kyanite eclogites, Weinschenk Island, North-East Greenland Caledonides: Lithos, v. 53, p. 127–147, doi: 10.1016/S0024-4937(00)00014-1.

Gebauer, D., Schertl, H.-P., Brix, M., and Schreyer, W., 1997, 35 Ma old ultrahigh-pressure metamorphism and evidence for very rapid exhumation in the Dora Maira Massif, Western Alps: Lithos, v. 41, p. 5–24.

Gerya, T.V., Stöckhert, B., and Perchuk, A.L., 2002, Exhumation of high-pressure metamorphic rocks in a subduction channel: A numerical simulation: Tectonics, v. 21, p. 6-1–6-19, doi: 10.1029/2002TC001406.

Gilotti, J.A., 1993, Discovery of a medium-temperature eclogite province in the Caledonides of North-East Greenland: Geology, v. 21, p. 523–526, doi: 10.1130/0091-7613(1993)021<0523:DOAMTE>2.3.CO;2.

Gilotti, J.A., 1994, Eclogites and related high-pressure rocks from North-East Greenland: Grønlands Geologiske Undersøgelse Rapport, v. 162, p. 77–90.

Gilotti, J.A., and Elvevold, S., 1998, Partial eclogitization of the Ambolten gabbro-norite North-East Greenland Caledonides: Schweizerische Mineralogische und Petrographische Mitteilungen, v. 78, p. 273–292.

Gilotti, J.A., and Ravna, E.J.K., 2002, First evidence for ultrahigh-pressure metamorphism in the North-East Greenland Caledonides: Geology, v. 30, p. 551–554.

Gilotti, J.A., Nutman, A.P., and Brueckner, H.K., 2004, Devonian to Carboniferous collision in the Greenland Caledonides: U-Pb zircon and Sm-Nd ages of high-pressure and ultrahigh-pressure metamorphism: Contributions to Mineralogy and Petrology, v. 148, p. 216–235, doi: 10.1007/s00410-004-0600-4.

Griffin, W.L., Austrheim, H., Brastad, K., Bryhni, I., Krill, A.G., Krogh, E.J., Mørk, M.-B.E., Qvale, H., and Tørudbakken, B., 1985, High-pressure metamorphism in the Scandinavian Caledonides, *in* Gee, D.G., and Sturt, B.A., eds., The Caledonide orogen—Scandinavia and related areas: Chichester, John Wiley, p. 783–801.

Hacker, B.R., and Peacock, S.M., 1995, Creation, preservation, and exhumation of UHPM rocks, *in* Coleman, R.G., and Wang, X., eds., Ultrahigh-pressure metamorphism: Cambridge, Cambridge University Press, p. 159–181.

Hacker, B.R., Ratschbacher, L., Webb, L., McWilliams, M., Calvert, A., Dong, S., Wenk, H.-R., and Chateigner, D., 2000, Exhumation of ultrahigh-pressure continental crust in east central China: Late Triassic–Early Jurassic tectonic unroofing: Journal of Geophysical Research, v. 105, p. 13,339–13,364.

Hacker, B.R., Andersen, T.B., Root, D.B., Mehl, L., Mattinson, J.M., and Wooden, J.L., 2003, Exhumation of high-pressure rocks beneath the Solund Basin, Western Gneiss Region of Norway: Journal of Metamorphic Geology, v. 21, p. 613–629, doi: 10.1046/j.1525-1314.2003.00468.x.

Hermann, J., Rubatto, D., Korsakov, A., and Shatsky, V.S., 2001, Multiple zircon growth during fast exhumation of diamondiferous, deeply subducted continental crust (Kokchetav Massif, Kazakhstan): Contributions to Mineralogy and Petrology, v. 141, p. 66–82.

Higgins, A.K., and Leslie, A.G., 2000, Restoring thrusting in the East Greenland Caledonides: Geology, v. 28, p. 1019–1022, doi: 10.1130/0091-7613(2000)028<1019:RTITEG>2.3.CO;2.

Higgins, A.K., Henriksen, N.H., Jepsen, H.F., Kalsbeek, F., Thrane, K., Elvevold, S., Escher, J.C., Frederiksen, K.S., Gilotti, J.A., Jones, K., Leslie, A.G., Smith, M.P., Kinny, P.D., and Watt, G.R., 2004, The foreland-propagating architecture of the East Greenland Caledonides

72°–75°N: Journal of the Geological Society of London, v. 161, p. 1009–1026.

Hoskin, P.W.O., and Black, L.P., 2000, Metamorphic zircon formation by solid-state recrystallization of protolith igneous zircon: Journal of Metamorphic Geology, v. 18, p. 423–439, doi: 10.1046/j.1525-1314.2000.00266.x.

Hoskin, P.W.O., and Ireland, T.R., 2000, Rare earth element chemistry of zircon and its use as a provenance indicator: Geology, v. 28, p. 627–630, doi: 10.1130/0091-7613(2000)028<0627:REECOZ>2.3.CO;2.

Hoskin, P.W.O., and Schaltegger, U., 2003, The composition of zircon and igneous and metamorphic petrogenesis, *in* Hanchar, J.M., and Hoskin, P.W.O., eds., Zircon: Reviews in Mineralogy and Geochemistry, v. 53, p. 29–62.

Hull, J.M., Friderichsen, J.D., Gilotti, J.A., Henriksen, N., Higgins, A.K., and Kalsbeek, F., 1994, Gneiss complex of the Skærfjorden region, North-East Greenland: Grønlands Geologiske Undersøgelse Rapport, v. 162, p. 35–51.

Kalsbeek, F., 1995, Geochemistry, tectonic setting, and poly-orogenic history of Paleoproterozoic basement rocks from the Caledonian fold belt of North-East Greenland: Precambrian Research, v. 72, p. 301–315, doi: 10.1016/0301-9268(94)00097-B.

Kalsbeek, F., Nutman, A.P., and Taylor, P.N., 1993, Palaeoproterozoic basement province in the Caledonian fold belt of North-East Greenland: Precambrian Research, v. 63, p. 163–178, doi: 10.1016/0301-9268(93)90010-Y.

Kaneko, Y., Katayama, I., Yamamoto, H., Misawa, K., Ishikawa, M., Rehman, H.U., Kausar, A.B., and Shiraishi, K., 2003, Timing of Himalayan ultrahigh-pressure metamorphism: Sinking rate and subduction angle of the Indian continental crust beneath Asia: Journal of Metamorphic Geology, v. 21, p. 589–599.

Katayama, I., Maruyama, S., Parkinson, C.D., Terada, K., and Sano, Y., 2001, Ion microprobe U-Pb zircon geochronology of peak and retrograde stages of ultrahigh-pressure metamorphic rocks from the Kokchetav Massif, northern Kazakhstan: Earth and Planetary Science Letters, v. 188, p. 185–198, doi: 10.1016/S0012-821X(01)00319-3.

Korotev, R.L., 1996, A self-consistent compilation of elemental concentration data for 93 geochemical reference samples: Geostandards Newsletter, v. 20, p. 217–245.

Kretz, R., 1983, Symbols for rock-forming minerals: The American Mineralogist, v. 68, p. 277–279.

Lang, H.M., and Gilotti, J.A., 2001, Plagioclase replacement textures in partially eclogitised gabbros from the Sanddal mafic-ultramafic complex, Greenland Caledonides: Journal of Metamorphic Geology, v. 19, p. 497–515, doi: 10.1046/j.0263-4929.2001.00325.x.

Lapen, T.J., Johnson, C.M., Baumgartner, L.P., Mahlen, N.J., Beard, B.L., and Amato, J.M., 2003, Burial rates during prograde metamorphism of an ultra-high-pressure terrane: An example from Lago di Cignana, western Alps, Italy: Earth and Planetary Science Letters, v. 215, p. 57–72, doi: 10.1016/S0012-821X(03)00455-2.

Lenze, A., Stöckhert, B., and Wirth, R., 2005, Grain scale deformation in ultrahigh-pressure metamorphism—An indicator of rapid phase transformation: Earth and Planetary Science Letters, v. 229, p. 217–230, doi: 10.1016/j.epsl.2004.10.012.

Liu, F., Xu, Z., Liou, J.G., Katayama, I., Masago, H., Maruyama, S., and Yang, J., 2002, Ultra-high pressure mineral inclusions in zircons from gneissic core samples of the Chinese Continental Scientific Drilling Site in eastern China: European Journal of Mineralogy, v. 71, p. 180–188.

Liu, F., Liou, J.G., and Xu, Z., 2005, U-Pb SHRIMP ages recorded in the coesite-bearing zircon domains of paragneisses in the southwestern Sulu terrane, eastern China: New interpretation: The American Mineralogist, v. 90, p. 790–800, doi: 10.2138/am.2005.1677.

Ludwig, K.R., 2001a, Squid version 1.02: A user's manual: Berkeley Geochronology Center Special Publication, v. 2, p. 1–22.

Ludwig, K.R., 2001b, Isoplot/EX version 2.49: A geochronological toolkit for Microsoft Excel: Berkeley Geochronology Center Special Publication, no. 1a, p. 1–55.

Mattinson, J.M., 2005, Zircon U-Pb chemical abrasion (CA-TIMS) method: Combined annealing and multi-step partial dissolution analysis for improved precision and accuracy of zircon ages: Chemical Geology, v. 220, p. 47–66, doi: 10.1016/j.chemgeo.2005.03.011.

Michard, A., Henry, C., and Chopin, C., 1995, Structures in UHPM rocks: A case study from the Alps, *in* Coleman, R.G., and Wang, X., eds., Ultrahigh-pressure metamorphism: Cambridge, Cambridge University Press, p. 132–158.

Mosenfelder, J.L., and Bohlen, S.R., 1997, Kinetics of the coesite to quartz transformation: Earth and Planetary Science Letters, v. 153, p. 133–147, doi: 10.1016/S0012-821X(97)00159-3.

Mosenfelder, J.L., Schertl, H.P., Smyth, J.R., and Liou, J.G., 2005, Factors in the preservation of coesite: The importance of fluid infiltration: The American Mineralogist, v. 90, p. 779–789, doi: 10.2138/am.2005.1687.

Nasdala, L., Zhang, M., Kempe, U., Panczer, G., Gaft, M., Andrut, M., and Plötze, M., 2003, Spectroscopic methods applied to zircon, *in* Hanchar, J.M., and Hoskin, P.W.O., eds., Zircon: Reviews in Mineralogy and Geochemistry, v. 53, p. 427–467.

Parrish, R.R., and Noble, S.R., 2003, Zircon U-Th-Pb geochronology by isotope dilution–thermal ionization mass spectrometry (ID-TIMS), *in* Hanchar, J.M., and Hoskin, P.W.O., eds., Zircon: Reviews in Mineralogy and Geochemistry, v. 53, p. 183–213.

Pearce, N.J.G., Perkins, W.T., Westgate, J.A., Gorton, M.P., Jackson, S.E., Neal, C.R., and Cheney, S.P., 1997, New data for National Institute of Standards and Technology 610 and 612 glass reference materials: Geostandards Newsletter, v. 21, p. 115–144.

Perrillat, J.P., Daniel, I., Lardeaux, J.M., and Cardon, H., 2003, Kinetics of the coesite-quartz transition: Application to the exhumation of ultrahigh-pressure rocks: Journal of Petrology, v. 44, p. 773–788, doi: 10.1093/petrology/44.4.773.

Puga, E., Fanning, C.M., Nieto, J.M., and Díaz de Federico, A., 2005, Recrystallization textures in zircon generated by ocean-floor and eclogite-facies metamorphism: A cathodoluminescence and U-Pb SHRIMP study, with constraints from REE elements: Canadian Mineralogist, v. 43, p. 183–202.

Ravna, E.J.K., 2000, The garnet-clinopyroxene Fe^{2+}-Mg geothermometer: An updated calibration: Journal of Metamorphic Geology, v. 18, p. 211–219, doi: 10.1046/j.1525-1314.2000.00247.x.

Ravna, E.J.K., and Terry, M.P., 2004, Geothermobarometry of UHP and HP eclogites and schists—An evaluation of equilibria among garnet-clinopyroxene-kyanite-phengite-coesite/quartz: Journal of Metamorphic Geology, v. 22, p. 579–592, doi: 10.1111/j.1525-1314.2004.00534.x.

Root, D.B., Hacker, B.R., Mattinson, J.M., and Wooden, J.L., 2004, Zircon geochronology and ca. 400 Ma exhumation of Norwegian ultrahigh-pressure rocks: An ion microprobe and chemical abrasion study: Earth and Planetary Science Letters, v. 228, p. 325–341, doi: 10.1016/j.epsl.2004.10.019.

Roselle, G.T., and Engi, M., 2002, Ultrahigh pressure (UHP) terrains: Lessons from thermal modeling: American Journal of Science, v. 302, p. 410–441.

Rubatto, D., 2002, Zircon trace element geochemistry: Partitioning with garnet and the link between U-Pb ages and metamorphism: Chemical Geology, v. 184, p. 123–138, doi: 10.1016/S0009-2541(01)00355-2.

Rubatto, D., and Gebauer, D., 2000, Use of cathodoluminescence for U-Pb zircons dating by ion microprobe: Some examples from the Western Alps, *in* Pagel, M., Barbin, V., Blanc, P., and Ohnenstetter, D., eds., Cathodoluminescence in geosciences: Berlin, Springer, p. 373–400.

Rubatto, D., and Hermann, J., 2001, Exhumation as fast as subduction?: Geology, v. 29, p. 3–6, doi: 10.1130/0091-7613(2001)029<0003:EAFAS>2.0.CO;2.

Rubatto, D., and Hermann, J., 2003, Zircon formation during fluid circulation in eclogites (Monviso, Western Alps): Implications for Zr and Hf budget in subduction zones: Geochimica et Cosmochimica Acta, v. 67, p. 2173–2187, doi: 10.1016/S0016-7037(02)01321-2.

Ryan, P.D., 2001, The role of deep basement during continent-continent collision: A review, *in* Miller, J.A., Holdsworth, R.E., Buick, I.S., and Hand, M., eds., Continental reactivation and reworking: Geological Society of London Special Publication 184, p. 39–55.

Schaltegger, U., Fanning, C.M., Günther, D., Maurin, J.C., Schulmann, K., and Gebauer, D., 1999, Growth, annealing and recrystallization of zircon and preservation of monazite in high-grade metamorphism: Conventional and in-situ U-Pb isotope, cathodoluminescence and microchemical evidence: Contributions to Mineralogy and Petrology, v. 134, p. 186–201, doi: 10.1007/s004100050478.

Stacey, J.S., and Kramers, J.D., 1975, Approximation of terrestrial lead isotope evolution by a two-stage model: Earth and Planetary Science Letters, v. 26, p. 207–221, doi: 10.1016/0012-821X(75)90088-6.

van Zuilen, M.A., Mathew, K., Wopenka, B., Lepland, A., Marti, K., and Arrhenius, G., 2005, Nitrogen and argon isotopic signatures in graphite from the 3.8-Ga-old Isua Supracrustal Belt: Southern West Greenland: Geochimica et Cosmochimica Acta, v. 69, p. 1241–1252, doi: 10.1016/j.gca.2004.08.033.

Vavra, G., Schmid, R., and Gebauer, D., 1999, Internal morphology, habit and U-Th-Pb microanalysis of amphibolite-to-granulite facies zircons: Geochronology of the Ivrea Zone (Southern Alps): Contributions to Mineralogy and Petrology, v. 134, p. 380–404, doi: 10.1007/s004100050492.

Williams, I.S., 1998, U-Pb by ion microprobe, *in* McKibben, M.A., Shanks, W.C., and Ridley, W.I., eds., Applications of microanalytical techniques to understanding mineralizing processes: Society of Economic Geologists Reviews Economic Geology, v. 7, p. 1–35.

Yang, J.S., Wooden, J.L., Wu, C.L., Liu, F.L., Xu, Z.Q., Shi, R.D., Katayama, I., Liou, J.G., and Maruyama, S., 2003, SHRIMP U-Pb dating of coesite-bearing zircon from the ultrahigh-pressure metamorphic rocks, Sulu terrane, east China: Journal of Metamorphic Geology, v. 21, p. 551–560, doi: 10.1046/j.1525-1314.2003.00463.x.

MANUSCRIPT ACCEPTED BY THE SOCIETY 21 SEPTEMBER 2005

Printed in the USA

Geological Society of America
Special Paper 403
2006

The Sino-Korean–Yangtze suture, the Huwan detachment, and the Paleozoic–Tertiary exhumation of (ultra)high-pressure rocks along the Tongbai-Xinxian-Dabie Mountains

Lothar Ratschbacher
Leander Franz
Eva Enkelmann
Raymond Jonckheere
Axel Pörschke
Geowissenschaften, Technische Universität Bergakademie Freiberg, D-09599 Freiberg, Germany
Bradley R. Hacker
Department of Geological Sciences, University of California, Santa Barbara, California 93106, USA
Shuwen Dong
Yueqiao Zhang
Chinese Academy of Geological Sciences, Beijing 100037, People's Republic of China

ABSTRACT

There are three sutures in the Qinling-Dabie-Sulu orogen in the Tongbai–Xinxian (northern Hong'an)–northern Dabie area: the Silurian Sino-Korean craton–Erlangping intra-oceanic arc suture, the Silurian Erlangping arc–Qinling unit (microcontinent) suture, and the Early Triassic Qinling unit–Yangtze craton suture. We resolve the controversy regarding the age of the Sino-Korean craton–Yangtze craton collision by recognizing that there was Paleozoic collision between the Qinling unit and the Sino-Korean craton and Mesozoic collision between the Qinling unit and the Yangtze craton. The Qinling unit constitutes a long and narrow microcontinent that extends through the Qinling-Dabie area and probably into the Sulu area. Its common characteristics are the Mesoproterozoic (ca. 1.0 Ga) Jinningian orogeny, ca. 0.8–0.7 Ga arc formation and rifting, and Late Silurian–Early Devonian (ca. 400 Ma) arc magmatism with concomitant regional contact metamorphism up to granulite-facies conditions (peak: 680–740 °C at 0.9–1.1 GPa). A common Proterozoic history links the Qinling microcontinent to the Yangtze craton. Its 400 Ma arc, forearc basin, and its separation from the Yangtze craton by the partly oceanic Huwan mélange make the Qinling microcontinent distinct. The forearc basin sits on the southern part of the 400 Ma arc and underlying Proterozoic continental basement, and detrital geochronology ties it to the Qinling microcontinent basement and its arc. The Huwan mélange is a subduction-accretion complex containing elements of the Qinling microcontinent and its arc, the Paleotethyan ocean floor, and possibly the Yangtze craton.

Ratschbacher, L., Franz, L., Enkelmann, E., Jonckheere, R., Pörschke, A., Hacker, B.R., Dong, S., and Zhang, Y., 2006, The Sino-Korean–Yangtze suture, the Huwan detachment, and the Paleozoic–Tertiary exhumation of (ultra)high-pressure rocks along the Tongbai-Xinxian-Dabie Mountains, *in* Hacker, B.R., McClelland, W.C., and Liou, J.G., eds., Ultrahigh-pressure metamorphism: Deep continental subduction: Geological Society of America Special Paper 403, p. 45–75, doi: 10.1130/2006.2403(03).

Quartz eclogites (540–590 °C, 2.1 GPa) signify ca. 315 Ma subduction. Devonian to Permian eclogite zircon ages, $^{40}Ar/^{39}Ar$ and Rb/Sr mineral ages in the forearc and its basement, and static, Permian blueschist metamorphism in the upper-plate basement testify to subduction throughout the late Paleozoic.

The ~10-km-wide Huwan detachment bounds the high- and ultrahigh-pressure rocks of the Xinxian–Hong'an block (pressure peak at older than 240 Ma) along their northern margin. It is partly responsible for exhumation of the high- and ultrahigh-pressure rocks, but the entire basement core of Hong'an–Dabie orogen is also strongly deformed. The Huwan shear-zone high-strain deformation indicates passage of rocks through the lithosphere by subhorizontal N-S extension and vertical contraction, showcased by condensed Triassic isograds (420 °C and ~0.4 GPa in the hanging wall and ~530 °C and 2.2 GPa in the footwall). The Huwan detachment produced Triassic crustal exhumation rates of 1.9–1.4 mm/yr; synkinematic phengite grew as early as ca. 235 Ma, and the main retrograde deformation occurred at 224–195 Ma. The Tongbai-Xinxian area shows a massive 130–115 Ma cluster of cooling ages, reflecting regional cooling after granitoid injection and regional Cretaceous heating. Apatite fission-track ages cluster at 80–55 Ma and signify cooling related to transtension that coincided with rifting marked by Late Cretaceous–Eocene red bed deposition throughout eastern China. Exhumation rates of for the last 70 m.y. have been slow: ~0.06 mm/yr. The India-Asia collision reactivated the orogen in the Eocene, particularly along the Tanlu fault zone and locally along fault zones in Tongbai-Xinxian.

Keywords: ultrahigh-pressure orogeny, Qinling-Dabie-Sulu orogen, Sino-Korean–Yangtze suture, Huwan detachment, Paleozoic-Holocene exhumation path.

INTRODUCTION

The Qinling-Tongbai-Xinxian-Dabie-Sulu orogen stretches for ~2000 km in east-central China (Fig. 1). Controversies exist about the location and number of sutures and the age of collision between the northern Sino-Korean and the southern Yangtze cratons. Resolving these controversies is important, because the orogen hosts two distinct ultrahigh-pressure events. Researchers in the Qinling have favored a Paleozoic amalgamation (e.g., Kröner et al., 1993) or a Paleozoic collision overprinted by Mesozoic intracontinental shortening (e.g., Mattauer et al., 1985). In contrast, work in the Dabie-Sulu area has demonstrated Triassic Yangtze craton subduction beneath a collage of rock units traditionally attributed to the Sino-Korean craton (e.g., Ames et al., 1996; Hacker et al., 1996a; Wallis et al., 1999). In the Qin Mountains (Qinling), a clearer picture has emerged (e.g., Ratschbacher et al., 2003, and references therein). There, intra-oceanic arc formation at ca. 490–470 Ma (the Erlangping-Danfeng-Heihe unit) was followed by accretion of the Qinling microcontinent (Qinling unit) to the intra-oceanic arc and the Sino-Korean craton and imprint of a ca. 400 Ma Andean-type magmatic arc onto the Qinling and Erlangping-Danfeng-Heihe units and the Sino-Korean craton. Oceanic subduction continued south of the Qinling unit, producing a Carboniferous, Franciscan-type high-pressure mélange belt (Sun et al., 2002), and terminated with the attempted north-directed subduction of the Yangtze craton (e.g., Hacker et al., 2000). Preservation of ultrahigh-pressure (UHP) minerals, including coesite in eclogites and host paragneisses in Hong'an–Dabie–Sulu, demonstrates subduction of supracrustal rocks of the Yangtze craton down to mantle depths (e.g., Zhou et al., 1993; Eide and Liou, 2000, for the Hong'an–Xinxian area).

Most models for exhumation of the Triassic UHP rocks (e.g., Hacker et al., 2000, 2004; Faure et al., 1999, 2003; Webb et al., 1999, 2001) suggest a major role of subhorizontal extension that apparently followed buoyant rise of the UHP rocks through the mantle. The north-dipping Huwan detachment was identified as the major high-strain, normal-sense shear zone at the top of the strongly deformed high-pressure and UHP rocks in northern Hong'an (this area is called "Xinxian" in the Chinese literature—a usage we follow in this paper; Rowley and Xue, 1996; Webb et al., 1996; Hacker et al., 1998, 2000; Webb et al., 1999, 2001). The Xinxian area has also been suggested to constitute the only portion of the orogen where the northern boundary of the high-pressure and UHP units coincides with the Sino-Korean craton–Yangtze craton suture (e.g., Hacker et al., 2000, 2004; Ratschbacher et al., 2003; Faure et al., 2001).

Although portions of the UHP rocks were exhumed to the surface by the Jurassic (Grimmer et al., 2003; Wang et al., 2003; Wan et al., 2006), Cretaceous and Cenozoic deformation contributed to exhumation of the present exposure level from mid-crustal depths. The associated structures dominate the orogenic architecture of the Dabie Shan (e.g., Ratschbacher et al., 2000).

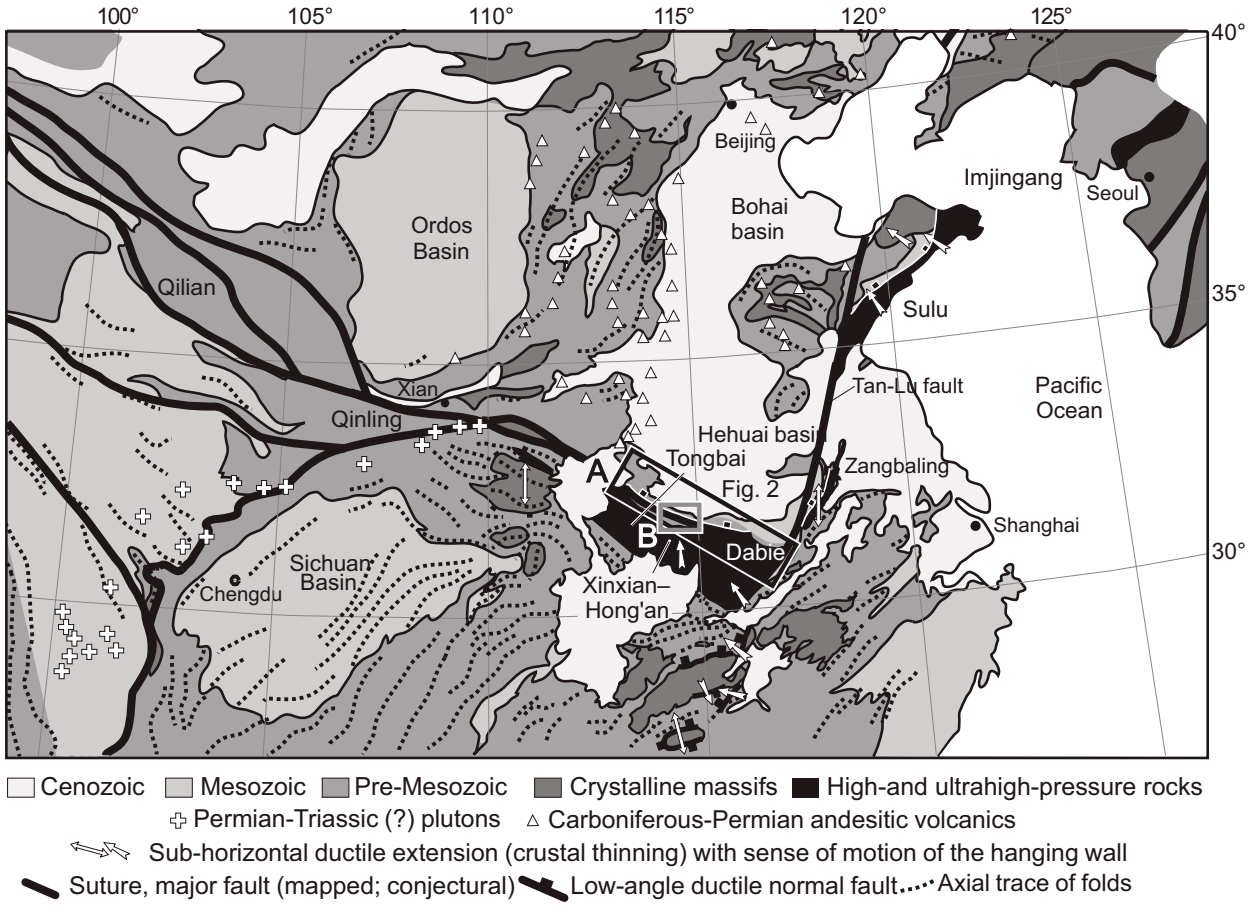

Figure 1. The Qilian–Qinling–Tongbai–Hong'an–Xinxian–Dabie–Sulu–Imjingang collisional orogen of eastern Asia. Structural interpretations of Triassic subhorizontal extension in crystalline basement domes are from Faure et al. (1996, 2003), Wallis et al. (1999), Lin et al. (2000), Hacker et al. (2000), and Ratschbacher et al. (2003). Andesitic volcanic rocks from Zhang (1997) and Permian–Triassic plutons from R.G.S. Sichuan (1991) and R.G.S. Shaanxi (1989) suggest pre–Late Permian arc magmatism related to Paleotethys subduction and postcollisional plutonism linked to crustal thickening.

SCOPE OF THIS STUDY

Herein, we address the following controversies by providing new and reviewing existing geologic, geochronologic, petrologic, and structural data from the Tongbai–Xinxian–northern Dabie area: Where is the suture between the Sino-Korean craton and Yangtze craton? Are there intervening microcontinents? What was the role of the Carboniferous high-pressure metamorphism along the northern edge of the Yangtze craton? What was the pressure–temperature–time–deformation (*P-T-t-d*) history of the Huwan detachment shear-fault zone during the Triassic orogeny? What was the *P-T-t-d* history of the Proterozoic–Paleozoic units, which are ascribed to the Sino-Korean craton, north of the well-documented Triassic high-pressure and UHP orogen? How was the collision zone overprinted in the Cretaceous–Tertiary? Our study highlights the differences between the high-pressure and UHP orogen and its northern foreland, shows that the foreland units are part of the Qinling microcontinent, and provides a comprehensive tectonic scenario for the Sino-Korean craton–Yangtze craton suture zone from the Paleozoic to Holocene.

GEOLOGIC UNITS OF THE NORTHERN TONGBAI–XINXIAN–DABIE REGION

The northern Tongbai–Xinxian–Dabie region is underlain by a number of fault-bounded units that are correlated with similar—often more complete—units in the Qinling farther west (e.g., Ratschbacher et al., 2003). These units are described in the following from north to south. Figure 2 summarizes important geologic and geochronologic data substantiating this subdivision.

Sino-Korean Craton and Kuanping Unit

The basement of the Sino-Korean craton is composed of the 2.6–2.0 Ga Taihua gneiss and the Xiong'er Group (e.g., Kröner et al., 1988). The Kuanping unit, chiefly amphibolite-

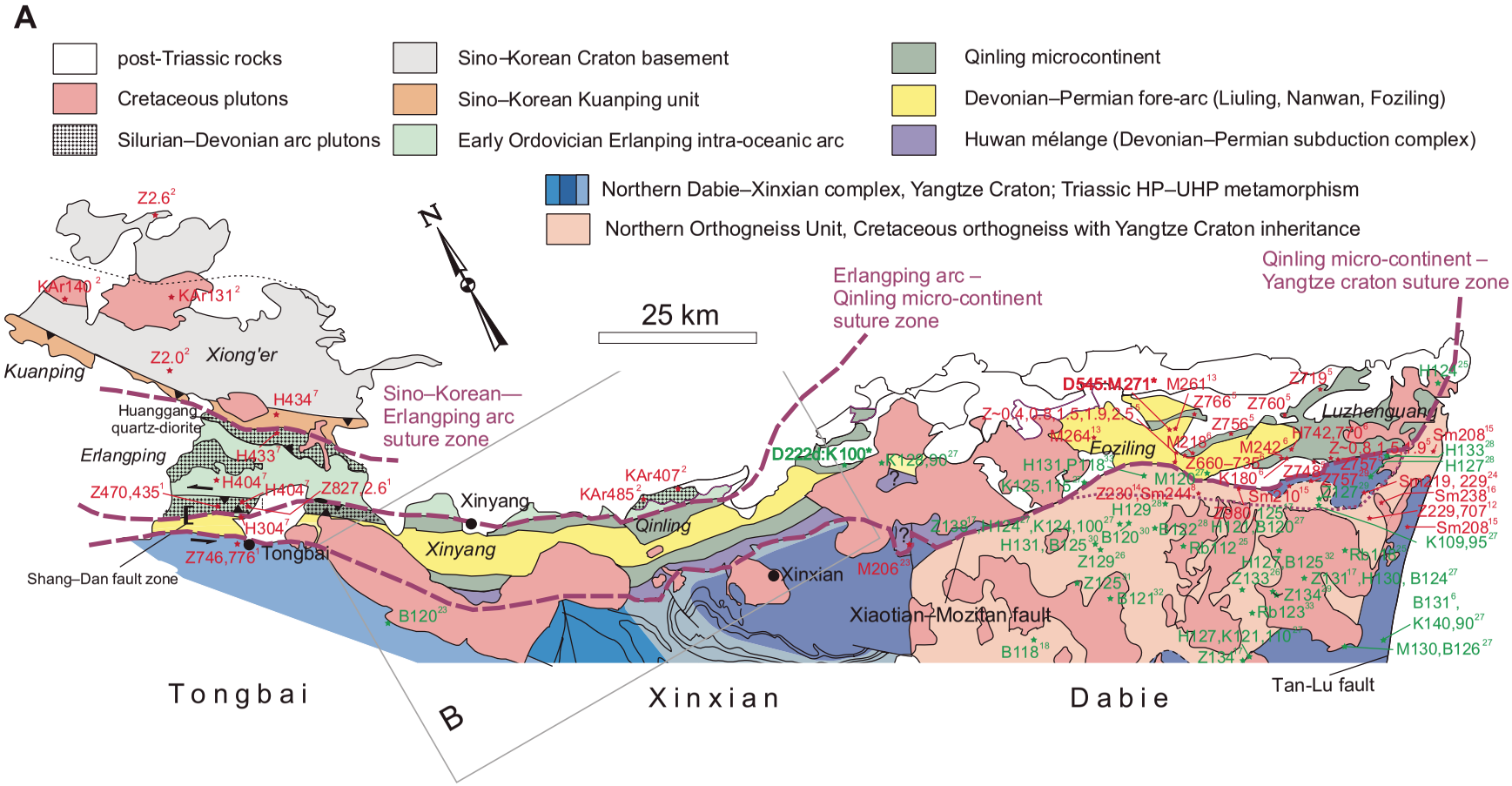

Figure 2. Correlation of geological units of the northern margin of Tongbai-Xinxian-Dabie orogenic belt, distribution of Early Cretaceous plutons, and reliable geochronological ages. Geochronological references: *—this paper; 1—Kröner et al. (1993); 2—R.G.S Henan (1989); 3—Ye et al. (1993); 4—Li et al. (2001); 5—Chen et al. (2003); 6—Hacker et al. (2000); 7—Zhai et al. (1998); 8—Li et al. (1989); 9—Jian et al. (1997); 10—Jian et al. (2001); 11—Sun et al. (2002); 12—Xie et al. (2001); 13—Niu et al. (1994); 14—Liu et al. (2002); 15—Liu et al. (2001); 16—Chen et al. (1998); 17—Hacker et al. (1998); 18—Eide et al. (1994); 19—Liu et al. (2004a); 20—Gao et al. (2002); 22—Xu et al. (2000); 23—Webb et al. (1999); 24—Xie et al. (2004); 25—Zhou et al. (1992); 26—Xie et al. (1998); 27—Ratschbacher et al. (2000); 28—Hacker and Wang (1995); 29—Xue et al. (1997); 30—Mattauer et al. (1991); 31—Zhang and Sun (1990); 32—Chen et al. (1995); 33—Jahn et al. (1999). The ages of Niu et al. (1994) were recalculated, thus they may deviate slightly from those given in the original publication. Sample numbers stand ahead of our data. HP–UHP—high-pressure–ultrahigh-pressure.

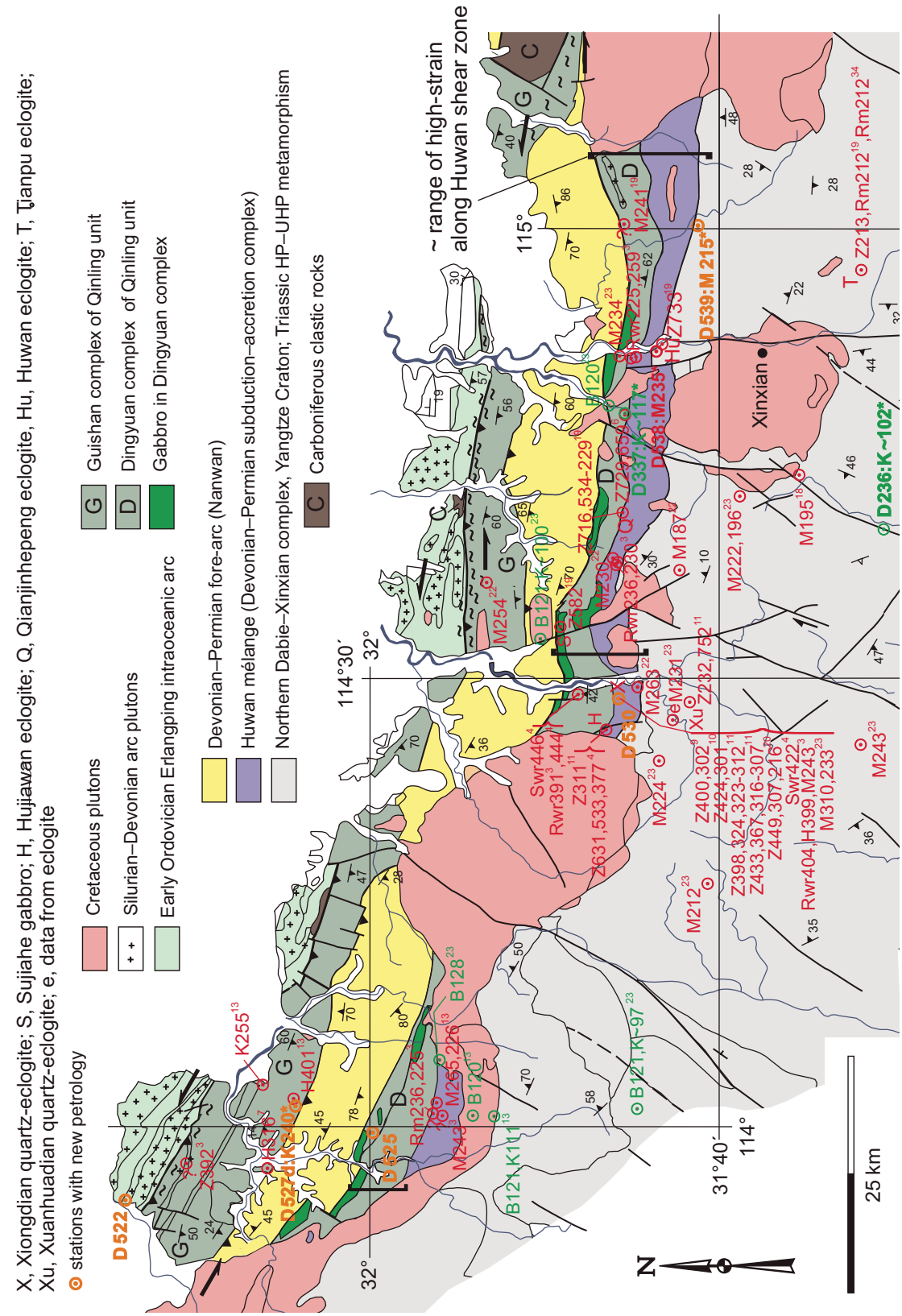

Figure 2. *(continued)*

to greenschist-facies marbles and two-mica quartz schists, was interpreted as overlying passive margin sedimentary rocks or an accretionary wedge (see e.g., Ratschbacher et al., 2003). Two $^{40}Ar/^{39}Ar$ ages (434 ± 2 Ma for metamorphic hornblende and 433 ± 2 Ma for magmatic hornblende in diorite of the Huanggang intrusive complex; Zhai et al., 1998) likely typify the Silurian–Devonian arc that overprints the Kuanping, Erlangping, and Qinling units (see following; Ratschbacher et al., 2003).

Erlangping Unit

The Erlangping Unit consists of greenschist- to amphibolite-facies volcanic and plutonic rocks, fine-grained clastic rocks, and chert with Cambrian–Silurian fossils (e.g., Niu et al., 1993); geochemical data suggest it is an Early Ordovician (ca. 470–490 Ma) intra-oceanic arc (e.g., Xue et al., 1996). In Tongbai and Xinxian, one ca. 485 Ma K/Ar age of unknown type (R.G.S. Henan, 1989) may date this complex; a 404 ± 5 Ma $^{40}Ar/^{39}Ar$ hornblende age from amphibolite (Zhai et al., 1998) and a ca. 407 Ma K/Ar age (again of unknown type, R.G.S. Henan, 1989) are likely associated with the Silurian–Devonian arc (see following).

Qinling Unit

In the Qin Mountains, the Qinling unit includes a variety of rocks, and its internal structure is not well understood (e.g., Ratschbacher et al., 2003). The structurally lower Qinling includes biotite–plagioclase gneisses, amphibolites, calc-silicate rocks, garnet–sillimanite gneiss, and marble (Xue et al., 1996); the upper Qinling consists of marble with minor amphibolite and garnet–sillimanite gneiss (You et al., 1993). In Tongbai-Xinxian, the Qinling unit has been subdivided into several units, the relationships of which are controversial. Our field survey results generally correspond with the subdivision proposed by Li S.-G. et al. (1995, 2001). In northwestern Tongbai, marble overlies felsic orthogneiss with abundant granulitic enclaves and xenoliths derived from mafic igneous and sedimentary protolith; zircon $^{207}Pb/^{206}Pb$ evaporation ages are 470 ± 20 Ma and 470 ± 14 Ma for the protoliths of two-pyroxene granulites (~800 °C and 1.0 GPa) and 435 ± 14 Ma for the enclosing granodioritic gneiss (Kröner et al., 1993). Metaquartzite and metasedimentary garnet granulite gave detrital zircon ages of 2555 ± 8 Ma and 827 ± 10 Ma, respectively. Okay et al. (1993) interpreted the orthogneiss as retrograde granulite and the marble as intercalations in the granulite-gneiss sequence. Here, we suggest that the mafic granulites are part of the intra-oceanic arc sequence of the Erlangping-Danfeng-Heihe unit, that the metasedimentary rocks are associated clastics, and that the enclosing orthogneiss likely belongs to the Silurian–Devonian arc, which has regional contact metamorphism dated by a 404 ± 2 Ma $^{40}Ar/^{39}Ar$ hornblende age (from a felsic, garnet–two-pyroxene granulite; Zhai et al., 1998).

The greenschist- to amphibolite-facies Guishan complex (the lower part of the Xinyang "Group" of the Chinese literature) consists of gneiss, amphibolite, garnet–mica schist, chlorite–albite schist, marble, and quartzite; the protoliths of some of these rocks were interpreted as metavolcanic: keratophyre, andesitic tuff, and basalt (e.g., Xu et al. 1992). This unit reappears south of the Nanwan "Formation" (the upper part of the Xinyang Group) as the Dingyuan complex (e.g., Suo et al., 1993; Li et al., 2001), suggesting that the overall structure of the Qinling unit in Xinxian is a synform. The Guishan complex yielded a 392 ± 25 Ma U/Pb zircon age for acid metavolcanic rock in its upper part (Ye et al., 1994; see also Figure 3B for a summary of important Qinling geochronology in Xinxian), $^{40}Ar/^{39}Ar$ hornblende ages of 401 ± 4 Ma (garnet amphibolite; Niu et al., 1994), 316 ± 1 Ma (amphibolite), and 304 ± 10 Ma (amphibolite of uncertain affinity, perhaps part of the Danfeng unit; Zhai et al., 1998), a 254 ± 1 Ma $^{40}Ar/^{39}Ar$ muscovite age (Xu et al., 2000), and two $^{40}Ar/^{39}Ar$ K-feldspar ages of 225 ± 6 Ma (Niu et al., 1994) and ca. 240 Ma (this study). Zircons from quartzofeldspathic gneiss with mafic layers at the very southern edge of the Dingyuan complex range from 739 Ma and 638 Ma (n = 10, peaks at 729 ± 15 Ma and 659 ± 19 Ma, U/Pb sensitive high-resolution ion microprobe [SHRIMP]; Hacker et al., 2000). The Sujiahe gabbro at the northern edge of the Dingyuan complex yielded 639–440 Ma zircon ages with a weighted mean of 22 spots at 582 ± 11 Ma (U/Pb SHRIMP; Liu et al., 2004a). Rb/Sr whole-rock isochrons yielded 391 ± 13 Ma and 444 ± 31 Ma (Ye et al., 1994; Li et al., 2001, respectively). A Sm/Nd whole-rock isochron gave 446 ± 23 Ma on greenschist-facies volcanic rocks; major- and trace-element geochemistry indicated that these rocks formed in a magmatic arc (Li et al., 2001). The Dingyuan complex has yielded $^{40}Ar/^{39}Ar$ phengite cooling ages of 241 ± 2 Ma from granite mylonite (Liu et al., 2004a; Balifan unit; the location of the sample is unclear), and 234 ± 2 Ma from mylonitic quartzofeldspathic schist (Webb et al., 1999).

The Luzhenguan complex in northern Dabie is correlated with the Guishan complex on the basis of lithology, and consists of a lower unit of metavolcaniclastic rocks, granitoid, and gneiss, and an upper quartz–mica schist; it is unclear whether nearby quartzite, phyllite, and marble belong to the Luzhenguan or the overlying Foziling unit (see following; Li et al., 2001; Chen et al., 2003). Six granites yielded U/Pb zircon ages of 766–719 Ma, one quartzite gave single-grain detrital zircon age components of ca. 0.75 Ga, ca. 1.5 Ga, and ca. 1.9 Ga (Pb/Pb evaporation; Chen et al., 2003), and one garnet–biotite schist gave ages ranging from 735 to 660 Ma (U/Pb SHRIMP; Hacker et al., 2000). Granodiorite and dioritic gneiss yielded $^{40}Ar/^{39}Ar$ hornblende ages of 742 ± 10 Ma and 770 ± Ma, and mica schist and garnet–biotite schist gave $^{40}Ar/^{39}Ar$ muscovite ages of ca. 242 Ma and ca. 218 Ma, and ca. 180 Ma for K-feldspar from a deformed granitic dike (Hacker et al., 2000).

The Nanwan unit contains greenschist-grade turbiditic slate, phyllite, quartz mica schist, and quartzite. Its equivalent

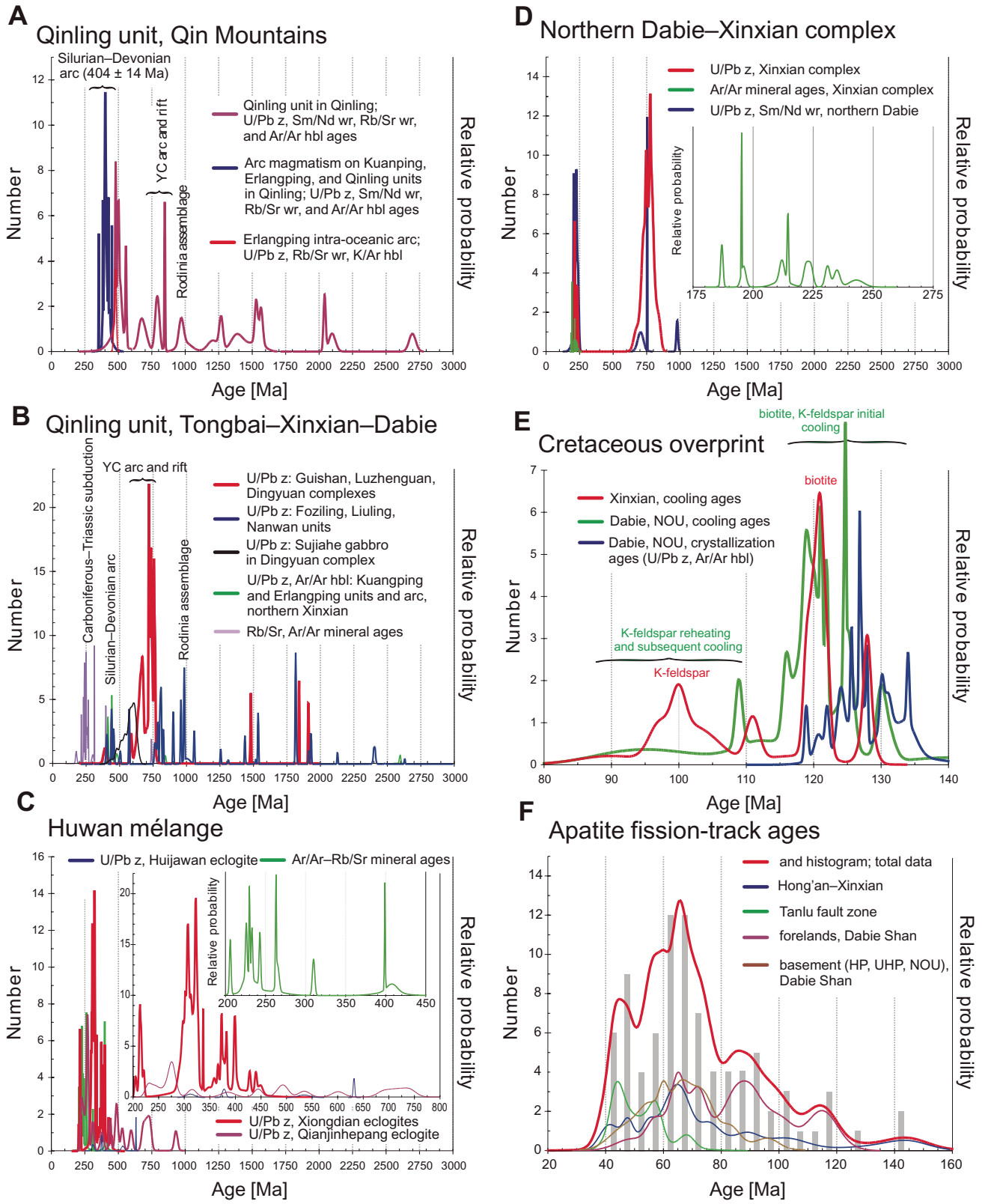

Figure 3. Histograms and relative frequencies of reliable ages from the Qinling-Tongbai-Xinxian-Dabie belt used for regional correlations and definition of tectonothermal events (see text). Data are given in the text, Figure 2, Tables 1–2, and are summarized in Table 12, which is available from the GSA Data Repository (see footnote 1, p. 58). Abbreviations: z—zircon, wr—whole rock, hbl—hornblende, YC—Yangtze craton, NOU—Northern Orthogneiss Unit.

in northern Dabie, the Foziling "Group," consists of greenschist- to amphibolite-facies, monotonous, mostly fine-grained, well-bedded siltstone and shale, minor volcanic rock, with a local basal quartzite and marble (e.g., Chen et al. 2003); the Foziling Group is thrust onto Carboniferous sandstone, siltstone, and shale (e.g., Okay et al., 1993). The Nanwan and Foziling units have been variably interpreted as Yangtze craton passive margin, Sino-Korean craton forearc flysch, Sino-Korean craton backarc flysch, or accretionary wedge (see Li et al., 2001, for discussion). Li et al. (2001) used Nd model ages and $\varepsilon_{Nd}(0)$ values to suggest that the Foziling rocks originated within an active continental margin along the Sino-Korean craton (equivalent to the Silurian–Devonian arc in this paper). Carboniferous coals with intercalated marine shales locally overlie these units. Here, we interpret the Nanwan and Foziling units as forearc basin sediments, deposited on the Guishan-Dingyuan-Luzhenguan complexes, which received detritus from these units, the Silurian–Devonian arc, and its Proterozoic basement (see following). This interpretation is supported by detrital zircons from Foziling quartzites that yielded age groups of 2.5 Ga, 1.9 Ga, 1.5 Ga, 0.8 Ga, and 0.4 Ga (Chen et al., 2003). The Foziling unit has given muscovite and biotite K/Ar ages from 225 to 204 Ma (Chen et al., 1993), and $^{40}Ar/^{39}Ar$ muscovite ages of ca. 271 Ma (this study), ca. 264 Ma, and ca. 261 Ma (Niu et al., 1994). Several Devonian conglomerate localities along the Shang-Dan fault (i.e., along the northern margin of the Liuling unit—the likely equivalent of the Nanwan unit in Qinling) are associated with turbidites and pyroclastic sediments derived from the Qinling unit, an ophiolitic assemblage, and basic volcanic rocks; Yu and Meng (1995) suggested a forearc origin for these conglomerates. The fossiliferous Upper Devonian siliciclastic rocks are conformably overlain by a sequence of shallow-marine carbonates, turbidites, debris-flow deposits, and slumps, and a shallowing-upward sequence of proven Lower Carboniferous and suspected Carboniferous to Permian age (Yu and Meng, 1995). Metaconglomerate near Danfeng, in the northernmost Liuling unit, gave detrital zircon ages of ca. 1.0 Ga ($n = 3$), 782 ± 11 Ma ($n = 3$), and 403 ± 7 Ma (three probably metamorphic overgrowths), indicating sources within the Qinling unit and the Silurian–Devonian arc (U/Pb SHRIMP; Ratschbacher et al., 2003).

Silurian–Devonian Magmatic Arc

Within the Qin Mountains, a suite of relatively undeformed Late Silurian–Early Devonian plutons intrude the Sino-Korean craton, the Kuanping, Erlangping-Danfeng-Heihe, and Qinling units; U/Pb zircon, Sm/Nd, and Rb/Sr whole-rock, and $^{40}Ar/^{39}Ar$ hornblende ages from these plutons and associated regional metamorphism cluster at ca. 404 Ma ($n = 25$; Fig. 3A). This magmatic-metamorphic event has been interpreted as an Andean-style continental margin arc, facing a subduction zone located south of the Qinling unit (e.g., Ratschbacher et al., 2003).

Huwan Mélange

Field mapping, geochronology, and locally distinctive lithology allow delineation of a separate unit between the Qinling unit in the north and the Yangtze craton in the south (compare also Li et al., 2001; Ye et al., 1993, 1994). Definition of this unit has been hindered by strong deformation within an ~5–10-km-wide zone straddling the southern part of the Qinling unit and the northern part of the high-pressure and UHP units in southern Xinxian (the northern Dabie–Xinxian unit, see following); here we attribute this deformation mostly to the Triassic Huwan shear zone (see following). Confusion arises because this unit has been assigned to various complexes; for example, the Xinyang Group has been divided in Xinxian into the northern Nanwan flysch and the southern Balifan tectonic mélange (Zhong et al., 1999; 2001; Xu et al., 2000; Sun et al., 2002; Liu et al., 2004a, 2004b), which likely corresponds to the Sujiahe mélange of Jian et al. (1997). In the Chinese literature, the Huwan mélange has also been named the eclogite-bearing Huwan "formation" and was considered to be the southern part of the Sujiahe "Group," the northern part of which is the Dingyuan "formation" (see preceding section). These ambiguities in the definition of units have hindered the assignment of dated rocks. For example, whereas Jian et al. (1997) defined their Xiongdian eclogite as part of the Sujiahe mélange, Sun et al. (2002) classified their Xiongdian eclogite body as part of the Huwan shear zone.

The Huwan mélange contains typically mylonitized, elongated blocks of eclogite, gabbro, (epidote-) amphibolite, marble, and quartzite; augen gneiss, quartzofeldspathic schist, and graphitic schist may form an argillic matrix to these blocks. The marbles contain Ordovician fossils (Ye et al., 1994). Where defined, the boundaries of the Huwan mélange are north-dipping deformation zones. Metamorphism is greenschist to amphibolite facies. The Balifan-Sujiahe eclogites yielded peak metamorphic conditions of 600–730 °C and 1.4–1.9 GPa and retrograde metamorphism at 530–685 °C and ~6 kbar, according to Fu et al. (2002), and 550–570 °C and ~2.1 GPa, according to Liu et al. (2004b); the latter values correspond to our own *P-T* estimates (540–600 °C and 2.0 GPa, see following). An enriched light rare earth element (LREE) signature and $\varepsilon_{Nd}(t)$ values of –1.9– +5.8 indicate oceanic basalts as protoliths; these characteristics distinguish these eclogites clearly from the Yangtze craton eclogites of Xinxian–Hong'an–Dabie (northern Dabie–Xinxian unit, see following; Fu et al., 2002).

The Xiongdian quartz-eclogite bodies have undergone four independent U/Pb zircon studies (Fig. 3C). Jian et al. (1997) obtained four concordant fractions; three yielded ages between 400 and 373 Ma, the fourth 300 ± 2 Ma. Jian et al. (2001) interpreted a 424 ± 5 Ma SHRIMP core age as the age of the protolith and a 301 ± 13 Ma rim age as the age of high-pressure metamorphism; ages of 408–335 Ma were taken as mixed. Sun et al. (2002) studied two different bodies: Zircon

cores from eclogite 99XD-1 gave a range of spot ages (SHRIMP, $n = 5$), of which 398 ± 5 Ma is likely the protolith age; a second group of core ages at 324 ± 4 Ma ($n = 8$) had unclear meaning. Zircon overgrowths with garnet-omphacite-phengite inclusions produced peaks at 323 ± 7 Ma ($n = 2$) and 312 ± 5 Ma ($n = 11$), likely dating the high-pressure metamorphism. Eclogite 99XD-2 yielded core ages between 450 and 350 Ma, with peaks at 433 ± 9 Ma and 367 ± 10 Ma, which were interpreted as the protolith age; two other core and overgrowth groups likely formed during high-pressure metamorphism and retrograde metamorphism outside the garnet stability field at 316 ± 8 Ma and 307 ± 4 Ma, respectively. Gao et al. (2002) found SHRIMP zircon spot ages of 449 ± 14 Ma and 307 ± 14 Ma, and a 216 ± 4 Ma ($n = 6$) cluster in their Xiongdian eclogite. Finally, one of the eclogite bodies gave a Sm/Nd garnet–whole-rock isochron of 422 ± 67 Ma, a Rb/Sr whole-rock age of 404 ± 34 Ma, and a $^{40}Ar/^{39}Ar$ barroisite age of 399 ± 1 Ma (Ye et al., 1993). Webb et al. (1999) reported a geologically questionable 310 ± 3 Ma $^{40}Ar/^{39}Ar$ phengite age from their Xiongdian eclogite and a 233 ± 2 Ma phengite age in a top-to-the-north shear band in the enclosing quartzofeldspathic gneiss and mica schist; the Triassic overprint is supported by a muscovite $^{40}Ar/^{39}Ar$ age of ca. 243 Ma from the Xiongdian rock formation (Ye et al., 1994). Major-, trace-element, and isotope geochemistry indicates little crustal contamination for the basaltic andesite and basaltic protoliths of the Xiongdian eclogites (Li et al., 2001). Most likely, the Xiongdian eclogites represent Middle Silurian–Early Devonian mafic volcanic rocks that were subducted in the late Carboniferous and overprinted in the Triassic during the subduction of the leading edge of the Yangtze craton (see following).

The Hujiawan eclogite crops out northwest of the Xiongdian bodies and yielded a SHRIMP zircon age of 311 ± 17 Ma without inherited components (Sun et al., 2002). Conventional U/Pb zircon geochronology gave concordant ages of 631 ± 3 Ma (one fraction; likely the protolith age), 533 ± 23 Ma (one fraction), 377 ± 7 Ma (two fractions, interpreted as mixed ages), and ca. 300 Ma (high-pressure metamorphism). The trace-element and isotopic characteristics of the Hujiawan eclogite suggest an island-arc basalt (Liu et al., 2001), which differs from the Xiongdian bodies.

The Qianjinhepeng eclogite (>1.2 GPa, 610 ± 40 °C) is embedded in quartzofeldspathic gneiss at the northern rim of the Huwan mélange. It gave zircon SHRIMP ages of 933 ± 25 Ma (one core), a cluster of 716 ± 28 Ma ($n = 4$), likely the protolith age, and a 534–229 Ma range of spot ages (8 spots between 315 ± 17 Ma and 229 ± 12 Ma); the youngest age was interpreted as the maximum age of the high-pressure metamorphism (Liu et al., 2004a).

The Huwan mélange has yielded Permian–Triassic cooling ages: $^{40}Ar/^{39}Ar$ muscovite ages of ca. 267 Ma, ca. 226 Ma (Niu et al., 1994), ca. 263 Ma (Xu et al., 2000), ca. 243 Ma, ca. 230 Ma (Ye et al., 1993), and ca. 206 Ma (Webb et al., 1999). Four Rb/Sr muscovite–plagioclase–whole-rock isochrons of 259 ± 33 Ma, 236 ± 11 Ma, 230 ± 40 Ma, and 225 ± 8 Ma of unspecified mylonitic rocks likely date deformation related to the Huwan shear zone (see following; Ye et al., 1993).

Northern Dabie–Xinxian Complex (High-Pressure–UHP Metamorphic Yangtze Craton)

The northern Dabie–Xinxian complex, also called the Xinxian "formation" in the Chinese literature, consists of granitic to granodioritic gneiss and supracrustal rock that experienced proven high-pressure to UHP conditions. Pressures apparently decrease both northward and southward within this unit (Zhang and Liou, 1994; Cui and Wang, 1995). Liu et al. (2004b) quantified the *P-T* conditions of eclogites within the northern high-pressure (quartz-eclogite) zone and southerly UHP (coesite-eclogite) zone at 470–500 °C, 1.4–1.7 GPa and 620–670 °C, 2.6–2.9 GPa, respectively; we obtained ~530 °C and 2.2 Ga for an eclogite from the quartz-eclogite zone (see following).

Sun et al. (2002) obtained a protolith age of 752 ± 17 Ma and a 232 ± 10 Ma age for the high-pressure Xuanhuadian quartz eclogite (SHRIMP U/Pb zircon; Fig. 2B; see also Fig. 3D for a summary of important northern Dabie–Xinxian geochronology). The Huwan eclogite (Fig. 2B; 570 ± 30 °C, >1.2 GPa), grouped into the southern part of the Huwan high-pressure unit by Liu et al. (2004a), gave a concordant zircon SHRIMP age of 733 ± 10 Ma ($n = 20$), likely its protolith age. From its location, lithological association, and the lack of a Paleozoic age component, we suggest that this eclogite is part of the northern Dabie-Xinxian complex. The Tianpu coesite-eclogite (Fig. 2B, 640 ± 30°, 2.9 ± 0.3 GPa), embedded in granitic gneiss, contains only metamorphic zircons that cluster at 213 ± 5 Ma ($n = 13$); as its phengite Rb/Sr age is 212 ± 7 Ma, these ages are best interpreted as dating post-UHP recrystallization (Liu et al., 2004a). In northern Dabie (the northern part of the Northern Orthogneiss Unit of Hacker et al., 1996a), pre-Cretaceous ages of gneisses were 757 ± 1 Ma (Xue et al., 1997) and 707 ± 42 (Xie et al., 2001). Ultramafic and mafic bodies distributed along the northern margin of Dabie also yielded Triassic ages (Hacker et al., 1998; Jahn et al., 1999; Ratschbacher et al., 2000; see summaries in Fig. 2A and in Liu et al., 2001), which are interpreted as dating the high-pressure and UHP conditions (e.g., Liu et al., 2001; Xie et al., 2004).

The $^{40}Ar/^{39}Ar$ phengite ages from the northern margin of the northern Dabie–Xinxian complex in Xinxian are: 187 ± 1 Ma (granitic gneiss; Xu et al., 2000), 235 ± 2 Ma (felsic gneiss), and 215 ± 1 Ma (mica schist–orthogneiss intercalation; this study). The $^{40}Ar/^{39}Ar$ phengite ages from within the northern Dabie–Xinxian complex are 243 ± 6 Ma (shear band in eclogite), 212 ± 2 Ma (retrograde epidote–actinolite schist), 231 ± 2 Ma (eclogite rim), 224 ± 2 Ma (shear band in gneiss), 222 ± 2 Ma (mylonitized eclogite), 196 ± 2 Ma (host paragneiss to the previous sample; Webb et al., 1999), and 195 ± 1 Ma (gneiss; Eide et al., 1994).

Cretaceous Magmatism and Related Regional Metamorphism

In contrast to northern Dabie, no well-documented U/Pb zircon ages are available from the Mesozoic granitoids of Xinxian (Fig. 2). The oldest group of $^{40}Ar/^{39}Ar$ ages in Xinxian, 130–125 Ma (Fig. 3E; 125–130 Ma; compiled from Niu et al., 1994; Webb et al., 1999; Ratschbacher et al., 2000) overlaps the crystallization ages of Early Cretaceous plutons in the Northern Orthogneiss Unit of the northern Dabie Shan and thus likely reflects postemplacement cooling. Cooling at ca. 120 Ma in northern Dabie is structurally controlled (Ratschbacher et al., 2000), and this same age is dominant in Xinxian (Fig. 3E). K-feldspar ages from Xinxian overlap the ca. 100–90 Ma reheating and subsequent cooling documented in Dabie (Ratschbacher et al., 2000).

NEW $^{40}Ar/^{39}Ar$ AND FISSION-TRACK GEOCHRONOLOGY

$^{40}Ar/^{39}Ar$ Geochronology

We measured $^{40}Ar/^{39}Ar$ ages on eight mineral concentrates (Fig. 4; Table 1). Analyses were performed at Stanford University and the University of Vienna following analytical procedures of Hacker et al. (1996b) and Frimmel and Frank (1998). Four K-feldspars were degassed following the heating schedule adopted for multiple-diffusion domain analysis (Lovera et al., 1997); we refrained, however, from a quantitative evaluation, because multiple isothermal, low-temperature steps identified significant Cl-correlated excess ^{40}Ar (Harrison et al., 1994), and the age spectra are not composed of monotonically increasing steps. Ratschbacher et al. (2003; their Appendix A) outlined adjustments allowing modeling and interpretation of parts of such spectra (e.g., D222d), but in this study, the quantitative evaluation does not yield information beyond the qualitative interpretation.

K-feldspar samples D222d and D527b are from the southern Guishan complex. At station D222, the active Jinzhai fault (Ratschbacher et al., 2000) overprints mylonitic rocks. A disturbed hornblende spectrum (deformed amphibolite; Ratschbacher et al., 2003) from this locality and two poorly located muscovite K/Ar ages (Chen et al., 1993) indicate a tectonometamorphic event at younger than 497 Ma and ca. 450–433 Ma, respectively. The K-feldspar records a regional thermal overprint at ca. 100 Ma, likely induced by a Cretaceous pluton to the south, that shows initial cooling through ~250 °C at ca. 128 Ma, and reheating and cooling at 90 ± 10 Ma (Ratschbacher et al., 2000). K-feldspar from a retrogressed, partly mylonitic amphibolite and tourmaline–hornblende gneiss with K-feldspar augen at station D527 suggests mylonitization older than 270 Ma and reheating at ca. 240 Ma. Niu et al.'s (1994) K-feldspar age of ca. 255 Ma supports a Permian–Triassic low-temperature overprint in this area; these data also constrain the age of the blueschist-grade overprint in these rocks (see following). Two hornblende ages at ca. 401 Ma (near D527, Niu et al., 1994) and ca. 316 Ma (Zhai et al., 1998) suggest a late Paleozoic age for the mylonitization. Sample D337a, from the southernmost margin of the Dingyuan complex, documents reheating and subsequent cooling of Neoproterozoic basement (Hacker et al., 2000; see preceding) by Cretaceous regional metamorphism at ca. 125–110 Ma; the pluton east of this station cooled through ~300 °C at ca. 120 Ma (Webb et al., 1999). K-feldspar ages of samples D236 and D329b document the regional Cretaceous (ca. 100–105 Ma) reheating of the high-pressure–UHP Xinxian–Hong'an area, in line with the data of Webb et al. (1999).

Two white-mica ages characterize cooling accompanying deformation within the Huwan shear zone along the northern margin of the Xinxian complex. D538d phengite, from mylonitic but weakly retrogressed gneiss containing numerous shear bands, dates early top-to-the-north flow at ca. 235 Ma; Liu et al. (2004b) obtained phengite Si values of 3.33 atoms per formula unit (p.f.u.) in shear bands in their eclogite HW01, likely at our station D538. D539c phengite (core and rim Si values of 3.48 and 3.28 p.f.u.) dates top-to-the-north flow along phengite-rich shear bands within the retrograde outer margin of a small eclogite body at ca. 215 Ma, demonstrating a Late Triassic age for late-stage deformation in the Huwan shear zone. White mica in two-mica, gneissic, likely volcaniclastic, quartzite D545c yielded ca. 271 Ma, in line with two other Permian white-mica ages (Niu et al., 1994) from the Foziling unit in Dabie.

Apatite and Titanite Fission-Track Geochronology

Twenty-eight samples from metamorphic and magmatic rocks from the northern Dabie and Hong'an–Xinxian areas were selected for apatite (AFT, $n = 22$) and titanite fission-track geochronology (TFT, $n = 6$). See Grimmer et al. (2002) for the methodological and technical aspects of AFT, including the calculation and comparison of ages obtained by the independent ϕ, Z, and ξ methods, the evaluation of the Durango, Fish Canyon, and Mount Dromedary standards, and our approach to $T[t]$-path modeling. We use ϕ ages in the following discussion. Table 2 lists the sample locations, the AFT dating parameters, and ages; Table 3 gives track-length parameters. Titanite was separated conventionally mounted in epoxy, and ground and polished with 6.0, 3.0, 1.0, and 0.3 μm diamond suspensions. The mounts were etched for 24 h in 0.4% HF at room temperature (Jonckheere and Wagner, 2000; Enkelmann et al., 2005), covered with muscovite external detectors, and irradiated in the course of two irradiations in the Thetis reactor at the Institute for Nuclear Sciences of the University at Gent. The muscovite external detectors were etched in 40% HF for 30 min at room temperature. Three mounts of Fish Canyon and Mount Dromedary age standards and four mounts of standard uranium glass (CN-5) were included in each irradiation to calculate the ζ calibration factor (423 ± 25 yr cm^2). Track counting was performed on clear titanite surfaces with homogeneous track densities at a

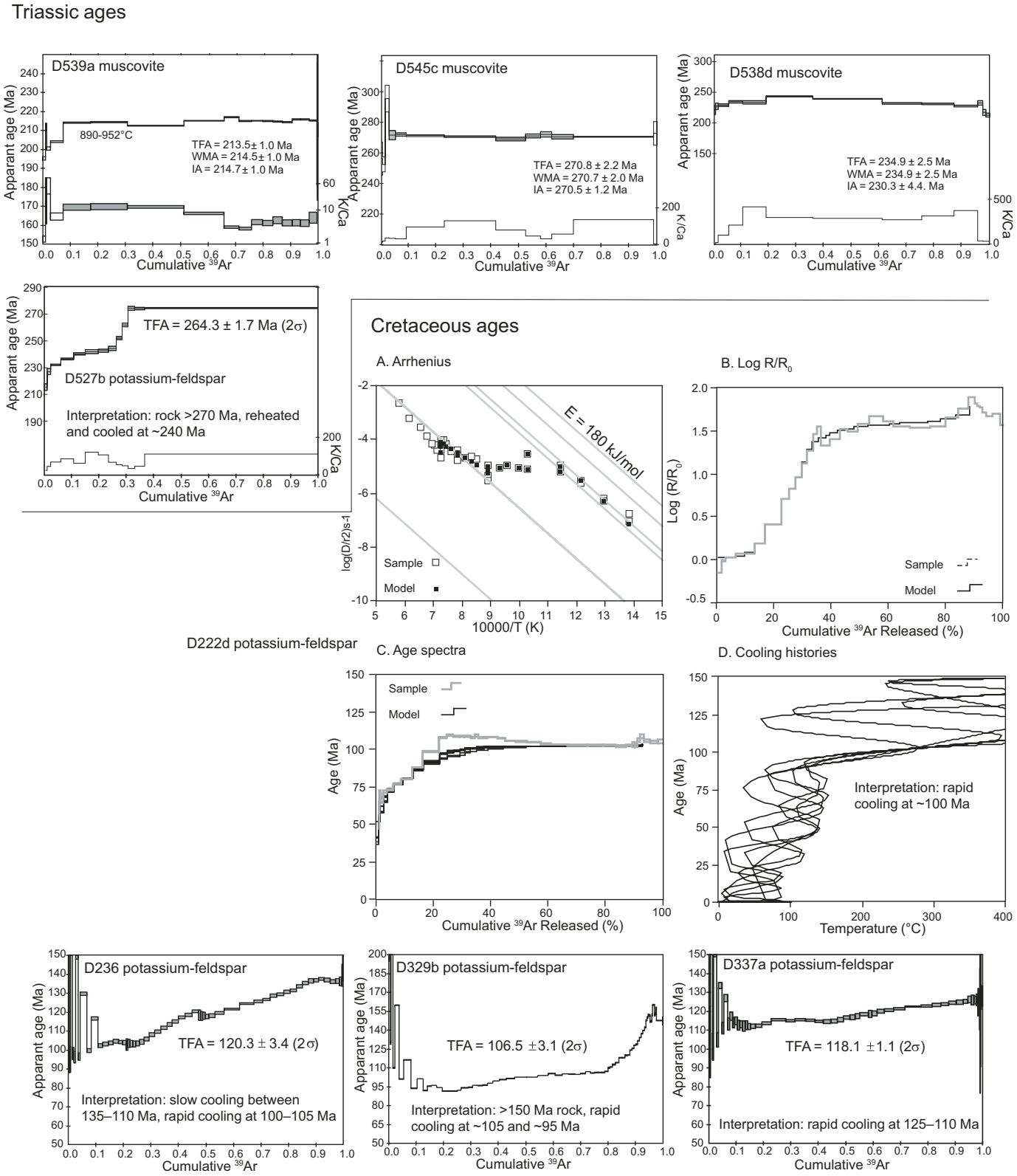

Figure 4. New $^{40}Ar/^{39}Ar$ data. See Table 1 for sample location, age data, and interpretations. Weighted mean ages (WMA) were calculated using shaded steps. TFA—total fusion age; IA—isochron age. Uncertainties are 1σ. Diffusion-domain analysis of metamorphic K-feldspars shows Arrhenius plot, log(R/R_0) plot, release spectrum, and range of cooling histories.

TABLE 1. $^{40}Ar/^{39}Ar$ DATA FROM XINXIAN–DABIE

Sample	Rock and Unit	Coordinates	
D222d	metavolcaniclastic mylonitic gneiss with amphibolite and leucocratic quartz-feldspar layers, Guishan	31°48.45′	115°15.15′
D236	potassium-feldspar vein in a garnet-hornblende-biotite orthogneiss, Xinxian	31°30.09′	114°39.62′
D329b	potassium-feldspar megacrystic quartzofeldspathic gneiss, Hong'an	31°16.0′	114°09.9′
D337a	banded gneiss with mafic layers, Dingyuan	31°45.197′	114°47.934′
D527b	potassium-feldspar augen in mylonitic tourmaline-hornblende gneiss, Guishan	32°03.966′	114°01.873′
D538d	felsic gneiss, northernmost Xinxian	31°43.406′	114°52.374′
D539a	felsic orthogneiss and micaschist, northernmost Xinxian	31°41.346′	115°00.356′
D545c	biotite-bearing, gneissic quartzite (metavolcanic), Foziling	31°28.975′	116°12.173′

Sample	J	Weight (mg)	Grain Size (μm)	Interpretation
Potassium–feldspar (multi-diffusion domain, qualitative interpretation)				
D222d	0.0040573	2.2	400	rapid cooling at ca. 100 Ma
D236	0.0042144	1.8	400	slow cooling between 135–110 Ma, rapid cooling 100–105 Ma
D329b	0.0040316	1.5	200	>150 Ma rock, Cretaceous reheating and rapid cooling at ca. 105 and ~95 Ma
D337a	0.0041142	1.7	400	rapid cooling from 110–125 Ma
D527b	0.008560	8.0	1000	>275 Ma rock, reheating at ca. 240 Ma

Sample	mineral	J	Weight (mg)	Grain size (μm)	TFA	WMA	isochron	MSWD or Correlation	40/36	% Ar
Muscovite										
D538d	mus	0.008560	4.0	200	234.9 ± 2.5	*234.9 ± 2.5*	230.3 ± 4.4	0.7243	360 ± 104	100
D539a	mus	0.0007004	4.1	400	213.5 ± 0.6	*214.5 ± 0.6*	214.7 ± 0.7	21/1.9	290 ± 6	92
D545c	mus	0.008560	6.1	200	270.8 ± 2.2	*270.7 ± 2.0*	270.5 ± 1.2	0.9964	402 ± 16	92

Note: Italics indicate preferred age. TFA—total fusion age; WMA—weighted mean average; MSWD—mean square of weighted deviates.

nominal magnification of 1000 using a Zeiss Axioplan microscope. All suitable grains were counted in samples that contained fewer than 20 grains. Table 4 lists the TFT sample locations, dating parameters, and ages.

Figure 5 combines the regional fission-track age distribution with an interpretation of Cretaceous (Fig. 5A) and Cenozoic structures (Fig. 5B) in Hong'an–Xinxian and northern Dabie (Fig. 5C); the structural interpretation updates that given by Ratschbacher et al. (2000). The AFT ages are Early Cretaceous to late Eocene (145–40 Ma). The subdued topography of the Hong'an–Xinxian area (our samples span ~250 m elevation difference) inhibits any age-altitude correlation. Figure 5 also presents *T*[*t*]-path modeling results (using AFTSolve 1.1.3, Ketcham et al., 2000) of samples with a large number of confined tracks. TFT ages are included in the diagrams, but were not used in the modeling. Because there are only weak geologic constraints on the cooling history of the Hong'an–Xinxian area, we set pairs of initial and final constraints. Two closely spaced initial constraints allow the thermal histories to start with cooling or heating; the two final constraints allow the model to find a thermal event that reduces all accumulated tracks and thus accounts for track shortening at ambient temperatures over geological times. Low-temperature track-length reduction has been described for fossil tracks in age standards and borehole samples; this reduction is not incorporated into the annealing equations derived from laboratory annealing experiments on induced fission tracks, which only account for annealing that takes part within the partial annealing zone (see discussion in Jonckheere, 2003a, 2003b).

We obtained similar, slow cooling paths throughout the study area, although we varied the initial constraints over a wide age range (Fig. 5). Assuming a geothermal gradient of 25 °C/km, the exhumation rate has been ~0.06 mm/yr for the last 70 m.y. (the average AFT age of Hong'an–Xinxian; Fig. 3F). Combining the TFT and AFT ages and assuming titanite and apatite closure temperatures of 300 °C and 100 °C, respectively, gives a slow Late Cretaceous cooling of 5–7 °C/m.y. for Xinxian and 3–4.5 °C/m.y. for the northern part of the Northern Orthogneiss Unit of Dabie; the relatively high assumed titanite closure temperature is supported by equivalent $^{40}Ar/^{39}Ar$ biotite and TFT ages for 4 of our 6 samples. The apatite confined track-length distributions are typically negatively skewed, broad, and unimodal. In line with the *T*[*t*]-path modeling results, this indicates continuous cooling through the ~100 °C isotherm to surface temperatures since the time given by the apparent fission-track ages.

Projecting all available AFT ages on a NW-SE section across Hong'an–Xinxian (Fig. 5A, inset) does not show age clusters, and, with the possible exception of the Tongbai fault zone (a Late Cretaceous–Early Tertiary strike-slip zone that was reactivated in the late Cenozoic; Webb et al., 1999; Ratschbacher et al., 2000), no unambiguous correlation with structures. The same indistinct picture (a large age range over small elevation difference) holds for the northern Dabie Shan, again suggesting slow exhumation rates.

Figure 3F plots all well-documented AFT ages from Tongbai–Hong'an–Xinxian–Dabie area and the northern, eastern, and southern forelands of the Dabie Shan (Grimmer et al., 2002; Reiners et al., 2003; Zhou et al., 2003; Xu et al., 2006). Two distinct maxima at 80–55 Ma and ca. 45 Ma contrast with a broad age range that spans the Cretaceous. These clusters may have significance at a smaller scale: Eocene ages occur mostly along the Tanlu fault in eastern Dabie, where the footwall Dabie block is juxtaposed against the Qianshan basin and, more rarely, in Tongbai-Xinxian. All areas show Late Cretaceous–Tertiary ages.

TABLE 2. SAMPLE LOCATIONS AND APATITE FISSION-TRACK DATING PARAMETERS

Sample	Latitude (N)	Longitude (E)	Elevation (m)	grains	N_s	N_i	ρ_d (10^5 cm^{-2})	ϕ (10^{15} cm^{-2})	ζ (a cm^2)	Z (10^8 a)	P(χ^2)	ϕ – age (Ma)	ζ-age (Ma)	Z –age (Ma)
DS43*	31°22.400′	116°11.500′	180	27	276	917	16.4	9.670	369	5.76	20	87.7 ± 6.3	90.2 ± 6.5	86.0 ± 6.4
DS58*	31°14.340′	116°20.390′	190	20	1912	6671	16.4	9.730	369	5.78	2	83.6 ± 3.0	85.8 ± 3.1	81.9 ± 3.0
DS72*	31°07.480′	116°31.520′	400	26	664	2885	16.5	9.670	369	5.79	26	67.2 ± 3.2	69.6 ± 3.4	66.3 ± 3.4
D516*	31°43.140′	116°30.584′	100	14	954	714	3.87	2.580	369	1.53	0	116.0 ± 6.7	105 ± 6	113 ± 6.5
D517	32°07.455′	114°00.285′	200	11	846	439	3.87	2.581	369	1.53	0	128 ± 14	117 ± 13	124 ± 13
D519	32°10.289′	113°57.335′	100	17	1580	2580	3.87	2.580	369	1.53	6	47.7 ± 1.8	43.6 ± 1.8	46.7 ± 2.3
D523	31°54.94-′	113°57.702′	100	7	150	126	3.87	2.579	369	1.53	43	92.5 ± 11.0	84.4 ± 10	90.4 ± 11
D524	31°53.823′	113°57.925′	100	23	1090	2106	3.87	2.578	369	1.53	0	48.2 ± 5.5	44.0 ± 5.0	47.1 ± 5.4
D527	32°03.966′	114°01.873′	80	25	1759	936	3.87	2.575	369	1.53	40	145.0 ± 6.6	133 ± 6.3	142 ± 7.8
D532	31°50.148′	114°27.146′	90	20	1535	1329	3.87	2.574	369	1.53	21	89.6 ± 3.8	81.9 ± 3.7	87.8 ± 4.6
D533	31°56.971′	114°38.547′	150	10	757	993	3.87	2.573	369	1.53	3	61.3 ± 4.6	56.1 ± 4.3	60.1 ± 4.6
D535	31°46.833′	114°48.748′	90	9	503	382	3.87	2.572	369	1.53	23	102.0 ± 7.2	93.3 ± 6.7	100 ± 7.7
D536	31°44.850′	114°48.864′	100	25	1262	1499	3.87	2.571	369	1.53	37	65.3 ± 2.8	59.8 ± 2.7	64.1 ± 3.4
D538	31°43.200′	114°52.473′	90	56	947	1066	3.87	2.540	369	1.53	37	68.1 ± 3.3	63.1 ± 5.1	67.6 ± 3.9
D539	31°41.346′	115°00.356′	100	14	153	210	3.87	2.530	369	1.53	14	55.7 ± 6.0	51.8 ± 5.7	55.5 ± 6.3
D540	31°42.134′	115°07.478′	260	20	286	520	3.87	2.519	369	1.53	65	41.9 ± 3.2	39.2 ± 7.8	41.9 ± 3.5
D543*	31°27.736′	116°10.498′	320	40	3204	3337	3.87	2.510	369	1.53	13	72.7 ± 2.3	68.2 ± 2.4	73.0 ± 3.3
D545*	31°28.975′	116°12.173′	280	7	343	402	3.87	2.490	369	1.53	78	64.1 ± 4.9	60.6 ± 4.7	64.9 ± 5.4
D546	31°21.877′	116°22.297′	100	10	140	247	6.21	4.009	341	2.14	12	67.1 ± 7.2	59.7 ± 6.4	60.4 ± 6.8
D549	31°12.511′	116°22.739′	190	23	565	1197	6.21	4.001	341	2.14	80	55.8 ± 3.1	53.9 ± 3.0	50.3 ± 3.3
D552	31°04.699′	116°21.012′	780	20	1121	1805	6.21	3.994	341	2.14	47	73.2 ± 3.1	65.4 ± 2.7	66.1 ± 3.7
D98-17*	31°10.299′	116°32.279′	—	34	4271	4844	3.87	2.410	369	1.53	0	60.2 ± 1.5	59.0 ± 1.3	63.1± 1.4
CN104	31°24.370′	114°40.158′	125	23	401	448	6.21	3.899	341	2.14	98	103.0 ± 7.4	94.1 ± 6.7	95.1 ± 7.6
CN106	31°19.737′	114°22.615′	148	30	752	1483	6.21	3,874	341	2.14	1	61.5 ± 3.9	56.6 ± 3.6	57.2 ± 3.6
CN110	32°04.573′	113°32.067′	325	14	757	2141	6.21	3.899	341	2.14	0	40.3 ± 3.1	37.3 ± 2..9	37.7 ± 2.9
CN111a	32°08.512′	113°35.225′	295	23	1255	2604	6.21	3.852	341	2.14	43	54.9 ± 2.2	50.8 ± 1.9	51.4 ± 2.7
CN112	32°20.518′	113°36.500′	75	26	2125	3907	6.21	3.806	341	2.14	0	66.6 ± 4.0	62.5 ± 3.7	63.1 ± 3.8
CN113	32°21.112′	113°25.868′	152	30	710	1229	6.21	3.776	341	2.14	84	64.4 ± 3.3	60.9 ± 3.0	61.5 ± 3.8
CN136	31°15.927′	113°53.312′	45	19	505	374	6.21	3.547	341	2.14	84	141 ± 10	141 ± 10	143 ± 11

Note: N_s: number of spontaneous tracks; N_i: number of induced tracks; ρ_d: track density on dosimeter; ϕ: neutron flux density; Z: Z-calibration factor; ζ: ζ_{CN5} -calibration factor; P(χ)^2 is the probability of obtaining χ^2 value for ν degrees of freedom (where ν = number of grains - 1).

*Data published in Grimmer et al. (2002)

TABLE 3: CONFINED TRACK-LENGTH PARAMETERS IN APATITE

Sample	*N*	MTL (μm)	Std.
D519	106	13.0	1.6
D524	33	13.0	1.4
D527	106	12.8	1.3
D532	108	11.9	1.9
D533	12	11.8	2.0
D536	70	12.7	1.6
D538	15	13.0	1.9
D540	10	10.9	2.5
D72	40	13.4	1.2
D98-17	105	12.0	1.6

Note: N: number of tracks; MTL: mean track length; Std.: standard deviation.

NEW PETROLOGY

We investigated ~100 samples from the main geological units of the Xinxian area with optical microscopy and selected nine samples for electron-probe microanalysis. We operated the five-spectrometer JEOL JXA-8900R electron microprobe at Freiberg at 15 kV accelerating voltage, 20 nA beam current, and counting times of 20 s for Si, Al, Mg, Ca, Sr, Ba, and K, and 30 s for Fe, Ni, Na, Cr, Mn, and Ti. Smithsonian Institute and MAC™ standards were used. Table 5 lists sample locations and parageneses, and summarizes our *P-T* estimates. Figure 6 depicts the *P-T* arrays derived from mineral assemblages and thermobarometry. Tables 6–11 provide microprobe analyses of representative minerals; they are available in the GSA Data Repository[1].

Northern Dabie–Xinxian Complex

Massive eclogite sample 98196 (station D539) shows the primary mineral assemblage garnet + omphacite + phengite + clinozoisite + quartz, with atoll-shaped garnet porphyroblasts and a weak alignment of the prismatic minerals. There is no petrographic indication for the former stability of coesite in the matrix or as inclusions. Along grain boundaries and cleavages, omphacite is altered to a felty mass of sheet silicates and amphibole. Garnet rims are overgrown by bluish-green amphibole and plagioclase. Other secondary minerals include biotite, formed at the expense of phengite, and sphene that mantles rutile. Garnet shows rimward decreasing Mn and Ca and a concomitant increase in Fe and Mg. Typical core and rim compositions are $Alm_{50}Grs_{35}Prp_3Sps_{12}$ and $Alm_{63}Grs_{25}Prp_{11}Sps_1$, respectively. The bell-shaped Mn profile probably developed during growth under greenschist- to amphibolite-facies conditions (cf. Spear, 1993), and increasing Mg# indicates heating during growth. Omphacite has jadeite contents of 28–44 mol% with variable and irregular zoning. Phengite is zoned with outward decreasing Si contents of 3.48 –3.28 atoms p.f.u. and decreasing X_{Mg}, highlighting Mg-Tschermaks exchange. Clinozoisite is unzoned with pistacite contents of ~12 mol%. Secondary clinoamphibole, growing at the rims of garnet porphyroblasts, is barroisite and magnesiokatophorite. Secondary plagioclase is albite with $An_{<01}$.

A *P-T* estimate for eclogite 98196 is difficult due to the distinct retrograde overprint. Phengite in paragenesis with garnet and omphacite allows an estimate of the peak pressure conditions based on the barometer of Waters and Martin (1993, updated 1996; activity models in Appendix). Garnet compositions yielding the highest activity factor $a^2_{Grs}a_{Prp}$, phengite with the highest Si content, and omphacite with the highest jadeite component were considered to reflect maximum pressure conditions. In sample 98196, the highest $a^2_{Grs}a_{Prp}$ point and the highest Mg# are at the rim, indicating coincidence of peak temperatures and pressures at 2.1–2.2 GPa and 500–550 °C. Precise temperature estimates in eclogites, mainly based on Fe-Mg exchange between garnet and omphacite or garnet and phengite (e.g., Krogh, 2000; Green and Hellmann, 1982), are problematic due to our inability to estimate Fe^{3+} in phengite and omphacite (e.g., Schliestedt, 1980; Carswell et al., 1997). For omphacite, Fe^{3+} estimates based on charge balance or Na content (e.g., Ryburn et al., 1976; Droop, 1987; Cawthorn and Collerson, 1974) are highly variable and depend critically upon the accuracy of the microprobe analyses. We assumed 50% Fe^{3+}, as recommended by Carswell et al. (2000) and as measured for Dabie eclogites using wet chemistry and XANES (Schmid et al., 2003); this gave 485–535 °C for the omphacites with the highest jadeite contents. Due to the small amount of Fe in phengite, methods to determine its ferric iron content often fail (e.g., Schliestedt, 1980). Assuming that ferrous

[1]GSA Data Repository item 2006051, Tables 6–12, is available online at www.geosociety.org/pubs/ft2006.htm, or on request from editing@geosociety.org or Documents Secretary, GSA, P.O. Box 9140, Boulder, CO 80301, USA.

TABLE 4. SAMPLE LOCATIONS AND SPHENE FISSION-TRACK DATING PARAMETERS

sample	Latitude (N)	Longitude (E)	grain	N_s	N_i	ρ_d (10^5cm^{-2})	ζ (a cm^2)	P(χ^2) (%)	ζ-age (Ma)
CN111b	32°08.307′	113°35.135′	20	1089	2089	7.66	423	67	83.9 ± 6.6
CN113	32°21.067′	113°25.521′	10	1263	2087	7.66	423	0	97.1 ± 6.5
DS58	31°14.340′	116°20.390′	8	1312	907	4.27	423	15	129.3 ± 9.7
DS72	31°07.480′	116°31.520′	18	1687	1340	4.27	423	77	112.7 ± 8.0
D98-17	31°10.299′	116°32.279′	11	1955	2381	7.66	423	85	131.7 ± 9.2
D536	31°44.850′	114°48.864′	20	1158	974	4.27	423	79	106.5 ± 8.0

Note: N_s: number of spontaneous tracks; N_i: number of induced tracks; ρ_d: track density on dosimeter; ϕ: neutron flux density; Z: Z-calibration factor; ζ: ζ_{CN5}-calibration factor; P(χ^2) is the probability of obtaining χ^2 value for ν degrees of freedom (where ν = number of grains - 1).

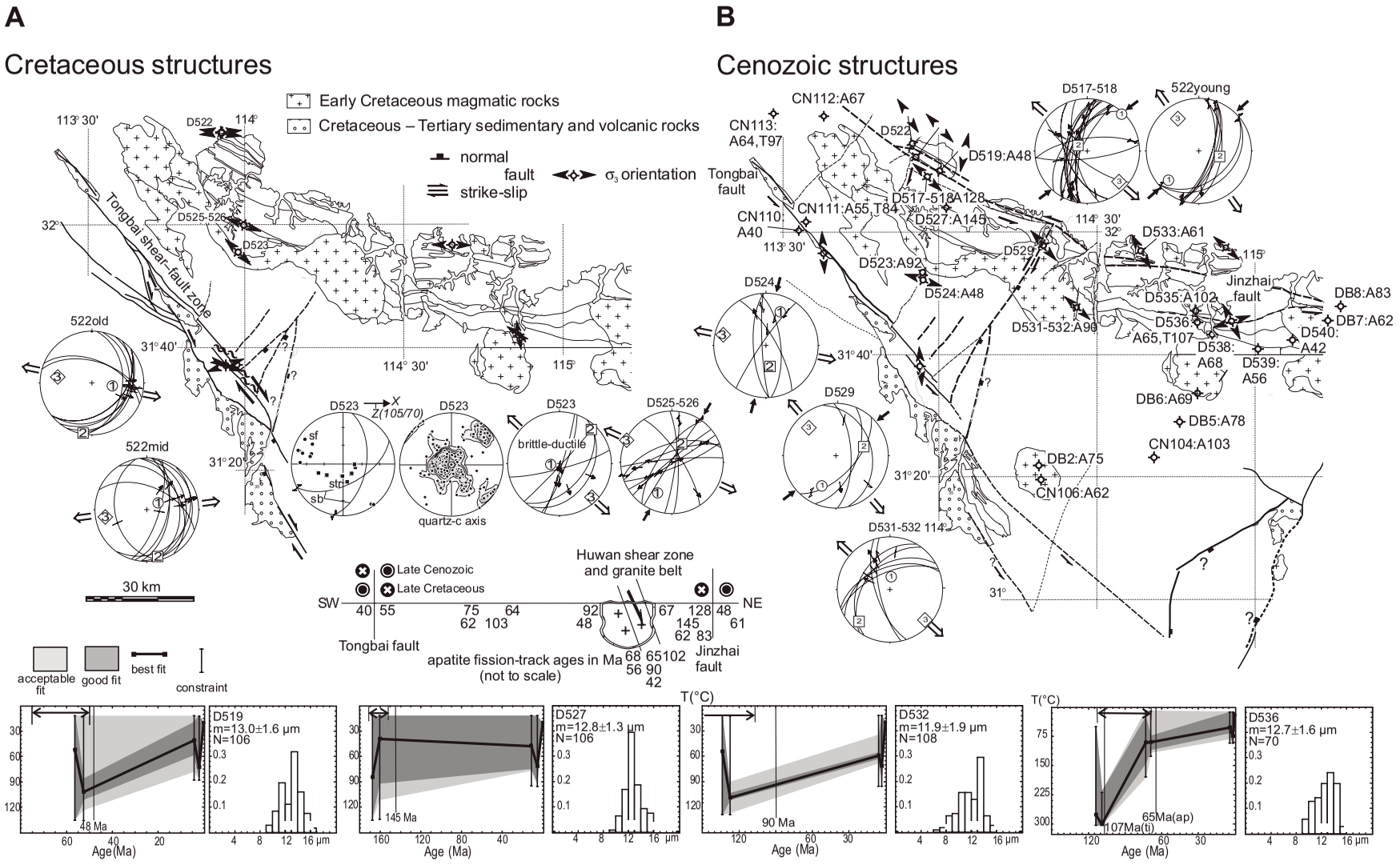

Figure 5. Simplified map of Cretaceous (A) and Cenozoic (B) structures in Tongbai-Xinxian and Cenozoic structures in northern Dabie (C). Maps are modified from and unlabeled data are taken from Ratschbacher et al. (2000). Lower-hemisphere, equal-area stereograms show ductile and brittle structural data: sf—foliation; str—mineral stretching lineation; sb—shear band; sz—shear zone; tg—tension gash. Fault-slip data and principal stress orientations 1–3: Faults are drawn as great circles, and striae are drawn as arrows pointing in the direction of displacement of the hanging wall. Confidence levels of slip-sense determination are expressed in the arrowhead style: solid—certain; open—reliable; half—unreliable; without head—poor. Arrows around the plots give calculated local orientation of subhorizontal principal compression and extension. In B and C, apatite fission-track (A) and titanite fission-track (T) data from this study are plotted together with reliable data from the literature (Grimmer et al., 2002; Reiners et al., 2003; Zhou et al., 2003; Xu et al., 2006). Inset in A gives schematic NE-SW profile across Tongbai-Xinxian with location of major faults, Cretaceous plutonism, and apatite fission-track ages. Insets in A–C: Confined track-length distributions and representative *T*[*t*] paths of representative samples. In the *T*[*t*]-path diagrams, the arrow at the top of each diagram indicates the range of initial constraints for which the depicted *T*[*t*]-path solutions are valid. The constraints are represented by the bold vertical lines. The vertical line with the number at the bottom of each diagram gives the apatite fission-track age in Ma.

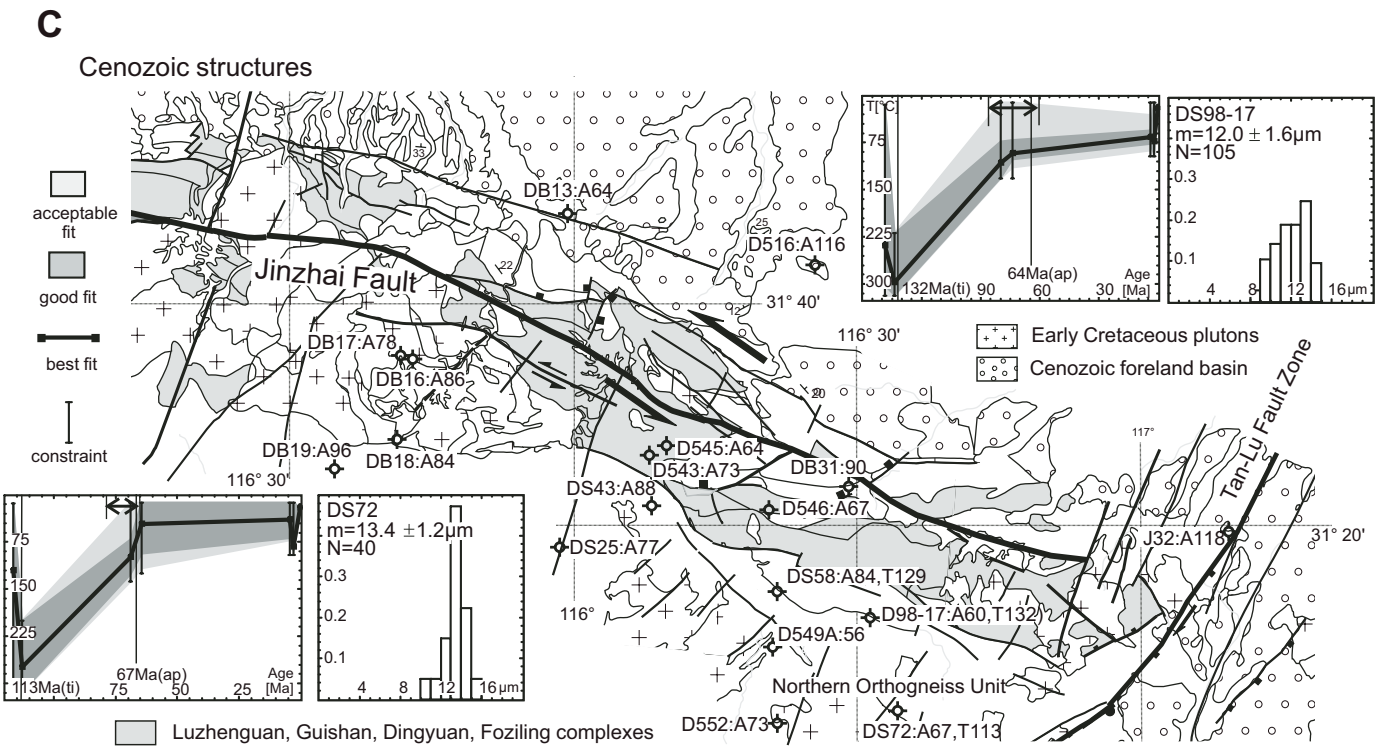

Figure 5. *(continued)*

TABLE 5. NEW PETROLOGY FROM XINXIAN

Sample/Station	Rock Type	Unit	Mineral Assemblage	Pressure–Temperature Estimate
98196/D539	eclogite	Xinxian complex	Grt - Omp - Phg - Czo - Qtz ± Rt, Ap	530 °C/2.21 GPa
98185/D530	eclogite	Huwan mélange (Xiongdian)	Grt - Omp - Phg - Czo - Qtz ± Rt, Ap	536 °C/2.01 GPa
D530c/D530	eclogite	Huwan mélange (Xiongdian)	Grt - Omp - Phg - Czo - Bar - Qtz ± Rt, Ap	595 °C/2.06 GPa
98181/D530	garnet amphibolite	Huwan mélange (Xiongdian)	Grt - Mg-Hbl - Pl (An_{10-12}) - Phg - Czo - Qtz ± Rt, Ilm, Ap	560 °C/1.1 GPa
98182/D530	garnet-mica schist	Huwan mélange (Xiongdian)	Grt - Phg - Czo - Qtz - Ab ± Rt, Spn	600 °C/1.8 GPa
D525a/D525	greenschist	Dingyuan complex	Act/Mg-Hbl - Ep - Chl - Ab - Phg - Qtz ± Cc, Spn, Zrn, Ap	core: 480 °C/0.71 GPa; rim: 420 °C/0.43 GPa
D527d/D527	amphibolite	Guishan complex	Ed/Prg - Pl (An_{34-41}) - Qtz - Bt ± Ilm, Ap	740 °C/0.9 GPa; HP/LT overprint: 250–300 °C/0.4–0.65 GPa
D527e/D527	amphibolite	Guishan complex	Mg-Hs - Pl (An_{33-37}) - Qtz - Bt ± Ilm, Ap	680 °C/1.1 Gpa
D522a/D527	amphibolite	Erlangping unit	Act/Mg-Hbl - Ep - Chl - Ab - Phg ± Qtz, Ilm	core: 350 °C/1 GPa; rim: 555 °C/0.63 GPa

Note: See Table 2 for locations (latitude, longitude), except for D530, 31°45.151′, 114°28.340′; D525, 32°00.052′, 113°59.243′. Mineral abbreviations follow Kretz (1983), except for Bar=barroisite, Phg=phengite.

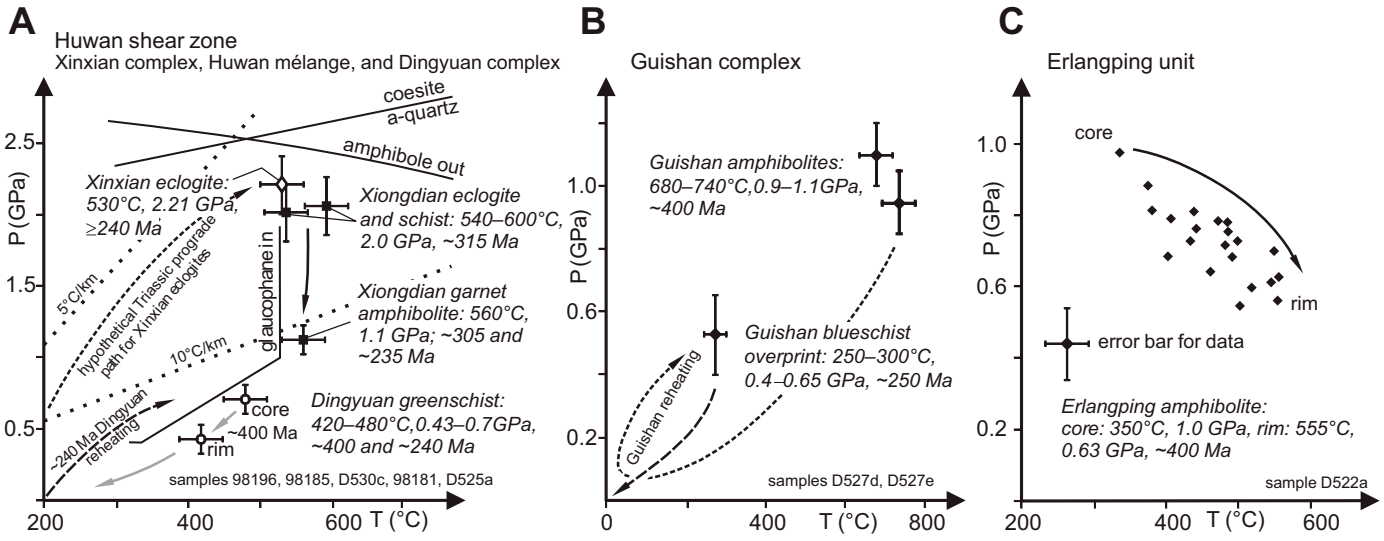

Figure 6. (A) Pressure-temperature-time (*P-T-t*) path for the Huwan shear-zone rocks straddling the Xinxian complex, the Huwan mélange, and the Dingyuan complex. *P-T* estimates with error bars are for the late Paleozoic Xiongdian eclogitic metabasites (squares), Triassic Xinxian eclogite (diamond), and early Paleozoic Dingyuan greenschist (circle; core and rim sections). Amphibole out after Carswell (1990), glaucophane in after Maresch (1977), quartz-coesite transition after Bohlen and Boetcher (1982). (B) *P-T-t* data of the Guishan complex with hypothetical *P-T-t* path; error bars indicate the spread of the analytical data. (C) Prograde, clockwise *P-T* loop for Erlangping amphibole schist; error due to Fe^{3+}-estimate indicated by cross bar.

iron equals total iron for garnet and white mica, thermometers provide maximum values; application of Green and Hellman's (1982) garnet-phengite thermometer yielded ~580 °C at 2.2 GPa, in accord with Liu et al.'s (2004b) eclogite data for this area. These *P-T* estimates (Fig. 6A) correspond within error to those from coeval quartz eclogites of the southern Dabie Shan (e.g., Okay et al., 1993; Liou et al., 1996; Franz et al., 2001); they also match estimates for the Paleozoic Xiongdian eclogites (see following, and Fu et al., 2002).

The metamorphism of eclogites and gneissic country rocks in the northern Dabie–Xinxian complex is exclusively Triassic–Jurassic (see preceding). The 232 ± 10 Ma zircon age of the pristine Xuanhuadian eclogite is identical to $^{40}Ar/^{39}Ar$ phengite ages from unaltered or weakly retrogressed rocks (243–231 Ma, $n = 3$), suggesting that peak *P-T* conditions (530 °C at 2.2 GPa; Fig. 6A) were attained prior to 240 Ma. Ages for phengites from retrograde, high-strain zones are 224–195 Ma ($n = 5$, including the ca. 215 Ma age of our station D539; excluding one 187 Ma age). The weak deformation recorded by the pristine mineral assemblage and the high-strain fabric traced by the retrograde minerals indicate that deformation along the Huwan shear zone occurred mostly during decompression, likely during passage through the crust.

Huwan Mélange

Xiongdian Eclogite and Garnet Amphibolite

The foliation in most samples is accentuated by porphyroblastic garnet and compositional banding that consists either of ≤90% large garnet porphyroblasts, oriented minor white mica, and quartz, or aligned, short prismatic omphacite accompanied by subordinate barroisite, quartz, and zoisite/clinozoisite. Elliptical inclusions and enveloping foliation suggest syntectonic growth of garnet (e.g., Passchier and Trouw, 1996). Accessory phases in eclogite are rutile, pyrite, and apatite. Some eclogites show thorough retrogression with the generation of chlorite + biotite + carbonate in foliation-parallel domains. A shear-band crenulation cleavage in garnet amphibolite 98181 contains retrograde hornblende + clinozoisite + plagioclase ± ilmenite in microfold hinges that erased all the eclogite-facies minerals other than rounded, corroded garnet and phengite.

Garnet in eclogite D530c shows prograde compositional zoning with cores and rims of $Alm_{62}Grs_{24}Prp_{14}Sps_{<01}$ and $Alm_{53}Grs_{25}Prp_{21}$ $Sps_{<01}$, respectively. Garnet in eclogite 98185 is unzoned $Alm_{49}Grs_{25}Prp_{24}Sps_{02}$. In retrogressed eclogite 98181, almandine decreases from garnet core to mantle and then increases toward the rim; the pyrope content varies inversely to this and grossular is irregular. Omphacite yields jadeite contents of <30–50 mol% (calculation after Banno, 1959) without pronounced zoning. Fe^{3+} contents, calculated from charge balance (Ryburn et al., 1976), are highly variable at 0%–75% of Fe_{total}. Phengite has Si contents of 3.25–3.45 p.f.u. and a paragonite component of 4–12 mol%. Si contents increase from core to rim, pointing to increasing pressure and/or decreasing temperature during growth (Massonne and Schreyer, 1987). Primary, bluish-green clinoamphibole is barroisite and magnesiokatophorite, whereas secondary, olive-green amphibole ranges in composition from edenite and pargasite to magnesiohornblende (classification of Leake et al., 1997). Clinozoisite composition varies from grain to grain with pistacite

contents of 4–16 mol%. Secondary plagioclase in the pristine eclogite is $An_{00–03}$ albite, whereas retrogressed eclogite 98181 shows $An_{10–12}$ plagioclase coexisting with magnesiohornblende along retrogressed garnet rims.

Thermobarometric calculations for eclogites 98185 and D530c, using garnet rims, high-jadeite omphacite and high-Si phengite, and Waters and Martin's (1993) geobarometer, yield 1.9–2.1 GPa at 500–600 °C. At these pressures, garnet-clinopyroxene thermometry (Krogh, 2000; assuming 50% Fe^{3+} of Fe_{total} in omphacite) indicates temperatures of 520–540 °C for 98185 and 580–610 °C for D530c. Application of Green and Hellman's (1982) garnet-phengite thermometer gives 650 °C (98185) and 750 °C (D530c) at 2.0 GPa. The empirical amphibole thermobarometer of Ernst and Liu (1998) supports this estimate, yielding 550–600 °C at 2.0–2.4 GPa for primary sodic-calcic amphibole prisms in contact with omphacite in D530c.

For garnet amphibolite 98181, which shows relics of the high-pressure metamorphism and secondary mineral assemblages, the identification of the retrograde paragenesis is crucial. As shown above, the microprobe traverse through garnet reveals eclogitic composition in the core, but a distinct change in composition at the rim adjacent to the amphibolite-facies assemblage hornblende + plagioclase ($An_{10–12}$) + ilmenite. Combined application of Graham and Powell's (1984) garnet-hornblende thermometer and Kohn and Spear's (1990) garnet-hornblende-plagioclase geobarometer yields 560–605 °C at 1.1–1.2 GPa. We obtain similar pressures with the GRIPS (garnet-rutile-ilmenite-plagioclase-quartz) geobarometer of Bohlen and Liotta (1986). Temperatures reproduced by the amphibole-plagioclase thermometer of Holland and Blundy (1994) and the Ti-in-hornblende thermometer of Colombi (1988) testify to retrogression under epidote-amphibolite–facies conditions.

Xiongdian Garnet-Mica Schist

Mica schist 98182 is interlayered with the Xiongdian eclogite and contains garnet + phengite + quartz + clinozoisite + plagioclase ± sphene ± rutile. The schist shows a lepidoblastic fabric and a compositional layering with quartz-rich bands and layers of white mica. Inclusions in the garnet porphyroblasts are quartz, white mica, sphene, and rutile. Similar to the eclogites, garnet shows a prograde compositional zoning with core and rim composition of $Alm_{67}Grs_{25}Prp_{07}Sps_{01}$ and $Alm_{63}Grs_{29}Prp_{7.5}Sps_{0.5}$, respectively. Phengite is zoned with increasing Si contents from core to rim (Si_{core}: 3.22 p.f.u.; Si_{rim}: 3.34 p.f.u.) and decreasing paragonite component (10 mol% to <5 mol%). Plagioclase is nearly pure albite ($An_{00–01}$). Clinozoisite yielded a pistacite component of ~14 mol%. Prismatic and anhedral sphene has Al_2O_3 contents of up to 2.5 wt% and very low Fe_2O_3 contents of >0.3 wt%.

Compositional zoning in 98182 garnet is similar to eclogitic garnet from the same outcrop (D530c, 98185). Phengite shows a rimward increase in celadonite. Assuming that the rim composition of garnet and associated high-Si phengite record peak metamorphism, we obtain 570–600 °C (at 2.0 GPa) using the calibration of Green and Hellmann (1982), which matches the estimate from the eclogites. Rutile inclusions in garnet and matrix sphene next to clinozoisite indicate the reaction 3 grossular + 5 rutile + 2 quartz + H_2O ↔ 5 sphene + 2 clinozoisite. A calculation of this reaction curve with TWEEQ (Berman, 1991; activity models see Appendix) results in ~1.8 GPa at 600 °C.

The ca. 315 Ma age for zircon overgrowths containing garnet-omphacite-phengite inclusions establishes a late Carboniferous age for eclogite-facies metamorphism in the Xiongdian rocks (see preceding). The age of the retrograde metamorphic history is more difficult to pin down; the synkinematic texture of the epidote-amphibole–facies minerals in both eclogite and mica schist suggests Paleozoic retrogression (ca. 305 Ma). Triassic zircon growth and the ca. 235 Ma phengite age out of the top-to-the-north shear-band fabric in the Xiongdian gneiss point to a Triassic age for the deformation, facilitating late-stage retrogression.

Qinling Unit

Dingyuan Complex Amphibolite-Greenschist

Sample D525a shows penetrative foliation and compositional variation with millimeter-sized mafic and felsic lenses and layers. The mafic sections consist of amphibole + chlorite + epidote + albite ± quartz ± calcite ± sphene; the felsic layers are quartz + albite + phengite + chlorite ± zircon ± apatite. Pale-green, aligned clinoamphibole is actinolite and magnesiohornblende with the highest Al, Ti, and Na contents in crystal cores. Chlorite has rather uniform composition, with Si contents of 5.38–5.60 p.f.u. and X_{Mg} of 0.54–0.56. Similar to clinoamphibole, epidote has a distinct chemical variability, with pistacite contents of 20–36 mol% in different grains. Plagioclase is $An_{00–02}$ albite, and carbonate is almost pure calcite with minor Mg and Fe. Phengite yields Si contents of 3.28–3.43 p.f.u., with the highest values in the cores. The highest paragonite contents (up to 25 mol%) parallel the high-Si contents, whereas X_{Mg} is rather uniform (0.51–0.55). Syntectonic sphene shows elevated concentrations of Al_2O_3 (up to 6.2 wt%) and Fe_2O_3 contents of up to 3.0 wt%.

Thermobarometry was performed using the amphibole-epidote-chlorite-albite-quartz thermobarometer of Triboulet et al. (1992), which is based on complex exchange equilibria (i.e., tremolite-edenite and pargasite/hastingsite-edenite) between amphibole and associated minerals. Using the midpoint method of Papike et al. (1974) for the calculation of the Fe^{3+} content of amphibole, we obtain peak temperatures of 480 °C at 0.7 GPa for amphibole, epidote, and chlorite cores. Calculations based on the maximum and minimum possible Fe^{3+} concentrations in amphibole result in errors of ±30 °C and ±0.1 GPa. The lowest *P-T* conditions are recorded for hornblende rims and adjacent epidote and chlorite crystals, for which Triboulet et al.'s (1992) thermometer yields 420 °C at 0.4 GPa. Temperatures from the Ti-in-amphibole thermometer of Colombi

(1988) are 485 °C (core) to 430 °C (rim). Metamorphic pressures are given by the elevated celadonite component of phengite in the felsic layers; Si contents >3.4 p.f.u. indicate minimum pressures of ~0.7 GPa at 450 °C (Massonne and Szpurka, 1997), whereas lower rim Si contents of <3.35 p.f.u. highlight the retrograde *P-T* path.

The Dingyuan metavolcanic rocks are part of the ca. 400 Ma magmatic arc (Sm/Nd and Rb/Sr geochronology, see preceding), and our *P-T* data characterize its regional contact metamorphism. Synkinematic white mica in mylonitic rocks related to the Huwan shear zone is ca. 240 Ma; we suggest that the retrograde overprint concentrated along shear zones is related to deformation associated with the Huwan detachment.

Guishan Amphibolites

These are medium-grained rocks, displaying a foliated, mainly nematoblastic microfabric formed by aligned brownish hornblende and subordinate biotite among equigranular plagioclase and quartz. Quartz in compositionally banded amphibolite D527e also forms large, rounded porphyroclasts, suggesting a tuffaceous protolith. Sample D527d features millimeter-sized, irregular retrogression spots formed by aggregates of pumpellyite, epidote, phengite, and chlorite. Accessories in the amphibolites are ilmenite, sphene, and apatite. Clinoamphibole in D527d is pargasite and edenite with elevated TiO_2 contents of up to 1.5 wt%, whereas D527e bears magnesiohastingsite with TiO_2 contents up to 1.1 wt%. Clinoamphiboles of both samples are characterized by elevated K_2O contents of up to 1.8 wt%. Al and Ti contents vary distinctly within the compositional layers and decrease slightly rimward. Individual plagioclase is unzoned, but varies from An_{32} to An_{41}. Biotite of D527e has high TiO_2 contents (3.5–3.9 wt%) and uniform X_{Mg} values of ~0.46. Epidote in the retrograde sections of D527d has pistacite contents of 15–25 mol%, whereas associated pumpellyite is a Mg-Al variety (classification of Passaglia and Gottardi, 1973) typical of blueschists (Terabayashi, 1988). Phengite yields Si contents of 3.25–3.45 p.f.u. and shows distinctly variable X_{Mg} values of 0.27–0.82, and secondary chlorite gives Si contents of 5.50–5.61 p.f.u. and X_{Mg} = 0.55–0.58.

Applying the thermobarometer of Ernst and Liu (1998) to amphibole cores of D527d gives 0.85–1.05 GPa at 700–780 °C. D527e amphibole core reveals 640–720 °C at 1.0–1.2 GPa; similar temperatures are reproduced by the thermometers of Colombi (1988) and Holland and Blundy (1994). These data highlight upper amphibolite– to granulite-facies conditions. Rimward decreasing Ti and Al contents in amphiboles record decreasing *P-T* conditions. The stability of pumpellyite and the pistacite content of coexisting epidote (Maryuama et al., 1986) in the retrogression spots of D527d provide temperatures of 250–300 °C. The breakdown curve of pumpellyite gives an upper pressure limit of 0.65 GPa (Evans, 1990), and phengite with Si contents of 3.45 p.f.u. constrain a minimum pressure of ~0.4 GPa (Massonne and Szpurka, 1997). This *P-T* estimate and the pumpellyite composition indicate low-grade high-pressure, low-temperature conditions typical of subduction zones.

Zircon and white mica geochronology positions the Guishan meta-igneous rocks into the ca. 400 Ma magmatic arc (see geochronology in preceding sections). Our K-feldspar age for D527 and neighboring K-feldspar and muscovite ages assign the static blueschist-facies overprint to the Triassic.

Erlangping Unit

Erlangping amphibole schist D522a shows a weak foliation obscured by a strongly recrystallized matrix of albite + epidote + chlorite + actinolite ± ilmenite ± apatite. Clinoamphibole is distinctly zoned, with Al, Ti, and Na contents that increase at the expense of Si from actinolite cores to magnesiohornblende rims (Leake et al., 1997). Chlorite yields Si contents of 5.30–5.60 p.f.u. and X_{Mg} values of 0.58–0.62. Whereas small epidotes have uniform pistacite components of 13–15 mol%, larger crystals show pistacite contents of ~25 mol% in cores and ~12 mol% in rims. Plagioclase forms lens-shaped matrix grains and is $An_{00–03}$ albite. Syntectonic and unoriented, recrystallized phengite yields Si contents of 3.15–3.21 p.f.u. with X_{Mg} values of 0.59–0.67, which vary from grain to grain; BaO reaches 1.3 wt%, and paragonite contents are ~2 mol%.

The prograde zoning in hornblende allows us to calculate a segment of the metamorphic loop. Applying the thermobarometer of Triboulet et al. (1992) to the actinolitic cores gives 350–375 °C at 0.9–1.0 GPa, which indicates the prograde, clockwise *P-T* evolution of the sample. The same thermobarometer gives maximum *P-T* conditions of 555 °C at 0.63 GPa for magnesiohornblende rims and associated epidote and chlorite. Pressures determined from the geobarometer of Cho (cited on page 442 in Laird, 1982) result in a well-defined range of 0.55–0.65 GPa for amphibole-chlorite equilibria. Colombi's (1988) thermometer gives 500–560 °C for the Ti-rich rims.

Hornblende geochronology in Tongbai suggests that the syntectonic metamorphism occurred ca. 400 Ma. It likely affected an older (ca. 480 [?] Ma, see geochronology in preceding) igneous protolith.

STRUCTURE AND KINEMATICS

Methods

In the field, we characterized the contacts of the main rock units along traverses by studying the relative amount of deformation, the sense of displacement or shear, and the pressures and temperatures of deformation. The amount of deformation was judged from the shape of deformed objects, the thickness and spacing of deformed zones, and the degree of grain-size reduction. Sense of shear was established in the field and in thin section by means of criteria such as offset

markers, σ and δ clasts, shear bands, asymmetric boudinage, schistosity-cisaillement (S-C) fabrics, and lattice-preferred orientation (texture) measurements of quartz. Our quartz-texture interpretation is based on comparisons with textures from deformation zones where the path and temperature have been established by independent criteria, and from polycrystal-plasticity models and experimental data. To understand the kinematics of fault arrays, we applied stress inversion techniques to mesoscopic fault-slip data. We refer the reader to Passchier and Trouw (1996), Angelier (1994), and Twiss and Unruh (1998) for comprehensive summaries and critical discussions of these structural methods. Our data are shown in Figures 5 (Cretaceous and Cenozoic deformation) and 7 (Paleozoic and Triassic deformation).

Xinxian Complex

Stations D537–538, D539, and D230 record Triassic deformation related to the Huwan shear zone along the very northern margin of the Xinxian complex (Fig. 7A); we did not observe pre-Triassic deformation in this complex. Adjacent stations D537 and D538, in nonmylonitic felsic gneiss with local mica-rich layers, garnet-mica schist, retrograde, low-grade, quartz-ribbon phyllonite, and small amphibolitized eclogite lenses show spectacular extensional shear bands. The near-vertical, locally overturned, top-NNE fabric indicates postshear tilting. Synkinematic phengite yields an age of ca. 235 Ma (this study). Station D539, felsic orthogneiss and garnet-mica schist surrounding amphibolite (relict eclogite), shows top-N shear bands with <a> slip along basal and prism planes in quartz; its late-stage (greenschist-grade) deformation is dated at ca. 215 Ma (this study). D230, mostly mylonitic, partly chloritic, biotite-orthogneiss, shows top-NE, dextral-normal slip.

Huwan Mélange

Stations D530 and D540 of this study, D231 of Hacker et al. (2000), and D335, D339, and D340 of Webb et al. (1999, 2001) record Triassic deformation related to the Huwan shear zone within the Huwan mélange; no older deformation has been quantified (Fig. 7A). Station D530, including one of the Xiongdian eclogite bodies, is in nonmylonitic quartzofeldspathic gneisses with asymmetric foliation boudinage and a dominant synthetic shear zone set with top-NNW flow. The deformation fabric formed when the footwall was rising, and these structures were tilted northward. Early top-NW shear zones dip steeply N, and conjugate shear zones dip shallowly S; late shear zones dip more shallowly to the N. Folds with subhorizontal, W-trending axes and subhorizontal axial planes overprint all structures. Folding affected steeply N-dipping layering and likely records subvertical shortening and subhorizontal N-S extension during late-stage activity along the then steeply dipping Huwan shear zone (compare Froitzheim, 1992, for similar structures in the Alps). The fabric in both of these stations and adjacent station D335 of Webb et al. (1999) formed late in the metamorphic history, clearly postdating the Carboniferous high-pressure metamorphism and coinciding with the 263–233 Ma phengite ages and the ca. 216 Ma zircon rim age obtained from the Xiongdian eclogite area (see preceding section). Station D540, in strongly foliated, locally mylonitic granitic gneiss containing fine-grained amphibolite boudins and dikes (possibly relict eclogite) and intruded by Cretaceous(?) subvolcanic andesite, shows greenschist-facies top-NE flow; the flow direction is poorly constrained. Top-NNE shear in Webb et al.'s (2001) station D340 is well dated between 236 and 230 Ma by Rb/Sr and $^{40}Ar/^{39}Ar$ white-mica ages (see preceding section; Ye et al., 1993; Xu et al., 2000).

Dingyuan Complex

The southern margin of the Dingyuan complex is subvertical or steeply N-dipping in most localities we visited. Station D525, in relict amphibolite layers in greenschist, and D232 (Webb et al., 1999), in mylonitic quartzofeldspathic schist, have subvertical shear zones and shear bands with top-N(E) flow, again suggesting that the deformation fabric was tilted northward during footwall uplift. Phengite in the low-temperature, top-N mylonite of D232 dates deformation at ca. 235 Ma (Webb et al., 1999).

Nanwan and Foziling Unit

Huwan detachment deformation dies out within the southern part of the Nanwan unit. All stations we analyzed show subvertical fabrics and record Triassic deformation related to the Huwan shear zone; no older deformation has been quantified. Ductile-to-brittle faults in station D526 are interpreted to have formed when the foliation and bedding was subhorizontal or shallowly N-dipping; displacement was then top-N. Station D535, just north of the Dingyuan–Nanwan boundary, shows steeply N-dipping, top-S shear bands and shears zones resulting in spectacular foliation boudinage; in the Chinese literature deformation of these well-bedded, phyllitic quartzites and chloritic quartzose phyllites is interpreted as top-S thrusting of the Nanwan unit onto the Dingyuan complex (e.g., Xu et al., 2000). In contrast, we suggest that an initially shallowly S-dipping, top-S extensional shear fabric, antithetic to the top-N shear along the Huwan detachment (and likely along the Dingyuan-Nanwan contact, not exposed at D535) was rotated into the apparent thrust geometry by large-scale N-S extension and later folding. Deformation during cooling, the excision of Triassic isograds across the Huwan detachment, and the progressive rotation of the deformation fabrics as observed at several outcrops (e.g., D530), support the subhorizontal extension interpretation (see following discussion). The greenschist-facies shales (phyllite and quartzose phyllite) of station D532, just north of the

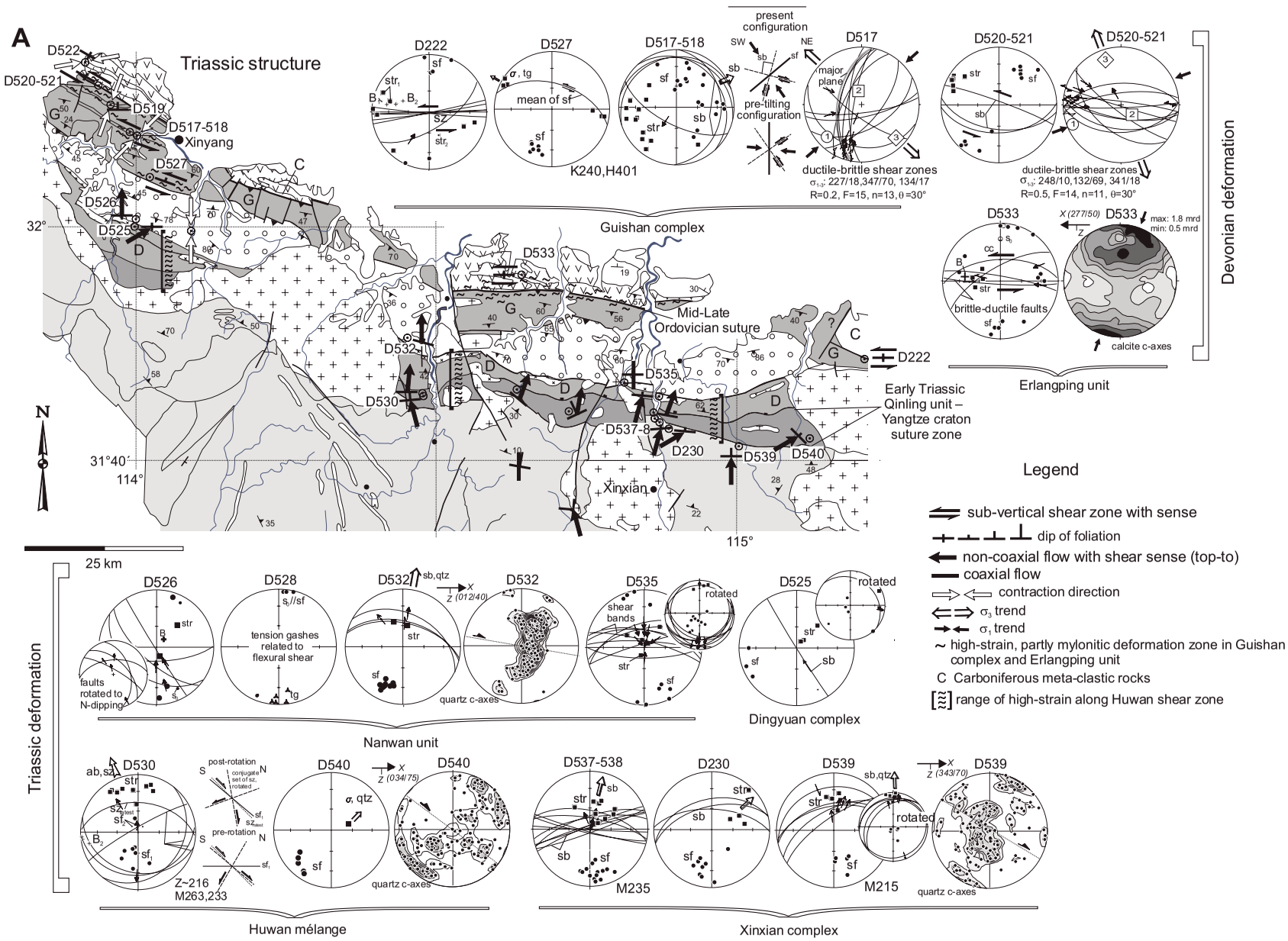

Figure 7 *(continued on following page)*. As Figure 5 but for Triassic and Silurian–Devonian structural data. B, fold axis; σ, shear sense from sigma-clasts; s_0, bedding.

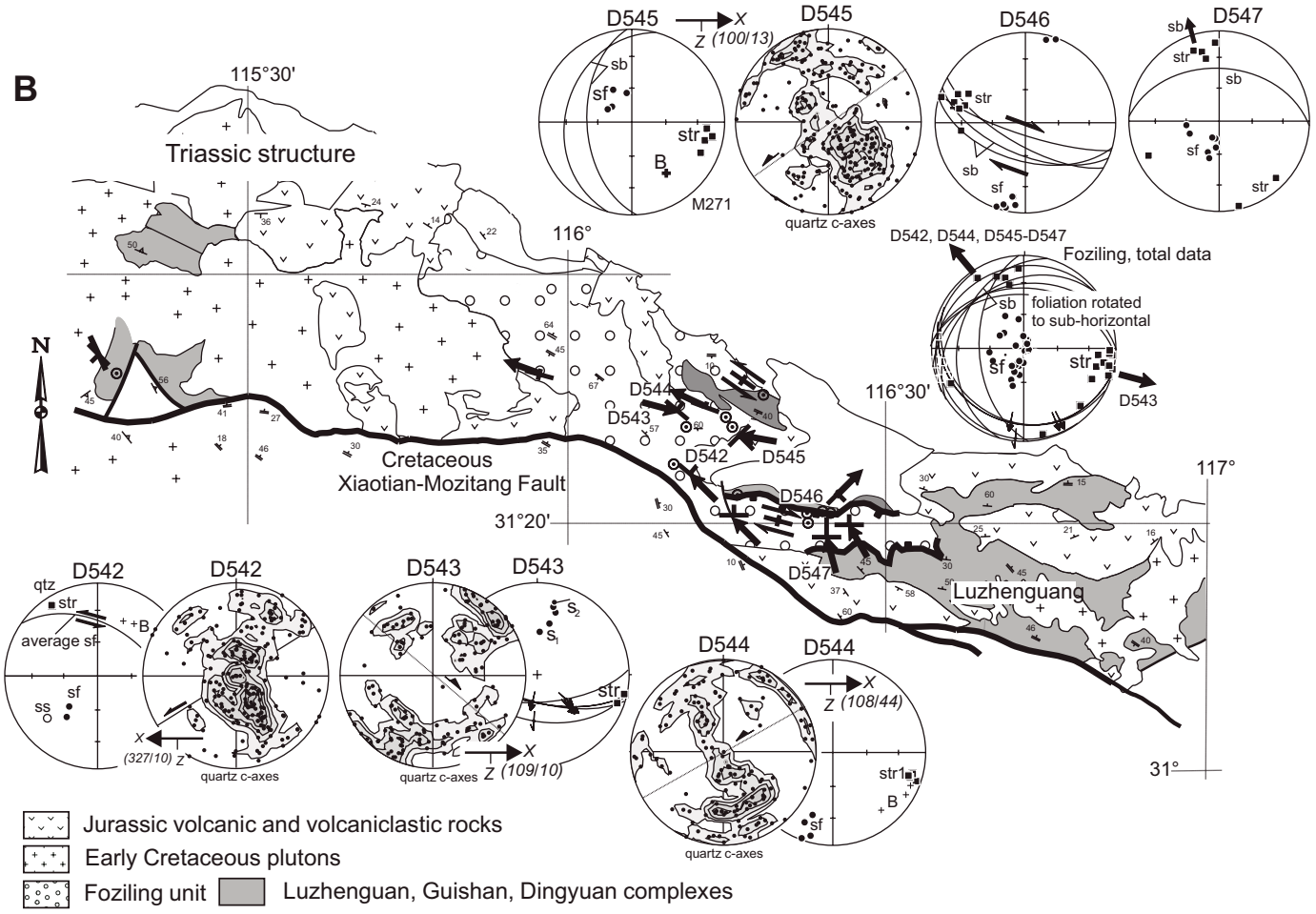

Figure 7. *(continued)*

boundary to the Dingyuan complex, are tightly folded and overprinted by ductile-brittle fault zones with top-N shear; this station likely portrays deformation along the northern margin of the Huwan shear zone. Station D528 records tight upright folding within the Nanwan complex; the relationship of this folding to normal shear along the Huwan detachment is unclear.

In the northern Dabie foreland, six stations portray Permian–Triassic, low-temperature deformation (Fig. 7B; muscovite cooling ages of 271 and 261 Ma, Fig. 2A) in the Foziling unit. Quartzite (D542, D543), partly mylonitic quartzose phyllite (D544) with <a> folds, and volcaniclastic, quartzose two-mica gneiss (D544) show variable but mostly vertical foliation, indicating folding with SE-trending axes. Unfolding suggests coaxial subhorizontal extension along the NW-SE mineral lineation with a non-coaxial top-NW component. Stations D546 and D547, (chlorite-)biotite quartz schists, are close to the Luzhenguan-Foziling contact and show dextral strike slip (D546) and top-NNW (D547) shear; unfolding suggests top-NW normal faulting for both stations, corroborating the interpretation of Hacker et al. (2000) of that contact; their ca. 242 Ma phengite is synkinematic.

Guishan Complex

Station D222 in the Guishan complex (Fig. 7A) consists of partly mylonitic amphibolite with leucocratic layers and metavolcaniclastic rocks. It has a vertical foliation and shear-band fabric with sinistral shear under amphibolite- to retrograde greenschist-facies conditions, all overprinted by active sinistral strike-slip faults. Early isoclinal <a> folds indicate high strain, and second-generation folds are strongly asymmetric and related to the sinistral shear. Because these rocks were overprinted by Cretaceous regional metamorphism (K-feldspar age of ca. 100 Ma), the recorded deformation is older, likely Paleozoic.

Stations D517–518, D519, and D527 characterize the deformation in the Guishan complex of northeastern Tongbai near Xinyang (Fig. 7A). Nearby stations D517–D518 consist of locally kyanite-staurolite–bearing mica schist and gneiss, marble, mylonite with feldspar and hornblende blasts, and its retrograde products; this sequence is interpreted as intercalated volcaniclastic rocks and limestone. Deformation began at amphibolite-facies conditions and continued during cooling through ductile-brittle shearing/faulting; isoclinal folds and late open

folds are present. An early conjugate set of shear bands indicates strong coaxial NE-SW shortening within the then-vertical foliation; the shear bands were later rotated into their apparent normal-fault geometry. A second set of shear zones were then imprinted, again indicating NE-SW contraction. Given the 316–401 Ma hornblende ages in the Guishan complex of northwestern Tongbai, the ductile deformation is likely Paleozoic; the outcrop at station D518 is cut by a probable Cretaceous dike that shows only brittle deformation. Station D519 is an L-tectonite orthogneiss with a similar structural pattern to D517–518; this gneiss likely yielded the 392 Ma protolith age reported by Ye et al. (1993). Station D527, just north of the boundary to the Nanwan unit, contains retrograde hornblende, tourmaline, and K-feldspar–bearing biotite gneiss and (garnet) amphibolite. An early mylonitic deformation developed during sinistral strike-slip flow was overprinted by high-pressure–low-temperature metamorphism (see preceding discussion). Niu et al.'s (1994) hornblende age of ca. 401 Ma dates deformation as Early Devonian, and our K-feldspar age of ca. 240 Ma indicates that the high-pressure–low-temperature overprint was Triassic.

Erlangping Unit

Stations D520–D521 lie in a spectacular sinistral strike-slip shear zone along the boundary between the Guishan complex and the Erlangping unit, in gabbro (partly retrogressed to talc-schist), serpentinized ultramafic rock, and mylonitic orthogneiss. Greenschist-grade mylonitization resulted in mostly symmetric boudinage of greenschist in a carbonate matrix and progressed into ductile-brittle faulting, expressed as flexural folds accommodating faults with calcite fibers. This zone is overprinted by later brittle, possibly active faulting (see following). Ca. 400 Ma hornblende ages farther west constrain the ductile deformation as Early Devonian. Station D533 shows a partly mylonitized, strongly boudinaged sequence of thick, well-bedded marble and amphibolite greenschist. High strain in a sinistral strike-slip setting is also indicated by isoclinal <a>-type flow folds; the structures are refolded by open folds.

Cretaceous and Cenozoic Structures

Stations D523 and D525–526 record Early Cretaceous (nearby 128–120 Ma biotite cooling ages) subhorizontal extension (Fig. 5A). At station D523, felsic orthogneiss, K-feldspar–rich granite, and pegmatite dikes intrude amphibolite-mica schist intercalations (likely relics of Huwan mélange rocks); the intrusions resemble the Northern Orthogneiss Unit of Dabie. Station D522 exemplifies the stress field in place during Late Cretaceous–Early Tertiary deformation, which is concentrated along the dextral Tongbai shear-fault zone (Webb et al., 1999; Ratschbacher et al., 2000). This shear-fault zone is associated with Upper Cretaceous, possibly lower Tertiary (K_2 on Chinese maps) basins. In Tongbai, $^{40}Ar/^{39}Ar$ biotite cooling and pseudotachylite ages (Webb et al., 1999) suggest (re)activation of the Tongbai shear zone at ca. 75 Ma.

Cenozoic faulting is concentrated along the Jinzhai fault in northernmost Xinxian and Tongbai and along the Tongbai shear-fault zone. Both fault zones are sinistral, and the Jinzhai fault is definitely active, as indicated by recent geomorphic features (e.g., Zhang et al., 1995). We encountered evidence of the associated regional stress field (NW-SE extension, NE-SW compression) at nearly every location visited, but accommodated strain appears to be small. Dextral faults, conjugate to the sinistral strike-slip faults, strike NNE and are transtensional. Such faults are active in the Dabie Shan (Zhang et al., 1995; Ratschbacher et al., 2000) and define the NNE-trending boundaries of blocks that segment the Hong'an–Dabie area into basement massifs and basins. A Tertiary faulting history is indicated by the Early Tertiary AFT ages along the Tongbai fault.

DISCUSSION

Location of the Sino-Korean–Yangtze Suture and Role of Carboniferous High-Pressure Metamorphism in the Qinling-Dabie Orogen

The Tongbai–Xinxian–northern Dabie area contains three sutures (Fig. 2A): (1) The Sino-Korean craton–Erlangping intra-oceanic arc suture is younger than the intra-oceanic arc rocks (ca. 480 Ma, but poorly defined in Tongbai-Xinxian) and older than the Silurian-Devonian arc rocks stitching the Sino-Korean craton (Kuanping unit), the Erlangping unit, and the Qinling units. (2) The Erlangping arc–Qinling unit suture has the same time constraints. (3) The Qinling unit–Yangtze craton suture formed ca. 240 Ma, based upon the oldest ages of high-pressure–UHP metamorphism in the northern Yangtze craton.

We resolve the controversies about the age of the Sino-Korean craton–Yangtze craton collision by suggesting that the Paleozoic collisions occurred between the Qinling unit and the Sino-Korean craton, postdating the amalgamation of the intervening Erlangping arc with these continental units. The Qinling unit constitutes a long and narrow microcontinent that extends at least through the Qinling-Dabie area and probably into the Sulu area. A suite of common characteristics delineate this microcontinent throughout the Qinling, Tongbai-Xinxian, and northern Dabie areas: (1) These areas experienced the Mesoproterozoic (ca. 1.0 Ga) Jinningian orogeny that assembled Rodinia (Fig. 3A–B; Li, 1999; Li Z.X. et al., 1995, 1999, 2002). (2) They have in common the ca. 0.8–0.7 Ga rifting event that marks Rodinia's breakup (Fig. 3A–B; e.g., Li Z.X. et al., 1995, 1999). In Xinxian and northern Dabie, portions of the Dingyuan and Luzhenguan complexes record the magmatic signature of this rifting event: quartzofeldspathic rocks (former volcanic and volcaniclastic rocks) intercalated with amphibolite (former mafic volcanic rocks), and granitoids, the intrusive part of the volcanic series. (3) Most importantly, these areas share the arc that developed on the Proterozoic microcontinent

and northern collage (Erlangping unit and Sino-Korean craton) in the Late Silurian–Early Devonian (Fig. 3A–B). In the Qinling, the arc sequence is mostly plutonic, as it is in Tongbai, where it is represented by, for example, the large Huanggang quartz diorite complex. Most of the Guishan and Dingyuan rocks in Xinxian seem to have been emplaced as volcanic rocks and were metamorphosed to up to granulite-facies conditions during regional metamorphism accompanying arc development, a local metamorphic signature that the Xinxian rocks share with those in Tongbai. No direct record of Silurian-Devonian arc rocks is known from the Luzhenguan unit, which seems to represent only the Neoproterozoic rift.

The Proterozoic history of the Qinling microcontinent also ties it to the Yangtze craton, and this has hindered the recognition of the Qinling unit as a separate microcontinent that lies between the Sino-Korean craton and the Yangtze craton all along the Qinling-Dabie-Sulu orogen. The Jinningian orogeny and the Neoproterozoic rifting are defined in the Yangtze craton. The north(west)ern margin of the Yangtze craton also suggests that the Neoproterozoic "rifting event" actually marks two distinct events that are difficult to separate based only on age, and particularly so in the Qinling microcontinent, where the geochronological database is limited and obscured by the overprinting Paleozoic arc. Local, petrochemically well-studied granitoids define an older age group at ca. 815 Ma that constitutes the Panxi-Hannan arc (e.g., Zhou et al., 2002), whereas a larger and better-defined group at ca. 732 Ma corresponds to rifting of Rodinia (e.g., Gao et al., 1990).

So it is the Paleozoic signature that undoubtedly differentiates the Qinling microcontinent from the Yangtze craton; this signature includes the Silurian-Devonian arc but also older components, e.g., the ca. 580 Ma Sujiahe gabbro and other, possibly coeval, gabbros that dot the Dingyuan complex, and which may hint to an early Paleozoic subduction history. It is also differentiated by the presence of a Paleozoic forearc basin on the Qinling microcontinent and the occurrence of the Huwan mélange (see following).

The Qinling microcontinent and its arc carry an incompletely preserved forearc basin, constituted by the Liuling unit of Qinling (or part of it), the Nanwan unit of Xinxian, and the Foziling unit of Dabie. We suggest a forearc setting due to the position of these units on the southern margin of the main volume of the presently exposed arc rocks and the presence of continental basement beneath them, indicated most clearly by the Guishan and Dingyuan complexes in Xinxian and the Luzhenguan complex in Dabie. Furthermore, detrital geochronology ties the Liuling and Foziling units to the Qinling microcontinent and its Paleozoic arc: both units carry the ca. 400 Ma and 700–800 Ma arc and rift signature of the Qinling microcontinent; the Liuling unit also shows the 1.0 Ga orogenic event. The ca. 400 Ma detrital zircon ages in the Foziling unit are important, as they indicate the presence of the Silurian-Devonian arc in the hinterland, for which evidence is lacking in the Qinling "basement," the underlying Luzhenguan complex (see preceding).

The geochronology of arc magmatism seems to imply that northward subduction beneath the Qinling microcontinent terminated during the Devonian. However, fossiliferous units in the Liuling unit reach up into the Lower Carboniferous. Furthermore, the paucity of volcanic rocks in most of the Nanwan and Foziling units, and also the apparent lack of volcanic rocks in the Carboniferous rocks that apparently overlie them suggest that the forearc basin partly postdates arc activity. However, the apparent end of arc magmatism on the Qinling microcontinent and the Erlangping unit remains to be explained and may simply reflect a change in subduction geometry in the Paleotethys ocean.

The Huwan mélange and the geochronology of the hanging wall serve as the bridge to tie the Paleozoic evolution of the collage along the southern margin of the Sino-Korean craton (Erlangping and Qinling units) to the subduction of the leading edge of the Yangtze craton. We interpret the Huwan mélange as a Carboniferous–Permian (and likely older) subduction-accretion complex with a tectonic and possibly sedimentary mixture of rocks from the Qinling microcontinent, the Silurian-Devonian arc, the Paleotethyan ocean floor, and the Yangtze craton. Most importantly, the eclogites involved in the mélange signify oceanic subduction during the Carboniferous (their age of high-pressure metamorphism). The geochemistry of some of the Huwan eclogites (e.g., Xiongdian) indicates that they are oceanic basalts, implying that they cannot be blocks scraped off the Yangtze craton, as such rocks do not exist in the Yangtze craton (see the studies on the origin of the Hong'an–Dabie eclogites, e.g., Jahn, 1998, and discussion on the Dabie Shan in the following). Other eclogites, e.g., the Hujiawan eclogite, seem to have magmatic arc affinity: The geochemistry, position along the northern margin of the Huwan mélange, and the Neoproterozoic and Paleozoic age components of the Hujiawan eclogite hint that this group of eclogites may constitute tuffs derived from the Silurian-Devonian arc. Other eclogites, e.g., the Qianjinhepeng eclogite with its 0.93 Ga component, and in particular the strong 0.72 Ga age component, may derive from the Yangtze craton. Again, the Qianjinhepeng eclogite position along the northern edge of the Huwan mélange and its Paleozoic age component make a Qinling origin more likely.

The age of high-pressure metamorphism in the Huwan mélange eclogites ranges from 325 to 312 Ma and does not span the proposed Paleozoic–Early Triassic subduction-accretion history. This may be the result of incomplete preservation or insufficient investigation. For example, Devonian to Permian zircon spot ages reported by Jian et al. (2001), Sun et al. (2002), and Gao et al. (2002) may reflect subduction-related recrystallization throughout the late Paleozoic in the Huwan mélange. This is supported by the range of cooling ages in the Nanwan and Foziling units (271–204 Ma)—which we interpret as the forearc—and in the Erlangping and Qinling units of Tongbai-Xinxian (316–234 Ma) that signifies Early Permian–Triassic and early Late Carboniferous–Triassic thermal events.

Whether arc magmatism ended in the Silurian-Devonian remains to be tested: It is possible that Middle Carboniferous–Early Permian andesitic breccia and tuff in the eastern half of the Sino-Korean craton (e.g., Zhang, 1997) may signify northward migration of the arc in the central part of the orogen, and that the Permian–Triassic plutons within the eastern Songpan–Garzê flysch belt are subduction related (Ratschbacher et al., 2003).

Why does the Silurian-Devonian arc signature diminish from Qinling-Tongbai-Xinxian into Dabie, and why is the arc apparently not present in Sulu? The paleomagnetic record shows that convergence and collision between the Sino-Korean craton and Yangtze craton involved a clockwise rotation of up to 70° (e.g., Zhao and Coe, 1987; Gilder et al., 1999). Thus, one might speculate that the Paleotethys ocean south of the Sino-Korean craton narrowed eastward (into the Dabie-Sulu area) and that no arc formed in the east (compare Li et al., 2001).

Finally, and very speculatively, the eclogites associated with mantle-derived ultramafic rocks in the northern Northern Orthogneiss Unit (type III eclogites of Jahn, 1998; e.g., Rizhao, Rongcheng) of Dabie may be in an analogous structural position to the Huwan mélange rocks. Thus, it may be that the Qinling microcontinent–Yangtze craton suture, here drawn along the Cretaceous Xiaotian-Mozitang shear-fault zone, south of the Foziling and Luzhenguan units in northern Dabie (Fig. 2A), should be drawn farther south within the Northern Orthogneiss Unit (the thin dotted line in Fig. 2A).

Pressure-Temperature-Time-Deformation History of the Huwan Detachment

Structural studies have not progressed far enough to define the boundaries of the Huwan shear-fault zone definitively. Our observations along a few transects suggest that high strain associated with the detachment sets in and overprints strong, often penetrative deformation in the Yangtze craton rocks along the very northern margin of the northern Dabie–Xinxian complex. We did not find high-strain ductile or brittle deformation related to Huwan normal shear north of the southern margin of the Nanwan unit in Xinxian; the Foziling unit is affected heterogeneously by normal shear. Thus, we place the northern margin of the Huwan detachment along the southern margin of the Nanwan unit.

We must emphasize that the Huwan detachment is not *the* only high-strain shear zone involved in exhuming the high-pressure–UHP rocks: the entire basement core of the Hong'an–Dabie orogen is strongly deformed (see Hacker et al., 2000; Webb et al., 1999, 2001, for structural data), and low-strain regions are confined to millimeter- to multiple-kilometer-scale boudins, hosting most of the spectacular high-pressure–UHP evidence (for a particularly spectacular example in Dabie, see Oberhänsli et al., 2002). Our observations also suggest that in general, strain is weaker in those parts of the Huwan detachment that preserve the high-pressure assemblages (both in the Huwan mélange and the northern Dabie–Xinxian complex) than in retrograde shear zones that are often mylonitic. Although the outcrops we found did not allow us to identify specific syn–high-pressure structures, and describe their formation in terms of vorticity, strain, and rheology, these structures bear similar overall orientation than those formed during retrograde overprint, but lack the noncoaxial flow criteria that are ubiquitous in the retrograde, high-strain portion of the detachment. Furthermore, our overall impression from relating critical mineral assemblages to deformation is that the Huwan shear-zone high-strain deformation describes passage of rocks through the crustal portion of the lithosphere.

The Huwan detachment deformation records subhorizontal N-S extension (although local stretching directions vary) and vertical contraction. That this deformation produced crustal thinning is clear from (1) the overall structural geometry (N-dipping flow planes and top-N kinematics), (2) the contraction of isograds across the detachment (Triassic pressures of ~0.4 GPa in the Dingyuan greenschist contrast with ~2.2 GPa along the northern margin of the Xinxian complex), and (3) the fact that deformation postdated the peak pressures. Although the nature of the initial contacts of the major units (the Xinxian complex, Huwan mélange, Dingyuan complex, and Nanwan unit) that the Huwan shear zone overprints are structurally undefined, the Triassic deformation is normal shear; local apparent thrust geometries within the Huwan shear zone are the result of rotation due to footwall uplift. Our petrologic work confirmed the suggestion that the coesite-bearing UHP core of Hong'an is rimmed in the north by a high-pressure zone that did not experience pressures high enough to form coesite. Assuming a pressure difference of Triassic metamorphism of ~1.6 GPa (~2.0 GPa or ~70 km depth in the Xinxian complex and ~0.4 GPa or ~15 km in the Dingyuan complex) at the onset of deformation along the Huwan detachment and a ~45° dip to the shear zone gives ~80 km displacement along the fault and ~55 km subhorizontal extension.

The Huwan detachment deformation was Triassic. As argued already, we suggest that the peak pressure predated 240 Ma. In the Xinxian complex, synkinematic phengite grew in mylonitic shear zones as early as ca. 235 Ma; late-stage high-strain shear was active at ca. 215 Ma. In the Huwan mélange and the Dingyuan complex, early top-N(NE) shear that can be clearly attributed to the Huwan detachment is 236–230 Ma; shear along the Luzhenguan-Foziling contact began as early as 242 Ma. We thus propose that deformation along the Huwan shear zone initiated at ca. 235 Ma. The main body of retrograde phengite ages within the Huwan shear zone is 224–195 Ma, bracketing its major activity. Rates of exhumation of ~1.9 and ~1.4 mm/yr apply, taking 31 m.y. (224–195 Ma) and 40 m.y. (235–195 Ma), respectively, for passage of rocks through ~55 km (see preceding); these are rates observed in active orogens today.

Pressure-Temperature-Time-Deformation History of the Xinxian-Dabie Foreland (North of the Huwan Detachment)

Our petrology and the available geochronology outline middle-lower crustal regional contact metamorphism in rocks of the Silurian-Devonian arc at ca. 400 Ma (Ratschbacher et al., 2003). Our peak *P-T* estimates (680–740 °C at 0.9–1.1 GPa) for the Guishan complex are similar to those derived from Qinling unit rocks in Qinling (0.9–1.0 GPa at 700–800 °C; e.g., Hu et al., 1993) and the garnet granulites in northwestern Tongbai (755–840 °C and ~0.97 GPa; Kröner et al., 1993). Metamorphic grade decreases from granulite facies in the Guishan complex to upper greenschist facies in the Erlangping unit. In Xinxian, a wide belt of high-strain sinistral wrench deformation that straddles the Guishan-Erlangping contact developed during but mostly after this ca. 400 Ma metamorphism. Similar high-strain, sinistral-transpressive mylonite zones have been observed in Qinling (see Ratschbacher et al., 2003); the most spectacular being the sinistral-transpressive Shang-Dan shear-fault zone that was active in the early Devonian (ca. 400 Ma).

The evidence of a static, ca. 255–240 Ma blueschist metamorphism in the Guishan complex of Tongbai, the 271–204 Ma range of cooling ages in the Nanwan and Foziling forearc units, and the 316–234 Ma cooling ages in the Erlangping and Qinling unit of Tongbai-Xinxian are best interpreted as originating from Paleotethys subduction along the Huwan mélange suture zone. This metamorphic signature is not related to the exhumation along the Huwan detachment, as it extends far north of the Triassic shear zone and is older.

Collision Zone Overprint in the Cretaceous–Tertiary

Despite its dominance in the Dabie Shan (Ratschbacher et al., 2000, 2003), surprisingly little Early Cretaceous deformation occurred in the Tongbai–Xinxian–Hong'an and Qinling areas. The massive 130–115 Ma cluster of cooling ages in Xinxian–Hong'an thus may simply reflect regional, locally rapid cooling after granitoid injection and regional Cretaceous heating. The intense concentration of Early Cretaceous magmatism along the Triassic Qinling microcontinent–Yangtze craton suture (the Huwan mélange) in Tongbai-Xinxian, and particularly in northern Dabie (Northern Orthogneiss Unit), has been interpreted as the result of Pacific subduction (Ratschbacher et al., 2000) or mantle delamination (Wu et al., 2005). In either case, it is a spectacular demonstration of the effect that preexisting heterogeneities can have on a subsequent, unrelated tectonic event.

Late Cretaceous–Early Tertiary deformation along dextral-transpressional shear-fault zones and associated basins is a characteristic feature of the entire Qinling-Xinxian-Dabie orogen. Deformation along similar zones has been loosely constrained between 101 and 63 Ma in Qinling (Ratschbacher et al., 2003), at ca. 75 Ma along the Tongbai shear-fault zone (Webb et al., 2001), and younger than ca. 115 Ma in Dabie (reactivation of the Xiaotian-Mozitang fault zone in a dextral-transtensional setting; Ratschbacher et al., 2000). The bulk of the AFT ages (80–55 Ma age cluster) are also Late Cretaceous–Early Tertiary and may signify cooling related to transtension during this event; the cooling might follow the time of reheating and subsequent cooling documented in Dabie at ca. 100–90 Ma (Ratschbacher et al., 2000), likely also recorded by the K-feldspar ages of Xinxian (Fig. 3E). Transtension within the Qinling-Dabie orogen coincides with rifting marked by Late Cretaceous–Eocene red bed deposition throughout eastern China (e.g., Ren et al., 2002).

Two major conclusions may be gleaned from the fission-track data: (1) Exhumation rates were slow throughout the Cretaceous–Tertiary; the spectacular exception is the Early Cretaceous exhumation of the Northern Orthogneiss Unit of northern Dabie. Our slow average exhumation rate of ~0.06 mm/yr for the last 70 m.y. for Xinxian and the foreland of Dabie is consistent with slow rates of Tertiary exhumation of ~0.02 mm/yr for the flanks of the Dabie Shan, and 0.05–0.07 mm/yr for the core of the range, derived from (U-Th)/He and AFT ages and considering erosion and topography (Reiners et al., 2003). The Cretaceous period prior to ca. 70 Ma was likely a time of extremely slow, continuous exhumation and peneplanation for most of the orogen. (2) The India-Asia collision may have induced reactivation of preexisting fault zones in the Eocene; we document enhanced cooling along the Tanlu fault zone (Grimmer et al., 2002) and along the faults zones in Tongbai-Xinxian (this study). Reiners et al. (2003) suggested a modest increase in exhumation rate within the Dabie Shan between 80 and 40 Ma (≤0.2 mm/yr).

CONCLUSIONS

The Qinling-Dabie-Sulu orogen contains three sutures in Tongbai-Xinxian (northern Hong'an)–northern Dabie: The Silurian Sino-Korean craton–Erlangping intra-oceanic arc suture; the Silurian Erlangping arc–Qinling unit (microcontinent) suture; and the Early Triassic Qinling unit–Yangtze craton suture. This recognition of three sutures resolves the controversies about the age of the Sino-Korean craton–Yangtze craton collision by placing the Paleozoic collisions between the Qinling unit and the Sino-Korean craton, and the Mesozoic collision between the Qinling unit and the Yangtze craton. The Qinling unit constitutes a long and narrow microcontinent that extends through Qinling-Dabie and probably into Sulu. Its common characteristics in Qinling, Tongbai-Xinxian, and northern Dabie are: the Mesoproterozoic (ca. 1.0 Ga) Jinningian orogeny, ca. 0.8–0.7 Ga arc formation and rifting events, and Late Silurian–Early Devonian (ca. 400 Ma) arc formation. In Xinxian, the arc is represented mostly by volcanic rocks (Guishan and Dingyuan complexes) that were metamorphosed to up to granulite facies (peak: 680–740 °C at 0.9–1.1 GPa) during regional contact metamorphism; this metamorphic signature is also found in Tongbai.

Whereas the Proterozoic history of the Qinling microcontinent ties it to the Yangtze craton, its Paleozoic arc signature, the presence of a mid(?) to late Paleozoic (the Liuling-Nanwan-Foziling) forearc basin, and the partly oceanic Huwan mélange make the Qinling microcontinent distinct from the Yangtze craton. Detrital geochronology ties the Liuling and Foziling units to the Qinling microcontinent basement and its Paleozoic arc.

The Huwan mélange is a Carboniferous–Permian (and likely older) subduction-accretion complex containing elements of the northern microcontinent and its arc, the Paleotethyan ocean floor, and possibly the Yangtze craton. Quartz eclogites (e.g., the 540–590 °C and 2.1 GPa Xiongdian eclogite) signify Carboniferous (ca. 315 Ma) subduction. Devonian to Permian zircon spot ages from the eclogites may reflect subduction throughout the late Paleozoic. This is supported by the 271–204 Ma and 316–234 Ma ranges of $^{40}Ar/^{39}Ar$ and Rb/Sr mineral ages in the forearc and its basement, and the static, ca. 255–240 Ma blueschist metamorphism in the basement of the upper plate.

The high- and ultrahigh-pressure rocks of the Xinxian–Hong'an block (pressure peak at ≥240 Ma) are bounded along their northern margin by the Huwan extensional detachment; the boundaries of this high-strain zone extend from the northernmost Yangtze craton to the southern margin of the Nanwan unit. The Huwan shear zone high-strain deformation describes the passage of rocks through the lithosphere by subhorizontal N-S extension and vertical contraction. This is evident from the condensed Triassic isograds (420 °C and ~0.4 GPa in the hanging wall Dingyuan greenschist and ~530 °C and 2.2 GPa in the Xinxian complex footwall). Apparent thrust geometries within the Huwan shear zone resulted from rotation due to footwall uplift. The Huwan detachment deformation was Triassic: synkinematic phengite grew as early as ca. 235 Ma, and the main deformation occurred during cooling from 224 to 195 Ma. Rates of exhumation were 1.9–1.4 mm/yr. The Huwan detachment is not the only high-strain shear zone involved in exhumation of the high-pressure–ultrahigh-pressure rocks: the entire basement core of Hong'an–Dabie orogen is strongly deformed.

The Tongbai-Xinxian area shows a massive 130–115 Ma cluster of cooling ages, reflecting regional, locally rapid cooling after granitoid injection and regional Cretaceous heating. Surprisingly little Early Cretaceous deformation occurred in the Qinling–Tongbai–Xinxian–Hong'an area, given its dominance in the Dabie Shan. Apatite fission-track ages cluster at 80–55 Ma and signify cooling related to transtension that coincides with rifting marked by Late Cretaceous–Eocene red bed deposition throughout eastern China. Slow average rates of ~0.06 mm/yr for the last 70 m.y. characterize Xinxian and Dabie. The Cretaceous period prior to ca. 70 Ma was likely a time of extremely slow, continuous exhumation and peneplanation for most of the Qinling-Dabie orogen; the spectacular exception is the Northern Orthogneiss Unit of northern Dabie. The India-Asia collision reactivated the orogen in the Eocene, particularly along the Tanlu fault zone and locally along the faults zones in Tongbai-Xinxian.

APPENDIX

Activity models used to calculate reaction curves are: Omphacite—Holland (1980, 1990); garnet—Hodges and Spear (1982); phengite, sphene, and clinozoisite: ideal (recommendations of Waters and Martin, 1996, and Carswell et al., 2000); quartz, $H_2O = 1$.

ACKNOWLEDGMENTS

Funded by Deutsche Forschungsgemeinschaft (DFG) grants Ra442/19, 20. Andy Calvert contributed multi-diffusion-domain modeling of K-feldspar sample D222s. The EBSD calcite texture of sample D533 was measured by Yanxia Xie in the lab of Rudy Wenk. We thank Juhn Liou, Mike Williams, and Michael Terry for constructive reviews.

REFERENCES CITED

Ames, L., Zhou, G., and Xiong, B., 1996, Geochronology and geochemistry of ultrahigh-pressure metamorphism with implications for collision of the Sino-Korean and Yangtze cratons, central China: Tectonics, v. 15, p. 472–489, doi: 10.1029/95TC02552.

Angelier, J., 1994, Fault-slip analysis and paleostress reconstruction, *in* Hancock, P.L. ed., Continental deformation: Tarrytown, New York, Pergamon, p. 53–100.

Banno, S., 1959, Aegirinaugites from crystalline schists in Sikoku: Journal of the Geological Society of Japan, v. 65, p. 652–657.

Berman, R., 1991, Thermobarometry using multi-equilibrium calculation: A new technique with petrologic applications: Canadian Mineralogist, v. 29, p. 833–855.

Bohlen, S., and Boetcher, A., 1982, The quartz-coesite transformation: A pressure determination and the effects of other components: Journal of Geophysical Research, v. 87, p. 7073–7078.

Bohlen, S., and Liotta, J., 1986, A barometer for garnet amphibolites and garnet granulites: Journal of Petrology, v. 27, p. 1025–1034.

Carswell, D., 1990, Eclogites and the eclogite facies, *in* Carswell, D., ed., Eclogite facies rocks: Glasgow, Blackie, p. 1–13.

Carswell, D., O'Brian, P., Wilson, N., and Zhai, M., 1997, Thermobarometry of phengite-bearing eclogites in the Dabie Mountains of central China: Journal of Metamorphic Geology, v. 15, p. 239–252, doi: 10.1111/j.1525-1314.1997.00014.x.

Carswell, D., O'Brian, P., Wilson, R., and Zhai, M., 2000, Metamorphic evolution, mineral chemistry and thermobarometry of schists and orthogneisses hosting ultrahigh pressure eclogites in the Dabieshan of central China: Lithos, v. 52, p. 121–155, doi: 10.1016/S0024-4937(99)00088-2.

Cawthorn, R., and Collerson, K., 1974, The recalculation of pyroxene end-member parameters and the estimation of ferrous and ferric iron content from electron microprobe analyses: The American Mineralogist, v. 59, p. 1203–1208.

Chen, D., Wu, Y., Wang, Y.-J., Zhi, X., Xia, Q., and Yang, J., 1998, Ages, Nd and Sr isotopic compositions of the Jiaoziyan gabbroic intrusion from the northern Dabie terrain: Scientia Geologica Sinica, v. 7, p. 29–35.

Chen, F., Guo, J.-H., Jiang, L.-L., Siebel, W., Cong, B., and Satir, M., 2003, Provenance of the Beihuaiyang lower-grade metamorphic zone of the

Dabie ultrahigh-pressure collision orogen, China: Evidence from zircon ages: Journal of Asian Earth Sciences, v. 22, p. 343–352, doi: 10.1016/S1367-9120(03)00068-3.

Chen, J., Dong, S., Deng, Y., and Chen, Y., 1993, Interpretation of K-Ar ages of the Dabie orogen—A differential uplifted block: Geological Review, v. 39, p. 15–22.

Chen, J.-F., Xie, Z., and Liu, S.-S., 1995, Cooling ages of the Dabie orogen, China, determined by ^{40}Ar-^{39}Ar and fission track techniques: Science in China, v. 38, p. 749–757.

Colombi, A., 1988, Métamorphisme et géohemie des roches mafiques des Alpes ouest-centrales (géopofil Viège Domodossola-Locarno) [Ph.D. thesis]: Lausanne, Switzerland, University Lausanne, 216 p.

Cui, W., and Wang, X., 1995, Eclogites of southern Henan and northern Hubei province, central China: The Island Arc, v. 4, p. 347–361.

Droop, G.T.B., 1987, A general equation for estimating Fe^{3+} concentrations in ferromagnesian silicates and oxides from microprobe analyses, using stoichiometric criteria: Mineralogical Magazine, v. 51, p. 431–435.

Eide, E., and Liou, J., 2000, High-pressure blueschists and eclogites in Hong'an: A framework: Lithos, v. 52, p. 1–22, doi: 10.1016/S0024-4937(99)00081-X.

Eide, L., McWilliams, M.O., and Liou, J.G., 1994, $^{40}Ar/^{39}Ar$ geochronologic constraints on the exhumation of HP-UHP metamorphic rocks in east-central China: Geology, v. 22, p. 601–604, doi: 10.1130/0091-7613(1994)022<0601:AAGAEO>2.3.CO;2.

Enkelmann, E., Jonckheere, R., and Ratschbacher, L., 2005, The effects of radiation damage accumulation and annealing on fission-track dating of titanite: Nuclear Instruments and Methods in Physics Research, sec. B, v. 227, p. 567–576.

Ernst, W., and Liu, J., 1998, Experimental phase-equilibrium study of Al and Ti contents of calcic amphibole in MORB—A semiquantitative thermobarometer: The American Mineralogist, v. 83, p. 952–969.

Evans, B., 1990, Phase relations of epidote blueschists, *in* Okrusch, M., ed., Third International Eclogite Conference: Lithos, v. 25, p. 3–23.

Faure, M., Sun, Y., Shu, L., Monié, P., and Charvet, J., 1996, Extensional tectonics within a subduction-type orogen: The case study of the Wugongshan dome (Jiangxi Province, SE China): Tectonophysics, v. 263, p. 77–108, doi: 10.1016/S0040-1951(97)81487-4.

Faure, M., Lin, W., Shu, L., Sun, Y., and Schärer, U., 1999, Tectonics of the Dabieshan (eastern China) and possible exhumation mechanism of ultra high-pressure rocks: Terra Nova, v. 11, p. 251–258, doi: 10.1046/j.1365-3121.1999.00257.x.

Faure, M., Lin, W., and Le Breton, N., 2001, Where is the North China–South China block boundary in eastern China?: Geology, v. 29, p. 119–122, doi: 10.1130/0091-7613(2001)029<0119:WITNCS>2.0.CO;2.

Faure, M., Lin, W., Monié, P., Le Breton, N., Poussineau, S., Panis, D., and Deloule, E., 2003, Exhumation tectonics of the ultrahigh-pressure metamorphic rocks in the Qinling orogen in east China: New petrological-structural-radiometric insights from the Shandong Peninsula: Tectonics, v. 22, doi: 10.1029/2002TC001450.

Franz, L., Romer, R., Klemd, R., Schmid, R., Oberhänsli, R., Wagner, T., and Dong, S., 2001, Eclogite-facies quartz veins within metabasites of the Dabie Shan (eastern China): Pressure-temperature-time-deformation-path, composition of the fluid phase and fluid flow during exhumation of high-pressure rocks: Contributions to Mineralogy and Petrology, v. 141, p. 322–346.

Frimmel, H.E., and Frank, W., 1998, Neoproterozoic tectono–thermal evolution of the Gariep Belt and its basement: Namibia and South Africa: Precambrian Research, v. 90, p. 1–28.

Froitzheim, N., 1992, Formation of recumbent folds during synorogenic crustal extension (Austroalpine nappes, Switzerland): Geology, v. 20, p. 923–926, doi: 10.1130/0091-7613(1992)020<0923:FORFDS>2.3.CO;2.

Fu, B., Zheng, Y.-F., and Touret, J.L.R., 2002, Petrological, isotopic and fluid inclusion studies of eclogites from Sujiahe, NW Dabie Shan (China): Chemical Geology, v. 187, p. 107–128, doi: 10.1016/S0009-2541(02)00014-1.

Gao, S., Zheng, B., and Li, Z., 1990, Geochemical evidence for Proterozoic continental arc and continental-margin rift magmatism along the northern margin of the Yangtze craton: South China: Precambrian Research, v. 47, p. 205–221.

Gao, S., Qiu, Y., Ling, W., McNaughton, N.J., Zhang, B., Zhang, G., Zhang, Z., Zhong, Z., and Suo, S., 2002, SHRIMP single zircon U-Pb geochronology of eclogites from Yingshan and Xiongdian: Earth Science Journal of China University of Geosciences, v. 27, p. 558–564.

Gilder, S.A., Leloup, P.H., Courtillot, V., Chen, Y., Coe, R.S., Zhao, X., Xiao, W., Halim, N., Cogné, J.-P., and Zhu, R., 1999, Tectonic evolution of the Tancheng-Lujiang (Tan-Lu) fault via Middle Triassic to Early Cenozoic paleomagnetic data: Journal of Geophysical Research, v. 104, p. 15,365–15,390, doi: 10.1029/1999JB900123.

Graham, C., and Powell, R., 1984, A garnet-hornblende thermometer: Calibration, testing, and application to the Pelona schists, southern California: Journal of Metamorphic Geology, v. 2, p. 13–31.

Green, D., and Hellmann, P., 1982, Fe-Mg partitioning between coexisting garnet and phengite at high pressures, and comments on a garnet-phengite thermometer: Lithos, v. 15, p. 253–266, doi: 10.1016/0024-4937(82)90017-2.

Grimmer, J.C., Jonckheere, R., Enkelmann, E., Ratschbacher, L., Blythe, A., Wagner, G.A., Liu, S., and Dong, S., 2002, Late Cretaceous–Tertiary history of the southern Tan-Lu fault zone: Apatite fission-track and structural constraints from the Dabie Shan: Tectonophysics, v. 359, p. 225–253, doi: 10.1016/S0040-1951(02)00513-9.

Grimmer, J.C., Ratschbacher, L., Franz, L., Gaitzsch, I., Tichomirowa, M., McWilliams, M.O., and Hacker, B.R., 2003, When did the ultrahigh-pressure rocks reach the surface? A $^{207}Pb/^{206}Pb$ zircon, $^{40}Ar/^{39}Ar$ white mica, Si-in-phengite single grain study of Dabie Shan synorogenic foreland sediments: Chemical Geology, v. 197, p. 87–110, doi: 10.1016/S0009-2541(02)00321-2.

Hacker, B.R., and Wang, Q., 1995, Ar/Ar geochronology of ultrahigh-pressure metamorphism in central China: Tectonics, v. 14, p. 994–1006, doi: 10.1029/95TC00932.

Hacker, B.R., Wang, X., Eide, E.A., and Ratschbacher, L., 1996a, Qinling–Dabie ultrahigh-pressure collisional orogen, *in* Yin, A., and Harrison, T.M., eds., The tectonic evolution of Asia: Cambridge, UK, Cambridge University Press.

Hacker, B.R., Modenfelder, J.L., and Gnos, E., 1996b, Rapid emplacement of the Oman ophiolite: Thermal and geochronologic constraints: Tectonics, v. 15, p. 1230–1247, doi: 10.1029/96TC01973.

Hacker, B.R., Ratschbacher, L., Webb, L., Ireland, T., Walker, D., and Dong, S., 1998, U/Pb zircon ages constrain the architecture of the ultrahigh-pressure Qinling-Dabie orogen, China: Earth and Planetary Science Letters, v. 161, p. 215–230, doi: 10.1016/S0012-821X(98)00152-6.

Hacker, B.R., Ratschbacher, L., Webb, L., McWilliams, M., Calvert, A., Dong, S., Wenk, H.R., and Chateigner, D., 2000, Exhumation of the ultrahigh-pressure continental crust in east-central China: Late Triassic–Early Jurassic tectonic unroofing: Journal of Geophysical Research, v. 105, p. 13,339–13,364, doi: 10.1029/2000JB900039.

Hacker, B.R., Ratschbacher, L., and Liou, J.G., 2004, Subduction, collision and exhumation in the ultrahigh-pressure Qinling-Dabie orogen, *in* Malpas, J., Fletcher, C.J.N., Ali, J.R., and Aitchison, J.C., eds., Aspects of the tectonic evolution of China: Geological Society of London Special Publication 226, p. 157–175.

Harrison, T.M., Heizler, M.T., Lovera, O.M., Wenji, C., and Grove, M., 1994, A chlorine disinfectant for excess argon released from K-feldspar during step heating: Earth and Planetary Science Letters, v. 123, p. 95–104, doi: 10.1016/0012-821X(94)90260-7.

Hodges, H., and Spear, F., 1982, Thermometry, geobarometry at Mt. Moosilake, New Hampshire: The American Mineralogist, v. 67, p. 1118–1134.

Holland, T.J.B., 1980, The reaction albite = jadeite + quartz determined experimentally in the range of 600–1200 °C: The American Mineralogist, v. 65, p. 129–134.

Holland, T.J.B., 1990, Activities of components in omphacite solid solutions: Contributions to Mineralogy and Petrology, v. 105, p. 446–453, doi: 10.1007/BF00286831.

Holland, T., and Blundy, J., 1994, Non-ideal interactions in calcic amphiboles and their bearing on amphibole-plagioclase thermometry: Contributions to Mineralogy and Petrology, v. 116, p. 433–447, doi: 10.1007/BF00310910.

Hu, N., Yang, J., An, S., and Hu, J., 1993, Metamorphism and tectonic evolution of the Shangdan fault zone, Shaanxi, China: Journal of Metamorphic Geology, v. 11, p. 537–548.

Jahn, B.-M., 1998, Geochemical and isotopic characteristics of UHP eclogites and ultramafic rocks in the Dabie orogen: Implications for continental subduction and collision tectonics, *in* Hacker, B.R., and Liou, J.G., eds., When continents collide: Geodynamics and geochemistry of ultrahigh-pressure rocks: Dordrecht, Kluwer Academic Publishers, p. 203–239,

Jahn, B.-M., Wu, F., Lo, Ch.-H., and Tsai, Ch.-H., 1999, Crust-mantle interaction induced by deep subduction of the continental crust: Geochemical and Sr-Nd isotopic evidence from post-collisional mafic-ultramafic intrusions of the northern Dabie complex, central China: Chemical Geology, v. 157, p. 119–146, doi: 10.1016/S0009-2541(98)00197-1.

Jian, P., Yang, W., Li, Z.C., and Zhou, H., 1997, Isotopic geochronological evidence for the Caledonian Xiongdian eclogite in the western Dabie mountains, China: Acta Geologica Sinica, v. 10, p. 455–465.

Jian, P., Liu, D., Yang, W., and Williams, I.S., 2001, SHRIMP dating of zircons from the Caledonian Xiongdian eclogite, western Dabie Mountains, China: Chinese Science Bulletin, v. 46, p. 77–79.

Jonckheere, R., 2003a, On the densities of etchable fission tracks in a mineral and co-irradiated external detector with reference to fission-track dating of minerals: Chemical Geology, v. 200, p. 41–58, doi: 10.1016/S0009-2541(03)00116-5.

Jonckheere, R., 2003b, On the methodical problems in estimating geological temperature and time from measurements of fission tracks in apatite: Radiation Measurements, v. 36, p. 43–55, doi: 10.1016/S1350-4487(03)00096-9.

Jonckheere, R., and Wagner, G.A., 2000, On the thermal stability of fossil and neutron-induced fission tracks in natural titanite: Nuclear Instruments and Methods in Physics Research, Section B, v. 168, p. 78–87.

Ketcham, R.A., Donelick, R.A., and Donelick, M.B., 2000, AFTSolve: A program for multikinetic modeling of apatite fission-track data: Geological Materials Research, v. 2, p. 1–32.

Kohn, M., and Spear, F., 1990, Two new geobarometers for garnet-amphibolites, with applications to southeastern Vermont: The American Mineralogist, v. 75, p. 89–96.

Kretz, R., 1983, Symbols for rock-forming minerals: The American Mineralogist, v. 68, p. 277–279.

Krogh, E., 2000, The garnet-clinopyroxene Fe/Mg thermometer: An updated calibration: Journal of Metamorphic Geology, v. 18, p. 211–219, doi: 10.1046/j.1525-1314.2000.00247.x.

Kröner, A., Compston, W., Zhang, G.W., Guo, A.L., and Todt, W., 1988, Age and tectonic setting of late Archean greenstone-gneiss terrane in Henan province, China, as revealed by single-grain zircon dating: Geology, v. 16, p. 211–215, doi: 10.1130/0091-7613(1988)016<0211:AATSOL>2.3.CO;2.

Kröner, A., Zhang, G., and Sun, Y., 1993, Granulites in the Tongbai area, Qinling belt, China: Geochemistry, petrology, single zircon geochronology, and implications for the tectonic evolution of eastern Asia: Tectonics, v. 12, p. 245–255.

Laird, J., 1982, Amphiboles in metamorphosed basaltic rocks, Chapter 2: Mineralogical Society of America Reviews in Mineralogy, v. 9B, p. 113–158.

Leake, B.E., Wooley, A.R., Arps, C., Birch, W., Gilbert, M., Grice, J., Hawthorne, F., Kato, A., Kisch, H., Krivovichev, V., Linthout, K., Mandarino, J.L.J., Maresch, V., Nickel, E., Rock, N., Schumacher, J., Smith, D., Stephenson, N., Ungaretti, L., Whittaker, E., and Youzhi, G., 1997, Nomenclature of amphiboles. Report of the Subcommittee on Amphiboles of the International Mineralogical Association Commission on New Minerals and Mineral Names: European Journal of Mineralogy, v. 9, p. 623–665.

Li, S.G., Hart, S.R., Zheng, S.G., Liu, D.L., Zhang, G.W., and Guo, A.L., 1989, Timing of collision between the North and South China blocks—The Sm-Nd isotopic age evidence: Science in China, v. 32, p. 1393–1400.

Li, S.G., Jagoutz, E., Zhang, Z.Q., Chen, W., and Lo, Q.H., 1995, Structure of high-pressure metamorphic belt in the Dabie mountains and its tectonic implications: Chinese Science Bulletin, v. 40, p. 138–140.

Li, S.G., Huang, F., Nie, Y.H., Han, W.L., Long, G., Li, H.M., Zhang, S.Q., and Zhang, Z.-H., 2001, Geochemical and geochronological constraints on the suture location between the North and South China blocks in the Dabie orogen, central China: Physics and Chemistry of the Earth, Part A: Solid Earth and Geodesy, v. 26, p. 655–672, doi: 10.1016/S1464-1895(01)00117-X.

Li, X.H., 1999, U-Pb zircon ages of granites from the southern margin of the Yangtze block: Timing of Neoproterozoic Jinning orogeny in SE China and implications for Rodinia assembly: Precambrian Research, v. 97, p. 43–57, doi: 10.1016/S0301-9268(99)00020-0.

Li, Z.-X., Zhang, L., and Powell, McA.Ch., 1995, South China in Rodinia: Part of the missing link between Australia–East Antarctica and Laurentia?: Geology, v. 23, p. 407–410.

Li, Z.X., Li, X.H., Kinny, P.D., and Wang, J., 1999, The breakup of Rodinia: Did it start with a mantle plume beneath South China?: Earth and Planetary Science Letters, v. 173, p. 171–181, doi: 10.1016/S0012-821X(99)00240-X.

Li, Z.X., Li, X.H., Zhou, H., and Kinny, P.D., 2002, Grenvillian continental collision in south China: New SHRIMP U-Pb zircon results and implications for the configuration of Rodinia: Geology, v. 30, p. 163–166, doi: 10.1130/0091-7613(2002)030<0163:GCCISC>2.0.CO;2.

Lin, W., Faure, M., Monié, P., Schärer, U., Zhang, L., and Sun, Y., 2000, Tectonics of SE China: New insights from the Lushan massif (Jiangxi Province): Tectonics, v. 19, p. 852–871, doi: 10.1029/2000TC900009.

Liou, J.G., Zhang, R.Y., Eide, E.A., Maruyama, S., Wang, X., and Ernst, W.G., 1996, Metamorphism and tectonics of high-*P* and ultrahigh-*P* belts in Dabie-Sulu regions, eastern central China, *in* Yin, A., and Harrison T.M., eds., The tectonic evolution of Asia: Cambridge, UK, Cambridge University Press, p. 300–343.

Liu, D., Tang, J., Zhou, Ch., Gao, T., Shen, H., and Yang, Ch., 2002, U-Pb zircon dating and its geological significance of the Taoyuanzhai volcanic rocks, central Dabie orogenic belt: Acta Geologica Sinica, v. 76, p. 217–221.

Liu, X., Jahn, B.-M., Liu, D., Dong, S., and Li, S., 2004a, SHRIMP U-Pb zircon dating of a metagabbro and eclogites from western Dabieshan (Hong'an block), China, and its tectonic implications: Tectonophysics, v. 394, p. 171–192, doi: 10.1016/j.tecto.2004.08.004.

Liu, X., Wei, C., Liu, S., Dong, S., and Liu, J., 2004b, Thermobaric structure of a traverse across western Dabieshan: Implications for collision tectonics between the Sino-Korean and Yangtze cratons: Journal of Metamorphic Geology, v. 22, p. 361–379, doi: 10.1111/j.1525-1314.2004.00519.x.

Liu, Y.-C., Li, S.-G., Xu, S.-T., Jahn, B.-M., Zheng, Y.-F., Zhang, Z.-Q., Jiang, L.-L., Chen, G.-B., and Wu, W.-P., 2001, Sm-Nd dating of eclogites from north Dabie and its constraints on the timing of granulite-facies retrogression: Geochimica, v. 30, p. 79–87.

Lovera, O.M., Grove, M., Harrison, T.M., and Mahon, K.I., 1997, Systematic analysis of K-feldspar $^{40}Ar/^{39}Ar$ step heating results; I, Significance of activation energy determinations: Geochimica et Cosmochimica Acta, v. 61, p. 3171–3192, doi: 10.1016/S0016-7037(97)00147-6.

Maresch, W., 1977, Experimental studies on glaucophane: An analysis of present knowledge: Tectonophysics, v. 43, p. 109–125, doi: 10.1016/0040-1951(77)90008-7.

Maruyama, S., Cho, M., and Liou, J., 1986, Experimental investigations of greenschist-blueschist transition equilibria: Pressure dependence of Al contents in sodic amphiboles: A new geobarometer: Geological Society of America Memoir 164, p. 1–16.

Massonne, H., and Schreyer, W., 1987, Phengite barometry based on the limiting assemblage with K-feldspar, phlogopite and quartz: Contributions to Mineralogy and Petrology, v. 96, p. 212–224, doi: 10.1007/BF00375235.

Massonne, H., and Szpurka, Z., 1997, Thermodynamic properties of white micas on the basis of high-pressure experiments in the system K_2O-MgO-Al_2O_3-SiO_2-H_2O and K_2O-FeO-Al_2O_3-SiO_2-H_2O: Lithos, v. 41, p. 229–250, doi: 10.1016/S0024-4937(97)82014-2.

Mattauer, M., Matte, P., Malavieille, J., Tapponnier, P., Maluski, H., Xu, Z.Q., Lu, Y.L., and Tang, Y.Q., 1985, Tectonics of the Qinling belt: Build-up and evolution of eastern Asia: Nature, v. 317, p. 496–500, doi: 10.1038/317496a0.

Mattauer, M., Matte, Ph., Maluski, H., Xu, Z., Zhang, Q., and Wang, Y.-M., 1991, La limite Chine du Nord-Chine du Sud au Paleozoique et au Trias. Nouvelles donnees structurales et radiometriques dans le massif de Dabie-Shan (chaine des Qinling): Compte Rendu Academie Science, Paris, v. 312, p. 1227–1233.

Niu, B., Liu, Z., and Ren, J., 1993, The tectonic relationship between the Qinling Mountains and Tongbai-Dabie Mountains with notes on the tectonic evolution of the Hehuai Basin: Bulletin of the Chinese Academy of Geological Sciences, v. 26, p. 1–12.

Niu, B., Fu, Y., Liu, Z., Ren, J., and Chen, W., 1994, Main tectonothermal events and $^{40}Ar/^{39}Ar$ dating of the Tongbai-Dabie Mts.: Acta Geoscientia Sinica, v. 1994, p. 20–34.

Oberhänsli, R., Martinotti, G., Schmid, R., and Liu, X., 2002, Preservation of primary volcanic textures in the ultrahigh-pressure terrain of Dabie Shan: Geology, v. 30, p. 699–702, doi: 10.1130/0091-7613(2002)030<0699:POPVTI>2.0.CO;2.

Okay, A., Sengör, A., and Satir, M., 1993, Tectonics of an ultrahigh-pressure metamorphic terrane: Dabie Shan, China: Tectonics, v. 12, p. 1320–1334.

Papike, J.J., Cameron, K.L., and Baldwin, K., 1974, Characterization of other than quadrilateral components and estimates of ferric iron from microprobe data: Geological Society of America Abstract with Programs, v. 6, no. 7, p. 1053–1054.

Passaglia, E., and Gottardi, G., 1973, Crystal chemistry and nomenclature of pumpellyites and jugoldites: Canadian Mineralogists, v. 12, p. 219–223.

Passchier, C., and Trouw, R., 1996, Microtectonics: Berlin, Springer-Verlag, 289 p.

Ratschbacher, L., Hacker, B., Webb, L., McWilliams, M., Ireland, T., Dong, S., Calvert, A., Chateigner, D., and Wenk, H.R., 2000, Exhumation of the ultrahigh-pressure continental crust in east-central China: Cretaceous and Cenozoic unroofing and the Tan-Lu fault: Journal of Geophysical Research, v. 105, p. 13,303–13,338, doi: 10.1029/2000JB900040.

Ratschbacher, L., Hacker, B.R., Calvert, A., Webb, L.E., Grimmer, J.C., McWilliams, M.O., Ireland, T.R., Dong, S., and Hu, J., 2003, Tectonics of the Qinling (central China): Tectonostratigraphy, geochronology, and deformation history: Tectonophysics, v. 366, p. 1–53, doi: 10.1016/S0040-1951(03)00053-2.

Reiners, P.W., Zhou, Z., Ehlers, T.A., Xu, C., Brandon, M.T., Donelick, R.A., and Nicolescu, S., 2003, Post-orogenic evolution of the Dabie Shan, eastern China, from (U-Th)/He and fission-track thermochronology: American Journal of Science, v. 303, p. 489–518.

Ren, J., Tamaki, K., Li, S., and Junxia, Z., 2002, Late Mesozoic and Cenozoic rifting and its dynamic setting in Eastern China and adjacent areas: Tectonophysics, v. 344, p. 175–205, doi: 10.1016/S0040-1951(01)00271-2.

R.G.S. Henan, 1989, Regional Geology of Henan Province (in Chinese): Geological Publishing House, Beijing, scale: 1:500,000.

R.G.S. Shaanxi, 1989, Regional Geology of Shaanxi Province (in Chinese): Geological Publishing House, Beijing, scale: 1:500,000.

R.G.S. Sichuan, 1991, Regional Geology of Sichuan Province (in Chinese): Geological Publishing House, Beijing, scale: 1:500,000.

Rowley, D.B., and Xue, F., 1996, Modeling the exhumation of ultra-high pressure metamorphic assemblages; observations from the Dabie/Tongbai region, China: Geological Society of America Abstracts with Programs, v. 28, no. 7, p. 249.

Ryburn, R., Rahem, A., and Green, D., 1976, Determination of the *PT*-path of natural eclogites during metamorphism—Record of a subduction: Lithos, v. 9, p. 161–164, doi: 10.1016/0024-4937(76)90033-5.

Schliestedt, M., 1980, Phasengleichgewichte in Hochdruckgesteinen von Sifnos, Griechenland [Ph.D. thesis]: TU Braunschweig, 142 p.

Schmid, R., Wilke, M., Oberhänsli, R., Janssens, K., Falkenberg, G., Franz, L., and Gaab, A., 2003, Micro-XANES determination of ferric iron and its application in thermobarometry: Lithos, v. 70, p. 381–392, doi: 10.1016/S0024-4937(03)00107-5.

Spear, F.S., 1993, Metamorphic phase equilibria and pressure-temperature-time paths: Mineralogical Society of America Monograph, Washington, 799 p.

Sun, W., Williams, I.S., and Li, S., 2002, Carboniferous and Triassic eclogites in the western Dabie Mountains, east-central China: Evidence for protracted convergence of the North and South China blocks: Journal of Metamorphic Geology, v. 20, p. 873–886, doi: 10.1046/j.1525-1314.2002.00418.x.

Suo, S.T., Sang, L., Han, Y., You, Z., and Zhou, N., 1993, The petrology and tectonics in Dabie Precambrian metamorphic terrane, central China: Wuhan, Press of the China University of Geosciences, p. 33–112.

Terabayashi, M., 1988, Actinolite-forming reactions at low pressure and the role of the Fe^{2+}-Mg substitution: Contributions to Mineralogy and Petrology, v. 100, p. 268–280, doi: 10.1007/BF00379738.

Triboulet, C., Thieblemont, D., and Audren, C., 1992, The (Na-Ca) amphibole-albite-chlorite- epidote-quartz thermobarometer in the system S-A-F-M-C-N-H_2O: An empirical calibration: Contributions to Mineralogy and Petrology, v. 10, p. 545–556.

Twiss, R.J., and Unruh, J.R., 1998, Analysis of fault slip inversions: Do they constrain stress or strain rate?: Journal of Geophysical Research, v. 103, p. 12,205–12,221, doi: 10.1029/98JB00612.

Wallis, S., Enami, M., and Banno, S., 1999, The Sulu UHP terrane: A review of the petrology and structural geology: International Geology Review, v. 41, p. 906–920.

Wan, Y., Li, R., Wilde, S.A., Liu, D., Chen, Z., Yan, L., Song, T., and Yin, X., 2005, UHP metamorphism and exhumation of the Dabie orogen, China: Evidence from SHRIMP dating of zircon and monazite from a UHP granitic gneiss cobble from the Hefei Basin: Geochimica et Cosmochimica Acta, v. 69, p. 4333–4348, doi: 10.1016/jgca.2005.03.055.

Wang, Q., Lia, R., Wang, D., and Li, S., 2003, Eclogites preserved as pebbles in Jurassic conglomerate, Dabie Mountains, China: Lithos, v. 70, p. 345–357, doi: 10.1016/S0024-4937(03)00105-1.

Waters, D., and Martin, H., 1993, Geobarometry of phengite-bearing eclogites (updated calibration of 1996 at: www.earth.ox.ac.uk/davewa/ecbar.html): Terra Abstracts, v. 5, p. 410–411.

Webb, L., Hacker, B.R., Ratschbacher, L., and Dong, S.W., 1996, Structures and kinematics of exhumation: Ultrahigh-pressure rocks in the Hong'an block of the Qinling-Dabie ultrahigh-pressure orogen, E. China: Geological Society of America Abstracts with Programs, v. 28, no. 7, p. 69.

Webb, L., Hacker, B., Ratschbacher, L., McWilliams, M., and Dong, S., 1999, Thermochronologic constraints on deformation and cooling history of high and ultrahigh-pressure rocks in Qinling-Dabie orogen, eastern China: Tectonics, v. 18, p. 621–638, doi: 10.1029/1999TC900012.

Webb, L.E., Ratschbacher, L., Hacker, B.R., and Dong, S., 2001, Kinematics of exhumation of high- and ultrahigh-pressure rocks in the Hong'an and Tongbai Shan of the Qinling-Dabie collisional orogen, eastern China, *in* Hendrix, M.S., and Davis, G.A., eds., Paleozoic and Mesozoic tectonic evolution of central Asia from continental assembly to intracontinental deformation: Geological Society of America Special Paper 194, p. 231–245.

Wu, F.-Y., Lin, J.-Q., Wilde, S.A., Zhang, X., and Yang, J.-H., 2005, Nature and significance of the Early Cretaceous giant igneous event in eastern China: Earth and Planetary Science Letters, v. 233, p. 103–119, doi: 10.1016/j.epsl.2005.02.019.

Xie, Z., Chen, J.-P., Zhou, T.-X., Li, H.-M., Zao, Y.-C., and Zhou, H.-Y., 1998, U-Pb zircon ages of the rocks in the north Dabie terrain, China: Scientia Geologica Sinica, v. 7, p. 501–511.

Xie, Z., Chen, J.-F., Zhang, X., Gao, T.-S., Dai, Z.-Q., Zhou, T.-X., and Li, H.-M., 2001, Zircon U-Pb dating of gneiss from Shizhuhe in north Dabie and its geological implications: Acta Petrologica Sinica, v. 17, p. 139–144.

Xie, Z., Zheng, Y.-F., Jahn, B.-M., Ballevre, M., Chen, J., Gautier, P., Gao, T., Gong, B., and Zhou, J., 2004, Sm-Nd and Rb-Sr dating of pyroxene-garnetite from north Dabie in east-central China: Problem of isotope disequilibrium due to retrograde metamorphism: Chemical Geology, v. 206, p. 137–158, doi: 10.1016/j.chemgeo.2004.01.013.

Xu, B., Grove, M., Wang, Ch., Zhang, L., and Liu, S., 2000, $^{40}Ar/^{39}Ar$ thermochronology from the northwestern Dabie Shan: Constraints on the evolution of Qinling-Dabie orogenic belt, east-central China: Tectonophysics, v. 322, p. 279–301, doi: 10.1016/S0040-1951(00)00092-5.

Xu, S.T., Jiang, L., Liu, Y., and Zhang, Y., 1992, Tectonic framework and evolution of the Dabie orogen in Anhui, eastern China: Acta Geologica Sinica, v. 66, p. 1–14.

Xu, X., Zhou, Z., Van Den Haute, P., Donelick, R.A., and Chen, H., 2006, (U-Th)/He and fission-track geochronology in the Dabie Shan: Chinese Science Bulletin (in press).

Xue, F., Lerch, F., Kröner, A., and Reischmann, T., 1996, Tectonic evolution of the East Qinling Mountains, China, in the Paleozoic: A review and a new tectonic model: Tectonophysics, v. 253, p. 271–284, doi: 10.1016/0040-1951(95)00060-7.

Xue, F., Rowley, D.B., Tucker, R.D., and Peng, Z.X., 1997, U-Pb zircon ages of granitoid rocks in the north Dabie complex, eastern Dabie Shan, China: The Journal of Geology, v. 105, p. 744–753.

Ye, B.D., Jiang, P., Xu, J., Cui, F., Li, Z., and Zhang, Z., 1993, The Sujiahe terrane collage belt and its constitution and evolution along the northern hillslope of the Tongbai-Dabie orogenic belt: Wuhan, Press of China University of Geoscience, p. 66–67.

Ye, B.D., Jiang, P., Xu, J., Cui, F., Li, Z., and Zhang, Z., 1994, Timing of the Sujiahe group in the Tongbai-Dabie orogenic belt, *in* Chen, H., ed., Research of isotope geochemistry: Hangzhou, Zhejiang University Press, p. 175–186.

You, Z., Han, Y., Suo, S., Chen, N., and Zhong, Z., 1993, Metamorphic history and tectonic evolution of the Qinling complex, eastern Qinling Mountains, China: Journal of Metamorphic Geology, v. 11, p. 549–560.

Yu, Z., and Meng, Q., 1995, Late Paleozoic sedimentary and tectonic evolution of the Shangdan suture zone, eastern Qinling, China: Journal of Southeast Asian Earth Sciences, v. 11, p. 237–242, doi: 10.1016/0743-9547(95)98084-F.

Zhai, X., Day, H.W., Hacker, B.R., and You, Z., 1998, Paleozoic metamorphism in the Qinling orogen, Tongbai mountains, central China: Geology, v. 26, p. 371–374, doi: 10.1130/0091-7613(1998)026<0371:PMITQO>2.3.CO;2.

Zhang, D., and Sun, G., 1990, Emplacement age of the Tiantangzhai granite massif, Dabie Mountains and its geological significance: Acta Petrologica Mineralogica, v. 6, p. 31.

Zhang, K.-J., 1997, North and South China collision along the eastern and southern North China margins: Tectonophysics, v. 270, p. 145–156, doi: 10.1016/S0040-1951(96)00208-9.

Zhang, R., and Liou, J., 1994, Coesite-bearing eclogite in Henan Province, central China: Detailed petrography, glaucophane stability and *PT*-path: European Journal of Mineralogy, v. 6, p. 217–233.

Zhang, Y.Q., Vergely, P., and Mercier, J.L., 1995, Active faulting in and along the Qinling Range (China) inferred from SPOT imagery analysis and extrusion tectonics of southern China: Tectonophysics, v. 243, p. 69–95, doi: 10.1016/0040-1951(94)00192-C.

Zhao, X., and Coe, R.S., 1987, Paleomagnetic constraints on the collision and rotation of North and South China: Nature, v. 327, p. 141–144, doi: 10.1038/327141a0.

Zhong, Z., Suo, S., and You, Z., 1999, Regional-scale extensional tectonic pattern of ultrahigh-*P* and high-*P* metamorphic belts from the Dabie massif, China: International Geologic Review, v. 41, p. 1033–1041.

Zhong, Z., Suo, S., You, Z., Zhang, H., and Zhou, H., 2001, Major constituents of the Dabie collisional orogenic belt and partial melting in the ultrahigh-pressure unit: International Geologic Review, v. 43, p. 226–236.

Zhou, G., Liu, J., Eide, E., Liou, J., and Ernst, W., 1993, High pressure/low temperature metamorphism in northern Hubei province, central China: Journal of Metamorphic Geology, v. 11, p. 561–574.

Zhou, M.-F., Yan, D.-P., Kennedy, A.K., Li, Y., and Ding, J., 2002, SHRIMP U-Pb zircon geochronological and geochemical evidence for Neoproterozoic arc-magmatism along the western margin of the Yangtze block: South China: Earth and Planetary Science Letters, v. 196, p. 51–67, doi: 10.1016/S0012-821X(01)00595-7.

Zhou, T., Chen, J., Li, X., and Foland, K.A., 1992, $^{40}Ar/^{39}Ar$ isotope dating of intrusions from Huoshan-Shucheng syenite zone: Anhui Geology, v. 2, p. 4–11.

Zhou, Z., Xu, C., Reiner, P.W., Yang, F., and Donelick, R.A., 2003, Late Cretaceous–Cenozoic exhumation history of Tiantangzhai region of Dabieshan orogen: Constraints from (U-Th)/He and fission-track analysis: Chinese Science Bulletin, v. 48, p. 1151–1156, doi: 10.1360/02wd0525.

MANUSCRIPT ACCEPTED BY THE SOCIETY 21 SEPTEMBER 2005

Geological Society of America
Special Paper 403
2006

$^{40}Ar/^{39}Ar$ thermochronology of the Sulu terrane: Late Triassic exhumation of high- and ultrahigh-pressure rocks and implications for Mesozoic tectonics in East Asia

L.E. Webb*
Department of Earth Sciences, Syracuse University, Syracuse, New York 13244, USA
M.L. Leech*
School of Earth Sciences, Stanford University, Stanford, California 94305, USA
T.N. Yang
Institute of Geology, Chinese Academy of Geological Sciences, Beijing, 100037, China

ABSTRACT

Structural and thermochronological data from the Sulu terrane of eastern China document the exhumation of high-pressure and ultrahigh-pressure (UHP) metamorphic rocks to upper-crustal depths by ca. 206 Ma. $^{40}Ar/^{39}Ar$ ages from K-bearing phases record recrystallization and cooling through amphibolite- and upper greenschist–facies conditions during top-to-the-NW noncoaxial shear and suggest cooling rates on the order of 55 °C/m.y. Integration of the $^{40}Ar/^{39}Ar$ data with U/Pb constraints on the timing of UHP metamorphism yields vertical exhumation rates of >6 mm yr^{-1} from mantle to upper-crustal depths. Qualitative thermal models of metamorphic K-feldspars suggest transient reheating in the Jurassic of a magnitude insufficient to reset mica ages. The Yantai-Qingdao-Wulian fault that currently delineates the boundary between the Yangtze and Sino-Korean cratons was active in the Early Cretaceous as a top-to-the-W extensional detachment fault. The youngest phase of deformation recorded by the $^{40}Ar/^{39}Ar$ data is consistent with mid to Late Cretaceous deformation associated with the Tan-Lu fault. In total, the data reveal that high-pressure and UHP rocks of the Sulu terrane reached and resided at higher structural levels by the end of the Late Triassic relative to the high-pressure and UHP rocks presently exposed in the Dabie Shan. Thus, our $^{40}Ar/^{39}Ar$ data from the Sulu terrane provide the tightest constraints thus far on the timing and rates of exhumation of high-pressure and UHP rocks to upper-crustal depths in the orogen.

Keywords: thermochronology, tectonics, eastern China, exhumation rates, microstructural analysis.

*E-mail, Webb: lewebb@syr.edu. Present address, Leech: Department of Geosciences, San Francisco State University, San Francisco, California 94132, USA.

Webb, L.E., Leech, M.L., and Yang, T.N., 2006, $^{40}Ar/^{39}Ar$ thermochronology of the Sulu terrane: Late Triassic exhumation of high- and ultrahigh-pressure rocks and implications for Mesozoic tectonics in East Asia, *in* Hacker, B.R., McClelland, W.C., and Liou, J.G., eds., Ultrahigh-pressure metamorphism: Deep continental subduction: Geological Society of America Special Paper 403, p. 77–92, doi: 10.1130/2006.2403(04). For permission to copy, contact editing@geosociety.org.

INTRODUCTION

The Sulu ultrahigh-pressure (UHP) metamorphic terrane is part of the Qinling-Dabie-Sulu orogenic belt in east-central China and records a history of profound subduction to, and subsequent exhumation from, mantle depths during Permian–Triassic collision between the Yangtze and Sino-Korean cratons. Metamorphic rocks of Yangtze affinity are known to include the world's most extensive exposures of high-pressure and UHP rocks, and thus offer a prime opportunity to study structural, petrological, geochemical, and isotopic systematics associated with regionally extensive subduction of continental lithosphere. Understanding the subduction-exhumation history of the orogen is complicated by multiple phases of deformation and widespread Late Jurassic–Early Cretaceous plutonism. Based on map relationships, the Sulu and Dabie terranes are separated by ~500 km of apparent sinistral offset along the Tan-Lu fault. The timing and nature of this relationship have been variously proposed to be both a primary feature of the Sino Korean–Yangtze collision (e.g., Yin and Nie, 1993) and a late Mesozoic to Cenozoic feature (e.g., Ratschbacher et al., 2000). To date, the Dabie–Hong'an–Qinling portion of the orogen has been the principal target of geochronological investigations (e.g., Ames et al., 1996; Chavagnac et al., 2001; Hacker et al., 1998, 2000; Li et al., 1993; Ratschbacher et al., 2000, 2003; Rowley et al., 1997; Webb et al., 1999b; Xue et al., 1997), while the Sulu region remained relatively understudied in this context until recently (e.g., Leech et al., this volume; Xu et al., this volume). This paper presents new $^{40}Ar/^{39}Ar$ thermochronologic and structural data from the Sulu terrane. Together, these data constrain the timing and rates of exhumation of the UHP rocks to upper-crustal depths and have further implications for the Mesozoic tectonic evolution of the orogen and East Asia.

GEOLOGY OF THE SHANDONG PENINSULA

Metamorphic rocks with Yangtze-craton affinities comprise the high-pressure and UHP units in the Sulu terrane (Fig. 1). Regional evidence for metamorphic coesite in part defines the UHP unit. High-pressure and UHP eclogite blocks are widespread, though volumetrically minor, in host gneiss, schist, and marble. Blocks of garnet peridotite of meter to kilometer scale are found locally throughout the terrane. Field and petrological evidence demonstrates that lithologies hosting UHP eclogites also record UHP metamorphism with peak conditions of ~4 GPa and 800 °C (e.g., Zhang and Liou, 1998; Ye et al., 2002; Liu et al., 2002, 2004a). Isotopic data suggest that the protoliths of the high-pressure and UHP crustal rocks have Proterozoic ages and were subjected to Middle to Late Triassic UHP metamorphism (e.g., Ames et al., 1996; Enami et al. 1993; Yang et al., 2003; Liu et al., 2004b; Leech et al., this volume) and granulite- to amphibolite-facies retrograde overprinting associated with isothermal decompression and local partial melting (Zhang and Liou, 1998; Wallis et al., 2005).

The high-pressure and UHP units are separated from amphibolite- and granulite-facies metamorphic rocks of the Sino-Korean craton by the Yantai-Qingdao-Wulian fault (Fig. 1). Correlation of the metamorphic rocks northwest of the Yantai-Qingdao-Wulian fault with the Sino-Korean craton was challenged by Faure et al. (2001, 2003) and have been interpreted by other workers as part of the Qinling microcontinent (Ratschbacher et al., this volume). Metamorphic rocks on both sides of the fault are unconformably overlain by Jurassic–Early Cretaceous volcanic and sedimentary cover and are intruded by postcollisional Mesozoic granites. Like the Qinling-Dabie portion of the orogen, Late Jurassic–Early Cretaceous igneous activity in the Shandong Peninsula is associated with ore genesis (e.g., Zhang et al., 2003).

Structural Observations

The high-pressure–UHP rocks of the Sulu terrane are characterized by a generally SE-dipping foliation, SE-plunging stretching lineations, and top-to-the-NW shear sense (Wallis et al., 1999; Webb et al., 2002; Faure et al., 2003; Xu et al., this volume; Fig. 1). The foliation within the UHP gneiss is folded about centimeter- to meter-scale folds with SSW- to ENE-plunging axes. Deformation was accompanied principally by recrystallization under amphibolite-facies conditions. The high-pressure unit displays a strong crenulation cleavage, in which S_2 and L_2 parallel the dominant (S_1, L_1) fabric observed in the UHP unit. Structural variability within the UHP unit includes: (1) top-to-the-S sense of shear and S-plunging stretching lineations in L-S tectonites between Lanshantou and Denshan (vicinity of stop 18; Fig. 1); and (2) both top-to-the-NW and top-to-the-W sense of shear and E- to SE-plunging stretching lineations in the Taolin-Shimen area (vicinity of stop 40; Fig. 1). Top-to-the-SE shear sense was recognized in the high-pressure unit by Faure et al. (2003) and Xu et al. (this volume) and was proposed to represent rare vestiges of deformation during subduction. Overall, the regional structure of the Sulu terrane is strikingly similar to that of Hong'an and Dabie Shan (cf. Hacker et al., 2000; Webb et al., 2001; Faure et al., 2003).

In order to better understand the significance of field observations and to select meaningful samples for $^{40}Ar/^{39}Ar$ analyses, we conducted microstructural studies of oriented samples (Leech et al., 2003; this study). Sample descriptions are summarized in Table 1. Petrographic observations reveal that eclogite bodies displaying mesoscopic deformation fabrics are commonly dominated by symplectite at the microscopic scale, suggesting that static recrystallization occurred after deformation was partitioned into the surrounding host gneisses. Syntectonic plagioclase porphyroblasts in retrogressed mafic schist interlayered within quartzofeldspathic gneiss contain folia of hornblende and rutile that are locally continuous with the external foliation defined by biotite and epidote, implying that the observed fabric developed during retrograde metamorphism

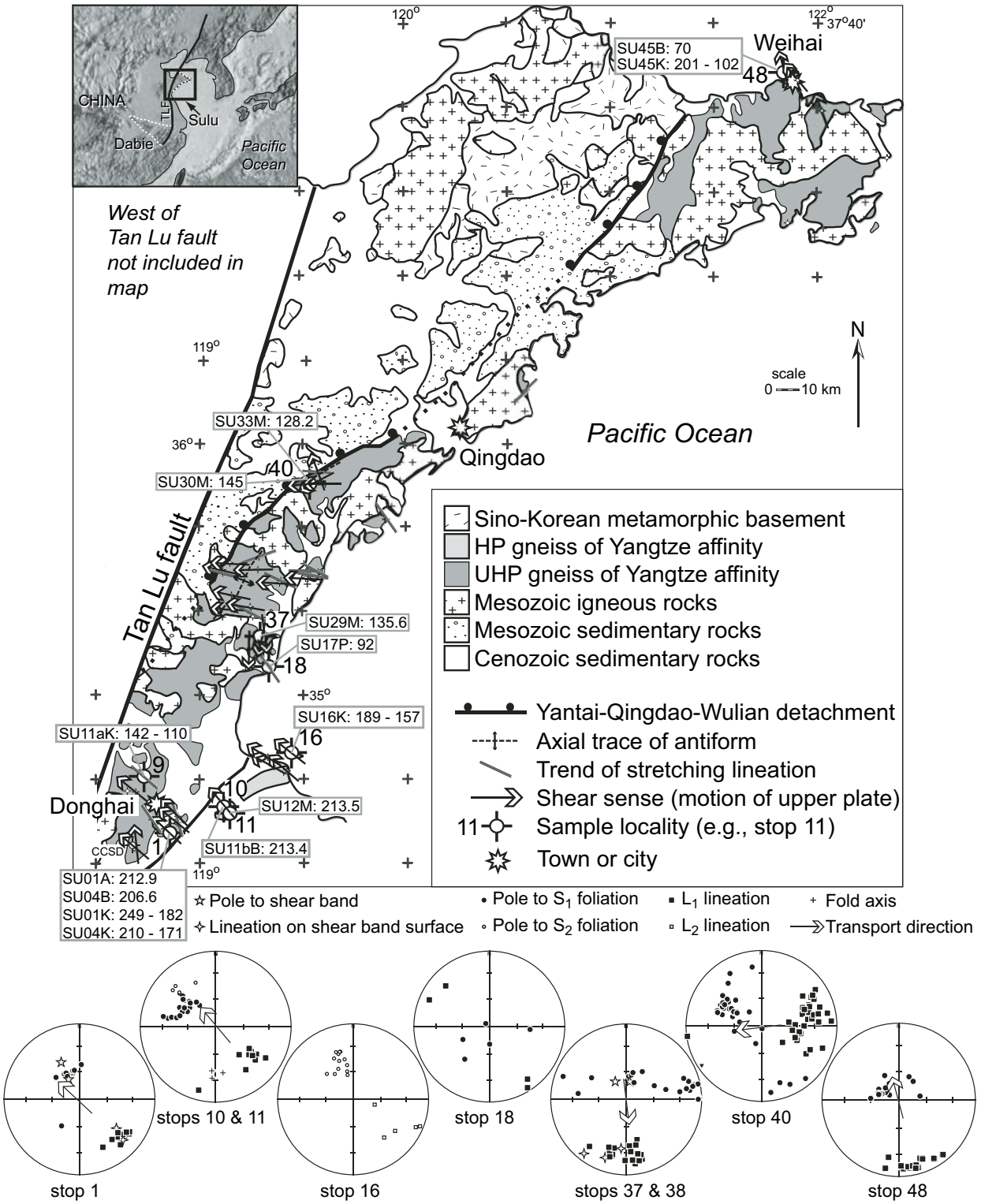

Figure 1. Geologic map of the Sulu terrane in eastern China. Inset shows relative locations of the Sulu terrane and Dabie Shan. TLF—Tan-Lu fault. Map indicates major rock types east of the Tan-Lu fault zone. Results of $^{40}Ar/^{39}Ar$ analyses are indicated with sample localities and are listed in the format of SU01*X: N*, where SU01 is the sample number and *X* corresponds to one of the following abbreviations: A—amphibole; B—biotite; K—K-feldspar; M—white mica; P—pseudotachylite (whole rock). *N* corresponds to the maximum and minimum ages obtained from K-feldspars and the preferred age for all other phases. Structural data collected at sample localities are presented in stereonets with equal-angle, lower-hemisphere projections. Structural data for all other localities visited during this study are summarized by map symbols. Refer to Table 1 to correlate sample numbers with sample localities (stop numbers). HP—high pressure, UHP—ultrahigh-pressure.

from high-pressure to upper greenschist–facies conditions. Polygonized quartz and feldspar lacking undulatory extinction in the core of the NE-trending UHP antiform suggest that at deeper structural levels annealing followed deformation. Greenschist-facies mylonitic fabrics associated with top-to-the-W shear sense are limited to the northwestern limb of the antiform in the vicinity of the Yantai-Qingdao-Wulian detachment fault. We return to a discussion of the timing and significance of these structural observations following presentation of the thermochronologic data.

THERMOCHRONOLOGY OF THE SULU TERRANE

Analytical Procedures

The $^{40}Ar/^{39}Ar$ analyses of samples from the Sulu terrane were performed at the Syracuse University Noble Gas Isotopic Research Laboratory (SUNGIRL). Following sample selection via petrographic analysis, high-purity mineral separates (>99%) were prepared by standard rock-crushing, mineral-separation, and handpicking techniques. After a final acetone wash, mineral separates were wrapped individually in Sn foil and stacked with GA1550 biotite standard (98.79 Ma; Renne et al., 1998), which was used to monitor the neutron dose. Samples were vacuum sealed in a Suprasil quartz tube and irradiated for 10 h in position L-67 of the Ford reactor at the University of Michigan.

The $^{40}Ar/^{39}Ar$ analyses of unknowns were achieved via double-vacuum resistance-furnace heating experiments. Gas was extracted during standard furnace dwell times of 12 min (except for K-feldspar diffusion experiments) and was then exposed for 10 min to hot and cold SAES ST-707 getters for purification. The purified gas was analyzed on a Micromass 5400 mass spectrometer equipped with an electron multiplier.

Sample data were corrected for blanks, mass discrimination, decay of ^{37}Ar and ^{39}Ar, neutron-induced interfering isotopes, and atmospheric argon. Correction factors used to account for interfering nuclear reactions were determined by analyzing argon extracted from irradiated optical grade, fused CaF_2 and K-glass. Correction factors used to account for interfering nuclear reactions for the irradiated samples are: $(^{40}Ar/^{39}Ar)_K = 2.12809 \times 10^{-2} \pm 1.32367 \times 10^{-3}$, $(^{36}Ar/^{37}Ar)_{Ca} = 2.62232 \times 10^{-4} \pm 5.90022 \times 10^{-6}$, $(^{39}Ar/^{37}Ar)_{Ca} = 7.11194 \times 10^{-4} \pm 9.24552 \times 10^{-6}$. All ages were calculated using the decay constants recommended by Steiger and Jäger (1977). Two-sigma analytical errors are reported in this manuscript, unless otherwise noted, and include an error associated with flux monitor age and the irradiation parameter, *J*, typically <1.0% (2σ). Age calculations for inverse isochron and apparent age data were achieved utilizing the program Isoplot 3.0 (Ludwig, 2003). Results of the thermochronologic analyses are summarized in Table 2. Apparent age spectra for samples are shown in Figure 2, with the exception of K-feldspar spectra, shown in Figures 3 and 4 along with multi-diffusion-domain models. Detailed experimental data for all samples are available from the GSA Data Repository.[1]

Geologic Context of Samples and Analytical Results

Below we describe the field, structural, and petrographic observations associated with each sample, because these data are critical to constructing valid interpretations of the thermochronologic data. Discussion of geologic context is followed by analytical results from the step-heating experiments of the respective samples.

Samples SU01 and SU04

Samples SU01 and SU04 come from Fangshan quarry, in the UHP unit southeast of Donghai (stop 1, Fig. 1). Quartzofeldspathic gneiss is the dominant lithology and is intercalated with biotite-rich seams and contains mafic boudins up to several meters in length. Foliation dips moderately to the SSE, and lineations plunge ~30° to the SE. Shear sense is top-to-the-NW, as indicated by amphibole-rich and pegmatitic shear bands, feldspar sigma clasts, and asymmetric boudinage of epidote-amphibolite layers. Field data and petrographic observations both indicate that deformation was synchronous with retrograde amphibolite-facies metamorphism. Thin-section analyses indicate that the dominant recovery mechanism was grain-boundary migration. Partial recovery of quartz and feldspar suggests that either temperature outlasted deformation or that static recrystallization occurred during a younger thermal event (Fig. 5A). Four mineral separates from two samples were dated from this locality: K-feldspar and amphibole from sample SU01, and biotite and K-feldspar from SU04.

SU01 amphibole was sampled from an amphibole-rich seam developed along a shear band surface in quartzofeldspathic gneiss from which the feldspar sample was derived. Step heating resulted in older apparent ages for the first three steps, which account for <1.5% of the cumulative ^{39}Ar released (Fig. 2). The remainder of the experiment produced apparent ages concordant at the 95% confidence interval, with the exception of the 1050 °C step, which was likely associated with in vacuo decomposition of amphibole (Wartho, 1995). The weighted mean age for the forced plateau of 212.9 ± 0.9 Ma is within error of the inverse isochron age defined by the data from the same steps. The inverse isochron defines an intercept within error of a trapped atmospheric component; the error is large because the steps are highly radiogenic.

The age spectrum for SU01 K-feldspar is characterized by ages ranging from 249 Ma to 182 Ma (Fig. 3). The spectrum is characterized by anomalously old ages in the lowest temperature steps, perhaps related to Ar release from adsorption sites or fluid inclusions. This portion of the spectrum is followed by

[1]GSA Data Repository item 2006052, supplementary data tables detailing results of $^{40}Ar/^{39}Ar$ furnace step-heating experiments, is available online at www.geosociety.org/pubs/ft2006.htm, or on request from editing@geosociety.org or Documents Secretary, GSA, P.O. Box 9140, Boulder, CO 80301, USA.

TABLE 1. $^{40}Ar/^{39}Ar$ SAMPLE DESCRIPTIONS

Sample	Locality	Dominant Mineralogy	Relict Phases	Sample Description
SU01	stop 1	Qtz + Pl + Kfs + Am + Bt + Ttn	Grt	QFP gneiss
SU04	stop 1	Qtz + Pl + Kfs + Bt + Ep + opaques	Am, Grt	QFP gneiss
SU11a	stop 9	Qtz + Pl + Kfs + Am + Ep + Ttn		weakly foliated hypabyssal intrusion
SU11b	stop 10	Bt + Pl + Ep + Qtz	Grt, Rt, Am	micaceous shear band
SU12	stop 11	Qtz + Pl + Kfs + Ms + Ep		schist
SU16	stop 16	Qtz + Pl + Kfs + Bt + Ms + Ep + Cal	Am	vein nodule in fold hinge
SU17	stop 18	Glass + Cal + Ser	Qtz , Pl, Kfs	pseudotachylite vein in QFP gneiss
SU29	stop 37	Qtz + Pl + Kfs + Bt + Ep + Ttn	Am, Grt	L-S tectonite
SU30	stop 40	Bt + Qtz + Pl	Phn, Ep, Kfs	micaceous mylonite
SU33	stop 40	Qtz + Kfs + Ms + Pl + Ep		deformed pegmatite
SU45	stop 40	Qtz + Pl + Kfs + Bt	Phn	QFP gneiss

Note: Am—amphibole; Bt—biotite; Cal—calcite; Ep—epidote; Grt—garnet; Kfs—K-feldspar; Ms—muscovite; Phn—phengite; Pl—plagioclase; QFP—quartzofeldspathic; Qtz—quartz; Rt—rutile; Ser—sericite; Ttn—titanite. Note that no chemical data exist for these samples and therefore white mica was inferred to be either muscovite or phengite based on paragenesis and textural relationships observed during microstructural analysis.

TABLE 2. SUMMARY OF RESULTS FOR $^{40}Ar/^{39}Ar$ ANALYSES

Sample	Locality	Phase dated	WMA (Ma)	Analytical error (Ma)	Total error (Ma)	MSWD	$\%^{39}Ar$	N	IIA (Ma)	Error (Ma)	$^{40}Ar/^{36}Ar$ intercept	Error	MSWD	N
SU01	stop 1	amphibole	212.9	1.3	1.7	7.5	98.6	12/17	211.0	2.5	469	330	0.22	12/17
SU04	stop 1	biotite	206.6	1.0	1.4	6.6	91.6	12/17	205.9	1.4	282	6	0.46	17/17
SU11b	stop 10	biotite	213.4	1.2	1.5	7.1	96.7	15/17	212.8	1.4	276	3	1.3	17/17
SU12	stop 11	white mica	213.5	1.4	1.6	11.1	98.4	12/15	214.5	1.5	290	2	1.2	15/15
SU17	stop 18	whole rock	92.1	0.3	1.0	0.52	33.9	4/14	87.7	2.1	3508	230	1.8	8/14
SU29	stop 37	biotite	135.6	0.5	0.9	3.3	88.0	12/16	140.9	3.4	294	13	23	16/16
SU30	stop 40	white mica	159.9	0.6	1.2	2.7	90.5	9/15	155.8	3.4	283	21	7.2	15/15
SU30[†]	stop 40	white mica	145.3	6.6	6.6	14	7.7	5/15	143.6	9.0	293	39	10.8	5/15
SU33	stop 40	white mica	128.2	0.7	1.3	2.3	82.3	6/13	128.8	1.0	296	2	0.74	13/13
SU45	stop 48	biotite	69.6	2.5	1.4	12	57	4/10	78.0	2.9	262	11	19	9/10

Note: Refer to Table 1 for sample descriptions and to Table 3 for K-feldspar summary. WMA—weighted mean age; MSWD—mean square weighted deviates; $\%^{39}Ar$—percentage of total ^{39}Ar released represented by steps used in WMA calculation; N—number of steps or data points, expressed as a fraction of the total, used in the respective calculation. IIA—inverse isochron age. All errors are reported at the 2σ level. WMA errors include the uncertainty in the irradiation parameter (J factor). Total errors further include uncertainties associated with decay constants.

[†] Reflects calculations utilizing the subset of data most clearly associated with argon loss.

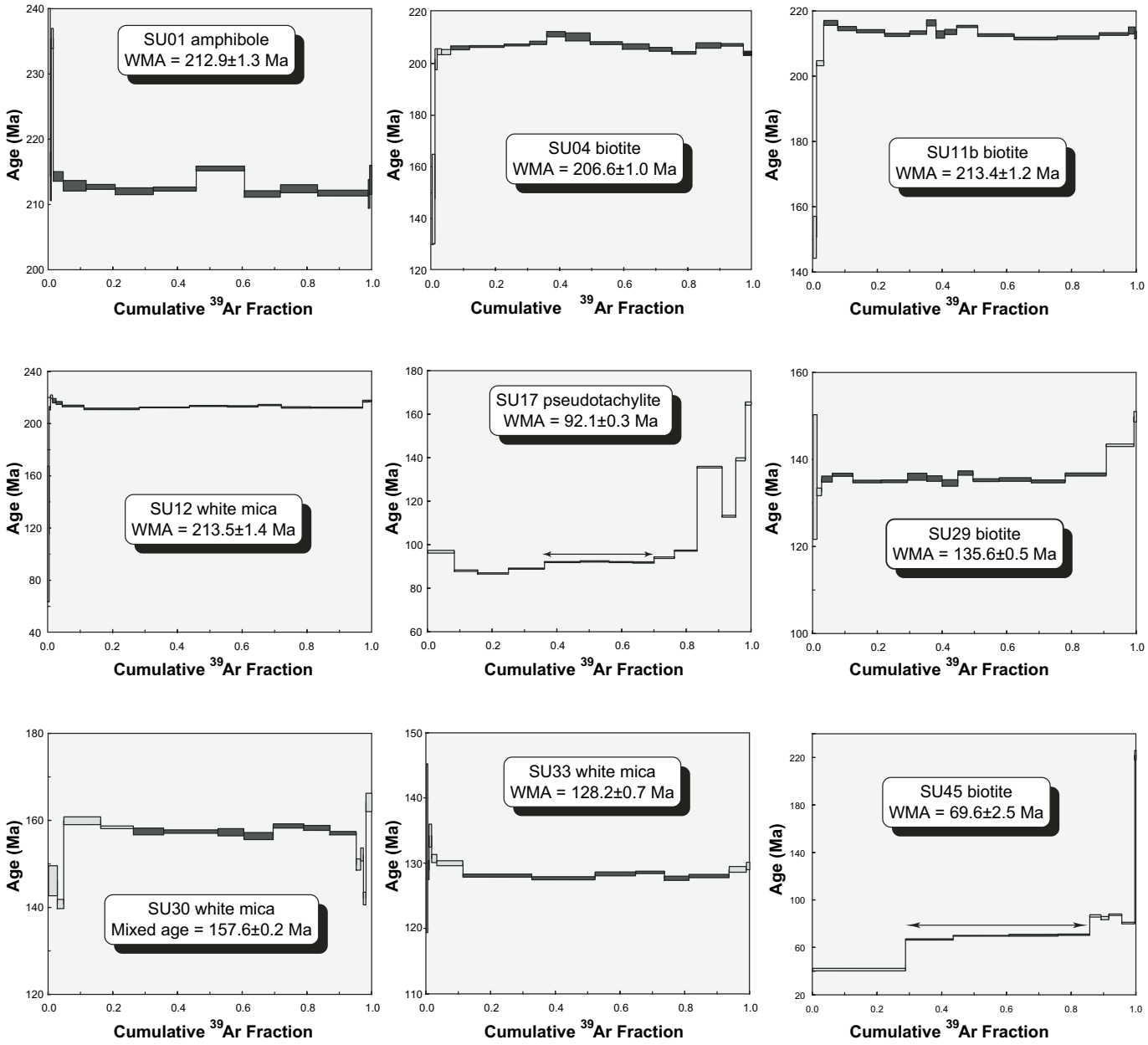

Figure 2. Results of $^{40}Ar/^{39}Ar$ analyses shown with apparent age spectra (see Figs. 3 and 4 for results of K-feldspar analyses); WMA—weighted mean age (forced plateau). Steps included in WMA are filled (or indicated by arrows when scale precludes recognition of filled boxes). Errors indicated in text are 2σ, whereas step ages are 1σ.

three, semiflat apparent age segments at ca. 188 Ma, 232 Ma, and 248 Ma. The isotopic data do not reveal a correlation between K/Ca or K/Cl ratio and age.

Step heating of SU04 biotite resulted in a reasonably flat age spectrum (Fig. 2). Twelve of seventeen steps were selected to calculate the weighted mean age of 206.6 ± 1.0 Ma. The inverse isochron defined a trapped $^{40}Ar/^{36}Ar$ component of 282 ± 6, slightly less than an atmospheric value of 295.5, and an inverse isochron age of 205.9 ± 1.4 Ma. An age of ca. 148 Ma for the first step and the slightly younger ages on the low- and high-temperature end of the steps chosen for the weighted mean age suggest that this sample may have experienced at least one episode of Ar loss, perhaps during the Late Jurassic–Early Cretaceous.

SU04 K-feldspar yielded an apparent age spectrum characterized by maximum and minimum apparent ages of 210 and 171 Ma, respectively (Fig. 3). Four of the five K-feldspar samples dated in this study yielded $^{36}Ar/^{40}Ar$ and $^{39}Ar/^{40}Ar$ isotopic ratios that are clustered rather than correlated. In contrast, the inverse isochron for SU04 K-feldspar is characterized by two discrete

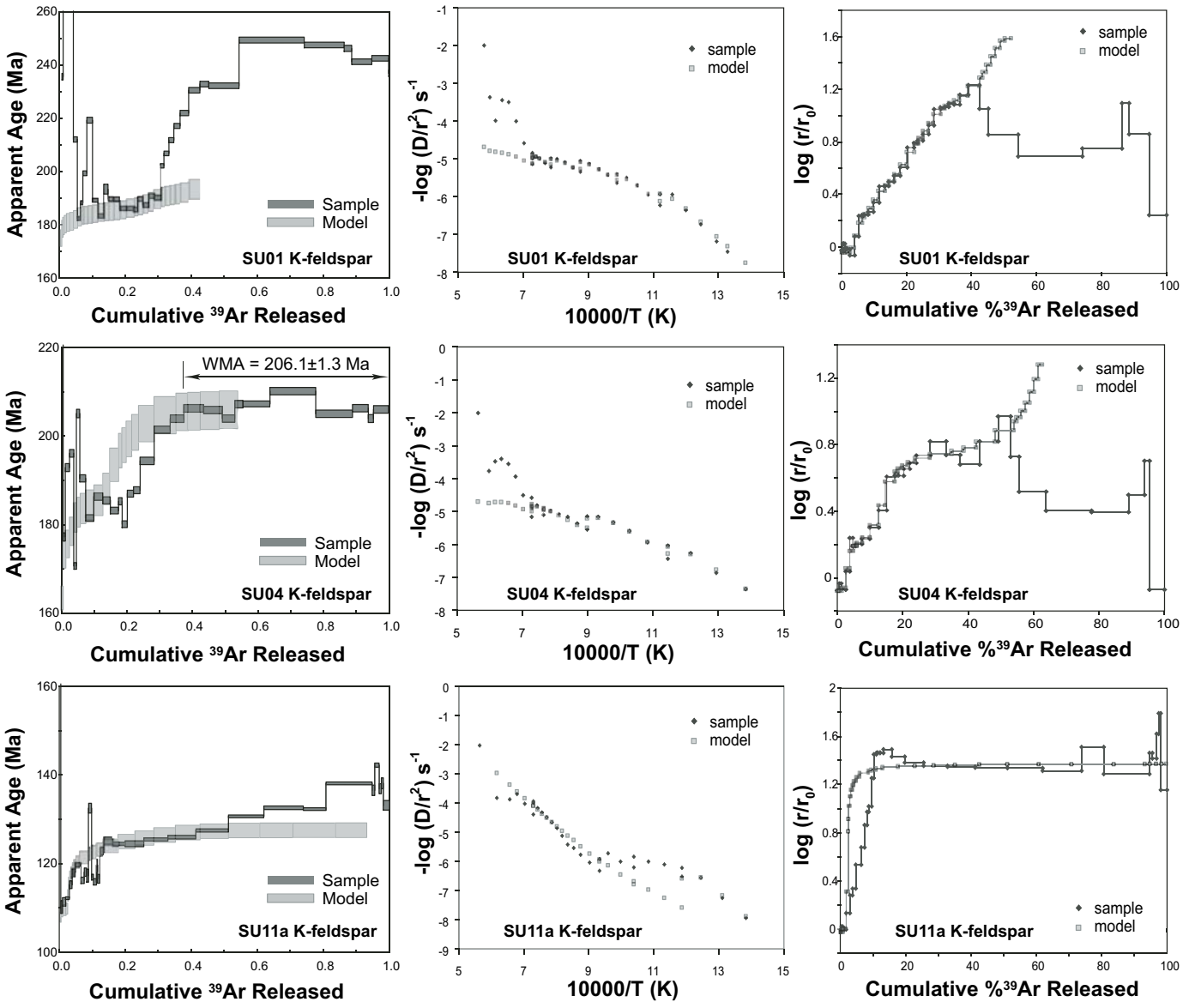

Figure 3. Apparent age spectra and qualitative thermal models for K-feldspar samples SU01, SU04, and SU11a. Step age uncertainties are 1σ. Modeled spectra are shown with 1% age errors. See Figure 7 for best-fit thermal histories associated with modeled spectra.

trends, each defined by data corresponding to temperature steps above and below 1100 °C—the expected breakdown temperature of K-feldspar (e.g., Lovera et al., 1997)—and corresponding to inverse isochron ages of 179 Ma and 204 Ma, respectively (Fig. 6). The isotopic data show no correlation between K/Ca or K/Cl ratios in the data defining the two trends.

Sample SU11a

Sample SU11a, from a weakly deformed hypabyssal intrusion, was sampled from a decimeter-scale outcrop on a hillside within the UHP unit (stop 9, Fig. 1). Within a hundred (covered) meters of the sample location, the lithology changes to quartzo-feldspathic gneisses with SSE-dipping foliation and gently SE-plunging stretching lineations defined by biotite, quartz, and feldspar. Deformation is concentrated in biotite-rich seams, but shear sense was not definitively deduced. In thin section, SU11a is characterized by large equant grains of quartz and feldspar with 120° triple junctions. The foam texture is overprinted by relatively planar zones of reduced grain size and sericitic alteration, accompanied by microcracks and undulatory extinction in neighboring large grains. Sample SU11a K-feldspar produced an apparent age spectrum characterized by maximum and minimum apparent ages of 142 Ma and 110 Ma, respectively (Fig. 3).

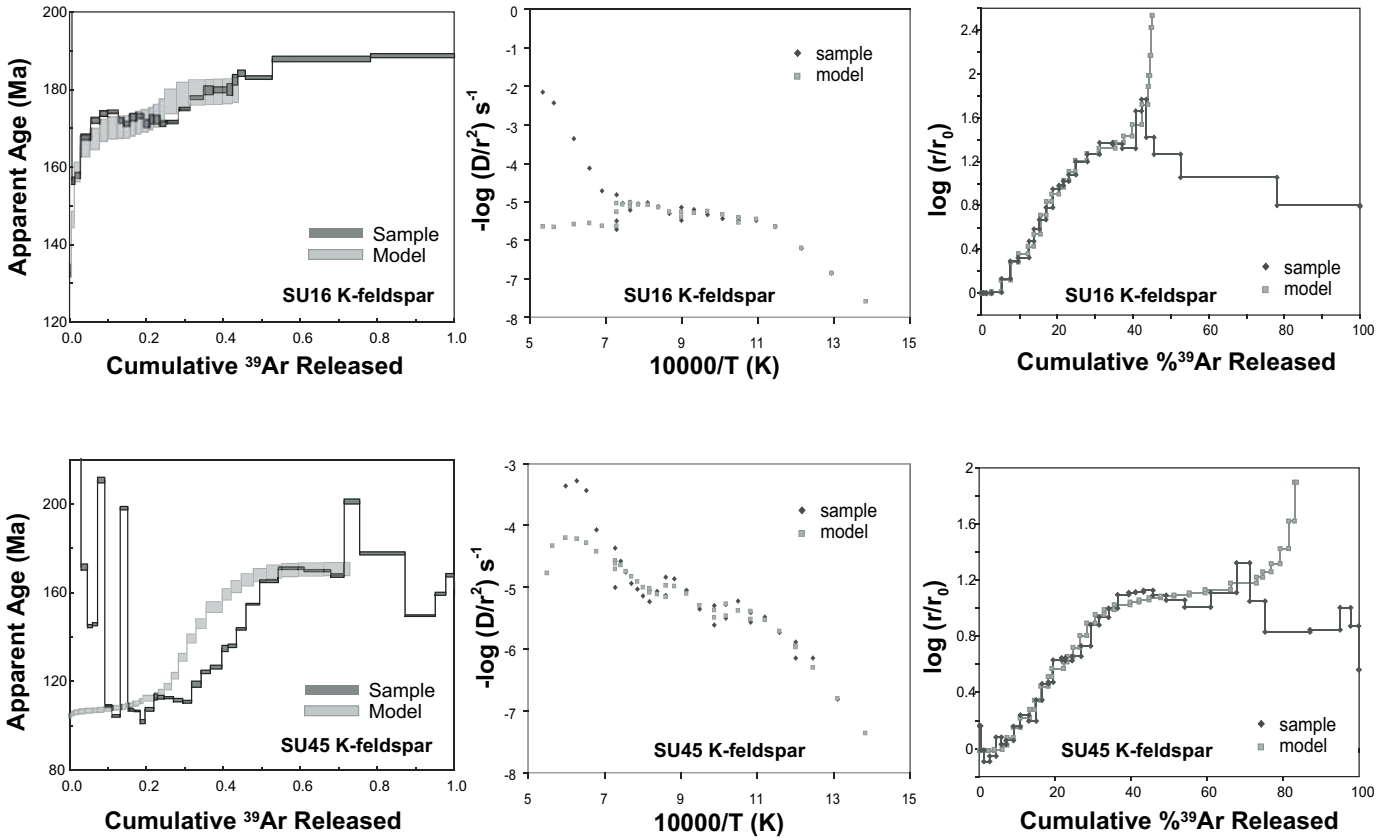

Figure 4. Apparent age spectra and qualitative thermal models for K-feldspar samples SU16 and SU45. Box heights on experimentally derived spectra are shown at 1σ. Modeled spectra are shown with 1% errors on age. See Figure 7 for best-fit thermal histories associated with modeled spectra.

Samples SU11b and SU12

Sample SU11b was taken from a biotite-rich top-to-NW shear band within the Jingping metavolcanic rocks of the high-pressure unit at locality 10, near the village of Paigou (Fig. 1). Sample 12 comes from the metavolcanic rocks at a nearby locality (stop 11). The dominant lithology, white mica–chlorite–albite–quartz schist, is characterized by a strong crenulation cleavage imparted by intense folding. An intersection lineation trends 105–110°. Significantly, S_2 foliations and L_2 stretching lineations defined by micas are essentially identical to those of the UHP unit. This suggests that the dominant S_1 and L_1 fabrics observed in the UHP unit in the Donghai region are likely equivalent to S_2 and L_2 in the high-pressure unit, and that any older fabrics of the UHP unit may have been fully transposed. The biotite-rich shear band displays only the S_2 fabric at mesoscopic scales, yet preserves the S_1 foliation as inclusion trails of rutile and amphibole within plagioclase porphyroblasts (Fig. 5B). Biotite and white mica define L_2 stretching lineations. Field and petrographic observations suggest that the amphibolite–upper greenschist facies overprint was synchronous with S_2 fabric development.

SU11b biotite yielded a weighted mean age of 213.4 ± 1.2 Ma (Fig. 2). The age spectrum suggests some Ar loss, apparent in the first two steps, which comprise <4% of the total ^{39}Ar released; the youngest apparent age is ca. 151 Ma. The inverse isochron, defined by the fifteen steps of the forced plateau, yielded an inverse isochron age of 212.8 ± 1.4 Ma, concordant with the weighted mean age, and a trapped ^{40}Ar/^{36}Ar component with a value of 276, a value less than atmospheric.

SU12 white mica also produced an apparent age spectrum with two younger initial steps that had cumulative ^{39}Ar accounting for ~1% of the total ^{39}Ar released (Fig. 2). The weighted mean age for this sample was 213.5 ± 1.4 Ma, identical to the weighted mean age obtained from sample SU11b. The inverse isochron for SU12, based on twelve of the fifteen total steps, gave an inverse isochron age of 214.5 ± 1.5 Ma and a trapped ^{40}Ar/^{36}Ar component of 290 ± 2, just slightly less than atmospheric.

Sample SU16

SU16 comes from a coastal island quarry within the high-pressure unit (locality 16, Fig. 1). This outcrop bears similarities to other exposures within the high-pressure unit, such as a strong crenulation cleavage and an intersection lineation that trends 110°. An S_1 foliation in felsic rocks is defined by compositional banding of quartzofeldspathic and mica-rich

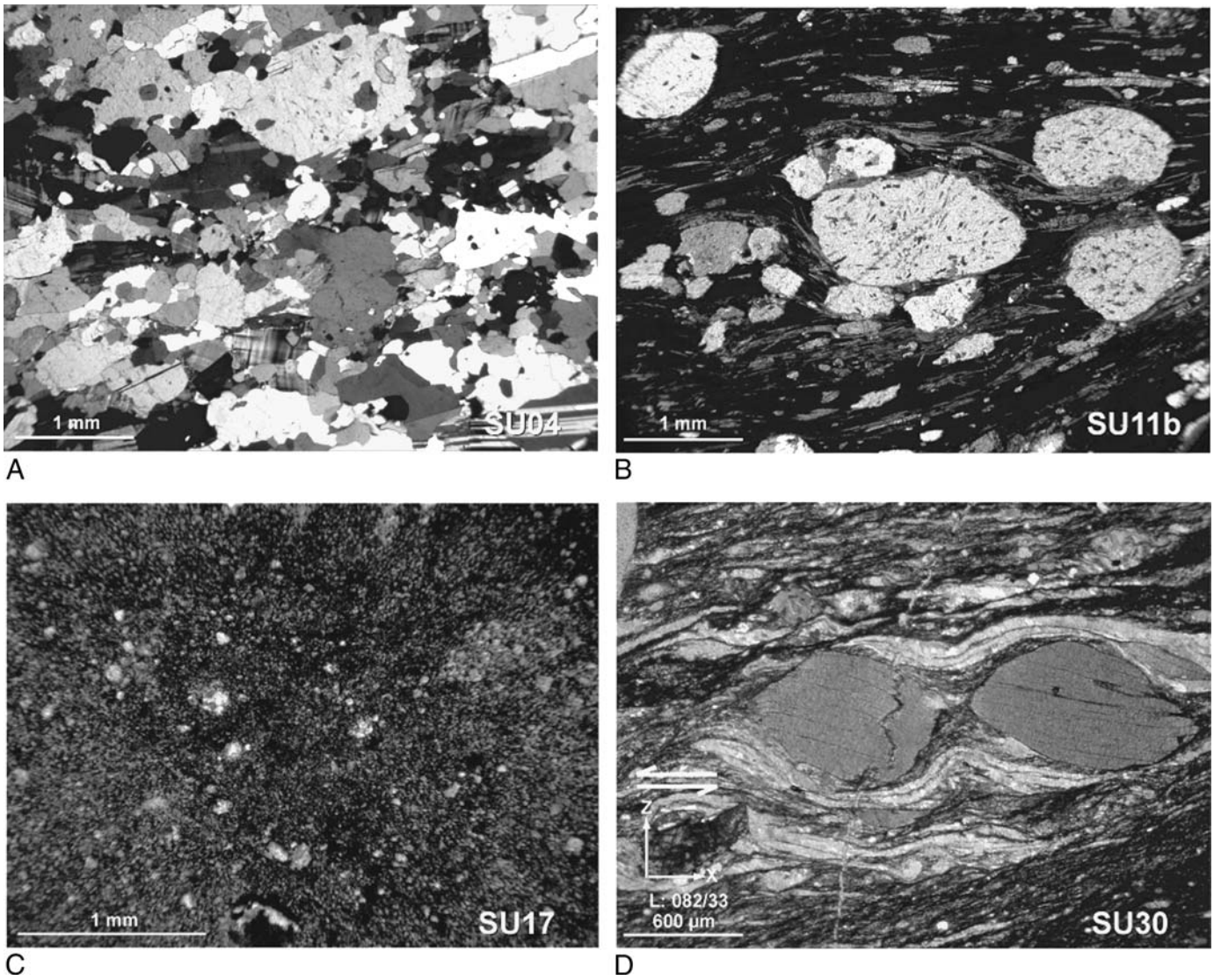

Figure 5. Photomicrographs of Sulu samples. (A) Gneissic texture resulting from recovery of quartz and feldspar in sample SU04 quartzofeldspathic gneiss (crossed polars). (B) Plagioclase porphyroblasts with internal foliation defined principally by rutile and amphibole in sample SU11b mafic schist (plane light). (C) Pseudotachylite sample SU17 is a mixture of glass and cataclasite (crossed polars). (D) Ultramylonite sample SU30 contains dynamically recrystallized quartz and very fine-grained biotite grown at the expense of white mica porphyroclasts (crossed polars). Top-to-the-W shear sense was deduced from both mesoscopic and microscopic features. Sample orientation is normal to the foliation and parallel to the stretching lineation.

domains. An S_2 foliation dips moderately to SSE, and L_2 stretching lineations plunge to the SE. The quartzofeldspathic gneiss contains euhedral chalcopyrite crystals and is host to larger swaths of biotite-epidote-albite seams and boudins. The S_1 and S_2 foliations within the mafic rocks are concordant with those of the host gneiss. Kinematic indicators include asymmetric boudins of quartz veins showing top-to-the-NW sense of shear. At least one episode of fluid infiltration is associated with pegmatitic veins, and nodules of K-feldspar and quartz are concentrated in fold hinges; SU16 comes from one of these nodules.

SU16 K-feldspar produced an age spectrum with maximum and minimum apparent ages of 189 Ma and 157 Ma (Fig. 4). The age spectrum has two apparent flat segments that correspond to ages of ca. 172 Ma and ca. 188 Ma.

Sample SU17

Sample SU17 comes from a hillside quarry, locality 18, within the mapped boundary of the UHP unit (Fig. 1). The dominant rock type is a two-mica amphibolite-grade quartzofeldspathic gneiss with mafic bands rich in epidote and amphibole. A SE-dipping foliation and SE-plunging lineation are heavily

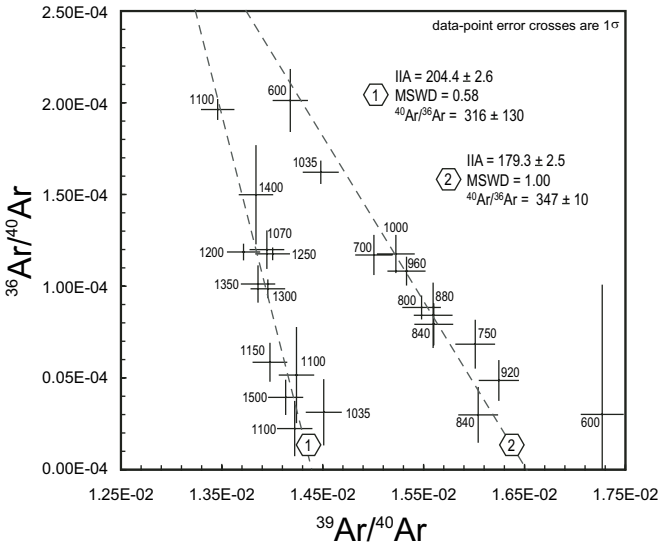

Figure 6. Inverse isochron analysis (IIA) for SU04 K-feldspar shows two discrete trends of data. Data show 1σ errors; adjacent numbers indicate temperature. Only data shown were used in regressions. The oldest age is within error of the weighted mean age (206 Ma) calculated for higher-temperature steps comprising >60% of the ^{39}Ar released (see Fig. 3). MSWD—mean square of weighted deviates.

obscured by chlorite-filled fractures and abundant massive to fine-grained pseudotachylite veins. SU17 is a sample of the pseudotachylite. Petrographic analysis of the pseudotachylite reveals that it is a mixture of glass and cataclasite with rare clasts up to ~100 μm in diameter (Fig. 5C).

Step heating of sample SU17 resulted in a weighted mean age of 92.1 ± 1.3 Ma, calculated utilizing data from our steps in the middle and flattest portion of the spectrum, accounting for 33.9% of the ^{39}Ar released. The spectrum is interpreted as a loss profile resulting from deformation-induced resetting of the Ar systematics of the gneissic protolith at ca. 92 Ma. Eight of the fourteen steps yielded an inverse isochron age of 87.7 ± 2.1 Ma, concordant with the weighted mean age at the 95% confidence level. The trapped ^{40}Ar/^{36}Ar component indicated by the inverse isochron was 3508 ± 230, much greater than atmospheric. This high trapped ^{40}Ar/^{36}Ar value supports the notion that the sample was incompletely reset during deformation, an interpretation supported by both the form of the age spectrum and the petrographic observations.

Sample SU29

Sample SU29 from locality 37 represents a unique structural domain within the mapped boundaries of the UHP unit that is dominated by L-S tectonites (Fig. 1). The rock is quartzofeldspathic gneiss with biotite and intermittent mafic lenses. Foliation is somewhat variable where recognizable and dips steeply WSW or SW. Stretching lineations plunge S and are defined by quartz rods and elongate K-feldspar. Shear sense is top-to-the-S. Thin-section textures indicate dynamic recrystallization of the constituent minerals.

SU29 biotite yielded a weighted mean age of 135.6 ± 0.5 Ma from twelve of sixteen steps, which account for 88% of the total ^{39}Ar released (Fig. 2). The inverse isochron calculated utilizing data from all sixteen steps resulted in an inverse isochron age of 140.9 ± 3.4 and an atmospheric ^{40}Ar/^{36}Ar intercept.

Samples SU30 and SU33

Two samples, SU30 and SU33 were collected from locality 40 along the Yantai-Qingdao-Wulian fault zone (Fig. 1). Rock types at this locality are diverse and include variably retrogressed eclogite blocks in quartzofeldspathic gneiss, abundant and massive pegmatitic veins, and marble (the latter as float). Deformation at greenschist-facies conditions produced foliations with shallow to moderate SW dips and subhorizontal E-W stretching lineations. This deformation is only weakly manifested in the eclogite boudins by vague lineations on boudin margins. Shear sense is top-to-the-W. SU30 is a micaceous ultramylonite that is dominated by white mica porphyroclasts and very fine-grained synkinematic biotite in thin section (Fig. 5D). SU33 is a synkinematic pegmatite vein with white mica. Both samples exhibit dynamically recrystallized quartz.

SU30 white mica produced a hump-shaped spectrum (Fig. 2). The plateau-like segment yielded a weighted mean age of 159.9 ± 0.6 Ma. An inverse isochron generated with all fifteen data resulted in an inverse isochron age of 155.8 ± 3.4 Ma and a ^{40}Ar/^{36}Ar intercept of 283 ± 21. Based on the hump-shaped spectrum and petrographic observations, the weighted mean age is interpreted to be a mixed age as a result of Early Cretaceous Ar loss. A weighted mean age calculated using the youngest apparent ages from the low- and high-temperature steps gave 145.3 ± 6.6 Ma, corresponding to ~8% of the total ^{39}Ar released. The inverse isochron age calculated for these steps resulted in 143.6 ± 9.0 Ma and corresponds to a trapped ^{40}Ar/^{36}Ar ratio of 293, within error of atmospheric.

SU33 white mica resulted in a weighted mean age of 128.2 ± 0.7 Ma based on six steps, which account for 82% of the total ^{39}Ar released. An inverse isochron age of 128.8 ± 1.0 Ma calculated from all 13 data recorded an atmospheric ^{40}Ar/^{36}Ar component.

Sample SU45

SU45 was sampled from an island to the north of Weihai area on the Shandong Peninsula (Fig. 1). Quartzofeldspathic gneiss encapsulates amphibolite boudins up to several meters in length. Foliations dip gently to the ESE, and stretching lineations defined by quartz, feldspar, biotite, and hornblende plunge to the SSE. Asymmetric boudinage of amphibolite layers and feldspar sigma clasts indicate top-to-the-NW shear. The sample shows evidence of late low-temperature deformation in the form of fractures in feldspars and undulatory extinction in quartz, with deformation concentrated along grain boundaries.

SU45 biotite produced an apparent age spectrum with two flat segments followed by a final step that yielded an age of ca. 220 Ma (Fig. 2). A weighted mean age of 69.6 ± 2.5 Ma was

calculated based on the intermediate steps that make up 57% of the total ^{39}Ar released. A short flat segment at high temperature corresponds to an apparent age of ca. 87 Ma. The spectrum is interpreted to reflect Ar loss associated with the low-temperature deformation observed in thin section. An inverse isochron calculated using the four steps associated with the weighted mean age yielded an inverse isochron age of 78.0 ± 2.9 Ma and a $^{40}Ar/^{36}Ar$ intercept of 262 ± 11.

SU45 K-feldspar yielded an apparent age spectrum with a steep profile (Fig. 4), which, neglecting steps with anomalously old ages in the first 15% of the ^{39}Ar released, is characterized by minimum and maximum ages of 102 and 201 Ma. The shape of the spectrum further indicates that the K-feldspar exhibited anomalous degassing behavior during the experiment at temperatures >1100 °C.

K-Feldspar Multi-Diffusion-Domain Models

The thermal histories of five K-feldspar samples were explored via the multi-diffusion-domain modeling (MDD) techniques of Lovera et al. (1989; http://sims.ess.ucla.edu/argon.htm). We refer the reader to McDougall and Harrison (1999) and Parsons et al. (1999) for detailed discussions and debates on the application and viability of MDD modeling. Model parameters were determined by modeling the experimental Arrhenius data with the program AUTOARR (Figs. 3 and 4; Table 3). All samples, with the exception of SU11a, yielded reasonably good fits to the experimentally derived diffusion data for temperatures <1100 °C, where onset of melting of K-feldspar typically commences and loss via volume diffusion ceases (McDougall and Harrison, 1999; Figs. 3 and 4). The poor fits for sample SU11a were most likely a result of the late brittle deformation seen in the microstructures. Sample SU45 also showed evidence for late brittle deformation. Activation energies determined for the metamorphic feldspars (i.e., all except for SU11a) were 30–38 kcal mol^{-1}, on the low end of the activation energies typical for K-feldspars from crystalline rocks (Lovera et al., 1997; Table 3).

The complex nature of apparent age spectra for all samples (e.g., multiple ramp-flat features as opposed to serially increasing ages, anomalous degassing behavior) indicates that the samples may be complicated by deformation-related Ar loss and/or low-temperature recrystallization, therefore precluding rigorous interpretation of the MDD models (Lovera et al., 2002). However, to place qualitative constraints on the time of cooling below ~300 °C, the apparent age spectra were modeled manually via the program AGESME. Various thermal histories were explored (e.g., monotonic cooling, isothermal holding, and transient reheating), taking into account independent temperature-time constraints from step-heating experiments described already and from other isotopic systems employed in our study (cf. Leech et al., this volume). Figure 7 presents the thermal histories that yielded the best model fits to the experimental age spectra obtained for each of the samples (see Figs. 3 and 4 for experimental and model spectra). Because these models allow reheating, they are nonunique solutions, and we emphasize that the models are only qualitative assessments of possible thermal histories of these K-feldspars. Next we discuss the interpretations associated with the MDD models in conjunction with the geologic constraints and the thermochronological data detailed previously.

DISCUSSION

The combined thermochronologic, structural, and petrographic data have implications for the Triassic exhumation history of the high-pressure–UHP rocks as well as for later Mesozoic tectonic events in East Asia. Fifteen $^{40}Ar/^{39}Ar$ step-heating analyses revealed information regarding what appear to be distinct tectonic events in the Sulu region: Late Triassic exhumation following peak metamorphism, Late Jurassic–Early Cretaceous igneous activity and detachment faulting, and mid to Late Cretaceous brittle faulting (Fig. 7). Qualitative MDD models of K-feldspar suggest the possibility of at least one, and possibly two, thermal excursions during Jurassic time (Fig. 7).

Late Triassic Exhumation to Upper-Crustal Depths

Field observations and microstructural data support an interpretation that the cluster of ages ca. 213 Ma corresponds to recrystallization at amphibolite- to upper greenschist–facies conditions. Field and microstructural evidence indicate that at that time, the UHP and high-pressure units were involved in top-to-NW noncoaxial shear during exhumation (Wallis et al., 1999; Faure et al., 2003; this study; Fig. 1). Petrographic observations

TABLE 3. SUMMARY OF RESULTS FOR $^{40}Ar/^{39}Ar$ ANALYSES OF K-FELDSPARS AND PARAMETERS USED IN QUALITATIVE MODELING OF THERMAL HISTORIES

Sample name	Sample locality	Apparent age (Ma)		E_a (kCal/mol)	$\log(D_0/r_0^2)$ (s^{-1})	# domains
		Minimum	Maximum			
SU01	stop 1	182.4	249.3	36.0	3.1	7
SU04	stop 1	170.8	210.2	30.0	1.6	8
SU11a	stop 9	110.3	142.2	46.0	6.0	3
SU16	stop 16	156.5	188.7	37.8	3.8	5
SU45	stop 48	102.0	201.1	35.2	3.3	6

Note: Ea—activation energy. Note that plane slab geometries yielded the best fit for all samples. For the purposes of these models, all domains were assumed to have the same activation energy.

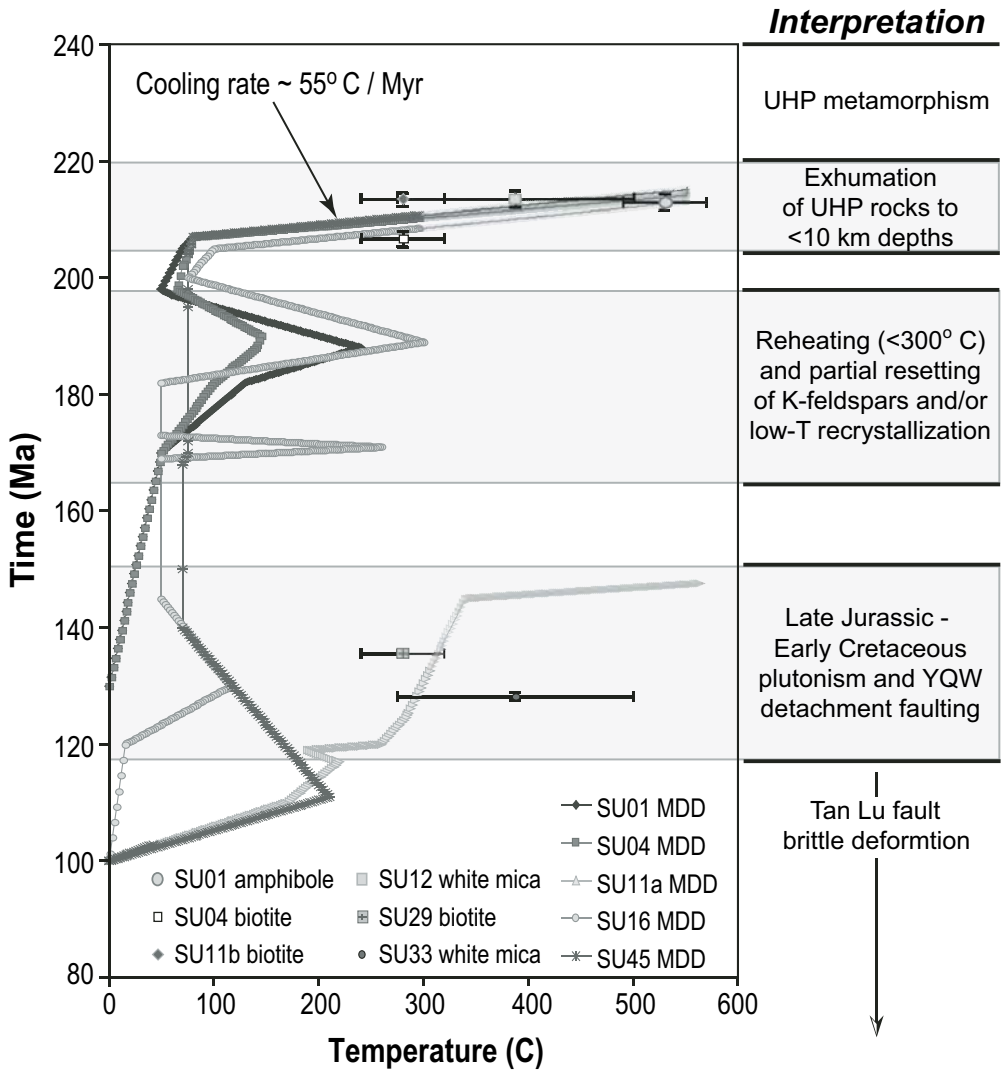

Figure 7. Temperature-time (*T-t*) plot for the Sulu terrane based on $^{40}Ar/^{39}Ar$ analyses and qualitative multi-diffusion-domain (MDD) modeling of K-feldspars. The K-feldspar thermal histories are those that yielded the best model fits to the experimental age spectra (Figs. 3 and 4). While these thermal models best constrain the *T-t* history below 300 °C, they are still sensitive to the higher-temperature history. Several samples from the high-pressure and ultrahigh-pressure (UHP) units constrain a cooling rate of 55 °C/m.y. associated with exhumation through crustal depths. Tectonic interpretations are summarized at the right and illustrate best estimates on the duration of events, as appropriate. YQW—Yantai-Qingdao-Wulian.

indicate that temperature outlasted deformation and facilitated the recovery of quartz and feldspar as the rocks cooled through biotite and K-feldspar (SU04) closure temperatures ca. 206 Ma. These data, in conjunction with thermal modeling of SU01 and SU04 K-feldspar, suggest that the UHP rocks were exhumed to upper-crustal levels by the Late Triassic ($T \approx 100$ °C; Fig. 7).

The data suggest that cooling rates of ~55 °C/m.y. accompanied exhumation through crustal depths (Fig. 7). This cooling must correspond to the portions of published *P-T* paths following near-isothermal decompression from depths associated with UHP conditions (see for example *P-T* path summaries in Wallis et al. [1999] and Faure et al. [2003]). How do the $^{40}Ar/^{39}Ar$ data bear on exhumation rates? If one assumes that the UHP rocks were at a minimum of 100 km depths at ca. 220 Ma (see Leech et al. [this volume] for a detailed discussion on the timing of UHP metamorphism and zircon growth under retrograde amphibolite-facies conditions that constrains this parameter), the Ar data suggest that by 206 Ma, the UHP rocks were at a maximum of 10 km depth. The required vertical exhumation rates are >6 mm yr^{-1}, slightly faster than those calculated by Liu et al. (2004b). Exhumation via top-to-the-NW shear along an extensional detachment fault with a dip of ≤35° requires transport along the shear zone at plate-

tectonic rates (cm yr^{-1}) through crustal depths. Such rates are in line with those that have been documented in the Hong'an portion of the orogen (Webb et al., 1999b) and are moderate in comparison to those documented in other high-pressure–UHP orogens (e.g., Rubatto and Hermann, 2001; Baldwin et al., 2004). However, a vertical exhumation rate of >6 mm yr^{-1} through the crust is fairly rapid, considering that most models for the exhumation of UHP rocks call upon buoyancy as a driving force for rapid exhumation and concede to neutral buoyancy and, thus, stagnation when the UHP rocks reach lower-crustal depths (e.g., Ernst, 2001; Walsh and Hacker, 2004).

Early and Middle Jurassic Reheating?

Evidence in this study for reheating of the Sulu high-pressure–UHP terrane in the Early Jurassic comes solely from thermal modeling of K-feldspar samples SU01, SU04, and SU16 (Fig. 7). All three models are permissive of transient reheating with temperatures peaking between ca. 190 and 187 Ma. Despite the fact that the models suggest that temperatures may have locally achieved 250–300 °C, no evidence for thermal resetting of biotite or white mica is documented in the vicinity of the respective K-feldspar sample localities. Though several spectra indicate Ar loss, it is generally of Late Jurassic–Early Cretaceous age (see low-temperature intercepts in apparent age spectra in Fig. 2). It is noteworthy, however, that there is abundant evidence in the Dabie Shan region for recrystallization of white mica (Hacker et al., 2000). White mica and biotite $^{40}Ar/^{39}Ar$ ages from that part of the orogen are commonly 195–180 Ma (Hacker and Wang, 1995; Hacker et al., 2000). In the Hong'an region, Early Jurassic $^{40}Ar/^{39}Ar$ ages ca. 195 Ma were linked to late-stage NE-SW extension under ductile-brittle conditions (Webb et al., 1999b). Whether there is any link between the modeled thermal histories for Sulu K-feldspars and the $^{40}Ar/^{39}Ar$ ages from Hong'an and Dabie is speculative. If so, the UHP rocks in Sulu reached and remained at higher structural levels in the Late Triassic–Early Jurassic compared to the Dabie Shan, where up to 15 km of Early Cretaceous exhumation has been documented (Hacker et al., 1995).

SU01 and SU04 were sampled from the UHP unit near the mapped boundary with the high-pressure unit (Fig. 1). SU16 was sampled from a chalcopyrite mine quarry in the high-pressure unit, just east of the along-strike projection of the boundary. The boundary between the high-pressure and UHP units is well defined by a regional study documenting the presence of high-pressure versus UHP mineral inclusions in zircons (Liu et al., 2004a). It has been variously mapped by some workers as the Haizhou-Siyang fault based on geophysical studies (Cong, 1996), or as a ductile shear zone based on field mapping (e.g., DF5 of Xu et al., this volume). However, structural transects conducted as part of this study yielded no evidence to support the presence of a major shear zone between the high-pressure and UHP units. If the boundary is indeed a fault, perhaps the feldspars recorded a related deformation event. However, we observed no mesoscopic or microstructural evidence to support such an interpretation. Similar thermal histories recorded by $^{40}Ar/^{39}Ar$ data from samples located on both sides of the boundary require that if the high-pressure–UHP boundary is a fault, it must have limited offset or the slip occurred before ca. 213 Ma.

The possibility of Middle Jurassic reheating is implied by the thermal model for SU16 K-feldspar (Fig. 7), as well as the younger apparent trend on the inverse isochron for sample SU04 feldspar (Fig. 6). Regional reheating, and possibly local recrystallization (e.g., SU04), may have been related to Jurassic plutonism documented in the Shandong Peninsula (e.g., Zhang et al., 2003; Xu et al., 2004). Several K-feldspar samples from the Dabie Shan modeled by Hacker et al. (2000) also suggest a thermal spike ca. 170 Ma. At present, any statement regarding the significance of this signal in the model for SU16 is premature. We note, however, that the U/Pb zircon age of ca. 166 Ma was from a granodiorite associated with a gold deposit in the northern Shandong Peninsula (Zhang et al., 2003), and sample SU16, from which the 171 Ma thermal spike was inferred, comes from a chalcopyrite mine in the high-pressure unit. One possible interpretation is that the Middle Jurassic may represent an early phase of igneous activity associated with ore genesis in the region. Plutons as old as Middle Jurassic are typically considered to be part of the Yanshanian orogeny in east China and traditionally are associated with the Pacific plate margin. However, recent geochemical and geochronological studies suggest that regional extension and igneous activity may be linked to removal of the lithospheric keel beneath the North China craton (e.g., Gao et al., 2002; Xu et al., 2004). At least some degree of Middle Jurassic regional tectonism is indicated by studies in the foreland, which reveal that siliciclastic sediments were deposited in a transpressive stress field (Grimmer et al., 2003).

Late Jurassic–Early Cretaceous Magmatism and Detachment Faulting

Early Cretaceous ages were obtained from SU11a K-feldspar, SU29 biotite, and SU30 and SU33 white mica (Fig. 2). These samples are associated with intrusive bodies and/or structures that cut the Late Triassic amphibolite-facies fabrics. The vast majority of lineations measured in the area east of the Yantai-Qingdao-Wulian fault between 35 and 36°N are oblique to lineations in the Late Triassic fabrics south of 35°N (Fig. 1). The thermochronologic data, combined with field and microstructural observations, suggest that the Yantai-Qingdao-Wulian fault was active as an Early Cretaceous top-to-the-W detachment fault. Our data are limited to the southern half of the peninsula, but studies in northern Shandong have described the Yantai-Qingdao-Wulian fault as an ~800-m-thick mylonitic-ultramylonitic shear zone (Faure et al., 2003). Wallis et al. (1999) recognized at least two stages of deformation in the vicinity of the fault, documenting E-W stretching lineations associated with top-to-the-W shear sense in a later stage of

mylonitic deformation, kinematic observations similar to ours from the Yantai-Qingdao-Wulian fault in the Wulian area, where deformation was attended by a maximum of lower greenschist-facies metamorphic conditions.

The thermochronologic data, including feldspar thermal models, suggest that extensional detachment faulting was active by 128 Ma, perhaps as early as 145 Ma, and may have continued to at least 120 Ma. In the case of SU29, from locality 37, an Early Cretaceous biotite age appears to be associated with top-to-the-S shear in dominantly L-S tectonites (Fig. 1). Feldspars and micas from the core of the orogen are largely unaffected by the Early Cretaceous extension and igneous activity, with the exception of minor Ar loss, as discussed earlier. The absence of regional resetting of the Ar systematics from samples south of 35°N suggests that Early Cretaceous exhumation in the Donghai region may have been limited to a couple of kilometers. Early Cretaceous detachment faulting along the Yantai-Qingdao-Wulian fault and plutonism on the Shandong Peninsula are temporally linked with detachment faulting and voluminous intrusions in the northern Dabie Shan (cf. Hacker et al., 1995; Ratschbacher et al., 2000). A similar time frame has been documented for Early Cretaceous extension associated with core complex formation as far inboard as southernmost Mongolia (Webb et al., 1999a). Xu et al. (2004) concluded that lithospheric thinning must have continued until the Late Cretaceous because of a change from lithospheric- to asthenospheric-sourced mafic magmas in the Shandong region west of the Yantai-Qingdao-Wulian fault at that time.

Mid to Late Cretaceous Deformation

Evidence for Late Cretaceous deformational and/or thermal resetting of Ar systematics in the Sulu terrane comes principally from samples SU17 and SU45, from localities 18 and 48, respectively (Figs. 1, 2, and 4). Sample SU17, a pseudotachylite vein that cuts the gneissic foliation, yielded an age consistent with faulting ca. 92 Ma. Sample SU45 showed evidence for late brittle deformation, and biotite yielded a complex spectrum consistent with Ar loss at ca. 70 Ma. The best-fit thermal model for SU45 K-feldspar called for reheating ca. 110 Ma, but this signal in the model could be alternatively related to deformation-related Ar loss. Though complicated, these data argue for Late Cretaceous brittle deformation in the Shandong region. We accept the possibility of a 110–75 Ma thermal pulse along the Tan-Lu fault that is indicated by K-feldspar and apatite fission-track thermochronology (Ratschbacher et al. 2000; Grimmer et al., 2002). Although the samples in our study are not from the present-day expression of the Tan-Lu fault zone, we interpret them to record deformation related to mid to Late Cretaceous sinistral-oblique slip along the Tan-Lu fault. Ratschbacher et al. (2000) documented ≥5.4 km of Cenozoic dip slip along the Tan-Lu fault, an observation that may explain why the hanging-wall Sulu terrane appears to expose shallower Mesozoic structural levels than the footwall Dabie Shan.

CONCLUSIONS

Combined structural and thermochronological studies in the Sulu terrane of eastern China document exhumation of the high-pressure and UHP metamorphic rocks from mantle to upper-crustal depths by ca. 206 Ma. Our $^{40}Ar/^{39}Ar$ dating of K-bearing phases that record recrystallization and cooling through amphibolite- and upper greenschist–facies conditions during top-to-the-NW noncoaxial shear indicates cooling rates on the order of 55 °C/m.y. Integration of the $^{40}Ar/^{39}Ar$ data with U/Pb constraints on the timing of UHP metamorphism gives vertical exhumation rates through crustal depths of >6 mm yr^{-1}. Similar thermal histories obtained from samples on both sides of the contact between the high-pressure and UHP rocks suggest that the boundary between the two units is either not a fault or was active before ca. 213 Ma.

Qualitative multi-diffusion-domain models for metamorphic feldspars sampled from the high-pressure and UHP units yield thermal histories consistent with the samples having resided at upper-crustal depths until at least Early Cretaceous time. While we cannot completely discount that samples may have experienced monotonic cooling or have been held at constant temperatures, at least three MDD models are consistent with mild to moderate reheating (<300 °C) ca. 190 Ma, followed by cooling ca. 180 Ma. One model further suggests a second thermal pulse ca. 170 Ma. Regional data from the orogen (i.e., including the Dabie Shan) are consistent with these thermal events being real. However, any thermal pulses in the Jurassic were insufficient to reset mica ages in the Sulu terrane.

The $^{40}Ar/^{39}Ar$ data also have implications for the history of Early Cretaceous extension in East Asia. The Yantai-Qingdao-Wulian fault, associated with mylonitic deformation in both the northern and southern parts of the Shandong Peninsula, was active by at least ca. 128 Ma as a top-to-the-W extensional detachment fault. Although postcollisional Mesozoic plutons are abundant on the Shandong Peninsula, they are volumetrically minor and relatively undeformed compared to the large-scale Early Cretaceous extension in the northern Dabie Shan.

The youngest phase of deformation recorded by the $^{40}Ar/^{39}Ar$ data is consistent with mid to Late Cretaceous deformation associated with sinistral-oblique slip on the Tan-Lu fault. The Tan-Lu fault, at least in its present expression, appears to truncate both the Early Cretaceous expression of the Yantai-Qingdao-Wulian fault on the Shandong Peninsula and the Xiaotian–Mozitang fault in the Dabie Shan; consideration of a possible linkage between these two detachment faults may prove useful in pre–Late Cretaceous restorations of the orogen.

Several factors suggest that the high-pressure and UHP rocks of the Sulu terrane reached and resided at higher structural levels by the Late Triassic relative to the high-pressure and UHP rocks exposed in the Dabie Shan. Significant exhumation associated with Early Cretaceous extension and later dip slip on the Tan-Lu fault has exposed rocks in the Dabie Shan that resided at deeper structural levels in Late Triassic–Early Jurassic

time. Therefore, we conclude that the $^{40}Ar/^{39}Ar$ data from the Sulu terrane presented herein provide the best constraints so far on the timing and rates of exhumation to upper-crustal depths of high-pressure and UHP rocks in the orogen.

ACKNOWLEDGMENTS

This research was supported by National Science Foundation (NSF) Continental Dynamics grant EAR-0003355 and also benefited from salary support to L.E. Webb from NSF grant EAR-IF-0130833. We would like to thank Suzanne Baldwin for discussions related to multi-diffusion-domain modeling, and reviewers B.R. Hacker, S. Johnston, J.G. Liou, M. Wong, and R.Y. Zhang for thoughtful comments that improved the manuscript.

REFERENCES CITED

Ames, L., Zhou, G., and Xiong, B., 1996, Geochronology and geochemistry of ultrahigh pressure metamorphism with implications for collision of the Sino-Korean and Yangtze cratons, central China: Tectonics, v. 15, p. 472–489, doi: 10.1029/95TC02552.

Baldwin, S.L., Monteleone, B., Webb, L.E., Fitzgerald, P.G., Grove, M., and Hill, E.J., 2004, Pliocene eclogite exhumation at plate tectonic rates in eastern Papua New Guinea: Nature, v. 431, p. 263–267, doi: 10.1038/nature02846.

Chavagnac, V., Jahn, B., Villa, I.M., Whitehouse, M.J., and Liu, D., 2001, Multichronometric evidence for an in situ origin of the ultrahigh-pressure metamorphic terrane of Dabieshan, China: The Journal of Geology, v. 109, p. 633–646, doi: 10.1086/321961.

Cong, B., 1996, Ultrahigh-pressure metamorphic rocks in the Dabieshan-Sulu region of China: Dordrecht, Netherlands, Kluwer Academic Publishers, 224 p.

Enami, M., Suzuki, K., Zhai, M., and Zheng, X., 1993, The chemical Th-U-total Pb isochron ages of Jiaodong and Jiaonan metamorphic rocks in the Shandong Peninsula, eastern China: The Island Arc, v. 2, p. 104–113.

Ernst, W.G., 2001, Subduction, ultrahigh-pressure metamorphism, and regurgitation of buoyant crustal slices—Implications for arcs and continental growth: Physics of the Earth and Planetary Interiors, v. 127, p. 253–275, doi: 10.1016/S0031-9201(01)00231-X.

Faure, M., Lin, W., and Le Breton, N., 2001, Where is the North China–South China block boundary in eastern China?: Geology, v. 29, p. 119–122, doi: 10.1130/0091-7613(2001)029<0119:WITNCS>2.0.CO;2.

Faure, M., Lin, W., Monié, P., Le Breton, N., Poussineau, S., Panis, D., and Deloule, E., 2003, Exhumation tectonics of the ultrahigh-pressure metamorphic rocks in the Qinling orogen in east China: New petrological-structural-radiometric insights from the Shandong Peninsula: Tectonics, v. 22, 1018, doi: 10.1029/2002TC001450.

Gao, S., Rudnick, R.L., Carlson, R.W., McDonough, W.F., and Liu, Y.-S., 2002, Re-Os evidence for replacement of ancient mantle lithosphere beneath the North China craton: Earth and Planetary Science Letters, v. 198, p. 307–322, doi: 10.1016/S0012-821X(02)00489-2.

Grimmer, J.C., Jonckheere, R., Enkelmann, E., Ratschbacher, L., Hacker, B.R., Blythe, A., Wagner, G.A., Liu, S. and Dong, S., 2002, Cretaceous–Tertiary history of the southern Tan-Lu fault zone: Apatite fission-track and structural constraints from the Dabie Shan: Tectonophysics, v. 359, p. 225–253.

Grimmer, J.C., Ratschbacher, L., Franz, L., Gaitzsch, I., Tichomirowa, M., McWilliams, M.O., Hacker, B.R., and Zhang, Y., 2003, When did the ultrahigh-pressure rocks reach the surface? A $^{207}Pb/^{206}Pb$ zircon, $^{40}Ar/^{39}Ar$ white mica, Si-in-phengite single grain study of Dabie Shan synorogenic foreland sediments: Chemical Geology, v. 197, p. 87–110, doi: 10.1016/S0009-2541(02)00321-2.

Hacker, B.R., and Wang, Q., 1995, Ar/Ar geochronology of ultrahigh-pressure metamorphism in central China: Tectonics, v. 14, p. 994–1006, doi: 10.1029/95TC00932.

Hacker, B.R., Ratschbacher, L., Webb, L., and Dong, S., 1995, What brought them up? Exhumation of the Dabie Shan ultrahigh-pressure rocks: Geology, v. 23, p. 743–746, doi: 10.1130/0091-7613(1995)023<0743:WBTUEO>2.3.CO;2.

Hacker, B.R., Ratschbacher, L., Webb, L., Ireland, T., Walker, D., and Dong, S., 1998, U/Pb zircon ages constrain the architecture of the ultrahigh-pressure Qinling-Dabie orogen, China: Earth and Planetary Science Letters, v. 161, p. 215–230, doi: 10.1016/S0012-821X(98)00152-6.

Hacker, B.R., Ratschbacher, L., Webb, L.E., Ireland, T.R., Calvert, A., Dong, S., Wenk, H.-R., and Chateigner, D., 2000, Exhumation of ultrahigh-pressure continental crust in east-central China: Late Triassic–Early Jurassic tectonic unroofing: Journal of Geophysical Research, v. 105, p. 13,339–13,364, doi: 10.1029/2000JB900039.

Leech, M.L., Webb, L.E., Yang, T., and Xu, Z., 2003, Microstructural analysis of the ultrahigh-pressure Sulu terrane, eastern China: Eos (Transactions, American Geophysical Union), v. 84, p. F1391.

Li, S., Ciao, Y., Liou, D., Chen, Y., Ge, N., Zhang, Z., Sun, S., Cong, B., Zhang, R., Hart, S.R., and Wang, S., 1993, Collision of the North China and Yangtse blocks and formation of coesite-bearing eclogites; timing and processes: Chemical Geology, v. 109, p. 89–111, doi: 10.1016/0009-2541(93)90063-O.

Liu, F., Xu, Z., Liou, J.G., Katayama, I., Masago, H., Maruyama, S., and Yang, J., 2002, Ultrahigh-pressure mineral inclusions in zircons from gneissic core samples of the Chinese Continental Scientific Drilling Site in eastern China: European Journal of Mineralogy, v. 14, p. 499–512.

Liu, F., Xu, Z., and Liou, J.G., 2004a, Tracing the boundary between UHP and HP metamorphic belts in the southwestern Sulu terrane, eastern China: Evidence from mineral inclusions in zircons from metamorphic rocks: International Geologic Review, v. 46, p. 409–429.

Liu, F., Xu, Z., Liou, J.G., and Song, B., 2004b, SHRIMP U-Pb ages of ultrahigh-pressure and retrograde metamorphism of gneisses, south-western Sulu terrane, eastern China: Journal of Metamorphic Geology, v. 22, p. 315–326, doi: 10.1111/j.1525-1314.2004.00516.x.

Lovera, M., Richter, F.M., and Harrison, T.M., 1989, The $^{40}Ar/^{39}Ar$ thermochronometry for slowly cooled samples having a distribution of diffusion domain sizes: Journal of Geophysical Research, v. 94, p. 17,917–17,935.

Lovera, M., Grove, M., Harrison, T.M., and Mahon, K.I., 1997, Systematic analysis of K-feldspar $^{40}Ar/^{39}Ar$ step heating results. I: Significance of activation energy determinations: Geochimica et Cosmochimica Acta, v. 61, p. 3171–3192, doi: 10.1016/S0016-7037(97)00147-6.

Lovera, M., Grove, M., and Harrison, T.M., 2002, Systematic analysis of K-feldspar $^{40}Ar/^{39}Ar$ step heating results. II: Relevance of laboratory argon diffusion properties to nature: Geochimica et Cosmochimica Acta, v. 66, p. 1237–1255, doi: 10.1016/S0016-7037(01)00846-8.

Ludwig, K.R., 2003, Isoplot/EX, rev. 3.00, A geochronological toolkit for Microsoft Excel: Berkeley Geochronology Center Special Publication, v. 4, 71 p.

McDougall, I., and Harrison, T.M., 1999, Geochronology and thermochronology by the $^{40}Ar/^{39}Ar$ method: New York, Oxford University Press, 212 p.

Parsons, I., Brown, W.L., and Smith, J.V., 1999, $^{40}Ar/^{39}Ar$ thermochronology using alkali feldspars: Real thermal history or mathematical mirage of microtexture?: Contributions to Mineralogy and Petrology, v. 136, p. 92–110, doi: 10.1007/s004100050526.

Ratschbacher, L., Hacker, B.R., Calvert, A., Webb, L.E., Ireland, T.R., McWilliams, M.O., Dong, S., Wenk, H.-R., and Chateigner, D., 2000, Exhumation of the ultrahigh-pressure continental crust in east-central China: Cretaceous and Cenozoic unroofing and the Tan-Lu fault: Journal of Geophysical Research, v. 105, p. 13,303–13,338, doi: 10.1029/2000JB900040.

Ratschbacher, L., Hacker, B.R., Calvert, A., Webb, L.E., Grimmer, J.C., McWilliams, M., Ireland, T.R., Dong, S., and Hu, J., 2003, Tectonics of the Qinling (central China): Tectonostratigraphy, geochronology, and

deformation history: Tectonophysics, v. 366, p. 1–53, doi: 10.1016/S0040-1951(03)00053-2.

Renne, P.R., Swisher, C.C., III, Deino, A.L., Karner, D.B., Owens, T., and DePaolo, D.J., 1998, Intercalibration of standards, absolute ages and uncertainties in $^{40}Ar/^{39}Ar$ dating: Chemical Geology, v. 145, p. 117–152, doi: 10.1016/S0009-2541(97)00159-9.

Rowley, D.B., Xue, F., Tucker, R.D., Peng, Z.X., Baker, J., and Davis, A., 1997, Ages of ultrahigh pressure metamorphism and protolith orthogneisses from the eastern Dabie Shan: U/Pb zircon geochronology: Earth and Planetary Science Letters, v. 151, p. 191–203, doi: 10.1016/S0012-821X(97)81848-1.

Rubatto, D., and Hermann, J., 2001, Exhumation as fast as subduction?: Geology, v. 29, p. 3–6, doi: 10.1130/0091-7613(2001)029<0003:EAFAS>2.0.CO;2.

Steiger, R.H., and Jäger, E., 1977, Subcommission on Geochronology: Convention on the use of decay constants in geo- and cosmochronology: Earth and Planetary Science Letters, v. 36, p. 359–362, doi: 10.1016/0012-821X(77)90060-7.

Wallis, S., Enami, E., and Banno, S., 1999, The Sulu UHP terrane: A review of the petrology and structural geology: International Geologic Review, v. 41, p. 906–920.

Wallis, S., Tsuboi, M., Suzuki, K., Fanning, M., Jiang, L., and Tanaka, T., 2005, Role of partial melting in the evolution of the Sulu (eastern China) ultrahigh-pressure terrane: Geology, v. 33, p. 129–132, doi: 10.1130/G20991.1.

Walsh, E.O., and Hacker, B.R., 2004, The fate of subducted continental margins: Two-stage exhumation of the high-pressure to ultrahigh-pressure Western Gneiss Region, Norway: Journal of Metamorphic Geology, v. 22, p. 671–687, doi: 10.1111/j.1525-1314.2004.00541.x.

Wartho, J.-A., 1995, Apparent argon diffusive loss $^{40}Ar/^{39}Ar$ age spectra in amphiboles: Earth and Planetary Science Letters, v. 134, p. 393–407, doi: 10.1016/0012-821X(95)00113-Q.

Webb, L.E., Graham, S.A., Johnson, C.L., Badarch, G., and Hendrix, M., 1999a, Occurrence, age, and implications of the Yagan–Onch Hayrhan metamorphic core complex, southern Mongolia: Geology, v. 27, p. 143–146, doi: 10.1130/0091-7613(1999)027<0143:OAAIOT>2.3.CO;2.

Webb, L.E., Hacker, B.R., Ratschbacher, L., McWilliams, M.O., and Dong, S., 1999b, $^{40}Ar/^{39}Ar$ thermochronologic constraints on deformation and cooling history of high and ultrahigh-pressure rocks in the Qinling-Dabie orogen: Tectonics, v. 18, p. 621–638, doi: 10.1029/1999TC900012.

Webb, L.E., Ratschbacher, L., Hacker, B.R., and Dong, S., 2001, Kinematics of exhumation of high- and ultrahigh-pressure rocks in the Hong'an and Tongbai Shan of the Qinling-Dabie collisional orogen, eastern China: Geological Society of America Memoir 194, p. 413–434.

Webb, L.E., Leech, M.L., Yang, T., and Xu, Z., 2002, Kinematics of structures of the ultrahigh-pressure Sulu terrane, eastern China: Eos (Transactions, American Geophysical Union), v. 83, p. F1245.

Xu, Y.G., Huang, X.-L., Ma, J.-L., Wang, Y.-B., Iizuka, Y., Xu, J.-F., Wang, Q., and Wu, X.-Y., 2004, Crust-mantle interaction during the tectono-thermal reactivation of the North China craton: Constraints from SHRIMP zircon U-Pb chronology and geochemistry of Mesozoic plutons from western Shandong: Contributions to Mineralogy and Petrology, v. 147, p. 750–767, doi: 10.1007/s00410-004-0594-y.

Xue, F., Rowley, D.B., Tucker, R.D., and Peng, Z.X., 1997, U-Pb zircon ages of granitoid rocks in the north Dabie complex, eastern Dabie Shan, China: The Journal of Geology, v. 105, p. 744–753.

Yang, J.S., Wooden, J.L., Wu, C.L., Liu, F.L., Xu, Z.Q., Shi, R.D., Katayama, I., Liou, J.G., and Maruyama, S., 2003, SHRIMP U-Pb dating of coesite-bearing zircon from the ultrahigh-pressure metamorphic rocks, Sulu terrane, east China: Journal of Metamorphic Geology, v. 21, p. 551–560, doi: 10.1046/j.1525-1314.2003.00463.x.

Ye, K., Liu, J., Cong, B., Ye, D., Xu, P., Omori, S., and Maruyama, S., 2002, Ultrahigh-pressure (UHP) low-Al titanites from carbonate-bearing rocks in Dabieshan-Sulu UHP terrane, eastern China: The American Mineralogist, v. 87, p. 875–881.

Yin, A., and Nie, S., 1993, An indentation model for the North and South China collision and the development of the Tanlu and Honam fault systems, eastern Asia: Tectonics, v. 12, p. 801–813.

Zhang, R.Y., and Liou, J.G., 1998, Ultrahigh-pressure metamorphism of the Sulu terrane, eastern China: A perspective view: Continental Dynamics, v. 3, p. 32–53.

Zhang, X., Cawood, P.A., Wilde, S.A., Liu, R., Song, H., Li, W., and Snee, L.W., 2003, Geology and timing of mineralization at the Cangshang gold deposit, north-western Jiaodong Peninsula, China: Mineral Deposita, v. 38, p. 141–153.

MANUSCRIPT ACCEPTED BY THE SOCIETY 21 SEPTEMBER 2005

Geological Society of America
Special Paper 403
2006

Polyphase subduction and exhumation of the Sulu high-pressure–ultrahigh-pressure metamorphic terrane

Zhiqin Xu
Lingsen Zeng
Fulai Liu
Jingsui Yang
Zeming Zhang
Key Laboratory for Continental Dynamics, Ministry of Land and Resources,
Institute of Geology, Chinese Academy of Geological Sciences, Beijing, 100037, China
M. McWilliams
J.G. Liou
Department of Geological and Environmental Sciences, Stanford University, Stanford, California 94305-2115, USA

ABSTRACT

Four structural-metamorphic zones separated by ductile shear zones comprise the Sulu high- to ultrahigh-pressure metamorphic terrane. From south to north, they are the southern high-pressure zone (0.2–0.4 GPa, 350–400 ºC), the central very high-pressure zone (1.5–2.5 GPa, 500–600 ºC), the northern ultrahigh-pressure (UHP) zone (>2.8 GPa, 650–800 ºC) dominated by paragneiss, and the northern UHP zone dominated by granitic gneiss. Exhumation was associated with retrograde amphibolite- to greenschist-facies metamorphism and oblique southeastward ductile extrusion within the subduction channel. Geologic observations and seismic reflection profiles suggest an eroded asymmetric antiformal slab intruded by numerous Mesozoic granitic plutons. Zircon U/Pb ages indicate that peak metamorphism in the UHP zone occurred at 240–220 Ma, and $^{40}Ar/^{39}Ar$ thermochronology documents later exhumation at 220–200 Ma. In contrast, in the high-pressure zone, peak metamorphism and exhumation ages are older than 253 Ma and 253–240 Ma, respectively, by the same mineral. Together with previous results, these new data suggest that subduction and exhumation of different parts of the Yangtze slab occurred at different times, depending upon vertical variations in the physical properties of the subducted continental crust.

Keywords: polyphase structural deformation, Sulu, high-pressure, ultrahigh-pressure, UHP slices.

INTRODUCTION

The Dabie-Sulu high-pressure–ultrahigh-pressure (UHP) metamorphic terrane of eastern China was created by Triassic collision between the Sino-Korean and Yangtze cratons (Li et al., 1989, 1996, 2000a, 2000b; Ames et al., 1993; Liou et al., 1998; Hacker et al., 1998). It is the largest and one of the best-preserved UHP terranes in the world. Much of the Sulu high-pressure and UHP terrane is Yangtze continental crust that was subducted to >100 km and then exhumed (Cong and Wang, 1999; Liou et al., 2000). Because these UHP rocks preserve important information about continental subduction processes,

Xu, Z., Zeng, L., Liu, F., Yang, J., Zhang, Z., McWilliams, M., and Liou, J.G., 2006, Polyphase subduction and exhumation of the Sulu high-pressure–ultrahigh-pressure metamorphic terrane, *in* Hacker, B.R., McClelland, W.C., and Liou, J.G., eds., Ultrahigh-pressure metamorphism: Deep continental subduction: Geological Society of America Special Paper 403, p. 93–113, doi: 10.1130/2006.2403(05).

they have been extensively studied (Ernst et al., 1997; Ernst, 2001; Chopin, 2003, and references therein). Published work has characterized the petrology, geochemistry, structural geology, and geochronology of these extraordinary UHP rocks, but most work has focused on the Hong'an and Dabie blocks. In contrast, the high-pressure and UHP rocks of the Sulu terrane are poorly exposed and less well known.

To better characterize the structure of the Sulu UHP eclogite terrane and its associated country rocks, we mapped the Lianyungang area at 1:250,000 scale and conducted detailed structural studies of rocks from the Sulu area, as well as the Chinese Continental Scientific Drilling (CCSD) drill cores. By combining large- and small-scale structural analyses with radiometric ages, we have attempted to (1) better define the structures in the Sulu high-pressure and UHP metamorphic slice, (2) determine the nature and mechanism of its deformation, (3) constrain the timing of subduction and exhumation, and (4) develop a tectonic model to explain the tectonic evolution of Sulu high-pressure and UHP rocks.

GEOLOGICAL SETTING AND TECTONIC FRAMEWORK

The Sulu high-pressure–ultrahigh-pressure metamorphic terrane extends NE-SW for ~750 km and is 180 km wide (Fig. 1). It is bounded on the north by the Wulian-Yantai fault and the Laiyang Cretaceous basin, and on the south by the Xiangshui fault and the North Jiangsu basin. Field observations and petrologic data suggest that the Sulu terrane is composed primarily of three parallel metamorphic zones: the southern Sulu high-pressure zone (0.2–0.4 GPa, 350–400 ºC), the central Sulu very high-pressure zone (1.5–2.5 GPa, 500–600 ºC), and the northern Sulu UHP zone (2.8 GPa, 650–800 ºC) (Xu et al., 2004). Detailed field mapping and recent seismic reflection experiments from Taoyuan to Lianshui (Fig. 2) have allowed us to identify a number of imbricated slices that are separated by ductile shear zones in each metamorphic zone. The CCSD main hole is located in the southern part of the UHP zone (Fig. 1). Petrology and structural data from the CCSD main hole have confirmed the overall structure for the Sulu high-pressure–UHP belt, as suggested in the seismic reflection profile.

Southern Sulu High-Pressure Zone (I)

The southern Sulu high-pressure zone is composed of glaucophane- and kyanite-bearing paragneiss, quartzite, and marble. The occurrences of glaucophane in the Yangji drill core (Zhang et al., 1991) and winchite, barroisite, and aragonite in Yuntaishan and Liandao (Qiu et al., 2002) define the range of the southern Sulu high-pressure slice. The protoliths for these high-pressure rocks are sedimentary with minor basic volcanic rocks. Textures and thermobarometric studies suggest early blueschist-facies metamorphism at 0.70–0.85 GPa and 300–360 °C, followed by greenschist-facies retrogression at 350–410 °C and 0.2–0.4 GPa (Qiu et al., 2002). From top to bottom, zone I is subdivided by ductile shear zones DF1, DF2, and DF3 into four imbricated slices: Guannan (Ia), Guanyun (Ib), Yuntaishan (Ic), and West Yuntaishan (Id), with a NE-SW–trending foliation that dips 20–35°SE, and a SE-plunging stretching lineation. The shear zones that separate these slices are 300 to 500 m thick (Xu et al., 2004) (Fig. 3).

Central Sulu Very High-Pressure Zone (II)

Zone II (Hanshan) is 5–12 km wide and is located to the north of the high-pressure zone. It was recognized recently by the presence of OH-topaz in kyanite quartzites from Hanshan. Its upper part is composed of kyanite-chlorite quartzite, kyanite-bearing phengite–quartz schist, and kyanite-bearing albite–quartz schist, and its lower part is marble, phosphatic marble, and phosphorite. Metamorphic mineral assemblages Toz + Ky + Qtz, Ky + Ms + Qtz + Ap, Ky + Qtz + Ab, and Grt + Bt + Ab + Qtz are common (mineral abbreviations are from Kretz, 1983, unless we specify otherwise). Petrologic studies show that zone II rocks experienced peak very high-pressure metamorphism, which was later overprinted by blueschist-facies retrogression. OH-topaz in kyanite quartzite from Hanshan indicates peak metamorphic conditions of 500–600 °C and 1.5–2.5 GPa, respectively (Zhang et al., 2002), substantially higher than zone I. The upper part of zone II is separated from the overlying West Yuntaishan slice Id by DF4, a 500-m-wide ductile shear zone in mylonitic granitoids that dips 15–20°SE. The lower part of zone II is strongly sheared and overlies the UHP zone along ductile shear zone DF5 (Fig. 2).

Northern Sulu UHP Zone (III and IV)

The northern Sulu UHP metamorphic zone is defined by the widespread occurrence of coesite within garnets and clinopyroxenes in eclogites, as well as micro-inclusions within zircons from gneisses and eclogites (Liu et al., 2002, 2004a). It covers an area bounded on the south by the DF5 shear zone, on the north by the Wulian-Yantai fault, and on the west by the Tan-Lu fault (Fig. 1). Within this zone, paragneiss (25%) and granitic gneiss (70%) are the dominant country rocks, enclosing blocks and lenses of eclogite and garnet peridotite. Based on the dominant rocks that host the eclogites and garnet peridotites, this zone is subdivided by ductile shear zone DF9 into UHP zone III and UHP zone IV. UHP zone III is composed of dominantly supracrustal rocks and UHP zone IV of granitic gneisses, both with minor eclogite and peridotite lenses and layers.

Northern Sulu UHP Zone III

Zone III consists mainly of UHP supracrustal rocks intercalated with eclogitic and ultramafic lenses. The supracrustal rocks include coesite-bearing paragneiss, kyanite quartzite,

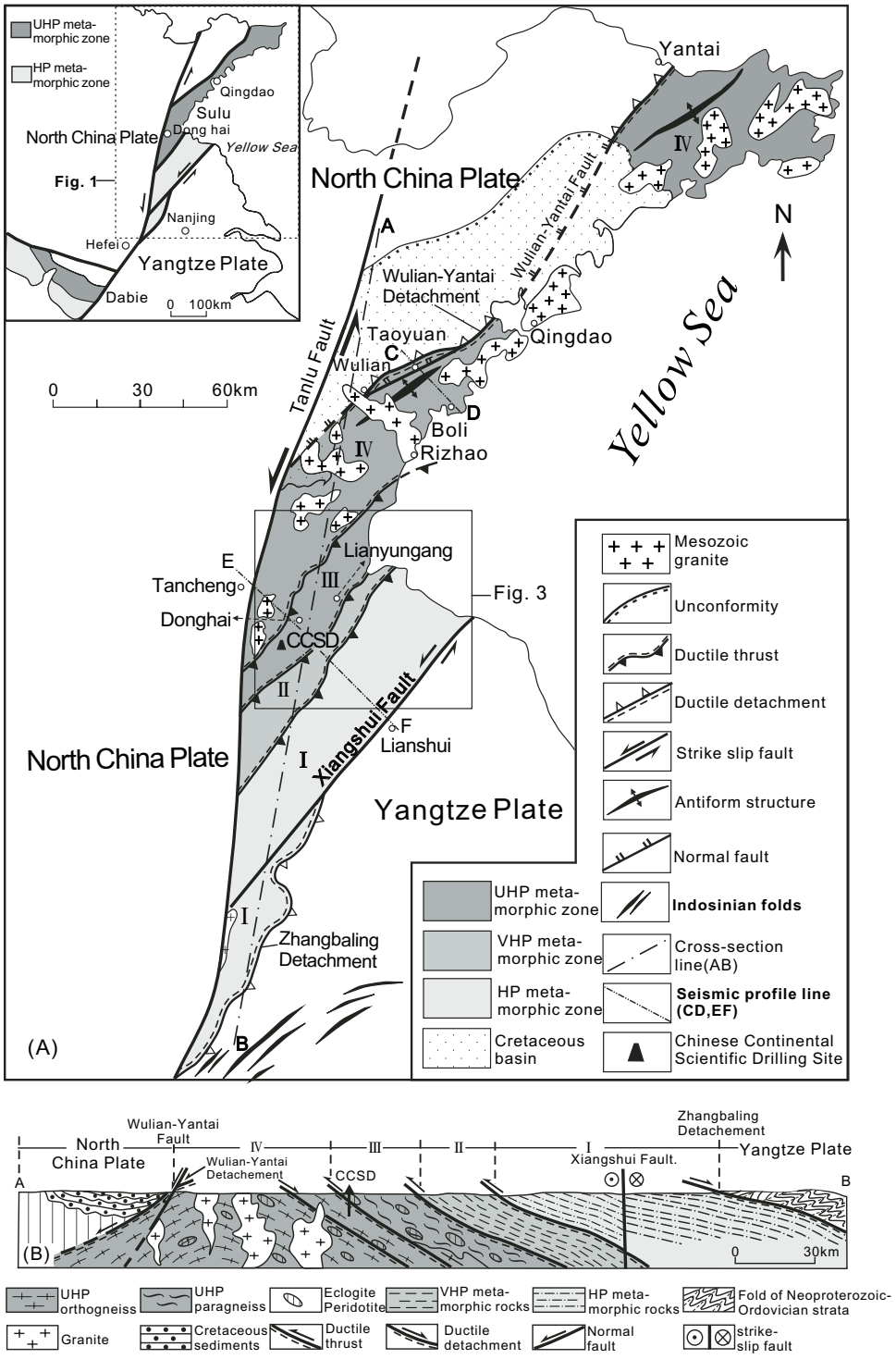

Figure 1. Tectonic sketch map (A) and a cross section (B) of the Sulu high-pressure–ultrahigh-pressure (HP-UHP) metamorphic terrane, showing: (1) high-pressure zone I, very high-pressure (VHP) zone II, and UHP (III and VI) zones separated by ductile shear zones; and (2) overall structure along the cross-section line A–B in (A). CCSD—location of the Chinese Continental Scientific Drilling Project site. Two seismic reflection profiles along lines C–D and E–F, respectively, are used to construct a continuous seismic reflection profile across the Sulu UHP belt as shown in Figure 2.

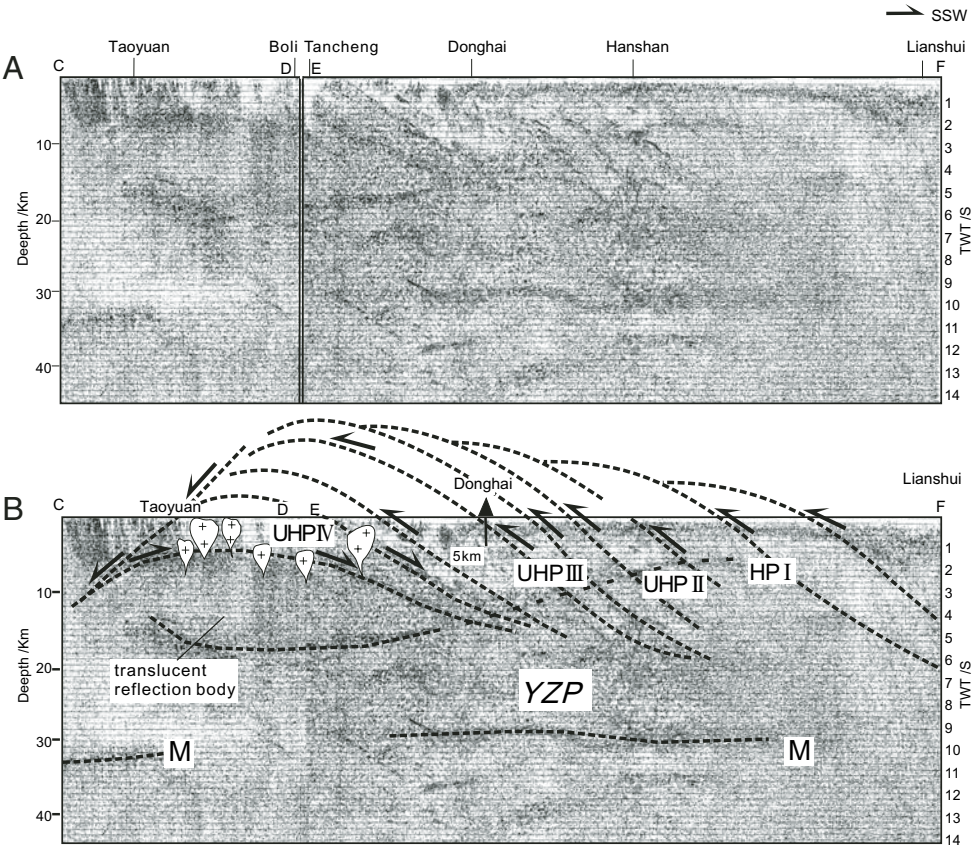

Figure 2. Original seismic reflection profile (A) (after Yang et al., 2004) with an updated interpretation (B) across the Sulu high-pressure–ultrahigh-pressure (UHP) terrane showing an eroded antiform structure in which the UHP zone IV is situated in the core and UHP zone III, very high-pressure (VHP) zone II, and high-pressure (HP) zone I are in the envelope. M—Moho, YZP—Yangtze craton; TWT—two-way traveltime.

jadeite quartzite, mica schist, and amphibolite. OH-topaz in kyanite quartzite at Hushan indicates metamorphic conditions of ~650 °C and 2.8–3.0 GPa (Zhang et al., 2002). The middle and upper parts of the supracrustal rocks south of Donghai are coesite- or aegirine-bearing gneiss. From SE to NW, the Lianyungang (IIIa), Maobei (IIIb), Donghai (IIIc) and Shilianghe (IIId) slices are separated by ductile shear zones DF6, DF7, and DF8, respectively (Fig. 2). In these shear zones, mylonites, mylonitic rocks, and type-A folds are abundant. These tectonic slices and their intervening shear zones have SE-dipping foliations and SE-plunging stretching lineations, similar to those in the high-pressure zone.

Peak metamorphic assemblages and textures related to the UHP metamorphism were strongly overprinted by retrogression during exhumation. Mineral assemblages diagnostic of UHP metamorphism within the paragneiss, such as Coe + Grt + Omp + Phe + Rt and Coe + Grt + Jd + Phe, are only preserved as inclusions in zircons (Liu et al., 2002, 2004a), where Coe, Omp, and Phe are coesite, omphacite, and phengite, respectively. Based on these mineral assemblages, we identify three main retrograde stages:

(1) Early exhumation: Grt + Coe + Rt + H_2O = Ttn + Ep + Qtz, at 750–850 °C and 2.5–2.8 GPa, where Ttn and Ep are titanite and epidote, respectively.

(2) Mid exhumation: Jd + Qtz = Ab, Agt = Cal, Grt + Jd + Qtz + H_2O = Hbl +Ab, at 680–780 °C and 1.2–1.8 GPa.

(3) Late exhumation: Amphibolite-facies mineral assemblages and textural relationships dominate the UHP rocks. Preserved mineral assemblages are Ep + Bt + Pl + Kfs + Qtz, Ms + Bt + Pl + Kfs + Qtz, Grt + Bt ± Ms + Pl + Kfs + Qtz, Grt + Hbl + Bt + Pl + Qtz, and Ep + Hbl + Bt + Ms + Pl + Kfs + Qtz. Pressure and temperature estimates from various geothermometers and geobarometers, such as Grt–Hbl, Grt–Hbl–Pl–Qtz, Grt–Bt, and Hbl–Pl, suggest metamorphism occurred at 550–650 °C and 0.5–0.7 GPa.

Northern Sulu UHP Zone IV

Zone IV is ~40 km wide and lies between the Wulian-Yantai fault and ductile shear zone DF9. It consists of granitic gneiss and subordinate supracrustal rock intercalated with eclogites and ultramafic blocks (Fig. 1). The supracrustal rocks, eclogites, and Weihai garnet peridotite contain coesite; the granitic gneiss does

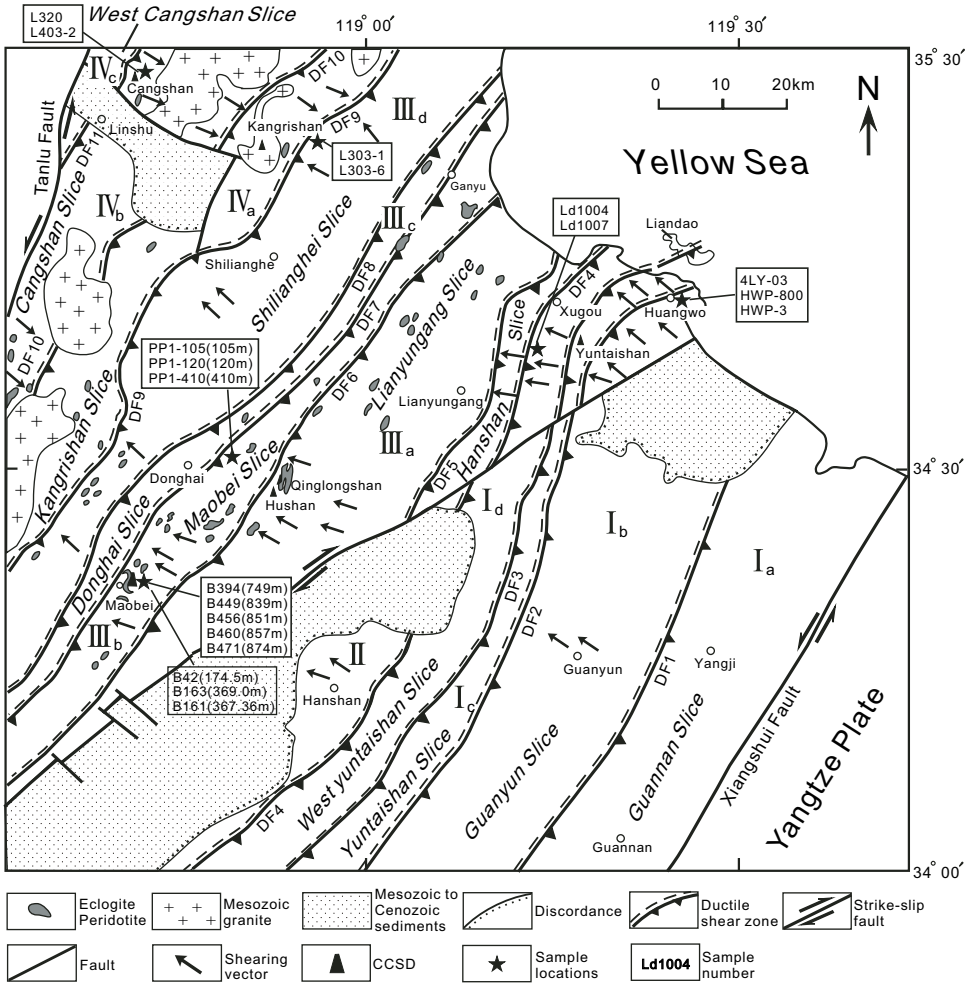

Figure 3. Tectonic map of the Lianyungang area showing the distribution of various high-pressure and ultrahigh-pressure (UHP) slices, major ductile shear zones DF_1 to DF_{11}, and samples for quartz lattice preferred orientation studies. CCSD—Chinese Continental Scientific Drilling Project.

not (Liu et al., 2002; Yang et al., 2003), but zircons separated from granitic gneisses contain coesite and UHP mineral assemblages typical of the area near the Wulian-Yantai fault. Foliations dip gently NW to WNW, but southeastward away from the fault, foliations dip gently SE to ESE. This regional change in dip direction suggests a broad antiform (Fig. 1), which is also shown by seismic reflection data (Fig. 2) (Yang et al., 2004). Such an antiform structure was also suggested by Faure et al. (2003). North of Lingshu, we identified three structural subslices. From top to bottom they are: Kangrishan (IVa), Cangshan (IVb), and West Cangshan (IVc); they are separated by ductile shear zones DF9, DF10, and DF11 (Fig. 3). Each shear zone consists of hundreds of meters of E-dipping mylonitic rocks.

The antiform was significantly modified by the emplacement of Triassic–Jurassic granites, which have U-Pb zircon and whole-rock Rb-Sr ages that range from 210 to 109 Ma, representing magmatic additions during and after exhumation (Wang et al., 2005).

POLYPHASE DEFORMATION IN THE SULU HIGH-PRESSURE–UHP BELT

The observed tectonic framework (tectonic slices bounded by ductile shear zones) was produced during exhumation as mid- to deep-level ductile deformation was superseded by shallower-level ductile deformation and, ultimately, brittle deformation. In particular, the deformation associated with the movement of the Tan-Lu fault, and large-scale post-Mesozoic extension in central and north China have greatly affected the early structures formed in subduction and early exhumation of the Sulu UHP terrane. Knowledge of the structure, kinematics, *P-T* conditions, and deformation mechanisms of the ductile shear zones is essential to an understanding of the structural evolution of the Sulu high-pressure–UHP belt, but in this strongly retrogressed and reworked UHP terrane, it is difficult to identify early structural details. Here, we try to reveal them through detailed examination of microstructures and strain

analyses, in combination with well-documented mineral assemblages for each episode of metamorphic evolution of the Sulu terrane. Detailed structural analyses were performed to delineate the structural relationships between the different tectonic units as discussed in the preceding section. Textural and structural relationships among various generations of mineral assemblages were also carefully examined to relate deformation episodes with metamorphic reactions from subduction to exhumation of the Sulu continental crust. Structural data, in conjunction with U-Pb zircon sensitive high-resolution ion microprobe (SHRIMP), biotite, and hornblende $^{40}Ar/^{39}Ar$ ages, allow us to differentiate subduction-related structures from those formed during exhumation.

We measured quartz lattice preferred orientation in the *x*-*z* plane of oriented thin sections on a U-stage to determine quartz plastic deformation mechanism and sense of shearing, and to obtain the corresponding *P*-*T* conditions for such plastic deformation. Previous studies (Mainprice et al., 1986; Ji, 1988) have identified four types of quartz lattice preferred orientations resulting from preferential activation of one of the slip systems in quartz to accommodate shear strain at various temperature conditions: (1) high-*T* (>650 °C) prismatic (10$\bar{1}$0) <c> slip system; (2) intermediate-*T* (650–550 °C) prismatic (10$\bar{1}$0) <a> slip system; (3) intermediate- to low-*T* (550–450 °C) prismatic (10$\bar{1}$1) <c> slip system; and (4) low-*T* (<400 °C) basal (10$\bar{1}$1) <c> slip system. Quartz lattice preferred orientation has been widely used to infer the shear sense as well as corresponding temperature conditions for the formation of a quartz-bearing ductile shear zone. Olivine lattice preferred orientation is also used in a similar fashion but for olivine-rich rocks. We used quartz lattice preferred orientation to infer temperature conditions for the ductile deformations observed in the Sulu high-pressure–UHP metamorphic belt. We also compared *P*-*T* conditions obtained from these analyses with those from olivine lattice preferred orientation studies on olivine-bearing ultramafic rocks and from thermobarometric studies both for the surface and CCSD borehole samples to evaluate the consistency between these independent data sets, and in turn to constrain the kinematics of deformation associated with subduction and exhumation.

Ductile Deformation During Subduction (D1)

Near Donghai, Maobei UHP slice IIIb is sandwiched between SE-dipping ductile shear zones DF6 and DF7 (Fig. 3). In the western part of the Maobei slice, the sigmoidal Maobei eclogite has an overall trend of NNE-SSW and dips 50° to 55°E (Fig. 4A). Refolding of "A" folds represented by small-scale folds of red garnet and green omphacite bands is common in the Maobei eclogites (Fig. 4). The CCSD drill hole at Maobei (Fig. 3) reveals 600 m of rutile eclogite, phengite eclogite, and quartz eclogite in its uppermost part, all of which experienced various degrees of retrogression (Zhang et al., 2004). During the drilling of the CCSD project, the core was restored to its original position with the image logging technique, and thus the structures observed in these core samples can be compared with those from surface geology. Early structures are recognized in fresh eclogites; they differ from the regional NE-SW–trending structures formed during exhumation. These early foliations trend nearly N-S and dip steeply 50–55°E (Fig. 4A), consistent with surface observations. Subhorizontal stretching lineations defined by elongated omphacite, rutile, and apatite grains are parallel to the strike of the Maobei eclogite. Strain measurements on oriented thin sections of fresh eclogite from samples B42R41P1d and B161R140P1 (Fig. 5; Table 1) yield a maximum aspect ratio of 26:1 for omphacite and 24:1 for rutile, respectively. Taking an undeformed rutile grain to be an equiaxis sphere and applying the Flinn index $K = (x/y - 1)/(y/z - 1)$, sheared rutiles have K = 1.26. Projected onto a Woods diagram (Fig. 5), the rutile data suggest 92%–160% elongation and 51%–60% shortening, assuming no strain along the intermediate axis (Fig. 5). Quartz eclogite from the borehole at 174.5 and 369.0 m exhibits a quartz lattice preferred orientation that suggests activity of the high-*T* (>650 °C) {10$\bar{1}$0} <c> slip system (Ji, 1988) and top-S shear sense (Fig. 5D). Rutile eclogite and phengite eclogite experienced a less intense retrograde overprint and record peak metamorphic conditions of 700–850 °C and >2.8 GPa. Quartz eclogite formed during early retrogression at 700–800 °C and >2.5 GPa (Zhang et al., 2005). Such temperature conditions are consistent with those inferred from quartz lattice preferred orientation studies.

In eastern Donghai, the Qinglongshan eclogite that is cut by shear zones DF6 and DF7 dips steeply to the east. But early structures preserved in the Qinglongshan eclogite include stretching lineations plunging 45°NNE and tight A folds, similar to those in the Maobei slice.

Using the electron-backscatter diffraction (EBSD) technique, Xu et al. (2005) measured lattice preferred orientation for olivines from the CCSD-PP1 peridotite samples. They found that Zhimafang peridotites have C-type olivine fabric of Jung and Karato's classification (Jung and Karato, 2001), in which the olivine [001] axis is subparallel to the stretching lineation and the (100) plane is subparallel to the foliation, despite different deformation intensity and strain regimes (simple shear or uniaxial compression). It was suggested that such olivine lattice preferred orientation was formed at UHP metamorphic conditions and was preserved during exhumation of the Zhimafang garnet peridotite, though olivine lattice preferred orientation was formed at a substantially higher temperature than high-*T* quartz lattice preferred orientation. Observations from quartz and olivine lattice preferred orientation measurements, as well as mineral assemblages, suggest that the nearly N-S–trending structure may represent the early structures formed during subduction of the Sulu continental crust.

Early Deformation (D1) in the High-Pressure Zone

In Zhangbaling area of the southern Sulu high-pressure zone, a mylonite belt with a subhorizontal foliation was found within the glaucophane-bearing metavolcanics (Fig. 6). Within

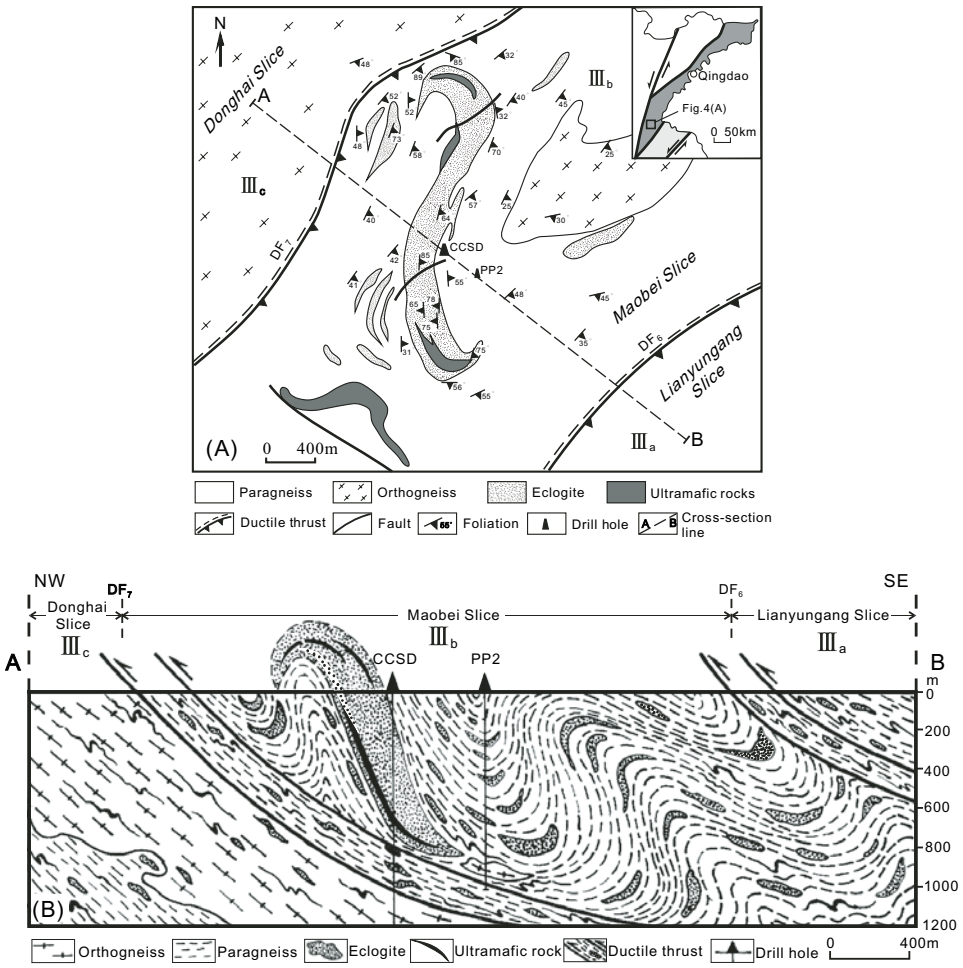

Figure 4. Geologic map (A) and cross section (B) of the Maobei area around the Chinese Continental Scientific Drilling Project (CCSD) drill site showing distribution of eclogite, ultramafic rocks, and major structures. DF—ductile shear zone.

this shear zone, penetrative cleavages, N-S–trending stretching lineations defined by preferentially oriented glaucophanes, quartzes, and feldspars, type-A folds and sheath folds are well preserved. Structures such as σ- and δ-type feldspar porphyroblasts, S-C fabric, and domino structure all indicate top-to-the-S shear sense. Quartz lattice preferred orientation measurements yield a low-*T* (<400 °C) basal (10$\bar{1}$1) <c> fabric and top-to-the-S shear sense (Xu et al., 1997). In the southeast of Zhangbaling, Neoproterozoic to Ordovician metasediments of lower-greenschist facies overlie the mylonite belt and have experienced progressive decreasing shear strain upward. Such a strain gradient resulted in the gradual transition from gently SSE-dipping penetrative foliations and nearly N-S-trending stretching lineations to steeply dipping spaced foliations and nearly vertical stretching lineations. Using a Dunnet diagram, strain analysis on the boulders (sample ZBL-Z1 and ZBL-Z2) in the Neoproterozoic conglomerate yields a Flint index of ~1.0 (Fig. 6B). These observations suggest that this mylonite zone is a gently southward-dipping ductile shear zone that was cut by the NW-SW–trending shear zones. We interpret this to mean that this shear zone may have resulted from deformation at high-pressure conditions during northward subduction of the Yangtze plate.

In summary, we conclude that simple shear was the principal mechanism for deformation in the subduction stage, probably including early exhumation (D1) both in UHP (700–850 °C and 2.5–2.8 GPa) and high-pressure conditions.

Shear Strain during Main Exhumation (D2)

Examination of subtle but systematic changes in the trend of stretching lineations helps to better define the deformation associated with the exhumation. The stretching lineations of this stage of deformation trend WNW-ESE overall, but change from E-W in the NE to NW-SE in the SW part of the metamorphic slice. During 1:250,000 regional mapping of the Lianyungang area, we identified 11 ductile shear zones as boundaries to the structural slices. Type-A folds and other structures indicative of high ductile shear strain are widespread within the shear

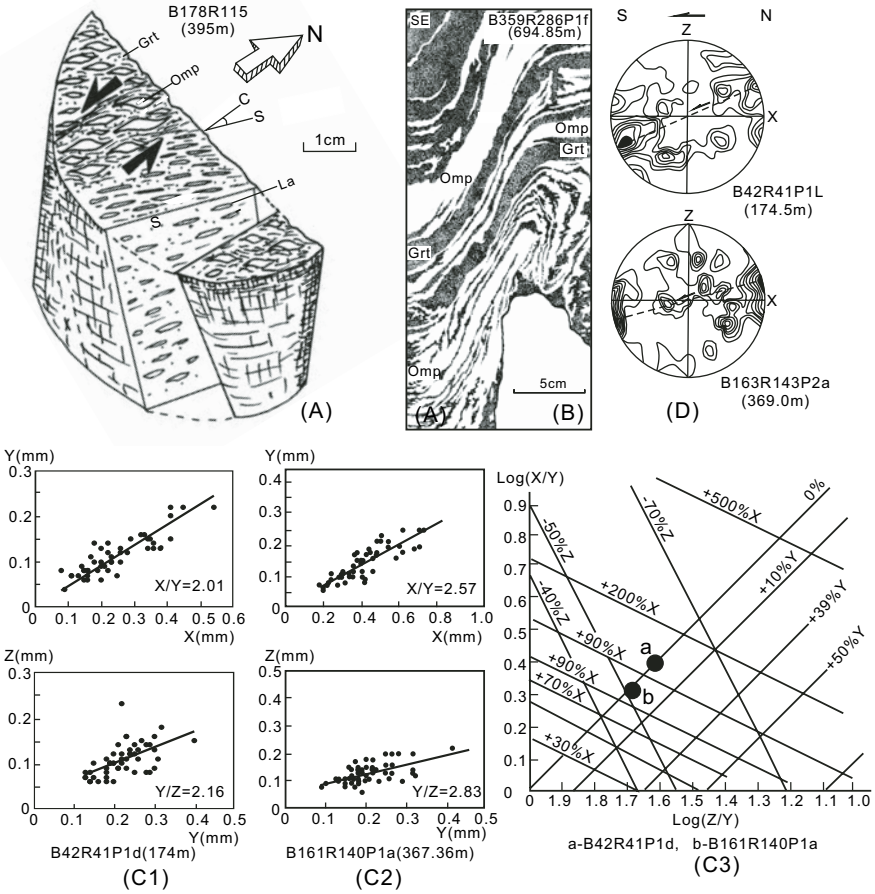

Figure 5. Features of early deformation (D1) in the eclogites of the Chinese Continental Scientific Drilling Project (CCSD) core. (A) Hand drawing of an eclogite core sample (396 m deep) from the CCSD main hole showing nearly N-S–trending stretching lineation and characteristics of shear deformation. Grt—garnet, Omp—omphacite, La—stretching lineation. (B) Hand drawing of an eclogite core sample (694.85 m deep) showing refolded A-type fold. (C) Strain analyses of rutile from eclogite core samples of the CCSD main hole showing shearing mechanism during early subduction deformation. C1 and C2 are for samples B42R41P1d (174.5 m) and B161R140P1a (369.0 m), respectively; C3 is a Wood diagram showing that rutile has undergone shearing; a—rutiles from sample B161R140P1a; b—rutiles from sample B42R41P1d. (D) Lattice preferred orientations of quartz in eclogite cores from the CCSD main borehole: (top) sample B42R41P1 (174.50 m), $N = 120$, contours at densities 0.8%, 1.7%, 2.5%, 3.3%, 4.2%, 5.0%, 5.8%, and 6.7%; (bottom) sample B163R143P2a (369 m), $N = 120$, contours at densities 0.8%, 1.7%, 2.5%, 3.3%, 4.2%, 5.0%, 5.8%, and 6.7%.

TABLE 1. SUMMARY OF STRAIN ANALYSES ON RUTILES AND OMPHACITES IN ECLOGITES FROM THE CHINESE CONTINENTAL SCIENTIFIC DRILLING PROJECT BOREHOLE

Sample	Depth (m)	Rutile			*N*	Omphacite			*N*
		x:y	x:z	y:z		x:y	x:z	y:z	
B42R41P1d	174.50	2.01		2.16	50				
B130R112P1-1	316.73	2.12	2.55	1.89	50	2.65	2.14	3.06	50
B161 R140P1	369.00	2.57		2.83	50				
B161R140P1c	369.10	2.54		2.71	50				
B208R185P1f	448.02	4.61	3.35	2.33	25	4.08		2.09	50
B270R226P2-2	545.00				50	3.80		1.70	50

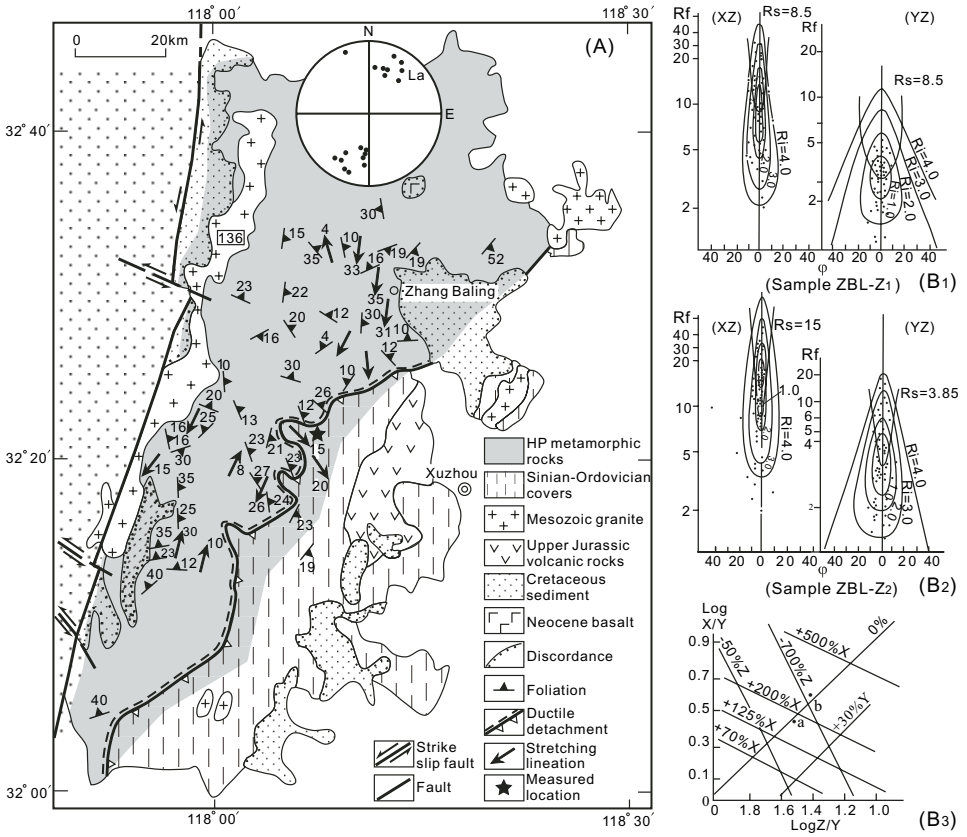

Figure 6. Simplified geologic map of the Zhangbaling area (A) and strain analyses (B) showing the early deformation (D1) in the high-pressure (HP) metamorphic unit. Strain analysis on the boulders from the Neoproterozoic conglomerates using the Dunnet diagram (B1 for ZBL-Z1 and B2 for ZBL-Z2) yielded a Flin index of ~1.0. These results were also resolved in a Wood diagram (B3), in which a and b represent strain values of rutile along *x*, *y*, and *z* axes for samples ZBL-Z1 and ZBL-Z2, respectively.

zones. Stretching lineations defined by elongations in metavolcaniclastic rocks, elongated quartzes, and strain shadows around garnet porphyroblasts, are common. These were used to infer the kinematics of the ductile shear zones (Fig. 7).

A series of imbricate, gently SE-dipping slices are separated by mylonites that dip gently SE. Structures in mylonitic paragneisses that enclose eclogitic lenses from 750 to 1105 m in the CCSD main borehole and from 950 to 1008 m in the CCSD-PP1 borehole, together with surface observations show that shear zone DF7 dips to the SE at 35° (Fig. 7).

Shear Strain of the South Sulu High-Pressure Imbricated Structural Slice

In zones I and II, the boundaries between the slices are mylonites that dip gently to the SE. On the *x*-*z* plane, variable scales of asymmetric folds, S-C structures, σ and δ porphyroclasts, and domino structures all suggest top-NW sense of shear (Fig. 7). In the ductile shear zones, syndeformational assemblages are dominated by transitional blueschist–greenschist facies retrogression at 400 °C and 1.2–2.0 GPa. Mineral assemblages are Wnc + Ab + Act + Grt + Phe + Arg, Bar + Ab + Phe + Grt + Act, Bar + Ab + Phe + Act, and Wnc + Ab + Act + Ep + Phe. These minerals are typically confined to strongly penetrative S_1 shear foliations. In contrast, greenschist-facies minerals, such as chlorite, epidote, actinolite, albite, biotite, and calcite, formed at 350–410 °C and 0.2–0.4 GPa (Qiu et al., 2002) and are distributed along S_2 spaced cleavages resulting from refolding of S_1 shear foliations.

Quartz lattice preferred orientations were determined from samples of metavolcanic mylonites (GLY-03, HWP-800-1, HWP-3 and HWP-4) from DF2 at Huanwo and from mylonitic kyanite-bearing schists (Ld1004 and Ld1007) at Hanshan, between the Yuntaishan slice Id and zone II. These measurements show that quartz exhibits an intermediate- to low-*T* (<400–450 °C) {10$\bar{1}$0} <a> fabric and low-*T* (<400 °C) {0001} <a> fabric suggestive of top-NW shear (Fig. 8A). The inferred temperature conditions for quartz plastic deformation are well matched to those that defined the syndeformational metamorphic mineral assemblages. Therefore, we conclude that ductile deformation in this part of high-pressure zone was mainly associated with exhumation, which is different from the Zhangbaling area, where early structures associated with subduction are preserved.

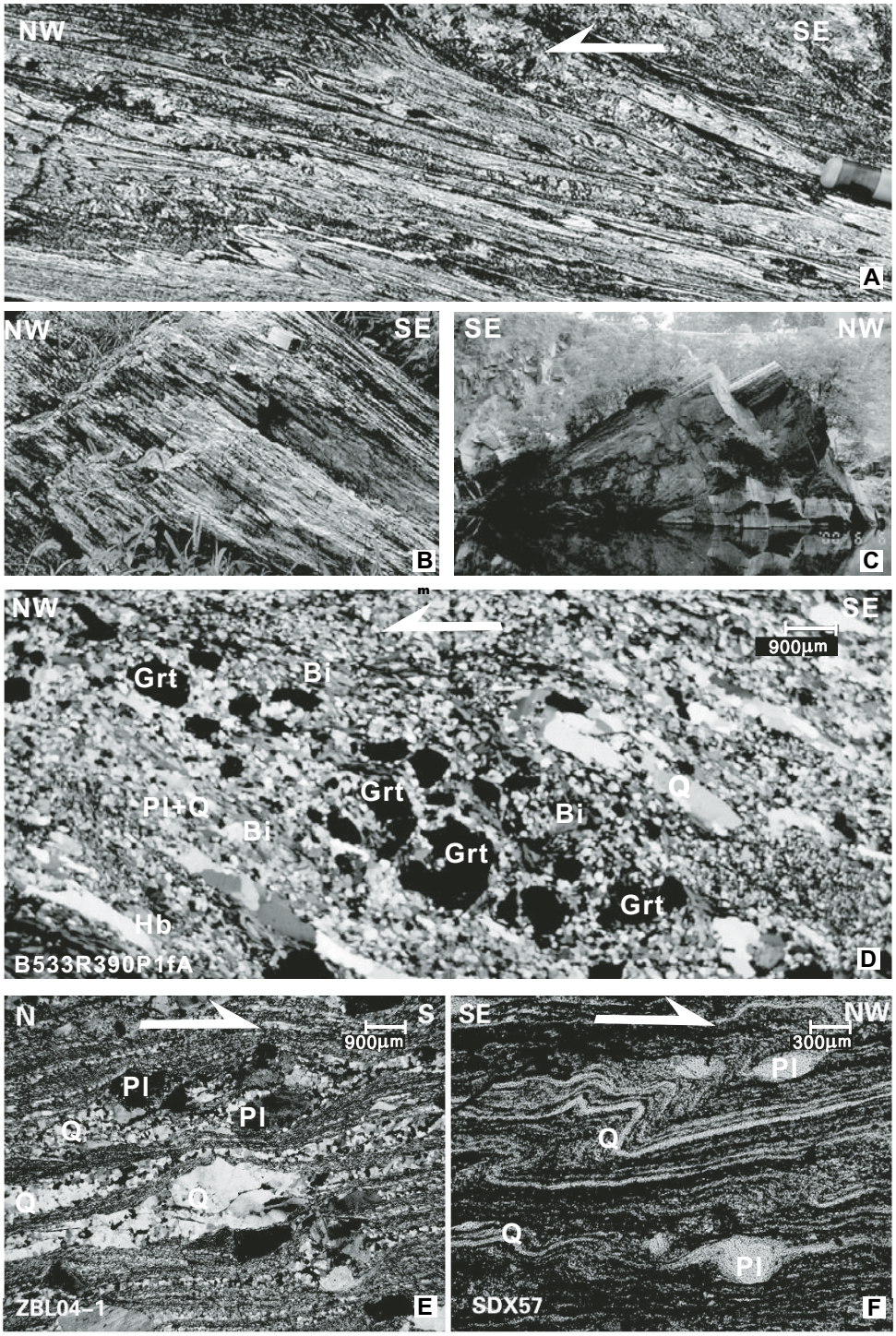

Figure 7. Field and microphotographs showing the nature of ductile deformation in the Sulu high-pressure–ultrahigh-pressure (UHP) terrane. (A) Structures in the metavolcanic mylonite of ductile shear zone 2 (DF2) between the Guanyun (Ib) and Yuntaishan slice (Ic), indicating the top-NW shear sense. (B.) SE-dipping stretching lineation near Xugou of DF4. (C) Structures in the amphibolite of DF6 between Lianyungang slice (IIIa) and Maobei slice (IIIb) showing the shear deformation of the A-type fold. (D) Mylonitic paragneiss in DF8 from Chinese Continental Scientific Drilling Project (CCSD) core composed of garnet, hornblende, quartz, and biotite porphyroclasts (sample B533R390P1fA, 970.80 m). (E) Metavolcanic mylonite from Zhangbaling ductile detachment that has S-C fabric and plagioclase porphyroblasts suggesting top-S shear sense. (F) Ultramylonite from the Wulian-Weihai ductile detachment, in which σ- and δ-type porphyroclasts, as well as shear folds, indicate top-NW shear sense. Q—quartz; Pl—plagioclase; Q + Pl—felsic; Bi—biotite; Grt—garnet; Hb—hornblende.

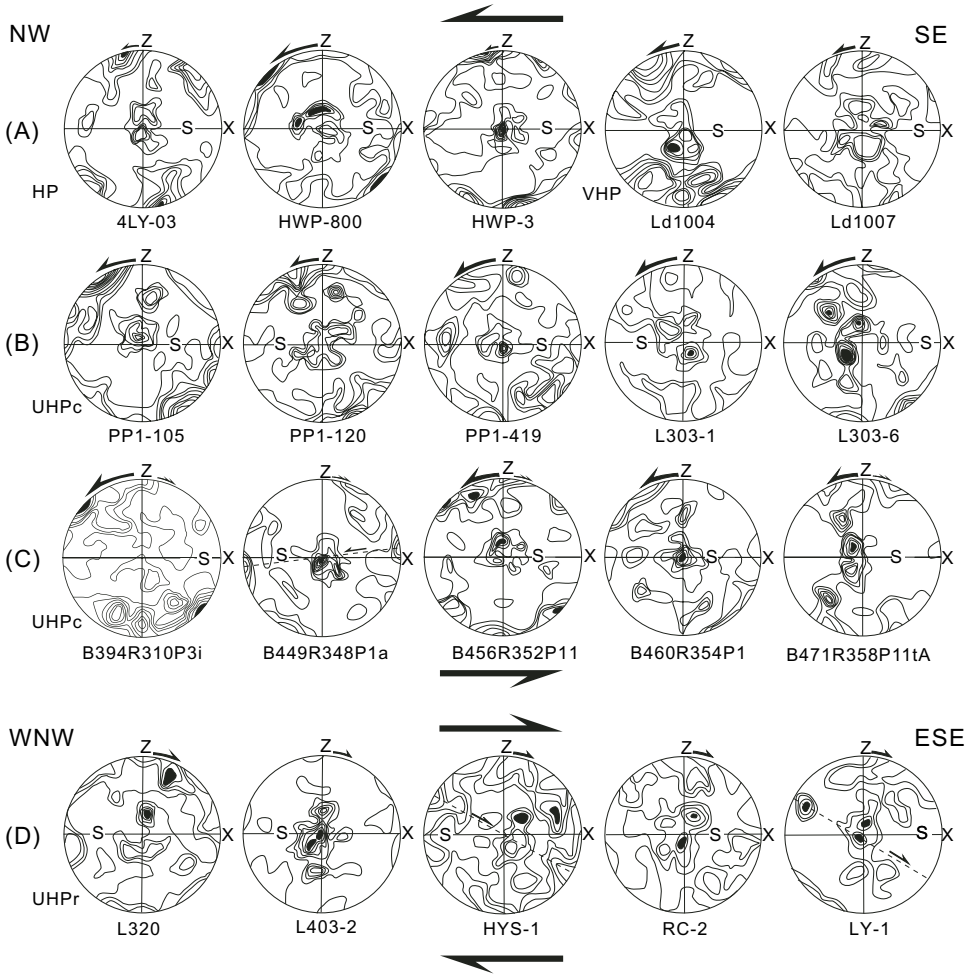

Figure 8. Lattice preferred orientations of quartz in the ductile shear zones from different structural units of the Sulu high-pressure–ultrahigh-pressure (UHP) terrane. (A) Samples 4LY-03, HWP-800, and HWP-3 from the high-pressure unit; Ld1004 and Ld1007 from the very high-pressure (VHP) unit; $N = 120$, contours at densities 0.8%, 1.7%, 2.5%, 3.3%, 4.2%, 5.0%, 5.8%, and 6.7%. (B) Samples PP1-105 (105 m), PP1-120(120 m), and PP1-419 (419 m) from Chinese Continental Scientific Drilling Project (CCSD) cores CCSD-PP1; L303-1, and L303-6 from surface in the UHP III unit; $N = 120$, contours at densities 0.8%, 1.7%, 2.5%, 3.3%, 4.2%, 5.0%, 5.8%, and 6.7%. (C) Samples B394R310P3i (748.9 m), B449R348P1a (838.65 m), B456R352P11 (851.50 m), B460R354P1 (856.95 m), and B471R358P11tA (873.67 m) from CCSD main hole in the UHP III unit; $N = 120$, contours at densities 0.8%, 1.7%, 2.5%, 3.3%, 4.2%, 5.0%, 5.8%, and 6.7%. (D) Samples L320, L403-2, HYS-1, RC-2, and LY-1 from the UHP IV unit; $N = 120$, contours at densities 0.8%, 1.7%, 2.5%, 3.3%, 4.2%, 5.0%, 5.8%, and 6.7%.

Shear Strain in the Northern Sulu UHP Slice

Seven structural slices and six ductile shear zones were identified in the northern Sulu UHP zones III and IV. They have penetrative foliations gently dipping SE to ESE. Rocks within these ductile shear zones include variably mylonitic granitic gneiss, metavolcanic gneiss, eclogite and marble with type-A folds, sheath folds, and two generations of folds. Microstructures, including asymmetric folds, S-C structures, and asymmetric strain shadows, mostly indicate top-NW shear, but in some areas top-SE shear sense is also observed. Mineral assemblages that formed concurrently with this stage of deformation—Kfs + Pl + Qtz + Mus + Bt + Ep, Kfs + Pl + Qtz + Grt + Bt + Ep, Kfs + Pl + Aeg + Bt, Pl + Qtz + Hbl + Bt ± Grt, and Kfs + Pl + Qtz + Ms + Bt—suggest deformation under amphibolite- to greenschist-facies conditions of 550–650 °C and 0.5–0.7 GPa. Additionally, some rocks within the shear zones exhibit various degrees of greenschist-facies overprinting at 300–400 °C and 0.30–0.35 GPa.

Three sample sets from the northern Sulu UHP slice were used to determine quartz lattice preferred orientation and deformation kinematics. The first set is from the CCSD-PP1 borehole and includes PP1-105, PP1-120 and PP1-419. The second

(L303 and L303-6) is from mylonitic paragneiss in shear zone DF6. The third (B394R310P3i, B449R348Pia, B456R352P11, B460R358P11tA, and B471R358P11tA) is from mylonitic paragneiss in DF7 of the main CCSD borehole. Quartz lattice preferred orientation studies show that, in addition to an intermediate- to low-*T* and low-*T* fabric of {10$\bar{1}$0}<a>, {10$\bar{1}\bar{1}$}<a>, and {0001}<a>, a high-*T* fabric (>650 °C) of {10$\bar{1}$0}<c> is present in samples PP1-419 and B449R348P1a. The lattice preferred orientation variation indicates that the ductile shear zones experienced shear during progressive cooling. The obliquities of the lattice preferred orientation concentrations indicate top-NW sense of shear, whereas the weak concentration of [0001] poles in the intermediate-temperature fabric is indicative of top from NW to SE shear, which may represent late brittle-ductile normal faulting (Fig. 8B–C).

To characterize the deformation kinematics in these UHP slices, quartz lattice preferred orientations were studied in samples L320 and L403-2 from DF10 and DF11 mylonitic granitic gneisses, and samples HyS-1, RC-2, and Ly-1 from zone IV in Rongcheng. These results (Fig. 8D) show that quartz fabrics in zone IV also record deformation at conditions varying from high-*T* {10$\bar{1}$0}<c>, intermediate-*T* {10$\bar{1}$0}<a>, intermediate–low-*T* {10$\bar{1}\bar{1}$}<a>, to low-*T* {0001}<a> fabric. These data also indicate top from WNW to ESE normal slip.

Our data show that ductile shear in the high-pressure–UHP slab during exhumation can be explained by extrusion with shear toward the NW or WNW at the top and toward the SE or ESE at the bottom.

Postexhumation Extension (D3)

Rocks from the Sulu high-pressure and UHP metamorphic slice experienced postexhumation extension accompanied by Mesozoic magmatism and the formation of continental sedimentary basins, signaling the transition to brittle deformation.

Wulian-Yantai Extensional Detachment

The NE-SW–striking Wulian-Yantai ductile shear zone is the northern boundary of the Sulu high-pressure–UHP terrane, separating the Sulu UHP zone from the Laiyan basin (Fig. 9). Granite mylonite and eclogite mylonite are abundant in this zone. Near Taolin in the NE, W-plunging stretching lineations occur on mylonite foliations that dip 20–25°W. Near Jiaozhou in the SW, stretching lineations trend at 60°NW with respect to the strike of mylonite foliations that dip 15–20°NW (Fig. 9B). S-C structures, σ and δ feldspar porphyroclasts, domino structures, and asymmetric drag folds of quartz bands indicate oblique-normal slip of the hanging wall. Quartz from five samples of granitic ultramylonites from Taoyuan and Taocun have lattice preferred orientations that suggest activity of the low-*T* (<350 °C) {0001}<a> slip system, and top-NW or -W shear sense (Fig. 9C). This slip system is compatible with the greenschist-facies retrogression common for the highly strained rocks within the Wulian-Yantai ductile shear zone. Movement on this fault contributed to the formation of the Cretaceous Laiyang basin and a NE-SW–trending antiform and facilitated emplacement of Mesozoic granites into the antiform. (Wang et al., 2005).

NW-SW–Trending Upright Concentric Folds

Upright flexural box folds with NW-SE–trending axial planes occur in the SE limb of the antiform in the UHP zone III. Axial cleavage is not well developed in these folds, which presumably formed at relatively shallow depths. Near Yushan and Sanqingge of Shilianghe slice IIId, these upright folds are superimposed on top-SE ductile shear zones. The upright concentric folds were formed during NE-SW contraction and NW-SE extension. These folds and the Wulian-Yantai ductile décollement shear zone appear to have formed in the same stress field.

In summary, our data presented herein indicate four types of quartz lattice preferred orientation in samples from the surface as well as from the CCSD boreholes. Some of the samples clearly have low-*T* fabric superimposed on the earlier high-*T* fabric. The data imply that these quartz-bearing rocks have undergone early high-*T* deformation, versus intermediate-*T* and intermediate- to low-*T*, and latest low-*T* deformation. Such a pattern is consistent with *P-T* paths inferred from metamorphic mineral assemblages (Fig. 10). The Sulu high-pressure–UHP metamorphic belt has experienced three episodes of deformation: (1) subduction-stage ductile deformation (D1), in which the high-pressure zone and UHP zone have undergone ductile deformation in corresponding peak metamorphic conditions; (2) exhumation-stage ductile deformation (D2); and (3) postexhumation deformation (D3). The latter two episodes of deformation have reworked and overprinted the earliest D1 deformation.

TIMING OF EXHUMATION OF THE SULU HIGH-PRESSURE–UHP METAMORPHIC BELT

To better constrain the timing and sequence of exhumation of the Sulu high-pressure–UHP slice, we dated biotite and muscovite from various rock types by $^{40}Ar/^{39}Ar$. These new data, in conjunction with published ages, help constrain the tectonic evolution of the Sulu high-pressure–UHP metamorphic slice.

Formation and Exhumation of Sulu UHP Metamorphic Terrane

The $^{40}Ar/^{39}Ar$ ages of biotites from the ductile shear zones in the CCSD main borehole were measured at the Guangzhou Institute of Geochemistry. The plateau ages of biotites from samples B475R359P3v (891 m), B527R388P1f (960 m), B608R432P1f (1097 m), and B627R441P3n (1130 m) of CCSD-MH cores range from 200.9 ± 1.1 to 214.1 ± 4.3 Ma, with corresponding isochron ages from 198.2 ± 3.9 to 218.7 ± 4.4 Ma (Table 2; Fig. 11A–B). These data are similar to those of Li et al. (2003) and Liu et al. (2004a), suggesting retrograde metamorphism at 220, 213, and 204 Ma (see also Webb et al., this volume). These results and our new biotite $^{40}Ar/^{39}Ar$ age

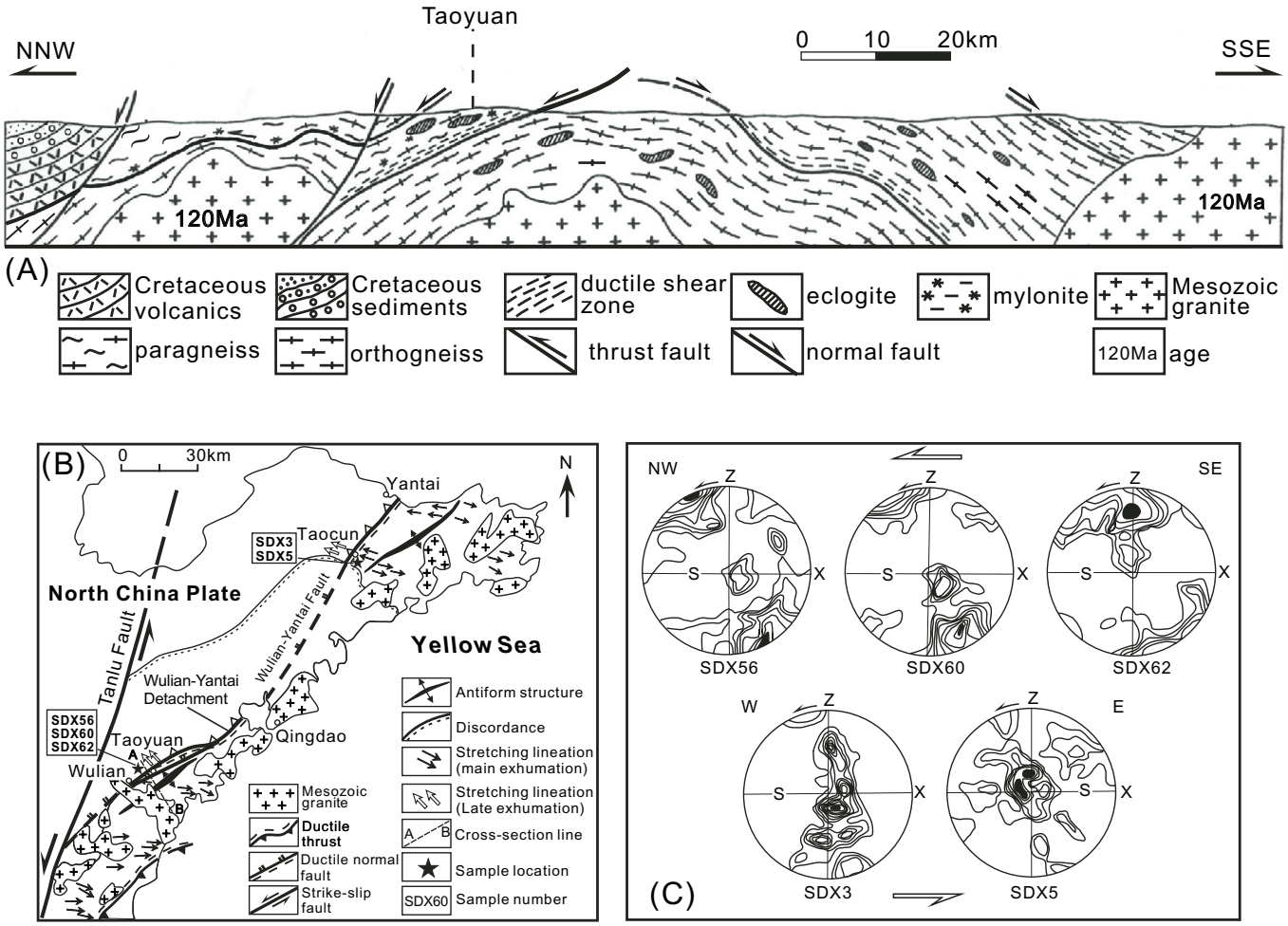

Figure 9. Cross section (A) and simplified geologic map (B) showing the major structures in the Sulu ultrahigh-pressure (UHP) IV zone. Quartz lattice preferred orientations for the Wulian-Yantai ductile detachment are shown in C. Samples SDX56, SDX60, and SDX62 are from Taoyuan, SW of the Wulian-Yantai detachment fault; samples SDX3 and SDX5 are from Taocun, NE of the Wulian-Yantai detachment fault.

data indicate that the earliest exhumation of the UHP rocks occurred at 220–200 Ma. The short interval between UHP metamorphism and early exhumation implies very rapid exhumation.

Age Constraints on the Exhumation of the Sulu High-Pressure Metamorphic Zone

Biotite and muscovite from the ductile shear zones of the high-pressure slice were dated at Stanford University. Biotite from sample L806 in Yuntaishan slice Ic does not yield a formal plateau age. A good estimate of the $^{40}Ar/^{39}Ar$ closure age of this biotite is its weighted mean age of 232.5 ± 2.4 Ma, with a corresponding isochron age of 232.9 ± 2.5 Ma (mean square of weighted deviates [MSWD] = 6.3, $^{40}Ar/^{36}Ar$ = 178 ± 70 Ma). Biotites from samples LYG1025-08 and LYG-20 in the Yuntaishan slice yield formal plateau ages of 253.8 ± 2.6 and 243.9 ± 2.6 Ma, and isochron ages of 254.0 ± 2.7 Ma (MSWD = 1.2, $^{40}Ar/^{36}Ar$ = 279 ± 23) and 244.2 ± 2.6 Ma (MSWD = 0.7, $^{40}Ar/^{36}Ar$ = 262 ± 28), respectively (Fig. 12). We analyzed muscovite from samples HWP-33 and SDX80 separated from gneiss and schist of the Yuntaishan slice by $^{40}Ar/^{39}Ar$, yielding weighted mean ages of 214.2 ± 2.3 and 218.7 ± 2.3 Ma and isochron ages of 213.8 ± 2.7 (MSWD = 5.52, $^{40}Ar/^{36}Ar$ = 307 ± 27) and 218.8 ± 2.4 Ma (MSWD = 1.41, $^{40}Ar/^{36}Ar$ = 293 ± 18) for muscovites from HWP-33 and SDX80, respectively (Table 3). These ages indicate that exhumation of the Sulu high-pressure slice started from 254 to 232 Ma to 214 Ma, earlier than the Sulu UHP slice (220–200 Ma; Fig. 12C–D), similar to the results of Li et al. (2000b).

Muscovite from the Wulian-Yantai ductile detachment yielded a $^{40}Ar/^{39}Ar$ isochron age of 148.7 ± 2.6 Ma and a plateau age of 146.7 ± 0.9 Ma (Yang et al., 2002), similar to the Cretaceous depositional age of the Laiyang sedimentary basin. This relationship suggests that normal slip along the Wulian-Yantai shear zone contributed to the formation and evolution of

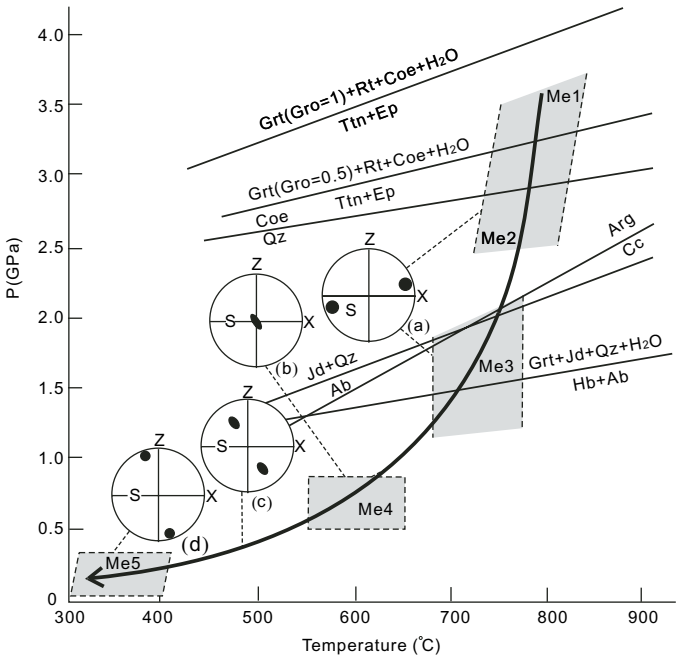

Figure 10. Relation between retrograde pressure-temperature (*P-T*) path and quartz lattice preferred orientations of Donghai ultrahigh-pressure (UHP) gneiss. Me2—first exhumation stage, T = 750–850 °C, P = 2.5–2.8 GPa; Me3—second exhumation stage, T = 680–780 °C, P = 1.2–1.8 GPa; Me4—third exhumation stage, T = 550–650 °C, P = 0.5–0.7 GPa; Me5—latest exhumation stage, T = 300–400 °C, P = 0.3–0.35 GPa. (a) High-T fabric of quartz with slip system of {10$\bar{1}$0}<c> (T > 650 °C). (b) Intermediate-T fabric of quartz with slip system of (10$\bar{1}$0) <a> (T = 550–650 °C). (c) Low–intermediate-T fabric of quartz with slip system of (10$\bar{1}\bar{1}$) <a> (T = 450–550 °C). (d) Low-T fabric of quartz with slip system of {0001} <a> (T < 400 °C). Mineral abbreviations are from Kretz (1983).

the Laiyang basin. Formation of an antiform in the slice III–IV, emplacement of a number of Mesozoic granitic plutons (210–101 Ma), and the occurrence of NW-SE–trending upright concentric folds testify to extensional deformation during the late exhumation of the Sulu UHP terrane.

DISCUSSION AND CONCLUSION

Surface samples and CCSD drill cores of the Sulu UHP rocks vary in composition and metamorphic grade (Zhang et al., 2000, 2004, 2005; Liu et al., 2004c). The eclogite and country rocks experienced in situ UHP metamorphism when large tracts of continental crust were subducted to >100 km and later exhumed (Liu et al., 2004c). The mechanism by which deeply subducted continental crust is exhumed and returned to Earth's surface is a challenging research problem (Ernst and Liou, 1999). Various hypotheses have been proposed to explain the rapid exhumation of UHP metamorphic rocks, including eroding and floating (Platt, 1993), extension (Harrison, 1992), vertical extrusion (Chemenda et al., 1995, 1996; Maruyama et al., 1994), and upper-crust extension and lower-crust shortening (Anderson et al., 1990; Ballevere et al., 1990). Chemenda et al. (1995, 1996) suggested that rocks that experience UHP metamorphism become relatively soft and are squeezed from the subduction channel by plate convergence. In the Dabie-Sulu area, models of extrusion and extension (Faure et al., 2001; Maruyama et al., 1994) have been invoked for the exhumation of this UHP metamorphic slice. Hacker et al. (2004) suggested that in Late Permian–Early Triassic times, the northern edge of the South China plate was subducted to >150 km, creating UHP metamorphic rocks of the Dabie and Sulu slice; exhumation by extension occurred between 245 and 195 Ma during clockwise rotation of the craton. All these models assume subduction and exhumation of an intact continental slab.

Recent petrologic, geochemical, structural, and seismic studies have generated new data that enable us to examine the tectonics of the Sulu high-pressure–UHP metamorphic slices in greater detail:

TABLE 2. $^{40}Ar/^{39}Ar$ AGES FOR BIOTITES AND MUSCOVITES FROM THE SULU HIGH PRESSURE AND ULTRAHIGH-PRESSURE BELTS

Sample	Depth (m)	Location	Tectonic unit	Host Rock	Mineral	Plateau age	Isochron age
B475R359P3v	891	Maobei CCSD	UHP (III)	Mylonitic paragneiss	Biotite	210.9±1.1 Ma	218.7±4.4 Ma
B527R388P1f	960	Maobei CCSD	UHP (III)	Mylonitic paragneiss	Biotite	214.1 ± 4.2 Ma	214.1±4.3 Ma
B608R432P1f	1097	Maobei CCSD	UHP (III)	Mylonitic paragneiss	Biotite	200.9±1.1 Ma	198.2±4.0 Ma
B627R441P3n	1130	Maobei CCSD	UHP (III)	Mylonitic paragneiss	Biotite	202.4±1.0 Ma	201.1±3.0 Ma
LYG-20	0	Pingshan, Lianyungang	HP (I)	Mylonitic Ep-Pl-gneiss	Biotite	243.7±2.5 Ma	244.2±2.6 Ma
LYG-1025-08	0	Xueqigou, Lianyungang	HP (I)	Mylonitic Ep-Pl-gneiss	Biotite	254.11±2.6 Ma	254.0±2.7 Ma
HWP-33	0	Dongxiliandao, Lianyungang	HP (I)	Mylonitic Ep-Pl-gneiss	Muscovite	215.1±2.3 Ma	213.8±2.7 Ma
SDX-80	0	Ganyu	HP (I)	Pl-gneiss	Muscovite	218.4±2.3 Ma	218.8±2.7 Ma

Note: $^{40}Ar/^{39}Ar$ biotite and muscovite dating performed at Guangzhou Institute of Geochemistry, Chinese Academy of Sciences, and Stanford University. CCSD—Chinese Continental Scientific Drilling Project; HP—high pressure; UHP—ultrahigh-pressure; Ep—epidote; Pl—plagioclase.

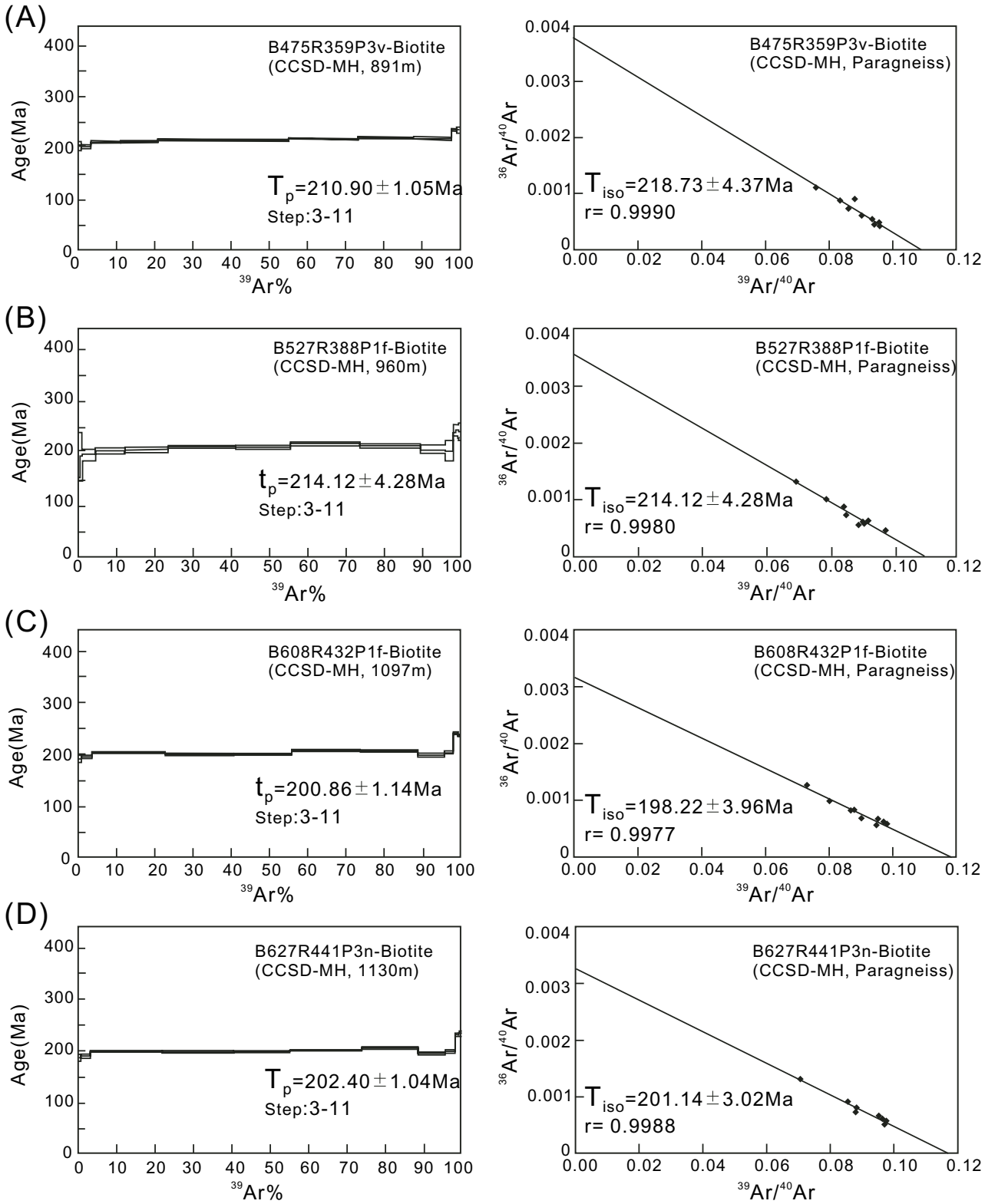

Figure 11. ^{40}Ar/^{39}Ar isochron and plateau ages of biotite from the Chinese Continental Scientific Drilling Project (CCSD) main hole in the ultra-high-pressure (UHP) III zone: (A) sample B475R359P3v (891 m); (B) sample B527R388P1f (960 m); (C) sample B608R432P1f (1097 m); and (D) sample B627R441P3n (1130 m).

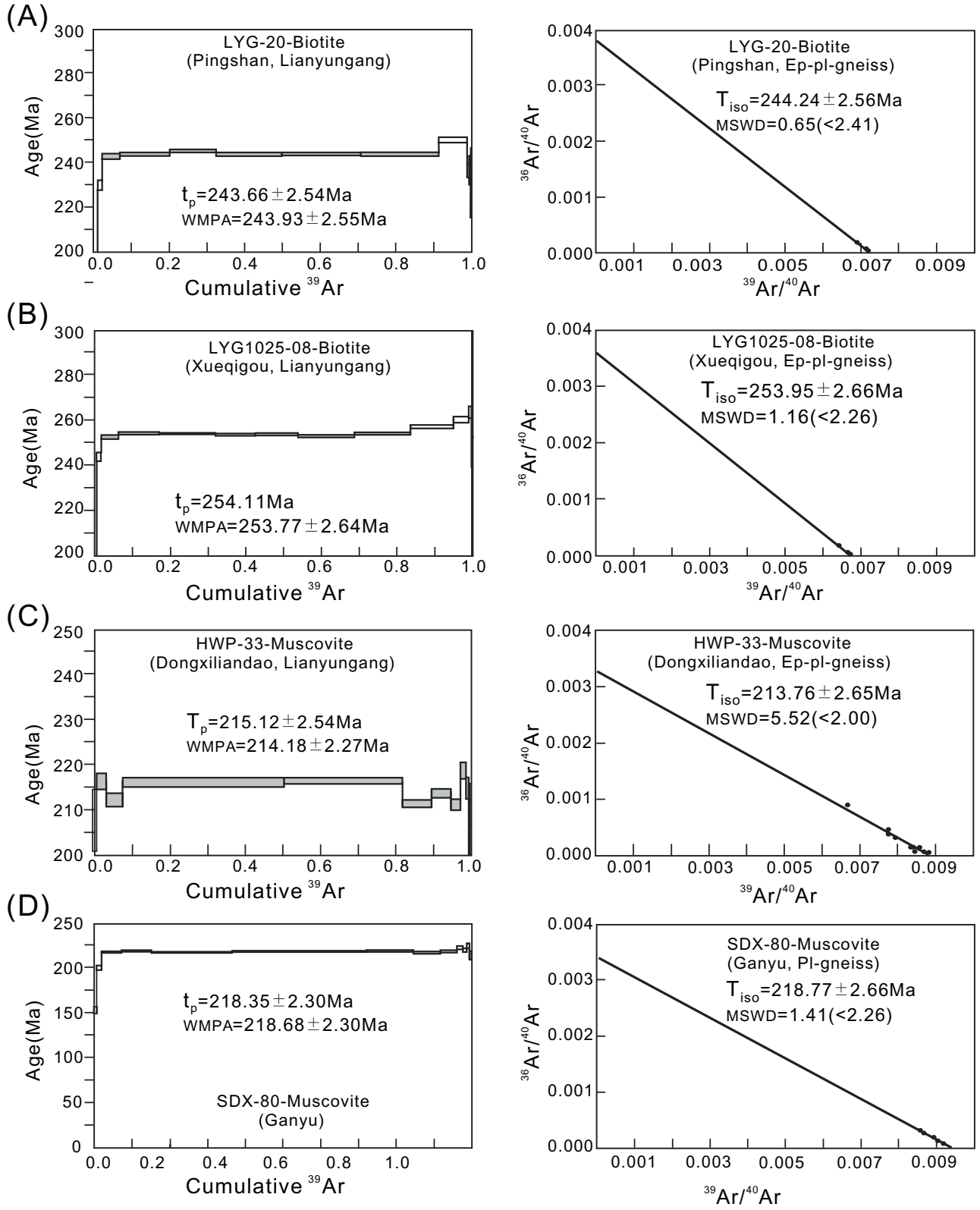

Figure 12. ^{40}Ar/^{39}Ar isochron and plateau ages of biotite and muscovite from ductile shear zones in the high-pressure zone: (A) sample LYG-20; (B) sample LYG-102-08; (C) sample HWP-33; and (D) sample SDX-80. MSWD—mean square of weighted deviates, WMPA—weighted mean plateau age.

TABLE 3. SUMMARY OF RADIOMETRIC DATA ON THE SULU HIGH PRESSURE (I) AND ULTRAHIGH-PRESSUREP (III AND IV) METAMORPHIC BELTS FROM PREVIOUS STUDIES

Location	Host Rock	Method	Age (Ma)	Reference
Sulu UHP belt IV				
Weihai	Garnet peridotite	SHRIMP U/Pb Zircon	225 ± 5 Ma	Yang et al., 2003
Rongcheng	Garnet peridotite	SHRIMP U/Pb zircon	229±39 Ma	Yang et al., 2003
Majiagou, Rizhao	Eclogite	Sm-Nd whole rock	209 ~211 Ma	Li et al., 1993
Zhubian	Eclogite	Sm-Nd whole rock	228±6 Ma	Li et al., 1993
Yangkou, Rizhao	Eclogite	U-Pb zircon	202±13Ma	Li et al., 1993
Linshu	Eclogite	U-Pb zircon	217.1±8.7 Ma	Ames et al., 1996
Yangkou, Rizhao	Eclogite	U-Pb zircon	224±14 Ma	Zheng et al., 2004
Lanshantou, Rizhao	Eclogite	U-Pb zircon	224 ± 27 Ma	Zheng et al., 2004
Sulu UHP belt III				
Qinglongshan, Donghai	Eclogite	Sm-Nd whole rock	226 ± 3 Ma	Li et al., 1993
Qinglongshan, Donghai	Eclogite	U-Pb zircon	218 ± 16 Ma	Zheng et al., 2004
Qinglongshan, Donghai	Orthogneiss	U-Pb zircon	221 Ma	Rumble et al., 2002
Zhimafang, Fangshan	Garnet peridotite	U-Pb zircon	216–233 Ma	Rumble et al., 2002
CCSD-PP2, Donghai	Orthogneiss	SHRIMP U/Pb zircon-mantle & core	232 ± 4.0Ma	Liu et al., 2004b
CCSD-PP2, Donghai	Paragneiss	SHRIMP U/Pb zircon-mantle & core	228 ± 5.0 Ma	Liu et al., 2004b
CCSD-PP2, Donghai	Orthogneiss	SHRIMP U/Pb zircon-rim	213 ± 5.0 Ma	Liu et al., 2004b
CCSD-PP2, Donghai	Paragneiss	SHRIMP U/Pb zircon-rim	208 ± 4.0 Ma	Liu et al., 2004b
CCSD-MH, Donghai	Orthogneiss	SHRIMP U/Pb zircon	227 ± 2.0 Ma	Liu et al., 2004c
CCSD-MH, Donghai	Orthogneiss	SHRIMP U/Pb zircon-rim	209 ± 3.0 Ma	Liu et al., 2004c
Niushan, Donghai	Eclogite	$^{40}Ar/^{39}Ar$ amphibole	213.4 ± 4.1 Ma	Li et al., 2003
Fangshan, Donghai	Eclogite	$^{40}Ar/^{39}Ar$ biotite	200.6 ± 3.1Ma	Li et al., 2003
Fangshan, Donghai	Eclogite	$^{40}Ar/^{39}Ar$ biotite	204 ± 2.0 Ma	Li et al., 2003
Sulu HP belt I				
Zhangbaling	Eclogite	$^{40}Ar/^{39}Ar$ Biotite	245.1 ± 0.5 Ma	Li et al., 1993

Note: CCSD—Chinese Continental Scientific Drilling Project; SHRIMP—sensitive high-resolution ion microprobe; HP—high pressure; UHP—ultrahigh-pressure.

(1) The paragneiss, granitic gneiss, marble, and quartzite that host the eclogite and ultramafic blocks and lenses account for ~95% of the Sulu slices. In these country rocks, coesite inclusions and other UHP diagnostic minerals are common in zircon (Liu et al., 2002, 2004b), demonstrating that large amounts of Yangtze craton continental crust was subducted below 100 km under the Sino-Korean craton at 240–220 Ma.

(2) The Sulu high-pressure and UHP slices preserve structures formed at crustal to mantle depths, corresponding to transitions from high-pressure–low-temperature, through very high-pressure–middle-temperature, to UHP metamorphism. As discussed above, the Sulu UHP belt can be subdivided into the supracrustal rock–dominant UHP III zone and granitic rock–dominant UHP IV zone, which is not only well expressed at the surface but also in the 5180 m CCSD borehole (Fig. 1). Such a stratigraphic relationship might suggest an original vertical crustal section of shallower supracrustal rocks underlain by granitic rocks. Both rock types were intruded by basaltic or gabbroic magma, the protolith of eclogites (Jahn, 1998). SHRIMP U-Pb zircon dating of Sulu high-pressure rocks suggests that the protoliths of eclogite and granitic gneiss formed at 700–800 Ma (see summaries in Leech et al., this volume, and Hacker et al., this volume; Liu et al., 2004b; Zheng et al., 2004). Together with the field relationships among eclogite, paragneiss, and granitic gneiss, these ages suggest that the eclogite protoliths were mafic magmas intruded into the country rocks as dikes or sills.

(3) A seismic refraction profile across the Sulu high-pressure–UHP terrane (Fig. 2) reveals an eroded dome or slab 10 km deep at its center and 15 km wide (Yang et al., 2004). UHP rocks dominate the core of this slab. High-pressure slices I, II, and III successively overlie the UHP slice and dip to the SE. To its NW, a high-pressure slice dipping to the NW overlies the UHP slice. Atop the UHP IV slab, shear sense is top from SE to NW (Fig. 10). Shear sense is top-SE at its bottom, suggesting that the whole slab experienced southeastward extrusion along the subduction channel. A strong N-dipping seismic reflector at depths of 18–20 km near Donghai may represent an intermediate-level detachment separating the Sulu high-pressure–UHP rocks from Yangtze continental rocks.

(4) Radiometric data from numerous U-Pb, Sm/Nd, and Rb/Sr studies (Table 3; Fig. 13) suggest that peak UHP metamorphism in the Sulu area occurred between 200 and 240 Ma (Liu et al.. 2004a; see summaries in Leech et al., this volume, and Hacker et al., this volume). The high-pressure metamorphic slice formed before 250 Ma and was exhumed from 250 to 210 Ma; subduction and exhumation of the high-pressure slices occurred earlier (240–220 Ma and 220–200 Ma, respectively) than in the UHP metamorphic slice.

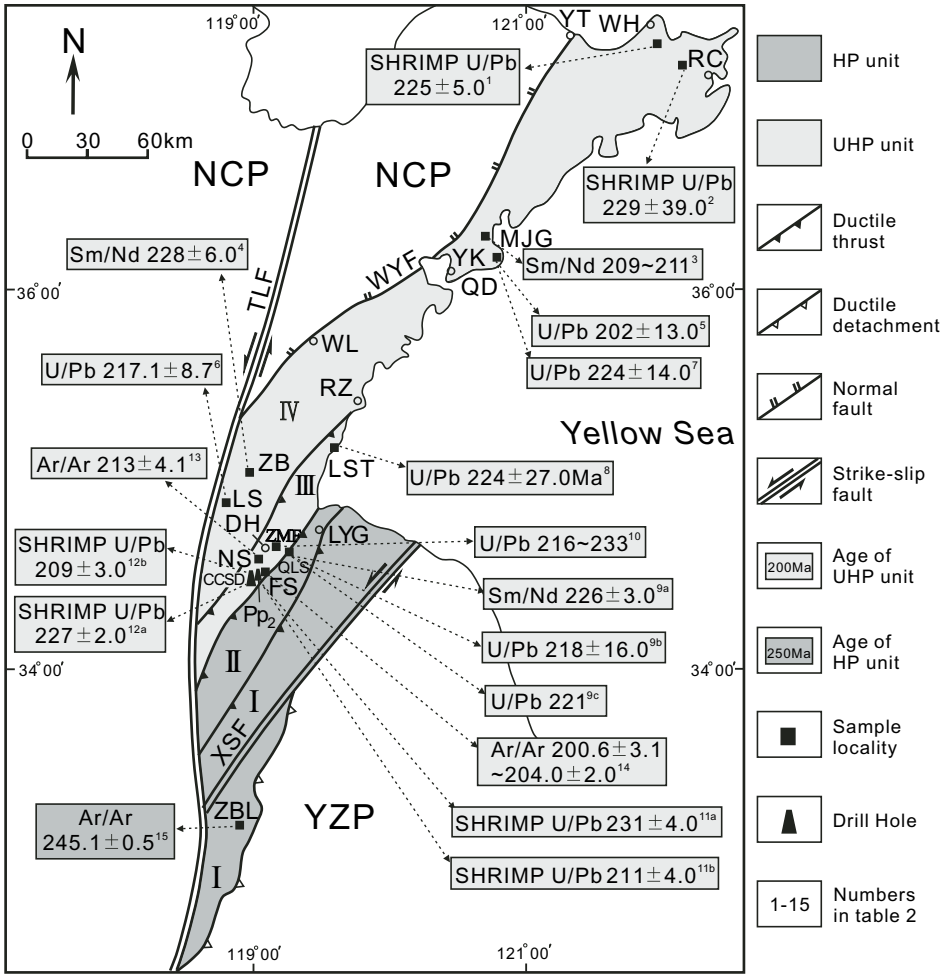

Figure 13. Summary of previous dating results using different methods in the Sulu high-pressure–ultrahigh-pressure (UHP) metamorphic terrane. For each location, dating method and corresponding result are shown in the box. CCSD—Chinese Continental Scientific Drilling Project site, TLF—Tan-Lu fault, XSF—Xiangshui fault, WYF—Wulian-Yantai fault, YT—Yantai, WH—Weihai, RC—Rongcheng, WL—Wulian, MJG—Majiagou, YK—Yangkou, QD—Qingdao, RZ—Rizhao, LST—Lanshantou, ZB—Zhubian, LS—Linshu, DH—Donghai, LYG—Lianyungang, ZMF—Zhimafang, NS—Niushan, QLS—Qinglongshan, FS—Fangshan, and ZBL—Zhangbaling.

These data suggest a working model that incorporates observations from surface geology and the CCSD boreholes. Prior to 250 Ma, passive-margin rocks from the leading edge of the Yangtze craton were subducted beneath the Sino-Korean craton. Sedimentary and granitic rocks, together with the enclosing mafic and ultramafic materials, were subducted and experienced variable high-pressure to UHP metamorphism.

Several lines of evidence imply a difference in timing of metamorphism between the Sulu high-pressure and UHP rocks. The four slices are separated by major ductile shear zones (Fig. 1). While the overall structural relations among these zones have been reworked by exhumation (particularly Mesozoic extension and intrusion of granitic plutons), their original relationship is probably similar to that observed today. Rocks in the high-pressure zone experienced metamorphism at 300–360 °C and 0.7–0.85 GPa, equivalent to subduction to a depth of 30 km. In contrast, rocks in the UHP zone experienced peak metamorphism at pressures equivalent to depths >100 km. Radiometric data indicate that high-pressure rocks underwent high-pressure metamorphism and were exhumed beginning at ca. 250 Ma and 254–232 Ma, respectively, substantially before the 220–240 Ma and 200–220 Ma ages observed for UHP rocks.

Based on the observations presented herein, we propose an alternate model (Fig. 14) for the formation and exhumation of the Sulu high-pressure–UHP metamorphic slice. High-pressure rocks represent the uppermost crustal rocks of the Yangtze craton. Because of their low density, they were only subducted to ~30 km, underwent peak high-pressure metamorphism at ca.

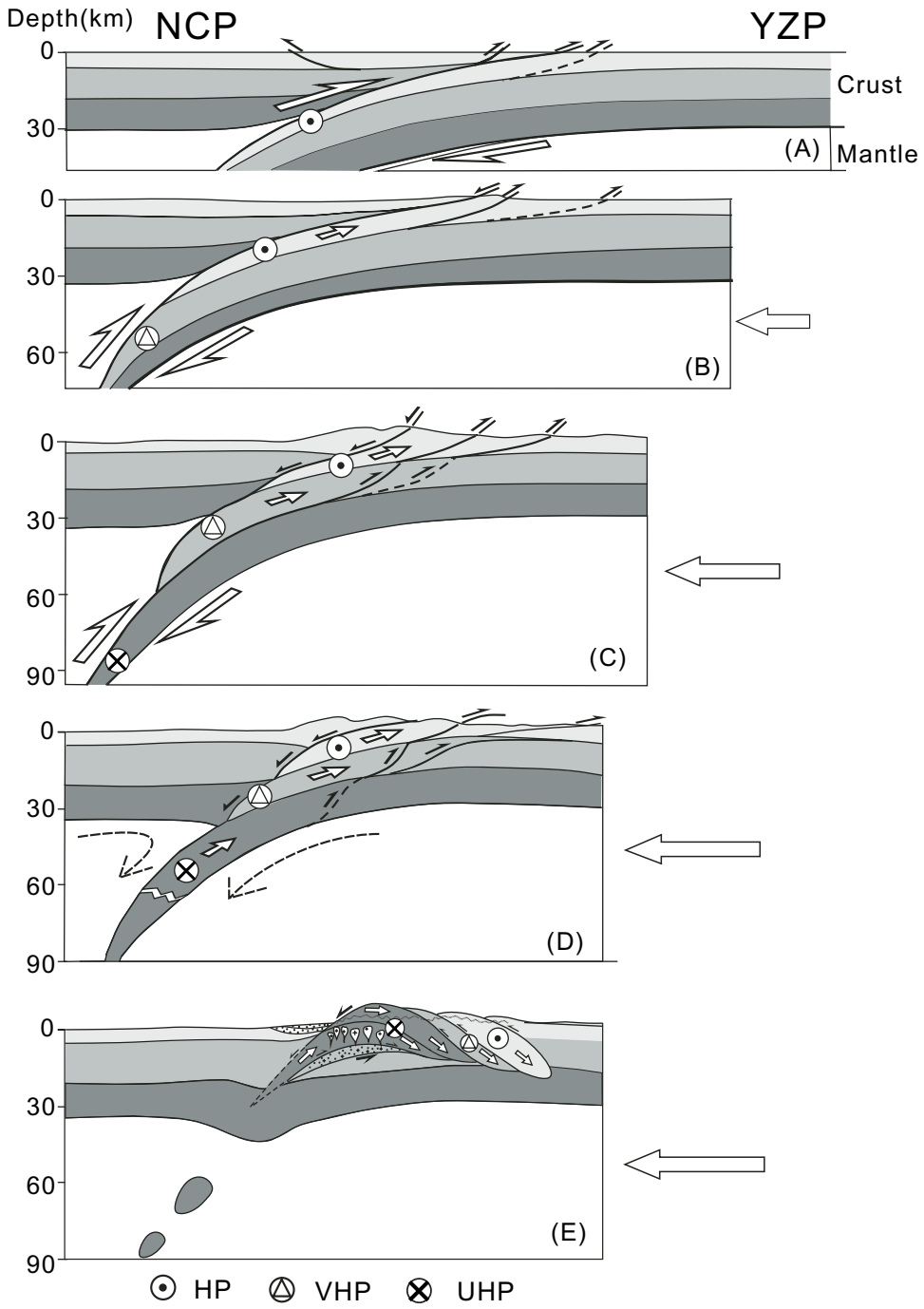

Figure 14. Model for the differential subduction and exhumation of a continental lithosphere proposed in this study: (A) older than 253 Ma, high-pressure (HP) rocks were formed at 30 km depth; (B) 250–240 Ma, very high-pressure (VHP) rocks were formed ~60 km deep, and the onset of exhumation of the high-pressure slabs occurred; (C) 240–220 Ma, ultrahigh-pressure (UHP) rocks were formed at ~100 km depth, and in contrast, very high-pressure and high-pressure slabs were exhumed; (D) 220–200 Ma, high-pressure, very high-pressure, and UHP slabs were exhumed; (E) postcollisional deformation resulted in a series of top-S thrusts and the antiform structure of the Sulu high-pressure–ultrahigh-pressure (UHP) metamorphic belt. NCP—North China plate (Sino-Korean craton), YZP—Yangtze craton (plate).

250 Ma, and began to be exhumed along the subduction channel as early as 232 Ma. In contrast, UHP rocks representing deeper levels in the Yangtze craton were denser and more easily subducted. They experienced peak UHP metamorphism below 80 km at 240–220 Ma and started exhumation at 220–200 Ma.

ACKNOWLEDGMENTS

This work was supported by Chinese National Science Foundation grant 40399141, Ministry of Science and Technology through a 973 National Basic Research Project 2003CB716500 and Chinese Geological Survey grant 121201056606. This is a China–United States cooperative project supported by National Science Foundation (NSF) grant EAR-003355. We thank Bradley Hacker, Mary Leech, Martin Wong, and an anonymous reviewer for critical and thoughtful reviews. Thanks are due to Fangyuan Chen, Fenghua Liang, and Xiaowei Zhang for their help in preparation of the figures.

REFERENCES CITED

Ames, L., Tilton, G.R., and Zhou, G., 1993, Timing of collision of the Sino-Korean and Yangtze cratons: U-Pb zircon dating of coesite-bearing eclogites: Geology, v. 21, p. 339–342, doi: 10.1130/0091-7613(1993)021<0339:TOCOTS>2.3.CO;2.

Ames, L., Zhou, G., and Xiong, B., 1996, Geochronology and isotopic character of ultrahigh-pressure metamorphism with implications for collision of the Sino-Korean and Yangtze cratons, central China: Tectonics, v. 15, p. 472–489, doi: 10.1029/95TC02552.

Anderson, T.B., and Jamerit, B., 1990, Uplift of deep crust during orogenic extensional collapse: A model based on field studies in the Sogn-Sunnfjord region of western Norway: Tectonics, v. 9, p. 1097–1111.

Ballevere, M., Lagabrille, Y., and Merlr, O., 1990, Tertiary ductile normal faulting as a consequence of lithospheric stacking in the Western Alps: Mémoires de la Société Géologique de France, v. 156, p. 227–236.

Chemenda, A.I., Mattauer, M., Malavielle, J., and Bokun, A.N., 1995, A mechanism for syn-collisional rock exhumation and associated normal faulting: Results from physical modeling: Earth and Planetary Science Letters, v. 132, p. 225–232, doi: 10.1016/0012-821X(95)00042-B.

Chemenda, A.I., Mattauer, M., and Bokun, A.N., 1996, Continental subduction and a mechanism for exhumation of high-pressure metamorphic rocks: New modeling and field data from Oman: Earth and Planetary Science Letters, v. 143, p. 173–182, doi: 10.1016/0012-821X(96)00123-9.

Chopin, C., 2003, Ultrahigh-pressure metamorphism: Tracing continental crust into the mantle: Earth and Planetary Science Letters, v. 212, p. 1–14, doi: 10.1016/S0012-821X(03)00261-9.

Cong, B.L., and Wang, Q.C., 1999, The Dabie-Sulu UHP rocks slice: Review and prospect: Chinese Science Bulletin, v. 44, p. 1074–1085.

Ernst, W.G., 2001, Subduction, ultrahigh-pressure metamorphism, and regurgitation of buoyant crustal slices—Implications for arcs and continental growth: Physics of the Earth and Planetary Interiors, v. 127, p. 253–275, doi: 10.1016/S0031-9201(01)00231-X.

Ernst, W.G., and Liou, J.G., 1999, Overview of UHP metamorphism and tectonics in well-studied collisional orogens: International Geology Review, v. 41, p. 477–493.

Ernst, W.G., Maruyama, S., and Wallis, S., 1997, Buoyancy-driven, rapid exhumation of ultrahigh-pressure metamorphosed continental crust: Proceedings of the National Academy of Sciences of the United States of America, v. 94, p. 9532–9537, doi: 10.1073/pnas.94.18.9532.

Faure, M., Lin, W., and Le Breton, N., 2001, Where is the North China–South China block boundary in eastern China?: Geology, v. 29, p. 119–122, doi: 10.1130/0091-7613(2001)029<0119:WITNCS>2.0.CO;2.

Faure, M., Lin, W., Monie, P., Le Breton, N., Poussineau, S., Panis, D., and Deloule, E., 2003, Exhumation tectonics of the ultrahigh-pressure metamorphic rocks in the Qinling orogen in east China: New petrological-structural-radiometric insights from the Shandong Peninsula: Tectonics, v. 22, p. 1018, doi: 10.1029/2002TC001450.

Hacker, B.R., Ratschbacher, L., Webb, L., Ireland, T., Walker, D., and Dong, S., 1998, U/Pb zircon ages constrain the architecture of the ultrahigh-pressure Qinling-Dabie orogen, China: Earth and Planetary Science Letters, v. 161, p. 215–230, doi: 10.1016/S0012-821X(98)00152-6.

Hacker, B.R., Ratschbacher, L., and Liou, J.G., 2004, Subduction, collision and exhumation in the ultrahigh-pressure Qinling-Dabie orogen, *in* Malpais, J., Fletcher, C.J.N., Ali, J.R., and Aitchison, J.C., eds., Aspects of the tectonic evolution of China: Geological Society of London Special Publication 226, p. 157–175.

Harrison, C.G.A., 1992, Rates of continental erosion and mountain building: Abstracts of the 29th International Geologic Congress, Kyoto, Japan, v. 1, p. 95.

Jahn, B.M., 1998, Geochemical and isotopic characteristics of UHP eclogites and ultramafic rocks of the Dabie orogen, *in* Hacker, B.R., and Liou, J.G., eds., When continents collide: Geochemistry of ultrahigh-pressure rocks: Dordrecht, Kluwer Academic Publishers, p. 203–239.

Ji, S.C., 1988, Tectonic significance of partial melting (1) Experiment study on transition of deformation mechanism: Acta Geoscientia Sinica, v. 4, p. 347–356.

Jung, H., and Karato, S., 2001, Water-induced fabric transitions in olivine: Science, v. 293, p. 1460–1463, doi: 10.1126/science.1062235.

Kretz, R., 1983, Symbols for rock-forming minerals: The American Mineralogist, v. 68, p. 277–279.

Li, J.Y., Yang, T.N., Chen, W., and Zhang, S.H., 2003, $^{40}Ar/^{39}Ar$ dating of deformation events and reconstruction of exhumation of ultrahigh-pressure metamorphic rocks in Donghai: East China: Acta Geologica Sinica, v. 77, p. 155–168.

Li, S.G., Hart, S.R., Zhang, S.G., Liu, D.L., Zhang, G.W., and Guo, A.L., 1989, Timing of collision between north and south China blocks—The Sm-Nd isotopic age evidence: Science in China, v. 32, p. 1393–1400.

Li, S.G., Xiao, Y.L., Liu, D.L., Chen, Y.Z., Ge, N.J., Zhang, Z.Q., Sun, S.S., Cong, B.L., Zhang, R.Y., Hart, S.R., and Wang, S.S., 1993, Collision of North China and Yangtze blocks and formation of coesite-bearing eclogites: Timing and processes: Chemical Geology, v. 109, p. 89–111, doi: 10.1016/0009-2541(93)90063-O.

Li, S.G., Jagoutz, E., Xiao, Y.L., Ge, N.J., and Chen, Y.Z., 1996, Chronology of ultrahigh-pressure metamorphism in the Dabie Mountains and Sulu terrane: Science in China, ser. D, Earth Science, v. 39, p. 597–609.

Li, S.G., Jagoutz, E., Chen, Y.Z., and Li, Q.L., 2000a, Sm-Nd and Rb-Sr isotopic chronology and cooling history of ultrahigh pressure metamorphic rocks and their country rocks at Shuanghe in the Dabie Mountains, central China: Geochimica et Cosmochimica Acta, v. 64, p. 1077–1093, doi: 10.1016/S0016-7037(99)00319-1.

Li, S.G., Jagoutz, E., Lo, C.H., Chen, Y.Z., Li, Q.L., and Xiao, Y.L., 2000b, Sm/Nd, Rb/Sr, and $^{40}Ar/^{39}Ar$ isotopic systematics of ultrahigh-pressure metamorphic rocks in the Dabie-Sulu slice, central China: A retrospective view, *in* Ernst, W.G., and Liou, J.G., eds., Ultra-high pressure metamorphism and geodynamics in collision-type orogenic slices: Pennsylvania, Sheridan Press, p. 234–244.

Liou, J.G., Zhang, R.Y., Ernst, W.G., Rumble, D., and Maruyama, S., 1998, High-pressure minerals from deeply subducted metamorphic rocks: Reviews in Mineralogy and Geochemistry, v. 37, p. 33–96.

Liou, J.G., Hacker, B.R., and Zhang, R.Y., 2000, Into the forbidden zone: Science, v. 287, p. 1215–1216, doi: 10.1126/science.287.5456.1215.

Liu, F.L., Xu, Z.Q., Liou, J.G., Katayama, I., Masago, H., Maruyama, S., and Yang, J.S., 2002, Ultrahigh-pressure mineral inclusions in zircons from gneissic core samples of the Chinese Continental Scientific Drilling site

in eastern China: European Journal of Mineralogy, v. 14, p. 499–512, doi: 10.1127/0935-1221/2002/0014-0015.

Liu, F.L., Zhang, Z.M., and Xu, Z.Q., 2003, Three-dimensional distribution of ultrahigh-pressure minerals in Sulu terrane: Acta Geologica Sinica, v. 77, p. 69–84.

Liu, F.L., Xu, Z.Q., and Liou, J.G., 2004a, Tracing the boundary between UHP and HP metamorphic slices in the southwestern Sulu terrane, eastern China: Evidence from mineral inclusions in zircons from metamorphic rocks: International Geology Review, v. 46, p. 409–425.

Liu, F.L., Xu, Z.Q., Liou, J.G., and Song, B., 2004b, SHRIMP U-Pb ages of ultrahigh-pressure and retrograde metamorphism of gneisses, southwestern Sulu terrain, eastern China: Journal of Metamorphic Geology, v. 22, p. 315–326, doi: 10.1111/j.1525-1314.2004.00516.x.

Liu, F.L., Xu, Z.Q., and Xue, H.M., 2004c, Tracing the protolith, UHP metamorphism, and exhumation ages of orthogneiss from the SW Sulu terrane (eastern China): SHRIMP U-Pb dating of mineral inclusion-bearing zircons: Lithos, v. 78, p. 411–429, doi: 10.1016/j.lithos.2004.08.001.

Mainprice, D., Boucher, T.-L., Blumenfeld, P., and Tubia, J.M., 1986, Dominant <c> slip in naturally deformed quartz: Implications for dramatic plastic softening at high temperature: Geology, v. 14, p. 819–822, doi: 10.1130/0091-7613(1986)14<819:DCSIND>2.0.CO;2.

Maruyama, S., Liou, J.G., and Zhang, R., 1994, Tectonic evolution of the ultrahigh-pressure (UHP) and high-pressure (HP) metamorphic slices from central China: The Island Arc, v. 3, p. 112–121.

Platt, J.P., 1993, Exhumation of high-pressure rocks: A review of concepts and processes: Terra Nova, v. 5, p. 119–133.

Qiu, H.J., Xu, Z.Q., Zhang, Z.M., Yang, J.S., Yang, T.N., Zhang, J.X., and Li, H.B., 2002, New mineral evidence of high-pressure metamorphism of the Subei high-pressure slice—Aragonite inclusions in garnet from greenschist: Geological Bulletin of China, v. 21, p. 617–624.

Rumble, D., Giorgis, D., Ireland, T., Zhang, Z.M., Xu, H.M., Yui, T.F., Yang, J.S., Xu, Z.Q., and Liou, J.G., 2002, Low $\delta^{18}O$ zircons, U-Pb dating, and the age of the Qinglongshan oxygen and hydrogen isotope anomaly near Donghai in Jiangsu Province, China: Geochimica et Cosmochimica Acta, v. 66, p. 2299–2306, doi: 10.1016/S0016-7037(02)00844-X.

Wang, L.M., Song, M.C., Wang, P.C., Wang, S.J., Song, Z.Y., Liu, J.W., Li, Y.Y., and Zhang, X.D., 2005, The structure and evolution of the Sulu ultrahigh-pressure metamorphic slice: Beijing, Geological Publishing House, 126 p. (in Chinese with English abstract).

Xu, Z.Q., Zhang, J.X., Xu, H.F., Wang, Z.X., Li, H.B., Yang, T.N., Qiu, X.P., Zeng, L.S., Shen, K., and Chen, W., 1997, Ductile shear zones in the main continental mountain chains of China and their dynamics: Beijing, Geological Publishing House, 294 p. (in Chinese and with an extended English abstract).

Xu, Z.Q., Zhang, Z.M., Liu, F.L., Yang, J.S., Tang, Z.M., Cheng, S.Z., Cai, Y.C., Li, T.F., and Cheng, F.Y., 2004, The structure profile of 0–1200 m in the main borehole, Chinese Continental Scientific Drilling and its preliminary deformation analysis: Acta Petrologica Sinica, v. 20, p. 53–72.

Xu, Z.Q., Chen, J., Wang, Q., Zeng, L.S., Yang, J.S., Chen, F.Y., Li, T.F., and Liang, F.H., 2005, Type-C olivine fabric in the Zhimafang garnet peridotite of the southern Sulu ultrahigh-pressure metamorphic terrane: Formation conditions and tectonic implications: Acta Petrologica Sinica, v. 21, p. 389–397.

Yang, J.S., Wooden, J.L., Wu, C.L., Liu, F.L., Xu, Z.Q., Shi, R.D., Katayama, L., Liou, J.G., and Maruyama, S., 2003, SHRIMP U-Pb dating of coesite-bearing zircon from the ultrahigh-pressure metamorphic rocks, Sulu terrane, east China: Journal of Metamorphic Geology, v. 21, p. 551–560, doi: 10.1046/j.1525-1314.2003.00463.x.

Yang, T.N., Chen, W., Li, J.Y., Xu, Z.Q., Yin, X.L., and Xu, W.H., 2002, Exhumation history of the Sulu UHPM terrane—Evidence from dating and deformation on its northern boundary: Geological Review, v. 48, p. 176–182.

Yang, W.C., Yang, W.Y., and Chen, Z., 2004, Interpretation of 3D seismic reflection data in the Chinese Continental Scientific Drilling site: Acta Petrologica Sinica, v. 20, p. 127–137.

Zhang, R.Y., Liou, J.G., and Shu, J.F., 2002, Hydroxyl-rich topaz in high-pressure and ultrahigh-pressure kyanite quartzite, with retrograde woodhouseite, from the Sulu terrane, eastern China: The American Mineralogist, v. 87, p. 445–453.

Zhang, S.Y., Hu, K., Qiao, L.Y., and Liu, X.C., 1991, Composition and petrogenesis of the collisions of old blocks inside the continent—Take example for the high-pressure metamorphic slice in the central of China: Proceeding of the Qinling orogen conference: Xian, The NW University Publishing House, p. 48–56 (in Chinese with English abstract).

Zhang, Z.M., Xu, Z.Q., and Xu, H., 2000, Petrology of ultrahigh pressure eclogites from the ZK703 drill hole in the Donghai, eastern China: Lithos, v. 52, p. 35–50, doi: 10.1016/S0024-4937(99)00083-3.

Zhang, Z.M., Xu, Z.Q., Liu, F.L., You, Z.D., Shen, K., Yang, J.S., Li, T.N., and Chen, S., 2004, Geochemistry of eclogites from the main hole (100–2050 m) of the Chinese Continental Scientific Drilling Project: Acta Petrologica Sinica, v. 20, p. 27–42.

Zhang, Z.M., Xiao, Y.L., Liu, F.L., Liou, J.G., and Hoefs, J., 2005, Petrogenesis of UHP metamorphic rocks from Qinglongshan, southern Sulu, east-central China: Lithos, v. 81, p. 189–207, doi: 10.1016/j.lithos.2004.10.002.

Zheng, Y.F., Wu, Y., Chen, F., Gong, B., Li, L., and Zhao, Z., 2004, Zircon U-Pb and oxygen isotope evidence for a large-scale ^{18}O depletion event in igneous rocks during the Neoproterozoic: Geochimica et Cosmochimica Acta, v. 68, p. 4145–4165, doi: 10.1016/j.gca.2004.01.007.

MANUSCRIPT ACCEPTED BY THE SOCIETY 21 SEPTEMBER 2005

Geological Society of America
Special Paper 403
2006

SHRIMP U-Pb zircon dating of the Rongcheng eclogite and associated peridotite: New constraints for ultrahigh-pressure metamorphism of mantle-derived mafic-ultramafic bodies from the Sulu terrane

Ruixuan Zhao
Juhn G. Liou
Ru Y. Zhang
Department of Geological and Environmental Sciences, Stanford University, Stanford, California 94305-2115, USA
Tianfu Li
Laboratory of Continental Dynamics, Institute of Geology, Chinese Academy of Geological Sciences, Beijing, 100037, China

ABSTRACT

New sensitive high-resolution ion microprobe (SHRIMP) U-Pb zircon ages from eclogite and associated peridotite near Rongcheng, Sulu terrane, eastern China, indicate that eclogite within peridotite experienced Triassic metamorphism at the same time as the surrounding host gneiss. Cathodoluminescence (CL) images reveal that most of the zircons from two eclogites and one dunite have unzoned, homogeneous or slightly mottled patterns, typical of metamorphic zircons. Some zircons from eclogite sample CJ4C have distinct nonluminescent U-rich cores and luminescent U-poor rims, but similar ages were obtained from both domains. SHRIMP U-Pb zircon analyses of one dunite (MC5A) and two eclogites (CJ4A, 4C) yielded ages of 242 ± 8 Ma, 238 ± 3 Ma, and 232 ± 7 Ma, respectively, which are considered to be the peak metamorphic ages. A much younger age (218 ± 5 Ma) was obtained from eclogite CJ4D, but no petrological evidence for a retrograde event was found in this sample, and therefore this age is also considered to reflect eclogite-facies growth. Thus, new geochronological data confirm that these mantle-derived mafic-ultramafic bodies were emplaced into the subducting slab in the Triassic and experienced the ultrahigh-pressure metamorphism together with the adjacent supracrustal rocks.

Keywords: U-Pb SHRIMP geochronology, eclogite, garnet peridotite, UHP metamorphism.

INTRODUCTION

The Dabie-Sulu ultrahigh-pressure (UHP) metamorphic belt of east-central China is one of the largest UHP terranes in the world. It has attracted a great deal of attention since the discovery of coesite and microdiamond in eclogite within country rock gneiss (Okay et al., 1989; Wang et al., 1989; Xu et al., 1992, 2003). Radiometric dating is a useful method to understand the complex UHP metamorphic history in this terrane. In particular, sensitive high-resolution ion microprobe (SHRIMP) U-Pb dating of zircon domains, combined with cathodoluminescence (CL) imaging, rare earth element (REE) geochem-

Zhao, R., Liou, J.G., Zhang, R.Y., and Li, T., 2006, SHRIMP U-Pb zircon dating of the Rongcheng eclogite and associated peridotite: New constraints for ultrahigh-pressure metamorphism of mantle-derived mafic-ultramafic bodies from the Sulu terrane, *in* Hacker, B.R., McClelland, W.C., and Liou, J.G., eds., Ultrahigh-pressure metamorphism: Deep continental subduction: Geological Society of America Special Paper 403, p. 115–125, doi: 10.1130/2006.2403(06).

istry, and Raman spectroscopic study of inclusions have contributed greatly to recent progress in the dating of UHP metamorphic rocks (e.g., Rubatto and Gebauer, 2000; Rubatto, 2002; F. Liu et al., 2001). Geochronology of gneisses and enclosed eclogites from the Sulu terrane suggests that the UHP metamorphism took place during the Triassic collision between the Sino-Korean and Yangtze cratons. For example, F. Liu et al. (2005) reported a weighted mean age of 227 ± 9 Ma obtained from coesite-bearing zircon rims for paragneisses from Chinese Continental Scientific Drilling (CCSD) drill holes; and Yang et al. (2003) reported a lower-intercept U-Pb zircon age of 232 ± 56 Ma (2σ) for an eclogite in country rock gneiss from the Weihai area in Sulu (see Table 1 for summary). The identification of coesite together with other eclogite-facies minerals (e.g., garnet, jadeite, omphacite, phengite) as inclusions in zircon from country rock gneisses (Ye et al., 2000a; F. Liu et al., 2001, 2002, 2005; J. Liu et al., 2001) further confirms that the host gneisses, together with the enclosed coesite-bearing eclogites, were subducted to mantle depths and underwent UHP metamorphism during the Triassic collision.

Garnet peridotites that contain coesite-bearing eclogites are volumetrically minor, but constitute important petrological components of the Sulu UHP terrane. Zhang and Liou (1998a) identified two types of garnet peridotites in the Dabie-Sulu terrane: type-A upper-mantle slivers incorporated into the continental slab during subduction, and type-B crustal mafic-ultramafic complexes that were emplaced into the continental crust prior to subduction (also see Zhang et al., 2000). Abundant exsolution textures found in UHP minerals in the garnet peridotites and associated eclogites (Hacker et al., 1997; Zhang and Liou, 1998b; Zhang et al., 1999, 2000; Ye et al., 2000b) suggest an ultra-deep origin for these rocks. These new findings have made the Sulu terrane an increasingly exciting area for interdisciplinary studies of the geodynamics of continental subduction and crust-mantle interaction. Garnet peridotites and associated eclogites, therefore, have became the focus of many studies, because they can provide important information on the petrogenesis of eclogite in the upper mantle, on the composition of the mantle beneath orogenic belts, and on the emplacement mechanism of mantle rocks into subducted continental crust.

The initial tectonic setting, emplacement mechanism, and metamorphic history of these mafic-ultramafic bodies remain controversial. Although petrological and geochemical data show that type-A garnet peridotites and their enclosed eclogite lenses were derived from the mantle and tectonically emplaced into the subducting slab (Zhang et al., 2000), arguments still exist about whether these peridotites experienced UHP metamorphism at the same time as the enclosed eclogites and host country rock gneisses. Therefore, systematic geochronological studies are needed to constrain the timing of (1) igneous crystallization of garnet peridotite and associated eclogite and (2) subsequent metamorphic events, including peak UHP metamorphism and retrograde overprinting. However, most geochronological studies have focused on the eclogites that are enclosed within the host gneiss, and a few have determined the ages of ultramafic rocks (Song et al., 2005; Zhang et al., 2005). Because ultramafic rocks are low in Zr, most of the published ages on mafic-ultramafic bodies from the Dabie-Sulu terrane are based on Sm-Nd decay (Cong et al., 1992; Chavagnac and Jahn, 1996; Jahn et al., 2003). Only a few SHRIMP U-Pb zircon ages are available for peridotites and associated eclogites from the Donghai and Weihai areas of the Sulu terrane (Rumble et al., 2002; Yang et al., 2003; Zhao et al., 2005; Zhang et al., 2005) (Table 1). In this paper, we present SHRIMP U-Pb zircon dating and cathodoluminescence (CL) studies of eclogites and associated type-A garnet peridotites from the Rongcheng area, north Sulu terrane, that provide constraints on the timing of the UHP metamorphism in this area.

TABLE 1. SUMMARY OF U-Pb AGE DATA FOR DIFFERENT ROCK TYPES IN THE SULU ULTRA-HIGH PRESSURE TERRANE

Locality	Rock type	U-Pb peak age (Ma)	Error (±Ma)	Type of age	Reference
Xugou	Eclogite in peridotite	237	8 (2σ)	Weighted mean average	Zhao et al., 2005
Rongcheng	Eclogite in peridotite	238	3 (2σ)	Weighted mean average	This study
Rongcheng	Eclogite in peridotite	232	7 (2σ)	Weighted mean average	This study
Rongcheng	Eclogite in peridotite	218	5 (2σ)	Weighted mean average	This study
Zhimafang	Garnet peridotite	216–233		Single grain	Rumble et al., 2002
Weihai	Peridotite	221	12 (2σ)	Weighted mean average	Yang et al., 2003
CCSD-PP1	Garnet peridotite	221	3 (2σ)	Weighted mean average	Zhang et al., 2005
Rongcheng	Dunite	242	8 (2σ)	Weighted mean average	This study
Southern Sulu	Eclogite in gneiss	217	9	Lower intercept	Ames et al., 1996
Weihai	Eclogite in gneiss	232	56 (2σ)	Lower intercept	Yang et al., 2003
CCSD-PP2	Paragneiss	228	5	Weighted mean average	F. Liu et al., 2004a
CCSD-PP2	Orthogneiss	232	4	Weighted mean average	F. Liu et al., 2004a
CCSD-MH	Orthogneiss	227	2 (2σ)	Weighted mean average	F. Liu et al., 2004b
CCSD-MH, PP2, ZK-2304	Paragneiss	227	9 (2σ)	Weighted mean average	F. Liu et al., 2005
Sulu	Gneiss	207–232		Weighted mean average and single grain	Leech et al. (this volume)

CCSD—Chinese Continental Scientific Drilling Program.

GEOLOGICAL SETTING

The Qinling-Dabie-Sulu collision zone lies between the Sino-Korean and Yangtze cratons. The Sulu terrane is the eastern extension of the Qinling-Dabie belt, bounded by the Yantai-Qingdao-Wulian fault on the northwest and the Jiashan-Xiangshui fault on the south (Fig. 1A). The Sulu terrane consists of two fault-bounded UHP and high-pressure belts, both intruded by postorogenic Cretaceous granite. The UHP belt consists of mainly amphibolite-granulite–facies orthogneiss, paragneiss, amphibolite, and minor marble. Metamorphosed garnet peridotite and pyroxenite are widespread, and occur sporadically as blocks (meter to kilometer size) and thin layers in the gneiss (Zhang and Liou, 1998b). More than 90% of the eclogite bodies occur as lenses and layers in gneiss; the remainder is enclosed in ultramafic rocks and in marble. Coesite is found in eclogites from many localities of Figure 1A, including those in Rongcheng, Yangkou, and Weihai (Liou et al., 1995). The high-pressure belt, southeast of the UHP belt, consists mainly of quartz-mica schist, chloritoid-kyanite-mica-quartz schist, marble, and rare blueschist (Zhang et al., 1995).

Rongcheng is located in the northeastern part of the Sulu terrane. Several garnet peridotite bodies containing eclogite lenses occur in this area. Zhang et al. (2000) classified these rocks, together with peridotites from the Rizhao, Junan, and Donghai areas, as type-A garnet peridotites. These peridotites have lower 'fertile element' and higher MgO concentrations than those of the primitive mantle as defined by Ringwood (1975), indicating that they originated from a depleted mantle source. Their oxygen isotopic compositions ($\delta^{18}O$ +5 to +5.6‰) and low total REE concentrations also consistently suggest that these peridotites are mantle fragments that may have been tectonically emplaced into the Dabie-Sulu collision zone during subduction (Zhang et al., 2000). Among type-A garnet peridotites, Rongcheng lherzolites are the least depleted and have higher FeO than primitive mantle, suggesting that they may represent a slightly depleted mantle that was refertilized by interaction with basaltic melt (Zhang et al., 2000).

The Chijiadian garnet peridotite body in Rongcheng (Fig. 1B) forms a small hill of 0.6 × 0.2 km size underlain mainly by gneiss. The garnet peridotite contains eclogites with quartz pseudomorphs after coesite included in garnet and omphacite (Zhang et al., 1994). The margins of the peridotite body are extensively serpentinized, but garnet peridotite is well preserved in the center of the body and contains primary olivine, orthopyroxene, clinopyroxene, and garnet, together with minor, late amphibole. Olivine from this locality contains ilmenite exsolution lamellae (Hacker et al., 1997). A Sm-Nd isochron age of 232 Ma has been obtained from the Chijiadian eclogite (Cong et al., 1992).

For this study, zircon was extracted from three eclogite samples (CJ4A, CJ4C, and CJ4D) enclosed in lherzolite from the Chijiadian body. Samples of the surrounding lherzolite did not yield sufficient zircon for geochronology. We also collected samples from the Macaokuang peridotite body, southeast of the Chijiadian body (Fig. 1B); we also dated zircon separates from a dunite sample (MC5A) there.

ANALYTICAL METHODS

Zircons were separated from eclogites and dunite according to the following procedure. (1) Samples of 1–2 kg were crushed and sieved to small grain size. (2) Hand magnets were used to remove iron fillings and metal oxides from the sample. (3) Slope magnetic separator was then used to separate lower susceptibility minerals such as zircon and apatite from minerals like garnet, olivine and pyroxene. (4) Apatite was separated from zircon by desilting using alcohol (or by heavy liquid technique), and minor metal sulfide was removed by high-frequency dielectric separation. Finally zircons were handpicked by binocular microscope.

Zircon separates were mounted in epoxy, polished, and coated with gold before analysis. Cathodoluminescence (CL) examination was carried out using a JEOL JSM 5600 scanning electron microscope; U-Pb analyses employed the SHRIMP-RG (sensitive high-resolution ion microprobe–reverse geometry) at Stanford–U.S. Geological Survey Microanalytical Center at Stanford University. Analytical spots ~30 μm in diameter were sputtered using an ~5 nA O_2^- primary beam. For low-U zircons from eclogite samples CJ4A and CJ4D, seven scans through a 9 mass spectrum were made, and for higher-U zircons from eclogite sample CJ4C and dunite sample MC5A, five scans were made. The measured $^{206}Pb/^{238}U$ ratios were calibrated against standard zircon R-33 (419 Ma, John Aleinikoff, 2002, personal commun.), and the U concentrations were calibrated against standard zircon CZ3 (550 ppm U). Data reduction and processing were conducted using the computer programs SQUID and ISOPLOT (Ludwig, 2001a, 2001b). Isotope ratios and single ages in Table 2 are reported with 1σ errors, but the weighted mean ages are quoted at 2σ.

Mineral compositions were analyzed at Stanford University using a JEOL 733 Superprobe equipped with five wavelength-dispersive spectrometers. Operating conditions were 15 kV acceleration potential, 12 nA beam current, and peak counting times of 20 s. The results are listed in Table 3.

SAMPLE DESCRIPTION

The three eclogite samples (CJ4A, CJ4C, and CJ4D) from Chijiadian selected for SHRIMP U-Pb zircon dating occur as isolated nodules (<1 m) in garnet lherzolite. They consist of bimineralic garnet and omphacite, with minor rutile. Most of the garnets and omphacites are ~2–3 mm in diameter. Sample CJ4A is fresh; some omphacites in samples CJ4C and CJ4D are replaced by minor clinopyroxene + plagioclase symplectite. Garnet is pyrope-rich ($Alm_{35–37}Prp_{39–40}Grs_{24–26}$), and omphacite has a compositional range of $Jd_{31–33}$. Zircons from these samples contain inclusions of omphacite with a similar compositional range of $Jd_{33–34}$ (Table 3).

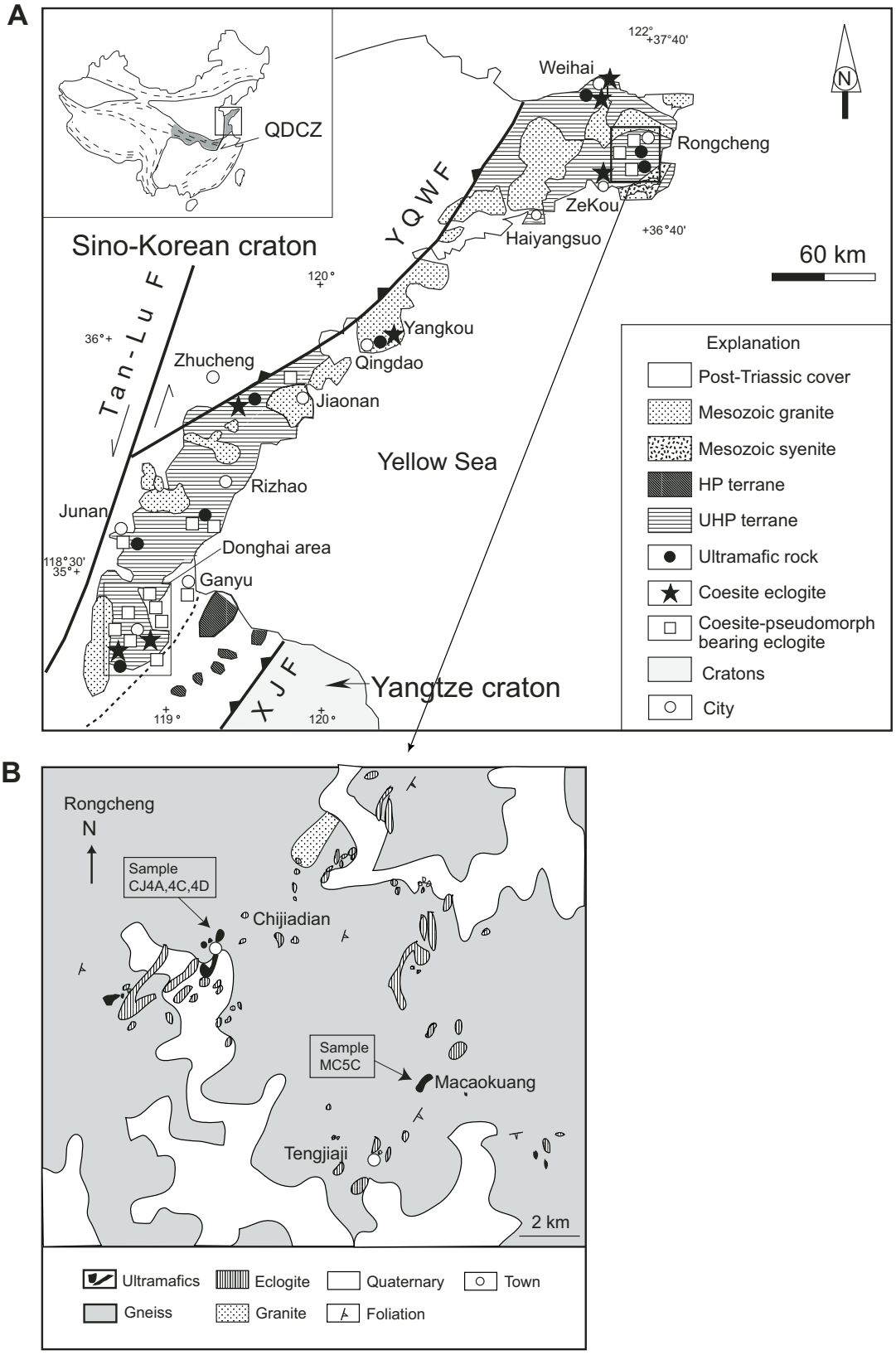

Figure 1. (A) Geologic map of the Sulu terrane in east-central China. (B) Eclogites and associated ultramafic rocks in the Rongcheng area (modified after Zhang et al., 2000). HP—high pressure, UHP—ultrahigh pressure, YQWF—Yantai-Qingdao-Wulian fault, QDCZ—Qinling-Dabie Collision Zone.

TABLE 2. U-Th-Pb SHRIMP ZIRCON DATA FROM THREE ECLOGITE SAMPLES (CJ4A, 4C, 4D) AND ONE DUNITE SAMPLE (MC5A) FROM RONGCHENG, SULU TERRANE

Spot name	U (ppm)	Th (ppm)	Th/U (%)	Common ^{206}Pb ^{238}U / ^{206}Pb	Uncorrected ^{207}Pb / ^{206}Pb	Uncorrected	$^{206}Pb^*$ / ^{238}U (Ma)	$^{206}Pb^*$ / ^{238}U age	Domain
Eclogite CJ4A									
CJ4A-1.1	32	5	0.15	0.00	26.71±3.7	.0467 ± 11.8	.0376 ± .0014	238.1 ± 9.0	homogeneous
CJ4A-2.1	30	3	0.09	0.00	28.03 ± 3.7	.0402 ± 19.0	.0361 ± .0014	228.9 ± 8.6	homogeneous
CJ4A-4.1	18	2	0.13	3.10	26.31 ± 4.1	.0756 ± 13.0	.0368 ± .0016	233.2 ± 10.0	homogeneous
CJ4A-6.1	36	10	0.27	7.58	24.45 ± 2.9	.1117 ± 7.4	.0378 ± .0012	239.1 ± 7.6	homogeneous
CJ4A-7.1	11	5	0.50	0.00	25.60 ± 5.3	.0468 ± 17.0	.0393 ± .0021	248.4 ± 13.3	homogeneous
CJ4A-8.1	27	24	0.93	0.40	29.19 ± 3.4	.0537 ± 10.2	.0341 ± .0012	216.3 ± 7.3	homogeneous
CJ4A-9.1	22	2	0.11	0.38	26.71 ± 3.6	.0539 ± 10.8	.0373 ± .0014	236.0 ± 8.5	homogeneous
Eclogite CJ4C									
CJ4C-1.1	1631	197	0.13	0.00	26.72 ± 0.7	.0504 ± 1.5	.0374 ± .0003	237.0 ± 1.6	Core
CJ4C-2.1	494	112	0.23	0.00	25.8 ± 1.2	.0492 ± 2.8	.0389 ± .0005	245.7 ± 3.0	Core
CJ4C-3.1	80	25	0.33	0.33	27.16 ± 3.1	.0535 ± 6.9	.0367 ± .0011	232.3 ± 7.1	Rim
CJ4C-6.1	69	35	0.52	0.66	27.46 ± 3.2	.0561 ± 7.0	.0362 ± .0012	229.1 ± 7.4	homogeneous
CJ4C-7.1	497	152	0.32	0.00	27.22 ± 1.2	.0502 ± 3.5	.0368 ± .0005	232.8 ± 2.9	Core
CJ4C-8.1	34	13	0.39	0.00	25.55 ± 4.6	.0510 ± 10.6	.0391 ± .0018	247.5 ± 11.3	Rim
CJ4C-8.2	177	93	0.54	0.00	26.83 ± 2.1	.0503 ± 4.8	.0373 ± .0008	236.1 ± 4.9	Core
CJ4C-10.1	280	149	0.55	2.89	25.98 ± 1.6	.0740 ± 3.0	.0374 ± .0006	236.5 ± 3.8	Core
CJ4C-11.1	115	55	0.49	0.06	26.64 ± 2.6	.0514 ± 9.3	.0375 ± .0010	237.4 ± 6.2	Core
CJ4C-12.1	226	181	0.83	1.66	25.81 ± 1.8	.0643 ± 3.6	.0381 ± .0007	241.0 ± 4.3	Core
Eclogite CJ4D									
CJ4D-1.1	4	1	0.19	2.85	28.6 ± 12.7	.0732 ± 30.9	.0340 ± .0045	215.3 ± 27.8	homogeneous
CJ4D-2.1	20	6	0.32	3.30	29.46 ± 4.9	.0766 ± 12.5	.0328 ± .0017	208.2 ± 10.5	homogeneous
CJ4D-3.1	27	21	0.82	0.29	29.19 ± 3.9	.0528 ± 12.2	.0342 ± .0014	216.5 ± 8.6	homogeneous
CJ4D-4.1	13	10	0.79	0.51	28.34 ± 5	.0546 ± 15.1	.0351 ± .0018	222.4 ± 11.2	homogeneous
CJ4D-5.1	11	3	0.26	0.66	28.58 ± 5.4	.0559 ± 16.6	.0348 ± .0019	220.3 ± 12.1	homogeneous
CJ4D-6.1	19	9	0.47	2.39	29.55 ± 4.3	.0694 ± 11.7	.0330 ± .0015	209.5 ± 9.2	homogeneous
CJ4D-7.1	78	16	0.21	0.34	29.91 ± 2.2	.0531 ± 6.7	.0333 ± .0008	211.3 ± 4.7	homogeneous
CJ4D-8.1	22	5	0.22	0.00	28.44 ± 6	.0452 ± 13.8	.0354 ± .0022	224.3 ± 13.5	homogeneous
CJ4D-9.1	12	5	0.41	1.42	28.95 ± 5.2	.0618 ± 14.5	.0341 ± .0018	215.9 ± 11.4	homogeneous
CJ4D-10.1	19	3	0.18	1.85	28.61 ± 4.5	.0652 ± 13.6	.0343 ± .0016	217.5 ± 9.9	homogeneous
CJ4D-11.1	15	5	0.33	2.12	26.09 ± 4.9	.0679 ± 13.4	.0375 ± .0019	237.4 ± 11.9	homogeneous
CJ4D-12.1	13	4	0.30	0.40	23.72 ± 4.8	.0547 ± 13.7	.0420 ± .0020	265.1 ± 12.7	homogeneous
CJ4D-13.1	28	7	0.26	2.32	29.43 ± 3.3	.0689 ± 10.0	.0332 ± .0011	210.5 ± 7.2	homogeneous
CJ4D-14.1	41	13	0.32	3.43	27.66 ± 4	.0780 ± 9.0	.0349 ± .0014	221.3 ± 9.0	homogeneous
CJ4D-15.1	5	1	0.14	7.46	30.58 ± 7.5	.1095 ± 17.2	.0303 ± .0024	192.2 ± 15.2	homogeneous
CJ4D-16.1	31	15	0.50	0.44	29.75 ± 3.2	.0539 ± 9.9	.0335 ± .0011	212.2 ± 6.9	homogeneous
CJ4D-17.1	3	1	0.21	6.12	24.79 ± 9.8	.1000 ± 20.3	.0379 ± .0039	239.6 ± 24.1	homogeneous
CJ4D-18.1	36	14	0.40	2.46	27.93 ± 3.1	.0702 ± 8.3	.0349 ± .0011	221.3 ± 7.0	homogeneous
CJ4D-19.1	18	6	0.37	1.67	26.67 ± 4.5	.0642 ± 12.2	.0369 ± .0017	233.4 ± 10.7	homogeneous
Dunite MC5A									
MC5A-3.1	70	2	0.03	0.00	26.58 ± 2.6	.0471 ± 8.6	.0378 ± .0010	239.2 ± 6.4	homogeneous
MC5A-4.1	57	1	0.01	0.00	25.77 ± 2.8	.0487 ± 10.2	.0389 ± .0011	246.2 ± 7.1	homogeneous
MC5A-5.1	84	5	0.06	0.07	26.23 ± 2.4	.0515 ± 7.6	.0381 ± .0009	241.0 ± 5.8	homogeneous

Note: Pb* corrected for common Pb using ^{207}Pb. All errors are 1 sigma of standard deviation.

TABLE 3. REPRESENTATIVE COMPOSITION OF MINERALS AND ZIRCON INCLUSIONS FROM RONGCHENG ECLOGITES AND DUNITE

Sample	Chijiadian eclogite CJ4A		Macaokuang dunite MC5A			Zircons from eclogite CJ4D	
Mineral	Grt	Omp	Ol	Opx	Spl	Omp inc[1]	Omp inc[2]
SiO_2	40.09	54.40	41.48	58.21	0.029	55.00	54.74
TiO_2	0.08	0.13	0.00	0.05	0.27	0.18	0.16
Cr_2O_3	0.09	0.13	0.03	0.07	44.81	0.09	0.05
Al_2O_3	22.43	7.33	0.00	0.45	18.10	8.01	7.25
FeO	17.26	5.019	7.64	5.52	24.51	4.62	4.73
MnO	0.36	0.02	0.11	0.12	0.34	0.01	0.03
MgO	10.51	10.32	50.00	35.43	9.11	10.28	9.98
CaO	8.87	15.07	0.00	0.076	0.00	15.89	14.77
Na_2O	0.01	5.85	0.00	0.00	0.04	5.06	5.38
Total	99.72	98.28	99.26	99.94	97.20	99.15	97.10
Si	3.01	2.00	1.01	2.00	0.00	1.99	2.02
Ti	0.00	0.00	0.00	0.00	0.01	0.00	0.00
Cr	0.01	0.00	0.00	0.00	1.18	0.00	0.00
Al	1.98	0.32	0.00	0.02	0.71	0.34	0.32
Fe^{2+}	1.08	0.15	0.16	0.16	0.68	0.14	0.15
Mn	0.02	0.00	0.00	0.00	0.01	0.00	0.00
Mg	1.18	0.56	1.82	1.81	0.45	0.56	0.55
Ca	0.71	0.59	0.00	0.00	0.00	0.62	0.58
Na	0.00	0.42	0.00	0.00	0.00	0.36	0.39
Total	20.00	10.05	6.99	10.00	7.05	10.01	10.01

Our dunite sample (MC5A) from the Macaokuang peridotite body consists of 0.2–0.3 mm olivine with minor orthopyroxene, clinopyroxene, amphibole, and Cr-spinel. The olivine is Fo_{92} and contains trace MnO (0.08–0.14 wt%); minor serpentine occurs at the rim of olivine. Orthopyroxene is En_{92} and low in Al_2O_3 (0.41–0.45 wt%). Spinel Cr/(Cr + Al) ratios are 0.59–0.63 (Table 3).

GEOCHRONOLOGICAL RESULTS

Chijiadian Eclogite (CJ4A)

Zircons from sample CJ4A are rounded 50–60 μm grains with luminescent but slightly mottled CL images (Fig. 2A). Seven analyses of seven zircon grains plot on a single mixing line with common Pb that defines an intercept age of 233 ± 7 Ma (Fig. 3A) (common Pb composition is assumed as Broken Hill Pb). This age is the same within error as the weighted mean $^{206}Pb/^{238}U$ age of 232 ± 7 Ma (n = 7). All zircons have low-U (11–36 ppm) and low-Th (2–24 ppm) concentrations.

Chijiadian Eclogite (CJ4C)

Zircons from sample CJ4C are rounded or ovoid and 100–200 μm in diameter. Some have a nonluminescent core surrounded by a luminescent rim in CL images (Figs. 2B and 2D), whereas others show homogeneous, luminescent CL patterns (Fig. 2C). The nonluminescent cores are rich in U (up to 1631 ppm) and Th (up to 197 ppm), but the luminescent rims and homogeneous luminescent grains have low-U (34–80 ppm) and low-Th (13–35 ppm) concentrations. Th/U ratios are similar (0.13–0.83) for the homogeneous, core, and rim domains. Spot analyses were conducted on the homogeneous domains, core domains, and rim domains and show no significant age difference (Table 2). Weighted mean $^{206}Pb/^{238}U$ ages were calculated separately for high-U (core) and low-U (homogeneous and rim) domains, and yielded 238 ± 3 Ma and 234 ± 9 Ma ages, respectively. These ages are statistically the same within error, and therefore we consider that these different domains represent a single age population. Ten spot analyses on nine zircons plot on a single mixing line with common Pb that defines an intercept age of 238 ± 3 Ma (Fig. 3B). This age is the same as the weighted mean $^{206}Pb/^{238}U$ age of 238 ± 3 Ma.

Chijiadian Eclogite (CJ4D)

Zircons from sample CJ4D are rounded to ovoid and 50–100 μm in diameter, and appear similar in CL to CJ4A (Fig. 2E). Some zircons have a very luminescent rim (<5 μm), too narrow to be analyzed. Nineteen analyses on nineteen zircons form a cluster (Fig. 3C) with a weighted mean $^{206}Pb/^{238}U$ age of 218 ± 6 Ma. Similar to CJ4A, all zircons are low in U (3–78 ppm) and Th (1–21 ppm).

Macaokuang Dunite (MC5A)

Zircons from sample MC5A are rounded to subrounded, 50–100 μm in diameter, and show luminescent but mottled CL images (Fig. 2F) similar to those from the eclogites. Due to the extremely small amount of zircon extracted from this sample, we made only three analyses on three zircons. These data are concordant (Fig. 3D) and define a weighted mean $^{206}Pb/^{238}U$ age of 242 ± 8 Ma. These zircons have low-U (57–84 ppm) and low-Th (1–5 ppm) concentrations and low Th/U ratios (0.01–0.06), similar to zircons from our Chijiadian eclogites.

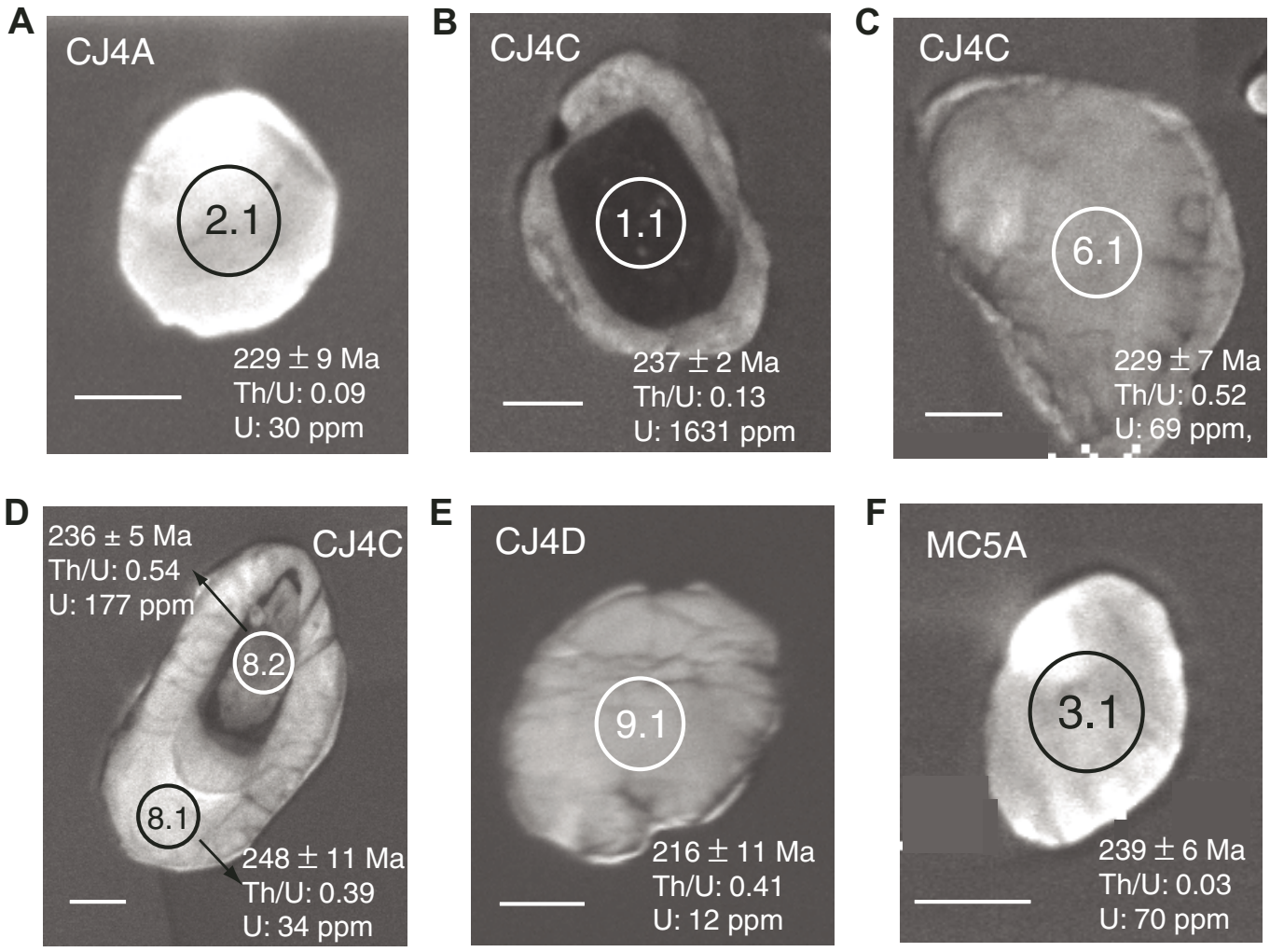

Figure 2. Cathodoluminescence (CL) images of zircons from eclogite sample CJ4A (A), CJ4C (B, C, and D), CJ4D (E), and dunite sample MC5A (F). Scale bars are 30 μm.

DISCUSSION AND CONCLUSIONS

Zircons from two eclogite samples (CJ4A, CJ4D) and one dunite sample (MC5A) show features that are typical of metamorphic zircons (Corfu et al., 2003). They are rounded to ovoid, and show unzoned, homogeneous, or slightly mottled CL patterns. Most zircons are characterized by Th/U ratios <0.5, with low-U (3–84 ppm) and low-Th (1–24 ppm) concentrations (Table 2; Fig. 4). These features are similar to zircons reported from eclogites and peridotites from other areas (Zhao et al., 2005; Song et al., 2005). On the other hand, zircons from eclogite-bearing gneiss show very different features. They are typically euhedral, elongate, and show distinct core, mantle, and rim zoning. They have higher U and Th contents, especially for the igneous core domains (up to several hundred ppm) (F. Liu et al., 2002, 2004a, 2005). Zircons from eclogite sample CJ4C show distinct cores and rims, but any age difference between these domains is too small for us to resolve.

Our SHRIMP U-Pb zircon data on two Chijiadian eclogites (CJ4A, CJ4C) from the Rongcheng area indicate that these eclogites experienced UHP metamorphism during the Triassic, from 238 ± 3 to 232 ± 7 Ma. This is in good agreement with the age of 242 ± 8 Ma for the Macaokuang dunite sample (MC5A) in the same area. The Rongcheng peridotites, including both Chijiadian and Macaokuang, are proposed to have been derived from the upper mantle based on whole-rock trace-element and REE compositions, and on mineral chemistries (Zhang et al., 1994, 2000). Chondrite-normalized La, Sm, and Lu abundances of Rongcheng eclogites suggest that some of them were derived from melts that were formed by various degrees of partial melting of mantle peridotite, and others formed by accumulation of garnet and clinopyroxene + trapped melt in the upper mantle (Zhang et al., 1994). The similar pressure-temperature (*P-T*) paths for the ultramafic rocks and eclogites (Zhang et al., 1994) indicate that they shared the same tectonometamorphic history. Because coesite pseudo-

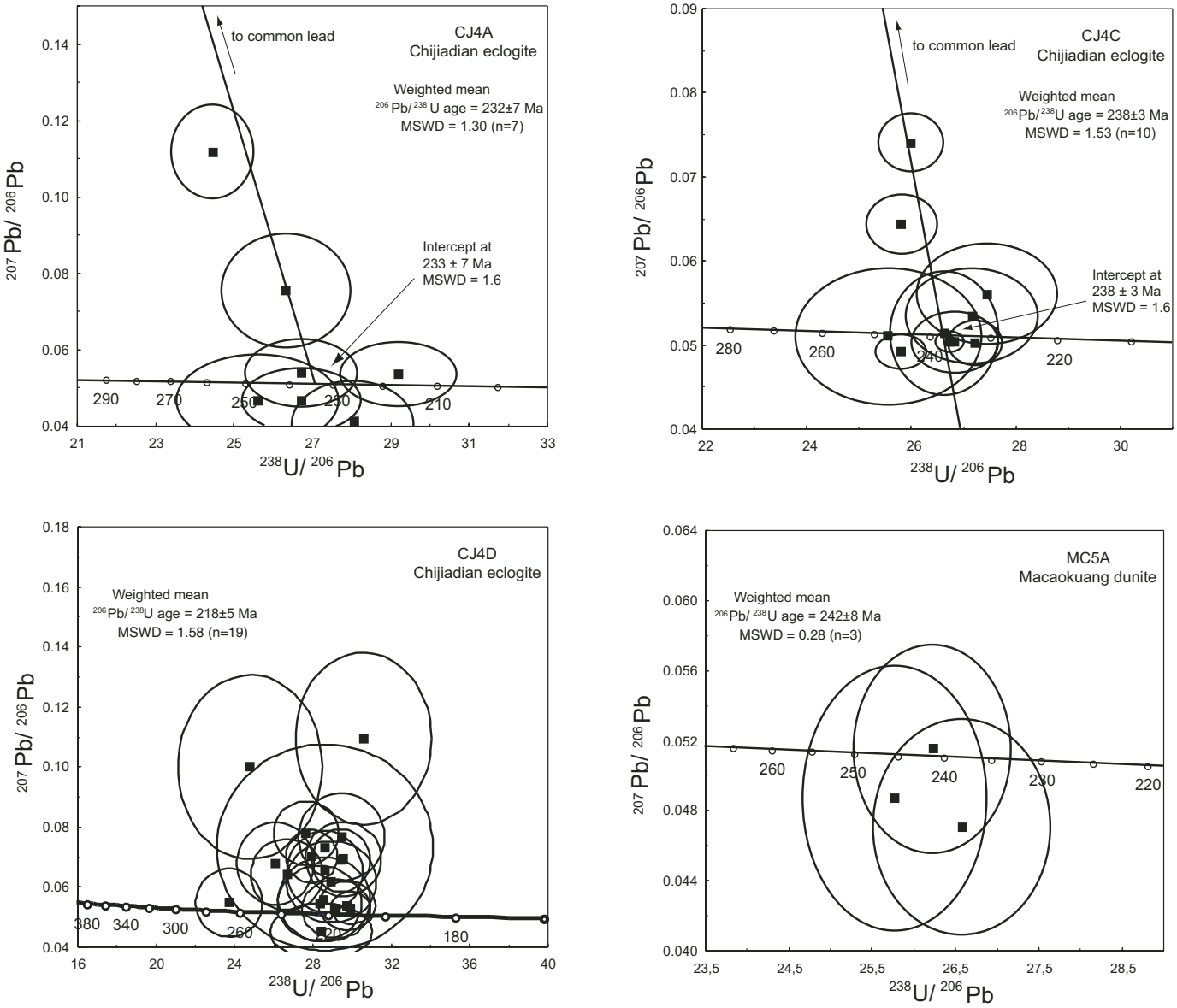

Figure 3. Tera-Wasserburg (TW) diagram showing sensitive high-resolution ion microprobe (SHRIMP) analyses of zircons from eclogite CJ4A (A), CJ4C (B), CJ4D (C), and dunite MC5A (D). Uncorrected ratios are plotted. Error ellipses are shown as 1σ, whereas the uncertainty of the weighted mean age is 2σ. MSWD—mean square of weighted deviates.

morphs are present in the Rongcheng eclogite (Zhang et al., 1994), the assemblage experienced a minimum pressure of 30 kbar. Our calculations using the garnet-clinopyroxene thermometer of Powell (1985) yield a peak temperature of ~940 °C for the eclogite CJ4A, which is close to the 840–930 °C range estimated for eclogites from the same body by Zhang et al. (1994). Peak *P-T* conditions for the Rongcheng lherzolite are estimated to be 820–920 °C and 40–60 kbar (Zhang et al., 1994; Hiramatsu et al., 1995). Thus, the eclogites and associated peridotites experienced the same UHP metamorphism, and the basaltic protoliths were emplaced into the ultramafic rocks before the UHP metamorphism.

Our ages are consistent with the weighted mean $^{206}Pb/^{238}U$ age of 237 ± 8 Ma from the Xugou eclogite (Zhao et al., 2005) and 221 ± 3 Ma from the Zhimafang garnet peridotites in the Donghai area (Zhang et al., 2005). These eclogites and peridotites also formed in the mantle before subduction and were tectonically emplaced into the subducting slab and then subjected to UHP metamorphism. All these rocks therefore experienced a similar history during the Triassic continental collision. No protolith domains were preserved in our zircons. A possible reason could be that Zr and Si contents were too low for zircons to have grown during the igneous crystallization of these mafic-ultramafic bodies. During the Triassic continental collision,

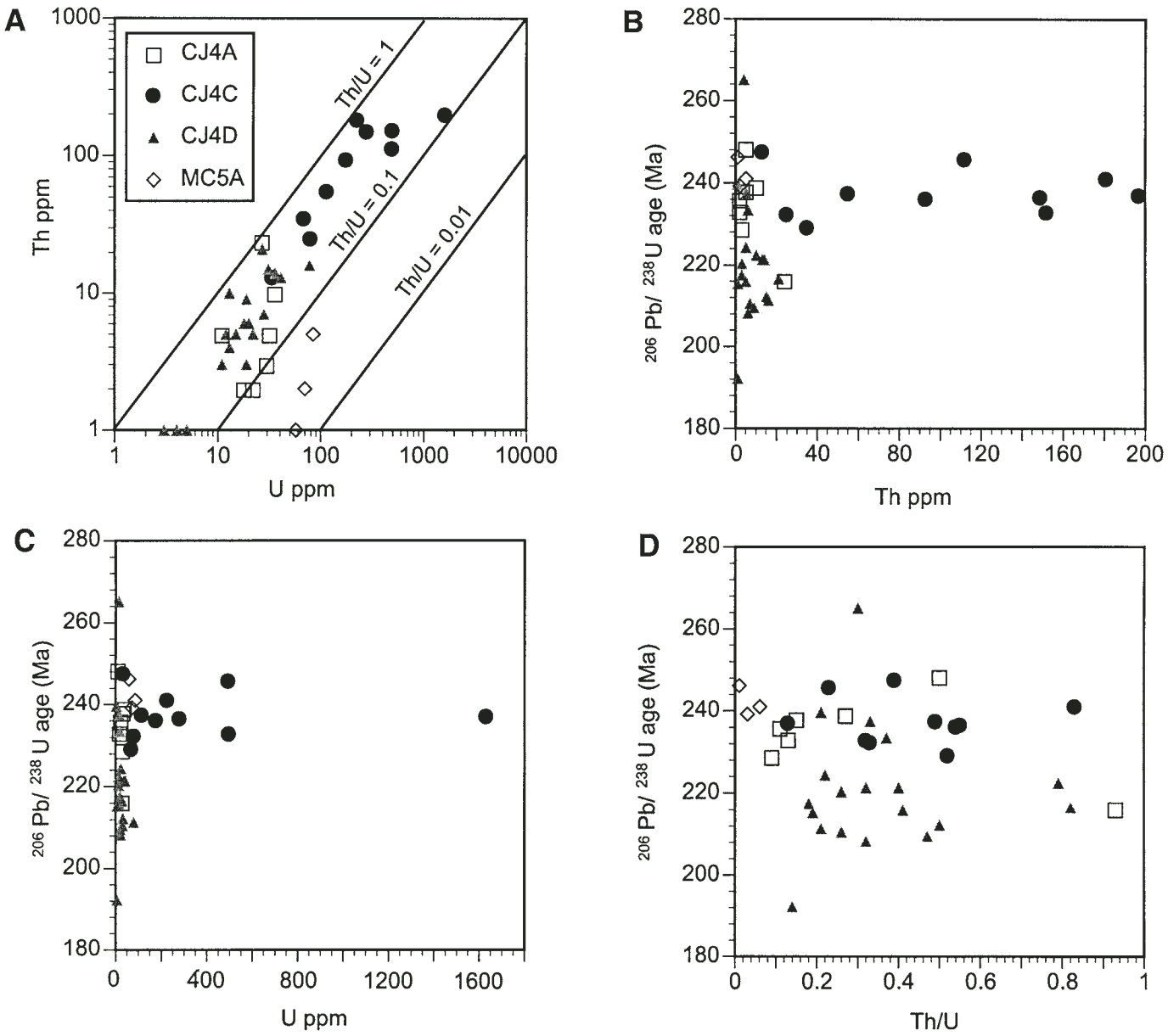

Figure 4. Th-U diagrams for samples CJ4A, CJ4C, CJ4D, and MC5A (A, B, and C). Zircons from CJ4C show a wider range of U and Th concentrations. (D) All zircons show low Th/U ratios and most are <0.5. ^{207}Pb corrected ^{206}Pb/^{238}U ages are used here.

these mafic-ultramafic bodies were tectonically emplaced into the subduction zone, and zircons formed from the metasomatic fluid derived either from the subducting slab or from the mantle. This suggestion is consistent with the observation of abundant hydrous phases in the zircon-bearing garnet peridotites (e.g., Zhang et al., 2005).

Our ages are similar to the 231–227 Ma ages of coesite-bearing core and mantle domains from zircons in paragneiss and orthogneiss in CCSD drill holes at Donghai, in the southwestern Sulu terrane (F. Liu et al., 2004a, 2004b, 2005). Our ages agree with U-Pb zircon ages of 217–232 Ma from eclogite within gneiss in the Sulu terrane (Ames et al., 1996; Yang et al., 2003) (Table 1). We conclude that the Rongcheng eclogite and peridotite experienced UHP metamorphism at the same time as the surrounding gneiss.

Eclogite sample CJ4D yielded a significantly younger age (218 ± 5 Ma), close to reported retrograde ages (Ayers et al., 2002; Hacker et al., 1998, 2000; Li et al., 2000; F. Liu et al., 2004a, 2004b; X. Liu et al., 2004). For example, F. Liu et al. (2004a) reported a 211 ± 4 Ma age for zircon rims corresponding to the amphibolite-facies overprint from gneiss in the Donghai area. X. Liu et al. (2004) also reported a U-Pb zircon retrograde age of 213 ± 5 Ma for Dabie eclogites within granitic gneiss. Based on the nearly uniform age and mottled CL texture, X. Liu

et al. (2004) interpreted these zircons to have been formed from complete post-UHP recrystallization.

Sample CJ4D is different from either case above. Zircons from CJ4D do not show pronounced zoning, but a homogeneous CL pattern. Inclusions of omphacite and no inclusions of low-pressure minerals in these zircon grains suggest formation under high-pressure metamorphic conditions. This sample was collected adjacent to the other eclogite samples (CJ4A, CJ4C) from the same body, and its zircons look similar. We conclude that these zircons also recorded the eclogite-facies metamorphism, but further investigation is needed to explain the reason for this young age.

We consider that the zircons from the three eclogites and the one dunite record the peak metamorphic event and provide new constraints for the timing of UHP metamorphism of mantle-derived garnet peridotites and their enclosed eclogites. Two of the eclogite samples yielded ages of 238 ± 3 and 232 ± 7 Ma, consistent with the age of 242 ± 8 Ma from the dunite sample. These data provide evidence that the Rongcheng eclogite and peridotite share the same metamorphic history and were emplaced into the subduction zone and subjected to peak metamorphism together.

ACKNOWLEDGMENTS

We thank W. Chu of Stanford University, J.S. Yang, S.Z. Chen, and C.L. Wu from Chinese Academy of Geological Sciences for logistical support and assistance in our field work, and F. Mazdab, B. Wiegand, and B. Jones for assistance with sensitive high-resolution ion microprobe (SHRIMP) U-Pb zircon dating, cathodoluminescence imaging, and electron microprobe analyses. We also greatly appreciate critical reviews of the manuscript by Bill McClelland, Brad Hacker, Chris Mattinson, Jeremy Hourigan, and Laura Webb. This study was supported in part by National Science Foundation grants EAR-0003355 and EAR-0506901 to J.G. Liou, and by a Geological Society of America research grant and Stanford University McGee research grant to R.X. Zhao.

REFERENCES CITED

Ames, L., Zhou, G.Z., and Xiong, B., 1996, Geochronology and geochemistry of ultrahigh-pressure metamorphism with implications for collision of the Sino-Korean and Yangtze cratons, central China: Tectonics, v. 15, p. 472–489, doi: 10.1029/95TC02552.

Ayers, J.C., Dunkle, S., Gao, S., and Miller, C.F., 2002, Constraints on timing of peak and retrograde metamorphism in the Dabie Shan ultrahigh-pressure metamorphic belt, east-central China, using U-Th-Pb dating of zircon and monazite: Chemical Geology, v. 186, p. 315–331, doi: 10.1016/S0009-2541(02)00008-6.

Chavagnac, V., and Jahn, B.-M., 1996, Coesite-bearing eclogites from the Bixiling Complex, Dabie Mountains, China: Sm-Nd ages, geochemical characteristics and tectonic implications: Chemical Geology, v. 133, p. 29–51, doi: 10.1016/S0009-2541(96)00068-X.

Cong, B.L., Zhang, R.Y., Li, S.G., Zhai, M.G., Wang, S.S., Cheng, C.Y., and Ishiwatari, A., 1992, Preliminary study of isotope chronology of northern Jiangsu and eastern Shandong province, China: Exploration of volcanoes and rocks in Japan, China and Antarctica: Yamakuchi, Yamakuchi University Press, p. 411–417.

Corfu, F., Hanchar, J.M., Hoskin, P.W.O., and Kinny, P.D., 2003, Atlas of zircon textures: Mineralogical Society of America Reviews in Mineralogy and Geochemistry, v. 53, p. 469–500.

Hacker, B., Sharp, T., Zhang, R.Y., Liou, J.G., and Hervig, R.L., 1997, Determining the origin of ultrahigh-pressure lherzolites: Science, v. 278, p. 702–704, doi: 10.1126/science.278.5338.702.

Hacker, B.R., Ratschbacher, L., Webb, L.E., Ireland, T., Walker, D., and Dong, S., 1998, Zircon ages constrain the architecture of the ultrahigh-pressure Qinling-Dabie orogen, China: Earth and Planetary Science Letters, v. 161, p. 215–230, doi: 10.1016/S0012-821X(98)00152-6.

Hacker, B.R., Ratschbacher, L., Webb, L.E., McWilliams, M.O., Ireland, T., Calvert, A., Dong, S., Wenk, H.-R., and Chateigner, D., 2000, Exhumation of ultrahigh-pressure continental crust in east-central China: Late Triassic–Early Jurassic tectonic unroofing: Journal of Geophysical Research, v. 105, p. 13,339–13,364, doi: 10.1029/2000JB900039.

Hiramatsu, N., Banno, S., Hirajima, T., and Cong, B., 1995, Ultrahigh-pressure garnet lherzolite from Chijiadian, Rongcheng County, in the Su-Lu region of eastern China: The Island Arc, v. 4, p. 324–333.

Jahn, B.-M., Fan, Q., Yang, J.-J., and Henin, O., 2003, Petrogenesis of the Maowu pyroxenite-eclogite body from the UHP metamorphic terrane of Dabieshan: Chemical and isotopic constraints: Lithos, v. 70, p. 243–267, doi: 10.1016/S0024-4937(03)00101-4.

Li, S., Jagoutz, E., Chen, Y., and Li, Q., 2000, Sm-Nd and Rb-Sr isotopic chronology and cooling history of ultrahigh pressure metamorphic rocks and their country rocks at Shuanghe in the Dabie Mountains, central China: Geochimica et Cosmochimica Acta, v. 64, p. 1077–1093, doi: 10.1016/S0016-7037(99)00319-1.

Liou, J.G., Banno, S., and Ernst, W.G., 1995, Ultrahigh-pressure metamorphism and tectonics: The Island Arc, v. 4, p. 233–239.

Liu, F.L., Xu, Z.Q., Katayama, I., Yang, J.S., Maruyama, S., and Liou, J.G., 2001, Mineral inclusions in zircons of para- and orthogneiss from pre-pilot drillhole CCSD-PP1, Chinese Continental Scientific Drilling Project: Lithos, v. 59, p. 199–215, doi: 10.1016/S0024-4937(01)00064-0.

Liu, F.L., Xu, Z.Q., Liou, J.G., Katayama, I., Masago, H., Maruyama, S., and Yang, J.S., 2002, Ultrahigh-pressure mineral inclusions in zircons from gneissic core samples of the Chinese Continental Scientific Drilling Site in eastern China: European Journal of Mineralogy, v. 14, p. 499–512, doi: 10.1127/0935-1221/2002/0014-0015.

Liu, F.L., Xu, Z.Q., Liou, J.G., and Song, B., 2004a, SHRIMP U-Pb ages of ultrahigh-pressure and retrograde metamorphism of gneisses, southwestern Sulu terrane, eastern China: Journal of Metamorphic Geology, v. 22, p. 315–326, doi: 10.1111/j.1525-1314.2004.00516.x.

Liu, F.L., Xu, Z.Q., and Xue, H., 2004b, Tracing the protolith, UHP metamorphism, and exhumation ages of orthogneiss from the SW Sulu terrane (eastern China): SHRIMP U-Pb dating of mineral inclusion-bearing zircons: Lithos, v. 78, p. 411–429, doi: 10.1016/j.lithos.2004.08.001.

Liu, F.L., Liou, J.G., and Xu, Z.Q., 2005, U-Pb SHRIMP ages recorded in the coesite-bearing zircon domains of paragneisses in the southwestern Sulu terrane, eastern China: New interpretation: The American Mineralogist, v. 90, p. 790–800, doi: 10.2138/am.2005.1677.

Liu, J., Ye, K., Maruyama, S., Cong, B., and Fa, H., 2001, Mineral inclusions in zircon from gneisses in the ultrahigh-pressure zone of the Dabie mountains, China: The Journal of Geology, v. 109, p. 523–535, doi: 10.1086/320796.

Liu, X., Jahn, B.M., Liu, D., Dong, S., and Li, S., 2004, SHRIMP U-Pb zircon dating of a metagabbro and eclogites from western Dabieshan (Hong'an block), China, and its tectonic implications: Tectonophysics, v. 394, p. 171–192, doi: 10.1016/j.tecto.2004.08.004.

Ludwig, K.R., 2001a, Squid 1.00: A user's manual: Berkeley Geochronology Center, Special Publication, no. 2, 17 p.

Ludwig, K.R., 2001b, Isoplot/Ex rev. 2.49: A geochronological tool kit for Microsoft Excel: Berkeley Geochronology Center, Special Publication, no. 1a, 55 p.

Okay, A.I., Xu, S., and Sengör, A.M.C., 1989, Coesite from the Dabie Mountains eclogite, central China: European Journal of Mineralogy, v. 1, p. 595–598.

Powell, R., 1985, Regression diagnostic and robust regression in geothermometer/geobarometer calibration: The garnet-clinopyroxene geothermometer revisited: Journal of Metamorphic Geology, v. 3, p. 231–243.

Ringwood, A.E., 1975, Composition and petrology of the Earth's mantle: New York, McGraw-Hill.

Rubatto, D., 2002, Zircon trace element geochemistry: Partitioning with garnet and the link between U-Pb ages and metamorphism: Chemical Geology, v. 184, p. 123–138, doi: 10.1016/S0009-2541(01)00355-2.

Rubatto, D., and Gebauer, D., 2000, Use of cathodoluminescence for U-Pb zircon dating by ion microprobe: Some examples from the Western Alps, *in* Pagel, M., Barbin, V., Blanc, P., and Ohnenstetter, D., eds., Cathodoluminescence in geosciences: Berlin, Germany, Springer, p. 373–400.

Rumble, D., Giorgis, D., Ireland, T., Zhang, Z., Xu, H., Yui, T.F., Yang, J., Xu, Z., and Liou, J.G., 2002, Low $\delta^{18}O$ zircons, U-Pb dating, and the age of the Qinglongshan oxygen and hydrogen isotope anomaly near Donghai in Jiangsu Province, China: Geochimica et Cosmochimica Acta, v. 66, p. 2299–2306, doi: 10.1016/S0016-7037(02)00844-X.

Song, S.G., Zhang, L.F., Niu, Y.L., Su, L., Jian, P., and Liu, D.Y., 2005, Geochronology of diamond-bearing zircons from garnet peridotite in the North Qaidam UHPM belt, northern Tibetan Plateau: A record of complex histories from oceanic lithosphere subduction to continental collision: Earth and Planetary Science Letters, v. 234, p. 99–118.

Wang, X.M., Liou, J.G., and Mao, H.G., 1989, Coesite-bearing eclogites from the Dabie mountains in central China: Geology, v. 17, p. 1085–1088, doi: 10.1130/0091-7613(1989)017<1085:CBEFTD>2.3.CO;2.

Xu, S., Okay, A.I., Ji, S., Sengör, A.M.C., Su, W., and Jiang, L., 1992, Diamond from the Dabie Shan metamorphic rocks and its implication for tectonic setting: Science, v. 256, p. 80–82.

Xu, S., Liu, Y., Chen, G., Compagnoni, R., Rolfo, F., He, M., and Liu, H., 2003, New findings of microdiamonds in eclogites from Dabie-Sulu region in central-eastern China: Chinese Science Bulletin, v. 48, p. 988–994, doi: 10.1360/03wd0085.

Yang, J.S., Wooden, J.L., Wu, C.L., Liu, F.L., Xu, Z.Q., Shi, R.D., Katayama, L., Liou, J.G., and Maruyama, S., 2003, SHRIMP U-Pb dating of coesite-bearing zircon from the ultrahigh-pressure metamorphic rocks, Sulu terrane, east China: Journal of Metamorphic Geology, v. 21, p. 551–560, doi: 10.1046/j.1525-1314.2003.00463.x.

Ye, K., Yao, Y., Katayama, I., Cong, B., Wang, Q., and Maruyama, S., 2000a, Large areal extent of ultrahigh-pressure metamorphism in the Sulu ultrahigh-pressure terrane of east China: New implications from coesite and omphacite inclusions in zircon of granitic gneiss: Lithos, v. 52, p. 157–164, doi: 10.1016/S0024-4937(99)00089-4.

Ye, K., Cong, B., and Ye, D., 2000b, The possible subduction of continental material to depths greater than 200 km: Nature, v. 407, p. 734–736, doi: 10.1038/35037566.

Zhang, R.Y., and Liou, J.G., 1998a, Dual origin of garnet peridotites of Dabie-Sulu UHP terrane, eastern-central China: Episodes, v. 21, p. 229–234.

Zhang, R.Y., and Liou, J.G., 1998b, Ultrahigh-pressure metamorphism of the Sulu terrane, eastern China: A prospective view: Continental Dynamics, v. 3, p. 32–53.

Zhang, R.Y., Liou, J.G., and Cong, B.L., 1994, Petrogenesis of garnet-bearing ultramafic rocks and associated eclogites in the Su-Lu ultrahigh-*P* metamorphic terrane, eastern China: Journal of Metamorphic Geology, v. 12, p. 169–186.

Zhang, R.Y., Hirajima, T., Banno, S., Cong, B.L., and Liou, J.G., 1995, Petrology of ultrahigh-pressure rocks from the southern Su-Lu region, eastern China: Journal of Metamorphic Geology, v. 13, p. 659–675.

Zhang, R.Y., Shu, J.F., Mao, H.G., and Liou, J.G., 1999, Magnetite lamellae in olivine and clinohumite from Dabie UHP ultramafic rocks, central China: The American Mineralogist, v. 84, p. 564–569.

Zhang, R.Y., Liou, J.G., Yang, J.S., and Yui, T.-F., 2000, Petrochemical constraints for dual origin of garnet peridotites from the Dabie-Sulu UHP terrane, eastern-central China: Journal of Metamorphic Geology, v. 18, p. 149–166, doi: 10.1046/j.1525-1314.2000.00248.x.

Zhang, R.Y., Yang, J.S., Wooden, J.L., Liou, J.G., and Li, T.F., 2005, U-Pb SHRIMP geochronology of zircon in garnet peridotite from the Sulu UHP terrane, China: Implications for mantle metasomatism and subduction-zone UHP metamorphism: Earth and Planetary Science Letters, v. 237, p. 729–743.

Zhao, R., Liou, J.G., Zhang, R.Y., and Wooden, J.L., 2005, SHRIMP U-Pb Dating of zircon from the Xugou UHP eclogite, Sulu terrane, eastern China: International Geology Review, v. 47, p. 805–814.

MANUSCRIPT ACCEPTED BY THE SOCIETY 21 SEPTEMBER 2005

Printed in the USA

Geological Society of America
Special Paper 403
2006

Late chloritoid-staurolite assemblage in a garnet-kyanite–bearing metapelite from the ultrahigh-pressure Brossasco-Isasca unit (Dora-Maira Massif, Western Alps): New petrological constraints for a portion of the decompressional path

C. Groppo
Department of Mineralogical and Petrological Sciences, via Valperga Caluso 35, I-10125 Torino, Italy
D. Castelli
R. Compagnoni
Department of Mineralogical and Petrological Sciences, via Valperga Caluso 35, I-10125 Torino, Italy, and CNR (National Research Council), Institute of Geosciences and Georesources–Torino, c/o DSMP (Department of Mineralogical and Petrological Sciences), via Valperga Caluso 35, I-10125 Torino, Italy

ABSTRACT

We conducted a detailed study of a unique metapelite from the ultrahigh-pressure (UHP) Brossasco-Isasca unit (Dora-Maira Massif). It consists of pre-Alpine porphyroblastic garnet (Grt1), Alpine-age idioblastic garnet (Grt2), phengite, and kyanite. The pre-Alpine garnet contains inclusions of staurolite, kyanite, paragonite, chloritoid, chlorite, quartz, ilmenite, and rutile. The metapelite also includes quartz aggregates after former coesite and fine-grained paragonite aggregates after jadeite. Late chloritoid and staurolite idioblasts, first reported from a Brossasco-Isasca unit metapelite, are also present in the rock matrix: they grew randomly across the main Alpine UHP foliation defined by phengite. The decompression pressure-temperature (*P-T*) path of the unit was constructed employing a *P-T* pseudosection calculated for the model MnNKFMASH (MnO-Na_2O-K_2O-FeO-MgO-Al_2O_3-SiO_2-H_2O) system in the pressure interval 0.6–1.8 GPa, i.e., below the coesite-quartz transition and within the albite stability field. The absence of albite and biotite, together with the compositions of staurolite, chloritoid, chlorite, and phengite allow us to constrain the 580–590 °C portion of the retrograde *P-T* path from *P* = 1.12–0.96 GPa. The results are in good agreement with previously estimated *P-T* paths, mostly inferred from retrograde assemblages in whiteschist and eclogite of the Brossasco-Isasca unit.

Keywords: southern Dora-Maira Massif, metapelite, decompression *P-T* path, pseudosection.

Groppo, C., Castelli, D., and Compagnoni, R., 2006, Late chloritoid-staurolite assemblage in a garnet-kyanite–bearing metapelite from the ultrahigh-pressure Brossasco-Isasca unit (Dora-Maira Massif, Western Alps): New petrological constraints for a portion of the decompressional path, *in* Hacker, B.R., McClelland, W.C., and Liou, J.G., eds., Ultrahigh-pressure metamorphism: Deep continental subduction: Geological Society of America Special Paper 403, p. 127–138, doi: 10.1130/2006.2403(07).

INTRODUCTION

In spite of numerous studies on the peak Alpine pressure-temperature (*P-T*) conditions of the Brossasco-Isasca unit (Chopin, 1984, 1987; Kienast et al., 1991; Schertl et al., 1991; Compagnoni et al., 1995; Sharp et al., 1993; Simon et al., 1997; Chopin and Schertl, 2000; Compagnoni and Hirajima, 2001), the postclimactic history has been poorly constrained. The decompression *P-T* path, mostly inferred from retrograde assemblages in whiteschist and eclogite (Compagnoni et al., 1995; Nowlan et al., 2000; Chopin and Schertl, 2000; Hermann, 2003), suggests that the Brossasco-Isasca unit experienced a complex evolution that consisted of significant decompression coupled with moderate cooling, followed by moderate heating and moderate decompression at the *P-T* boundary between the upper greenschist– and amphibolite-facies conditions.

The Brossasco-Isasca unit metapelites have not been used to reconstruct the retrograde portion of the Alpine *P-T* evolution of the unit because the minerals reequilibrated during exhumation, and only the latest mineral assemblage was preserved. However, chloritoid and staurolite idioblasts in the matrix of an ultrahigh-pressure (UHP) metapelite sample can be used to constrain the *P-T* path. In the absence of suitable geothermobarometers, we used thermodynamic modeling to calculate a *P-T* pseudosection in the pressure interval from 1.8 to 0.6 GPa, i.e., below the coesite-quartz transition and within the albite stability field. The modeled *P-T* path was then compared with the results previously obtained from petrologic studies of whiteschist and eclogite from the Brossasco-Isasca unit.

GEOLOGICAL SETTING

The Dora-Maira Massif, together with Monte Rosa and Gran Paradiso, belongs to the Internal Crystalline Massif of the Pennine Domain of the Western Alps. The Dora-Maira Massif is a composite basement nappe in which several slices of continental crust, locally separated by thin ocean-derived units of the Piemonte zone, are juxtaposed (e.g., Sandrone et al., 1993) (Fig. 1A).

The coesite-bearing Brossasco-Isasca unit is located in the southern Dora-Maira Massif and is tectonically sandwiched between other similar continent-derived tectonic slices that experienced different early-Alpine peak metamorphism, ranging from epidote-blueschist (Chopin et al., 1991; Avigad et al., 2003; Compagnoni and Rolfo, 2003) to coesite-eclogite facies (Chopin, 1984, 1987; Chopin et al., 1991; Kienast et al., 1991; Schertl et al., 1991; Sharp et al., 1993; Compagnoni et al., 1994; Matsumoto and Hirajima, 2000; Compagnoni and Rolfo, 2003; Hermann, 2003) (Fig. 1B).

Two main lithostratigraphic complexes have been recognized by Compagnoni et al. (1995) in the Brossasco-Isasca unit: a Monometamorphic Complex and a Polymetamorphic Complex. The Monometamorphic Complex, which experienced only the Alpine polyphase metamorphic recrystallization, con-

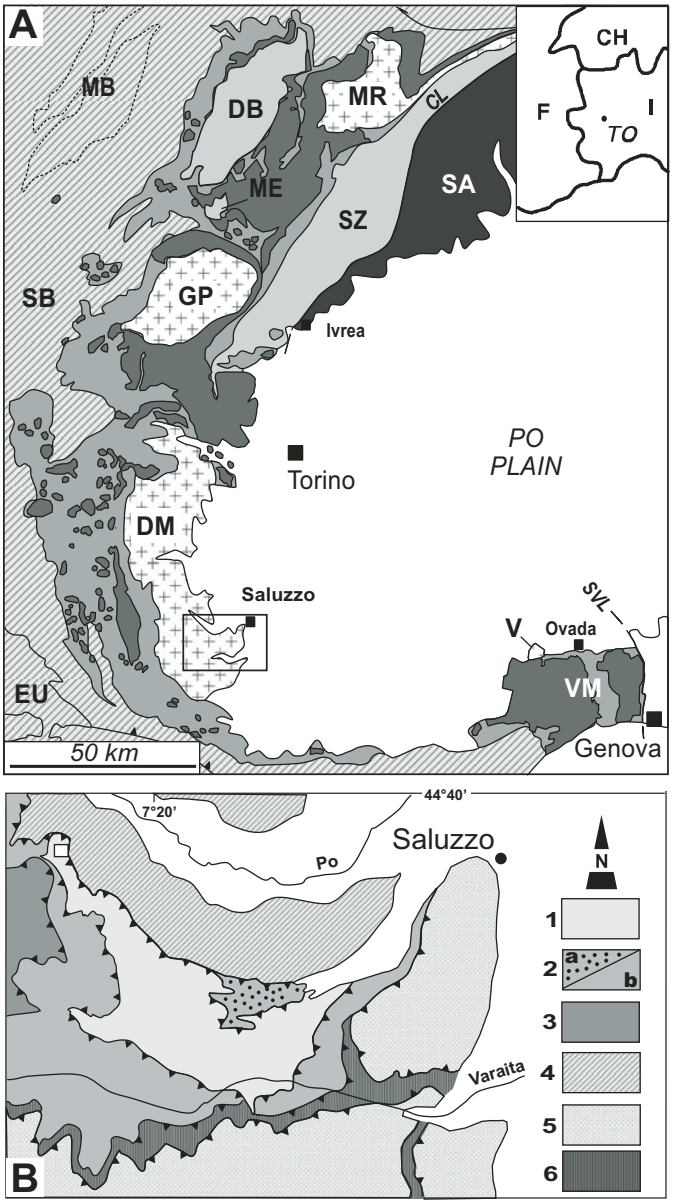

Figure 1. (A) Simplified tectonic sketch map of the Italian Western Alps. Helvetic Domain—Mont Blanc–Aiguilles Rouges (MB); Penninic Domain—Grand St. Bernard zone (SB), and Monte Rosa (MR), Gran Paradiso (GP), Dora-Maira (DM) and Valosio (V) Internal Crystalline Massifs; Austroalpine Domain—Dent Blanche nappe (DB), Monte Emilius nappe (ME), and Sesia zone (SZ). Southern Alps (SA); Embrunais–Ubaye Flysch nappe (EU); Voltri Massif (VM); Piemonte zone of calc-schists (light gray) with meta-ophiolites (dark gray). Other abbreviations and patterns: Canavese line (CL); Sestri-Voltaggio line (SVL); CH—Switzerland; F—France, TO—Torino. (B) Enlargement of the southern Dora-Maira Massif with location of the studied sample (small white square). 1—coesite-eclogite facies Brossasco-Isasca unit; 2—quartz-eclogite facies San Chiaffredo (a) and Rocca Solei (b) units; 3—quartz-eclogite facies "Upper Polymetamorphic" unit; 4—epidote-blueschist facies Pinerolo unit; 5—quartz-eclogite facies Dronero-Sampeyre unit; 6—lawsonite-blueschist to eclogite-facies meta-ophiolites of the Piemonte Zone.

sists of augen gneiss grading into medium- to fine-grained orthogneiss, locally with relict metagranitoids. Layers of pyrope-bearing whiteschist, derived from the metasomatic transformation of the granitoid protolith along ductile shear zones in the presence of a hydrous fluid phase (Gebauer et al., 1997; Compagnoni and Hirajima, 2001), are locally included in the orthogneiss.

The Polymetamorphic Complex experienced both pre-Alpine (most likely Variscan) and Alpine metamorphic cycles. It consists dominantly of paragneiss and paraschist with marble and eclogite intercalations. The paraschists contain rare textural and/or mineralogical relics of the pre-Alpine amphibolite-facies regional metamorphism (Biino and Compagnoni, 1991; Compagnoni and Hirajima, 1991; Compagnoni et al., 1994, 1995). Pre-Alpine intrusive contacts between the Variscan basement (corresponding to the Polymetamorphic Complex) and the late Variscan granitoids (the Monometamorphic Complex) are locally well preserved. For more detailed information about the Brossasco-Isasca unit, see Compagnoni and Rolfo (2003). The metapelite studied herein was sampled in the northwestern end of the Brossasco-Isasca unit and belongs to the Polymetamorphic Complex (Fig. 1B).

PETROGRAPHY

The studied metapelite is a medium-grained, garnet-kyanite-quartz/(coesite) + (jadeite) + high-Si phengite schist with accessory rutile and apatite. In spite of the seemingly pervasive Alpine deformation and metamorphism, pre-Alpine mineralogical relics are still preserved. We document two different generations of garnet: a pre-Alpine porphyroblastic garnet (Grt1) (mineral abbreviations according to Bucher and Frey, 2002) up to 2 cm in diameter; and an Alpine garnet (Grt2), which occurs both as thin coronas overgrowing Grt1 and as small idioblasts in the rock matrix (Fig. 2A). Grt1 contains inclusions of staurolite, kyanite, chloritoid, chlorite, paragonite, quartz, and ilmenite (partially transformed to rutile) and shows complex zoning, suggesting a polyphase pre-Alpine metamorphic evolution. The smaller Grt2 idioblasts include rutile needles with "sagenitic" arrangement, suggesting that they developed during the Alpine UHP metamorphic recrystallization event after a former pre-Alpine Ti-bearing biotite (Fig. 2B).

Phengite defines the main schistosity and is concentrated in millimeter-thick layers alternating with discontinuous, lensoidal quartz-rich domains. The phengite flakes are partially

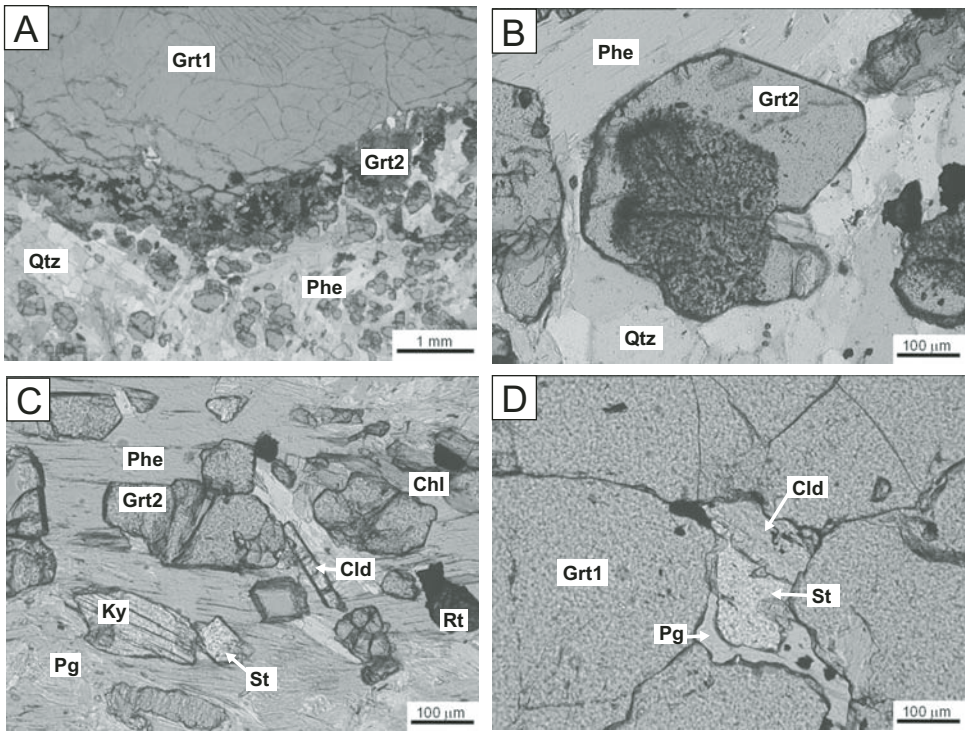

Figure 2. (A) Pre-Alpine porphyroblastic garnet (Grt1), ~2 cm in diameter rimmed with smaller Alpine garnets (Grt2). The overgrowth of Alpine Grt2 is evident from the presence of sagenitic rutile (darker Grt2). (B) Detail of an Alpine garnet (Grt2), the core of which is crowded with sagenitic rutile needles, suggesting its growth at the expense of a former pre-Alpine Ti-bearing biotite. (C) Alpine retrograde chloritoid and staurolite idioblasts grown in the metapelite matrix, which consists of Alpine Grt2, phengite, paragonite aggregates after former jadeite, kyanite, and quartz. (D) Alpine retrograde chloritoid and staurolite inclusions in pre-Alpine Grt1, developed along a fracture. Their chemical composition is the same as that of chloritoid and staurolite in the matrix. Chl—chlorite; Cld—chloritoid; Grt1—pre-Alpine garnet; Grt2—Alpine garnet; Ky—kyanite; Pg—paragonite; Phe—phengite; Qtz—quartz; Rt—rutile; St—staurolite.

replaced by finer-grained, less celadonitic phengite. No coesite relic is observed, but its former occurrence is suggested by the presence of polycrystalline quartz aggregates. Porphyroblastic kyanite, occurring within the phengitic domains, is locally fractured and corroded. Jadeite is not preserved, but its former occurrence is inferred from fine-grained rounded aggregates of paragonite.

Fine-grained chloritoid and staurolite idioblasts statically overgrew the main foliation (Fig. 2C). Staurolite is extremely rare and difficult to recognize with optical microscopy because of the absence of its typical yellow pleochroism. Chloritoid occurs as elongated prisms randomly cutting the schistosity, and shows weak greenish-blue to pale-blue pleochroism. Staurolite and chloritoid occur as inclusions near fractures in the pre-Alpine Grt1 (Fig. 2D). Chlorite occurs as aggregates concentrated in quartz-rich domains and appears to be in equilibrium with chloritoid. Albite does not occur in this paragenesis, in agreement with the observations of Hoschek (1967) that chloritoid is not stable with albite. Therefore, it may be concluded that in addition to the UHP peak assemblage, retrograde chloritoid, staurolite, quartz, paragonite/muscovite, and chlorite are preserved in the metapelite.

MINERAL CHEMISTRY

Garnet, white mica, chloritoid, staurolite, and chlorite were analyzed with a Cambridge Stereoscan 360 scanning electron microscope (SEM) equipped with an energy-dispersive spectrometer (EDS) Energy 200 and a Pentafet detector (Oxford Instruments) at the Department of Mineralogical and Petrological Sciences, University of Torino, Italy. The operating conditions were: 50 s counting time and 15 kV accelerating voltage. Microprobe data were acquired and managed using the Microanalysis Suite Issue 12, INCA Suite version 4.01; the raw data were calibrated on natural mineral standards and the ZAF (atomic number Z, Absorbance, Fluorescence) correction method was applied.

Garnet and phengite compositions were also checked with an electron microprobe (EMPA) Jeol JXA-8600 equipped with wavelength-dispersive spectrometers (WDS) at CNR (National Research Council), Institute of Geosciences and Georesources, Firenze, Italy. The operating conditions were 15 kV accelerating voltage and 10 nA beam current. The raw data were calibrated on natural mineral standards. The B-A correction method (Bence and Albee, 1968) was used to convert counts into concentrations by means of the TN-56 TRACOR-NORTHERN software package. Si, Ca, Fe, Al, Mg, Mn, Cr, K, and Ti counts were collected for 15 s and Na counts for 10 s.

Representative compositions of Alpine garnet, phengite, paragonite, margarite, staurolite, chloritoid, and chlorite are given in Tables 1 and 2. The pre-Alpine Grt1 is an Alm-Prp-Sps-(Grs) (mineral abbreviations according to Bucher and Frey, 2002) solid solution, characterized by complex concentric zoning with average composition from $Alm_{83}Prp_{10}Sps_4Grs_3$ in the core to $Alm_{78}Prp_{16}Sps_3Grs_3$ in the rim. Comparison with other zoned garnets from the same unit (e.g., Compagnoni and Hirajima, 2001) suggests that Grt1 underwent a polyphase pre-Alpine metamorphic evolution. Alpine Grt2 is relatively homogeneous and is characterized by a high almandine ($Alm_{72–77}$) and very low grossular ($Grs_{3–5}$) contents (Fig. 3); this suggests growth from a Ca-poor pelitic composition. In contrast to the pre-Alpine porphyroblastic Grt1, the smaller Grt2 is weakly zoned in Ca; the rutile needles–crowded core contains higher Ca.

We recognized four different types of white mica in the rock matrix: (1) Large flakes along the main foliation are high-Si phengite, with celadonitic substitution decreasing with increasing degree of recrystallization. The highest Si content, observed in the core of the largest flakes (Si = 3.55 atoms p.f.u. on the basis of 11 oxygen), decreases toward the rim (3.33 atoms p.f.u.) (Fig. 4). (2) Small flakes recrystallized from high-Si phengite contain very low celadonitic component (Si = 3.15–3.05 a.p.f.u), and a low Na content (up to 0.24 atoms p.f.u.) (Fig. 4). (3) Very fine-grained mica aggregates replacing jadeite are paragonite. (4) Rare margarite replaces the staurolite idioblasts.

Matrix chloritoid is relatively Fe-rich (from 0.78 to 0.80 mol%) and homogeneous. Staurolite is strongly zoned, with a Mg-rich core (X_{Mg} = 0.20) and an Fe-rich rim (X_{Mg} = 0.12). Both staurolite and chloritoid included adjacent to fractures in Grt1 are probably the products of late retrogressive reactions, such as (cf. Rodríguez Aller, 2003):

$$Alm + 5\ Ky + 3\ H_2O = 3\ St + 2\ Qtz$$

and

$$2\ St + 5\ Alm + 12\ H_2O = 23\ Cld + 7\ Qtz,$$

since they have exactly the same chemical composition as matrix chloritoid (Cld) and staurolite (St) (Table 2).

Chlorite, in equilibrium with chloritoid, shows X_{Mg} ranging from 0.47 to 0.53.

P-T PSEUDOSECTION

Effective Bulk-Rock Chemistry

Because of a lack of suitable geothermobarometers, the decompression *P-T* path was estimated by calculating a *P-T* pseudosection at fixed bulk-rock composition (e.g., Hensen, 1971; Zeh, 2001). Traditionally, two methods can be used to calculate the bulk composition of a rock. The first is based on mineral mode and mineral composition, obtained by point counting thin sections and by electron microprobe analysis, respectively (Zeh, 2001; Wei and Powell, 2003; Wei et al., 2004). As indicated by Zeh (2001), this method involves some problems, such as the presence of mineralogical heterogeneities, the definition of the mineral composition used for bulk-composition recalculation (important in the case of strongly

TABLE 1. REPRESENTATIVE ENERGY-DISPERSIVE SPECTROMETRY AND WAVELENGTH-DISPERSIVE SPECTROMETRY (in bold) ANALYSES OF ALPINE GARNET (Grt2), PHENGITE, PARAGONITE, AND MARGARITE

	Grt2 (site9)				Grt2 (site6)		Grt2 (site11)	
	rim	core	core	rim	rim	core	rim	core
Analyses	9.6	9.9	9.12	9.7	6.3	6.6	**11.4**	**11.5**
SiO_2	37.27	37.35	37.27	37.50	37.17	38.47	38.13	38.25
TiO_2	0.00	0.00	0.00	0.00	0.00	0.00	0.00	0.06
Al_2O_3	20.94	21.02	21.08	21.32	20.91	21.12	21.14	20.41
FeO	33.44	34.25	33.74	33.63	33.02	34.33	32.58	34.69
MnO	1.05	1.38	1.11	1.08	0.98	1.06	1.14	1.57
MgO	4.94	5.07	5.01	5.10	4.13	4.71	5.04	3.84
CaO	1.78	1.18	1.73	1.66	1.66	1.22	1.70	1.07
Total	99.42	99.85	99.14	100.29	99.37	100.91	99.75	99.99
Numbers of ions on the basis of 12O								
Si	2.99	2.98	2.98	2.98	3.02	3.03	3.03	3.06
Al	1.98	1.99	2.01	2.00	1.96	1.96	1.98	1.92
Ti	0.00	0.00	0.00	0.00	0.00	0.00	0.00	0.00
Fe^{2+}	2.24	2.30	2.28	2.23	2.20	2.26	2.16	2.32
Mn	0.07	0.09	0.08	0.07	0.07	0.07	0.08	0.11
Mg	0.59	0.61	0.60	0.60	0.49	0.55	0.60	0.46
Ca	0.15	0.10	0.15	0.14	0.14	0.10	0.14	0.09
Total	8.02	8.03	8.03	8.02	7.98	7.99	7.99	7.98
Molecular percentages of end-members								
Grs	0.05	0.03	0.05	0.05	0.05	0.03	0.05	0.03
Alm	0.75	0.77	0.76	0.74	0.73	0.75	0.72	0.77
Prp	0.20	0.20	0.20	0.20	0.16	0.18	0.20	0.15
Sps	0.02	0.03	0.03	0.02	0.02	0.02	0.03	0.04
X_{Mg}	0.21	0.21	0.21	0.21	0.18	0.20	0.22	0.16

	Phengite								Paragonite		Margarite
	core	core	core	core			rim	late			
Analyses	**2.2**	**11.1**	**11.2**	1.14	1.13	1.12	1.11	**2.3**	7.4	10.25	10.23
SiO_2	51.95	53.92	53.81	53.38	53.06	52.50	51.81	47.23	47.47	47.19	31.45
TiO_2	0.23	0.18	0.24	0.00	0.00	0.00	0.00	0.29	0.00	0.00	0.00
Al_2O_3	26.55	25.12	25.18	25.20	26.08	26.06	28.00	35.80	40.18	40.67	50.42
Cr_2O_3	0.01	0.08	0.04	0.00	0.00	0.00	0.00	0.04	0.00	0.00	0.00
FeO	2.02	2.03	1.87	1.86	2.12	2.03	2.03	0.74	0.00	0.00	0.00
MnO	0.00	0.00	0.00	0.00	0.00	0.00	0.00	0.06	0.00	0.00	0.00
MgO	3.47	3.98	3.97	4.14	3.67	3.89	3.26	0.65	0.00	0.00	0.00
CaO	0.01	0.00	0.00	0.00	0.00	0.00	0.00	0.06	0.00	0.40	12.75
Na_2O	0.19	0.17	0.05	0.00	0.00	0.00	0.56	2.03	7.32	7.17	1.25
K_2O	11.05	10.71	11.22	10.95	11.30	11.09	9.92	8.66	0.89	0.83	0.00
Total	95.49	96.20	96.39	95.52	96.23	95.57	95.58	95.56	95.85	96.26	95.86
Numbers of ions on the basis of 11O											
Si	3.46	3.55	3.54	3.54	3.50	3.49	3.42	3.10	3.01	2.98	2.07
Al^{IV}	0.54	0.45	0.46	0.46	0.50	0.51	0.58	0.90	0.99	1.02	1.93
Al^{VI}	1.54	1.49	1.49	1.50	1.53	1.53	1.60	1.88	2.01	2.01	1.99
Ti	0.01	0.01	0.01	0.00	0.00	0.00	0.00	0.01	0.00	0.00	0.00
Fe^{2+}	0.11	0.11	0.10	0.10	0.12	0.11	0.11	0.04	0.00	0.00	0.00
Mn	0.00	0.00	0.00	0.00	0.00	0.00	0.00	0.00	0.00	0.00	0.00
Mg	0.34	0.39	0.39	0.41	0.36	0.39	0.32	0.06	0.00	0.00	0.00
Sum	6.01	6.00	6.00	6.02	6.01	6.02	6.03	6.00	6.01	6.01	5.99
Ca	0.00	0.00	0.00	0.00	0.00	0.00	0.00	0.00	0.00	0.03	0.90
Na	0.03	0.02	0.01	0.00	0.00	0.00	0.07	0.26	0.90	0.88	0.16
K	0.94	0.90	0.94	0.93	0.95	0.94	0.84	0.73	0.07	0.07	0.00
Sum	0.96	0.92	0.95	0.93	0.95	0.94	0.91	0.99	0.97	0.97	1.06

TABLE 2. REPRESENTATIVE ENERGY-DISPERSIVE SPECTROMETRY ANALYSES OF STAUROLITE, CHLORITOID, AND CHLORITE

	Staurolite						Chloritoid							Chlorite			
	core	core	rim	rim	in Grt1	in Grt1							in Grt1				
Analyses	10.17	10.20	10.21	10.22	A.1	A.3		2.3	2.4	5.8	8.11	8.4	A.1		1.23	5.12	3.15
SiO_2	28.89	29.35	28.02	28.84	29.11	28.86	SiO_2	25.01	24.92	25.53	24.88	25.14	25.09	SiO_2	24.81	24.59	24.97
TiO_2	0.00	0.00	0.00	0.00	0.00	0.00	TiO_2	0.00	0.00	0.00	0.00	0.00	0.00	TiO_2	0.00	0.00	0.00
Al_2O_3	54.11	54.57	54.38	54.85	53.02	53.57	Al_2O_3	41.19	41.29	40.93	41.08	41.07	41.26	Cr_2O_3	0.00	0.00	0.00
FeO	10.33	10.59	10.23	10.75	10.97	11.51	FeO	22.83	22.58	22.78	23.13	23.81	23.23	Al_2O_3	22.66	22.36	22.06
ZnO	3.40	2.66	4.21	2.88	3.13	2.16	MnO	0.19	0.25	0.00	0.36	0.33	0.39	FeO	26.10	25.02	24.20
MnO	0.00	0.00	0.00	0.00	0.00	0.00	MgO	3.81	3.79	3.70	3.23	3.12	3.45	MnO	0.00	0.00	0.00
MgO	1.11	1.02	0.80	0.83	1.41	1.17	CaO	0.00	0.00	0.00	0.00	0.00	0.00	MgO	13.73	14.46	15.36
Total	97.84	98.19	97.64	98.14	97.65	97.28	Total	93.03	92.84	92.94	92.69	93.47	93.42	Total	87.30	86.43	86.59
Number of ions on the basis of 46O							Number of ions on the basis of 12O							Number of ions on the basis of 14O			
Si	8.12	8.16	7.96	8.05	8.01	7.93	Si	2.03	2.03	2.07	2.03	2.04	2.03	Si	2.64	2.63	2.65
Al	17.92	17.87	18.21	18.04	17.19	17.34	Al	3.94	3.96	3.91	3.96	3.93	3.94	Ti	0.00	0.00	0.00
Ti	0.00	0.00	0.00	0.00	0.00	0.00	Ti	0.00	0.00	0.00	0.00	0.00	0.00	Cr	0.00	0.00	0.00
Fe^{2+}	2.43	2.46	2.43	2.51	2.52	2.64	Fe^{2+}	1.55	1.54	1.54	1.58	1.62	1.57	Al	2.85	2.82	2.76
Zn	0.71	0.55	0.88	0.59	0.64	0.44	Mn	0.01	0.02	0.00	0.03	0.02	0.03	Fe^{2+}	2.33	2.24	2.15
Mn	0.00	0.00	0.00	0.00	0.00	0.00	Mg	0.46	0.46	0.45	0.39	0.38	0.42	Mn	0.00	0.00	0.00
Mg	0.47	0.42	0.34	0.34	0.58	0.48	Ca	0.00	0.00	0.00	0.00	0.00	0.00	Mg	2.18	2.31	2.43
Sum	28.92	28.91	28.94	28.93	28.94	28.83	Sum	8.00	8.00	7.97	7.99	7.99	7.99	Sum	10.00	10.00	10.00
X_{Mg}	0.16	0.15	0.12	0.12	0.19	0.15	X_{Mg}	0.23	0.23	0.22	0.20	0.19	0.21	X_{Mg}	0.48	0.51	0.53

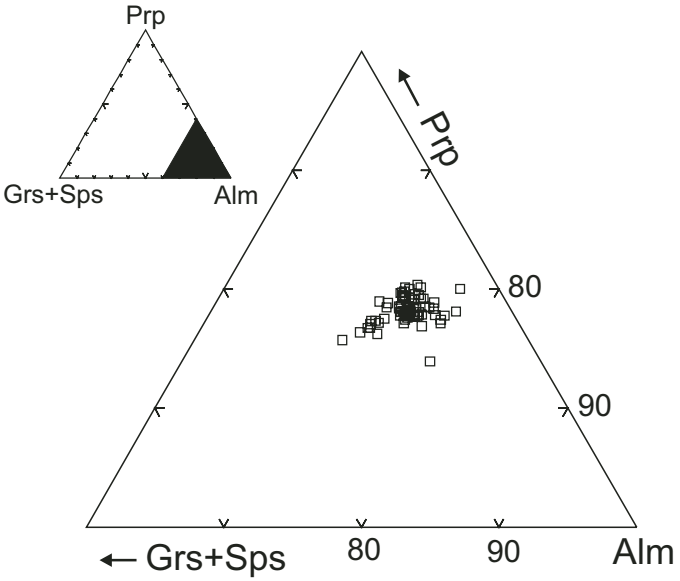

Figure 3. Composition of alpine garnets (Grt2) plotted in the (grossular [Grs] + spessartine [Sps])–pyrope [Prp]–almandine [Alm] diagram.

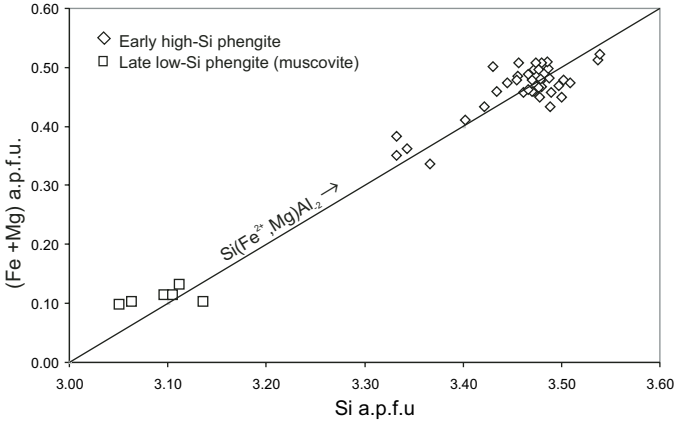

Figure 4. Phengite compositions plotted in the Si (atoms p.f.u. on the basis of 11 oxygens) versus (Fe + Mg) diagram. The line indicates the ideal celadonitic substitution.

zoned minerals), and the reduction of complex natural rock composition to a simpler model system. Alternatively, the bulk chemistry of the rock sample can be obtained by X-ray fluorescence (XRF) or inductively coupled plasma–mass spectrometry (ICP-MS) techniques. In this case, the composition must be simplified, and some corrections may be required (Zeh, 2001).

However, when a *P-T* pseudosection approach is used to reconstruct the *P-T* path of a rock, it is important that the composition accurately represents the system that was operating during metamorphism (Evans, 2004). The term "effective bulk composition" is used to distinguish between the measured bulk composition of the sample, and the composition of the chemical system available for mineral reaction in that sample (Stüwe, 1997).

In the studied metapelite, the pre-Alpine Grt1 occurs as porphyroblasts up to 2 cm in diameter, thus representing a significant portion of the modal composition. However, relict Grt1 appears to have been much less involved in the Alpine metamorphic reactions, and was not considered in the bulk-rock composition used to model the retrogressive *P-T* path. Therefore, the effective bulk composition was calculated by analyzing, by SEM-EDS, a representative number of metamorphic domains including only the Alpine mineral assemblage formed by low-celadonite phengite, paragonite, Grt2, chloritoid, staurolite, and chlorite. The bulk composition used in the calcula-

tion, which is the average of six SEM-EDS analyses of 4.70 × 3.20 mm areas is: SiO_2 = 49.81, TiO_2 = 1.09, Al_2O_3 = 27.78, FeO = 10.47, MgO = 2.28, MnO = 0.05, CaO = 0.50, K_2O = 4.26, and Na_2O = 1.79 (wt%). These data are reported on a molar basis in Figure 5.

Results of *P-T* Pseudosection Calculation

A *P-T* pseudosection in the system MnNKFMASH (MnO-Na_2O-K_2O-FeO-MgO-Al_2O_3-SiO_2-H_2O) was constructed for the Brossasco-Isasca unit metapelite using the effective whole-rock composition as discussed in the preceding section. CaO was not considered because it is minor. Na_2O was included in the system to model the paragonite-albite transition. The *P-T* pseudosection was calculated following the approach of Connolly (1990), and using the internally consistent thermodynamic data set and equation of state for H_2O of Holland and Powell (1998, upgrade 2002). The phases considered in the calculation were garnet, staurolite, chloritoid, phengite, paragonite, biotite, chlorite, albite, and quartz. Solid-solution models and mixing parameters used for garnet, staurolite, chloritoid, phengite, biotite, and chlorite are briefly described in the Appendix. Albite was treated as the pure end member.

In the calculation, the following assumptions were made: (1) H_2O was the only fluid phase affecting mineral equilibria and was in excess, as suggested by the presence of hydrous minerals and the absence of carbonates; and (2) the system was SiO_2 saturated.

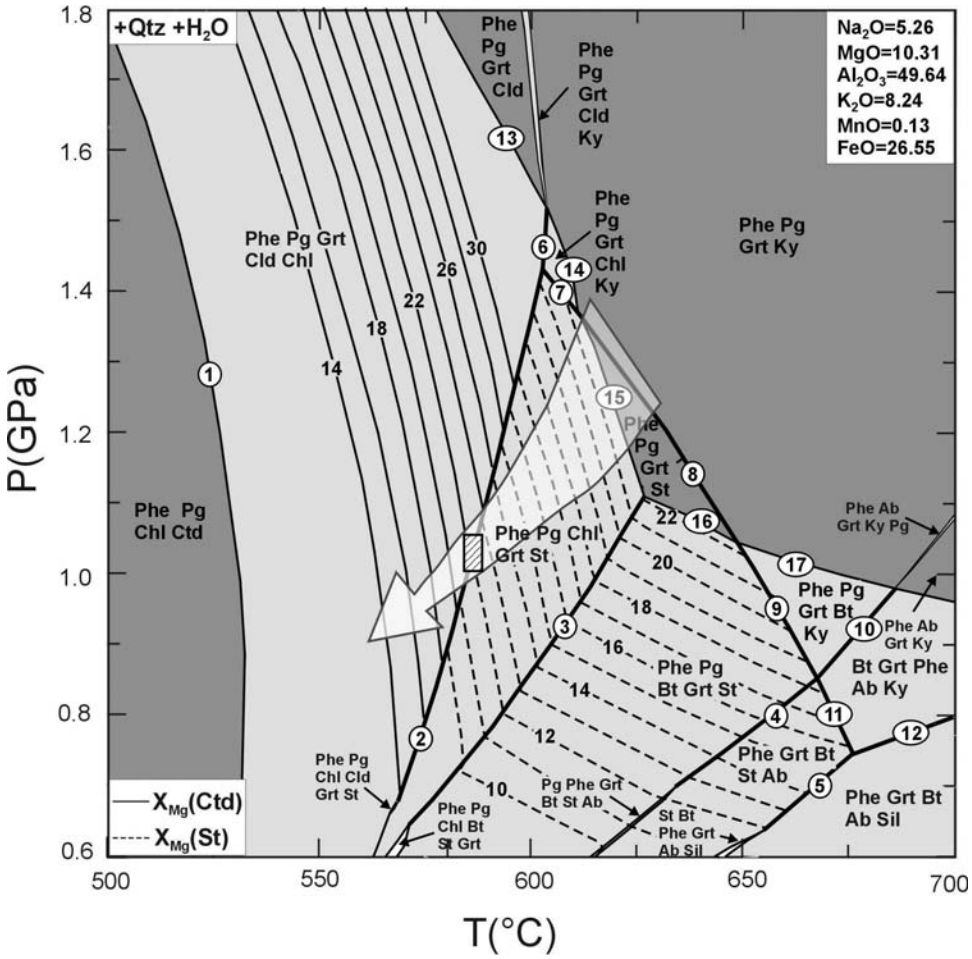

Figure 5. Pressure-temperature (*P-T*) pseudosection for the studied metapelite calculated in the MnNKFMASH system, using the effective bulk composition obtained from the average SEM-EDS analyses, which are reported in the top right inset. White, light-gray, and dark-gray fields are quadri-, tri-, and divariant fields, respectively. Thick lines are discontinuous reactions. Circled numbers refer to the reactions listed in Table 3. Chloritoid and staurolite X_{Mg} [Mg/(Mg + Fe + Mn)]% isopleths are reported as thin continuous and dashed lines, respectively. The small ruled rectangle shows the match of the X_{Mg}(St) = 12 and X_{Mg}(Cld) = 22 isopleths, which constrain the retrograde Alpine *P-T* path. The proposed *P-T* trajectory is shown as a white arrow. Mineral abbreviations according to Bucher and Frey (2002): Ab—albite; Bt—biotite; Chl—chlorite; Cld—chloritoid; Grt2—Alpine garnet; Ky—kyanite; Pg—paragonite; Phe—phengite; Qtz—quartz; Rt—rutile; Sil—sillimanite; St—staurolite.

The *P-T* pseudosection, calculated in the range T = 500–700 °C and P = 0.6–1.8 GPa, consists of 5 quadrivariant, 10 trivariant, and 4 divariant fields (Fig. 5). The most relevant equilibrium assemblages along boundary curves that involve garnet, phengite, chloritoid, staurolite, biotite, kyanite, albite, and chlorite are given in Table 3. Focusing on staurolite- and chloritoid-bearing assemblages, the staurolite stability field, limited by the two reactions,

St-in: Cld + Qtz = St + Grt + Chl + H_2O
(reaction 2 in Table 3)

and

St-out: St + Qtz = Grt + Ky + H_2O (reaction 8 in Table 3),

occurs below the invariant point [Ctd,Ky,St], at $P \approx 1.4$ GPa and $T \approx 600$ °C.

From Figure 5 it is evident that the staurolite Mg content progressively decreases with decreasing pressure and temperature (X_{Mg} isopleths from 0.22 to 0.10). The chloritoid upper-stability limit is mainly controlled by reactions 2 and 6 of Table 3: its Mg content progressively decreases with decreasing temperature. Chlorite occurs at temperatures below 625 °C; its upper-stability limit is constrained by reactions 3, 13, 14, and 15 of Table 3. Garnet forms according to reaction 1 at $T > 525$ °C. The X_{Mg} isopleths of chlorite and garnet, which show approximately the same trend as the chloritoid isopleths, are not shown in the pseudosection of Figure 5 for clarity. The phengite stability field covers all the investigated pressure intervals, with its Si content ranging from 3.38 atoms p.f.u. at 1.8 GPa to 3.10 atoms p.f.u. at 0.6 GPa. The paragonite-albite transition is constrained by the discontinuous reactions 4 and 10; the albite-bearing assemblages are restricted to low pressures. The albite stability field is controlled by the Al_2O_3 content in the bulk-rock composition (Zeh, 2001; Proyer, 2003a, 2003b); the paragonite stability field expands toward lower pressures and higher temperatures with increasing Al_2O_3 content. The biotite stability field is constrained by reactions 3, 16, and 17 at low-pressure and high-temperature conditions.

TABLE 3. MODELED EQUILIBRIUM ASSEMBLAGES ALONG THE RELEVANT BOUNDARY CURVES OF FIGURE 5*

(1)	$Chl_1 + Cld_1 + Qtz = Cld_2 + Grt + Chl_2 + H_2O$
(2)	$Cld + Qtz = Grt + Chl + St + H_2O$
(3)	$Grt + Phe + Chl = Pg + Bt + St + Qtz + H_2O$
(4)	$Pg + Grt + Qtz = Phe + Ab + Bt + St + H_2O$
(5)	$Ab + Bt + St + Qtz = Phe + Sil + Grt + H_2O$
(6)	$Cld + Qtz = Grt + Chl + Ky + H_2O$
(7)	$Chl + St + Qtz = Grt + Ky + H_2O$
(8)	$St + Grt + Qtz = Grt + Ky + H_2O$
(9)	$Pg + Bt + St + Qtz = Phe + Ky + Grt + H_2O$
(10)	$Pg + Bt + Grt + Qtz = Ab + Ky$
(11)	$Ab + Bt + St + Qtz = Phe + Grt + Ky + H_2O$
(12)	$Ky = Sil$
(13)	$Grt_1 + Chl + Cld + Qtz = Grt_2 + H_2O$
(14)	$Ky + Grt_1 + Chl + Qtz = Grt_2 + H_2O$
(15)	$Grt_1 + St + Chl + Qtz = Grt_2 + H_2O$
(16)	$Pg + Grt_1 + St + Bt + Qtz = Phe + Grt_2 + H_2O$
(17)	$Ky + Bt + Grt_1 + Pg + Qtz = Grt_2 + Phe + H_2O$

*Due to pseudocompounds approximation (Connolly, 1990), an assemblage along a boundary curve may contain more than one compound belonging to the same solid solution. These modeled compounds are identified by numeral subscripts.

Reconstruction of the Retrograde *P-T* Path

Combining the calculated *P-T* pseudosection (Fig. 5) with petrological observations, the following constraints can be inferred for the retrograde *P-T* path of the metapelite:

(1) paragonite is the only Na-bearing phase in the metapelite; therefore, the retrograde *P-T* trajectory must lie at pressures exceeding the paragonite-albite reactions (4, 10);
(2) biotite was not observed in the metapelite; so the *P-T* path must pass above reaction curve 3: Grt + Phe + Chl = Pg + Bt + St + Qtz + H_2O;
(3) staurolite and chloritoid are both present in the rock matrix; therefore, the retrograde *P-T* trajectory first must enter the staurolite stability field and then the chloritoid stability field;
(4) staurolite has a Mg-rich core and an Fe-rich rim (X_{Mg} from 0.20 to 0.12), and chloritoid composition ranges from X_{Mg} = 0.22 to X_{Mg} = 0.18; therefore, the *P-T* path must cross the corresponding isopleths.

All this information tightly constrains the retrograde *P-T* path of the metapelite in the *P-T* interval 550–650 °C and 0.9–1.4 GPa (Fig. 5). The inferred trajectory is not only consistent with the staurolite and chloritoid compositional zoning, but also with the compositions of garnet, chlorite, and phengite. Microstructural data, which suggest that chlorite and chloritoid are in equilibrium, are confirmed by the overlap of the chlorite-chloritoid isopleths. Finally, late fine-grained phengite, derived from recrystallization of the high-Si phengite, is characterized by a Si content ranging from 3.16 to 3.10 atoms p.f.u.; these values correspond to a pressure range between 1.1 and 0.6 GPa.

The *P-T* pseudosection was also calculated at reduced activity of H_2O to evaluate the influence of aH_2O on the stability of phase equilibria. For aH_2O = 0.75, the topology of the phase diagram is similar, but all reaction curves are shifted toward lower pressure and temperature (Fig. 6). For example, the piercing point resulting from intersection of the staurolite and chloritoid isopleths (X^{St}_{Mg} = 0.12 and X^{Ctd}_{Mg} = 0.22, respectively) shifts from T = 585 °C, P = 1.03 GPa at aH_2O = 1 (Fig. 5), to T = 565 °C, P = 0.98 GPa at aH_2O = 0.75.

DISCUSSION

Microstructural and mineral chemistry data, together with the calculated *P-T* pseudosection allow us to reconstruct a small portion of the decompression *P-T* path of the Brossasco-Isasca unit from about T = 700 °C at P = 1.8 GPa to T = 500 °C at P =

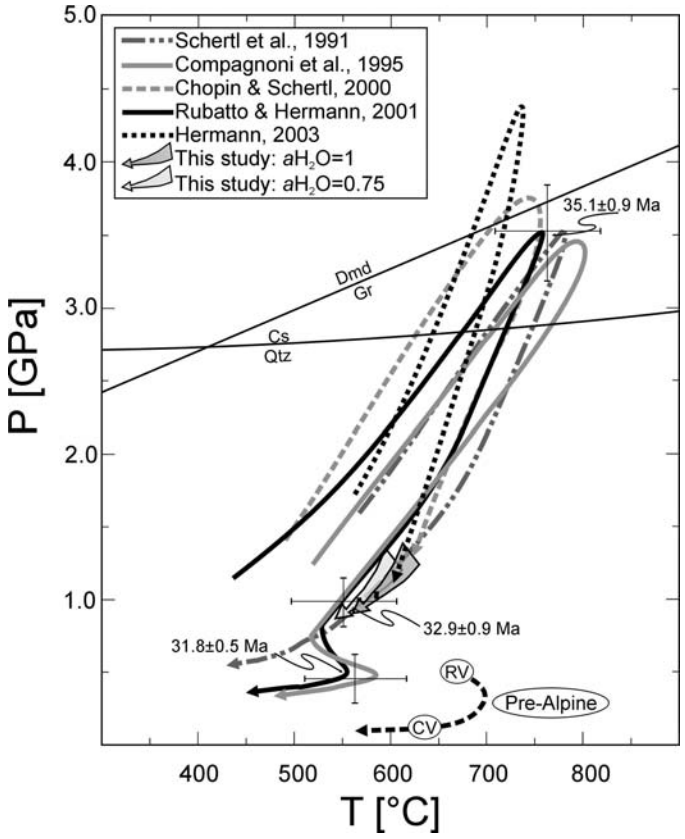

Figure 6. Comparison between the pressure-temperature (*P-T*) paths modeled for $aH_2O = 1$ and $aH_2O = 0.75$, respectively, and the *P-T* paths obtained from other lithologies by Schertl et al. (1991), Compagnoni et al. (1995), Chopin and Schertl (2000), Rubatto and Hermann (2001), and Hermann (2003). For the *P-T* trajectory of Rubatto and Hermann (2001), the age estimates of the most relevant metamorphic events are indicated. The pre-Alpine *P-T* path of the Polymetamorphic Complex is also reported; RV—Variscan regional metamorphism; CV—Variscan contact metamorphism; Cs—coesite, Qtz—quartz, Gr—graphite, Dmd—diamond.

0.6 GPa. The resulting *P-T* trajectory is well constrained by the relatively narrow stability field of each of the parageneses discussed herein and by the chemical composition of the minerals involved in the retrograde path. In particular, the *P-T* trajectory must intersect the reaction Cld + Qtz = St + Grt + H_2O (reaction 2 in Fig. 5) in a narrow *P-T* range ($580 < T < 590$ °C and $1.00 < P < 1.06$ GPa) where staurolite with modeled $X_{Mg} = 0.12$ reacts to give a chloritoid with modeled $X_{Mg} = 0.22$ (Fig. 5).

As reported herein, most constraints on the Brossasco-Isasca unit retrograde history derive from pyrope-bearing whiteschist (Schertl et al., 1991; Hermann, 2003) and eclogites (Nowlan, 1998; Chopin and Schertl, 2000). Schertl et al. (1991) described a retrograde *P-T* path consisting of two parts: a first, almost-isothermal decompression from 3.5 to 1.7 GPa coupled with cooling from 800 to 780 °C, and a second decompression from 1.7 to 0.5 GPa associated with cooling from 780 °C to 500 °C, respectively (Fig. 6).

On the basis of data reported by Chopin (1984, 1987), Kienast et al. (1991), and Sharp et al. (1993), Compagnoni et al. (1995) suggested a new *P-T* path for the Brossasco-Isasca unit. The climax conditions are constrained as $P = 3.3 \pm 0.3$ GPa and $T = 750 \pm 30$ °C—i.e., within the graphite stability field (Fig. 6). The subsequent evolution is marked by significant decompression coupled with moderate and continuous cooling (Fig. 6). A later tectonometamorphic event, developed at relatively low pressures, is characterized by a thermal peak at the boundary between upper greenschist– and low amphibolite–facies conditions (Fig. 6). Compagnoni et al. (1995) also recognized a pre-Alpine polyphase amphibolite-facies regional metamorphic event in the paraschists of the Polymetamorphic Complex, most likely Variscan in age (at ca. 330 Ma; Fig. 6). This regional event is locally overprinted by a high-temperature–low-pressure contact metamorphic recrystallization connected to the emplacement of late Variscan granitoids (at ca. 280 Ma; Gebauer et al., 1997).

Chopin and Schertl (2000) used the data of Nowlan (1998) to suggest a quite different retrograde path. Their *P-T* estimates were obtained using the garnet-clinopyroxene-phengite geobarometer of Waters and Martin (1993) coupled with the garnet-clinopyroxene geothermometer applied to the rim compositions of matrix phengite and omphacite from Brossasco-Isasca unit eclogites; these data defined a slightly cooler path than that of Schertl et al. (1991), corresponding to 2.4 GPa at 650 °C and 1.4 GPa at 620 °C (Fig. 6).

Rubatto and Hermann (2001) reconstructed the Brossasco-Isasca unit *P-T-t* (time) path combining petrological observations and geochronological data from calc-silicate nodules in marbles. They recognized an initial, fast exhumation stage from 3.5 to 1.0 GPa (i.e., from 110 to 35 km depth), with an exhumation rate of 3.4 cm/yr. This was followed by a second decompression stage from 1.0 to 0.5 GPa (from 35 to 17 km depth), at a mean exhumation rate of 1.6 cm/yr, associated with a slight heating. This exhumation rate is consistent with the earlier estimate by Borghi et al. (1996) for the Internal Penninic nappes and by Gebauer et al. (1997) for the Brossasco-Isasca unit (2–2.4 cm/yr). A later, slower exhumation, associated with a cooling to 250 °C, occurred at 0.5 cm/yr. Hermann (2003) reconstructed the retrograde *P-T* path for the whiteschist by using microstructural data (three different coronas along garnet-phengite contacts) combined with the Si content in phengite. The proposed trajectory shows decompression from 4.3 to 1.1 GPa accompanied by cooling from 730 to 600 °C (Fig. 6).

The retrograde *P-T* path obtained in this study from the metapelite is in good agreement with the last portion of the trajectory proposed by Chopin and Schertl (2000) and Hermann (2003), and is a reasonable extrapolation of their results toward the lower *P-T* portion of the Brossasco-Isasca unit path. Our *P-T* path ($aH_2O = 1$) is slightly warmer than the *P-T-t* trajectory of Rubatto and Hermann (2001). The *P-T* path by Schertl et al. (1991) lies at even higher temperature; as suggested by Chopin and Schertl (2000), the temperature might have been

overestimated due to the use of a unit H_2O activity to calculate the position of the reaction Tlc + Ky = Prp + Cs + H_2O.

The exhumation path modeled after calculation of the pseudosection at $aH_2O = 0.75$ is very close to the *P-T* paths proposed by Schertl et al. (1991), Compagnoni et al. (1995), and Hermann (2003). Most of the differences among these *P-T* trajectories may be due to the aH_2O values used for the thermobarometric estimates. In the Brossasco-Isasca unit, the aH_2O was estimated as >0.8 (Schertl et al., 1991) or in the range 0.4–0.7 (Sharp et al., 1993) in whiteschist, but its actual value is difficult to estimate because it is a function of temperature, pressure, and composition.

Though aH_2O may have played an important role in the stability of mineral assemblages and phase equilibria, the modeled portion of the retrograde *P-T* path is consistent with those previously obtained from other rock types of the Brossasco-Isasca unit. This work clearly indicates that partially reequilibrated rocks with relict minerals may give information useful for reconstructing the *P-T* path even of polymetamorphic rocks, provided a suitable ("effective") bulk-rock chemical composition is used for thermodynamic calculations.

ACKNOWLEDGMENTS

Careful reviews by G. Ernst, E. Ghent, B. Hacker, J.G. Liou, and H.-P. Schertl, which improved the article, are greatly appreciated. We are very grateful to J.A.D. Connolly for sharing his skill in phase diagram calculation and analysis. Daniele Castelli and Roberto Compagnoni acknowledge the financial support from CNR (National Research Council), Institute of Geosciences and Georesources.

Appendix. Solid Solution Models and Mixing Parameters

Solid solution models, end members, and mixing parameters are given in Table A, with the relevant references.

TABLE A. SOLID SOLUTION MODELS AND MIXING PARAMETERS

Phase solution models	End members		References
Garnet (Grt) $Fe_{3x}Ca_{3y}Mg_{3z}Mn_{3(1-x-y-z)}Al_2Si_3O_{12}$ $x + y + z \leq 1$	Spessartine Almandine Pyrope Grossular	$Mn_3Al_2Si_3O_{12}$ $Fe_3Al_2Si_3O_{12}$ $Mg_3Al_2Si_3O_{12}$ $Ca_3Al_2Si_3O_{12}$	Holland and Powell (1998)
Phengite (Phe) $K_xNa_{1-x}Mg_yFe_zAl_{3-2(y+z)}Si_{3+y+z}O_{10}(OH)_2$	Celadonite Fe-celadonite Muscovite Paragonite	$KMgAlSi_4O_{10}(OH)_2$ $KFeAlSi_4O_{10}(OH)_2$ $KAl_3Si_3O_{10}(OH)_2$ $NaAl_3Si_3O_{10}(OH)_2$	Holland and Powell (1998)
Biotite (Bt) $KMg_{(3-w)x}Fe_{(3-w)y}Mn_{(3-w)(1-x-y)}Al_{1+2w}Si_{3-w}O_{10}(OH)_2$ $x + y \leq 1$	Annite Eastonite Mn-biotite Phlogopite mnts_i = 1 east + 2/3 mnbi - 2/3 phl sdph_i = 1 east + 2/3 ann - 2/3phl	$KFe_3AlSi_3O_{10}(OH)_2$ $KMg_2Al_3Si_2O_{10}(OH)_2$ $KMn_3AlSi_3O_{10}(OH)_2$ $KMg_3AlSi_3O_{10}(OH)_2$	Powell & Holland (1999)
Chlorite (Chl) $Mg_{(5-y+z)x}Fe_{(5-y+z)w}Mn_{(5-y+z)(1-x-w)}Al_{2(1+y+z)}Si_{3-y+z}O_{10}(OH)_8$ $x + w \leq 1$	Clinochlore Daphnite Mn-chlorite	$Mg_5Al_2Si_3O_{10}(OH)_4$ $Fe_5Al_2Si_3O_{10}(OH)_4$ $Mn_5Al_2Si_3O_{10}(OH)_4$	Holland et al. (1998)
Staurolite (St) $Mg_{4x}Fe_{4y}Mn_{4(1-x-y)}Al_{18}Si_{7.5}O_{48}H_4$ $x + y \leq 1$	Fe-staurolite Mg-staurolite Mn-staurolite	$Fe_4Al_{18}Si_{7.5}O_{48}H_4$ $Mg_4Al_{18}Si_{7.5}O_{48}H_4$ $Mn_4Al_{18}Si_{7.5}O_{48}H_4$	Holland and Powell (1998)
Chloritoid (Cld) $Mg_xFe_yMn_{(1-x-y)}Al_2SiO_5(OH)_2$ $x + y \leq 1$	Fe-chloritoid Mg-chloritoid Mn-chloritoid	$FeAl_2SiO_5(OH)_2$ $MgAl_2SiO_5(OH)_2$ $MnAl_2SiO_5(OH)_2$	Holland and Powell (1998)

Note: mnts—Mn-tschermack; east—eastonite; mnbi—Mn-biotite; phl—phlogopite; sdph—siderophillite; ann—annite

REFERENCES CITED

Avigad, D., Chopin, C., and Le Bayon, R., 2003, Thrusting and extension in the southern Dora Maira ultra-high-pressure massif (Western Alps): View from below the coesite-bearing unit: The Journal of Geology, v. 111, p. 57–70, doi: 10.1086/344664.

Bence, A.E., and Albee, A.L., 1968, Empirical correction factors for the electron microanalysis of silicates and oxides: The Journal of Geology, v. 76, p. 382–402.

Biino, G., and Compagnoni, R., 1991, Evidence for a polymetamorphic crystalline basement in the very high pressure Brossasco-Isasca complex, Dora-Maira Massif, Western Alps: EUG VI Meeting, Strasbourg: Terra Abstracts, v. 3, p. 84.

Borghi, A., Compagnoni, R., and Sandrone, R., 1996, Composite *P-T* path in the Internal Penninic massifs of the Western Alps: Petrological constraints on their thermo-mechanical evolution: Eclogae Geologicae Helvetiae, v. 89, p. 345–367.

Bucher, M., and Frey, K., 2002, Petrogenesis of metamorphic rocks (7th edition): Berlin, Springer-Verlag, 341 p.

Carswell, D.A., O'Brien, P.J., Wilson, R.N., and Zhai, M., 1997, Thermobarometry of phengite-bearing eclogites in the Dabie Mountains of central China: Journal of Metamorphic Geology, v. 15, p. 239–252, doi: 10.1111/j.1525-1314.1997.00014.x.

Chopin, C., 1984, Coesite and pure pyrope in high-grade blueschists of the Western Alps: A first record and some consequences: Contributions to Mineralogy and Petrology, v. 86, p. 107–118, doi: 10.1007/BF00381838.

Chopin, C., 1987, Very high-pressure metamorphism in the Western Alps: New petrological and field data: Terra Cognita, v. 7, p. 94.

Chopin, C., and Schertl, H.P., 2000, The UHP unit in the Dora-Maira Massif, Western Alps, *in* Ernst, W.G., and Liou, J.G., eds., Ultrahigh-pressure metamorphism and geodynamics in collision-type orogenic belts: Final Report of the Task Group III-6 of the International Lithosphere Project: Bellwether Publishing Ltd. and Geological Society of America International Book Series, v. 4, p. 133–148

Chopin, C., Henry, C., and Michard, A., 1991, Geology and petrology of coesite-bearing terrane, Dora-Maira Massif, Western Alps: European Journal of Mineralogy, v. 3, p. 263–291.

Compagnoni, R., and Hirajima, T., 1991, Geology and petrology of the Brossasco-Isasca complex, southern Dora-Maira Massif, Western Alps: EUG VI Meeting, Strasbourg: Terra Abstracts, v. 3, p. 84.

Compagnoni, R., and Hirajima, T., 2001, Superzoned garnets in the coesite-bearing Brossasco-Isasca unit, Dora-Maira Massif, Western Alps, and the origin of the whiteschists: Lithos, v. 57, p. 219–236, doi: 10.1016/S0024-4937(01)00041-X.

Compagnoni, R., and Rolfo, F., 2003, UHPM units in the Western Alps, *in* Carswell, D.A., and Compagnoni, R., eds., Ultrahigh pressure metamorphism: EMU (European Mineralogical Union) Notes in Mineralogy, Volume 5: Budapest, Eötvös University Press, p. 13–49.

Compagnoni, R., Messiga, B., and Castelli, D., 1994, High pressure metamorphism in the Western Alps, *in* Guidebook to the field excursion B1, 16th General Meeting of the International Mineralogical Association, Pisa: Torino, Italy, Ovidiografica, Pino Torinese, 148 p.

Compagnoni, R., Hirajima, T., and Chopin, C., 1995, Ultra-high-pressure metamorphic rocks in the Western Alps, *in* Coleman, R.G., and Wang, X., eds., Ultrahigh pressure metamorphism: Cambridge, Cambridge University Press, p. 206–243.

Connolly, J.A.D., 1990, Multivariable phase diagrams: An algorithm based on generalized thermodynamics: American Journal of Science, v. 290, p. 666–718.

Evans, T.P., 2004, A method for calculating effective bulk composition modification due to crystal fractionation in garnet-bearing schist: Implication for isopleth thermobarometry: Journal of Metamorphic Geology, v. 22, p. 547–557, doi: 10.1111/j.1525-1314.2004.00532.x.

Gebauer, D., Schertl, H.P., Brix, M., and Schreyer, W., 1997, 35 Ma old ultrahigh-pressure metamorphism and evidence for very rapid exhumation in the Dora-Maira Massif, Western Alps: Lithos, v. 41, p. 5–24, doi: 10.1016/S0024-4937(97)82002-6.

Hensen, B.J., 1971, Theoretical phase relations involving cordierite and garnet in the system MgO-FeO-Al_2O_3-SiO_2: Contributions to Mineralogy and Petrology, v. 33, p. 191–214, doi: 10.1007/BF00374063.

Hermann, J., 2003, Experimental evidence for diamond-facies metamorphism in the Dora-Maira Massif: Lithos, v. 70, p. 163–182, doi: 10.1016/S0024-4937(03)00097-5.

Holland, T.J.B., and Powell, R., 1998, An internally consistent thermodynamic data set for phases of petrologic interest: Journal of Metamorphic Geology, v. 16, p. 309–343, doi: 10.1111/j.1525-1314.1998.00140.x.

Holland, T., Baker, J., and Powell, R., 1998, Mixing properties and activity-composition relationships of chlorites in the system MgO-FeO-Al_2O_3-SiO_2-H_2O: European Journal of Mineralogy, v. 10, p. 395–406.

Hoschek, G., 1967, Untersuchungen zum Stabilitätsbereich von Chloritoid und Staurolith: Contributions to Mineralogy and Petrology, v. 14, p. 123162, doi: 10.1007/BF00377530.

Kienast, J.R., Lombardo, B., Biino, G., and Pinardon, G., 1991, Petrology of very high pressure eclogitic rocks from the Brossasco-Isasca complex, Dora-Maira Massif, Italian Western Alps: Journal of Metamorphic Geology, v. 9, p. 19–34.

Matsumoto, N., and Hirajima, T., 2000, Garnet in pelitic schists from a quartz-eclogite unit of the southern Dora-Maira Massif, Western Alps: Schweizerische Mineralogische und Petrographische Mitteilungen, v. 80, p. 53–62.

Nowlan, E.U., 1998, Druck-Temperatur-Entwicklung und Geochemie von Eklogiten des Dora Maira Massivs, Westalpen [Ph.D. thesis]: Bochum, Ruhr-Universität, 167 p.

Nowlan, E.U., Schertl, H.P., and Schreyer, W., 2000, Garnet-omphacite-phengite thermobarometry of eclogites from the coesite-bearing unit of the southern Dora-Maira Massif, Western Alps: Lithos, v. 52, p. 197–214, doi: 10.1016/S0024-4937(99)00091-2.

Powell, R., and Holland, T., 1999, Relating formulations of the thermodynamics of mineral solid solutions: Activity modeling of pyroxenes, amphiboles, and micas: The American Mineralogist, v. 84, p. 1–14.

Proyer, A., 2003a, The preservation of high-pressure rocks during exhumation: Metagranites and metapelites: Lithos, v. 70, p. 183–194, doi: 10.1016/S0024-4937(03)00098-7.

Proyer, A., 2003b, Metamorphism of pelites in NKFMASH—A new petrogenetic grid with implications for the preservation of high pressure rocks during exhumation: Journal of Metamorphic Geology, v. 21, p. 493–509, doi: 10.1046/j.1525-1314.2003.00457.x.

Rodríguez Aller, J., 2005, Recristalización y deformación de litologías supracorticales sometidas a metamorfismo de alta presión (complejo de Malpica-Tuy, NO del Macizo Ibérico) [Ph.D. thesis]: Universidad de Coruña, Pais Vasco, Laboratorio Xeolóxico de Laxe, Área de Xeolóxia e Minería do Seminario de Estudos Galegos, Serie Nova Terra, v. 29, Ediciós do Castro, 542 p.

Rubatto, D., and Hermann, J., 2001, Exhumation as fast as subduction?: Geology, v. 16, p. 577–588.

Sandrone, R., Cadoppi, P., and Vialon, P., 1993, The Dora-Maira Massif, *in* von Raumer, J.F., and Neubauer, F., eds., Pre-Mesozoic geology in the Alps: Berlin, Springer, p. 315–323.

Schertl, H.P., Schreyer, W., and Chopin, C., 1991, The pyrope-coesite rocks and their country rocks at Parigi, Dora-Maira Massif, Western Alps: Detailed petrography, mineral chemistry and *P-T* path: Contributions to Mineralogy and Petrology, v. 108, p. 1–21.

Sharp, Z.D., Essene, E.J., and Hunziker, J.C., 1993, Stable isotope geochemistry and phase equilibria of coesite-bearing whiteschists, Dora Maira Massif, Western Alps: Contributions to Mineralogy and Petrology, v. 114, p. 1–12, doi: 10.1007/BF00307861.

Simon, G., Chopin, C., and Schenk, V., 1997, Near end-member magnesiochloritoid in prograde-zoned pyrope, Dora-Maira Massif, Western Alps: Lithos, v. 41, p. 37–57, doi: 10.1016/S0024-4937(97)82004-X.

Stüwe, K., 1997, Effective bulk composition changes due to cooling: A model predicting complexities in retrograde reaction textures: Contributions to Mineralogy and Petrology, v. 129, p. 43–52, doi: 10.1007/s004100050322.

Waters, D.J., and Martin, H.N., 1993, Geobarometry of phengite-bearing eclogites: Terra Abstracts, v. 5, p. 410–411.

Wei, C.J., and Powell, R., 2003, Phase relations in high-pressure metapelites in the system KFMASH (K_2O-FeO-MgO-Al_2O_3-SiO_2-H_2O) with application to natural rocks: Contribution to Mineralogy and Petrology, v. 145, p. 301–315, doi: 10.1007/s00410-003-0454-1.

Wei, C.J., Powell, R., and Clarke, G.L., 2004, Calculated phase equilibria for low- and medium-pressure metapelites in the KFMASH and KMnFMASH systems: Journal of Metamorphic Geology, v. 22, p. 495–508, doi: 10.1111/j.1525-1314.2004.00530.x.

Zeh, A., 2001, Inference of a detailed *P-T* path from *P-T* pseudosections using metapelitic rocks of variable composition from a single outcrop, Shackleton Range, Antarctica: Journal of Metamorphic Geology, v. 19, p. 329–350, doi: 10.1046/j.0263-4929.2000.00314.x.

Manuscript Accepted by the Society 21 September 2005

Printed in the USA

Geological Society of America
Special Paper 403
2006

Hydroxyl in diopside of diamond-free ultrahigh-pressure dolomitic marble from the Kokchetav Massif, Kazakhstan

Minoru Kikuchi*
Yoshihide Ogasawara
Department of Earth Sciences, Waseda University, 1-6-1 Nishiwaseda, Shinjuku-ku, Tokyo 169-8050, Japan

ABSTRACT

Hydroxyl (OH) content in diopside of one diamond-free ultrahigh-pressure (UHP) marble from the Kokchetav Massif, Kazakhstan, was estimated by a micro–Fourier transform infrared (FTIR) spectrometer. Two intrinsic diopside OH bands of FTIR absorption spectra were identified at 3645 and 3465 cm^{-1}, with the former band dominating the spectra. Another band occurred at 3685 cm^{-1}, which seemed to be accompanied by trivial bands at 3750, 3730, 3585, and 3565 cm^{-1}. Intensity variation of the 3685 cm^{-1} band within a single diopside crystal and its location may suggest that the cause of this band was submicroscopic amphibole lamellae. The OH concentration of diopside was estimated to be no less than 850 ppm by weight. Using the previously published experimental data, this OH content indicates that diopside formed at pressures >5 GPa and in a high water activity (aH_2O) environment.

Keywords: diamond-free UHP dolomitic marble, hydroxyl in diopside, FTIR, Kokchetav Massif.

INTRODUCTION

The Kokchetav Massif has been well known as one of the most abundant occurrences of microdiamonds in world ultrahigh-pressure (UHP) terranes. Diamond-bearing dolomite marble with an extremely high concentration of microdiamonds at Kumdy-Kol is a representative UHP carbonate rock in this massif (Ogasawara et al., 2000; Yoshioka et al., 2001). A unique UHP calcite marble at Kumdy-Kol contains titanite with coesite exsolution needles/lamellae (Ogasawara et al., 2002); minor amounts of microdiamonds have recently been identified in limited domains or layers (Ogasawara et al., 2004). Moreover, diopsides with K_2O-bearing exsolved lamellae (phengite or phlogopite in dolomite marble and phengite and K-feldspar in calcite marble) also occur in these two types of marbles. This texture indicates that precursor diopsides incorporated significant K_2O under UHP conditions, corresponding to experimentally determined K_2O solubility in clinopyroxenes (e.g., Harlow, 1997; Luth, 1997; Okamoto and Maruyama, 1998). The peak metamorphic pressure condition has been estimated at >6 GPa (Ogasawara et al., 2000, 2002).

The third carbonate from Kumdy-Kol is a Ti-clinohumite–bearing dolomitic marble that lacks microdiamond, and has been regarded as a product of extremely low-X_{CO_2} fluid conditions during UHP metamorphism (Ogasawara et al., 2000). Recently, one dolomitic marble sample with a thin layer of dolomite marble, containing diopside with phlogopite lamellae, was reported as evidence for the local heterogeneity of fluid conditions during UHP metamorphism (Ogasawara and Aoki, 2005). Ti-clinohumite–bearing diamond-free dolomitic marble contains a remarkable amount of diopside that lacks K_2O lamellae. Because diopside incorporates significant hydroxyl under UHP conditions (Locke

*m-kikuchi@suou.waseda.jp.

Kikuchi, M., and Ogasawara, Y., 2006, Hydroxyl in diopside of diamond-free ultrahigh-pressure dolomitic marble from the Kokchetav Massif, Kazakhstan, *in* Hacker, B.R., McClelland, W.C., and Liou, J.G., eds., Ultrahigh-pressure metamorphism: Deep continental subduction: Geological Society of America Special Paper 403, p. 139–145, doi: 10.1130/2006.2403(08).

et al., 2000), Ogasawara and Aoki (2005) speculated that hydroxyl may be present in the lamella-free diopside in this marble.

Fourier transform infrared (FTIR) studies on clinopyroxene (Cpx) reveal significant amounts of OH (>1000 ppm by weight) in mantle-derived omphacites (e.g., Skogby et al., 1990; Smyth et al., 1991). OH content varies in different geological settings and shows a positive correlation with pressure (e.g., Katayama and Nakashima, 2003). The purpose of this paper is to estimate hydroxyl content of lamella-free diopside in diamond-free dolomitic marble using micro-FTIR spectra and to discuss the formation conditions of dolomitic marble.

PETROLOGY OF DIAMOND-FREE DOLOMITIC MARBLE

Geological Outline

In the Kokchetav Massif, northern Kazakhstan, the high-pressure and UHP rocks occur in a large area (10–15 × 150 km^2) along a NW-SE direction (e.g., Dobretsov et al., 1995; Kaneko et al., 2000; Maruyama and Parkinson, 2000). Four metamorphic units (I, II, III, and IV) have been identified for the high-pressure–UHP rocks on the basis of their geological structures and lithology, and are fault-bounded by lower-pressure units (unit V and Daulet suite) (Kaneko et al., 2000). At Kumdy-Kol, the highest metamorphic unit in the Kokchetav Massif, unit II, consists predominantly of pelitic and psammitic gneisses, white schist, eclogite, and small amounts of orthogneiss, Ti-clinohumite-garnet ultramafic rocks, and metacarbonate rocks, including diamond-free dolomitic marble (Kaneko et al., 2000; Ogasawara et al., 2000; Muko et al., 2002; Katayama et al., 2003).

The minimum peak pressure condition has been estimated at >6 GPa, based on excess silica content of the precursor titanite in calcite marble (Ogasawara et al., 2002). The temperature condition has been determined to be 1000–1250 °C, based on the mineral assemblages in diamond-bearing dolomite marble and diamond-free dolomitic marble (Ogasawara et al., 2000). These *P-T* estimates are consistent with those of coherent blocks, such as eclogite and metapelites, in the Kumdy-Kol region (e.g., Okamoto et al., 2000; Katayama et al., 2002). The Kokchetav UHP rocks have an age of ca. 530 Ma (e.g., Claoue-Long et al., 1991; Katayama et al., 2001).

Characteristic Features of Diamond-Free Dolomitic Marble

Significant contrasts between diamond-bearing dolomite marble and diamond-free dolomite marble at Kumdy-Kol have been described previously (Ogasawara et al., 2000). Dolomitic marble lacks microdiamond and exsolution lamellae in diopside; however, this rock is useful for constraining the fluid composition under UHP conditions (Ogasawara et al., 2000). The presence of Ti-clinohumite with $CaCO_3$ phase in this rock requires extremely low-X_{CO_2} conditions (X_{CO_2} < 0.01) under UHP compared with X_{CO_2} ~ 0.1 based on coexisting diopside-dolomite pairs in diamond-bearing dolomite marble.

Although diopside in the diamond-bearing dolomite marble has phengite (rarely phlogopite) exsolution lamellae, diopside in the diamond-free dolomitic marble lacks such lamellae. Ogasawara and Aoki (2005) interpreted this by leaching of K_2O component through extremely low-X_{CO_2} (H_2O-rich) fluid.

Ohta et al. (2003) carried out C, O, and Sr isotope studies on constituent carbonates in the Kokchetav UHP marbles. The diamond-free dolomitic marble had a limited range of variation in $\delta^{18}O$ (+10.6 to +13.3‰) and $\delta^{13}C$ (–2.2 to –1.5‰) values. Conversely, the diamond-bearing dolomite marble had a wider range of variation in $\delta^{18}O$ (+9.1 to +20.5‰) and $\delta^{13}C$ (–9.4 to –1.0‰) values. The $^{87}Sr/^{86}Sr$ values of dolomitic marble (0.7259–0.7273) were lower than those of dolomite marble (0.7500–0.8050). Based on these results, they concluded that the dolomitic marble escaped later-stage hydrothermal alteration, whereas alteration was rather strong in the diamond-bearing dolomite marble.

Diopside in the diamond-free dolomitic marble was unaltered. In contrast, diopside in the diamond-bearing dolomite marble was often partly replaced by tremolite. Therefore, it has been suggested that the diamond-free dolomitic marble may preserve a significant amount of OH as evidence of fluid-rock interaction under UHP conditions (Ogasawara and Aoki, 2005).

Petrography of Diamond-Free Dolomitic Marble

The diamond-free dolomitic marble sample used for the present study is no. Y676. This marble exhibits granoblastic texture and consists mainly of Mg-calcite (30% by volume), dolomite (20%), forsterite (15%), diopside (10%), Ti-clinohumite (<10%), and symplectite (10%) (diopside + spinel + Mg-calcite) after garnet (Fig. 1). Diopside shows granular form and has an

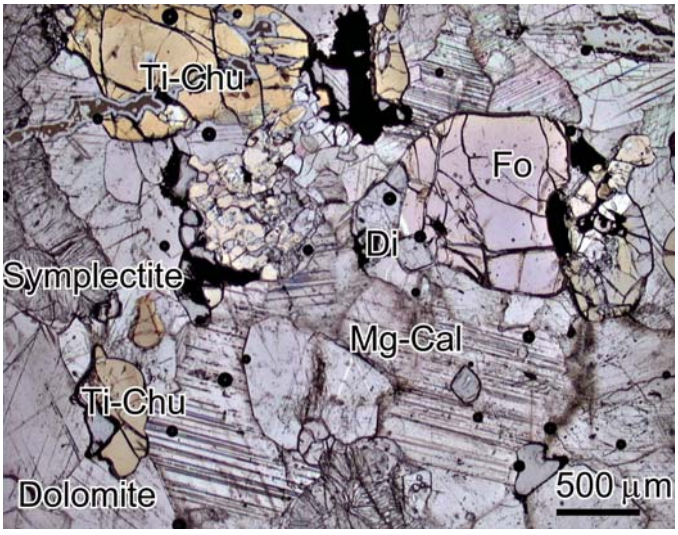

Figure 1. Photomicrograph of diamond-free dolomitic marble (sample no. Y676). Mineral abbreviations: Mg-Cal—Mg-calcite, Di—diopside, Dol—dolomite, Fo—forsterite, Ti-Chu—Ti-clinohumite.

average grain size of ~0.5 mm in longer dimension. All diopside grains in this marble are fresh and lack lamellae. No microdiamond has been identified. No later-stage alteration has been found by microscopic observation. Ogasawara and Aoki (2005) demonstrated that the peak-stage mineral assemblage was dolomite + aragonite + diopside + garnet + Ti-clinohumite (+ forsterite?) (see also Ogasawara et al., 1998, 2000).

Chemical compositions of diopside in sample no. Y676 were analyzed with a JEOL JXA-8900 electron microprobe using wavelength-dispersive mode with an accelerating voltage of 15 kV, beam current of 20 nA, and beam diameter of 10 μm. Five representative analyses are listed in Table 1. Diopside shows no chemical zoning and contains 0.6–0.9 wt% of FeO and 1.2–2.0 wt% of Al_2O_3. K_2O was below the detection limit.

TABLE 1. REPRESENTATIVE CHEMICAL COMPOSITIONS OF DIOPSIDE

Oxides (wt%)					
SiO_2	53.95	54.01	54.36	53.91	54.07
TiO_2	0.12	0.22	0.11	0.17	0.15
Al_2O_3	1.88	1.71	1.20	1.77	1.56
Cr_2O_3	0.02	0.01	0.00	0.00	0.07
FeO	0.65	0.88	0.80	0.80	0.86
MnO	0.04	0.05	0.05	0.05	0.05
MgO	17.68	17.83	18.00	17.69	17.62
CaO	25.61	25.28	25.32	25.67	25.61
K_2O	BDL	BDL	BDL	BDL	BDL
Na_2O	BDL	BDL	0.02	0.03	BDL
Total	99.95	99.99	99.86	100.09	99.99
Cations per 6 oxygen atoms					
Si	1.9523	1.9543	1.9683	1.9508	1.9583
Ti	0.0034	0.0059	0.0030	0.0047	0.0041
Al	0.0800	0.0728	0.0513	0.0753	0.0666
Cr	0.0005	0.0003	0.0000	0.0000	0.0020
Fe	0.0197	0.0268	0.0243	0.0241	0.0260
Mn	0.0012	0.0014	0.0017	0.0015	0.0017
Mg	0.9538	0.9615	0.9715	0.9540	0.9513
Ca	0.9933	0.9803	0.9825	0.9955	0.9938
K	BDL	BDL	BDL	BDL	BDL
Na	BDL	BDL	0.0015	0.0020	BDL

Note: Total Fe calculated as FeO. BDL: below detection limit.

METHODS OF STUDY

Sample Preparation

For micro-FTIR spectrometry, a 150-μm-thick section was prepared. In order to polish the section, an adhesive (Toagosei Co., Tokyo) was used to fix the sample on a deck glass. Both sides of the section were polished with diamond abrasives (grain size: 1 μm). After polishing with diamond paste, the sample was immersed in acetone to dissolve the glue. The thickness of the section was measured with a digital caliper. We confirmed that these chemicals, the glue, and acetone used in sample preparation, did not interfere with FTIR spectra.

Micro-FTIR Spectrometer

FTIR absorption spectra of diopside were acquired with a Thermo Nicolet Continuμm microscope with Avatar 370 Fourier transform IR spectrometer equipped with IR light source, KBr beam-splitter, and MCT-A detector. An aperture of 30 μm in diameter was used. Unpolarized light was used in the measurements. Each FTIR spectrum of unoriented diopside grains was accumulated from 100 scans. The wavenumber resolution of spectrum was 4 cm^{-1}. In order to avoid the effect of inclusions and/or cracks, optically clear parts of diopside were selected. We calculated the peak intensities with the software OMNIC, correcting the base line linearly around the objective bands.

Estimation of OH Content in Diopside

Ideally, polarized spectra in the three principal optical directions (*x*, *y*, and *z*) are necessary to determine the OH amount in diopside. However, since we used a randomly oriented thin section sample, we took the following method to reduce the absorption anisotropic effect. Unpolarized light, which brings spectra resulting from two perpendicular directions of each grain, was utilized, and 30 spectra were averaged. Water contents in clinopyroxenes have been determined from FTIR spectra using both peak heights (Skogby et al., 1990) and peak integration (Bell et al., 1995). Katayama and Nakashima (2003) compared both methods and found the results differed by <5%. The peak height method was utilized in the present study. The calculation method for unoriented samples, modified after Katayama and Nakashima (2003), is as follows: C_{OH} (wt%) = 1.8 {Abs /($\rho \times \varepsilon \times \zeta \times t$)}, where C_{OH}, Abs, ρ, ε, ζ, and t are OH concentration, total sum of absorbances of intrinsic OH of diopside, the density of diopside, molar absorptivity, the correction coefficient for unoriented samples, and thickness of the sample (path length), respectively. The molar absorptivity of 150(L/[mol × cm]) calibrated by Skogby et al. (1990) was used. The value 1/3 is generally applied as the correction coefficient for unoriented samples. We used the pure diopside density of 3.22 from Deer et al. (1992).

RESULTS

Optically clear diopside grains were selected for acquisition of FTIR spectra. Fifty FTIR spectra were obtained from 35 diopside grains. Eight representative spectra that were normalized to 1 mm thick are shown in Figure 2. Two apparent bands, 3645 and 3685 cm^{-1}, were detected in the range 4000–3200 cm^{-1}; their intensities are listed in Table 2. The former band appears in every spectrum, and usually is the strongest. Some spectra have a strong peak at 3685 cm^{-1} (e.g., spectra E, F, G, H of Fig. 2), but others have no band at 3685 cm^{-1} (e.g., spectra A, B, C of Fig. 2). In addition to the two bands, spectra exhibit some subtle bands at 3750, 3730, 3585, 3565, and rarely 3465 cm^{-1} (especially in spectra H and G in Fig. 2).

The peak intensity of the band at 3645 cm^{-1} is homogeneous in a single diopside grain, but varies between distinct

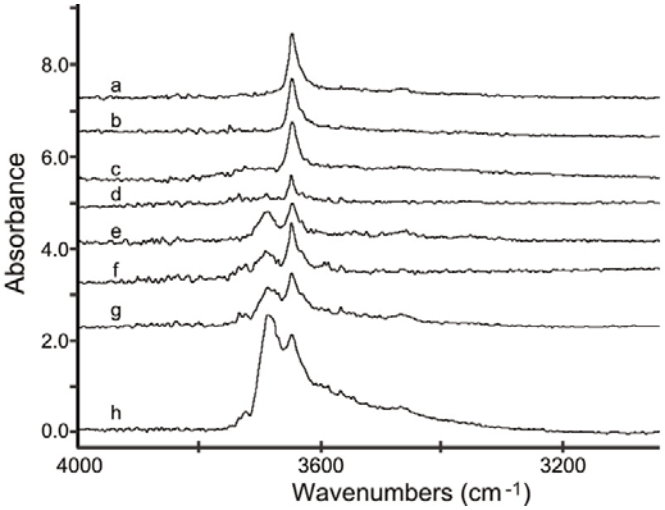

Figure 2. Representative unpolarized Fourier transform infrared (FTIR) spectra of diopsides in diamond-free dolomitic marble. Diopsides were unoriented; optically clear parts without inclusions or cracks were selected for analyses. Spectra were normalized to a thickness of 1-mm thickness and were on the same absorbance scale for comparison. Two obvious bands were found in the FTIR spectra: 3645 and 3685 cm^{-1}.

TABLE 2. INTENSITIES OF THE BANDS AT 3685 AND 3645 CM^{-1} IN 8 SPECTRA OF FIGURE 2

	3685 cm^{-1}	3645 cm^{-1}
a	0.000	1.236
b	0.000	1.008
c	0.000	0.993
d	0.141	0.503
e	0.275	0.460
f	0.300	0.987
g	0.468	0.639
h	1.414	0.573

Note: The peak intensities were calculated with the software OMNIC, correcting the background linearly.

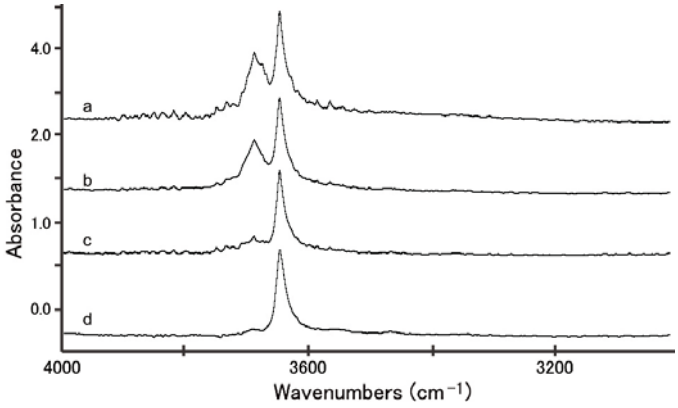

Figure 3. Unpolarized Fourier transform infrared (FTIR) spectra obtained within a single diopside grain, which were normalized to 1 mm thickness. Peak intensity of the 3645 cm^{-1} band is homogeneous, whereas that of the 3685 cm^{-1} band varies. Other bands at 3750, 3730, 3585, and 3565 cm^{-1} seem to be associated with the 3685 cm^{-1} band.

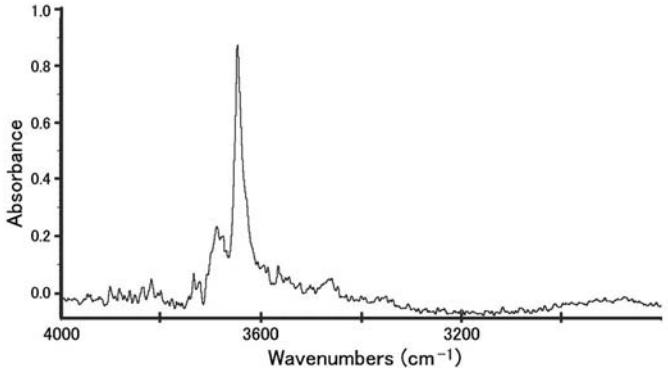

Figure 4. Averaged Fourier transform infrared (FTIR) spectrum calculated using 30 spectra of diopsides with relatively weak band at 3685 cm^{-1}. The spectrum was normalized to 1 mm thickness.

grains from 0.41 to 1.51 (avg. 0.83). This variation of the peak intensities is caused by the absorption anisotropic effect. Johnson et al. (2002) used diopside from a marble xenolith to demonstrate that the peak intensity of the 3645 cm^{-1} band varies in three optical directions with $x = y >> z$. On the other hand, the peak intensity of the band at 3685 cm^{-1} varies even within a single diopside grain (Fig. 3). Figure 3 also indicates that the bands at 3750, 3730, 3585, and 3565 cm^{-1} seem to be associated with the 3685 cm^{-1} band.

Because only the 3645 and 3465 cm^{-1} bands have been reported as intrinsic OH bands of diopside (e.g., Skogby et al., 1990; Johnson et al., 2002), an average spectrum was calculated using 30 spectra that have a relatively weak band at 3685 cm^{-1} and other related bands in order to estimate the amount of OH in our diopside (Fig. 4). In the resultant spectrum, we could not recognize the 3465 cm^{-1} band, because this band rarely appeared in spectra of our diopside sample. Therefore, OH amount in our diopside was estimated with only the 3645 cm^{-1} band; the peak intensity of this band was 0.788 in the averaged spectrum. The resultant OH content was >850 ppm.

DISCUSSION

Evaluation of Micro-FTIR Spectra

Previous studies have demonstrated that diopside generally exhibits four intrinsic OH bands: 3645, 3530, 3450, and 3350 cm^{-1} (e.g., Skogby and Rossman, 1989; Skogby et al., 1990; Skogby, 1994; Johnson et al., 2002). These four bands are classified into two groups on the basis of their pleochroic behavior: group I (3645 cm^{-1}) and group II (3530, 3450, and 3350 cm^{-1}) (for review, see Ingrin and Skogby, 2000). Johnson et al. (2002), however, reported only one major OH band at 3645 cm^{-1} from a marble xenolith. Based on these previous studies

and the homogeneity of the peak intensity in a single grain, the 3645 cm^{-1} band obtained in our sample can be regarded as an intrinsic OH vibration of diopside. A weak band at 3465 cm^{-1} sometimes occurs (e.g., spectra G and H in Fig. 2) and is also an intrinsic diopside OH band.

The 3685 cm^{-1} band shows a different behavior compared with the 3645 cm^{-1} band. The peak intensity of the 3685 cm^{-1} band varies even within a single diopside grain (Fig. 3), indicating that this band is not intrinsic. Figure 3 also indicates that the 3685 cm^{-1} band seems to be accompanied by trivial bands at 3750, 3730, 3585, and 3565 cm^{-1}. Koch-Müller et al. (2004) described a band at 3624–3600 cm^{-1} in omphacite that showed strong variation in a single grain; they concluded that this band was caused by nanometer-sized inclusions of sheet silicates. Usually, a sharp band at 3675 cm^{-1} accompanies four intrinsic OH bands of diopside and is thought to result from submicroscopic amphibole lamellae and/or disordered pyribole layers (Ingrin et al., 1989; Skogby et al., 1990). Some amphiboles show OH bands in the range 3690–3680 cm^{-1} (Kodama, 1985). Based on these previous studies, the 3685 cm^{-1} band in our diopside can be attributed to submicroscopic amphibole lamellae in diopside. The broadness of the 3685 cm^{-1} band may be related to disorder in the submicroscopic lamellae. These inferences can be tested by transmission-electron microscope (TEM) study.

Source of the OH Associated with Nonintrinsic Diopside Band

Ohta et al. (2003) demonstrated that C, O, and Sr isotopic composition of Mg-calcite and dolomite in the diamond-free dolomitic marble was homogeneous, whereas the diamond-bearing dolomite marble exhibited isotopic heterogeneity and disequilibrium. They concluded that the diamond-free dolomitic marble was isolated from retrograde fluids. Therefore, diopside in diamond-free dolomitic marble had no chance to incorporate OH from fluids during the retrograde stage. The only possible source of OH in submicroscopic amphibole is the host precursor diopside, because the precursor diopside could contain much higher concentrations of OH than the estimated value in this study. Submicroscopic amphibole lamellae were exsolved from diopside during the exhumation stage due to decompression. Conclusively, the source of the OH detected as the amphibole band (3685 cm^{-1}) was originally OH in diopside.

Estimated OH Content in Diopside and its Geological Implications

Locke et al. (2000) showed that the amount of OH in diopside increased with pressure, <120 ppm at 5 GPa and 1150 °C and ~1500 ppm at 7.5 GPa and 1200 °C, and their results indicated that OH content in diopside greatly increases from 5 to 7 GPa. Other previous studies have shown that several factors control the OH concentration in clinopyroxenes, these include pressure, oxygen fugacity, water activity, and chemical compositions (e.g., Skogby et al., 1990; Johnson et al., 2002; Bromiley et al., 2004). Among these, water contents in clinopyroxenes are proportional to pressure conditions if other variables are constant. Clinopyroxenes in mantle-derived rocks usually contain larger amounts of OH than those of crustal origin (e.g., Skogby et al., 1990; Smyth et al., 1991). Katayama and Nakashima (2003) reported that the OH content of omphacite from the Kokchetav Massif increases with the peak pressure conditions: ~1000 ppm in quartz eclogite; ~2000 ppm in coesite eclogite; and ~3000 ppm in diamond-grade eclogite. Bromiley et al. (2004) performed annealing experiments on natural chromian diopside and found that the hydrogen solubility increased with pressure at a controlled oxygen fugacity with Ni-NiO buffer. Based on experimental results by Locke et al. (2000), the diopside analyzed in our study has preserved a pressure condition >5 GPa.

Considering the presence of submicroscopic amphibole and the effect of hydrogen loss from OH-bearing diopside, the OH content of diopside in diamond-free dolomitic marble might have been much larger than the estimated value. Since we ignored the OH content of submicroscopic amphibole lamellae, precursor diopside could have incorporated much greater OH content. In addition, the effect of hydrogen loss in OH-bearing diopside during the exhumation stage cannot be ruled out. Skogby and Rossman (1989) found that the intensity of OH band at 3645 cm^{-1} was controlled by the following reduction-oxidation reaction in Fe-bearing systems:

$$Fe^{2+} + OH^- = Fe^{3+} + O^{2-} + 1/2H_2. \quad (1)$$

They demonstrated that the hydrogen diffusion rate in diopside is so large that hydrogen loss could occur in the order of hours. Johnson et al. (2002) conducted Mössbauer analyses of diopsides and showed that the diopside in the marble xenolith having one major OH band at 3645 cm^{-1} contained a high ratio of Fe^{3+}:Fe^{total} (~50%). They suggested that, if all the Fe had been originally Fe^{2+}, their diopside could have originally incorporated >1300 ppm OH, which is 10 times greater than the detected value.

The other important factor that controls the quantity of OH in diopside is H_2O activity, aH_2O. Johnson et al. (2002) compared OH content of diopside in various marbles and demonstrated that OH contents increased with increasing aH_2O. Koch-Müller et al. (2004), however, found an OH-poor (<30 ppm) omphacite in a diamond-bearing eclogite xenolith from the Mir kimberlite pipe, which formed under sufficient pressure to incorporate a significant amount of OH. They attributed the low water content in the omphacite to formation of the host eclogite under low aH_2O. Therefore, the significant amount of OH in diopside of diamond-free dolomitic marble from the Kokchetav Massif is evidence for the high aH_2O conditions during UHP metamorphism. Such results are consistent with previous studies that indicated diamond-free dolomitic marble had formed under extremely low-X_{CO_2} conditions (Ogasawara et al., 2000; Ogasawara and Aoki, 2005; Kikuchi and Ogasawara, 2003).

CONCLUSIONS

A major intrinsic OH band of diopside was found at 3645 cm^{-1} in the FTIR spectra of diopside in diamond-free dolomitic marble from the Kokchetav UHP Massif using micro-FTIR. The other OH band occurred at 3685 cm^{-1}, intensity varied even within a single grain, and this band was caused by submicroscopic amphibole lamellae exsolved from diopside during the exhumation stage.

The estimated OH content in diopside is >850 ppm by weight, and this value corresponds to a pressure condition of >5 GPa based on the experimental study by Locke et al. (2000). The OH content in diopside under peak metamorphic conditions was probably much larger for the following reasons: (1) OH in submicroscopic amphibole lamellae was originally in diopside, and (2) hydrogen loss from OH-bearing diopside could occur during decompression. The significant quantity of OH in diopside in the diamond-free dolomitic marble also indicates the high H_2O activity under UHP metamorphism. These results are consistent with previous studies (e.g., Ogasawara et al., 2000), which infer that the diamond-free dolomitic marble formed under extremely low-X_{CO_2} conditions at pressures >6 GPa.

ACKNOWLEDGMENT

The authors thank two reviewers, J. Mosenfelder (Caltech) and I. Katayama (Yale University), and co-editor J.G. Liou (Stanford University) for their constructive comments on the manuscript. We also thank T. Fagan for helpful discussions and improving the manuscript. Our thanks are also due to G. Rossman (Caltech) for helpful comments. This study was financially supported by Grant in Aid from JSPS (nos. 13640485 and 15204050) to Ogasawara

REFERENCES CITED

Bell, D.R., Ihinger, P.D., and Rossman, G.R., 1995, Quantitative analysis of trace OH in garnet and pyroxenes: The American Mineralogist, v. 80, p. 465–474.

Bromiley, G.D., Keppler, H., McCammon, C., Bromiley, F.A., and Jacobsen, S.D., 2004, Hydrogen solubility and speciation in natural, gem-quality chromian diopside: The American Mineralogist, v. 89, p. 941–949.

Claoue-Long, J.C., Sobolev, N.V., Shatsky, V.S., and Sobolev, A.V., 1991, Zircon response to diamond-pressure metamorphism in the Kokchetav Massif, USSR: Geology, v. 19, p. 710–713, doi: 10.1130/0091-7613(1991)019<0710:ZRTDPM>2.3.CO;2.

Deer, W.A., Howie, R.A., and Zussman, J., 1992, An introduction to the rock-forming minerals (second edition): London, Pearson Prentice Hall, p. 143–154.

Dobretsov, N.L., Sobolev, N.V., Shatsky, V.S., Coleman, R.G., and Ernst, W.G., 1995, Geotectonic evolution of diamondiferous paragneisses, Kokchetav complex, northern Kazakhstan—The geologic enigma of ultrahigh-pressure crustal rocks within a Paleozoic foldbelt: The Island Arc, v. 4, p. 267–279.

Harlow, G.E., 1997, K in clinopyroxene at high pressure and temperature: An experimental study: The American Mineralogist, v. 82, p. 259–269.

Ingrin, J., and Skogby, H., 2000, Hydrogen in nominally anhydrous upper-mantle minerals: Concentration levels and implications: European Journal of Mineralogy, v. 12, p. 543–570.

Ingrin, J., Latrous, K., Doukhan, J.C., and Doukhan, N., 1989, Water in diopside: An electron microscopy and infrared spectroscopy study: European Journal of Mineralogy, v. 1, p. 327–341.

Johnson, E.A., Rossman, G.R., Dyar, M.D., and Valley, J.W., 2002, Correlation between OH concentration and oxygen isotope diffusion rate in diopsides from the Adirondack Mountains, New York: The American Mineralogist, v. 87, p. 899–908.

Kaneko, Y., Maruyama, S., Terabayashi, M., Yamamoto, H., Ishikawa, M., Anma, R., Parkinson, C.D., Ota, T., Nakajima, Y., Katayama, I., Yamamoto, J., and Yamauchi, K., 2000, Geology of the Kokchetav UHP-HP metamorphic belt, northern Kazakhstan: The Island Arc, v. 9, p. 264–283, doi: 10.1046/j.1440-1738.2000.00278.x.

Katayama, I., and Nakashima, S., 2003, Hydroxyl in clinopyroxene from the deep subducted crust: Evidence for H_2O transport into mantle: The American Mineralogist, v. 88, p. 229–234.

Katayama, I., Maruyama, S., Parkinson, C.D., Terada, K., and Sano, Y., 2001, Ion micro-probe U-Pb zircon geochronology of peak and retrograde stages of ultrahigh-pressure metamorphic rocks from the Kokchetav Massif, northern Kazakhstan: Earth and Planetary Science Letters, v. 188, p. 185–198, doi: 10.1016/S0012-821X(01)00319-3.

Katayama, I., Ohta, M., and Ogasawara, Y., 2002, Mineral inclusions in zircon from diamond-bearing marble in the Kokchetav Massif, northern Kazakhstan: European Journal of Mineralogy, v. 14, p. 1103–1108, doi: 10.1127/0935-1221/2002/0014-1103.

Katayama, I., Muko, M., Iizuka, T., Maruyama, S., Terada, K., Tsutsumi, Y., Sano, Y., Zhang, R.Y., and Liou, J.G., 2003, Dating of zircon from Ti-clinohumite–bearing garnet peridotite: Implication for timing of mantle metasomatism: Geology, v. 31, p. 713–716, doi: 10.1130/G19525.1.

Kikuchi, M., and Ogasawara, Y., 2003, Stability relations in Ti-bearing assemblages in the Kokchetav UHP marbles: Eos (Transactions, American Geophysical Union), v. 84, no. 46, p. V22D–0619.

Koch-Müller, M., Matsyuk, S.S., and Wirth, R., 2004, Hydroxyl in omphacites and omphacitic clinopyroxenes of upper mantle to lower crustal origin beneath the Siberian platform: The American Mineralogist, v. 89, p. 921–931.

Kodama, H., 1985, Infrared spectra of minerals: Reference guide to identification and characterization of minerals for the study of soils: Agriculture Canada Research Establishments, Technical Bulletin 1985–1E, 197 p.

Locke, D.L., Holloway, J.R., and Hervig, R., 2000, Experimental determination of H_2O solubility in mantle clinopyroxene at 5 GPa and 7.5 GPa [abs.]: Eos (Transactions, American Geophysical Union), v. 81, no. 19, p. V52D–05.

Luth, R.W., 1997, Experimental study of the system phlogopite-diopside from 3.5 to 17 GPa: The American Mineralogist, v. 82, p. 1198–1209.

Maruyama, S., and Parkinson, C.D., 2000, Overview of the geology, petrology and tectonic framework of the high-pressure–ultrahigh-pressure metamorphic belt of the Kokchetav Massif, Kazakhstan: The Island Arc, v. 9, p. 439–455, doi: 10.1046/j.1440-1738.2000.00288.x.

Muko, A., Okamoto, K., Yoshioka, N., Zhang, R.Y., Parkinson, C.D., Ogasawara, Y., and Liou, J.G., 2002, Petrogenesis of Ti-clinohumite–bearing garnetiferous ultramafic rocks from Kumdy-Kol, *in* Parkinson, C.D., et al., eds., The diamond-bearing Kokchetav Massif, Kazakhstan: Tokyo, Universal Academy Press, Inc., p. 343–359.

Ogasawara, Y., and Aoki, K., 2005, The role of fluid for diamond-free dolomitic marble from the Kokchetav Massif: International Geological Review, v. 47, p. 1178–1193.

Ogasawara, Y., Zhang, R.Y., and Liou, J.G., 1998, Petrogenesis of dolomitic marbles from Rongcheng in the Su-Lu ultrahigh-pressure metamorphic terrane, eastern China: The Island Arc, v. 7, p. 82–97, doi: 10.1046/j.1440-1738.1998.00177.x.

Ogasawara, Y., Ohta, M., Fukasawa, K., Katayama, I., and Maruyama, S., 2000, Diamond-bearing and diamond-free metacarbonate rocks from Kumdy-Kol in the Kokchetav Massif, northern Kazakhstan: The Island Arc, v. 9, p. 400–416, doi: 10.1046/j.1440-1738.2000.00285.x.

Ogasawara, Y., Fukasawa, K., and Maruyama, S., 2002, Coesite exsolution from supersilicic titanite in UHP marble from the Kokchetav Massif, northern Kazakhstan: The American Mineralogist, v. 87, p. 454–461.

Ogasawara, Y., Adachi, A., and Aoki, K., 2004, Occurrence of microdiamond in UHP calcite marble from the Kokchetav Massif: Eos (Transactions, American Geophysical Union), v. 85, no. 47, p. T21A–0503.

Ohta, M., Mock, T., Ogasawara, Y., and Rumble, D., 2003, Oxygen, carbon, and strontium isotope geochemistry of diamond-bearing carbonate rocks from Kumdy-Kol, Kokchetav Massif: Kazakhstan: Lithos, v. 70, p. 77–90, doi: 10.1016/S0024-4937(03)00093-8.

Okamoto, K., and Maruyama, S., 1998, Multi-anvil re-equilibration experiments of Dabie Shan ultrahigh-pressure eclogite within the diamond-stability fields: The Island Arc, v. 7, p. 52–69, doi: 10.1046/j.1440-1738.1998.00179.x.

Okamoto, K., Liou, J.G., and Ogasawara, Y., 2000, Petrology of diamond-grade eclogite in the Kokchetav Massif, northern Kazakhstan: The Island Arc, v. 9, p. 379–399, doi: 10.1046/j.1440-1738.2000.00284.x.

Skogby, H., 1994, OH incorporation in synthetic clinopyroxene: The American Mineralogist, v. 79, p. 240–249.

Skogby, H., and Rossman, G.R., 1989, OH^- in pyroxene: An experimental study of incorporation mechanisms and stability: The American Mineralogist, v. 74, p. 1059–1069.

Skogby, H., Bell, D.R., and Rossman, G.R., 1990, Hydroxide in pyroxene: Variations in the natural environment: The American Mineralogist, v. 75, p. 764–774.

Smyth, J.R., Bell, D.R., and Rossman, G.R., 1991, Incorporation of hydroxyl in upper-mantle clinopyroxenes: Nature, v. 351, p. 732–735, doi: 10.1038/351732a0.

Yoshioka, N., Muko, A., and Ogasawara, Y., 2001, Extremely high diamond concentration in dolomite marble: UHPM Workshop 2001—Fluid/slab/mantle interactions and ultrahigh-*P* minerals (extended abstract): Tokyo, Waseda University, p. 51–55.

Manuscript Accepted by the Society 21 September 2005

Geological Society of America
Special Paper 403
2006

Petrologic characterization of Guatemalan lawsonite eclogite: Eclogitization of subducted oceanic crust in a cold subduction zone

Tatsuki Tsujimori*
Department of Geological and Environmental Sciences, Stanford University, Stanford, California 94305-2115, USA
Virginia B. Sisson
Department of Earth and Planetary Sciences, American Museum of Natural History, New York, New York 10024-5192, USA
Juhn G. Liou
Department of Geological and Environmental Sciences, Stanford University, Stanford, California 94305-2115, USA
George E. Harlow
Department of Earth and Planetary Sciences, American Museum of Natural History, New York, New York 10024-5192, USA
Sorena S. Sorensen
Department of Mineral Sciences, National Museum of Natural History, Smithsonian Institution, Washington, D.C. 20560-0119, USA

ABSTRACT

Early Cretaceous lawsonite eclogites and related high-pressure rocks occur as tectonic inclusions within serpentinite mélange south of the Motagua fault zone, Guatemala. Petrologic and microtextural analyses of mafic high-pressure rocks reveal three metamorphic stages linked to several deformational textures. The prograde stage represents an incipient eclogitization and is preserved in prograde garnet, along with an older S_1–S_2 foliation. The prograde assemblage is garnet (X_{Mg} = ~0.22) + omphacite (~52 mol% jadeite) or jadeite (~83 mol % jadeite) + lawsonite + chlorite + rutile + quartz ± phengite (3.6 Si p.f.u.); some rocks also have ilmenite and rare ferro-glaucophane. Lawsonite in garnet of some lawsonite eclogites contains rare pumpellyite inclusions. The presence of synmetamorphic brittle deformation, inclusions of pumpellyite, Fe^{2+}-Mg distribution coefficients between omphacite inclusions and adjacent garnet with Ln(K_D) = 2.7–4.5, and garnet-clinopyroxene-phengite thermobarometry suggest that eclogitization initiated at temperature (T) = ~300 °C and pressure (P) > 1.1 GPa, and continued to T = ~480 °C and P = ~2.6 GPa. In contrast, the retrograde eclogite-facies assemblage is characterized by reversely zoned garnet rims and omphacite ± glaucophane + lawsonite + rutile + quartz ± phengite (3.5 Si p.f.u.) along the S_3 foliation. Garnet-phengite-clinopyroxene thermobarometry yields P = ~1.8 GPa and T = ~400 °C. The youngest, blueschist-facies assemblage (glaucophane + lawsonite + chlorite + titanite + quartz ± phengite) locally replaces earlier mineral assemblages along S_4 crenulations. The inferred prograde P-T trajectory lies near a geotherm of ~5 °C km^{-1}, comparable to the calculated thermal and petrologic structure of the NE Japan subduction zone. These petrologic characteristics indicate:

*tatsukix@pangea.stanford.edu.

Tsujimori, T., Sisson, V.B., Liou, J.G., Harlow, G.E., and Sorensen, S.S., 2006, Petrologic characterization of Guatemalan lawsonite eclogite: Eclogitization of subducted oceanic crust in a cold subduction zone, *in* Hacker, B.R., McClelland, W.C., and Liou, J.G., eds., Ultrahigh-pressure metamorphism: Deep continental subduction: Geological Society of America Special Paper 403, p. 147–168, doi: 10.1130/2006.2403(09). For permission to copy, contact editing@geosociety.org.

(1) the basalt-eclogite transformation may occur at T = ~300 °C in cold subduction zones, (2) glaucophane-bearing prograde assemblages are rare during incipient eclogitization in cold subduction zones, and (3) the chlorite-consuming reactions that form Fe-Mg-Mn garnet are more effective than the lawsonite-consuming reaction that forms a grossular component. At depths of ~100 km in cold subduction zones, dehydration embrittlement may be caused by such chlorite-consuming reactions.

Keywords: cold subduction, HP-UHP metamorphism, lawsonite eclogite, P-T trajectory, Guatemala.

INTRODUCTION

An incredibly cool paleogeotherm near ~5 °C km^{-1} is one of the critical features of diamond-bearing ultrahigh-pressure (UHP) metamorphic rocks as well as lawsonite eclogites (e.g., Liou et al., 2000; Rumble et al., 2003; Maruyama and Liou, 2005). Although preservation of such an extremely low geotherm is rare in orogenic belts, thermal models of subduction zones predict cold temperatures in subduction zones where old lithosphere is rapidly subducting, such as beneath present-day Tonga and NE Japan (e.g., Kirby et al., 1996; Peacock and Wang, 1999; Peacock, 2001; Hacker et al., 2003a, 2003b). Also, experiments using mid-ocean-ridge basalt (MORB) compositions as precursors predict that subducted oceanic crust transforms to lawsonite eclogite from blueschist (e.g., Pawley, 1994; Poli and Schmidt, 1995; Pawley et al., 1996; Okamoto and Maruyama, 1999). Furthermore, lawsonite is stable along a cold geotherm down to 300 km depth and is proposed to be a major H_2O reservoir in subducted oceanic crust. The occurrence of lawsonite eclogite xenoliths in ultramafic diatremes of the Colorado Plateau (Watson and Morton, 1969; Helmstaedt and Schulze, 1988; Usui et al., 2003) implies that lawsonite-eclogite–facies conditions may be common in Pacific-type subduction. Questions about this process include: how does downgoing oceanic crust transform to lawsonite eclogite in a cold subduction? What are the pressure-temperature (*P-T*) paths for lawsonite eclogites? What prograde dehydration events are preserved in lawsonite eclogites during eclogitization?

So far, at least ten localities of lawsonite eclogite are known (excluding xenoliths), including (1) Motagua fault zone, Guatemala (McBirney et al., 1967; Smith and Gendron, 1997; Harlow et al., 2003, 2004; Tsujimori et al., 2005), (2) Samaná Peninsula, Hispaniola (Dominican Republic) (Zack et al., 2004), (3) Schistes Lustrés, Corsica (Caron et al., 1981; Caron and Péquignot, 1986), (4) Central Pontides, Turkey (Altherr et al., 2004), (5) Port Macquarie, New England fold belt, Australia (Och et al., 2003), (6) Pinchi Lake, British Columbia, Canada (Ghent et al., 1993), (7) Ward Creek, Franciscan complex, California, USA (Maruyama and Liou, 1988; Oh et al., 1991; Shibakusa and Maekawa, 1997), (8) Barru complex, Sulawesi, Indonesia (Parkinson et al., 1998), (9) Pam Peninsula, New Caledonia (Clarke et al., 1997), and (10) Motalafjella, western Spitsbergen (Hirajima et al., 1988) (See review of Tsujimori et al., 2006). Elsewhere higher-*T* epidote-bearing assemblages variably overprint most lawsonite-eclogite assemblages. In contrast, the Guatemalan lawsonite eclogite contains garnet porphyroblasts that grew only within the lawsonite stability field (Tsujimori et al., 2005). In this paper, we describe the detailed petrologic characteristics of the Guatemalan lawsonite eclogite. Together with microstructural features, these data are used to establish the prograde and retrograde *P-T* paths. This characterization of lawsonite eclogite helps us to understand metamorphic processes in a cold subduction zone with an extremely low geotherm.

Mineral abbreviations are after Kretz (1983); we also use aegirine (Ae), ferroglaucophane (Fgl), phengite (Phe), and coesite (Coe) throughout this paper.

GEOLOGIC SETTING

Active volcanic arcs or strike-slip fault systems characterize the present-day Caribbean plate margins. Along the northern and southern plate margins, there are Cretaceous blueschists, and eclogites (±rare garnet peridotites) extending from Guatemala (e.g., Tsujimori et al., 2005), through Cuba (e.g., Schneider et al. 2004), Jamaica (Draper, 1986), and Dominican Republic (e.g., Giaramita and Sorensen, 1994; Abbott et al., 2005) and farther south to Venezuela (e.g., Sisson et al., 1997) and Colombia (Green et al., 1968) (Fig. 1). These high-pressure rocks are associated with serpentinite, Jurassic-Cretaceous ophiolites, and/or accretionary complexes. The protoliths for these various high-pressure terranes vary from MORB to continental lithologies to island-arc volcanics (e.g., Sorensen et al., 1997, 2005; Beccaluva et al., 1995; Unger et al., 2005).

The northern boundary of the Caribbean plate in Guatemala is the Motagua fault zone, a left-lateral strike-slip fault that is part of the suture zone juxtaposing the Maya and Chortís continental blocks. The Motagua fault zone extends into the Caribbean plate along the Swan Islands fracture zone to the Cayman Trough. Along the Motagua fault zone in central Guatemala, serpentinite bodies are exposed on either side of the Río Motagua; the serpentinite-matrix mélange stretches ~220 km throughout central and eastern Guatemala (e.g., Harlow et al., 2004) (Fig. 2). The strike-slip fault system includes the E-W–trending Sierra de Chuacús and Sierra de Las Minas. To the north, the Motagua fault zone is bounded by epidote-amphibolite– to amphibolite-facies gneiss and schist with rare relict eclogites of the Chuacús

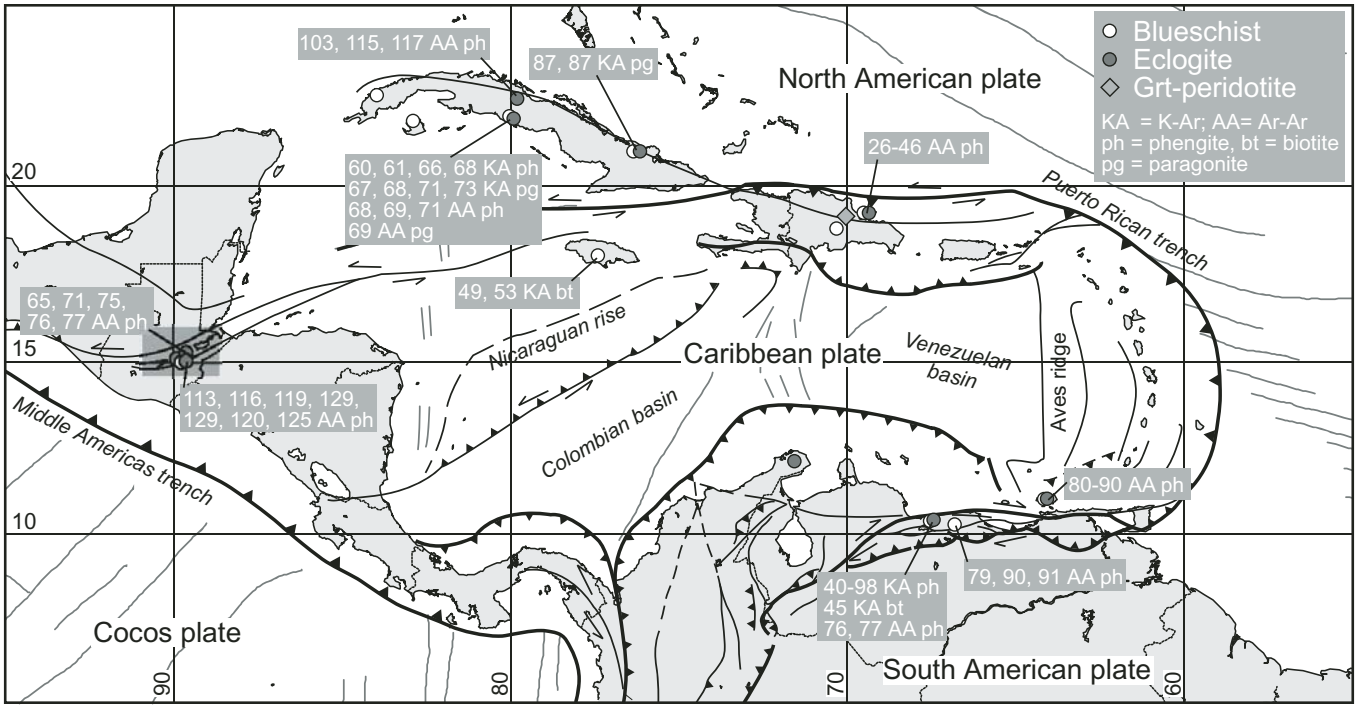

Figure 1. Tectonic framework of the Caribbean region showing representative localities of Cretaceous high-pressure–ultrahigh-pressure (UHP) rocks. Phengite and paragonite K-Ar and Ar-Ar ages are from Somin et al. (1992), Stöckhert et al. (1995), Smith et al. (1999), Gonçalves et al. (2000), Schneider et al. (2004), and Harlow et al. (2004).

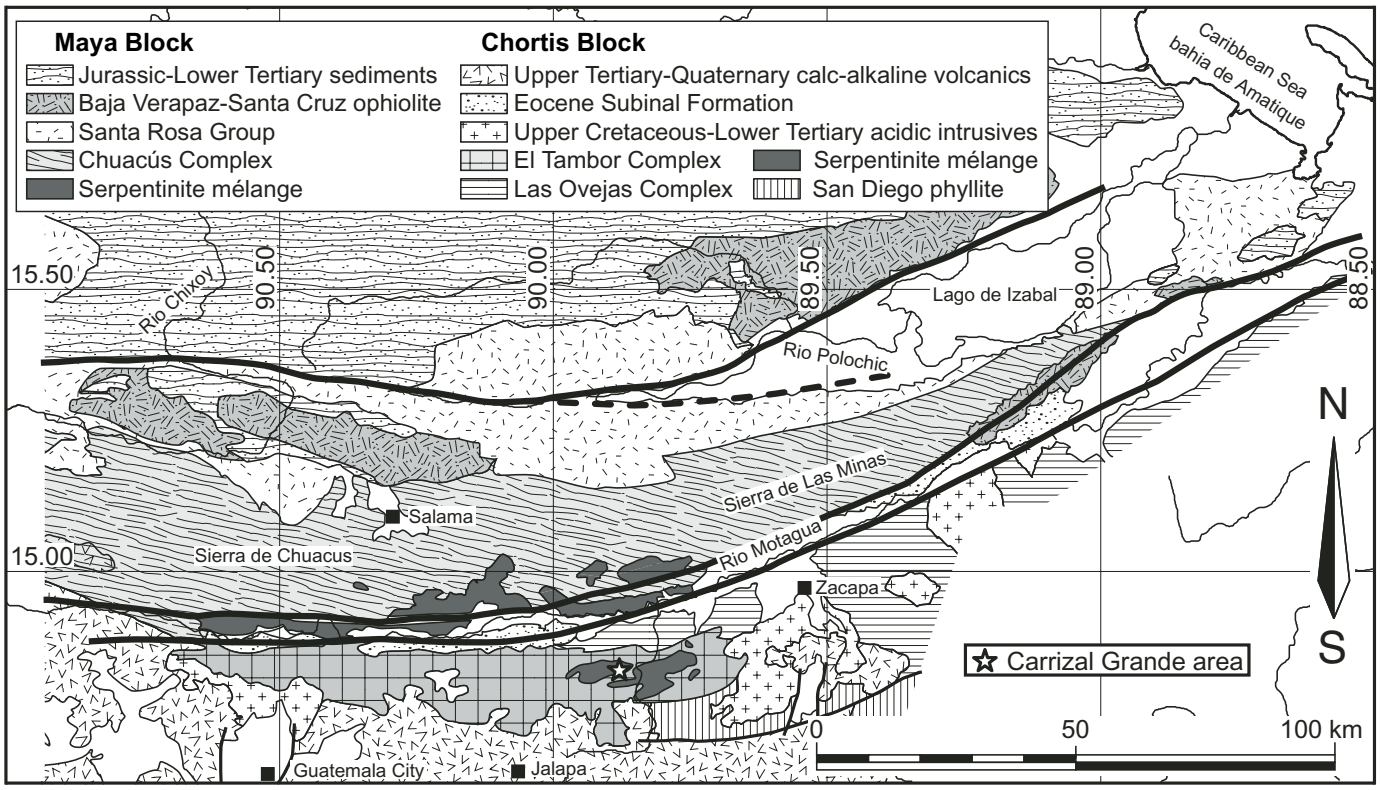

Figure 2. Simplified geologic map of central Guatemala, showing eclogite localities (modified after Beccaluva et al., 1995).

terrane (Ortega-Gutiérrez et al., 2004). North of the Chuacús terrane, Paleozoic Santa Rosa Group sediment and deformed granite constitute the basement of the Maya block. To the south, the basement of the Chortís block is the low-grade greenschist-facies San Diego phyllite and amphibolite-facies Las Ovejas complex.

The serpentinite-matrix mélange along the Motagua fault zone consists of meter-size blocks of ophiolitic rocks, high-pressure metamorphic rocks, and various metasomatic rocks. Some of the serpentinites host world-class localities of jadeitite (e.g., Harlow, 1994). Based on dissimilar rock assemblages and $^{40}Ar/^{39}Ar$ phengite geochronology, the serpentinite-matrix mélange can be divided into northern and southern belts (Harlow et al., 2004). The northern belt consists of amphibolite, gneiss, amphibolitized epidote-eclogite, and jadeitite with phengite $^{40}Ar/^{39}Ar$ integrated ages of 77–65 Ma. In contrast, the southern belt is characterized by blueschist, lawsonite eclogite, and lawsonite-bearing jadeite with phengite $^{40}Ar/^{39}Ar$ integrated ages of 125–116 Ma. The southern eclogite has an Sm-Nd garnet–omphacite–whole-rock isochron age of 135 Ma (Sisson et al., 2003). These Cretaceous cooling ages are mostly comparable to those of eclogites and blueschists from Cuba, Hispaniola, and Venezuela (e.g., Somin et al., 1992; Gonçalves et al., 2000; Schneider et al., 2004; Sisson et al., 2005).

ECLOGITES IN THE QUEBRADA DEL MICO AND QUEBRADA SECA

Mode of Occurrence

A fault-bounded eclogite-bearing serpentinite mélange unit occurs in the Carrizal Grande area, south of the Motagua fault zone (Fig. 2). A large amount of eclogite and related rocks are exposed as loose blocks (<10 m) in landslide debris along the Quebrada El Silencio, Quebrada del Mico, and the Quebrada Seca, streams that feed into Río Jalapa or El Tambor. The eclogitic blocks are sandwiched between antigorite serpentinite and phyllite, and the exposures cover an area of ~4 × 0.5 km. The blocks include eclogitic rocks, minor jadeitite, and mica schist (phengite-rich schist); rare eclogites intercalated with graphite-bearing quartz mica schists suggest a protolith mixture of mafic rocks with some semipelagic sedimentary rocks. Serpentinite associated with eclogitic blocks consist of schistose, friable antigorite serpentinite. The eclogitic blocks are rounded; rare tremolite- or glaucophane-rich rinds are observed. At least four types of eclogitic rocks are recognized: jadeite-bearing lawsonite eclogite, type I lawsonite eclogite, type II lawsonite eclogite, and garnet-bearing lawsonite blueschist (Fig. 3). The jadeite-bearing lawsonite eclogite is a pale-green, weakly foliated, rare rock containing up to 75 vol% garnet + clinopyroxene; it can be subdivided into fine- and coarse-grained varieties based on the size of the garnet porphyroblasts. In particular, the coarse-grained jadeite-bearing lawsonite eclogite has garnet porphyroblasts up to 1.5–2.5 cm in diameter (Tsujimori et al., 2005) (Fig. 3A). Type I lawsonite eclogite, dominant in Quebrada del Mico, is green and massive, with 0.5–1.0 cm garnet (Fig. 3B). Type I lawsonite eclogite is cut by irregularly shaped, retrograde, glaucophane-rich hydrous veins (1–15 cm wide). Type II lawsonite eclogite is well-foliated glaucophane-bearing eclogite (Fig. 3C), and the dominant rock in Quebrada Seca. Most have millimeter- to centimeter-scale compositional banding defined by omphacite- and glaucophane-bearing layers. The modal abundance of garnet + omphacite reaches locally up to 80% in type I and II lawsonite eclogite. Garnet-bearing lawsonite blueschist is a well-foliated schist that contains omphacite (<10 vol%) (Fig. 3D).

Textural Variation and Structural Framework

Most eclogitic rocks in the Carrizal Grande area preserve textural evidence for multiple stages of deformation, prograde metamorphism, and retrograde metamorphism prior to the formation of the mélange (Fig. 3). Similar deformation relationships in various blocks enable us to explain their synmetamorphic deformational history.

Meso- and microstructural analyses show four phases of deformations: D_1, D_2, D_3, and D_4 (Fig. 4), based on overprinting relationships among polyphase tight-isoclinal folds, boudinaged layers, inclusion trails in garnet, and late crenulations. The D_3 phase of deformation and recrystallization is dominant in most rocks. In particular, penetrative S_3 schistosity can be observed in all type II lawsonite eclogite and garnet-bearing quartz–phengite schist (Figs. 3C, 4E, and 4I). The early S_2 schistosity is preserved in jadeite-bearing lawsonite eclogite, type I lawsonite eclogite, and rare type II lawsonite eclogite (Fig. 3A). The transition from S_2 to S_3 is observed in F_3 folds; S_2 was folded during D_3 with the development of newly formed S_3 along the axial planes of F_3 folds (Figs. 3H and 3I). The schistosity in garnet-bearing quartz–phengite schist is presumed equivalent to S_3, and inclusion trails in garnet that are nearly perpendicular to matrix schistosity may be equivalent to S_2 (Fig. 3E). During D_3, type I lawsonite eclogite was boudinaged within its glaucophane-rich host type II lawsonite eclogite (Fig. 3D). Jadeite-bearing lawsonite eclogite that preserves pre-D_3 structures is interpreted as meter-scale boudins barely affected by D_3. Evidence of D_1 includes S_1 inclusion trails in garnet of jadeite-bearing lawsonite eclogite (Fig. 3A); inclusion trails comparable to S_1 are rarely observed in garnet cores in garnet-bearing quartz–phengite schist (see later section). D_4 deformation is minor, but includes open F_4 crenulations in garnet-bearing lawsonite blueschist (Fig. 3D). Centimeter-scale chevron folds in a loose block of serpentinite may be part of D_4 (Fig. 3F). Note, these stages of deformation are mostly within the eclogite blocks and are different from the five generations of ductile and four stages of brittle deformation observed in the basement and host serpentinite (e.g., Francis et al., 2005; Francis, 2005). For example, chevron folds in serpentinite can also be related to chevron folds formed during the D_5 deformation seen in the San Diego phyllite (Francis, 2005).

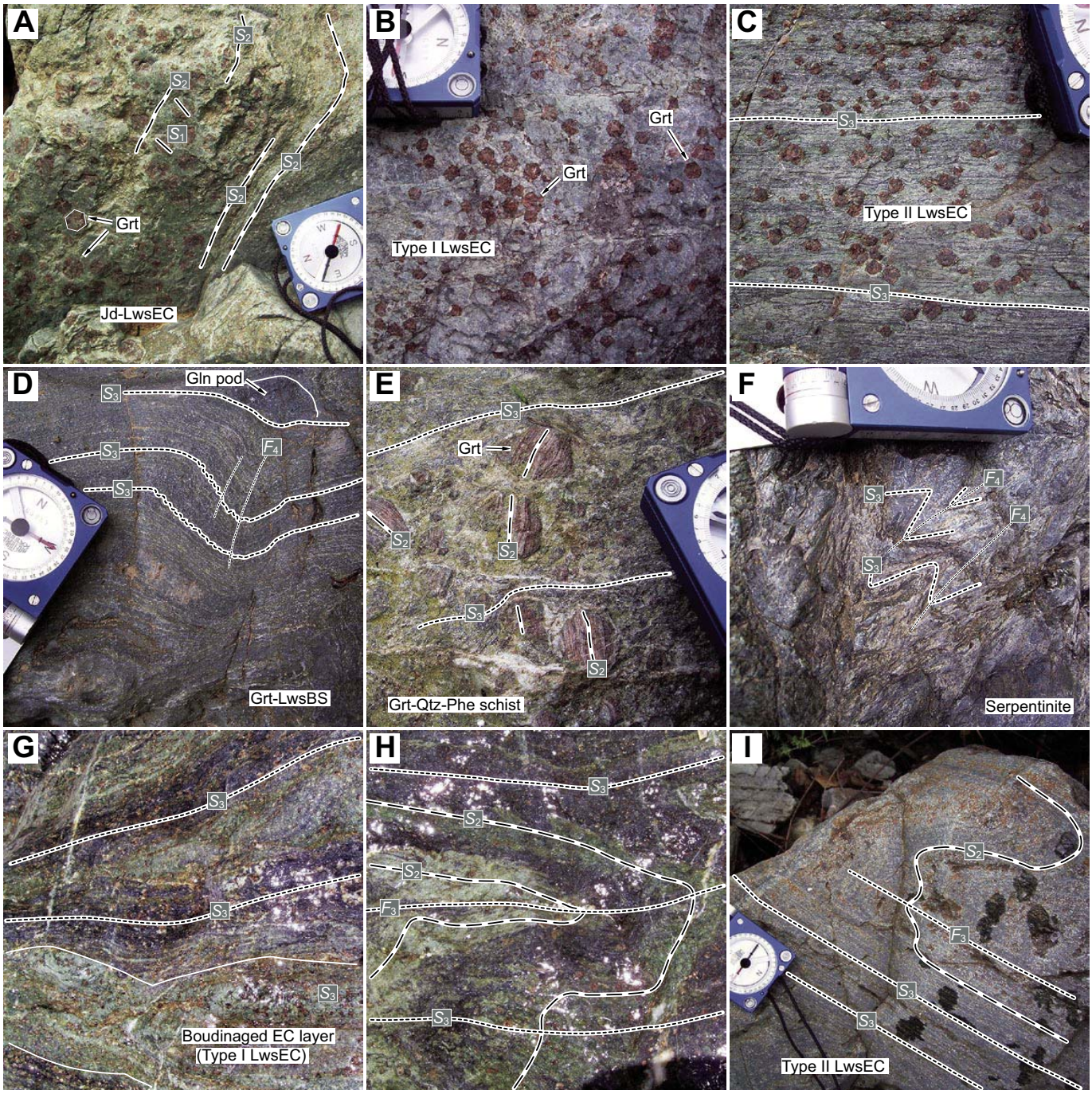

Figure 3. Representative structures of the Carrizal Grande high-pressure rocks. Geologic compass (7 cm wide) is for scale. (A) Coarse-grained jadeite-bearing lawsonite eclogite (Jd-LwsEc) containing large euhedral garnets (Grt) up to 2.5 cm. S_1 inclusion trails in garnet are nearly perpendicular to matrix schistosity S_2. (B) Type I lawsonite eclogite containing euhedral garnets. (C) Type II lawsonite eclogite showing a penetrative S_3 schistosity. (D) Garnet-bearing lawsonite blueschist (Grt-LwsBS) showing D_4 deformation and glaucophane (Gln) pod. (E) Coarse-grained garnet-bearing quartz–phengite (Grt-Qtz-Phe) schist containing garnets up to 2.5 cm. (F) Schistose antigorite serpentinite with chevron folds. (G) Boudinaged type I lawsonite eclogite layer. Field of view is about 20 cm. (H) Isoclinal fold of partially hydrated type I lawsonite eclogite showing the transition from S_2 to S_3; S_2 was folded during D_3 with the development of S_3 along the F_3 axial planes. Field of view is about 30 cm. (I) Isoclinal folds in type II lawsonite eclogite showing the transition from S_2 to S_3.

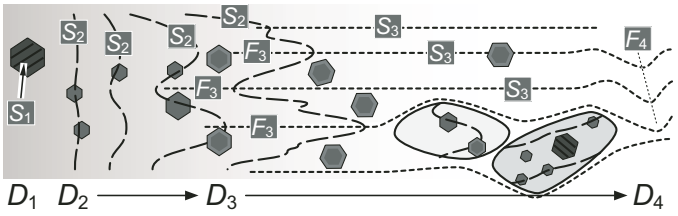

Figure 4. Schematic illustration showing development of the structural relationships.

PETROGRAPHY

Jadeite-Bearing Lawsonite Eclogites

The jadeite-bearing lawsonite eclogites are subdivided into coarse- and fine-grained rocks. The coarse-grained jadeite-bearing lawsonite eclogites have two generations of jadeitic pyroxene, which consist of sodic pyroxene and garnet, with minor rutile, phengite, chlorite, ferroglaucophane, lawsonite, titanite, ilmenite, and quartz (Tsujimori et al., 2005). Large garnet porphyroblasts (1.5–2.5 cm) contain oriented inclusions of sodic pyroxene, rutile, ferroglaucophane, quartz, lawsonite, and phengite with inclusions of chlorite and ilmenite are restricted to garnet cores. Inclusion trails in garnet define an internal S_1 foliation. The weakly foliated matrix consists of sodic pyroxene with minor lawsonite, rutile, quartz, and phengite; the preferred orientation of phengite and fine-grained sodic pyroxene define an S_2 foliation at a high angle to the internal fabric S_1 in garnet. Impure first-generation jadeite (Jd-I) occurs as subhedral blasts up to 1.5 mm in length, while second generation jadeitic pyroxene (Jd-II) occurs in fine-grained aggregates associated with minor omphacite (Fig. 5A). Matrix rutile is often rimmed by titanite; rare matrix jadeitic pyroxene may be replaced by albite. Although the effects of D_3 and D_4 were not recognized, the matrix was partly recrystallized during retrogression.

The fine-grained lawsonite eclogite lacks the centimeter-size large garnet (Fig. 5B); garnet porphyroblasts, up to 4 mm in size, are scattered in a nematoblastic foliation S_2 defined by preferred orientation of prismatic omphacite (<1 mm in length) and phengite. It contains omphacite and garnet with minor amounts of lawsonite, jadeite, phengite, quartz, and rutile. Rare albite is found as a secondary mineral replacing jadeite. Subhedral garnet contains mineral inclusions of omphacite, phengite, rutile, and tiny (<0.05 mm) lawsonite and rare quartz; inclusion trails are in continuity with external foliation S_2. Another important feature is that the older inclusion trail S_1 is not present. In some samples, matrix omphacite is partially contained within garnet. Omphacite is optically zoned, and contains oriented tiny mineral inclusions (<0.02 mm) of quartz and lawsonite in the greenish cores (Fig. 5B). Jadeite occurs as discrete grains (<0.5 mm) and contains rare rutile inclusions. Matrix rutile does not have a titanite rim.

Type I Lawsonite Eclogites

Type I lawsonite eclogite has 5–10 mm euhedral garnet scattered in a fine-grained, granoblastic, weakly foliated matrix (Figs. 5C and 5D). The matrix consists of omphacite and lawsonite, with minor chlorite, titanite, phengite and quartz; locally, omphacite occurs as fine-grained aggregates. Garnet porphyroblasts contain abundant inclusions of lawsonite, omphacite, rutile, ilmenite, and chlorite; most lack ilmenite and chlorite in their rims. Lawsonite inclusions in garnet cores contain rare <0.02 mm pumpellyite. Rutile in garnet does not have a titanite rim. In some samples, nearly inclusion-free garnet rims enclose inclusion-rich garnet. Late-stage phengite occurs along garnet grain boundaries and fills some fractures in garnet. Two different schistosities, S_2 and S_3, are recognized in the matrix. Lawsonite-rich seams and laminae define S_2; also, titanite overgrowths around rutile are aligned parallel to S_2. The S_2 is weakly crenulated, and locally cut by S_3 (Fig. 5D). In some samples, inclusions within garnet show a strong fabric comparable to S_2 that is not continuous with S_3 (Figs. 5D and 5E). These textures indicate that the main growth of garnet occurred during D_2. Crack-seal veins of elongate-blocky omphacite and lawsonite locally break up the matrix (Fig. 5C); these crack-seal veins can be traced into euhedral garnet as bands of oriented coarser omphacite and lawsonite (Fig. 5C). These textures indicate that D_2 involved brittle deformation during eclogite-facies conditions.

In the retrograde glaucophane-rich hydrous veins, the matrix is intensely recrystallized into fine-grained aggregates of glaucophane and omphacite (<0.3 mm) and unoriented, poikiloblastic subhedral to euhedral titanite (<1.5 mm in length). Glaucophane is intergrown with recrystallized omphacite, and titanite contains abundant tiny inclusions of glaucophane and omphacite. Rare coarse-grained phengite also grew in the hydrous veins.

Type II Lawsonite Eclogites

The type II lawsonite eclogite is a glaucophane-bearing nematoblastic matrix containing subhedral to euhedral 3–10 mm garnet, and is composed of omphacite, glaucophane, garnet, and lawsonite, with minor titanite, phengite, chlorite, and quartz. A penetrative S_3 schistosity is defined by oriented prismatic omphacite and glaucophane with granoblastic lawsonite (Figs. 3C and 5G). Garnet porphyroblasts contain inclusions of omphacite, lawsonite, rutile, quartz, and rare phengite. Some garnet cores contain rare K-feldspar—rather than phengite—inclusions. The internal fabric of the inclusions in garnet is discontinuous with the external foliation S_3. In some garnets, nearly inclusion-free rims enclose inclusion-rich cores. Some prismatic omphacites (<0.5 mm in length) contain inclusions of needle-like quartz, lawsonite, rutile, with rare glaucophane in the core. Pale violet glaucophane contains inclusions of rutile, lawsonite, omphacite, and rare zircon. Most lawsonite is twinned and contains rare inclusions of rutile. Titanite replaces most rutile (Fig. 5G), except for rutile inclusions in garnet.

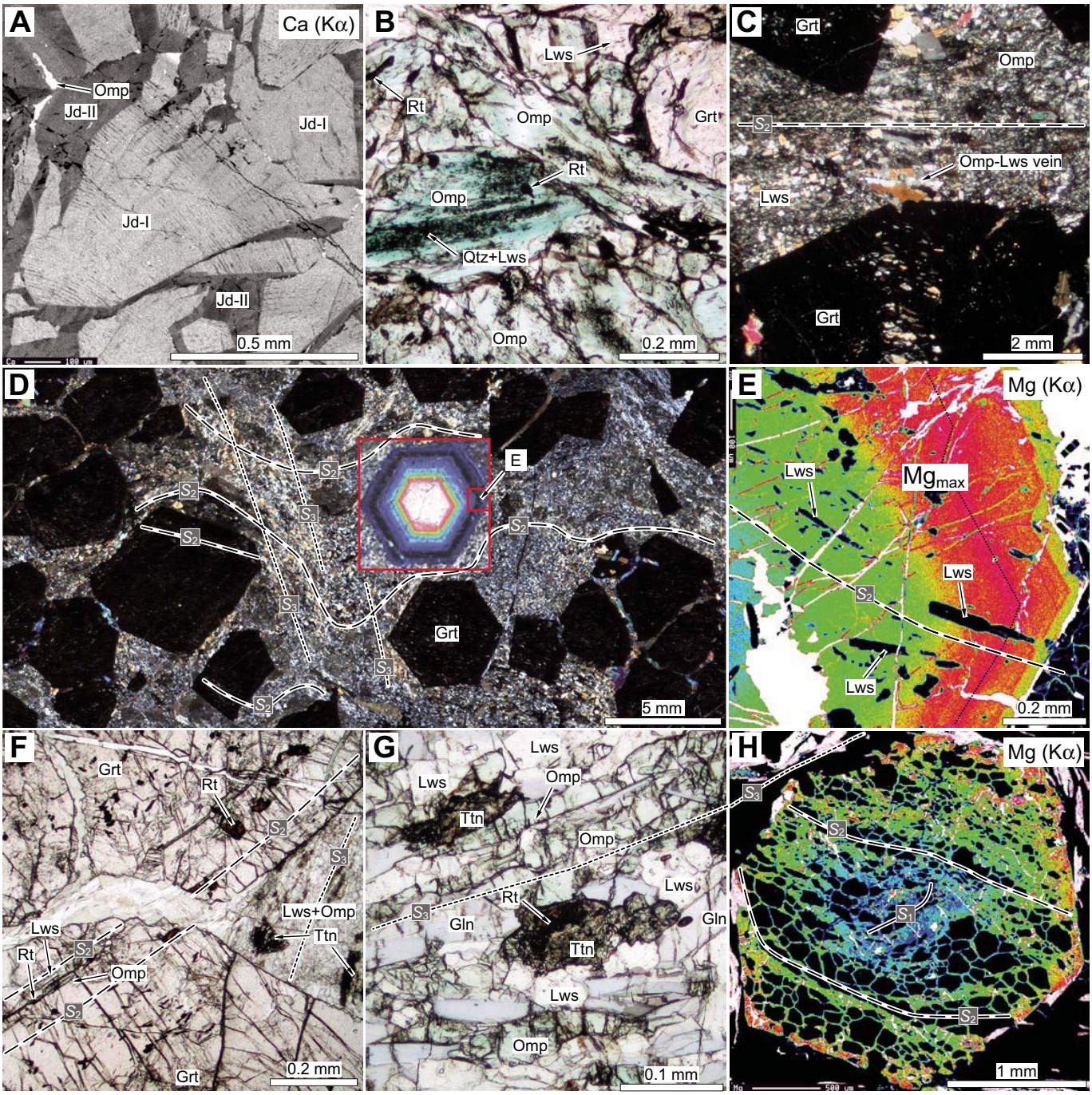

Figure 5. Microtextures of the Carrizal Grande rocks. (A) Backscattered-electron (BSE) image shows two stages of sodic clinopyroxene in the coarse-grained jadeite eclogite. Jd-I is replaced by Jd-II plus minor omphacite (Omp). (B) Photomicrograph in plane polarized light showing inclusion-rich omphacite and garnet in fine-grained jadeite eclogite. Grt—garnet, Lws—lawsonite, Rt—rutile, Qtz—quartz. (C) A synmetamorphic omphacite + lawsonite vein in type I lawsonite eclogite (crossed polarized light). (D) Weakly deformed matrix of type I lawsonite eclogite (crossed polarized light). Image is color X-ray of Mn concentration overlain on a garnet grain. (E) X-ray image of Mg in the rim of the same garnet. (F) Internal inclusion trails within garnets in type I lawsonite eclogite. Ttn—titanite. (G) Glaucophane (Gln)-bearing foliated matrix of type II lawsonite eclogite (plane polarized light). (H) X-ray image of Mg in a garnet showing two internal foliations.

Garnet-Bearing Lawsonite Blueschist

The garnet-bearing lawsonite blueschist is petrographically similar to the type II lawsonite eclogite, but has <10 vol% omphacite. It has a similar mineral assemblage of glaucophane, lawsonite, and garnet with minor omphacite, titanite, phengite, chlorite, and quartz. Garnet porphyroblasts (5–8 mm in size) contain inclusions of omphacite, lawsonite, rutile, quartz, and rare ferroglaucophane. Titanite in the matrix contains rare relict rutile. Recrystallization is more extensive than in the type II lawsonite eclogite. Most garnets have chloritized fractures with rare stilpnomelane. Secondary albite is associated with other retrograde minerals, such as titanite, chlorite and stilpnomelane.

Garnet-Bearing Quartz–Phengite Schist

The garnet-bearing quartz–phengite schist is a lepidoblastic, micaceous metapelite composed of quartz and phengite, minor garnet, lawsonite, glaucophane, rutile, titanite, and graphite. A penetrative S_3 schistosity defined by the preferred orientation of phengite is locally gently folded and crenulated (F_4) (Fig. 3D). Garnet occurs as euhedral to subhedral grains with a bimodal size distribution. Most millimeter-size garnets (normally 0.2–4 mm; rarely up to 2 cm) are poikiloblastic, with inclusions of granoblastic quartz, lawsonite, and fine-grained phengite (Fig. 5H) that preserve an early S_2 schistosity (Figs. 3E and 5H). In contrast, small garnet grains (<0.5 mm) are inclusion free and lie parallel to S_3. Pre-S_2 inclusion trails interpreted as S_1 can be seen in the large garnet cores (Fig. 5H). Lawsonite occurs as poikiloblastic, subhedral prisms (<1.5 mm) containing inclusions of quartz, rutile, garnet, and phengite; rare pumpellyite is included in lawsonite. Nearly colorless, nematoblastic glaucophane is <2 mm wide and contains inclusions of garnet and rutile. Some glaucophane is replaced by fine-grained aggregates of actinolite and chlorite.

MINERAL PARAGENESES AND METAMORPHIC STAGES

At least two metamorphic stages, an eclogite stage and a blueschist stage, can be distinguished in all rock types. Moreover, the eclogite stage can be subdivided further into prograde eclogite and retrograde eclogite stages. Mineral parageneses for the different metamorphic stages are summarized in Figure 6. The prograde eclogite stage is recorded in prograde-zoned garnet with older S_2 (or S_1) foliation, whereas the retrograde eclogite stage is recorded in reversely zoned narrow garnet rims and in the mineral assemblage formed during S_3. The blueschist stage represents post–eclogite-facies recrystallization and hydration during decompression.

The mineral assemblages and their pseudomorphs formed during S_2 (or S_1) characterize the prograde eclogite stage. This includes Grt + Omp + Lws + Rt + Qtz in mafic lithologies; some rocks also have chlorite, phengite, ferroglaucophane, ilmenite, and K-feldspar. Jadeite occurs instead of omphacite in jadeite eclogite. Eclogite-stage chlorite can be texturally distinguished from later blueschist-stage chlorite. Rare lawsonite contains pumpellyite as precursor inclusions. The minerals of this metamorphic stage are best preserved in the prograde-zoned garnets in all mafic lithologies and in the matrix of the fine-grained jadeite eclogite. The retrograde eclogite stage includes the reversely zoned rims of Grt plus Omp + Lws ± Gln + Rt + Qtz ± Phe ± Chl. This assemblage is

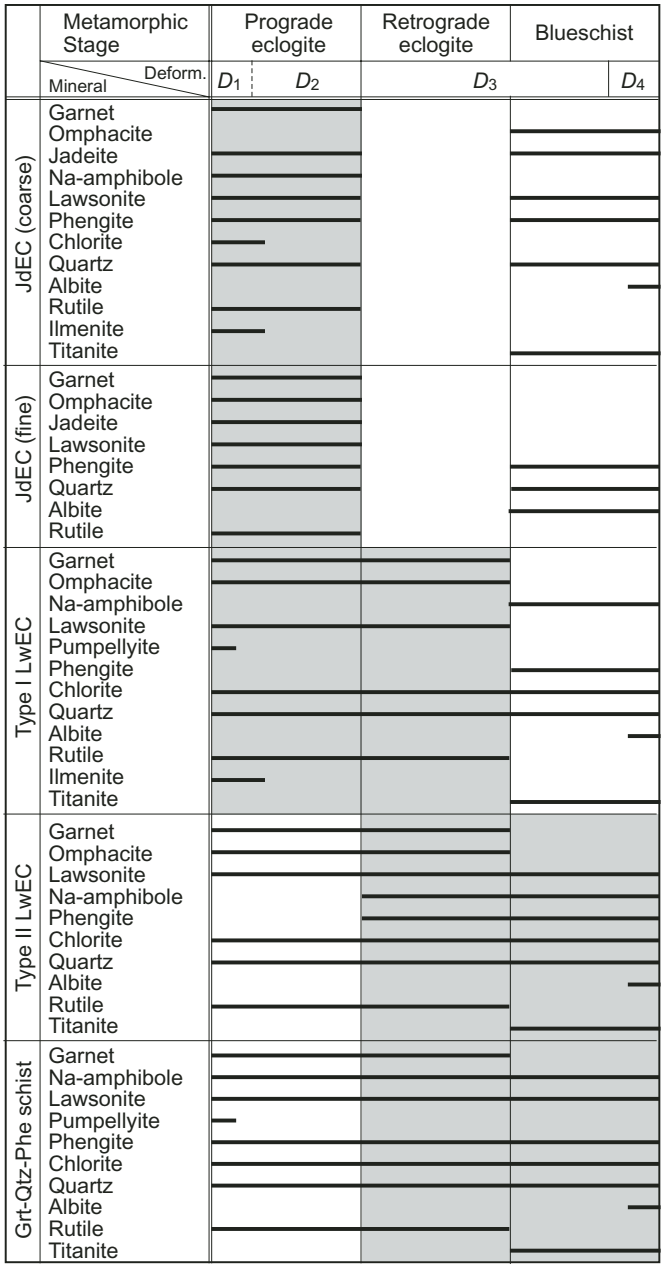

Figure 6. Mineral parageneses for the different stages of metamorphic recrystallization. Grt-Qtz-Phe schist—garnet-bearing quartz–phengite schist; LwEC—lawsonite eclogite; JdEC—jadeite eclogite.

best preserved in type II lawsonite eclogite and garnet-bearing lawsonite blueschist. Glaucophane and lawsonite containing rutile or omphacite inclusions are interpreted to be part of this stage. The post–eclogite-stage blueschist-facies overprint that locally replaces earlier mineral assemblages is Gln + Lws + Chl + Phe + Ttn + Qtz (±rare Ab). Titanite overgrowths on rutile and glaucophane-rich hydrous veins are typical features for this stage. In the coarse-grained jadeite eclogite, retrograde jadeite described by Tsujimori et al. (2005) may be part of this stage.

MINERAL CHEMISTRY

Electron microprobe analysis was carried out with a JEOL JXA-8900R at Okayama University of Science. Quantitative analyses were performed with 15 kV accelerating voltage, 12 nA beam current, and 3–5 μm beam size. Natural and synthetic silicates and oxides were used as standards for calibration. The CITZAF method (Armstrong, 1988) was employed for matrix corrections. Representative analyses are listed in Table 1. Fe was assumed to be Fe^{2+} unless otherwise noted.

Garnet

All of the garnet is zoned with spessartine-rich cores, except for garnet in the fine-grained jadeite eclogite (Fig. 7). X_{Mg} [= Mg/(Mg + Fe^{2+})] increases continuously from core to rim, but the nature of this trend varies with rock type. For example, the lowest X_{Mg} values are type I lawsonite eclogite (0.22), type II lawsonite eclogite/garnet-bearing lawsonite blueschist/garnet-bearing quartz–phengite schist (0.16–0.17), and jadeite eclogite (0.12–0.14). Reversely zoned rims, some with micron-scale oscillatory zoning, can be observed in some type I lawsonite eclogite, type II lawsonite eclogite, and garnet-bearing lawsonite blueschist (Fig. 7E). Garnet in coarse-grained jadeite eclogite has an almandine-rich composition: $alm_{55–76}grs_{17–28}prp_{0.8–10}sps_{0–22}$, with X_{Mg} = 0.02–0.12. Garnet in fine-grained jadeite eclogite has a spessartine-poor composition: $alm_{63–71}grs_{20–25}prp_{2–11}sps_{1–4}$, with X_{Mg} = 0.07–0.14; spessartine-rich cores were not observed. Garnet in the type I lawsonite eclogite is Ca and Mg rich relative to other rock types. It has a wider compositional range: $alm_{54–69}grs_{24–30}prp_{2–16}sps_{1–17}$, with X_{Mg} = 0.04–0.22; the highest X_{Mg} rim values are higher than in the other rock types. Garnet in type II lawsonite eclogite is $alm_{54–75}grs_{18–24}prp_{4–14}sps_{0.5–22}$, with X_{Mg} = 0.04–0.17; in some samples, the maximum X_{Mg} is similar to that in coarse-grained jadeite eclogite. Garnet in garnet-bearing lawsonite blueschist is $alm_{59–73}grs_{17–26}prp_{4–13}sps_{0.3–15}$, with X_{Mg} = 0.09–0.16. Poikiloblastic garnet in the garnet-bearing quartz–phengite schist is relatively poor in spessartine at the cores and has the composition: $alm_{63–72}grs_{18–24}prp_{4–13}sps_{0.3–7}$, with X_{Mg} = 0.05–0.16. In contrast, fine-grained garnet in garnet-bearing quartz–phengite schist is richer in spessartine: $alm_{49–68}grs_{16–22}prp_{3–12}sps_{4–31}$, with X_{Mg} = 0.05–0.15.

Clinopyroxene

Figure 8 shows clinopyroxene compositions from each rock type; the Fe^{2+}/Fe^{3+} ratio and end-member components were calculated following Harlow (1999). Jadeite eclogites contain a bimodal compositional distribution of omphacitic and jadeitic clinopyroxene. The coarse-grained jadeite eclogite contains two generations of sodic pyroxene (Tsujimori et al., 2005). The prograde jadeitic pyroxene (Jd-I) has a composition intermediate between jadeite and omphacite ($jd_{62–75}di$+$hd_{16–24}ae_{0–18}$; X_{Mg} = 0.09–0.93). Later-stage (blueschist-stage) jadeitic pyroxene (Jd-II) has a significantly higher jadeite component ($jd_{74–87}di$ + $hd_{9–16}ae_{0–11}$; X_{Mg} = 0.30–0.90), and coexists with minor omphacite ($jd_{42–50}di$ + $hd_{36–46}ae_{7–16}$; X_{Mg} = 0.70–0.88). Some Jd-I inclusions in garnet are also partly recrystallized into two pyroxenes. In contrast, the fine-grained jadeite eclogite contains two coexisting prograde pyroxenes: omphacite ($jd_{33–52}di$ + $hd_{36–53}ae_{0.2–19}$; X_{Mg} = 0.58–0.97) and jadeite ($jd_{69–83}di$ + $hd_{9–17}ae_{0–15}$; X_{Mg} = 0.47–1); the inclusion-rich green cores are slightly enriched in aegirine. Omphacite in type I lawsonite eclogite is $jd_{32–51}di$ + $hd_{40–50}ae_{0–23}$; X_{Mg} ranges from 0.62 to 0.98. Omphacite inclusions within garnet are commonly enriched in aegirine, whereas recrystallized grains in the matrix are poor in aegirine. Omphacite in type II lawsonite eclogite is aegirine rich and jadeite poor relative to the other rock types ($jd_{25–44}di$ + $hd_{37–52}ae_{5–30}$; X_{Mg} = 0.65–0.97). Some omphacite inclusions within garnet have a higher aegirine component than matrix omphacite. Omphacite in garnet-bearing lawsonite blueschist has similar compositions to that of type II lawsonite eclogite ($jd_{26–43}di$ + $hd_{43–54}ae_{5–17}$; X_{Mg} = 0.69–0.94); the omphacite inclusions in garnet are rich in aegirine.

Amphiboles

Compositions of sodic amphibole are plotted in Figure 9; the structural formulae of amphiboles were calculated based on O = 23, and the Fe^{2+}/Fe^{3+} ratio was estimated with total cation = 13, excluding Ca, Na, and K. All sodic amphibole is low in Ca (0.02–0.25 p.f.u.) and ^{IV}Al (0–0.16 p.f.u.). The inferred $Fe^{3+}/(Fe^{3+} + Al)$ ratio is typically <0.2. Ferroglaucophane inclusions in garnet of coarse-grained lawsonite eclogite have a low X_{Mg} of 0.18–0.49. Prograde inclusions of ferroglaucophane and glaucophane with X_{Mg} = 0.46–0.52 were also found in garnet of garnet-bearing lawsonite blueschist. No compositional differences in glaucophane grown during the retrograde eclogite stage and blueschist stage were found; these amphiboles have high Al and X_{Mg} values. Glaucophane in the retrograde veins of type I lawsonite eclogite has X_{Mg} = 0.59–0.76, similar to matrix glaucophane in type II lawsonite eclogite (X_{Mg} = 0.62–0.70), garnet-bearing lawsonite blueschist (X_{Mg} = 0.63–0.72), and garnet-bearing quartz–phengite schist (X_{Mg} = 0.63–0.74). Retrograde actinolite replacing glaucophane in the garnet-bearing quartz–phengite schist has 0.21–0.41 ^{M4}Na, 0.15–0.20 ^{IV}Al (p.f.u.), and X_{Mg} = 0.81–0.86.

TABLE 1. REPRESENTATIVE MICROPROBE ANALYSES OF MINERALS FROM HIGH-PRESSURE ROCKS FROM THE CARRIZAL GRANDE AREA

Mineral		SiO_2	TiO_2	Al_2O_3	Cr_2O_3	FeO*	MnO	MgO	CaO	Na_2O	K_2O	Total	O=	Si	Ti	Al	Cr	Fe^{3+}	Fe^{2+}	Mn	Mg	Ca	Na	K	Total
JdEC (coarse-grained)																									
Grt	rim	37.8	0.1	21.1	0.0	31.6	0.1	2.1	8.1	0.1	0.0	100.9	*12*	3.00	0.00	1.97	0.00	0.00	2.09	0.01	0.24	0.69	0.01	0.00	8.01
Grt	rim	36.9	0.2	21.3	0.0	32.8	0.1	1.6	7.7	0.0	0.0	100.5	*12*	2.96	0.01	2.01	0.00	0.00	2.20	0.01	0.19	0.66	0.01	0.00	8.03
Grt	core	37.3	0.3	20.3	0.0	27.5	6.7	0.3	8.6	0.0	0.0	100.9	*12*	3.00	0.02	1.92	0.00	0.00	1.85	0.46	0.04	0.74	0.00	0.00	8.02
Jd	inc. G	57.2	0.0	16.8	0.0	6.0	0.1	2.8	5.9	11.7	0.0	100.5	*6*	1.99	0.00	0.69	0.00	0.13	0.04	0.00	0.14	0.22	0.79	0.00	4.00
Jd	Jd-I	57.6	0.1	17.4	0.0	5.6	0.1	2.3	5.1	12.0	0.0	100.2	*6*	2.00	0.00	0.71	0.00	0.09	0.07	0.00	0.12	0.19	0.81	0.00	4.00
Jd	Jd-I	57.4	0.1	17.0	0.0	5.4	0.0	2.8	5.6	11.7	0.0	99.9	*6*	2.00	0.00	0.70	0.00	0.09	0.07	0.00	0.14	0.21	0.79	0.00	4.00
Jd	Jd-II	58.2	0.1	20.3	0.0	3.7	0.1	1.5	2.9	13.1	0.0	99.7	*6*	2.01	0.00	0.82	0.00	0.03	0.08	0.00	0.08	0.11	0.87	0.00	4.00
Jd	Jd-II	57.8	0.1	19.9	0.0	4.2	0.0	1.5	3.1	13.1	0.0	99.6	*6*	2.00	0.00	0.81	0.00	0.07	0.05	0.00	0.08	0.11	0.88	0.00	4.00
Omp		56.0	0.0	10.7	0.0	6.5	0.0	6.8	11.7	8.0	0.0	99.9	*6*	1.99	0.00	0.45	0.00	0.12	0.08	0.00	0.36	0.45	0.55	0.00	4.00
Omp		55.8	0.1	10.9	0.0	7.6	0.0	6.1	11.3	8.2	0.0	100.0	*6*	1.99	0.00	0.46	0.00	0.12	0.10	0.00	0.32	0.43	0.56	0.00	4.00
Fgl	inc. G	56.2	0.0	11.5	0.0	17.1	0.1	5.3	0.3	7.4	0.0	97.9	*23*	7.94	0.00	1.91	0.00	0.07	1.95	0.01	1.12	0.05	2.03	0.00	15.08
Lws	inc. G	38.9	0.1	31.4	0.1	0.5	0.0	0.0	17.1	0.0	0.0	88.2	*8*	2.04	0.01	1.94	0.01	0.02	0.00	0.00	0.00	0.96	0.00	0.00	4.97
Lws		38.1	0.0	31.6	0.1	0.3	0.0	0.0	17.1	0.0	0.0	87.2	*8*	2.02	0.00	1.97	0.01	0.01	0.00	0.00	0.00	0.97	0.00	0.00	4.98
Phe	inc. G	53.3	0.2	24.1	0.0	3.1	0.0	4.5	0.0	0.2	8.9	94.4	*11*	3.56	0.01	1.90	0.00	0.00	0.17	0.00	0.45	0.00	0.02	0.76	6.87
Chl	inc. G	23.5	0.0	19.4	0.0	42.0	1.1	2.3	0.0	0.0	0.0	88.4	*28*	5.44	0.00	5.30	0.01	0.00	8.14	0.22	0.79	0.00	0.01	0.01	19.92
JdEC (fine-grained)																									
Grt	rim	37.7	0.0	21.5	0.1	28.6	1.3	2.6	8.2	0.0	0.0	100.1	*12*	2.99	0.00	2.01	0.00	0.00	1.89	0.09	0.31	0.70	0.01	0.00	8.01
Grt	rim	37.8	0.0	21.3	0.0	29.6	1.1	2.5	7.9	0.0	0.0	100.4	*12*	2.99	0.00	1.99	0.00	0.00	1.96	0.08	0.30	0.67	0.00	0.00	8.01
Grt	core	37.8	0.1	21.3	0.0	30.6	1.6	1.3	8.4	0.0	0.0	101.1	*12*	3.00	0.01	1.99	0.00	0.00	2.03	0.11	0.15	0.71	0.00	0.00	8.00
Jd		57.2	0.2	17.8	0.0	5.4	0.2	2.5	4.1	12.0	0.0	99.4	*6*	2.00	0.00	0.73	0.00	0.07	0.09	0.01	0.13	0.15	0.81	0.00	4.00
Omp	rim	56.2	0.0	11.5	0.0	5.3	0.0	6.8	12.2	7.8	0.0	99.9	*6*	2.00	0.00	0.48	0.00	0.05	0.10	0.00	0.36	0.47	0.53	0.00	4.00
Omp	core	55.4	0.1	9.1	0.0	8.5	0.0	7.1	13.3	7.0	0.0	100.4	*6*	1.98	0.00	0.38	0.00	0.13	0.12	0.00	0.38	0.51	0.49	0.00	4.00
Lws		38.6	0.1	32.1	0.0	0.3	0.1	0.0	17.1	0.0	0.0	88.2	*8*	2.02	0.00	1.98	0.00	0.01	0.00	0.00	0.00	0.96	0.00	0.00	4.98
Phe		54.4	0.2	23.0	0.0	2.3	0.0	5.2	0.0	0.2	9.1	94.5	*11*	3.62	0.01	1.80	0.00	0.00	0.13	0.00	0.51	0.00	0.02	0.77	6.87
Type I LwEC																									
Grt	rim	38.5	0.0	21.7	0.1	25.6	0.2	4.0	9.5	0.0	0.0	99.5	*12*	3.02	0.00	2.01	0.01	0.00	1.67	0.01	0.47	0.79	0.00	0.00	7.98
Grt	rim	38.3	0.0	21.6	0.1	26.6	0.2	4.2	9.1	0.0	0.0	100.0	*12*	3.00	0.00	1.99	0.01	0.00	1.74	0.01	0.49	0.76	0.00	0.00	8.01
Grt	core	37.3	0.1	20.7	0.0	32.0	1.7	1.1	7.2	0.0	0.0	100.0	*12*	3.01	0.01	1.97	0.00	0.00	2.16	0.11	0.13	0.62	0.00	0.00	8.00
Grt	outer r.	38.3	0.1	21.4	0.0	28.7	0.1	3.4	8.6	0.0	0.0	100.6	*12*	3.01	0.00	1.98	0.00	0.00	1.88	0.01	0.39	0.72	0.00	0.00	8.00
Omp	inc. G	55.6	0.2	8.7	0.1	10.2	0.2	6.0	11.2	8.2	0.0	100.4	*6*	1.99	0.01	0.37	0.00	0.20	0.10	0.01	0.32	0.43	0.57	0.00	4.00
Omp		55.9	0.0	10.7	0.1	6.5	0.1	6.7	11.3	8.3	0.0	99.6	*6*	1.99	0.00	0.45	0.00	0.14	0.06	0.00	0.35	0.43	0.57	0.00	4.00
Omp		56.0	0.1	10.5	0.0	6.3	0.0	7.1	12.0	7.8	0.0	99.9	*6*	1.99	0.00	0.44	0.00	0.11	0.08	0.00	0.37	0.46	0.54	0.00	4.00
Lws	inc. G	38.4	0.1	31.3	0.1	1.3	0.0	0.0	17.4	0.0	0.0	88.6	*8*	2.02	0.00	1.93	0.00	0.05	0.00	0.00	0.00	0.98	0.00	0.00	4.99
Lws		38.1	0.0	31.2	0.1	0.5	0.0	0.0	17.3	0.0	0.0	87.3	*8*	2.02	0.00	1.95	0.00	0.02	0.00	0.00	0.00	0.98	0.00	0.00	4.99
Pmp	inc. L	36.2	0.6	23.1	0.1	8.3	0.2	0.9	22.3	0.2	0.0	91.7	*24.5*	6.05	0.07	4.54	0.01	0.00	1.16	0.02	0.21	4.00	0.07	0.00	16.14
Chl	inc. G	28.2	0.1	19.1	0.0	20.8	0.3	18.2	0.1	0.0	0.0	86.8	*28*	5.83	0.01	4.66	0.00	0.00	3.61	0.06	5.62	0.03	0.00	0.00	19.82
Phe		50.7	0.1	25.5	0.0	3.4	0.0	3.7	0.0	0.1	10.0	93.6	*11*	3.45	0.01	2.05	0.00	0.00	0.20	0.00	0.37	0.00	0.02	0.87	6.96

(continued)

TABLE 1. REPRESENTATIVE MICROPROBE ANALYSES OF MINERALS FROM HIGH-PRESSURE ROCKS FROM THE CARRIZAL GRANDE AREA *(continued)*

Mineral		SiO_2	TiO_2	Al_2O_3	Cr_2O_3	FeO*	MnO	MgO	CaO	Na_2O	K_2O	Total	O=	Si	Ti	Al	Cr	Fe^{3+}	Fe^{2+}	Mn	Mg	Ca	Na	K	Total
Type II LwEC																									
Grt	rim	38.2	0.0	21.3	0.0	28.8	0.7	3.2	7.9	0.0	0.0	100.2	*12*	3.02	0.00	1.98	0.00	1.90	0.05	0.37	0.67	0.00	0.00	8.00	15.99
Grt	core	37.3	0.2	20.7	0.0	26.0	7.2	0.8	8.1	0.0	0.0	100.3	*12*	3.00	0.01	1.96	0.00	0.00	1.75	0.49	0.10	0.70	0.00	0.00	8.01
Grt	outer r.	37.9	0.1	21.5	0.0	30.7	1.7	2.6	6.4	0.0	0.0	101.0	*12*	3.00	0.00	2.00	0.00	0.00	2.03	0.12	0.30	0.54	0.01	0.00	8.00
Omp	inc. G	55.0	0.0	7.8	0.1	9.8	0.0	6.9	11.9	7.8	0.0	99.3	*6*	1.99	0.00	0.33	0.00	0.23	0.06	0.00	0.37	0.46	0.55	0.00	4.00
Omp		55.5	0.0	8.0	0.0	9.8	0.0	6.6	11.0	8.4	0.0	99.3	*6*	2.00	0.00	0.34	0.00	0.24	0.05	0.00	0.36	0.42	0.58	0.00	4.00
Omp		56.0	0.0	10.1	0.0	7.2	0.0	6.6	11.5	8.0	0.0	99.4	*6*	2.01	0.00	0.43	0.00	0.11	0.10	0.00	0.35	0.44	0.56	0.00	4.00
Gln		58.2	0.0	11.2	0.0	10.5	0.0	9.8	0.4	7.4	0.0	97.4	*23*	7.99	0.00	1.81	0.00	0.14	1.07	0.00	2.00	0.05	1.97	0.00	15.03
Lws	inc. G	38.1	0.1	30.5	0.0	1.4	0.0	0.0	17.4	0.0	0.0	87.5	*8*	2.03	0.00	1.91	0.00	0.00	0.06	0.00	0.00	0.99	0.00	0.00	4.99
Lws		37.7	0.1	30.7	0.0	1.3	0.0	0.0	16.9	0.0	0.0	86.8	*8*	2.02	0.00	1.93	0.00	0.00	0.05	0.00	0.00	0.97	0.00	0.00	4.98
Chl	inc. G	25.7	0.0	18.2	0.0	32.8	0.5	10.4	0.0	0.0	0.0	87.7	*28*	5.65	0.00	4.73	0.00	0.00	6.05	0.10	3.43	0.00	0.02	0.01	19.99
Phe		52.5	0.2	23.9	0.0	3.6	0.0	4.3	0.0	0.3	10.1	94.8	*11*	3.53	0.01	1.89	0.00	0.00	0.20	0.00	0.43	0.00	0.04	0.86	6.96
Grt-LwBS																									
Grt	rim	37.7	0.1	21.3	0.0	30.5	0.3	3.3	6.8	0.0	0.0	99.9	*12*	2.99	0.00	2.00	0.00	0.00	2.03	0.02	0.39	0.58	0.00	0.00	8.01
Grt	core	37.7	0.1	20.8	0.0	28.3	4.5	1.0	8.4	0.0	0.0	100.9	*12*	3.01	0.01	1.96	0.00	0.00	1.89	0.30	0.12	0.72	0.00	0.00	8.01
Omp	inc. G	54.8	0.0	7.9	0.0	8.3	0.0	7.8	13.5	6.7	0.0	99.0	*6*	1.99	0.00	0.34	0.00	0.15	0.11	0.00	0.42	0.52	0.47	0.00	4.00
Omp		56.0	0.0	10.2	0.0	6.3	0.1	7.2	12.0	7.7	0.0	99.6	*6*	2.00	0.00	0.43	0.00	0.10	0.09	0.00	0.38	0.46	0.54	0.00	4.00
Omp		55.2	0.0	7.5	0.0	8.5	0.0	7.9	14.2	6.5	0.0	99.8	*6*	2.00	0.00	0.32	0.00	0.14	0.11	0.00	0.42	0.55	0.45	0.00	4.00
Gln		58.4	0.0	10.5	0.0	9.6	0.0	10.7	0.4	7.4	0.0	97.1	*23*	8.00	0.00	1.70	0.00	0.21	0.89	0.00	2.18	0.06	1.95	0.00	15.01
Lws	inc. G	38.5	0.0	31.4	0.0	0.6	0.0	0.0	17.5	0.0	0.0	88.2	*8*	2.02	0.00	1.95	0.00	0.03	0.00	0.00	0.00	0.99	0.00	0.00	4.99
Lws		38.2	0.0	31.4	0.1	0.5	0.0	0.0	17.5	0.0	0.0	87.8	*8*	2.02	0.00	1.96	0.00	0.02	0.00	0.00	0.00	0.99	0.00	0.00	4.99
Chl	inc. G	26.1	0.0	18.6	0.0	31.5	0.4	10.5	0.2	0.0	0.0	87.3	*28*	5.73	0.00	4.80	0.00	0.00	5.79	0.08	3.43	0.04	0.00	0.00	19.87
Phe	inc. G	54.0	0.1	22.8	0.0	2.7	0.0	4.3	0.1	0.1	9.9	94.0	*11*	3.63	0.01	1.81	0.00	0.00	0.15	0.00	0.43	0.00	0.02	0.85	6.89
Phe		52.5	0.1	23.2	0.1	3.4	0.1	4.1	0.1	0.2	10.2	93.8	*11*	3.56	0.01	1.86	0.00	0.00	0.19	0.00	0.41	0.01	0.02	0.88	6.95
Grt-Qtz-Phe schist																									
Grt-L	rim	37.6	0.0	21.2	0.0	30.8	0.5	2.5	7.2	0.0	0.0	99.9	*12*	3.00	0.00	1.99	0.00	2.06	0.00	0.04	0.30	0.61	0.00	0.00	8.00
Grt-L	core	37.3	0.1	21.2	0.0	31.2	1.6	1.1	7.6	0.1	0.0	100.1	*12*	2.99	0.01	2.01	0.00	2.09	0.00	0.11	0.13	0.65	0.01	0.00	8.00
Grt-S		37.5	0.1	21.0	0.0	25.3	9.0	1.2	6.4	0.0	0.0	100.5	*12*	3.01	0.00	1.98	0.00	1.70	0.00	0.61	0.14	0.55	0.01	0.00	8.00
Gln		58.1	0.1	11.4	0.0	10.5	0.0	9.3	0.1	7.5	0.0	97.0	*23*	8.01	0.01	1.85	0.00	0.10	1.12	0.00	1.92	0.02	1.99	0.00	15.01
Lws	inc. G	37.8	0.2	31.5	0.0	0.5	0.0	0.0	17.5	0.0	0.0	87.5	*8*	2.00	0.01	1.97	0.00	0.02	0.00	0.00	0.00	0.99	0.00	0.00	4.99
Lws		38.6	0.1	32.1	0.0	0.2	0.0	0.0	17.4	0.0	0.0	88.4	*8*	2.02	0.00	1.98	0.00	0.01	0.00	0.00	0.00	0.97	0.00	0.00	4.99
Pmp	inc. L	36.6	0.1	24.5	0.0	3.8	0.8	2.2	22.3	0.1	0.0	90.4	*24.5*	6.07	0.01	4.78	0.00	0.00	0.53	0.11	0.55	3.96	0.04	0.01	16.06
Phe		53.5	0.2	24.0	0.1	2.3	0.0	4.3	0.0	0.2	9.2	93.8	*11*	3.58	0.01	1.90	0.00	0.00	0.13	0.00	0.43	0.00	0.02	0.78	6.86

FeO* = total Fe as Fe^{2+}. See text for calculation of Fe^{3+}/Fe^{2+} ratio of clinopyroxene.
inc. G = inclusion in garnet; inc. L = inclusion in lawsonite; outer r. = outermost rim
Grt-L = porphyroblastic garnet in Grt-Qtz-Phe schist; Grt-S = small garnet in Grt-Qtz-Phe schist.

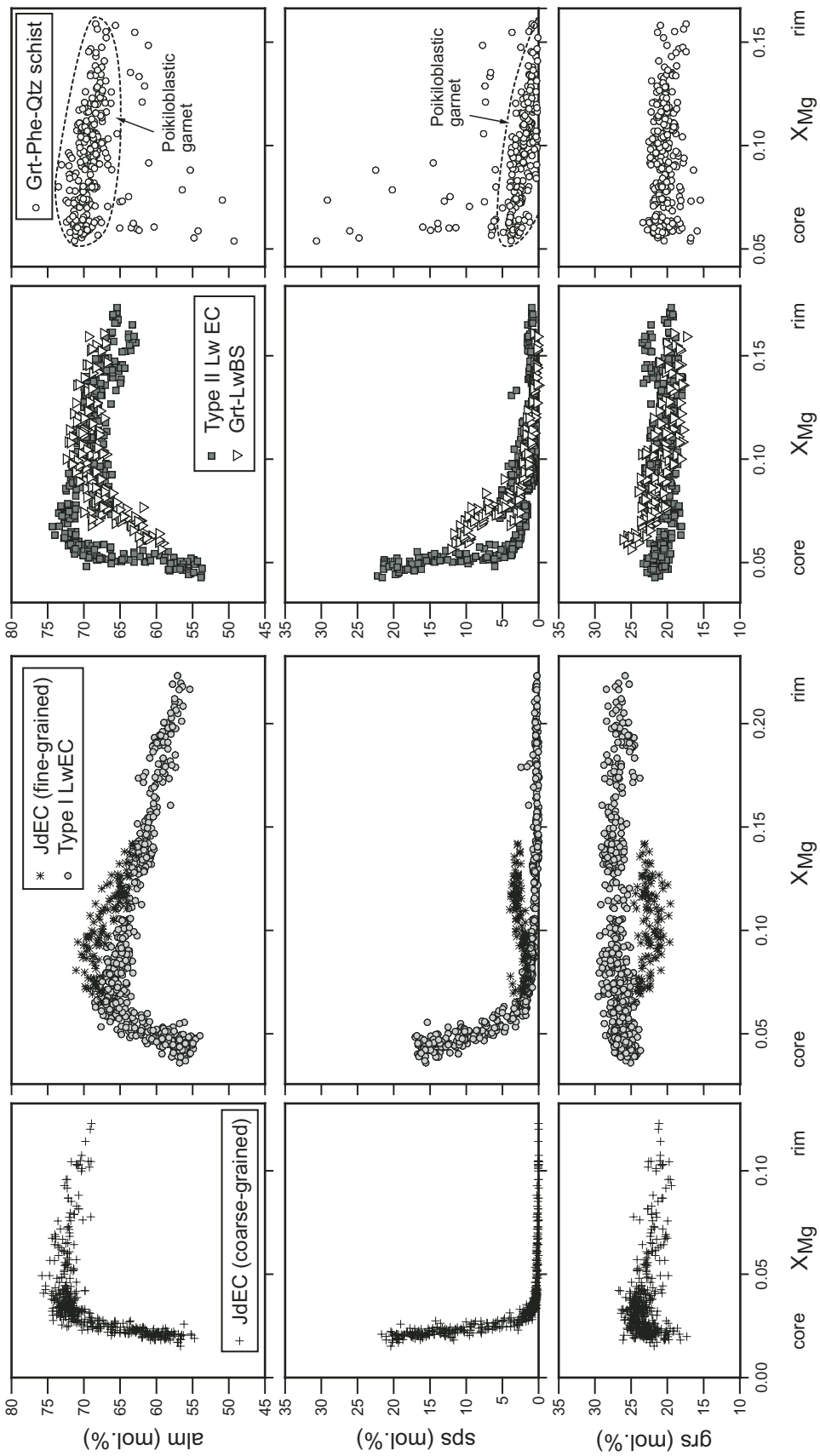

Figure 7. Compositional trends of garnet in high-pressure rocks from Carrizal Grande. Grt-Qtz-Phe schist—garnet-bearing quartz–phengite schist; LwEC—lawsonite eclogite; Grt-LwBS—garnet-bearing lawsonite blueschist; JdEC—jadeite eclogite; grs—grossular, sps—spessartine; alm—almandine.

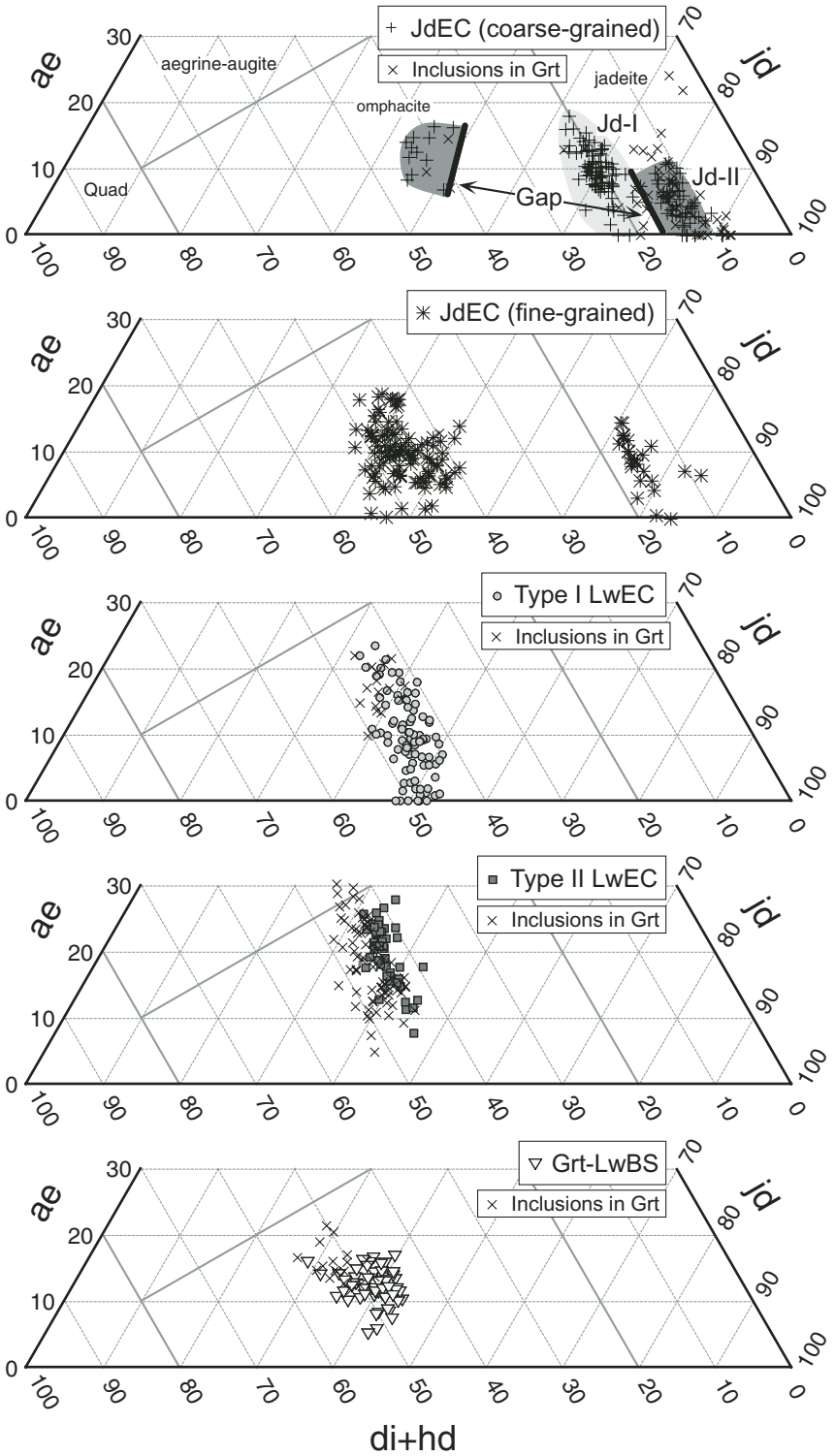

Figure 8. Compositional trends of clinopyroxene in high-pressure rocks from Carrizal Grande. LwEC—lawsonite eclogite; Grt-LwBS—garnet-bearing lawsonite blueschist; JdEC—jadeite eclogite; jd—jadeite; ae—aegirine; di + hd—diopside plus hedenbergite.

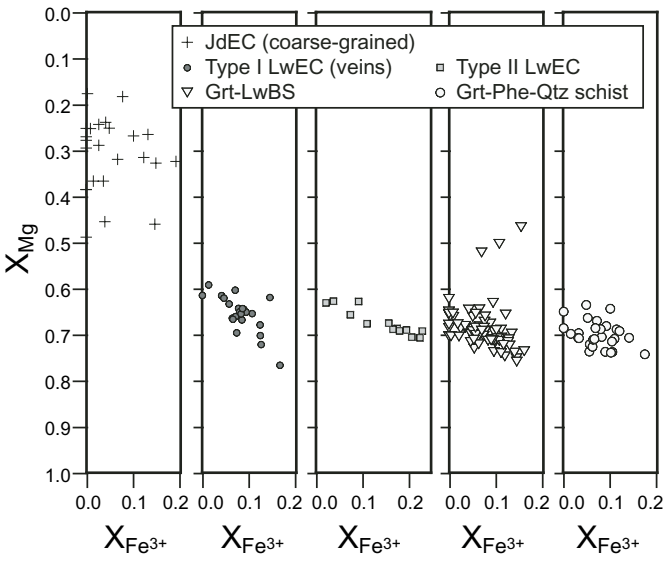

Figure 9. Compositional variations of sodic amphibole in high-pressure rocks from Carrizal Grande. Grt-Qtz-Phe schist—garnet-bearing quartz–phengite schist; LwEC—lawsonite eclogite; Grt-LwBS—garnet-bearing lawsonite blueschist; JdEC—jadeite eclogite.

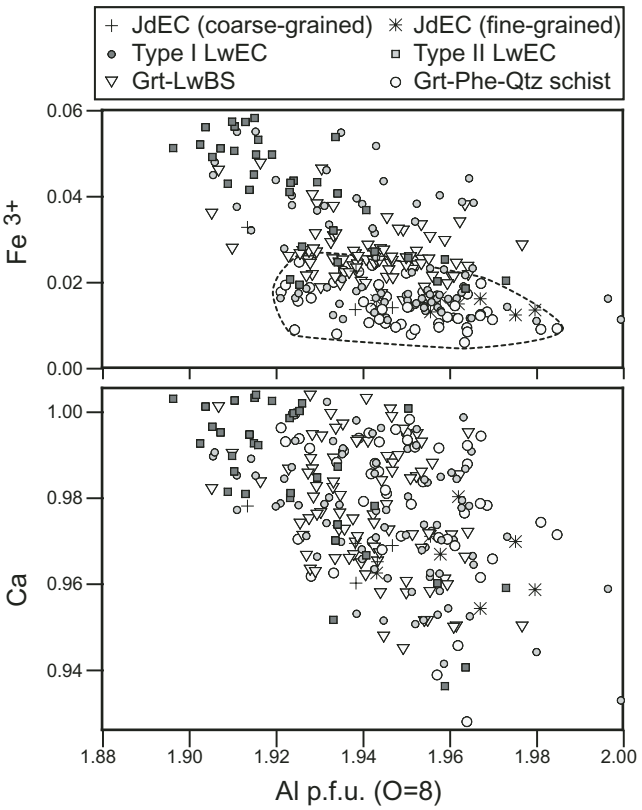

Figure 10. Compositional variation of lawsonite in high-pressure rocks from Carrizal Grande. Grt-Qtz-Phe schist—garnet-bearing quartz–phengite schist; LwEC—lawsonite eclogite; Grt-LwBS—garnet-bearing lawsonite blueschist; JdEC—jadeite eclogite.

Lawsonite

The compositions of lawsonite are plotted in Figure 10; all Fe is assumed to be Fe^{3+}. The lawsonite has 0.01–0.06 Fe^{3+}, 1.90–2.00 Al, and 0.93–1.00 Ca p.f.u. of 8 oxygen. The $Fe^{3+}/(Fe^{3+}$ + Al) ratio ranges from 0.003 to 0.03. There is no systematic chemical zoning, however, a negative correlation between Al and Fe^{3+} suggests substitution of Fe^{3+} for Al in the octahedral site. There are no compositional differences between different textural types of lawsonite within the same sample. Lawsonite in garnet-bearing quartz–phengite schist contains a significantly lower Fe^{3+} concentration, consistent with the occurrence of graphite.

Chlorite

Chlorite shows a wide compositional variation that varies with rock type (Fig. 11). Mn content has a good negative correlation with X_{Mg}. Chlorite inclusions in garnet in coarse-grained jadeite eclogite are low in X_{Mg} (0.09–0.10) and Si (5.4–5.5), and high in Al (5.2–5.3 p.f.u.), in contrast to other rock types (X_{Mg} = 0.30–0.70 and 4.4–5.1 Al p.f.u.). The X_{Mg} values increase from type I lawsonite eclogite (0.48–0.70) to type II lawsonite eclogite/garnet-bearing lawsonite blueschist/garnet-bearing quartz–phengite schist (0.30–0.52) to jadeite eclogite (0.12–0.14).

Phengite

Phengite in the investigated rocks has a wide compositional range with high Si (3.45–3.65 p.f.u.) and low Na/(Na^+K) (0.01–0.06); X_{Mg} varies from 0.63 to 0.82 (Fig. 12). There are no apparent differences in composition among different textural types of phengite in individual samples. However, late-stage phengite in the type I lawsonite eclogite is relatively low in Si.

Pumpellyite

Pumpellyite inclusions within lawsonite of type I lawsonite eclogite and garnet-bearing quartz–phengite schist are Al rich, with Al/(Al + Fe + Mg) = 0.78–0.88, and contain 0.09–0.21 wt% Na_2O (Fig. 13). Pumpellyite in type I lawsonite eclogite is less magnesian (X_{Mg} = 0.15–0.16) than in the garnet-bearing quartz–phengite schists (X_{Mg} = 0.51–0.55).

Other Minerals

Ilmenite inclusions in the cores of garnet in coarse-grained jadeite eclogite and type II lawsonite eclogite contain 2.8–7 wt% MnO. Titanite in the mafic rock types contains 0.6–1.2 wt% Al_2O_3, whereas rare titanite in garnet-bearing quartz–phengite schist contains <2.5 wt% Al_2O_3. Stilpnomelane in type II lawsonite eclogite and garnet-bearing lawsonite blueschist has X_{Mg} = 0.36–0.40.

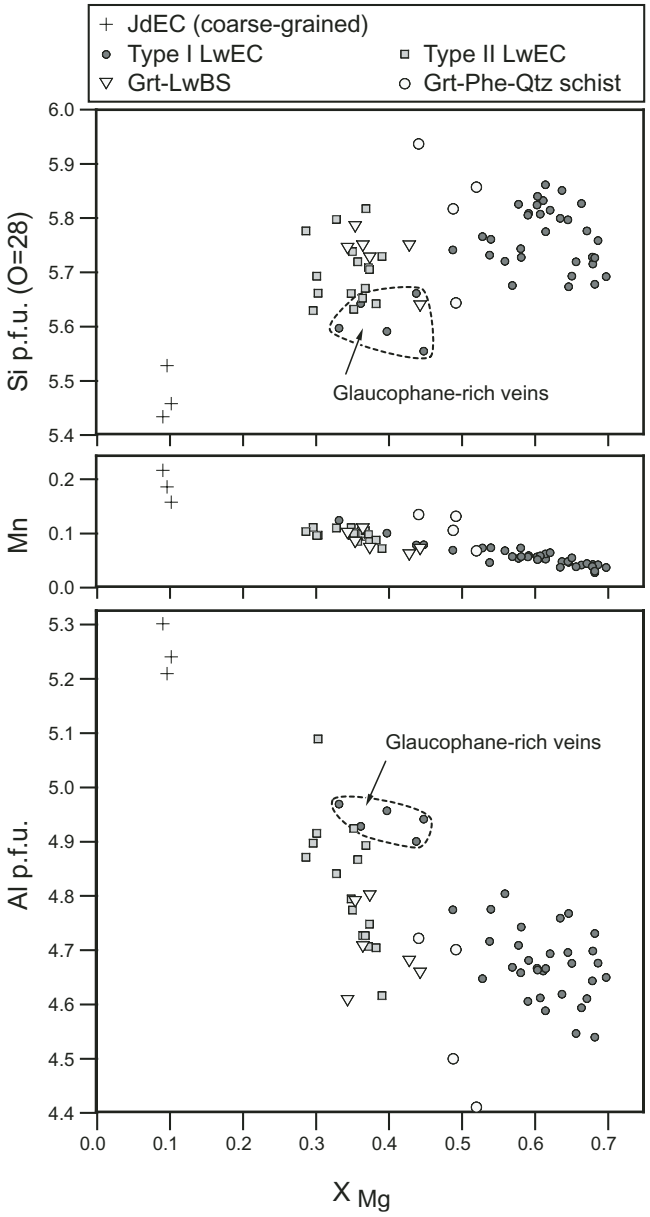

Figure 11. Compositional variations of chlorite in high-pressure rocks from Carrizal Grande. Grt-Qtz-Phe schist—garnet-bearing quartz–phengite schist; LwEC—lawsonite eclogite; Grt-LwBS—garnet-bearing lawsonite blueschist; JdEC—jadeite eclogite.

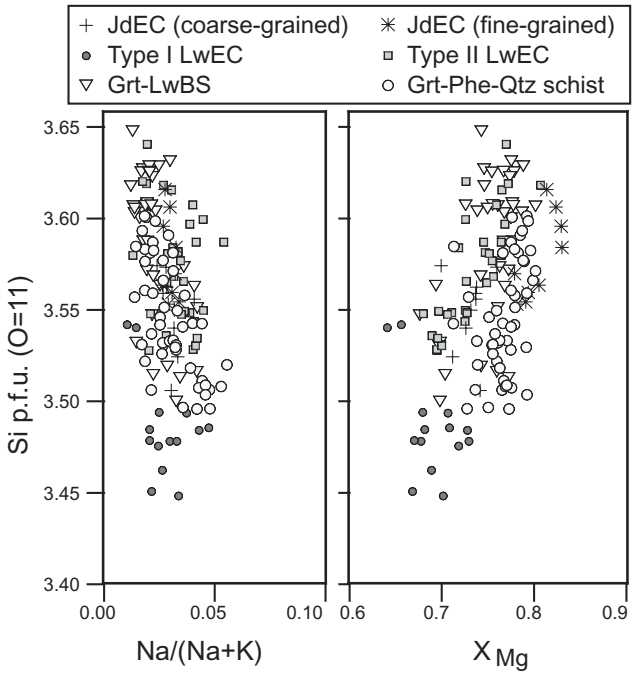

Figure 12. Compositional variations of phengite in high-pressure rocks from Carrizal Grande. Grt-Qtz-Phe schist—garnet-bearing quartz–phengite schist; LwEC—lawsonite eclogite; Grt-LwBS—garnet-bearing lawsonite blueschist; JdEC—jadeite eclogite.

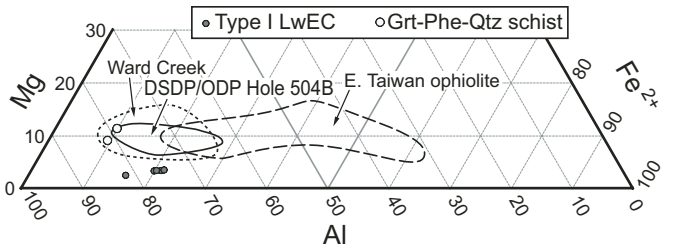

Figure 13. Compositional variations of pumpellyite in high-pressure rocks from Carrizal Grande. Compositional fields of pumpellyite from the Ward Creek blueschist (Maruyama and Liou, 1987), ocean-floor basalt of Deep Sea Drilling Project (DSDP)/Ocean Drilling Program (ODP) Hole 504B (Ishizuka, 1999), and East Taiwan ophiolite (Liou, 1979) are also shown. Grt-Qtz-Phe schist—garnet-bearing quartz–phengite schist; LwEC—lawsonite eclogite.

P-T CONDITIONS OF METAMORPHISM

The *P-T* conditions for each metamorphic stage can be constrained through the use of phase equilibria, thermobarometry, and petrogenetic grids. In this study, calculations to obtain phase equilibria were carried out using version 3.25 of THERMOCALC (Powell et al., 1998); the activities of mineral end members for calculations were obtained using the AX program of T.J.B. Holland (http://www.earthsci.unimelb.edu.au/tpg/thermocalc/). Characteristic features for each stage are described below.

Prograde Eclogite Stage

The prograde eclogite-facies assemblage is Grt + Omp (or Jd) + Lws + Chl + Rt + Qtz ± Ilm ± Fgl ± Phe in mafic rock types. As described in the preceding section, the X_{Mg} of garnet increases continuously from spessartine-rich cores to almandine-

rich rims. This implies a progressive increase in temperature during the growth of garnet by consumption of chlorite (e.g., Enami, 1998; Inui and Toriumi, 2004). Rutile and lawsonite are ubiquitous garnet inclusions in all rock types, and ilmenite occurs in the cores of some garnets in type I lawsonite eclogite. The lower temperature for garnet with lawsonite inclusions is limited by the equilibrium:

$$3\ \mathrm{Lws}\ [CaAl_2Si_2O_7(OH)_2{\cdot}H_2O] + 2\ \mathrm{Fe\text{-}Tlc} = 2\ \mathrm{Alm}\ [Fe_3Al_2Si_3O_{12}] + \mathrm{Grs}\ [Ca_3Al_2Si_3O_{12}] + 5\ \mathrm{Qtz}\ [SiO_2] + 8\ H_2O \quad (1)$$

(Okay, 2002).

The absence of talc suggests a minimum temperature around 290–300 °C for the core compositions of eclogitic garnets with S_1 or S_2 for this reaction (Fig. 14A). The presence of Lws + Rt + Ilm in the garnet core suggests that the metamorphic temperature is limited by the equilibria:

$$\mathrm{Lws}\ [CaAl_2Si_2O_7(OH)_2{\cdot}H_2O] + 2\ \mathrm{Ttn}\ [CaTiSiO_5] = \mathrm{Grs}\ [Ca_3Al_2Si_3O_{12}] + 2\ \mathrm{Rt}\ [TiO_2] + \mathrm{Qtz}\ [SiO_2] + 2\ H_2O \quad (2)$$

and

$$3\ \mathrm{Lws}\ [CaAl_2Si_2O_7(OH)_2{\cdot}H_2O] + 6\ \mathrm{Ilm}\ [FeTiO_3] + 3\ \mathrm{Qtz}\ [SiO_2] = 6\ \mathrm{Rt}\ [TiO_2] + 2\ \mathrm{Alm}\ [Fe_3Al_2Si_3O_{12}] + \mathrm{Grs}\ [Ca_3Al_2Si_3O_{12}] + 6\ H_2O. \quad (3)$$

This constraint indicates a metamorphic temperature of ~380–390 °C for the garnet core in coarse-grained jadeite eclogite (Fig. 14A). Moreover, the presence of Jd + Lws + Rt and the absence of paragonite in the jadeite eclogite constrain the pressure (P > 1.4 GPa at T = ~400 °C) with the reactions (Fig. 14A):

$$\mathrm{Jd} + 4\ \mathrm{Lws}\ [CaAl_2Si_2O_7(OH)_2{\cdot}H_2O] = 2\ \mathrm{Czo}\ [Ca_2Al_3Si_3O_{12}(OH)] + \mathrm{Pg}\ [Na_2Al_4(Si_6Al_2)O_{20}(OH)_4] + \mathrm{Qtz}\ [SiO_2] + 6\ H_2O \quad (4)$$

(Ghent et al., 1993), and

$$\mathrm{Jd} + \mathrm{Lws}\ [CaAl_2Si_2O_7(OH)_2{\cdot}H_2O] + \mathrm{Rt}\ [TiO_2] = \mathrm{Pg}\ [Na_2Al_4(Si_6Al_2)O_{20}(OH)_4] + \mathrm{Ttn}\ [CaAl_2Si_2O_7(OH)_2{\cdot}H_2O] + 2\ H_2O \quad (5)$$

(Okay, 2002).

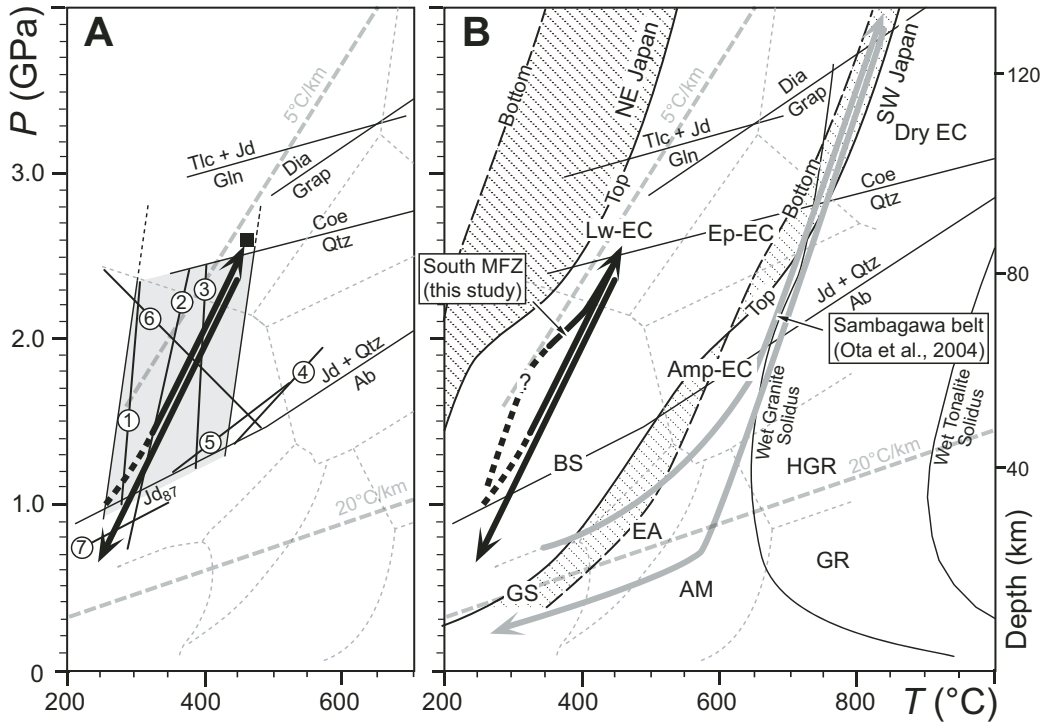

Figure 14. Qualitative pressure-temperature (P-T) path of lawsonite eclogite from Carrizal Grande. (A) Selected reaction curves to constrain metamorphic conditions. Numbered reactions are discussed in the text. Gray area represents the P-T field of the prograde eclogite stage constrained by the Jd + Qtz = Ab equilibria (Holland, 1983), and garnet-clinopyroxene thermometry (Krogh Ravna, 2000). (B) Comparisons of P-T path for Guatemalan lawsonite eclogite (this study) with the inferred P-T path of the highest-grade rocks of the Sanbagawa metamorphic belt (gray arrows: Ota et al., 2004) and P-T conditions for oceanic crust beneath present-day NE Japan (cold) and SW Japan (warm) subduction zones (hachured areas: Peacock and Wang, 1999). The metamorphic facies and their abbreviations are after Liou et al. (2004). MFZ—Motagua fault zone, EC—eclogite.

In coarse-grained lawsonite eclogite, the equilibrium

$$\begin{gathered}\text{Pg } [Na_2Al_4(Si_6Al_2)O_{20}(OH)_4] + \\ 2 \text{ Fgl } [Na_2Fe_3Al_2Si_8O_{22}(OH)_2] = \\ 6 \text{ Jd } [NaAlSi_2O_6] + 2 \text{ Alm } [Fe_3Al_2Si_3O_{12}] + \\ 4 \text{ Qtz } [SiO_2] + 4 \text{ } H_2O \text{ (Miyazaki et al., 1998)}\end{gathered} \quad (6)$$

further limits the minimum pressure to >1.6–2.0 GPa at temperature to ~350–450 °C for the Grt + Jd + Fgl assemblage (Tsujimori et al., 2005) (Fig. 14A). The Fe^{2+}-Mg distribution between omphacite and garnet also provides geothermobarometric information. The change in the Fe^{2+}-Mg distribution coefficient (K_D) between omphacite inclusions and adjacent garnet basically decreases from core to rim, suggesting heating during growth. The peak thermal condition was achieved at the highest X_{Mg} portion of the garnet rims within the lawsonite stability field (Figs. 5E and 7). A summary of the garnet-clinopyroxene thermometry at 2 GPa, applying the calibration of Krogh Ravna (2000), is shown in Figure 15: at P = 2.0 GPa, T = 290–490 °C (Fig. 14A). A relatively wide range of variations might be caused from the Fe^{2+}/Fe^{3+} estimation of omphacite and incomplete equilibrium between omphacite inclusions with adjacent garnet. Although the omphacite and garnet may not have achieved equilibrium at these low temperatures, the preservation of pumpellyite in lawsonite supports this low-T interpretation (e.g., Schiffman and Liou, 1980, 1983). Garnet-clinopyroxene-phengite thermobarometry (Krogh Ravna and Terry, 2004) of composite mineral inclusions in garnet rims near the highest X_{Mg} portion in the coarse-grained jadeite eclogite, and of matrix pairs in fine-grained jadeite eclogite, yields a maximum P = ~2.4–2.6 at T = ~480 °C (Fig. 14A). Therefore, it is likely that eclogitization initiated at T = ~300 °C and P > 1.1 GPa, and continued to T = ~480 °C and P = ~2.6 GPa.

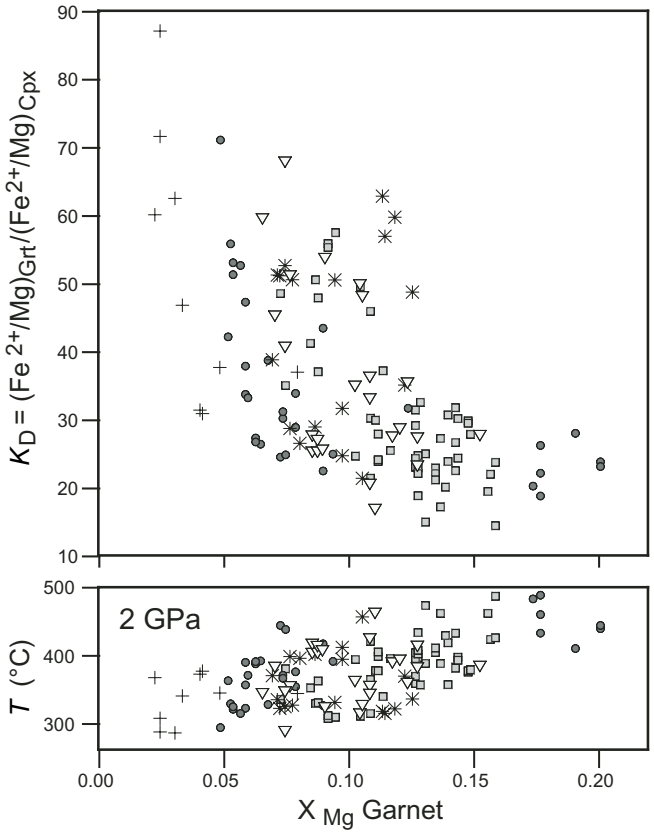

Figure 15. Relationships between X_{Mg} of garnet and K_D of garnet (Grt) + coexisting clinopyroxene (Cpx) inclusions and temperature at P = 2 GPa. Temperature was calculated using the garnet-clinopyroxene thermobarometer of Krogh Ravna (2000).

Retrograde Eclogite Stage

Folding of the pre-existing S_2 foliation and formation of the S_3 foliation accompanied the retrograde eclogite stage. The mineral assemblage is best preserved in type II lawsonite eclogite and garnet-bearing lawsonite blueschist, and has reversely zoned garnet rims and Omp ± Gln + Lws + Rt + Qtz ± Phe within S_3; these glaucophanes and lawsonites contain rutile inclusions. Garnet-clinopyroxene-phengite thermobarometry (Krogh Ravna and Terry, 2004) yields P = ~1.8 GPa and T = ~400 °C (Fig. 14A). It may be improbable that garnet grew during retrogression at such low T, however, retrograde garnet growth with a distinct X_{Mg} drop at the outermost rims has been described from eastern Alpine (Hoschek, 2001) and Sanbagawa eclogites (Ota et al., 2004). In a simplified Al_2O_3-CaO-MgO system with five phases (Lws, Chl, Prp, Grs, and Di) and excess Qtz and H_2O, the phase rule specifies a single invariant point and five univariant curves. Among these curves, a garnet-forming reaction within the stability field of Di + Grt (Prp +Grs):

$$\begin{gathered}3 \text{ Lws } [CaAl_2Si_2O_7(OH)_2 \cdot H_2O] + 3 \text{ Di } [CaMgSi_2O_6] = \\ 2 \text{ Grs } [Ca_3Al_2Si_3O_{12}] + \text{Prp } [Fe_3Al_2Si_3O_{12}] + \\ 3 \text{ Qtz } [SiO_2] + 6 \text{ } H_2O\end{gathered} \quad (7)$$

has a positive dP/dT slope of ~0.2 GPa/100 °C for garnet ($prp_{10}grs_{25}$) and omphacite (di_{35}). Therefore minor retrograde garnet overgrowth may be explained by this reaction.

Blueschist Stage

The late blueschist-facies assemblage is Gln + Lws + Chl + Phe + Ttn + Qtz ± Ab. No Fe-Mg exchange geothermobarometer is applicable to the observed mineral assemblage, however, this paragenesis suggests T < 300 °C (e.g., Maruyama and Liou, 1988; Evans, 1990. In coarse-grained jadeite eclogite, the retrograde assemblage Jd-II ± Omp + Ttn + Chl + Qtz ± Ab may represent this same stage. The simultaneous growth of two clinopyroxenes with a wide compositional gap and the Jd + Qtz = Ab sliding equilibrium (equation 7) (Holland, 1983) suggest approximate P-T conditions of P = ~0.7 GPa and T <~300 °C (Tsujimori et al., 2005) (Fig. 14A).

DISCUSSION

P-T-D Paths of Subduction and Exhumation

Detailed petrologic and microstructural examination of various high-pressure rock types in the Carrizal Grande area constrains the *P-T*-deformation (D) history during the subduction and exhumation of the eclogitized oceanic crust. As described herein, there are four deformational stages: D_1, D_2, D_3, and D_4; D_3 was the dominant stage.

The D_1–D_2 stages correspond to prograde eclogite stages, and D_3 represents a retrograde eclogite stage. The *P-T* constraints suggest that eclogitization during the D_1–D_2 stage initiated at T = ~300 °C and P > 1.1 GPa and continued to T = ~480 °C and P = ~2.6 GPa (Fig. 14). This prograde eclogitization was accompanied by ductile to partly brittle deformation.

In contrast, the D_3 stage, with P = ~1.8 GPa and T = ~400 °C, postdates the thermal maximum, because S_3 minerals are texturally in equilibrium with reversely zoned garnet rims that lack the S_2 fabric.

Furthermore, hydration and blueschist-facies recrystallization at shallower levels occurred in the high-pressure rocks of the Carrizal Grande area; the breakdown of rutile is critical to defining this later stage. The development of the blueschist-facies hydration was heterogeneous, limited by fluid introduction, seen as irregular-shaped glaucophane-rich hydrous veins. However, it appears to have been coeval with the minor but ubiquitous D_4 deformation defined by open folds, crenulations, and shear. The D_4 deformation may have affected the serpentinite associated with the high-pressure rocks. Metasomatic rocks, such as jadeitite, omphacitite, lawsonite-jadeite rock, and omphacite-glaucophane rock, are closely associated with the serpentinite and high-pressure rocks (e.g., Harlow, 1994; Harlow et al., 2003; Harlow and Sorensen, 2005). The available petrologic information for these metasomatic rocks suggests that they were synchronous with the blueschist-facies stage and accompanying D_4 deformation. Formation of the serpentinite mélange then postdated D_4.

As shown in Figure 14B, the inferred *P-T* trajectory lies near a geotherm of ~5 °C km^{-1}, i.e., near the "forbidden zone" of Liou et al. (2000), and shows a characteristic hairpin-like path. Such a *P-T* path suggests that the rocks were refrigerated during exhumation such that no greenschist- or amphibolite-facies recrystallization took place. The eclogitized oceanic crust was thus most likely exhumed up a subduction channel, and then trapped in serpentinite at shallow levels (<40 km), where the lawsonite blueschist developed.

Eclogitization in a Cold Subduction Zone

According to the calculated steady-state thermal structure of subduction zones (e.g., Peacock and Wang, 1999; Peacock, 2001), phase relationships in the MORB + H_2O system (e.g., Kerrick and Connolly, 2001; Hacker et al., 2003a, 2003b), and high-pressure experiments of the MORB + H_2O system (e.g., Schmidt and Poli, 1998; Okamoto and Maruyama, 1999; Spandler et al., 2003), the eclogitization of oceanic crust within Pacific-type subduction zones is likely to take place in the lawsonite stability field. Although the occurrence of lawsonite eclogite in orogenic belts is extremely rare (Tsujimori et al., 2006), the discovery of coesite-bearing lawsonite eclogite xenoliths on the Colorado Plateau (Usui et al., 2003) supports the hypothesis of lawsonite eclogite formation in Pacific-type subduction zones.

What are the implications of lawsonite eclogitization in cold subduction zones? Lawsonite can accommodate up to 11.5 wt% H_2O plus Sr, rare earth elements (REEs), and Pb, and is stable in cold subduction zones to at least 300 km depth (e.g., Schmidt, 1995; Pawley, 1994; Okamoto and Maruyama, 1999). Consequently, the dehydration of lawsonite likely plays an important role in the generation of arc magmatism, slab seismicity, and the recycling of volatiles and high field strength elements into mantle (Schmidt and Poli, 1998; Kerrick and Connolly, 2001; Connolly and Kerrick, 2002; Hacker et al., 2003a, 2003b; Spandler et al., 2003; Rüpke et al., 2004). Intermediate-depth earthquakes (50–300 km in depth) may be triggered by dehydration of the descending oceanic plate (Kirby et al., 1996; Helffrich, 1996; Peacock and Wang, 1999; Peacock and Hyndman, 1999; Peacock, 2001; Dobson et al., 2002; Omori et al., 2002; Hacker et al., 2003a, 2003b; Yamasaki and Seno, 2003).

How do the petrologic observations of this study fit with the calculated thermal and petrologic structure of cold subduction zones? For example, the thermal structure of the NE Japan subduction zone (Peacock and Wang, 1999; Hacker et al., 2003b) is shown in Figure 16. Present-day NE Japan is a cold subduction zone where the 130 Ma Pacific plate is subducting beneath the Eurasian plate at 91 mm/yr (Peacock and Wang, 1999). Figure 16 shows that the inferred prograde *P-T* trajectory of the Guatemalan lawsonite eclogite is slightly hotter than the calculated *P-T* conditions of the oceanic crust beneath NE Japan (Peacock and Wang, 1999). However, our *P-T* estimates for the initiation of eclogitization (T = ~300 °C and P > 1.1 GPa) and metamorphic peak (T = ~480 °C and P = ~2.6 GPa) are nearly consistent with the thermal structure of Peacock and Wang (1999) (Fig. 16). Our inferred prograde *P-T* path lies within the jadeite–lawsonite blueschist and lawsonite–amphibole eclogite fields of Hacker et al. (2003b) (Fig. 16). Zhang et al. (2004) reported high Vp/Vs ratios (~1.79–1.81) within the oceanic crust at 60–100 km depth beneath NE Japan, and interpreted this as a mixture of blueschist and eclogite.

What are the realistic dehydration reactions producing earthquakes within the slab crust? The experimental study by Okamoto and Maruyama (1999) showed a continuous lawsonite-consuming dehydration reaction within the lawsonite eclogite field. If lawsonite breakdown occurs, the grossular component in the crystallizing garnet should increase; in fact lawsonite

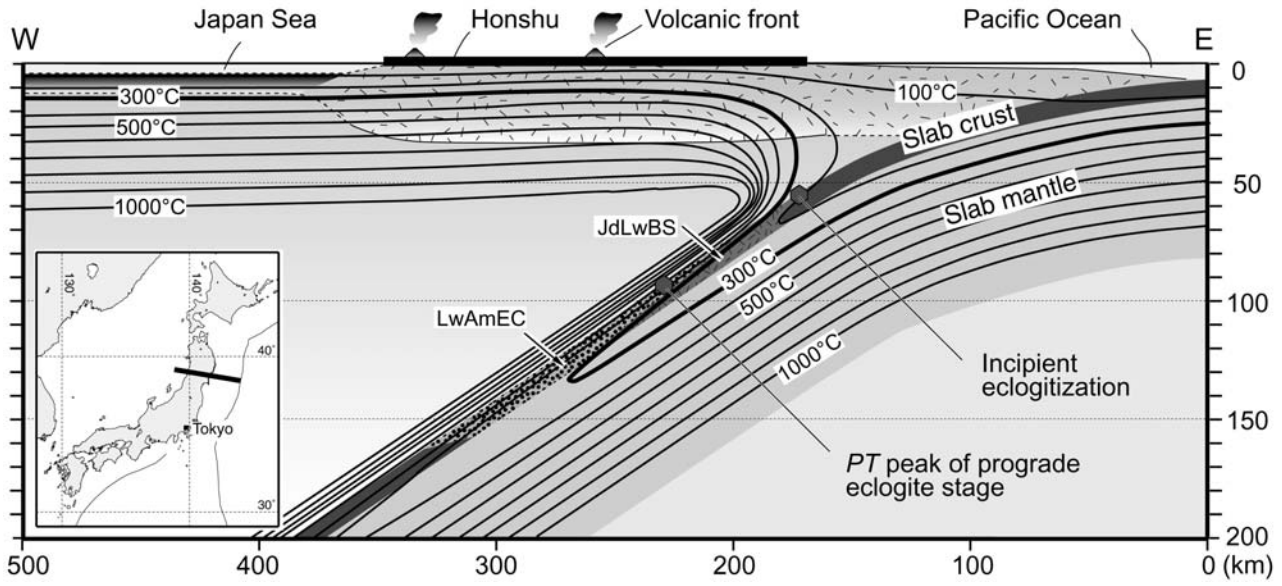

Figure 16. Thermal structure of the NE Japan subduction zone (Peacock and Wang, 1999; Hacker et al., 2003b) is similar to the prograde pressure-temperature (*P-T*) trajectory for Guatemalan lawsonite eclogite. The areas marked JdLwBS and LwAmEC represent jadeite lawsonite blueschist and lawsonite amphibole eclogite fields of Hacker et al. (2003a, 2003b). Isotherm contour interval is 100 °C.

eclogite xenoliths from the Colorado Plateau show this change (Helmstaedt and Schulze, 1988; Usui et al., 2003). In the Guatemalan lawsonite eclogites, the grossular component is essentially constant or decreases slightly from core to rim (Fig. 7). This indicates that the chlorite-consuming reactions to form almandine-pyrope-spessartine garnet were more effective than the lawsonite-consuming reaction to form the grossular component. At ~100 km depth in cold subduction zones, dehydration-induced seismicity may be caused by these chlorite-consuming reactions.

ACKNOWLEDGMENTS

This research was supported by the Japanese Society for the Promotion of Science through Research Fellowship for Research Abroad of the first author (Tsujimori). The authors acknowledge support by the National Science Foundation through grants EAR-0003355 and EAR-0510325 (Liou), EAR-0309320 (Harlow and Sorensen), and EAR-0309321 (Sisson). Tsujimori thanks Robert Coleman, William Rohtert, John Cleary, and Pieter Lee for their guidance during a field trip to Guatemala. We also thank Dick Mandell for alerting us to the presence of abundant eclogite uncovered by Hurricane Mitch. Thomas Zack, John Goodge, Roberto Compagnoni, and Bradley Hacker critically reviewed this manuscript.

REFERENCES CITED

Abbott, R.N., Draper, G., and Keshav, S., 2005, UHP magma paragenesis, garnet peridotite, and garnet clinopyroxenite: An example from the Dominican Republic: International Geology Review, v. 47, p. 233–247.

Altherr, R., Topuz, G., Marschall, H., Zack, T., and Ludwig, T., 2004, Evolution of a tourmaline-bearing lawsonite-eclogite from the Elekdag area (central Pontides, N Turkey): Evidence for infiltration of slab-derived B-rich fluids during exhumation: Contributions to Mineralogy and Petrology, v. 148, p. 409–425.

Armstrong, J.T., 1988, Quantitative analysis of silicate and oxide minerals: Comparison of Monte Carlo, ZAF and Phi-Rho-Z procedures, *in* Newbury, D.E., ed., Analysis microbeam: San Francisco, California, San Francisco Press, p. 239–246.

Beccaluva, L., Bellia, S., Coltorti, M., Dengo, G., Giunta, G., Mendez, J., Romero, J., Rotolo, S., and Siena, F., 1995, The northwestern border of the Caribbean plate in Guatemala: New geological and petrological data on the Motagua ophiolitic belt: Ofioliti, v. 20, p. 1–15.

Caron, J.-M., and Péquignot, G., 1986, The transition between blueschists and lawsonite-bearing eclogites based on observations from Corsican metabasites: Lithos, v. 19, p. 205–218, doi: 10.1016/0024-4937(86)90023-X.

Caron, J.-M., Kiénast, J.-R., and Triboulet, C., 1981, High-pressure/low-temperature metamorphism and polyphase Alpine deformation at Sant'Andrea di Cotone (eastern Corsica, France): Tectonophysics, v. 78, p. 419–451, doi: 10.1016/0040-1951(81)90023-8.

Clarke, G.L., Atchison, J.C., and Cluzel, D., 1997, Eclogites and blueschists of the Pam Peninsula, NE New Caledonia: A reappraisal: Journal of Petrology, p. 38, p. 843–876.

Connolly, J.A.D., and Kerrick, D.M., 2002, Metamorphic controls on seismic velocity of subducted oceanic crust at 100–250 km depth: Earth and Planetary Science Letters, v. 204, p. 61–74, doi: 10.1016/S0012-821X(02)00957-3.

Dobson, D.P., Meredith, P.G., and Boon, S.A., 2002, Simulation of subduction zone seismicity by dehydration of serpentinite: Science, v. 298, p. 1407–1410, doi: 10.1126/science.1075390.

Draper, G., 1986, Blueschists and associated rocks in eastern Jamaica and their significance for Cretaceous plate-margin development in the northern Caribbean: Geological Society of America Bulletin, v. 97, p. 48–60, doi: 10.1130/0016-7606(1986)97<48:BAARIE>2.0.CO;2.

Enami, M., 1998, Pressure-temperature path of Sanbagawa prograde metamorphism deduced from grossular zoning of garnet: Journal of Metamorphic Geology, v. 16, p. 97–106, doi: 10.1111/j.1525-1314.1998.00058.x.

Evans, B.W., 1990, Phase relations of epidote-blueschists: Lithos, v. 25, p. 3–23, doi: 10.1016/0024-4937(90)90003-J.

Francis, A.H., 2005, Deformation history of the Maya and Chortís blocks: Insight to the evolution of the Motagua fault zone, Guatemala [M.S. thesis]: Houston, Rice University, 149 p.

Francis, A.H., Avé Lallemant, H.G., and Sisson, V.B., 2005, Tectonic history of two disparate high-pressure, low-temperature metamorphic belts along the Motagua fault zone, Guatemala: Geological Society of America Abstracts with Programs, v. 37, no. 3, p. 5.

Ghent, E.D., Stout, M.Z., and Erdmer, P., 1993, Pressure-temperature evolution of lawsonite-bearing eclogites, Pinchi Lake, British Columbia: Journal of Metamorphic Geology, v. 11, p. 279–290.

Giaramita, M.J., and Sorensen, S.S., 1994, Primary fluids in low-temperature eclogites: Evidence from two subduction complexes (Dominican Republic, and California, USA): Contributions to Mineralogy and Petrology, v. 117, p. 279–292, doi: 10.1007/BF00310869.

Gonçalves, P., Guillot, S., Lardeaux, J.M., Nicollet, C., and Mercier de Lepinay, B., 2000, Thrusting and sinistral wrenching in a pre-Eocene HP-LT Caribbean accretionary wedge (Samana Peninsula, Dominican Republic): Geodinamica Acta, v. 13, p. 119–132, doi: 10.1016/S0985-3111(00)00116-9.

Green, D.H., Lockwood, J.P., and Kiss, E., 1968, Eclogite and almandine-jadeite-quartz rock from the Guajira Peninsula, Colombia, South America: The American Mineralogist, v. 53, p. 1320–1335.

Hacker, B.R., Abers, G.A., and Peacock, S.M., 2003a, Subduction factory 1. Theoretical mineralogy, densities, seismic wave speeds, and H_2O contents: Journal of Geophysical Research, v. 108, no. 2029, doi: 10.1029/2001JB001127.

Hacker, B.R., Peacock, S.M., Abers, G.A., and Holloway, S., 2003b, Subduction factory 2. Intermediate-depth earthquakes in subducting slabs are linked to metamorphic dehydration reactions: Journal of Geophysical Research, v. 108, 2030, doi: 10.1029/2001JB001129.

Harlow, G.E., 1994, Jadeitites, albitites and related rocks from the Motagua fault zone, Guatemala: Journal of Metamorphic Geology, v. 12, p. 49–68.

Harlow, G.E., 1999, Interpretation of Kcpx and CaEs components in clinopyroxene from diamond inclusions and mantle samples, *in* Gurney, J.J., Gurney, J.L., Pascoe, M.D., and Richardson, S.H., eds., Proceedings of Seventh International Kimberlite Convention: Cape Town, Redroof Design Company, vol. I, p. 321–331.

Harlow, G.E., and Sorensen, S.S., 2005, Jade (nephrite and jadeitite) and serpentinite: Metasomatic connections: International Geology Review, v. 47, p. 113–146.

Harlow, G.E., Sisson, V.B., Avé Lallemant, H.G., Sorensen, S.S., and Seitz, R., 2003, High-pressure, metasomatic rocks along the Motagua fault zone, Guatemala: Ofioliti, v. 28, p. 115–120.

Harlow, G.E., Hemming, S.R., Avé Lallemant, H.G., Sisson, V.B., and Sorensen, S.S., 2004, Two high-pressure–low-temperature serpentinite-matrix mélange belts, Motagua fault zone, Guatemala: A record of Aptian and Maastrichtian collisions: Geology, v. 32, p. 17–20, doi: 10.1130/G19990.1.

Helffrich, G., 1996, Subducted lithospheric slab velocity structure: Observations and mineralogical inferences, *in* Bebout, G.E., Scholl, D., Kirby, S., and Platt, J.P., eds., Subduction: Top to bottom: American Geophysical Union Geophysical Monograph 96, p. 215–222.

Helmstaedt, H., and Schulze, D.J., 1988, Eclogite-facies ultramafic xenoliths from Colorado Plateau diatreme breccias: Comparison with eclogites in crystal environments, evaluation of the subduction hypothesis, and implications for eclogite xenoliths from diamondiferous kimberlites, *in* Smith, D.C., ed., Eclogite and eclogite facies rocks: New York, Elsevier Science, p. 387–450.

Hirajima, T., Banno, S., Hiroi, Y., and Ohta, Y., 1988, Phase petrology of eclogites and related rocks from the Motalafjella high-pressure metamorphic complex in Spitsbergen and its significance: Lithos, v. 22, p. 75–97, doi: 10.1016/0024-4937(88)90018-7.

Holland, T.J.B., 1983, The experimental determination of activities in disordered and short-range ordered jadeitic pyroxenes: Contributions to Mineralogy and Petrology, v. 82, p. 214–220, doi: 10.1007/BF01166616.

Hoschek, G., 2001, Thermobarometry of metasediments and metabasites from the eclogite zone of the Hohe Tauern, eastern Alps, Austria: Lithos, v. 59, p. 127–150, doi: 10.1016/S0024-4937(01)00063-9.

Inui, M., and Toriumi, M., 2004, A theoretical study on the formation of growth zoning in garnet consuming chlorite: Journal of Petrology, v. 45, p. 1369–1392, doi: 10.1093/petrology/egh016.

Ishizuka, H., 1999, Pumpellyite from the oceanic crust, DSDP/ODP Hole 504B: Mineralogical Magazine, v. 63, p. 891–900, doi: 10.1180/002646199548998.

Kerrick, D.M., and Connolly, J.A.D., 2001, Metamorphic devolatilization of subducted oceanic metabasites: Implications for seismicity, arc magmatism and volatile recycling: Earth and Planetary Science Letters, v. 189, p. 19–29, doi: 10.1016/S0012-821X(01)00347-8.

Kirby, S.H., Stein, S., Okal, E.O., and Rubie, D.C., 1996, Metastable mantle phase transformations and deep earthquakes in subducting oceanic lithosphere: Reviews of Geophysics, v. 34, p. 261–306, doi: 10.1029/96RG01050.

Kretz, R., 1983, Symbols for rock-forming minerals: The American Mineralogist, v. 68, p. 277–279.

Krogh Ravna, E., 2000, The garnet-clinopyroxene Fe^{2+}-Mg geothermometer: An updated calibration: Journal of Metamorphic Geology, v. 18, p. 211–219, doi: 10.1046/j.1525-1314.2000.00247.x.

Krogh Ravna, E., and Terry, M.P., 2004, Geothermobarometry of UHP and HP eclogites and schists—An evaluation of equilibria among garnet-clinopyroxene-kyanite-phengite-coesite/quartz: Journal of Metamorphic Geology, v. 22, p. 579–592.

Liou, J.G., 1979, Zeolite facies metamorphism of basaltic rocks from the East Taiwan ophiolite: The American Mineralogist, v. 64, p. 1–14.

Liou, J.G., Hacker, B.R., and Zhang, R.Y., 2000, Into the forbidden zone: Science, v. 287, p. 1215–1216, doi: 10.1126/science.287.5456.1215.

Liou, J.G., Tsujimori, T., Zhang, R.Y., Katayama, I., and Maruyama, S., 2004, Global UHP metamorphism and continental subduction/collision: The Himalayan model: International Geology Review, v. 46, p. 1–27.

Maruyama, S., and Liou, J.G., 1988, Petrology of Franciscan metabasites along the jadeite-glaucophane type facies series, Cazadero, California: Journal of Petrology, v. 29, p. 1–37.

Maruyama, S., and Liou, J.G., 2005, From snowball to Phanerozoic Earth: International Geology Review, v. 47, p. 775–791.

McBirney, A., Aoki, K., and Bass, M.N., 1967, Eclogites and jadeite from the Motagua fault zone, Guatemala: The American Mineralogist, v. 52, p. 908–918.

Miyazaki, K., Sopaheluwakan, J., Zulkarnain, I., and Wakita, K., 1998, A jadeite-quartz-glaucophane rock from Karangsambung, central Java, Indonesia: The Island Arc, v. 7, p. 223–230, doi: 10.1046/j.1440-1738.1998.00164.x.

Och, D.J., Leitch, E.C., Caprarelli, G., and Watanabe, T., 2003, Blueschist and eclogite in tectonic mélange, Port Macquarie, New South Wales, Australia: Mineralogical Magazine, v. 67, p. 609–624, doi: 10.1180/0026461036740121.

Oh, C.W., Liou, J.G., and Maruyama, S., 1991, Low-temperature eclogites and eclogitic schists in Mn-rich metabasites in Ward Creek, California; Mn and Fe effects on the transition between blueschist and eclogite: Journal of Petrology, v. 32, p. 275–301.

Okamoto, K., and Maruyama, S., 1999, The high-pressure synthesis of lawsonite in the MORB + H_2O system: The American Mineralogist, v. 84, p. 362–373.

Okay, A.I., 2002, Jadeite-chloritoid-glaucophane-lawsonite blueschists in northwest Turkey: Unusually high *P*/*T* ratios in continental crust: Journal of Metamorphic Geology, v. 20, p. 757–768, doi: 10.1046/j.1525-1314.2002.00402.x.

Omori, S., Kamiya, S., Maruyama, S., and Zhao, D., 2002, Morphology of the intraslab seismic zone and devolatilization phase equilibria of the subducting slab peridotite: Earthquake Research Institute Bulletin, v. 76, p. 455–478.

Ortega-Gutiérrez, F., Solari, L.A., Solé, J., Martens, U., Gómez-Tuena, A., Morán-Ical, S., Reyes-Salas, M., and Ortega-Obregón, C., 2004, Polyphase, high-temperature eclogite-facies metamorphism in the

Chuacús Complex, central Guatemala: Petrology, geochronology, and tectonic implications: International Geology Review, v. 46, p. 445–470.

Ota, T., Terabayashi, M., and Katayama, I., 2004, Thermobaric structure and metamorphic evolution of the Iratsu eclogite body in the Sanbagawa belt, central Shikoku, Japan: Lithos, v. 73, p. 95–126, doi: 10.1016/j.lithos.2004.01.001.

Parkinson, C.D., Miyazaki, K., Wakita, K., Barber, A.J., and Carswell, D.A., 1998, An overview and tectonic synthesis of the pre-Tertiary very-high-pressure metamorphic and associated rocks of Java, Sulawesi, and Kalimantan, Indonesia: The Island Arc, v. 7, p. 184–200, doi: 10.1046/j.1440-1738.1998.00184.x.

Pawley, A.R., 1994, The pressure and temperature stability limits of lawsonite: Implications for H_2O recycling in subduction zones: Contributions to Mineralogy and Petrology, v. 118, p. 99–108, doi: 10.1007/BF00310614.

Pawley, A.R., Redfern, S.A.T., and Holland, T.J.B., 1996, Volume behavior of hydrous minerals at high pressure and temperature: I. Thermal expansion of lawsonite, zoisite, clinozoisite, and diaspore: The American Mineralogist, v. 81, p. 335–340.

Peacock, S.M., 2001, Are the lower planes of double seismic zones caused by serpentine dehydration in subducting oceanic mantle?: Geology, v. 29, p. 299–302, doi: 10.1130/0091-7613(2001)029<0299:ATLPOD>2.0.CO;2.

Peacock, S.M., and Hyndman, R.D., 1999, Hydrous minerals in the mantle wedge and the maximum depth of subduction thrust earthquakes: Geophysical Research Letters, v. 26, p. 2517–2520.

Peacock, S.M., and Wang, K., 1999, Seismic consequences of warm versus cool subduction metamorphism: Examples from southwest and northeast Japan: Nature, v. 286, p. 937–939.

Poli, S., and Schmidt, M.W., 1995, Water transport and release in subduction zones: Experimental constraints on basaltic and andesitic systems: Journal of Geophysical Research, v. 100, p. 22,299–22,314, doi: 10.1029/95JB01570.

Powell, R., Holland, T.J.B., and Worley, B., 1998, Calculating phase diagrams involving solid solutions via non-linear equations, with examples using THERMOCALC: Journal of Metamorphic Geology, v. 16, p. 577–588.

Rumble, D., Liou, J.G., and Jahn, B.M., 2003, Continental crust subduction and ultrahigh-pressure metamorphism, *in* Rudnick R.L., ed., The crust, Volume 3, Treatise on geochemistry (Holland, H.D., and Turekian, K.K., eds.): Oxford, Elsevier, p. 293–319.

Rüpke, L.H., Morgan, J.P., Hort, M., and Connolly, J.A.D., 2004, Serpentine and the subduction zone water cycle: Earth and Planetary Science Letters, v. 223, p. 17–34, doi: 10.1016/j.epsl.2004.04.018.

Schiffman, P., and Liou, J.G., 1980, Synthesis and stability relations of Mg-Al pumpellyite, $Ca_4Al_5MgSi_6O_{21}(OH)_7$: Journal of Petrology, v. 21, p. 441–474.

Schiffman, P., and Liou, J.G., 1983, Synthesis of Fe-pumpellyite and its stability relations with epidote: Journal of Metamorphic Geology, v. 1, p. 91–101.

Schmidt, M.W., 1995, Lawsonite: Upper pressure stability and formation of higher density hydrous phases: The American Mineralogist, v. 80, p. 1286–1292.

Schmidt, M.W., and Poli, S., 1998, Experimentally based water budgets for dehydrating slabs and consequences for arc magma generation: Earth and Planetary Science Letters, v. 163, p. 361–379, doi: 10.1016/S0012-821X(98)00142-3.

Schneider, J., Bosch, D., Monie, P., Guillot, S., Carcía-Casco, A., Lardeaux, J.M., Torres-Roldán, L., and Trujillo, G.M., 2004, Origin and evolution of the Escambray Massif (central Cuba): An example of HP/LT rocks exhumed during intraoceanic subduction: Journal of Metamorphic Geology, v. 22, p. 227–247, doi: 10.1111/j.1525-1314.2004.00510.x.

Shibakusa, H., and Maekawa, H., 1997, Lawsonite-bearing eclogitic metabasites in the Cazadero area, northern California: Mineralogy and Petrology, v. 61, p. 163–180, doi: 10.1007/BF01172482.

Sisson, V.B., Ertan, I.E., and Avé Lallemant, H.G., 1997, High pressure (~200 MPa) kyanite- and glaucophane-bearing schist and eclogite from the Cordillera de la Cost belt, Venezuela: Journal of Petrology, v. 38, p. 65–83, doi: 10.1093/petrology/38.1.65.

Sisson, V.B., Harlow, G.E., Sorensen, S.S., Brueckner, H.K., Sahm, E., Hemming, S., and Avé Lallemant, H.G., 2003, Lawsonite eclogite and other high-pressure assemblages in the southern Motagua fault zone, Guatemala: Implications for Chortís collision and subduction zones: Geological Society of America Abstracts with Programs, v. 35, no. 6, p. 639.

Sisson, V.B., Avé Lallemant, H.G., Ostos, M., Blythe, A.E., Snee, L.W., Copeland, P., Wright, J.E., Donelick, R.A., and Guth, L.R., 2005, Overview of radiometric ages in three allochthonous belts of northern Venezuela: Old ones, new ones, and their impact on regional geology, *in* Avé Lallemant, H.G., and Sisson, V.B., eds., Caribbean/South American plate interactions: Geological Society of America Special Paper 394, p. 91–117.

Smith, C.A., Sisson, V.B., Avé Lallemant, H.G., and Copeland, P., 1999, Two contrasting pressure-temperature-time paths in the Villa de Cura blueschist belt, Venezuela: Possible evidence for Late Cretaceous initiation of subduction in the Caribbean: Geological Society of America Bulletin, v. 111, p. 831–848, doi: 10.1130/0016-7606(1999)111<0831:TCPTTP>2.3.CO;2.

Smith, D.C., and Gendron, F., 1997, New locality and a new kind of jadeite jade from Guatemala; rutile-quartz-jadeitite: Fifth International Eclogite Conference: Terra Nova, Abstract supplement, no. 1, v. 9, p. 35.

Somin, M.L., Arakelyants, M.M., and Kolesnikov, E.M., 1992, Age and tectonic significance of high-pressure metamorphic rocks of Cuba: International Geology Review, v. 34, p. 105–118.

Sorensen, S.S., Grossman, J.N., and Perfit, M.R., 1997, Phengite-hosted LILE enrichment in eclogite and related rocks: Implications for fluid mediated mass transfer in subduction zones and arc magma genesis: Journal of Petrology, v. 38, p. 3–34.

Sorensen, S.S., Sisson, V.B., and Avé Lallemant, H.G., 2005, Geochemical evidence for possible trench provenance and fluid-rock histories, Cordillera de la Costa eclogite belt, Venezuela, *in* Avé Lallemant, H.G., and Sisson, V.B., eds., Caribbean/South American plate interactions: Geological Society of America Special Paper 394. p. 173–192.

Spandler, C., Hermann, J., Arculus, R., and Mavrogenes, J.A., 2003, Redistribution of trace elements during prograde metamorphism from lawsonite blueschist to eclogite facies; implications for deep subduction-zone processes: Contributions to Mineralogy and Petrology, v. 146, p. 205–222, doi: 10.1007/s00410-003-0495-5.

Stöckhert, B., Maresch, W.V., Brix, M., Kaiser, C., Toetz, A., Kluge, R., and Krückhans-Lueder, G., 1995, Crustal history of Margarita Island (Venezuela) in detail: Constraint on the Caribbean plate-tectonic scenario: Geology, v. 23, p. 787–790.

Tsujimori, T., Liou, J.G., and Coleman, R.G., 2005, Coexisting retrograde jadeite and omphacite in a jadeite-bearing lawsonite eclogite from the Motagua fault zone, Guatemala: The American Mineralogist, v. 90, p. 836–842, doi: 10.2138/am.2005.1699.

Tsujimori, T., Sisson, V.B., Liou, J.G., Harlow, G.E., and Sorensen, S.S., 2006, Very low-temperature record in subduction process: a Review of worldwide lawsonite eclogites: Lithos (in press).

Unger, L.S., Sisson, V.B., and Avé Lallemant, H.G., 2005, Tectonic setting of the Villa de Cura blueschists, Venezuela, based on major, minor, and trace elements, *in* Avé Lallemant, H.G., and Sisson, V.B., eds., Caribbean/South American plate interactions: Geological Society of America Special Paper 394, p. 233–249.

Usui, T., Nakamura, E., Kobayashi, K., and Maruyama, S., 2003, Fate of the subducted Farallon plate inferred from eclogite xenoliths in the Colorado Plateau: Geology, v. 31, p. 589–592, doi: 10.1130/0091-7613(2003)031<0589:FOTSFP>2.0.CO;2.

Watson, K.D., and Morton, D.M., 1969, Eclogite inclusions in kimberlite pipes at Garnet Ridge, northeastern Arizona: The American Mineralogist, v. 54, p. 267–285.

Yamasaki, T., and Seno, T., 2003. Double seismic zone and dehydration embrittlement of the subducting slab: Journal of Geophysical Research, v. 108, 2212, doi: 10.1029/2002JB001918.

Zack, T., Rivers, T., Brumm, R., and Kronz, A., 2004, Cold subduction of oceanic crust: Implications from a lawsonite eclogite from the Dominican Republic: European Journal of Mineralogy, v. 16, p. 909–916, doi: 10.1127/0935-1221/2004/0016-0909.

Zhang, H., Thurber, C.H., Shelly, D., Ide, S., Beroza, G.C., and Hasegawa, A., 2004, High-resolution subducting slab structure beneath northern Honshu, Japan, revealed by double-difference tomography: Geology, v. 32, p. 361–364, doi: 10.1130/G20261.2.

MANUSCRIPT ACCEPTED BY THE SOCIETY 21 SEPTEMBER 2005

Printed in the USA

Geological Society of America
Special Paper 403
2006

Non-ultrahigh-pressure unit bordering the Sulu ultrahigh-pressure terrane, eastern China: Transformation of Proterozoic granulite and gabbro to garnet amphibolite

Ru Y. Zhang
Juhn G. Liou
Tatsuki Tsujimori
Department of Geological and Environmental Sciences, Stanford University, Stanford, California 94305, USA
Shigenori Maruyama
Department of Earth and Planetary Sciences, Tokyo Institute of Technology, Tokyo, Japan

ABSTRACT

The Haiyangsuo area of the NE Sulu ultrahigh-pressure terrane, eastern China, consists of gneisses with minor granulite and amphibolite layers, metagabbros, and granitic dikes. The peak-stage assemblages of the granulites (garnet + orthopyroxene + clinopyroxene + plagioclase ± pargasite ± biotite ± quartz) formed at >750 °C and 9–11 kbar and were overprinted by amphibolite-facies phases characterized by well-developed corona layers of │garnet│amphibolite + quartz│at contacts between plagioclase and clinopyroxene or orthopyroxene, as well as by the exsolution of (orthopyroxene + ilmenite + amphibole) from clinopyroxene. These textures indicate a near-isobaric cooling history of the granulite-bearing gneiss terrane. The metagabbro preserves a relict igneous assemblage (orthopyroxene + clinopyroxene + plagioclase + pargasite ± ilmenite ± quartz) in its core, but in its margins has a metamorphic corona texture similar to the granulite that formed at ~600–700 °C and 7–10 kbar. Sensitive high-resolution ion microprobe (SHRIMP) U-Pb dating of zircons indicates that the protolith age of the garnet-biotite gneiss is older than 2500 Ma, whereas the granulite-facies metamorphism (the first regional metamorphic event) occurred at 1846 ± 26 Ma. Gabbro intrusion took place at 1734 ± 5 Ma, and the formation of amphibolite assemblages in both metagabbro and granulite occurred at ca. 340–370 Ma. Both gneiss and metagabbro were intruded by granitic dikes, with one dated at 158 ± 3 Ma. These data, together with a lack of eclogitic assemblages, suggest that this granulite-amphibolite–facies complex is exotic relative to the Triassic Sulu high-pressure–ultrahigh-pressure terrane; juxtaposition took place in Jurassic time.

Keywords: non-ultrahigh-pressure unit, Sulu UHP terrane, gabbro, garnet amphibolite, geochronology.

Zhang, R.Y., Liou, J.G., Tsujimori, T., and Maruyama, S., 2006, Non-ultrahigh-pressure unit bordering the Sulu ultrahigh-pressure terrane, eastern China: Transformation of Proterozoic granulite and gabbro to garnet amphibolite, *in* Hacker, B.R., McClelland, W.C., and Liou, J.G., eds., Ultrahigh-pressure metamorphism: Deep continental subduction: Geological Society of America Special Paper 403, p. 169–206, doi: 10.1130/2006.2403(10).

INTRODUCTION

Since coesite was first identified in Donghai eclogite in 1990 (Hirajima et al., 1990), this phase has been reported as inclusions in eclogitic garnet, omphacite, kyanite, and epidote and gneissic zircons in many Sulu ultrahigh-pressure (UHP) rocks (Fig. 1). Hence, in situ Triassic UHP metamorphism has been considered a characteristic of the subducted supracrustal rocks of the northern Yangtze craton (Zhang et al., 1995; Wallis et al., 1999; Ye et al. 2000; Liu et al. 2004a, 2004b, 2005). However, we recently identified a non-UHP unit composed of granulite-bearing amphibolite-facies gneiss with Proterozoic gabbroic bodies larger than 15 km^2 (Fig. 2) at Haiyangsuo, along the southern coast of the northeastern Shandong Peninsula. The gabbroic rock has been considered an important component of the "Jaiodong Proterozoic ophiolite sequence" (Wang et al., 1995), which consists of widely separated blocks of ultramafic rock, chert and metavolcanic rocks, all of which are significantly deformed and recrystallized ophiolitic rocks. Subsequently, Ye et al. (1999) described granulite relics (Opx + Cpx + Grt + Pl + Amp; abbreviations after Kretz, 1983) within amphibolite displaying garnet coronae between plagioclase and mafic minerals. They named rocks with the assemblage Grt_2 + Cpx_2 (Omp/Di) + Pl_2 (Ab) + Zo + Hbl_2 + Ky + Rt "transitional eclogite." They further suggested that the Haiyangsuo area is similar to the "cold eclogite" belt in Dabie, and represents a southern unit of the Sulu UHP metamorphic belt. As granulite-facies protoliths are rare for Dabie-Sulu UHP rocks, their findings motivated us to investigate the lithology, pressure-temperature (*P-T*) paths, and geochronology of various Haiyangsuo rocks. We conclude that the Haiyangsuo area is exotic with respect to the Sulu high-pressure–ultrahigh-pressure rocks; the two must be separated by a tectonic boundary, but the intervening area is covered by Quaternary sediments.

GEOLOGICAL OUTLINE

The Sulu metamorphic terrane is an eastern extension of the Triassic Qinling-Dabie collision zone between the Yangtze and Sino-Korean cratons, and consists of an UHP belt to the

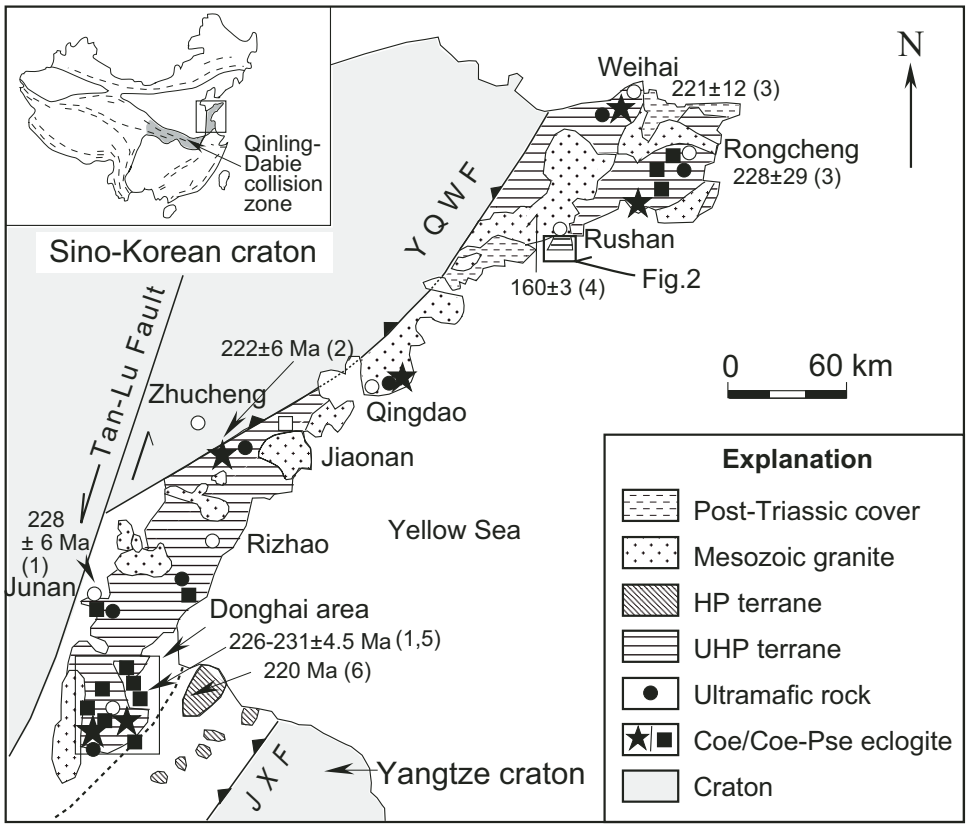

Figure 1. Simplified geological map of the study area and the Sulu region, showing major tectonic units and distribution of coesite (Coe)-bearing and coesite pseudomorph (Coe pse)–bearing eclogites. Metamorphic ages: (1) Sm-Nd ages of eclogite after Li et al. (1993), (2) Sm-Nd isochron age after Han et al. (1993); (3) zircon sensitive high-resolution ion microprobe (SHRIMP) U-Pb age for peridotite (Weihai) and eclogite (Rongcheng) after Yang et al. (2003); (4) monazite SHRIMP U-Pb age of Rushan granite from Hu et al. (2004); (5) zircon SHRIMP U-Pb age of CCSD-PP2 gneiss at Donghai after Liu et al. (2004b), and (6) $^{40}Ar/^{39}Ar$ plateau age of white mica for high-pressure belt mica and quartz schist after Cong et al. (1992). Abbreviations: JXF—Jiashan-Xianshui fault; YQWF—Yantai-Qingdao-Wulian fault; HP—high pressure; UHP—ultrahigh pressure.

north and a high-pressure belt to the south (Fig. 1; Zhang et al., 1995); the boundary in the vicinity of Donghai has recently been confirmed by a systematic study of mineral inclusions in zircons and is characterized by a mylonitic zone (e.g., Liu et al., 2004a). The UHP belt is composed of gneiss, amphibolite, and small amount of marble and quartzite. Widespread coesite-bearing eclogites occur as lenses and layers in gneiss, marble, and ultramafic rocks. Most of the UHP metamorphic garnet peridotites occur as block in gneiss. Most of the protolith ages of the eclogites and the country-rock gneisses range from 600 to 800 Ma, and UHP metamorphic ages are 220–240 Ma (Fig. 1; Li et al., 1993; Ames et al., 1996; Liu et al., 2004b, 2005; Leech et al., this volume; Webb et al., this volume; Hacker et al., 2006). The high-pressure belt in Sulu consists of gneiss, mica schist, kyanite-bearing mica schist, kyanite-topaz–bearing quartzite, marble, phosphatic rocks, and minor blueschist (Zhang and Kang, 1989); no eclogite has been found. These UHP and high-pressure belts of the Sulu terrane are intruded by Mesozoic granites and are unconformably overlain by Jurassic–Cretaceous volcanic-sedimentary cover sequences.

FIELD INVESTIGATION

The Haiyangsuo area in the northeastern Sulu UHP terrane, along the coast of southern Rushan county (Fig. 1), consists of three lithological units: (1) gneiss with granulite lenses and amphibolite layers, (2) metamorphosed gabbro intrusions, and (3) granitic dikes. Units 1 and 2 are dominant and display several stages of deformation and metamorphic recrystallization. Widespread gabbro bodies of ~15 km^2 (Fig. 2) exhibit clear crosscutting relationships with their host gneiss (Fig. 3); some show concordant contacts (e.g., gabbro intruded along the foliation of the gneiss). Some gneisses and late granitic dikes show a mylonitic foliation that wraps around the margins of some of the mafic bodies (Fig. 4A). A fine-grained, pale-red coronal metagabbro occurs in the cores of some of the metagabbro bodies (Fig. 4B); it is easy to misidentify as eclogite. Toward the margins of the mafic bodies, the rock becomes dark green due to amphibolite-facies recrystallization; the boundary between the outer amphibolite and inner coronal metagabbro is gradational. The red metagabbro core varies in size; most are 1–10 m in diameter. Young granitic dikes cut across all lithologic units, including the gneiss and metagabbro (Fig. 3).

PETROGRAPHY

Unit 1: Gneiss with Granulite Lens and Amphibolite Layer

Relics of granulite occur as meter-scale lenses or layers in the gneiss rock; they exhibit various extents of retrogression to garnet amphibolite. In our collections, three granulite-facies mineral assemblages were identified at different locations. (1) Biotite-bearing granulite consists of coarse-grained garnet, clinopyroxene, orthopyroxene, plagioclase, and quartz with

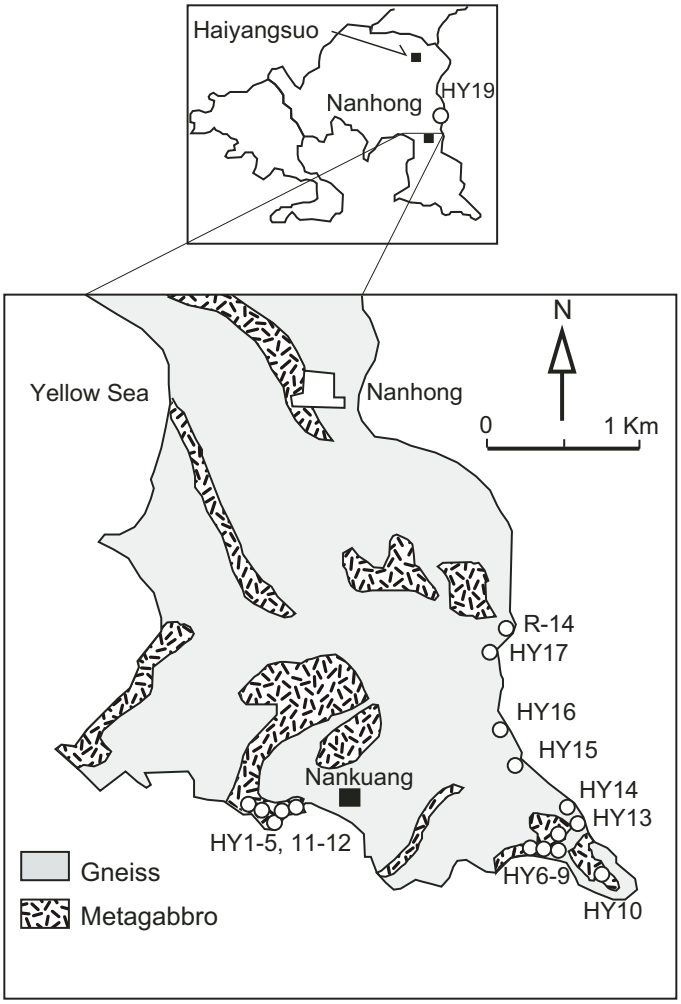

Figure 2. Schematic geologic map of the Haiyangsuo area showing distribution of metagabbro in gneissic rocks and sample locations.

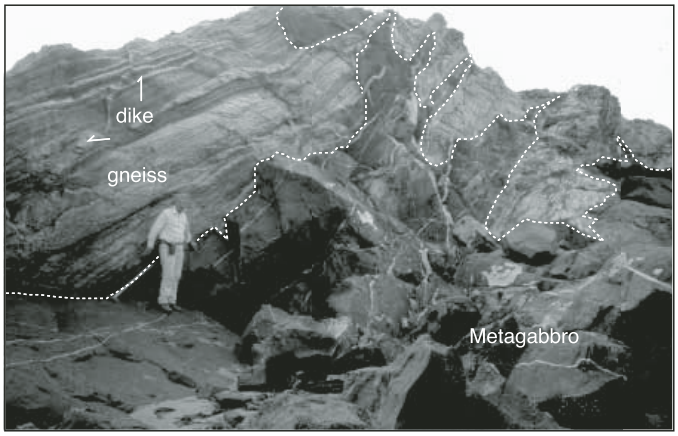

Figure 3. Field view showing relationship of various rock types. Gabbro intrusives crosscut gneiss, and thin granitic dikes either are along foliation or crosscut both gabbro and gneiss.

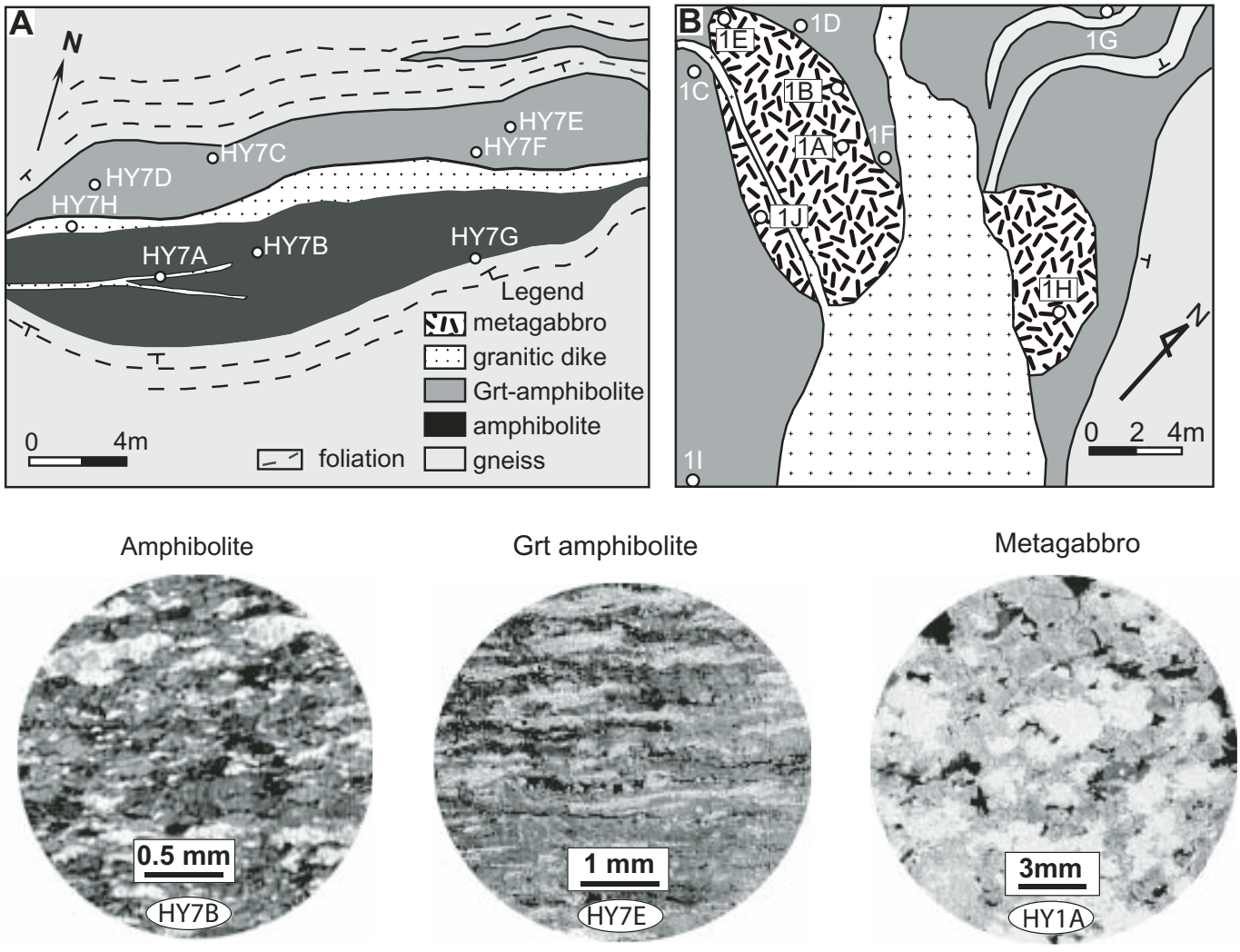

Figure 4. Geological mapping of two outcrops and scanning images of three thin sections for representative samples in the Haiyangsuo area. (A) Gneiss wraps around garnet-free (e.g., HY7B) and garnet-bearing amphibolite (e.g., HY7E). Very fine-grained garnet amphibolite with gabbroic protolith shows strong deformation and distribution of coronic garnets along foliation (HY7E). (B) A small gabbro body is intruded by a granitic dike; metamorphosed gabbro (e.g., HY1A) occurs in the core of the gabbro body and changes to garnet amphibolite at the margin.

minor biotite and ilmenite (Fig. 5A). Most garnets are ~4 mm across. Most pyroxenes of 1–3 mm show undulatory extinction and exsolution (sample 03-R14). Biotite occurs as relict coarse-grained blocky crystals or as secondary fine-grained scaly aggregates. (2) Pargasite-bearing granulite (Fig. 5B) contains Grt + Opx + Cpx + Pl + Prg + Rt/Ilm assemblages; garnet is 0.5–1.75 mm across, and the two pyroxenes are 0.3–1 mm in size; amphibole is pale yellow–brown and varies in abundance from 3 to 15 vol% (sample 12A-B). (3) Garnet pyroxenite consists of Grt, Opx, Cpx, and minor Ilm (samples 15A-D). Round garnet is the most abundant phase (60–70 vol%), 0.5–5 mm across, occurs as isolated grains and patches composed of garnets of variable size, and contains ilmenite inclusions. Pyroxene is an interstitial phase between garnets and is smaller (1–2 mm) than most garnets. Porphyroblastic garnet, 2 cm across in some pyroxenites (e.g., HY15E), is set in a finer matrix of Grt, Opx, Cpx, and ilmenite, and contains abundant ilmenite lamellae (Fig. 5C).

All granulites are weakly deformed and granoblastic. Clinopyroxenes contain submicron exsolved phases, such as Opx + Ilm + Amp (HY12B; Fig. 5D) or Ilm + rare earth element (REE)-bearing epidote (03-R14). The garnet-amphibolite–facies overprinting is characterized by the formation of fine-grained garnet corona along the contacts between plagioclase and mafic phases; the common replacements are green Amp ± Qtz after Cpx, cummingtonite or calcic amphibole ± Qtz after orthopyroxene, Pl_2 + Zo after Pl_1, and titanite after ilmenite. Zoisite of various sizes occurs as prisms or laths within pseudomorphs after the primary plagioclase. Fine-grained (0.05–0.1 mm) garnet coronas are common between plagioclase and pyroxene, but diminish to small thicknesses at boundaries

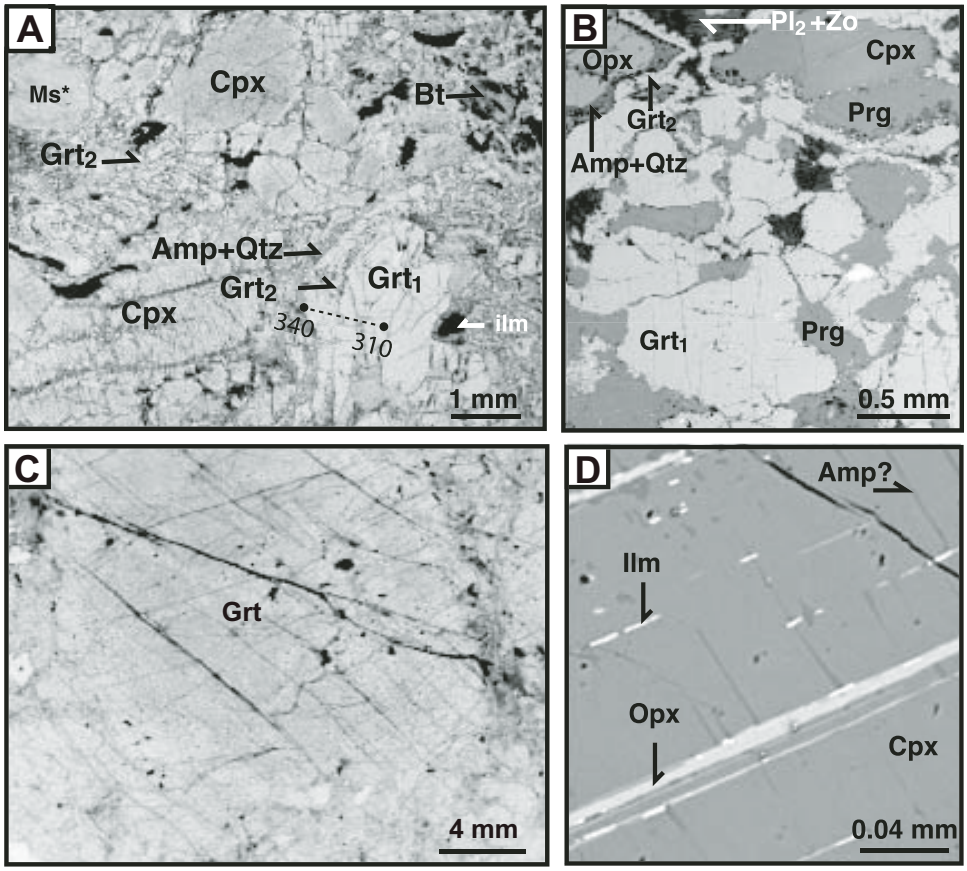

Figure 5. (A) Photomicrograph showing mineral assemblage and texture of granulite (03-R14) (plane light). In sample 03-R14, orthopyroxene is totally replaced by Amp + Qtz and coarse-grained garnet (Grt_1) is rimed by fine-grained garnets (Grt_2); fine-grained garnet coronas separate plagioclase from clinopyroxene. Ms*—white mica after plagioclase. Dashed line and number—probe analyses. (B) Backscattered-electron image (BSE) showing pargasite-bearing granulite (HY12B) with corona texture. (C) Photomicrograph of garnet pyroxenite (HY15E) showing porphyroblastic texture (plane light). (D) Exsolved lamellae of Opx, Ilm, and Amp in clinopyroxene (BSE); Amp lamellae are too thin for microanalysis. Abbreviations are after Kretz (1983).

between coarse-grained garnet (Grt_1) and pyroxene. Three corona mineral assemblages were identified: (1) Cpx (or Opx)|Amp + Qtz|Grt|Pl (Fig. 6A–B), (2) Cpx|Grt|Pl (Fig. 6C), and (3) Grt_1|Grt_2|Amp + Qtz|Cpx (Fig. 5A). In addition, some recrystallized fine-grained Cpx|Pl|Grt corona-like domains were found in plagioclase (Figs. 6D and 7).

Gneisses with distinct compositional layers include garnet-free, garnet-bearing, and quartz-rich paragneiss, orthogneiss, and mafic amphibolite. A representative sample of granitic gneiss (sample HY3) is composed of perthite, antiperthite, and quartz with no mafic minerals; it is mylonitic. Porphyroclasts (1–2 mm in size) of feldspar are set in a fine-grained matrix of fine-grained feldspar and quartz, with the minimum grain size <10 μm. Some felsic gneisses (e.g., sample HY5E) contain additional ~5 vol% amphibole; plagioclase includes abundant fine laths of zoisite and minor epidote. Sample HY17A is a garnet-rich (>40 vol%) gneiss composed of coarse, 1–6 mm garnet in a fine-grained (0.05–1 mm) matrix of pale green pargasite, colorless cummingtonite, quartz, and minor plagioclase; biotite and garnet-bearing gneisses are also common.

Most of the dark layers in the gneiss are unmylonitized Pl + Hbl ± Grt + Ttn ± Ep ± Qtz amphibolites. A foliated amphibolite (sample HY7B) consists of 90 vol% amphibole, plagioclase, and very minor titanite; the amphiboles are idioblastic and have a uniform grain size of 0.3–0.4 mm. Fine-grained titanite aggregates occur along the foliation. Garnet amphibolite (sample HY 19A) with a granoblastic texture consists of 0.5–0.8 mm euhedral garnet, 0.2–0.6 mm amphibole, plagioclase, minor quartz (~4%), and titanite.

Unit 2: Metagabbro

Gabbroic intrusive rocks exhibit various extents of amphibolite-facies recrystallization. Incipiently metamorphosed gabbro preserves intrusive relationships in its central parts and grades progressively outward to garnet amphibolite at the

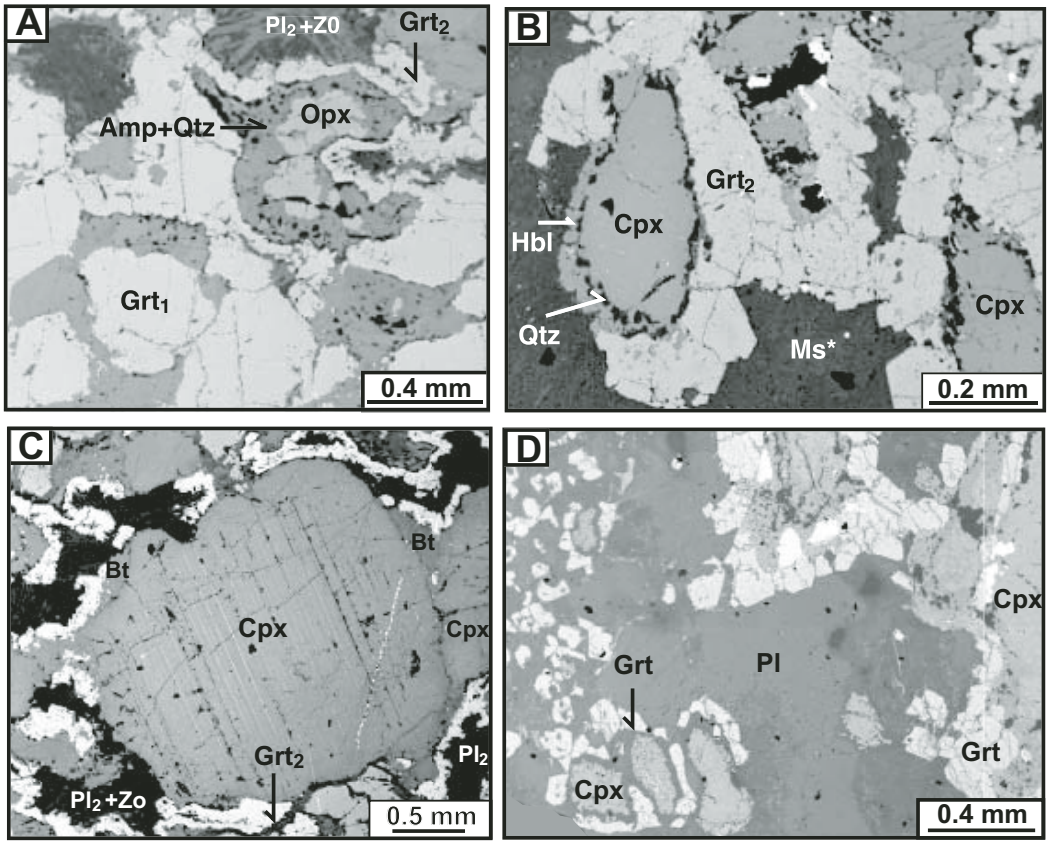

Figure 6. Backscattered-electron images showing representative corona mineral sequences of granulite (HY12B and 03-R14) and metagabbro (HY1E): Opx (or Cpx)|Amp + Qtz|Grt|Pl (A: HY12B and B: 03-R14); Cpx |Grt| Pl (C: HY12B). Small domains of Cpx (multicrystal)-Pl-Grt occur in plagioclase (D: HY1E). Abbreviations are after Kretz (1983).

margins. Coronal metagabbro in the center contains relict 0.5–1.5 mm igneous minerals, Opx + Cpx + Pl + Amp + Ilm ± Qtz (Fig. 7), some clinopyroxene, and amphibole crystals are up to 3 mm across. Plagioclase shows albite twining and only rare to minor replacement by fine-grained neoblastic anorthite, zoisite, and kyanite. Greenish clinopyroxene and pale-brown orthopyroxene contain exsolution lamellae; orthopyroxene shows greater extents of amphibole replacement than clinopyroxene. Igneous amphibole (Amp_1) shows strong pale yellowish-brown to dark yellow-green pleochroism. Ilmenite is an interstitial phase and rimmed by fine-grained titanite. The distinctive petrographic feature of the metagabbro is the presence of reaction rims separating primary orthopyroxene and clinopyroxene from plagioclase; reaction rims also occur around igneous amphibole and ilmenite. The common mineral sequences of corona layers between clinopyroxenes and plagioclase are Cpx (or Opx)|Amp_2 + Qtz|Grt|Pl_2 with zoisite and kyanite needles, or Opx|Amp_2 + Qtz + Di|Ab|Grt|Pl_2 with zoisite and kyanite needles (e.g., HY12G; Fig. 8). Rare garnet lamellae occur in clinopyroxene. In addition, some plagioclase contains isolated, 0.15–0.30-mm-diameter domains composed of clinopyroxene aggregates ± tiny Amp rimmed by Pl and then coronitic garnet (Fig. 6D; HY1E). With increasing recrystallization, the coronal metagabbro is transformed into garnet amphibolite.

The garnet amphibolite is developed at the margin of the intrusions where orthopyroxene has disappeared; only minor clinopyroxene relics are preserved. In weakly recrystallized garnet amphibolite (e.g., HY1F, HY11A, HY11B), fine-grained amphibole replaces pyroxene, long prismatic zoisite/epidote crystals form in Pl_2, and garnet corona texture is well preserved. Some garnet amphibolites are strongly deformed, with oriented Pl_2 and garnet coronas. With advanced recrystallization, garnet (~0.4 mm), hornblende (0.2–0.5 mm), and zoisite (up to 0.3 mm) coarsen (HY1C, HY1I and HY7E), and the coronal texture is no longer apparent (Fig. 4A). Mafic dikes within the gneiss were also metamorphosed at amphibolite-facies conditions. For example, sample HY19B is composed of 90 vol% amphibole, subordinate plagioclase, quartz, and very minor garnet and zoisite.

Unit 3: Felsic Dikes

Felsic dikes of various stages are abundant and cut across both gneiss and metagabbro. As these dikes are not the focus of

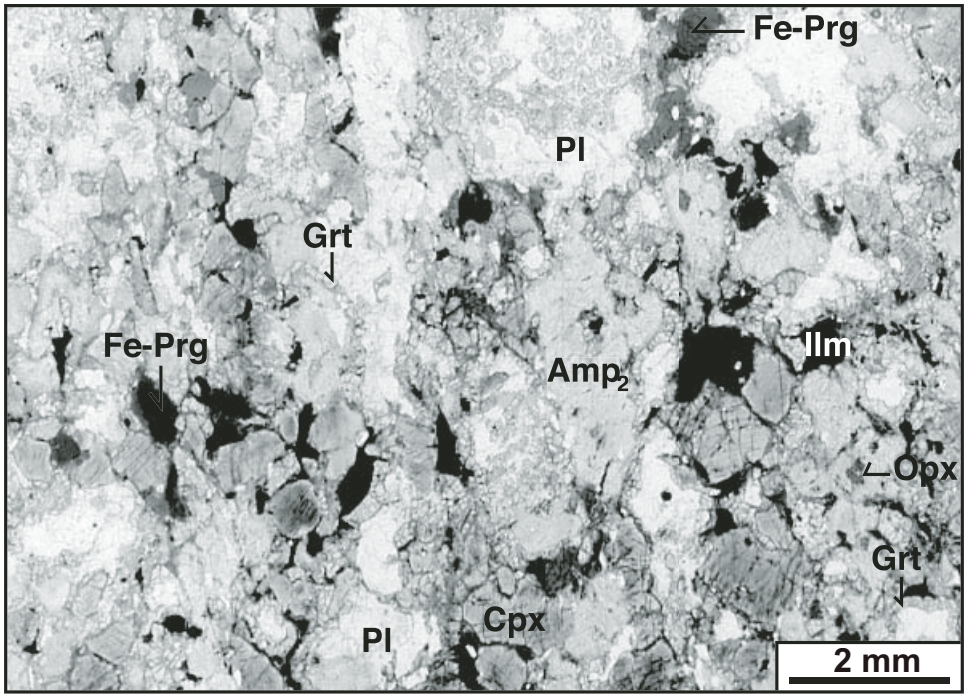

Figure 7. Photomicrograph of a metagabbro thin section (HY1E) showing assemblage (Prg + Opx + Cpx + Pl + Ilm) and texture. Only minor relict Opx is preserved; fine-grained garnet coronas occur at the contacts of pyroxenes and plagioclase. Abbreviations are after Kretz (1983).

this manuscript, we discuss only a few examples. The dikes are medium to coarse grained; some are pegmatitic. They (e.g., HY7A and HY7H) show a pronounced mylonitic texture. Porphyroclasts of plagioclase, rare microcline, quartz, and their aggregates, ranging from 0.2 to 2 mm constitute 40%–50% of the rock. These porphyroclasts are wrapped by thin layers of fine-grained, 50 μm quartz, minor white mica (±biotite ± epidote), and <10 μm quartz and feldspar. Some plagioclase porphyroclasts preserve compositional zoning and polysynthetic twinning. Minor garnets also occur in the matrix.

ZIRCON U-PB SHRIMP DATING OF GRANULITE

Few geochronologic studies of amphibolite and dikes have been carried out in Haiyangsuo. A less well-constrained (only 4 analyses) U-Pb upper intercept of 1784 ± 11 Ma and a lower intercept of 448 ± 13 Ma were obtained for the Haiyangsuo garnet amphibolite by Li et al. (1994). U-Pb sensitive high-resolution ion microprobe (SHRIMP) dating of a strongly deformed K-feldspar-rich dike from Haiyangsuo was recently reported by Wallis et al. (2005). Seven SHRIMP U-Th-Pb analyses of zircon yield a wide $^{208}Pb/^{238}U$ age range of 155.2–755.7 Ma; these analyses in the Tera-Wasserburg concordia diagram could not yield a meaningful weighted mean $^{206}Pb/^{238}U$ age or define a regression trend. In the present study, zircon separates from one granulite sample (03-R14, see description herein) were dated by the SHRIMP U-Pb method. The U-Pb SHRIMP dating results of gneiss, metagabbro, amphibolite, and granitic dike by Chu (2005) are also described.

Analytical Method

U-Th-Pb analyses were performed with the SHRIMP-RG (reverse geometry) in the Stanford–U.S. Geological Survey cooperative ion microprobe facility. Instrumental conditions and data acquisition were similar to the procedures described by Williams (1998). Analytical spots ~30 μm in diameter were sputtered using an ~5 nA O^{2-} primary beam. The data were collected in sets of 5 scans through 9 mass spectra. The primary beam was rastered across the analytical spot for 120 s before analysis to reduce surficial common Pb resulting from sample preparation and Au coating. Concentration data were calibrated against CZ3 zircon (550 ppm U), and isotope ratios were calibrated against R33 (419 Ma, John Aleinikoff, 2002, personal commun.). Data reduction followed Williams (1998) and utilized Squid (Ludwig, 2001). Isoplot 3 (Ludwig, 2003) was used to calculate all ages, which are reported here at the 95% confidence level.

Results

Most zircons were rounded, ranged in size from 50 to 150 μm, and showed weak cathodoluminescence (CL) response without obvious cores (Fig. 9). Twenty-one zircon grains from sample 03-R14 were analyzed, and yielded medium to high U contents of 111–1232 ppm, with one exception (76 ppm). The Th content ranged from 9 to 359 ppm, and the Th/U ratios from 0.03 to 0.67 (Table 1). The 21 analyses define a good discordia,

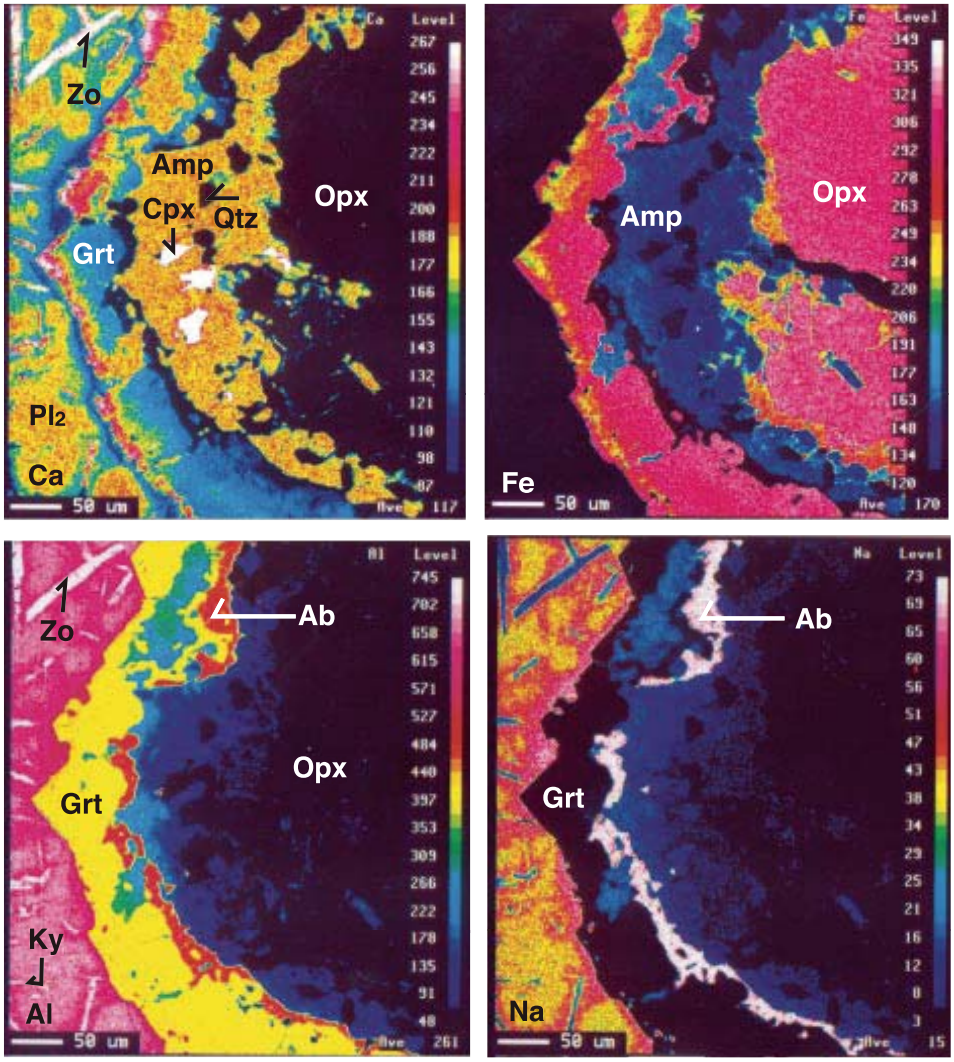

Figure 8. Compositional (Ca, Fe, Al and Na) X-ray maps for a corona mineral assemblage at the contact between orthopyroxene (Opx) and plagioclase (Pl) (HY12G). Abbreviations are after Kretz (1983).

yielding an upper intercept age of 1846 ± 26 Ma (t_1) and a lower intercept age of 373 ± 65 Ma (t_2) (Fig. 9). The t_1 age of 1846 Ma is interpreted as the age of the granulite-facies metamorphism and t_2 as the age of the garnet-amphibolite overprint.

U-Pb SHRIMP dating of zircons from all rock types by Chu (2005) at Stanford showed that (1) the protolith of one garnet- and biotite-bearing gneiss is older than 2500 Ma, (2) the crystallization age of the gabbro is 1734 ± 5 Ma, (3) amphibolite-facies recrystallization of the gabbro and amphibolites within the gneiss occurred at 339 ± 59 Ma, and (4) intrusion of one late granitic dike with inherent metamorphic zircons of 780–375 Ma took place at 158 ± 3 Ma; the igneous age is coeval with the SHRIMP age for intrusion of the Rushan granite (Hu et al., 2004), 20 km west of this area. One garnet amphibolite (03-HY6C) collected at the same outcrop as 03-R14 by Chu (2005) is a retrogressed granulite in which orthopyroxene and clinopyroxene were totally replaced by amphibole, leaving only relict coarse-grained garnets. Zircon U-Pb SHRIMP dating of this rock yielded upper and lower intercept ages of 1854 ± 18 Ma and 459 ± 47 Ma. Our age for the granulite-facies metamorphism is consistent with Chu's, but the overprinting age of the amphibolite-facies assemblage is younger than his result.

MINERAL CHEMISTRY

Field investigation, petrographic observation, and geochronologic data indicate that both the gabbros and the granulites experienced amphibolite-facies overprinting. The amphibolite-facies metamorphism at 370–340 Ma affected most of the lithologies in this region except for the young granitic dikes. The Haiyangsuo granulites are characterized by Opx + Cpx +

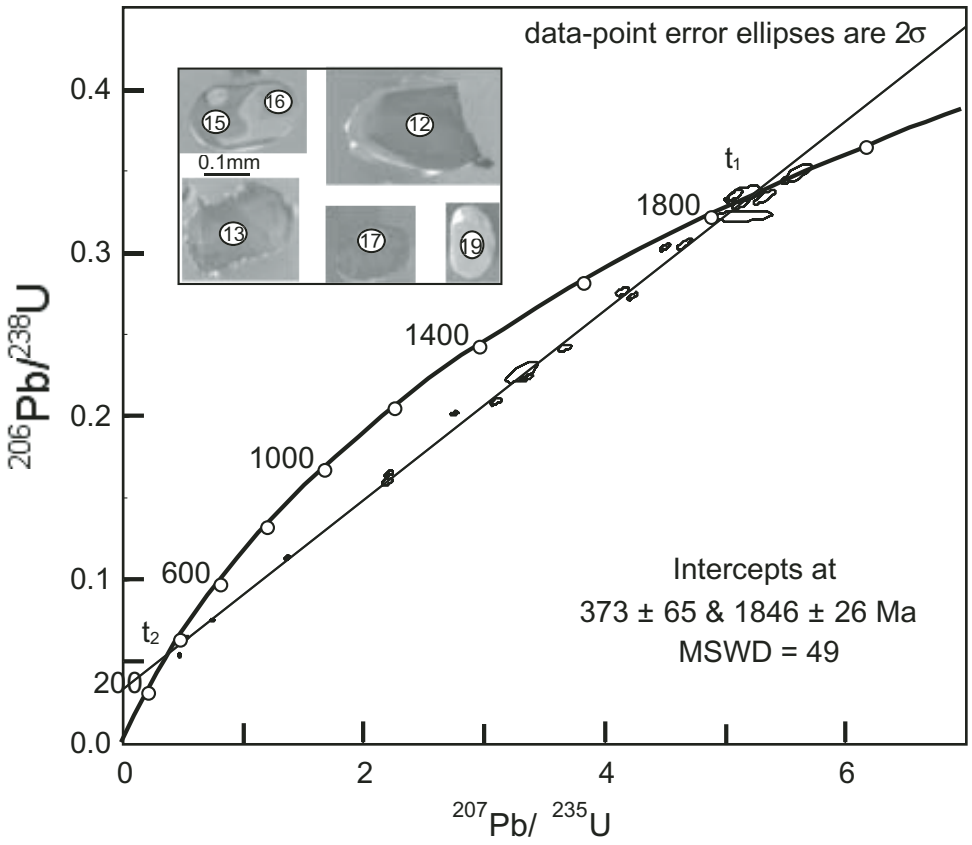

Figure 9. Concordia diagram for granulite (03-R14) showing metamorphic age (t_1) of granulite-facies rock and amphibolite overprint age (t_2). Some representative zircon cathodoluminescence images with metamorphic origin are also shown. MSWD—mean square of weighted deviation.

TABLE 1. U-Th-Pb MICROANALYSES OF ZIRCONS FROM GRANULITE (03-R14)

					204 corrected					
Spot name	% com Pb	U (ppm)	Th (ppm)	Th/U	$^{207}Pb/^{235}U$	% err	$^{206}Pb/^{238}U$	% err	$^{206}Pb/^{238}U$ Age (Ma)	1σ err
03-R14-1	0.00	371	51	0.14	4.15	1.0	.2764	0.7	1573.0	9.7
03-R14-2	0.00	435	281	0.67	3.67	1.2	.2422	0.7	1398.3	8.4
03-R14-3	0.02	914	196	0.22	2.75	0.9	.2020	0.5	1186.0	5.4
03-R14-4	0.00	994	230	0.24	4.23	0.8	.2735	0.6	1558.7	8.8
03-R14-5	0.05	561	84	0.15	3.10	1.2	.2091	0.9	1223.8	9.9
03-R14-6	0.00	781	129	0.17	3.35	1.2	.2236	0.8	1300.6	10.0
03-R14-7	0.00	639	108	0.17	4.66	1.1	.3057	0.9	1719.5	14.0
03-R14-8	0.00	76	10	0.13	3.31	3.3	.2273	2.4	1320.2	28.8
03-R14-9	0.00	590	115	0.20	5.13	1.1	.3295	0.8	1835.9	12.5
03-R14-10	0.00	1232	359	0.30	4.50	0.7	.3035	0.6	1708.7	8.6
03-R14-11	0.00	650	112	0.18	0.74	1.7	.0755	0.9	469.4	4.1
03-R14-12	0.02	507	78	0.16	5.07	1.2	.3348	0.9	1861.4	14.4
03-R14-13	0.00	552	71	0.13	1.36	1.5	.1137	0.9	694.2	6.2
03-R14-14	0.03	677	118	0.18	5.15	3.8	.3226	0.9	1802.3	14.1
03-R14-15.1	0.00	188	15	0.08	5.59	1.8	.3483	1.4	1926.7	23.6
03-R14-15.2	0.00	402	12	0.03	5.32	1.3	.3339	1.0	1857.2	16.9
03-R14-16	0.15	452	63	0.14	0.47	2.8	.0545	1.2	341.8	3.9
03-R14-17	0.00	333	45	0.14	2.19	1.8	.1600	1.2	956.8	10.8
03-R14-18	0.02	427	74	0.18	5.16	2.2	.3359	1.1	1867.0	18.3
03-R14-19	0.00	111	9	0.08	0.52	5.1	.0649	2.3	405.3	8.9
03-R14-20	0.00	562	105	0.19	2.21	1.3	.1650	0.9	984.7	8.2

Grt + Pl ± Prg ± Bt ± Qtz ± Kfs + Rt/Ilm assemblages and by the development of reaction coronas similar to those described in the previous section in the metagabbro. The garnet amphibolite contains a typical metamafic assemblage of Hbl + Pl + Grt + Ilm.

Mineral compositions of Haiyangsuo rocks were analyzed employing a JEOL superprobe 880 at the Tokyo Institute of Technology, and a JEOL 733 superprobe with five wavelength-dispersive spectrometers at Stanford University. Both machines were operated at 15 kV and 12 nA beam current. Total Fe is expressed as FeO except for zoisite/epidote. Ferric iron for calcic amphibole was calculated using the procedure of Schumacher (1991). The compositions of representative minerals are listed in Tables 2–6; characteristic features are described below.

Orthopyroxene

Orthopyroxene in granulite ranges in enstatite component [Mg/(Fe + Mg + Ca)] from 0.53 to 0.65 (Fig. 10) and contains very low wollastonite component (0.5–0.7 mol%). The Al_2O_3 content is 1.0–1.3 wt% and some grains (e.g., sample HY12A) are zoned in the enstatite component from core and mantle (64–65 mol%) to rim (59 mol%). Orthopyroxene in the metagabbro contains clinopyroxene lamellae and has slightly lower En (49–54 mol%) and higher Wo (0.7–3.1 mol%) than the granulitic orthopyroxene, which has an Al_2O_3 content of <1 wt% (HY1A). The metagabbroic orthopyroxene also shows weak zoning, with decreasing Wo from core to rim.

Clinopyroxene

Clinopyroxene in the granulites ($En_{40–37}Fs_{11–14}Wo_{48–49}$) and metagabbro ($En_{30–34}Fs_{19–23}Wo_{47–48}$) is diopside (Fig. 10); the jadeite component ranges from 2 to 7 mol% and 4–9 mol%, respectively. Most coarse-grained clinopyroxenes in both granulite and metagabbro are homogeneous, although weak zoning was identified. In granulitic diopside the Mg/Fe decreases from core to rim, whereas diopside in the metagabbro shows the opposite (Table 2). Fine-grained neoblastic clinopyroxenes in granulite ($En_{43}Fs_{10}Wo_{47}$) and metagabbro ($En_{36–38}Fs_{14–17}Wo_{47–48}$) have slightly different compositions. Relict clinopyroxene grains with 10 mol% Jd component were found in some garnet amphibolites (HY7E) derived from metagabbro. The tie lines between orthopyroxene and clinopyroxene are roughly parallel (Fig. 10), indicating that the compositional variation of pyroxene is related to bulk composition.

Garnet

Garnet, except for those from granitic dikes, contains very low spessartine (~1–2 mol%), which is therefore combined with the almandine component in the following description. Coarse-grained garnet (Grt_1) in the plagioclase-bearing granulite and relict garnet in the amphibolitized granulite are almandine rich ($Alm_{55–64}Grs_{17–23}Prp_{18–25}$); garnets from plagioclase-free garnet pyroxenite (HY15D and HY15E) are even richer ($Alm_{62–68}Grs_{15–19}Prp_{17–20}$). The coronal garnets ($Grt_2$) in the plagioclase-bearing granulite and metagabbro show distinct variations in composition due to variable bulk composition and disequilibrium in local domains (Tables 2 and 3; Fig. 11). Most Grt_2 grains are characterized by a higher Grs component ($Alm_{51–67}Grs_{18–29}Prp_{11–25}$) than Grt_1 in individual rocks. The Grt_2 grains with the highest Grs component ($Alm_{42–50}Grs_{31–44}Prp_{14–19}$) are adjacent to plagioclase (Fig. 11). Almandine-rich garnet coronas occur along ilmenite grain boundaries. Garnet from garnet amphibolite developed within gabbroic protoliths is relatively homogeneous ($Alm_{56–58}Grs_{19}Prp_{23–25}$, for sample HY1C; $Alm_{53–54}Grs_{28–32}Prp_{15–18}$ for sample HY7D).

Garnets from the gneiss and garnet amphibolite interlayers are homogeneous in single samples, but differ from sample to sample. Those from garnet-rich gneiss (HY17A) are almandine ($Alm_{69}Grs_{16}Prp_{13}Sps_2$) with lower grossular component than garnets ($Alm_{54}Grs_{35}Prp_8Sps_3$) from garnet amphibolite (HY19A). Garnets from metamorphosed dikes are characterized by high MnO (13.6 wt% in a metafelsic dike vs. 3.3–3.5 wt% in metamafic dikes) and very low in MgO (0.6–2.2 wt%); the garnets from felsic dikes are rich in Alm and Grs components ($Alm_{53}Grs_{31}Prp_9Sps_7$), whereas those from metamafic dikes are rich in Alm and Sps ($Alm_{59}Grs_{12}Prp_3Sps_{26}$).

Amphibole

Amphibole has three modes of occurrences: (1) coarse-grained pargasitic amphibole (Amp_1) as an igneous phase in gabbro and as a metamorphic phase in granulite; (2) fine-grained coronal hornblende after clinopyroxene, and calcic Amp ± cummingtonite after orthopyroxene in granulite and metagabbro (Amp_2), and (3) recrystallized hornblende (±garnet) in amphibolite (Amp_3) (Tables 2-2, 3-2, and 5). The igneous amphiboles include ferropargasite and edenite in gabbro, and are characterized by high contents of TiO_2, FeO, Al_2O_3, Na_2O, and K_2O. For example, the brownish-green ferropargasite in metagabbro HY1A contains the highest TiO_2 (~2 wt%) and K_2O (2.4 wt%) among the studied amphiboles. Other than higher MgO, the compositions of the coarse-grained pargasite and edenite in granulite are similar to that of metagabbroic amphibole. Most of the edenitic amphiboles contain less K_2O (<1 wt%) than the pargasite and ferropargasite, and occur as inclusions or lamellae in clinopyroxene or as a transitional product between primary pargasite and magnesiohornblende in the mantle of coarse-grained pargasite. Some coarse-grained amphiboles (Amp_1) grade outward to magnesiohornblende (Amp_2) at the rims. Amp_2 after clinopyroxene in both metagabbro and granulite is magnesiohornblende (or actinolite) characterized by low Al^{IV}, Ti, and K (Fig. 12); Amp_2 after orthopyroxene is either cummingtonite or actinolite with minimal CaO (0.7–3.0 wt%). Most amphiboles from the garnet amphibolite are magnesiohornblende with a wide range in composition, and have low Ti and K.

TABLE 2-1. MINERAL COMPOSITIONS OF HAIYANGSUO GRANULITE

Sample No.:	HY12A												
Mineral:	Grt1	Grt2	Grt2	Cpx	Cpx	Opx	Opx	Opx	Opx	Pl	Pl	Pl	Grt1
Texture:	rim	crn	crn-pl	core	af opx		core	mantle	rim	pse	pse	needle	core
SiO_2	37.95	37.99	37.99	52.5	53.36	52.36	53.26	53.71	53.31	49.69	59.20	44.16	38.90
TiO_2	0.05	0.01	0.01	0.18	0.07	0.03	0.35	0.04	0.03	0.00	0.00	0.00	0.08
Cr_2O_3	0.05	0.00	0.01	0.04	0.03	0.05	0.06	0.01	0.05	0.00	0.03	0.00	0.04
Al_2O_3	21.46	21.45	21.09	2.06	1.58	1.05	1.21	1.25	1.1	31.67	25.19	34.67	22.19
FeO	26.60	25.24	19.26	6.56	6.12	23.57	22.09	21.74	24.72	0.03	0.34	0.13	25.53
MnO	0.75	0.49	0.28	0.08	0.01	0.10	0.18	0.15	0.13	0.02	0.00	0.00	0.76
MgO	6.02	5.93	3.58	13.51	14.53	22.29	22.09	23.08	20.63	0.01	0.01	0.04	6.47
CaO	6.75	7.83	16.08	22.90	22.45	0.26	0.34	0.25	0.35	14.23	6.55	18.05	6.45
Na_2O	0.00	0.00	0.00	0.80	0.78	0.01	0.03	0.02	0.02	3.36	7.59	1.04	0.03
K_2O	0.00	0.00	0.00	0.03	0.00	0.00	0.00			0.05	0.11	0.02	0.01
Total	99.63	98.94	98.30	98.66	98.93	99.72	99.61	100.18	100.25	99.06	99.02	98.11	100.45
Si	2.978	2.988	2.996	1.969	1.986	1.964	1.983	1.981	1.992	2.285	2.665	2.076	2.999
Ti	0.003	0.001	0.001	0.005	0.002	0.001	0.010	0.001	0.001	0.000	0.000	0.000	0.005
Cr	0.003	0.000	0.001	0.001	0.001	0.001	0.002	0.000	0.001	0.000	0.001	0.000	0.002
Al	1.985	1.988	1.961	0.091	0.069	0.046	0.053	0.054	0.048	1.717	1.337	1.921	2.017
Fe	1.746	1.660	1.270	0.206	0.190	0.739	0.688	0.671	0.772	0.001	0.013	0.005	1.646
Mn	0.039	0.025	0.015	0.002	0.000	0.002	0.004	0.004	0.003	0.001	0.000	0.000	0.039
Mg	0.704	0.695	0.421	0.755	0.806	1.246	1.226	1.269	1.149	0.001	0.001	0.003	0.744
Ca	0.568	0.660	1.359	0.920	0.895	0.010	0.014	0.010	0.014	0.701	0.316	0.909	0.533
Na	0.000	0.000	0.000	0.058	0.056	0.001	0.002	0.001	0.001	0.300	0.662	0.095	0.004
K	0.000	0.000	0.000	0.001	0.000	0.000	0.000	0.000	0.000	0.003	0.006	0.001	0.001
Total	8.025	8.017	8.023	4.009	4.006	4.012	3.981	3.991	3.983	5.008	5.001	5.011	7.989

(*continued*)

TABLE 2-1. MINERAL COMPOSITIONS OF HAIYANGSUO GRANULITE (*continued*)

Sample No.:	HY12A							HY12B					
Mineral:	Grt2	Grt2	Cpx	Cpx	Cpx	Pl	Pl	Grt1	Cpx	Opx	Grt1	Grt1	Grt1
Texture:	crn	crn-pl	core	mantle	rim	pse	needle	core	core	core	core	mantle	rim
SiO_2	39.99	38.23	53.18	52.67	52.67	59.57	45.43	39.00	52.34	52.64	39.18	39.28	39.17
TiO_2			0.00	0.22	0.17	0.07	0.00	0.10	0.34	0.00	0.00	0.08	0.06
Cr_2O_3	0.03	0.01	0.00	0.00	0.03		0.02	0.05	0.03	0.01	0.12	0.11	0.06
Al_2O_3	22.25	22.59	1.88	3.11	2.77	25.84	35.54	22.05	3.39	1.10	21.87	22.00	22.07
FeO	25.16	22.95	6.77	7.78	7.81	0.02	0.04	25.81	7.26	22.33	26.18	26.08	25.54
MnO	0.38	0.36	0.04	0.05	0.09	0.01	0.02	0.94	0.07	0.11	0.89	0.75	0.79
MgO	6.43	4.95	13.73	12.79	12.35		0.00	6.60	12.58	22.59	6.52	6.59	6.53
CaO	7.58	11.00	23.38	22.62	22.72	7.29	18.36	6.24	21.93	0.22	6.22	6.32	6.36
Na_2O	0.03	0.00	0.59	0.67	0.73	6.98	0.98	0.03	0.92	0.02	0.05	0.01	0.19
K_2O	0.01	0.00	0.00	0.00	0.00	0.12	0.02	0.02	0.01	0.03	0.02	0.03	0.02
Total	101.85	100.09	99.73	99.90	99.34	99.90	100.40	100.83	98.87	99.06	101.05	101.23	100.79
Si	3.030	2.960	1.976	1.955	1.968	2.653	2.084	2.997	1.957	1.974	3.009	3.007	3.007
Ti	0.000	0.000	0.000	0.006	0.005	0.002	0.000	0.005	0.010	0.000	0.000	0.004	0.003
Cr	0.002	0.001	0.000	0.000	0.001	0.000	0.001	0.003	0.001	0.000	0.008	0.006	0.004
Al	1.987	2.061	0.082	0.136	0.122	1.357	1.922	1.998	0.150	0.049	1.980	1.985	1.997
Fe	1.594	1.486	0.210	0.241	0.244	0.001	0.002	1.659	0.227	0.700	1.681	1.670	1.640
Mn	0.019	0.018	0.001	0.001	0.002	0.000	0.001	0.061	0.002	0.004	0.058	0.048	0.052
Mg	0.726	0.571	0.761	0.708	0.688	0.000	0.000	0.756	0.701	1.263	0.746	0.752	0.747
Ca	0.615	0.912	0.931	0.900	0.910	0.348	0.903	0.514	0.878	0.009	0.512	0.518	0.523
Na	0.004	0.000	0.043	0.048	0.053	0.603	0.087	0.004	0.067	0.002	0.007	0.001	0.029
K	0.001	0.000	0.000	0.000	0.000	0.007	0.001	0.001	0.001	0.001	0.002	0.003	0.002
Total	7.979	8.009	4.004	3.995	3.992	4.971	4.999	7.999	3.992	4.003	8.002	7.995	8.004

(*continued*)

TABLE 2-1. MINERAL COMPOSITIONS OF HAIYANGSUO GRANULITE *(continued)*

Sample No.:	HY12B												
Mineral:	Grt2	Grt2	Grt2	Cpx	Opx	Cpx	0px	Cpx	Opx	Pl	Pl	Pl	Grt1
Texture:	crn	crn	crn		la i Cpx	host	la i Cpx	host	la i Cpx	pse	needle	af amp	m
SiO_2	39.28	39.42	38.77	52.83	51.68	51.55	50.78	51.61	50.88	58.85	45.06	59.95	38.77
TiO_2	0.00	0.00	0.02	0.25	0.19	0.29	0.11	0.30	0.04	0.00	0.04	0.03	0.00
Cr_2O_3	0.01	0.06	0.02	0.06	0.02	0.00	0.00	0.16	0.02	0.00	0.02	0.04	0.00
Al_2O_3	22.15	22.07	22.55	2.79	2.72	3.30	2.56	3.51	2.52	26.00	35.51	25.94	21.68
FeO	24.74	24.79	23.52	7.20	24.06	8.21	27.64	8.31	27.67	0.08	0.06	0.50	28.52
MnO	0.70	0.50	0.46	0.10	0.27	0.06	0.44	0.21	0.34	0.00	0.01	0.00	0.71
MgO	5.70	6.00	6.38	13.35	16.75	12.44	17.11	12.69	17.31	0.00	0.00	0.00	5.01
CaO	8.11	8.14	8.66	21.99	5.69	21.90	0.87	21.50	0.66	7.77	18.70	7.31	6.82
Na_2O	0.00	0.00	0.00	0.91	0.17	0.72	0.06	0.73	0.01	7.15	0.82	7.22	0.05
K_2O	0.00	0.03	0.01	0.00	0.01	0.02	0.00	0.01	0.03	0.10	0.03	0.07	0.02
Total	100.69	101.01	100.40	99.48	101.56	98.47	99.57	99.03	99.49	99.95	100.24	101.06	101.58
Si	3.020	3.017	2.976	1.963	1.938	1.945	1.950	1.937	1.954	2.629	2.073	2.647	2.998
Ti	0.000	0.000	0.001	0.007	0.005	0.008	0.003	0.008	0.001	0.000	0.001	0.001	0.000
Cr	0.001	0.003	0.001	0.002	0.001	0.000	0.000	0.005	0.001	0.000	0.001	0.001	0.000
Al	2.007	1.991	2.041	0.122	0.120	0.147	0.116	0.155	0.114	1.369	1.926	1.350	1.977
Fe	1.591	1.587	1.510	0.224	0.754	0.259	0.888	0.261	0.888	0.003	0.002	0.019	1.845
Mn	0.036	0.032	0.030	0.002	0.007	0.002	0.014	0.007	0.011	0.000	0.000	0.000	0.046
Mg	0.653	0.684	0.730	0.739	0.936	0.700	0.979	0.710	0.991	0.000	0.000	0.000	0.577
Ca	0.668	0.668	0.712	0.876	0.229	0.886	0.036	0.865	0.027	0.372	0.922	0.346	0.565
Na	0.000	0.000	0.000	0.066	0.012	0.052	0.004	0.053	0.001	0.619	0.074	0.618	0.007
K	0.000	0.003	0.000	0.000	0.000	0.001	0.000	0.001	0.001	0.006	0.001	0.004	0.002
Total	7.976	7.987	8.002	4.001	4.003	4.000	3.991	4.001	3.989	4.998	5.000	4.987	8.018

(*continued*)

TABLE 2-1. MINERAL COMPOSITIONS OF HAIYANGSUO GRANULITE *(continued)*

Sample No.:	03-R14												
Mineral:	Grt2	Grt1	Grt1	Grt2	Grt2	Grt2	Cpx	Cpx	Cpx	Grt2	Cpx	Pl	Pl
Texture:		312	314	327	328	330	core	mantle	rim	f	f		
SiO_2	38.63	38.80	38.68	38.92	39.51	38.45	51.11	51.83	52.55	38.32	52.40	57.54	56.75
TiO_2	0.03	0.01	0.01	0.03	0.00	0.06	0.17	0.29	0.08	0.03	0.11	0.06	0.01
Cr_2O_3	0.04	0.00	0.00	0.00	0.06	0.02	0.00	0.00	0.01	0.00	0.05	0.01	0.00
Al_2O_3	21.70	21.59	21.84	21.58	22.10	21.28	2.38	2.00	1.29	21.99	1.55	26.11	26.56
FeO	25.98	29.03	28.80	27.26	27.30	26.33	11.37	11.00	9.39	25.42	8.59	0.24	0.34
MnO	0.55	0.69	0.80	0.64	0.55	0.48	0.03	0.06	0.11	0.43	0.06	0.00	0.00
MgO	4.64	4.43	4.67	4.46	4.55	4.21	11.43	11.52	12.48	3.45	12.83	0.00	0.01
CaO	8.91	6.64	6.40	8.47	8.60	8.94	21.51	21.51	22.40	10.83	23.17	8.28	8.59
Na_2O	0.01	0.02	0.00	0.04	0.00	0.01	0.44	0.39	0.36	0.05	0.39	6.90	6.67
K_2O	0.01	0.03	0.03	0.01	0.02	0.02	0.00	0.04	0.04	0.01	0.02	0.20	0.15
Total	100.49	101.25	101.22	101.42	102.67	99.80	98.44	98.63	98.72	100.53	99.17	99.33	99.08
Si	3.003	3.015	3.003	3.010	3.011	3.017	1.956	1.974	1.990	2.986	1.973	2.597	2.572
Ti	0.002	0.001	0.001	0.002	0.000	0.004	0.005	0.008	0.002	0.002	0.003	0.002	0.000
Cr	0.002	0.000	0.000	0.000	0.003	0.001	0.000	0.000	0.000	0.000	0.002	0.000	0.000
Al	1.988	1.978	1.998	1.968	1.985	1.968	0.108	0.090	0.058	2.020	0.069	1.389	1.418
Fe	1.689	1.887	1.870	1.763	1.740	1.728	0.364	0.351	0.297	1.657	0.271	0.009	0.013
Mn	0.036	0.046	0.053	0.042	0.035	0.032	0.001	0.002	0.004	0.029	0.002	0.000	0.000
Mg	0.538	0.513	0.540	0.515	0.517	0.493	0.652	0.654	0.704	0.401	0.720	0.000	0.001
Ca	0.742	0.553	0.532	0.702	0.702	0.752	0.882	0.878	0.909	0.905	0.935	0.400	0.417
Na	0.002	0.004	0.000	0.007	0.001	0.001	0.033	0.029	0.027	0.008	0.028	0.604	0.586
K	0.001	0.003	0.003	0.001	0.002	0.002	0.000	0.002	0.002	0.001	0.001	0.012	0.009
Total	8.002	7.999	7.999	8.009	7.996	7.997	4.001	3.988	3.993	8.007	4.003	5.014	5.016

(*continued*)

TABLE 2-1. MINERAL COMPOSITIONS OF HAIYANGSUO GRANULITE *(continued)*

Sample No.:				HY15D								HY15E	
Mineral:	Kfs	Ms	Ilm	Grt	Grt	Grt	Grt	Opx	Opx	Cpx	Cpx	Grt-por	Grt-por
Texture:		af pl										rim	mantle
SiO_2	63.99	49.38	0.05	38.54	38.61	37.89	38.13	52.21	51.56	52.47	51.99	38.54	38.48
TiO_2	0.00	0.02	55.27	0.00	0.02	0.00	0.03	0.02	0.06	0.06	0.10	0.06	0.21
Cr_2O_3	0.04	0.01	0.07	0.09	0.10	0.11	0.11	0.05	0.08	0.12	0.12	0.05	0.07
Al_2O_3	18.29	34.79	0.00	21.39	21.35	21.36	21.44	0.59	0.70	1.20	1.28	21.95	22.25
FeO	0.05	0.75	44.55	27.67	28.09	28.27	28.25	28.31	27.73	9.14	9.23	29.65	28.60
MnO	0.06	0.02	0.00	0.78	0.78	0.79	0.81	0.24	0.20	0.06	0.09	0.77	0.61
MgO	0.00	0.27	1.22	4.71	4.30	4.01	4.58	18.36	18.40	12.85	12.59	4.01	5.04
CaO	0.01	0.32	0.03	6.83	6.68	6.69	6.46	0.30	0.37	22.09	22.53	6.78	6.60
Na_2O	0.14	1.20	0.01	0.04	0.00	0.00	0.00	0.01	0.02	0.36	0.31	0.00	0.00
K_2O	16.21	9.68	0.00	0.03	0.00	0.00	0.01	0.00	0.00	0.00	0.01	0.01	0.04
Total	98.79	96.43	101.20	100.08	99.93	99.12	99.82	100.08	99.12	98.35	98.25	101.81	101.89
Si	2.995	3.359	0.001	3.022	3.034	3.011	3.005	1.994	1.987	1.991	1.980	2.989	2.965
Ti	0.000	0.001	1.019	0.000	0.001	0.000	0.002	0.000	0.002	0.002	0.003	0.003	0.012
Cr	0.001	0.001	0.001	0.006	0.006	0.007	0.007	0.002	0.002	0.004	0.004	0.003	0.004
Al	1.009	2.792	0.000	1.977	1.978	2.001	1.992	0.027	0.032	0.054	0.058	2.006	2.021
Fe	0.002	0.043	0.913	1.814	1.846	1.879	1.862	0.904	0.894	0.290	0.294	1.923	1.843
Mn	0.002	0.001	0.000	0.040	0.041	0.041	0.042	0.006	0.005	0.002	0.002	0.051	0.040
Mg	0.000	0.027	0.044	0.550	0.504	0.475	0.538	1.045	1.057	0.727	0.715	0.464	0.579
Ca	0.001	0.023	0.001	0.574	0.563	0.570	0.546	0.012	0.015	0.898	0.920	0.563	0.545
Na	0.013	0.157	0.001	0.006	0.000	0.000	0.000	0.000	0.001	0.026	0.023	0.000	0.000
K	0.968	0.840	0.000	0.003	0.000	0.000	0.001	0.000	0.000	0.000	0.000	0.001	0.004
Total	4.991	7.243	1.980	7.992	7.973	7.985	7.994	3.991	3.995	3.992	3.998	8.003	8.013

(continued)

VTABLE 2-1. MINERAL COMPOSITIONS OF HAIYANGSUO GRANULITE *(continued)*

Sample No.:	HY15E												
Mineral:	Grt-por	Grt-por	Grt-por	Grt-por	Grt-por	Grt	Opx	Grt	Opx	Grt	Opx	Bt	Ilm
Texture:	core	core	mantle	rim	rim	core	core	rim	rim	core	305	inc	inc
$Si0_2$	38.40	38.21	37.78	38.22	38.64	39.28	52.41	38.56	51.29	38.74	51.89	36.88	0.18
TiO^2	0.02	0.03	0.00	0.02	0.00	0.00	0.00	0.01	0.03	0.10	0.00	2.45	51.69
Cr_2O_3	0.04	0.02	0.04	0.04	0.07	0.01	0.06	0.09	0.00	0.08	0.00	0.09	0.01
Al_2O_3	22.08	22.24	21.68	21.53	21.72	21.96	0.79	21.50	0.49	21.39	0.38	15.10	0.05
FeO	29.23	27.73	28.30	28.21	29.24	30.93	32.28	30.60	31.95	30.43	32.37	19.50	46.70
MnO	0.70	0.67	0.79	0.67	0.85	0.83	0.28	0.82	0.28	0.84	0.24	0.02	0.08
MgO	4.69	5.00	4.53	4.64	4.04	3.61	16.01	3.41	15.61	3.48	16.30	12.14	0.78
CaO	6.58	6.74	6.04	6.71	6.88	7.03	0.84	6.79	0.31	6.94	0.33	0.05	0.50
Na_2O	0.02	0.01	0.04	0.10	0.01	0.03	0.04	0.00	0.01	0.00	0.06	0.25	0.04
K_2O	0.02	0.02	0.03	0.03	0.00	0.02	0.04	0.02	0.06	0.01	0.00	8.63	0.05
Total	101.78	100.68	99.22	100.17	101.45	103.70	102.74	101.79	100.03	102.00	101.57	95.11	100.09
Si	2.972	2.972	2.992	2.998	3.004	3.004	1.986	3.006	3.994	3.012	1.990	2.808	0.018
Ti	0.001	0.002	0.000	0.001	0.000	0.000	0.000	0.001	0.002	0.006	0.000	0.140	3.916
Cr	0.003	0.001	0.002	0.003	0.005	0.001	0.002	0.005	0.000	0.005	0.000	0.006	0.006
Al	2.015	2.039	2.024	1.991	1.990	1.980	0.035	1.976	0.045	1.960	0.017	1.355	0.000
Fe	1.892	1.804	1.874	1.851	1.901	1.978	1.023	1.995	2.081	1.979	1.038	1.242	0.054
Mn	0.046	0.044	0.053	0.045	0.056	0.053	0.009	0.054	0.019	0.055	0.008	0.001	3.935
Mg	0.542	0.580	0.534	0.542	0.468	0.411	0.904	0.396	1.812	0.404	0.932	1.378	0.116
Ca	0.546	0.562	0.512	0.564	0.573	0.576	0.034	0.567	0.026	0.578	0.013	0.004	0.007
Na	0.002	0.001	0.007	0.014	0.002	0.005	0.003	0.000	0.001	0.000	0.004	0.036	0.007
K	0.002	0.002	0.003	0.003	0.000	0.002	0.002	0.002	0.006	0.001	0.000	0.838	0.009
Total	8.020	8.008	8.001	8.013	7.999	8.009	3.998	8.004	7.985	8.000	4.003	7.808	8.070

Note: crn—corona; crn-pl—corona contact with Pl; af—after; por—porphyroblast (see Fig. 5C); pse—pseudomorph; la i Cpx—lamellae in Cx; f—in small domain of Cpx-Pl-Grt (see text).

TABLE 2-2. MINERAL COMPOSITIONS OF RETROGRADE GARNET AMPHIBOLITE FROM GRANULITE

Sample No.:	HY12C												
Mineral:	Grt	Grt	Ilm	Zo	Ttn	Ms	Amp	Amp	Amp	Amp	Amp	Amp	Ttn
Texture:							relict-c	relict-m	relict-r				
SiO_2	38.74	38.86	0.34	39.07	30.09	48.49	42.2	42.32	44.03	43.71	42.81	40.83	30.66
TiO_2	0.09	0.04	51.42	0.07	38.39	0	1.15	0.88	0.41	0.44	0.75	0.6	37.97
Cr_2O_3	0.11	0.1	0.08	0.05	0.07	0.05	0.18	0.25	0.2	0.11	0.17	0.14	0.06
Al_2O_3	21.80	21.72	0.11	29.50	1.47	35.66	14.54	15.05	14.84	15.36	14.48	16.2	1.31
FeO	25.92	24.8	41.68	4.90	0.09	0.85	13.5	13.45	13.37	13.21	13.66	13.57	0.60
MnO	1.17	1.18	4.00	0.05	0.05	0.06	0.16	0.16	0.19	0.15	0.14	0.18	0.03
MgO	5.85	6.44	0.13	0.06	0.03	0.58	9.77	9.69	9.88	10.09	9.84	9.04	0.00
CaO	6.84	6.8	0.60	23.41	27.85	0.17	11.42	11.2	11.48	11.66	11.51	11.46	27.45
Na_2O	0.00	0.04	0.00	0.00	0.00	0.22	1.32	1.33	1.29	1.37	1.38	0.02	0.03
K_2O	0.00	0.04	0.01	0.00	0.00	8.37	1.35	0.82	0.48	0.47	0.92	0.02	0.00
Total	100.53	99.28	98.37	96.63	98.85	94.45	95.59	95.15	96.17	96.57	95.65	95.58	98.11
Si	3.003	3.013	0.009	6.059	0.999	3.186	6.361	6.362	6.515	6.441	6.242	6.230	1.017
Ti	0.005	0.002	0.994	0.008	0.959	0.000	0.130	0.100	0.046	0.049	0.085	0.065	0.947
Cr	0.007	0.006	0.002	0.006	0.002	0.003	0.022	0.030	0.023	0.013	0.020	0.017	0.002
Al	1.992	1.985	0.003	5.393	0.058	2.761	2.584	2.667	2.589	2.668	2.520	2.914	0.051
Fe^{3+}	0.000	0.000	0.000	0.572	0.000	0.000	0.049	0.144	0.105	0.114	0.078	0.127	
Fe^{2+}	1.681	1.608	0.896	0.000	0.002	0.047	1.653	1.547	1.547	1.514	1.636	1.605	0.017
Mn	0.060	0.060	0.068	0.005	0.001	0.003	0.020	0.020	0.024	0.019	0.018	0.023	0.001
Mg	0.676	0.744	0.005	0.014	0.001	0.057	2.195	2.171	2.179	2.216	2.201	2.056	0.000
Ca	0.568	0.565	0.017	3.890	0.991	0.012	1.845	1.804	1.820	1.841	1.851	1.874	0.975
Na	0.000	0.006	0.000	0.000	0.000	0.028	0.386	0.388	0.370	0.391	0.402	0.423	0.002
K	0.000	0.004	0.000	0.000	0.000	0.702	0.260	0.157	0.091	0.088	0.176	0.110	0.000
Total	7.992	7.994	1.994	15.947	3.013	6.797	15.505	15.390	15.309	15.354	15.229	15.444	3.011

(*continued*)

TABLE 2-2. MINERAL COMPOSITIONS OF RETROGRADE GARNET AMPHIBOLITE FROM GRANULITE (*continued*)

Sample No.:	HY12C	HY15B			
Mineral:	Ttn	Grt	Amp	Cum	Amp
Texture:					
SiO_2	30.85	38.47	45.12	54.27	52.43
TiO_2	38.67	0.01	0.42	0.00	0.16
Cr_2O_3	0.00	0.07	0.10	0.04	0.02
Al2O3	0.88	22.14	12.86	0.53	3.75
FeO	0.13	27.08	14.73	24.34	15.13
MnO	0.06	0.62	0.07	0.22	0.08
MgO	0.00	5.22	10.50	16.66	14.84
CaO	29.02	6.50	11.09	0.74	9.30
Na_2O	0.00	0.01	1.61	0.03	0.42
K_2O	0.00	0.03	0.30	0.00	0.04
Total	99.28	100.15	96.80	96.83	96.15
Si	1.010	2.997	6.645	8.016	7.673
Ti	0.952	0.001	0.047	0.000	0.018
Cr	0.000	0.004	0.012	0.005	0.002
Al	0.034	2.033	2.233	0.092	0.647
Fe^{3+}			0.227		0.049
Fe^{2+}	0.004	1.765	1.588	3.007	1.803
Mn	0.001	0.032	0.009	0.028	0.010
Mg	0.000	0.606	2.305	3.667	3.237
Ca	1.018	0.543	1.750	0.117	1.458
Na	0.000	0.002	0.460	0.009	0.119
K	0.000	0.003	0.056	0.000	0.008
Total	3.020	7.985	15.332	14.941	15.024

Note: c—core; m—mantle; r—rim. Ferric iron for calcic amphibole was calculated using a procedure by Schumacher (1991).

TABLE 3-1. COMPOSITIONS OF MINERALS FROM THE HAIYANGSUO METAGABBRO

Sample No.:	HY1A												
Mineral:	Grt	Grt	Grt	Grt	Grt	Grt	Cpx	Cpx	Cpx	Cpx	Opx	Opx	Opx
Texture:	crn	crn	crn	crn	crn	f	f	f	core	rim	core	mantle	rim
SiO_2	38.43	37.93	39.21	38.99	38.50	38.64	52.65	52.82	50.47	52.18	51.57	51.50	51.08
TiO_2	0.00	0.01	0.05	0.34	0.32	0.03	0.09	0.08	0.25	0.17	0.05	0.04	0.00
Cr_2O_3	0.03	0.04	0.00	0.00	0.05	0.06	0.02	0.02	0.05	0.03	0.04	0.01	0.05
Al_2O_3	21.55	21.40	21.91	21.88	21.41	21.10	1.69	1.60	2.49	2.02	0.90	0.82	0.88
FeO	27.09	27.24	27.99	27.15	26.91	31.85	9.91	8.46	13.00	11.73	29.29	29.92	29.81
MnO	1.05	0.91	0.92	0.20	0.19	1.04	0.04	0.01	0.12	0.11	0.35	0.29	0.33
MgO	3.77	3.32	4.11	4.21	3.84	1.78	12.08	12.73	9.77	10.97	16.25	16.45	16.31
CaO	7.38	8.47	7.53	7.26	8.26	6.76	22.15	22.53	21.15	21.47	1.44	0.65	0.36
Na_2O	0.04	0.00	0.02	0.04	0.05	0.02	0.82	0.93	0.90	0.71	0.11	0.06	0.06
K_2O	0.00	0.00	0.02	0.00	0.01	0.00	0.00	0.03	0.01	0.00	0.01	0.00	0.02
Total	99.34	99.32	101.76	100.07	99.55	101.28	99.46	99.21	98.21	99.39	100.01	99.74	98.90
					0								
Si	3.036	3.011	3.026	3.036	3.026	3.048	1.983	1.984	1.956	1.980	1.990	1.993	1.994
Ti	0.000	0.001	0.003	0.020	0.019	0.002	0.003	0.002	0.007	0.005	0.001	0.001	0.000
Cr	0.002	0.003	0.000	0.000	0.003	0.004	0.001	0.001	0.002	0.001	0.001	0.000	0.002
Al	2.006	2.002	1.993	2.008	1.984	1.962	0.075	0.071	0.114	0.090	0.041	0.037	0.040
Fe	1.790	1.808	1.807	1.768	1.769	2.101	0.312	0.266	0.421	0.372	0.945	0.969	0.973
Mn	0.055	0.048	0.047	0.010	0.010	0.069	0.001	0.000	0.003	0.003	0.009	0.007	0.009
Mg	0.444	0.393	0.473	0.489	0.450	0.209	0.678	0.713	0.564	0.620	0.935	0.949	0.949
Ca	0.625	0.720	0.623	0.606	0.696	0.571	0.894	0.907	0.878	0.873	0.060	0.027	0.015
Na	0.006	0.000	0.003	0.006	0.008	0.003	0.060	0.068	0.068	0.052	0.008	0.005	0.005
K	0.000	0.000	0.002	0.000	0.001	0.000	0.000	0.001	0.000	0.000	0.000	0.000	0.001
Total	7.963	7.986	7.977	7.943	7.966	7.969	4.007	4.013	4.013	3.996	3.991	3.989	3.988

(*continued*)

TABLE 3-1. COMPOSITIONS OF MINERALS FROM THE HAIYANGSUO METAGABBRO (*continued*)

Sample No.:	HY1A								HY1B				
Mineral:	Cpx	Grt	Grt	Grt	Zo	Pl	Pl	Ilm	Grt	Grt	Grt	Grt	Opx
Texture:		crn-cpx	core	crn-pl	needle	pse			crn	crn	crn	crn	
SiO_2	51.15	38.33	38.46	38.79	40.44	52.44	53.88	0.04	38.42	38.10	38.34	38.27	51.42
TiO_2	0.20	0.07	0.06	0.03	0.08	0.00	0.02	52.68	0.07	0.09	0.07	0.21	0.02
Cr_2O_3	0.00	0.00	0.02	0.00	0.04	0.02	0.07	0.00	0.08	0.05	0.07	0.08	0.07
Al_2O_3	2.36	21.14	21.59	21.35	30.01	30.31	28.85	0.04	21.49	21.55	21.60	21.58	0.92
FeO	12.68	28.53	27.59	26.32	4.07	0.09	0.10	45.01	27.90	31.00	29.04	31.20	29.05
MnO	0.14	0.14	0.11	0.05	0.02	0.03	0.00	0.19	1.29	1.19	0.99	1.27	0.34
MgO	9.85	2.77	3.04	3.00	0.09	0.00	0.01	0.34	3.64	2.62	3.12	2.28	16.11
CaO	21.29	8.40	8.93	9.81	23.10	12.82	10.91	0.00	7.40	6.84	7.26	6.82	1.25
Na_2O	0.86	0.05	0.01	0.04	0.20	3.99	5.19	0.05	0.04	0.00	0.02	0.00	0.08
K_2O	0.00	0.00	0.00	0.00	0.02	0.04	0.08	0.00	0.01	0.00	0.00	0.00	0.00
Total	98.53	99.43	99.81	99.39	98.05	99.74	99.11	98.35	100.34	101.44	100.51	101.71	99.24
					0								
Si	1.970	3.041	3.027	3.054	6.172	2.381	2.453	0.001	3.021	2.999	3.018	3.007	1.997
Ti	0.006	0.004	0.004	0.002	0.009	0.000	0.001	1.010	0.004	0.005	0.004	0.012	0.000
Cr	0.000	0.000	0.001	0.000	0.005	0.001	0.003	0.000	0.005	0.003	0.004	0.005	0.002
Al	0.107	1.977	2.003	1.981	5.399	1.622	1.548	0.001	1.992	2.000	2.004	1.998	0.042
Fe	0.408	1.893	1.816	1.733	0.468	0.003	0.004	0.959	1.835	2.041	1.912	2.050	0.944
Mn	0.004	0.007	0.006	0.003	0.002	0.001	0.000	0.003	0.067	0.062	0.051	0.066	0.009
Mg	0.565	0.328	0.357	0.352	0.019	0.000	0.001	0.013	0.427	0.307	0.366	0.267	0.932
Ca	0.879	0.714	0.753	0.827	3.778	0.624	0.532	0.000	0.623	0.577	0.612	0.574	0.052
Na	0.064	0.008	0.002	0.006	0.059	0.351	0.458	0.002	0.006	0.000	0.003	0.000	0.006
K	0.000	0.000	0.000	0.000	0.003	0.002	0.005	0.000	0.001	0.000	0.000	0.000	0.000
Total	4.003	7.971	7.968	7.957	15.914	4.985	5.003	1.990	7.980	7.994	7.975	7.979	3.984

(*continued*)

TABLE 3-1. COMPOSITIONS OF MINERALS FROM THE HAIYANGSUO METAGABBRO (*continued*)

Sample No.:	HY1B								HY1E				
Mineral:	Opx	Cpx	Cpx	Cpx	Cpx	Pl	Pl	Ky	Grt	Grt	Grt	Cpx	Cpx
Texture:				core	rim	pse	pse	needle	crn	crn	crn	412c	413m
SiO_2	51.63	52.10	52.44	51.42	51.98	55.42	63.31	40.72	38.77	38.43	38.60	51.99	51.99
TiO_2	0.02	0.10	0.09	0.18	0.09	0.01	0.00	0.02	0.03	0.01	0.01	0.12	0.08
Cr_2O_3	0.01	0.12	0.07	0.08	0.07	0.07	0.08	0.05	0.04	0.00	0.00	0.02	0.03
Al_2O_3	0.69	1.99	1.85	2.77	1.82	27.93	22.90	55.98	21.76	21.68	21.91	2.09	1.98
FeO	32.29	12.17	11.77	12.76	11.62	0.29	0.60	1.43	27.97	26.63	29.12	11.58	11.66
MnO	0.25	0.17	0.08	0.17	0.15	0.00	0.01	0.00	0.73	0.71	0.82	0.11	0.04
MgO	15.01	11.18	11.21	9.92	10.59	0.02	0.00	0.17	3.50	3.43	3.91	11.32	11.40
CaO	0.41	20.43	21.48	20.83	21.73	10.19	4.38	1.11	8.76	9.78	7.12	21.27	21.30
Na_2O	0.02	0.88	0.43	0.99	0.88	5.54	8.92	0.87	0.02	0.00	0.00	0.85	0.89
K_2O	0.01	0.01	0.00	0.00	0.03	0.08	0.04	0.05	0.03	0.02	0.03	0.00	0.01
Total	100.34	99.14	99.39	99.12	98.96	99.55	100.24	100.40	101.60	100.70	101.52	99.34	99.38
Si	2.005	1.982	1.986	1.966	1.985	2.506	2.797	1.106	3.007	3.001	2.999	1.973	1.973
Ti	0.001	0.003	0.002	0.005	0.003	0.000	0.000	0.000	0.002	0.001	0.001	0.003	0.002
Cr	0.000	0.004	0.002	0.002	0.002	0.003	0.003	0.001	0.002	0.000	0.000	0.001	0.001
Al	0.032	0.089	0.083	0.125	0.082	1.489	1.192	1.793	1.989	1.995	2.006	0.093	0.089
Fe	1.049	0.387	0.373	0.408	0.371	0.011	0.022	0.032	1.814	1.739	1.892	0.368	0.370
Mn	0.006	0.004	0.002	0.004	0.004	0.000	0.000	0.000	0.048	0.047	0.054	0.004	0.001
Mg	0.869	0.634	0.633	0.565	0.603	0.001	0.000	0.007	0.405	0.400	0.453	0.640	0.645
Ca	0.017	0.833	0.872	0.853	0.889	0.494	0.207	0.032	0.728	0.818	0.593	0.865	0.866
Na	0.002	0.065	0.031	0.073	0.065	0.486	0.764	0.046	0.003	0.000	0.000	0.063	0.065
K	0.000	0.000	0.000	0.000	0.001	0.005	0.002	0.002	0.003	0.002	0.003	0.000	0.001
Total	3.980	4.001	3.984	4.002	4.004	4.994	4.989	3.020	7.999	8.002	7.999	4.008	4.013

(*continued*)

TABLE 3-1. COMPOSITIONS OF MINERALS FROM THE HAIYANGSUO METAGABBRO (*continued*)

Sample No.:	HY1E										HY12G		
Mineral:	Cpx	Pl	Pl	Grt	Grt	Grt	Cpx	Cpx	Cpx	Pl	Opx*	Grt*	Grt*
Texture:	rim			f	f	f	f-core	f-mantle	f-rim	f		crn-opx	crn
SiO_2	52.60	52.51	54.04	38.46	38.84	38.77	53.02	53.94	52.33	60.72	51.33	38.77	38.94
TiO_2	0.09	0.00	0.00	0.00	0.00	0.06	0.09	0.06	0.11	0.00	0.03	0.00	0.02
Cr_2O_3	0.02	0.06	0.06	0.00	0.00	0.00	0.00	0.00	0.00	0.00	0.02	0.02	0.00
Al_2O_3	1.70	30.52	29.46	21.69	21.95	21.90	1.78	1.54	2.15	25.54	0.60	21.64	21.33
FeO	11.52	0.24	0.00	27.35	27.74	27.64	8.34	8.89	8.90	0.24	28.78	27.63	27.55
MnO	0.10	0.00	0.00	0.64	0.72	0.58	0.05	0.06	0.05	0.00	0.25	0.84	0.83
MgO	11.38	0.01	0.02	3.90	4.00	3.83	12.62	13.16	12.40	0.01	17.47	3.43	3.36
CaO	21.22	12.59	11.19	8.67	8.40	8.81	22.52	22.78	22.19	6.44	0.35	7.60	8.44
Na_2O	0.93	4.28	5.04	0.01	0.01	0.00	0.74	0.76	0.77	8.12	0.01	0.01	0.00
K_2O	0.02	0.05	0.09	0.02	0.01	0.00	0.01	0.01	0.02	0.06	0.01	0.03	0.01
Total	99.59	100.25	99.89	100.73	101.66	101.58	99.18	101.19	98.93	101.12	98.85	99.97	100.48
Si	1.989	2.374	2.440	3.001	3.002	3.000	1.988	1.986	1.973	2.675	1.994	3.045	3.049
Ti	0.003	0.000	0.000	0.000	0.000	0.004	0.003	0.002	0.003	0.000	0.001	0.000	0.001
Cr	0.000	0.002	0.002	0.000	0.000	0.000	0.000	0.000	0.000	0.000	0.001	0.001	0.000
Al	0.076	1.626	1.568	1.995	1.999	1.997	0.079	0.067	0.096	1.326	0.027	2.004	1.968
Fe	0.364	0.009	0.000	1.785	1.793	1.789	0.262	0.274	0.281	0.009	0.935	1.815	1.804
Mn	0.003	0.000	0.000	0.042	0.047	0.038	0.002	0.002	0.002	0.000	0.006	0.044	0.043
Mg	0.641	0.000	0.001	0.453	0.461	0.442	0.705	0.722	0.697	0.000	1.011	0.402	0.392
Ca	0.860	0.610	0.541	0.725	0.696	0.730	0.905	0.899	0.897	0.304	0.015	0.640	0.708
Na	0.068	0.376	0.442	0.001	0.001	0.000	0.054	0.054	0.056	0.694	0.000	0.002	0.000
K	0.001	0.003	0.005	0.002	0.001	0.000	0.001	0.001	0.001	0.003	0.000	0.003	0.001
Total	4.005	5.001	4.998	8.003	8.000	7.999	3.997	4.006	4.005	5.011	3.991	7.955	7.966

(*continued*)

TABLE 3-1. COMPOSITIONS OF MINERALS FROM THE HAIYANGSUO METAGABBRO (*continued*)

Sample No.:	HY12G												
Mineral:	Grt*	Grt*	Grt*	Grt*	Ky*	Pl*	Pl*	Zo*	Grt	Grt	Grt	Grt	Cpx
Texture:	crn	crn	crn	crn- pl	needle	pse	pse	needle	crn	crn	crn	in pl	
SiO_2	38.97	39.04	38.62	38.99	38.32	55.16	49.99	39.90	38.67	38.73	39.22	38.82	52.90
TiO_2	0.00	0.03	0.00	0.02	0.00	0.02	0.00	0.06	0.02	0.01	0.07	0.07	0.13
Cr_2O_3	0.00	0.00	0.00	0.00	0.05	0.03	0.01	0.00	0.01	0.02	0.00	0.01	0.01
Al_2O_3	21.55	21.66	21.63	21.94	61.37	29.05	32.08	30.47	21.76	22.31	21.91	21.83	2.20
FeO	26.61	26.54	22.04	21.13	0.24	0.02	0.23	3.92	29.03	26.16	23.35	26.52	11.05
MnO	0.71	0.67	0.51	0.48	0.00	0.01	0.00	0.00	1.03	0.76	0.75	0.65	0.08
MgO	3.02	3.13	2.40	2.30	0.00	0.01	0.15	0.06	3.41	2.95	2.43	3.26	10.90
CaO	9.38	10.15	14.80	15.19	0.78	10.83	14.83	24.22	7.31	10.22	13.48	10.08	21.80
Na_2O	0.06	0.01	0.00	0.01	0.19	5.09	1.75	0.03	0.03	0.01	0.02	0.01	0.99
K_2O	0.00	0.02	0.04	0.02	0.00	0.07	1.15	0.00	0.01	0.01	0.00	0.01	0.00
Total	100.30	101.25	100.04	100.08	100.95	100.27	100.19	98.66	101.29	101.18	101.23	101.26	100.05
Si	3.049	3.030	3.015	3.028	1.028	2.474	2.279	6.073	3.018	3.004	3.029	3.012	1.987
Ti	0.000	0.002	0.000	0.001	0.000	0.001	0.000	0.007	0.001	0.001	0.004	0.004	0.004
Cr	0.000	0.000	0.000	0.000	0.001	0.001	0.000	0.000	0.000	0.001	0.000	0.001	0.000
Al	1.987	1.981	1.990	2.008	1.940	1.536	1.724	5.466	2.001	2.040	1.994	1.997	0.097
Fe	1.741	1.723	1.439	1.372	0.005	0.001	0.009	0.449	1.895	1.697	1.508	1.721	0.347
Mn	0.037	0.034	0.026	0.025	0.000	0.000	0.000	0.000	0.053	0.039	0.038	0.033	0.002
Mg	0.352	0.362	0.279	0.266	0.000	0.000	0.010	0.014	0.397	0.341	0.280	0.377	0.610
Ca	0.786	0.844	1.238	1.264	0.022	0.520	0.725	3.950	0.612	0.850	1.115	0.838	0.877
Na	0.009	0.002	0.000	0.002	0.010	0.443	0.155	0.009	0.005	0.002	0.003	0.002	0.072
K	0.000	0.002	0.004	0.002	0.000	0.004	0.067	0.000	0.001	0.001	0.000	0.001	0.000
Total	7.962	7.980	7.992	7.968	3.007	4.980	4.969	15.967	7.983	7.976	7.972	7.986	3.996

(*continued*)

TABLE 3-1. COMPOSITIONS OF MINERALS FROM THE HAIYANGSUO METAGABBRO (*continued*)

Sample No.:	HY12G						
Mineral:	Cpx	Grt	Cpx	Opx	Opx	Ilm	Pl
Texture:	host	la i cpx					
SiO_2	52.23	37.95	53.00	51.45	51.95	0.03	54.34
TiO2	0.05	0.01	0.08	0.00	0.06	52.44	0.01
Cr_2O_3	0.00	0.06	0.02	0.00	0.02	0.04	0.04
Al_2O_3	2.11	20.87	2.18	0.90	0.66	0.02	28.81
FeO	12.49	29.65	11.15	30.96	29.28	46.07	0.13
MnO	0.12	1.26	0.06	0.38	0.20	0.37	0.00
MgO	10.57	2.37	11.07	16.72	17.32	0.38	0.02
CaO	21.90	8.12	21.99	0.34	0.29	0.00	10.99
Na_2O	0.98	0.02	0.95	0.00	0.00	0.02	4.85
K_2O	0.00	0.01	0.00	0.00	0.00	0.00	0.03
Total	100.43	100.29	100.50	100.75	99.78	99.37	99.22
Si	1.972	3.021	1.983	1.980	1.999	0.001	2.466
Ti	0.001	0.000	0.002	0.000	0.002	0.999	0.000
Cr	0.000	0.003	0.001	0.000	0.001	0.001	0.001
Al	0.094	1.958	0.096	0.041	0.030	0.001	1.541
Fe	0.394	1.974	0.349	0.996	0.942	0.976	0.005
Mn	0.003	0.066	0.001	0.010	0.005	0.006	0.000
Mg	0.595	0.281	0.617	0.959	0.993	0.014	0.001
Ca	0.886	0.693	0.882	0.014	0.012	0.000	0.534
Na	0.072	0.002	0.069	0.000	0.000	0.001	0.427
K	0.000	0.001	0	0.000	0.000	0.000	0.002
Total	4.016	8.000	4.001	4.000	3.984	2.000	4.977

*From Opx through garnet corona to plagioclase pseudomorph, see Fig. 9; other explanations are same as Table 2.

TABLE 3-2. COMPOSITIONS OF MINERALS FROM GARNET AMPHIBOLITE WITH GABBROIC PROTOLITH

Sample No.:	HY1C						HY7D						
Mineral:	Grt	Grt	Grt	Amp	Pl	Zo	Grt	Grt	Cpx	Pl	Amp	Amp	Amp
Texture:												relic-r	
SiO_2	38.71	38.46	38.49	41.60	57.01	38.19	39.17	38.93	53.39	65.58	50.35	41.60	46.11
TiO2	0.06	0.02	0.06	0.38	0.01	0.15	0.05	0.03	0.10	0.00	0.15	0.95	0.54
Cr_2O_3	0.04	0.05	0.13	0.09	0.06	0.04	0.01	0.03	0.08	0.01	0.02	0.04	0.01
Al_2O_3	21.22	21.25	21.11	14.91	26.67	26.62	21.68	21.92	2.04	21.84	5.89	13.81	10.46
FeO	27.40	27.87	27.56	19.85	0.23	8.35	24.85	23.93	9.53	0.26	13.35	16.57	14.19
MnO	0.78	2.12	0.92	0.26	0.00	0.08	0.48	0.41	0.09	0.00	0.09	0.01	0.04
MgO	4.83	2.46	3.82	6.58	0.01	0.02	4.51	3.83	12.21	0.01	13.10	9.02	11.48
CaO	7.44	8.18	7.53	11.14	8.40	23.61	9.87	11.33	21.28	2.34	12.06	11.57	11.26
Na_2O	0.02	0.04	0.02	1.72	6.29	0.00	0.08	0.05	1.15	9.48	0.64	1.67	1.43
K_2O	0.00	0.00	0.00	0.61	0.06	0.00	0.01	0.02	0.01	0.08	0.23	1.36	0.74
Total	100.50	100.45	99.64	97.13	98.72	97.06	100.71	100.450	99.86	99.60	95.88	96.60	96.26
Si	3.022	3.041	3.039	6.310	2.583	6.023	3.028	3.016	1.993	2.886	7.427	6.309	6.844
Ti	0.004	0.001	0.004	0.043	0.000	0.018	0.003	0.002	0.003	0.000	0.017	0.108	0.060
Cr	0.002	0.003	0.008	0.011	0.002	0.005	0.001	0.002	0.002	0.000	0.002	0.005	0.001
Al	1.953	1.981	1.965	2.667	1.424	4.948	1.975	2.002	0.090	1.133	1.024	2.469	1.830
Fe^{3+}				0.239		0.991					0.030	0.113	0.145
Fe^{2+}	1.789	1.843	1.820	2.279	0.009		1.607	1.551	0.297	0.010	1.617	1.988	1.616
Mn	0.040	0.111	0.048	0.034	0.000	0.008	0.025	0.021	0.002	0.000	0.011	0.001	0.005
Mg	0.562	0.290	0.450	1.488	0.000	0.005	0.520	0.442	0.679	0.001	2.880	2.039	2.539
Ca	0.622	0.693	0.637	1.811	0.408	3.990	0.818	0.940	0.851	0.110	1.906	1.880	1.791
Na	0.003	0.006	0.003	0.506	0.552	0.000	0.012	0.007	0.083	0.809	0.183	0.491	0.412
K	0.000	0.000	0.000	0.117	0.003	0.000	0.001	0.001	0.000	0.004	0.043	0.263	0.140
Total	7.998	7.969	7.973	15.503	4.982	15.987	7.988	7.984	4.000	4.954	15.140	15.666	15.383

(*continued*)

TABLE 3-2. COMPOSITIONS OF MINERALS FROM GARNET AMPHIBOLITE WITH GABBROIC PROTOLITH (*continued*)

Sample No.:	HY7D	HY11A							HY11D				
Mineral:	Ilm	Grt	Zo	Pl	Ms	Amp	Amp	Ilm	Zo	Amp	Amp	Pl	Ms
Texture:			needle									pse	
SiO_2	0.03	38.29	39.36	60.76	48.57	51.82	48.34	0.05	39.18	45.90	46.24	65.83	49.21
TiO_2	52.37	0.04	0.01	0.00	0.00	0.29	0.53	52.43	0.19	0.41	0.96	0.00	0.01
Cr_2O_3	0.04	0.07	0.02	0.03	0.00	0.05	0.09	0.08	0.00	0.04	0.12	0.02	0.00
Al_2O_3	0.03	21.10	29.26	24.54	39.19	3.15	7.40	0.03	29.16	12.57	12.17	22.00	39.04
FeO	44.53	28.75	5.27	0.32	0.15	15.64	17.25	46.05	5.67	14.62	8.93	0.02	0.16
MnO	0.97	1.23	0.07	0.05	0.02	0.07	0.05	0.29	0.08	0.20	0.01	0.00	0.01
MgO	0.35	3.31	0.05	0.00	0.02	13.21	10.85	0.37	0.04	10.61	14.78	0.00	0.20
CaO	0.07	7.51	23.86	6.39	0.07	11.87	11.57	0.00	24.31	11.87	12.12	2.45	0.07
Na_2O	0.05	0.05	0.04	7.41	0.21	0.43	1.01	0.03	0.03	1.25	1.76	10.18	0.30
K_2O	0.00	0.01	0.03	0.06	8.88	0.12	0.25	0.00	0.00	0.31	0.89	0.05	9.11
Total	98.44	100.34	97.44	99.56	97.10	96.65	97.32	99.32	98.08	97.79	97.98	100.55	98.11
Si	0.001	3.024	6.067	2.711	3.096	7.630	7.154	0.001	6.017	6.704	6.622	2.876	3.110
Ti	1.006	0.002	0.001	0.000	0.000	0.032	0.059	0.999	0.022	0.045	0.103	0.000	0.000
Cr	0.001	0.004	0.002	0.001	0.000	0.006	0.011	0.002	0.000	0.005	0.014	0.001	0.000
Al	0.001	1.965	5.316	1.290	2.945	0.547	1.291	0.001	5.278	2.164	2.055	1.133	2.908
Fe^{3+}	0.000		0.611			0.135	0.170		0.655	0.132	0.069		
Fe^{2+}	0.951	1.900		0.012	0.008	1.791	1.965	0.976		1.654	1.000	0.001	0.008
Mn	0.016	0.064	0.007	0.001	0.001	0.009	0.006	0.005	0.008	0.025	0.001	0.000	0.000
Mg	0.013	0.389	0.011	0.000	0.002	2.899	2.393	0.014	0.009	2.310	3.155	0.000	0.019
Ca	0.002	0.635	3.942	0.305	0.005	1.873	1.835	0.000	4.001	1.858	1.860	0.115	0.005
Na	0.002	0.008	0.010	0.641	0.025	0.123	0.290	0.001	0.008	0.354	0.489	0.862	0.037
K	0.000	0.001	0.006	0.003	0.722	0.023	0.047	0.000	0.000	0.058	0.163	0.003	0.734
Total	1.994	7.993	15.975	4.966	6.805	15.068	15.221	1.999	15.998	15.309	15.531	4.990	6.822

(*continued*)

TABLE 3-2. COMPOSITIONS OF MINERALS FROM GARNET AMPHIBOLITE WITH GABBROIC PROTOLITH (*continued*)

Sample No.:	HY11D			HY12F					
Mineral:	Ms	Ilm	Ttn	Grt	Grt	Pl	Zo	Amp	Amp
Texture:				crn-amp	crn-pl		needle	af cpx	
SiO_2	54.90	0.02	30.85	38.60	39.06	52.95	39.51	50.26	49.40
TiO_2	0.02	53.56	38.67	0.03	0.00	0.00	0.07	0.06	0.14
Cr_2O_3	0.05	0.00	0.00	0.00	0.00	0.00	0.05	0.02	0.01
Al_2O_3	31.33	0.00	0.88	21.91	21.75	30.37	29.20	5.75	6.52
FeO	0.36	41.76	0.13	27.33	27.09	0.01	6.58	15.24	17.47
MnO	0.00	2.57	0.06	1.06	1.14	0.00	0.03	0.11	0.12
MgO	0.17	0.13	0.00	3.09	2.13	0.00	0.07	12.38	11.21
CaO	1.02	0.08	29.02	8.64	10.61	12.81	23.90	11.35	11.50
Na2O	2.29	0.03	0.00	0.00	0.02	4.10	0.00	1.04	0.99
K2O	6.55	0.00	0.00	0.00	0.00	0.03	0.02	0.18	0.21
Total	96.69	98.15	99.28	100.66	101.80	100.27	99.43	96.39	97.57
Si	3.484	0.001	1.010	3.019	3.033	2.389	6.023	7.416	7.279
Ti	0.001	1.028	0.952	0.002	0.000	0.000	0.008	0.007	0.016
Cr	0.003	0.000	0.000	0.000	0.000	0.000	0.006	0.002	0.001
Al	2.344	0.000	0.034	2.020	1.991	1.615	5.247	1.000	1.133
Fe^{3+}							0.755	0.148	0.206
Fe^{2+}	0.019	0.891	0.004	1.788	1.759	0.000		1.733	1.947
Mn	0.000	0.043	0.001	0.055	0.058	0.000	0.003	0.014	0.015
Mg	0.016	0.005	0.000	0.360	0.247	0.000	0.016	2.722	2.462
Ca	0.069	0.002	1.018	0.724	0.883	0.619	3.904	1.795	1.816
Na	0.282	0.001	0.000	0.000	0.003	0.359	0.000	0.298	0.283
K	0.530	0.000	0.000	0.000	0.000	0.002	0.004	0.034	0.040
Total	6.748	1.972	3.020	7.969	7.973	4.984	15.966	15.169	15.198

TABLE 4. MINERAL COMPOSITIONS OF GNEISS AND AMPHIBOLITE INTERLAYER

Sample No.:	HY3				HY5E			HY7B			HY17A		
Mineral:	Pl	Kfs	Kfs	Pl	Pl	Pl	Amp	Pl	Pl	Amp	Grt	Amp	Cum
Texture:	host	exs	host	exs									
SiO_2	60.26	64.13	63.00	61.56	63.23	58.65	41.74	63.29	59.88	42.52	37.31	43.43	52.33
TiO_2	0.00	0.00	0.13	0.00	0.01	0.00	0.55	0.00	0.00	0.77	0.02	0.70	0.06
Cr_2O_3	0.00	0	0.00	0.07	0.00	0.00	0.00	0.04	0.00	0.01	0.00	0.02	0.01
Al_2O_3	24.41	18.19	18.53	23.03	22.26	25.33	13.51	21.99	25.17	12.39	21.07	12.30	1.50
FeO	0.02	0.00	0.16	0.07	0.09	0.03	16.80	0.16	0.12	16.67	31.10	16.11	23.87
MnO	0.02	0.00	0.00	0.01	0.00	0.00	0.14	0.00	0.02	0.27	1.04	0.09	0.21
MgO	0.00	0.00	0.00	0.03	0.01	0.00	9.14	0.00	0.00	9.24	3.22	9.89	15.94
CaO	5.58	0.00	0.00	3.95	2.91	6.72	10.73	3.98	6.49	11.62	5.62	10.77	1.11
Na_2O	8.41	0.78	0.94	9.42	9.52	7.76	2.07	8.80	7.14	1.90	0.01	1.72	0.18
K_2O	0.21	16.23	15.72	0.15	0.35	0.06	0.37	0.12	0.09	0.68	0.01	0.45	0.00
Total	98.91	99.33	98.48	98.29	98.36	98.55	95.05	98.38	98.91	96.07	99.40	95.47	95.19
Si	2.709	2.991	2.964	2.775	2.834	2.653	6.363	2.836	2.687	6.470	2.996	6.551	7.886
Ti	0.000	0.000	0.005	0.000	0.000	0.000	0.064	0.000	0.000	0.088	0.001	0.079	0.007
Cr	0.000	0.000	0.000	0.002	0.000	0.000	0.000	0.001	0.000	0.001	0.000	0.002	0.001
Al	1.293	1.000	1.028	1.224	1.176	1.350	2.429	1.162	1.331	2.223	1.994	2.188	0.266
Fe^{3+}							0.334			0.114		0.304	
Fe^{2+}	0.001	0.000	0.006	0.003	0.003	0.001	1.808	0.006	0.005	2.007	2.089	1.728	3.008
Mn	0.001	0.000	0.000	0.000	0.000	0.000	0.018	0.000	0.001	0.035	0.055	0.012	0.021
Mg	0.000	0.000	0.000	0.002	0.001	0.000	2.078	0.000	0.000	2.095	0.385	2.222	3.581
Ca	0.269	0.000	0.000	0.191	0.140	0.326	1.754	0.191	0.312	1.894	0.484	1.741	0.179
Na	0.733	0.071	0.086	0.823	0.827	0.681	0.613	0.765	0.621	0.561	0.002	0.503	0.051
K	0.012	0.966	0.944	0.009	0.020	0.003	0.072	0.007	0.005	0.132	0.001	0.087	0.000
Total	5.017	5.027	5.032	5.028	5.001	5.014	15.533	4.968	4.961	15.620	8.007	15.419	14.999

(*continued*)

TABLE 4. MINERAL COMPOSITIONS OF GNEISS AND AMPHIBOLITE INTERLAYER (*continued*)

Sample No.:	HY17A	HY19A				
Mineral:	Pl	Grt	Amp	Pl	Pl	Ttn
Texture:						
SiO_2	63.29	38.16	42.37	59.79	56.72	30.39
TiO_2	0.00	0.02	0.86	0.03	0.00	39.19
Cr_2O_3	0.04	0.01	0.00	0.00		0.01
Al_2O_3	21.99	21.30	13.16	25.05	26.78	0.96
FeO	0.16	25.06	17.00	0.00	0.04	0.29
MnO	0.00	1.91	0.12	0.00	0.02	0.03
MgO	0.00	2.05	8.48	0.00	0.01	0.00
CaO	3.98	12.08	11.31	6.12	8.43	28.79
Na_2O	8.80	0.00	1.79	8.01	6.83	0.02
K_2O	0.12	0.01	0.36	0.06	0.05	0.00
Total	98.38	100.57	95.45	99.06	98.88	99.68
Si	2.836	3.008	6.462	2.683	2.570	0.996
Ti	0.000	0.001	0.099	0.001	0.000	0.966
Cr	0.001	0.000	0.000	0.000	0.000	0.000
Al	1.162	1.979	2.366	1.325	1.430	0.037
Fe^{3+}	0.000	0.000	0.137	0.000	0.000	0.000
Fe^{2+}	0.006	1.652	2.031	0.000	0.002	0.008
Mn	0.000	0.099	0.016	0.000	0.001	0.001
Mg	0.000	0.240	1.928	0.000	0.001	0.000
Ca	0.191	1.020	1.848	0.294	0.409	1.011
Na	0.765	0.000	0.529	0.697	0.600	0.001
K	0.007	0.001	0.070	0.003	0.003	0.000
Total	4.968	8.001	15.487	5.004	5.016	3.020

TABLE 5. COMPOSITIONS OF AMPHIBOLES FROM GRANULITE AND METAGABBRO

Sample No.:	HY12A			HY12B					03-R14				HY15E
Texture:	Amp1	in cpx	af opx	Amp1	Amp1	Ia in cpx	Amp2	Amp2	Amp1	Amp2	Amp2	Amp2	inc
SiO_2	44.06	46.71	54.38	44.42	46.24	44.96	50.94	51.60	43.50	43.95	53.92	53.71	41.13
TiO2	1.56	0.86	0.14	1.32	0.96	1.05	0.41	0.42	1.04	0.85	0.03	0.18	0.91
Cr_2O_3	0.15	0.09	0.04	0.16	0.12	0.07	0.00	0.05	0.01	0.01	0.00	0.01	0.05
Al_2O_3	13.85	10.88	3.31	13.43	12.17	12.36	7.52	5.53	14.24	13.54	0.54	2.94	14.98
FeO	9.90	10.56	8.25	9.30	8.93	12.73	8.12	8.62	12.39	12.43	24.67	14.22	17.51
MnO	0.04	0.00	0.02	0.04	0.01	0.12	0.09	0.06	0.09	0.03	0.05	0.07	0.03
MgO	12.94	13.34	18.07	13.47	14.78	11.77	17.92	17.37	11.02	10.98	16.84	15.96	8.53
CaO	11.71	12.33	12.10	11.78	12.12	11.95	11.23	11.80	11.88	11.63	1.00	10.23	11.10
Na_2O	1.78	1.47	0.42	1.88	1.76	2.40	1.45	1.08	1.33	1.10	0.09	0.35	1.86
K_2O	1.41	0.83	0.10	1.23	0.89	0.03	0.02	0.34	1.29	1.32	0.04	0.15	1.53
Total	97.40	97.06	96.83	97.03	97.98	97.46	97.69	96.87	96.80	95.85	97.18	97.81	97.64
Si	6.417	6.802	7.703	6.470	6.622	6.592	7.131	7.353	6.440	6.546	7.960	7.719	6.183
Ti	0.171	0.094	0.015	0.145	0.103	0.116	0.043	0.045	0.115	0.096	0.004	0.020	0.103
Cr	0.017	0.010	0.005	0.018	0.014	0.008	0.000	0.006	0.002	0.001	0.000	0.002	0.006
Al	2.378	1.868	0.553	2.306	2.055	2.136	1.241	0.929	2.486	2.377	0.094	0.498	2.655
Fe^{3+}	0.007	0.000	0.063	0.005	0.069	0.000	0.206	0.098	0.001	0.018	0.000	0.000	0.114
Fe^{2+}	1.199	1.286	0.914	1.128	1.000	1.561	0.540	0.831	1.514	1.512	3.046	1.709	1.973
Mn	0.005	0.000	0.002	0.005	0.001	0.015	0.010	0.007	0.012	0.004	0.006	0.008	0.004
Mg	2.809	2.895	3.815	2.924	3.155	2.572	3.740	3.689	2.433	2.438	3.705	3.419	1.912
Ca	1.827	1.924	1.837	1.839	1.860	1.877	1.684	1.802	1.885	1.856	0.159	1.576	1.789
Na	0.503	0.415	0.115	0.531	0.489	0.682	0.393	0.298	0.382	0.318	0.024	0.096	0.541
K	0.262	0.154	0.018	0.229	0.163	0.007	0.004	0.061	0.243	0.250	0.007	0.027	0.293
Total	15.595	15.448	15.040	15.600	15.531	15.566	14.992	15.118	15.512	15.417	15.005	15.073	15.572

(*continued*)

TABLE 5. COMPOSITIONS OF AMPHIBOLES FROM GRANULITE AND METAGABBRO *(continued)*

Sample No.:	HY1A				HY1B			HY12G		
Texture:	Amp1	Amp2	Amp2	Amp2	Amp1	Amp2	Amp2	Amp2	Amp2	af opx
SiO_2	38.50	47.58	51.05	44.06	40.23	45.94	52.74	52.54	53.09	47.54
TiO_2	2.01	0.85	0.39	1.10	1.72	0.51	0.14	0.23	0.09	0.74
Cr_2O_3	0.03	0.04	0.04	0.03	0.12	0.10	0.10	0.07	0.02	0.03
Al_2O_3	12.97	7.82	4.73	10.85	12.46	9.30	1.28	3.21	2.24	7.82
FeO	22.53	16.54	17.29	17.59	21.30	18.99	23.85	12.60	17.64	14.59
MnO	0.13	0.07	0.11	0.09	0.08	0.09	0.15	0.05	0.30	0.07
MgO	5.72	11.23	13.42	10.25	6.70	9.47	14.27	15.71	12.83	12.79
CaO	11.04	11.01	9.71	11.06	11.30	11.26	4.23	11.71	11.40	11.04
Na_2O	1.67	1.13	0.42	1.81	1.86	1.39	0.19	0.50	0.34	1.40
K_2O	2.43	0.66	0.31	0.93	2.11	0.64	0.08	0.13	0.02	0.38
Total	97.03	96.93	97.47	97.77	97.85	97.66	97.03	96.75	97.97	96.40
Si	6.071	7.058	7.475	6.569	6.225	6.868	7.869	7.604	7.762	7.017
Ti	0.238	0.095	0.043	0.123	0.200	0.058	0.016	0.025	0.010	0.082
Cr	0.004	0.005	0.005	0.004	0.015	0.012	0.012	0.008	0.002	0.004
Al	2.398	1.368	0.817	1.907	2.273	1.637	0.225	0.548	0.386	1.361
Fe^{3+}	0.158	0.238	0.124	0.300	0.089	0.113		0.183	0.097	0.303
Fe^{2+}	2.814	1.814	1.993	1.893	2.668	2.139	2.976	1.342	2.060	1.498
Mn	0.017	0.009	0.014	0.011	0.011	0.011	0.015	0.006	0.037	0.009
Mg	1.344	2.483	2.928	2.278	1.545	2.109	3.174	3.388	2.796	2.813
Ca	1.866	1.750	1.523	1.767	1.874	1.804	0.676	1.816	1.786	1.746
Na	0.511	0.325	0.119	0.523	0.558	0.403	0.055	0.140	0.096	0.401
K	0.489	0.125	0.058	0.177	0.417	0.122	0.015	0.024	0.004	0.072
Total	15.910	15.270	15.099	15.552	15.875	15.273	15.032	15.084	15.967	15.306

Note: Ferric iron for calcic amphibole was calculated using a procedure by Schumacher (1991). HY12A–HY15E: granulite; others: metagabbro. af opx: after opx; la: lamellae; inc: inclusion.

TABLE 6. MINERAL COMPOSITIONS OF METAMORPHIC MAFIC AND GRANITIC DIKES

Sample No:	HY19B							HY7H				
Mineral:	Grt	Grt	Amp	Zo	Pl	Ilm	Ttn	Pl	Kfs	Bt	Ms	Grt
SiO_2	38.67	38.47	42.02	38.83	57.78	0.02	31.01	64.00	63.00	34.51	45.14	36.31
TiO_2	0.02	0.05	0.79	0.20	0.02	51.55	38.50	0.00	0.00	3.08	0.91	0.02
Cr_2O_3	0.01	0.04	0.02	0.00	0.01	0.01	0.00	0.00	0.00	0.00	0.01	0.00
Al_2O_3	21.28	21.31	15.02	29.65	26.31	0.00	1.14	22.33	18.73	16.55	28.36	20.67
FeO	23.42	23.96	16.22	4.54	0.11	44.03	0.16	0.00	0.00	25.11	5.65	24.51
MnO	3.48	3.30	0.14	0.03	0.00	0.90	0.00	0.00	0.00	0.33	0.02	13.60
MgO	2.24	2.24	8.25	0.06	0.01	0.91	0.00	0.00	0.00	4.88	1.35	0.63
CaO	11.37	10.76	11.26	23.01	8.22	0.64	27.02	3.11	0.01	0.03	0.00	4.00
Na_2O	0.01	0.03	1.42	0.01	6.51	0.02	0.01	9.68	1.02	0.11	0.19	0.04
K_2O	0.00	0.00	1.19	0.00	0.10	0.00	0.00	0.30	14.99	9.10	10.92	0.00
Total	100.50	100.16	96.33	96.33	99.07	98.08	97.84	99.42	97.75	93.70	92.55	99.75
Si	3.032	3.028	6.359	6.035	2.606	0.001	1.028	2.838	2.970	2.762	3.189	3.028
Ti	0.001	0.003	0.090	0.023	0.001	0.992	0.957	0.000	0.000	0.185	0.048	0.001
Cr	0.000	0.002	0.002	0.000	0.000	0.000	0.000	0.000	0.000	0.000	0.001	0.000
Al	1.966	1.977	2.679	5.432	1.399	0.000	0.044	1.167	1.041	1.561	2.361	2.031
Fe^{total}	1.535	1.577	2.053	0.590	0.004	0.942	0.004	0.000	0.000	1.689	0.335	1.709
Mn	0.231	0.220	0.018	0.003	0.000	0.019	0.000	0.000	0.000	0.018	0.001	0.749
Mg	0.262	0.263	1.861	0.014	0.001	0.035	0.000	0.000	0.000	0.582	0.142	0.078
Ca	0.955	0.907	1.826	3.832	0.397	0.018	0.957	0.148	0.001	0.003	0.000	0.357
Na	0.002	0.004	0.417	0.003	0.569	0.001	0.001	0.832	0.093	0.017	0.026	0.006
K	0.000	0.000	0.230	0.000	0.006	0.000	0.000	0.017	0.902	0.929	0.984	0.000
Total	7.984	7.981	15.534	15.932	4.983	2.008	2.991	5.003	5.007	7.745	7.087	7.958

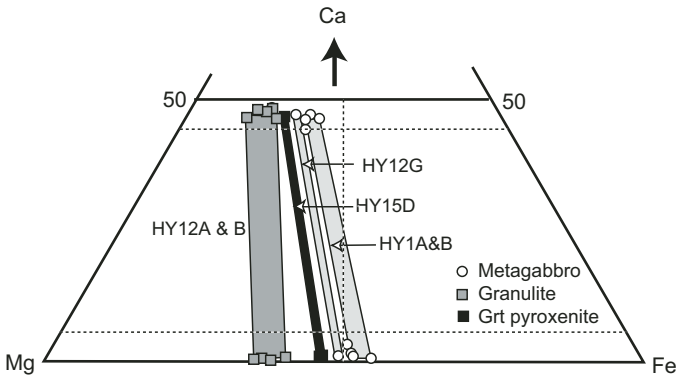

Figure 10. Compositional plots of representative clinopyroxene and orthopyroxene from granulite, metagabbro, and garnet pyroxenite.

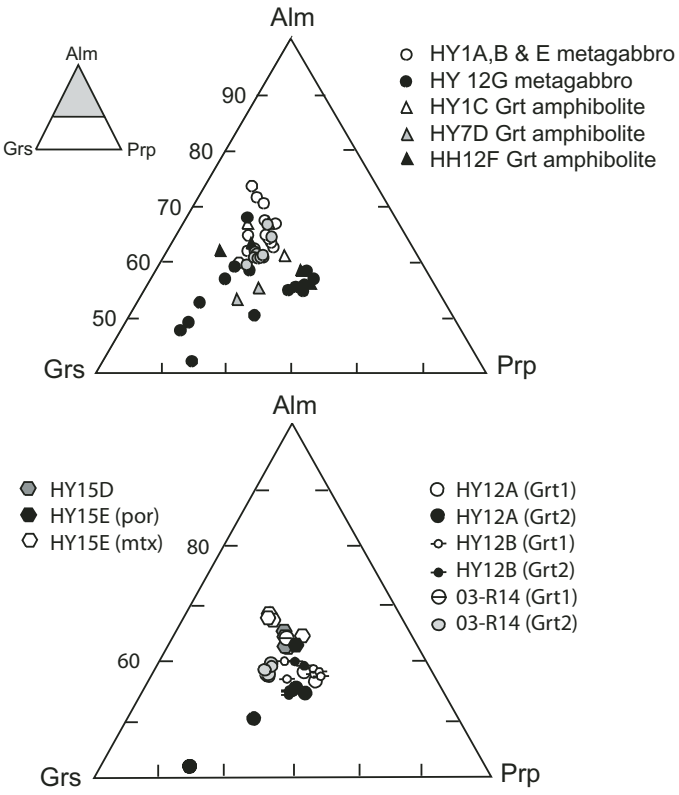

Figure 11. Almandine (Alm)-grossular (Grs)-pyrope (Prp) compositional plots of garnets from metagabbro and garnet amphibolite with gabbro protolith (A) and granulite (B). mtx—matrix; por—porphyroblast.

Plagioclase

Primary plagioclase (Pl_1) is only locally preserved in incipiently metamorphosed gabbro; most Pl_1 have been replaced by Pl_2 + Zo ± Grt ± Ms + An (pseudomorph after Pl_1) in granulite, and by Pl_2 + Zo ± Ky ± Grt + An in metagabbro. Only minor relict Pl_1 spots were analyzed (e.g., metagabbro HY1E, which has An_{55}). Pl_2 crystals are both calcic ($An_{50–77}$) and sodic ($An_{21–36}$) with gradational boundaries. Minor anorthite laths ($An_{>90}$) occur in plagioclase pseudomorphs after Pl_1. Most plagioclase from garnet amphibolite is sodic ($Ab_{36–88}$).

METAMORPHIC REACTIONS AND *P-T* CONDITIONS

Mineral reaction textures record *P-T*-assemblage evolution. The most common coronas observed in this study contain two layers of $|\text{Amp} \pm \text{Qtz}|\text{Grt}|$ or a single layer of garnet separating pyroxene (clinopyroxene or orthopyroxene) from plagioclase, and define the following reactions:

$$\text{Cpx} + \text{Pl} + \text{H}_2\text{O} = \text{Hbl} + \text{Qtz} + \text{Grt}, \quad (1)$$

$$\text{Opx} + \text{Cpx} + \text{Pl} + \text{H}_2\text{O} = \text{Hbl} + \text{Grt} + \text{Qtz}, \quad (2)$$

$$\text{Cpx} + \text{Pl} = \text{Grt}. \quad (3)$$

The coronae of $|\text{Grt}_2|\text{Amp} + \text{Qtz}|$ that separate garnet (Gr_1) from clinopyroxene define the reaction:

$$\text{Grt}_1\ (\text{Alm-rich}) + \text{Cpx} + \text{H}_2\text{O} = \text{Grt}_2\ (\text{Grs-rich}) + \text{Amp} + \text{Qtz}. \quad (4)$$

In metagabbro, the reactions forming $|\text{Grt}|\text{Amp} + \text{Qtz}|$ coronae between plagioclase and pyroxene may follow the same reactions 1, 2, and 3. Plagioclase is replaced by fine-grained assemblages of Zo + Pl_2 + Ky ± An + Qtz ± Grt. Zoisite, Pl_2, minor Ky, and An are the main products; grossular-rich garnet is only locally developed. These newly grown crystals are randomly distributed and coarsen with advanced recrystallization. Plagioclase breakdown in a closed system is a function of pressure (Goldsmith, 1982) and can be approximated by the following reactions:

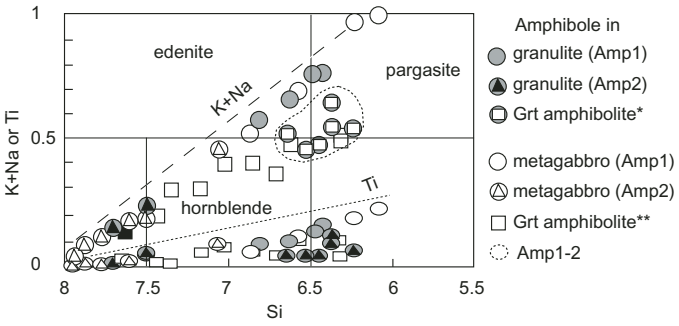

Figure 12. Si versus (Na + K) and Si versus Ti plots of amphiboles from granulite, metagabbro, and garnet amphibolite. Amp_1 from metagabbro and granulite have high contents of Ti and (Na + K) in p.f.u. Amphiboles include actinolite and cummingtonite in the field of Na + K < 0.5 and Si > 7.5; others are calcic amphibole (Ca_B > 1.5). * and ** represent garnet amphibolites with minor relict Amp_1 derived from granulite and gabbro, respectively.

$$Pl + H_2O \rightarrow Zo + Ky + Qtz + (NaSiCa_{-1}Al_{-1})_{Pl} \text{ and} \quad (5)$$

$$Pl \rightarrow Grt + Ky + Qtz + (NaSiCa_{-1}Al_{-1})_{Pl} \quad (6)$$

The process can be more complex and involve reactions with mafic minerals.

As described above, most pyroxenes underwent exsolution and reaction with plagioclase. The compositions of the original minerals in the Haiyangsuo granulite may have been modified to various extents, hence estimating *P-T* conditions based on mineral compositions is a difficult task. Only the compositions of less-altered minerals were used to estimate *P-T* conditions. Metamorphic pressures and temperatures of granulites were calculated at 800, 700, and 600 °C, and 5, 10, and 15 kbar (see Table 7-1). The Grt-Opx (Wood, 1974; Harley and Green, 1982) and Grt-Cpx-Opx-Pl-Qtz barometers (Paria et al., 1988) were employed to estimate pressure, and yielded 10 ± 1 kbar at 700 °C. The Grt-Cpx (Powell, 1985) and Grt-Opx thermometers (Harley, 1984) yielded similar temperatures of 605–665 °C at 10 kbar. The Opx-Cpx thermometer (Wood and Banno, 1973) independently gave higher temperature of 740–805 °C for coarse-grained Cpx and Opx from samples HY12A and HY15D; the clinopyroxene host and exsolved orthopyroxene lamellae yielded 650–730 °C (average 690 °C). These estimates represent post-peak equilibration after exsolution, because high cation-diffusion rates generally preclude the preservation of early, prograde, or maximum-*T* segments of a *P-T* path (Harley, 1989). The metamorphic temperature of the granulite-facies recrystallization was likely higher than the temperature obtained from clinopyroxene with orthopyroxene exsolution lamellae (>690 °C).

Amphibole-plagioclase thermometry (Blundy and Holland, 1990; Holland and Blundy, 1994) and Hbl-Grt-Pl thermobarometry (Dale et al., 2000) were employed to estimate *P-T* conditions for the Haiyangsuo garnet amphibolites, including the various gabbro and mafic dike protoliths. In these calibrations, both garnet and amphibole were assumed to obey a regular solution model; plagioclase was modeled using the expressions in Holland and Powell (1992). As shown in Table 7, the average recrystallization temperatures of T_A (Ed + 4Qtz = Tr + Ab) and T_B (Ed + Ab = richterite + Act) were 725, 685, and 655 °C for metamafic dike HY19B, and 545–680, 550–655, and 555–645 °C for metagabbro, at 10, 8, and 6 kbar, respectively. Sample HY19B is a completely recrystallized amphibolite, which is consistent with a higher-*T* estimate. The most-recrystallized metagabbros have higher temperature estimates than those in which plagioclase pseudomorphs are preserved. Pressure estimates range from 6.5 to 11 kbar at 600 °C.

DISCUSSION

Granulite *P-T-t* Path and Its Possible Origin

The U-Pb SHRIMP dating of zircons from the present study and that of Chu (2005) yielded the following results. The Haiyangsuo granulite experienced two recrystallization events: (1) granulite-facies recrystallization at 1846 ± 26 Ma, and (2) an amphibolite-facies overprint at 373 ± 65 Ma. Emplacement of the gabbro intrusions occurred at 1734 ± 5 Ma, and the amphibolite-facies recrystallization of the metagabbro was at 339 ± 59 Ma. The amphibolite-facies recrystallization of both granulite and gabbro produced identical corona textures, and has a similar age within uncertainty, suggesting that both resulted from one tectonometamorphic event. Based on the observed textures, age data, and *P-T* estimates described in the previous sections, the Haiyangsuo granulites show a near-isobaric cooling (IBC) *P-T-t* path (Fig. 13).

Ye et al. (1999) described a fine-grained diopside ± omphacite assemblage around the edges of relict clinopyroxene porphyroblasts, and suggested that the granulites recrystallized during compression from the granulite to the eclogite stability field. The Grt + Di + Pl paragenesis is also present in local domains in plagioclase from our granulite and metagabbro samples. In general, the Grt + Cpx + Pl ± Qtz assemblage represents a paragenetic link between a plagioclase-free eclogite-facies metabasite and an orthopyroxene-bearing granulite-facies metabasite, and the Grt + Cpx + Pl paragenesis occurs in local domains in plagioclase of the Haiyangsuo granulite and metagabbro. However, this assemblage may also occur in lower amphibolite–facies rocks (Fig. 13B) and is not definitive of high-*P* granulite (Pattison, 2003).

In fact, omphacite with a measurable Jd (~24 mol%) component was encountered only in one analysis in the Haiyangsuo granulite (Ye et al., 2000); more than 99% of the coronal assemblages between pyroxene and plagioclase were │Amp ± Qtz│Grt│ or garnet rather than omphacite-garnet. Even though a transitional eclogite *P-T* field has been suggested for these rocks, isobaric cooling can also explain such a transition. Holland and Powell (1998, Fig. 8) proposed a *P-T* pseudosection for the NCFMAS system to explain the phase relationship and *P-T* conditions of the granulite-eclogite transition. As shown in Figure 13D, the transition from a trivariant field of granulite (Grt + Cpx + Opx + Pl) to another trivariant field (Grt + Omp + Ky + Pl) and a divariant field (Grt + Omp + Cpx + Ky + Pl) can happen through either near-isobaric cooling (IBC) or increasing pressure. Granulites showing an isobaric cooling history have been considered to have formed at various origins and settings (Harley, 1989). The Haiyangsuo granulite may have been derived from a Proterozoic granulite-amphibolite terrane. The low recrystallization temperature and the counterclockwise isobaric cooling *P-T* path of the Haiyangsuo granulite may indicate formation during the thickening of extended thin crust, as proposed by Harley (1989).

Non-UHP Unit in the Sulu UHP Terrane

The whole Sulu UHP terrane (see Fig. 1) has long been considered to be a coesite-eclogite (UHP) belt in fault contact with the eclogite-free high-pressure belt in southern Sulu. The

TABLE 7-1. PRESSURE-TEMPERATURE CALCULATIONS OF GRANULITE

	T(°C)			P(kbar)		
	Opx1-Cpx1 Wood and Banno (1973)	Grt1-Cpx1 Powell (1985)	Grt1-Opx1 Harley (1984)	Grt1-Opx1 Wood (1974)	Grt1-Opx1 Harley and Green (1982)	Grt-Px-Pl Paria et al. (1988)
HY12A	740					
15/800		630	675	14.4	10	14.4
10/700		620	650	9.6	9.4	10.7
5/600		610	625	4.9	8.7	7.0
HY12B	650-730*					
15/800		680	650	14.1	9.7	15.2
10/700		665	625	9.4	9.0	11.5
5/600		655	600	4.7	8.4	7.6
HY15D	805					
15/800				17.8	11.3	
10/700				12.5	10.7	
5/600				7.2	9.9	
HY15E						
15/800		640	630	15.4	11.8	
10/700		630	605	10.3	11.4	
5/600		615	580	5.2	10.5	

Note: Temperature and pressure were calculated at 15, 10, and 5 kbar, and at 800, 700, and 600 °C, respectively.
*host Cpx - exsolved Opx

TABLE 7-2. PRESSURE-TEMPERATURE CALCULATIONS OF GARNET AMPHIBOLITE

	T (°C)				P (kbar)			
Sample	Grt-Hbl GR(1984) (Graham and Powell,1984)	Amp-Pl (Blundy and Holland, 1990)	Amp-Pl at 10 kbar (Holland and Blundy, 1994)		Grt-Pl-Amp at 600°C (Dale et al., 2000)			Pl-Amp (Blundy and Holland,1990)
			Ta metagabbro	Tb	P1	P2	P3	
HY1C	891	752	687	653	12.8	12.4	12.1	10
HY12F	557	596	623	687	6.7	7.4	7.7	1.9
HY19B	666	744	769	655	11	10.4	11.6	9.9

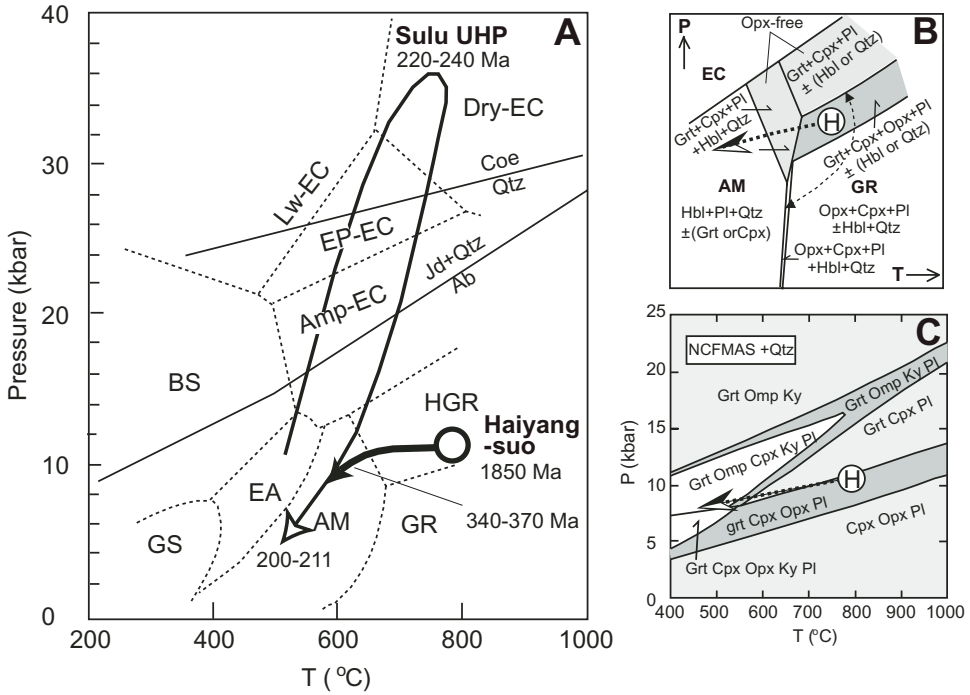

Figure 13. (A) Estimated pressure-temperature-time (*P-T-t*) path of the Haiyangsuo granulite showing near-isobaric cooling (IBC) history. For comparison, a simplified *P-T-t* path of Sulu ultrahigh-pressure (UHP) rocks is also shown. (B) Schematic *P-T* diagram showing the *P-T* domains of granulite and amphibolite mineral assemblages modified after Pattison (2003) and the Haiyangsuo granulite near-isobaric cooling path. (C) A *P-T* pseudosection for an aluminous andesitic basalt bulk composition showing the transformation from granulite to eclogite (EC) after Holland and Powell (1998). Abbreviations are after Kretz (1983). EC—eclogite; EP—epidote; BS—blueschist; GS—greenschist, EA—epidote-amphibolite; HGR—high-P granulite; AM—amphibolite; GR—granulite.

rock association and metamorphic evolution histories in the Haiyangsuo area are different, however, from both Sulu UHP and high-pressure rocks. Ye et al. (1999) correlated the Haiyangsuo "transitional eclogite" with the "cold eclogite" of south Dabie, and interpreted the Haiyangsuo area as an equivalent to the Dabie "cold eclogite belt," which is widespread in Dabie.

The Haiyangsuo granulite, however, was overprinted by garnet amphibolite rather plagioclase-bearing "transitional eclogite" to garnet amphibolite. The presence of very rare omphacite in a plagioclase-stable terrane may simply reflect metastable growth during isobaric cooling. Furthermore, most of the zircons from Dabie-Sulu high-pressure and UHP eclogites and gneisses have Neoproterozoic cores ranging from ca. 625 to 800 Ma (Hacker et al., 2000, 2006; Liu et al., 2004b, 2005). Moreover, $^{40}Ar/^{39}Ar$ ages from the Sulu UHP rocks are ca. 220–200 Ma (Cong et al., 1992; Webb et al., this volume; Xu et al., this volume). In the Haiyangsuo area, the protoliths for the gneissic and mafic rocks—including the gabbroic intrusions—have Early Proterozoic ages; some could be Archean. The 600–800 Ma Late Proterozoic protolith ages and the Triassic high-pressure and UHP metamorphic ages common in Dabie-Sulu high-pressure and UHP rocks were not observed. Based on the geochronologic and petrological data documented above, we suggest that the Haiyangsuo granulite-amphibolite facies complex is exotic to the Sulu UHP–high-pressure terrane. However, the correlation of the Haiyangsuo unit with other tectonic terranes in eastern China and the Korean peninsula remains to be investigated.

CONCLUSION

The Haiyangsuo area exposes three lithological units: (1) gneiss with granulite lenses and amphibolite layers, (2) metagabbro, and (3) granitic dikes. Unit 1 is dominant, displays several stages of metamorphism, and has a protolith age older than 2500 Ma. The granulite (Grt + Cpx + Opx ± Pl +Ilm/Rt ± Qtz ± Prg ± Bt) is volumetrically minor; most has been retrogressed to garnet amphibolite (Grt + Hbl + Ilm + Pl ± Qtz) at the margins of the granulite lenses. Coronas of │Grt│ Qtz ± Amp│ at the contacts between plagioclase and pyroxene indicate an isobaric cooling history. A SHRIMP U-Pb age of ca. 1850 Ma for metamorphic zircon from the granulite probably represents the first metamorphic event of unit 1, when the amphibolite-facies gneiss, granulite, and garnet amphibolite layers were metamorphosed. An amphibolite-facies overprint took place at 373 ± 65 Ma. Unit 2 exhibits various extents of transformation, with

incipient corona textures in the cores of the gabbros to a garnet amphibolite along the margins. Gabbroic rocks with primary phases (Opx + Opx + Pl + Ilm ± Qtz) formed at 1734 ± 5 Ma; they were subsequently recrystallized in amphibolite facies at 339 ± 59 Ma. The amphibolite-facies recrystallization of the granulite and gabbro probably resulted from a single tectonometamorphic event. The granitic dikes are much younger (160 ± Ma) but coeval with the SHRIMP age of the Rushan granite, ~20 km farther west (Hu et al., 2004; Fig. 1). The rock associations and metamorphic history indicate that the Haiyangsuo area is exotic to the Triassic Sulu high-pressure–UHP terrane, with which it was juxtaposed in the Jurassic.

ACKNOWLEDGMENTS

This research resulted from a U.S.-China cooperative project supported by the National Science Foundation (NSF) grant EAR-0003355 and EAR-0506901. We thank F. Mazdab, R. Zhao, and K. Okamoto for their assistance in sensitive high-resolution ion microprobe (SHRIMP) and microprobe laboratories, and W. Chu for his unpublished age data and generous help. We appreciate B. Hacker, S. Wallis, M. Terry, and W.G. Ernst for their critical review and material improvement of the manuscript.

REFERENCES CITED

Ames, L., Zhou, G.Z., and Xiong, B., 1996, Geochronology and geochemistry of ultrahigh-pressure metamorphism with implications for collision of the Sino-Korean and Yangtze cratons, central China: Tectonics, v. 15, p. 472–489, doi: 10.1029/95TC02552.

Blundy, J.D., and Holland, T.J.B., 1990, Calcic amphibole equilibria and a new amphibole plagioclase geothermometer: Contributions to Mineralogy and Petrology, v. 104, p. 208–224, doi: 10.1007/BF00306444.

Chu, W., 2005, Geochronological and petrological studies of Haiyangsuo region Sulu UHP terrane, eastern China [M.S. thesis]: Stanford, Stanford University, 80 p.

Cong, B.L., Zhang, R.Y., Li, S.G., Zhai, M.G., Wang, S.S., Cheng, C.Y., and Ishiwatari, A., 1992, Preliminary study of isotope chronology of northern Jiangsu and eastern Shandong province, China, *in* Ishda, S., ed., Exploration of volcanoes and rocks in Japan, China and Antarctica: Yamaguchi, Yamaguchi University, p. 411–419.

Dale, J., Holland, T., and Powell, R., 2000, Hornblende-garnet-plagioclase thermobarometry: A natural assemblage calibration of the thermodynamics of hornblende: Contributions to Mineralogy and Petrology, v. 140, p. 353–362, doi: 10.1007/s004100000187.

Goldsmith, J.R., 1982, Plagioclase stability at elevated temperatures and pressures: The American Mineralogist, v. 66, p. 1183–1188.

Harley, S.L., 1984, An experimental study of the partitioning of Fe-Mg between garnet and orthopyroxene: Contributions to Mineralogy and Petrology, v. 86, p. 359–373, doi: 10.1007/BF01187140.

Harley, S.L., 1989, The origins of granulites: A metamorphic perspective: Geological Magazine, v. 126, p. 215–247.

Harley, S.L., and Green, D.H., 1982, Garnet-orthopyroxene barometry for granulite and peridotites: Nature, v. 300, p. 697–701, doi: 10.1038/300697a0.

Hacker, B.R., Ratschbacher, L., Webb, L., McWilliams, M.O., Ireland, T., Calvet, A., Dong, S., Wenk, H.R., and Chateigner, D., 2000, Exhumation of ultrahigh-pressure continental crust in east central China: Journal of Geophysical Research, v. 105, p. 13,339–13,364, doi: 10.1029/2000JB900039.

Hacker, B.R., Wallis, S., Grove, M., and Gehrels, G., 2006, U-Pb SIMS and LA-ICP-MS zircon and monazite ages constrain the architecture of the ultrahigh-pressure Sulu orogen: Tectonics (in press).

Han, Z., Zhang, G., Guo, H., Zhang, Z., and Wang, L., 1993, Sm-Nd isochronism age of eclogite from southern Shandong province and its tectonics significance: Journal of Ocean University of Qingdao, v. 23, p. 120–124.

Hirajima, T., Ishiwatari, A., Cong, B.L., Zhang, R.Y., Banno, S., and Nozaka, T., 1990, Identification of coesite in Mengzhong eclogite from Donghai county, northeastern Jiangsu province, China: Mineralogical Magazine, v. 54, p. 579–584.

Holland, T., and Blundy, J., 1994, Non-ideal interactions in calcic amphiboles and their bearing on amphibole-plagioclase thermometry: Contributions to Mineralogy and Petrology, v. 116, p. 433–447, doi: 10.1007/BF00310910.

Holland, T.J.B., and Powell, R., 1992, Plagioclase feldspars: Activity-composition relations based upon Darken's Quadratic Formalism and Landau theory: The American Mineralogist, v. 77, p. 53–61.

Holland, T., and Powell, R., 1998, An internally consistent thermodynamic data set for phases of petrological interest: Journal of Metamorphic Geology, v. 16, p. 309–343, doi: 10.1111/j.1525-1314.1998.00140.x.

Hu, F., Fang, H., Yang, J., Wan, Y., Liu, D., Zhai, M., and Jin, C., 2004, Mineralizing age of the Rushan Iode gold deposit in the Jiaodong Peninsula: SHRIMP U-Pb dating on hydrothermal zircon: Chinese Science Bulletin, v. 49, p. 1629–1636, doi: 10.1360/04wd0105.

Kretz, R., 1983, Symbols for rock-forming minerals: The American Mineralogist, v. 68, p. 277–279.

Li, S., Xiao, Y., Liou, D., Chen, Y., Ge, N., Zhang, Z., Sun, S-S., Cong, B., Zhang, R., Hart, S.R., and Wang, S., 1993, Collision of the North China and Yangtze blocks and formation of coesite-bearing eclogite: Timing and processes: Chemical Geology, v. 109, p. 89–111, doi: 10.1016/0009-2541(93)90063-O.

Li, S., Chen, Y., Song, M., Zhang, Z., Yang, C., and Zhao, D., 1994, U-Pb zircon ages of amphibolite from the Haiyangsuo area, eastern Shandong Province: An example for influence of multi-metamorphism to lower and upper intercepts of zircon discordia line at the concordia curve: Acta Geoscientia Sinica, v. 12, p. 37–42 (in Chinese with English abstract).

Liu, F., Xu, Z., and Liou, J.G., 2004a, Tracing the boundaries between UHP and HP metamorphic belts in southwestern Sulu region, eastern China: Evidence from mineral inclusions in zircons from metamorphic rocks: International Geology Review, v. 46, p. 409–452.

Liu, F., Xu, Z., and Liou, J.G., 2004b, SHRIMP U-Pb ages of ultrahigh-pressure and retrograde metamorphism of gneisses from southwestern Sulu terrane, eastern China: Journal of Metamorphic Geology, v. 22, p. 315–326, doi: 10.1111/j.1525-1314.2004.00516.x.

Liu, F., Liou, J.G., and Xu, Z., 2005, U-Pb SHRIMP ages recorded in the coesite-bearing zircon domains of paragneisses in the southwestern Sulu terrane, eastern China: New interpretation: The American Mineralogist, v. 90, p. 790–800, doi: 10.2138/am.2005.1677.

Ludwig, K.R., 2001, SQUID 1.02: Berkeley Geochronology Center Special Publication 2, 19 p.

Ludwig, K.R., 2003, Isoplot 3: Berkeley Geochronology Center Special Publication 4, 70 p.

Paria, P., Bhattacharya, A., and Sen, S.K., 1988, The reaction garnet + clinopyroxene + quartz = 2 orthopyroxene + anorthite: A potential geobarometer for granulites: Contributions to Mineralogy and Petrology, v. 99, p. 126–133, doi: 10.1007/BF00399372.

Pattison, D.R.M., 2003, Petrogenetic significance of orthopyroxene-free garnet + clinopyroxene + plagioclase ± quartz-bearing metabasites with respect to the amphibolite and granulite facies: Journal of Metamorphic Geology, v. 21, p. 21–24, doi: 10.1046/j.1525-1314.2003.00415.x.

Powell, R., 1985, Regression diagnostic and robust regression in geothermometer/geobarometer calibration: The garnet-clinopyroxene geothermometer revisited: Journal of Metamorphic Geology, v. 3, p. 231–243.

Schumacher, J.C., 1991, Empirical ferric iron corrections: Necessity, assumptions and effects on selected geothermobarometers: Mineralogical Magazine, v. 55, p. 3–18.

Wallis, S., Enami, M., and Banno, S., 1999, The Sulu UHP terrane: A review of the petrology and structural geology: International Geology Review, v. 41, p. 906–920.

Wallis, S., Tsuboi, M., Suzuki, K., Fanning, M., Jiang, L., and Tanaka, T., 2005, Role of partial melting in the evolution of the Sulu (eastern China) ultrahigh-pressure terrane: Geology, v. 33, p. 129–162, doi: 10.1130/G20991.1.

Wang, R., An, J., and Lai, X., 1995, Discovery of an ophiolite suite in eastern Shandong Peninsula and its significance: Acta Petrologica Sinica, v. 11, p. 221–228.

Williams, I.S., 1998, U-Th-Pb geochronology by ion microprobe, *in* Mickibbeen, M.A., Shanks, W.C., III, and Ridley, I., eds., Application of microanalytical techniques to understanding mineralizing processes: Society of Economic Geologists Reviews in Economic Geology, v. 7, p. 1–35.

Wood, B.J., 1974, The solubility of alumina in orthopyroxene coexisting with garnet: Contributions to Mineralogy and Petrology, v. 46, p. 1–14, doi: 10.1007/BF00377989.

Wood, B.J., and Banno, S., 1973, Garnet-orthopyroxene and orthopyroxene-clinopyroxene relationships in simple and complex systems: Contributions to Mineralogy and Petrology, v. 42, p. 109–124, doi: 10.1007/BF00371501.

Yang, J.S., Wooden, J.L., Wu, C.L., Liu, F.L., Xu, Z.Q., Shi, R.D., Liou, J.G., and Maruyama, S., 2003, SHRIMP U-P dating of coesite-bearing zircon from the ultrahigh-pressure metamorphic rocks, Sulu terrane, east China: Journal of Metamorphic Geology, v. 21, p. 551–560.

Ye, K., Cong, B., Hirajima, T., and Banno, S., 1999, Transformation from granulite to transitional eclogite at Haiyangsuo, Rushan County, eastern Shandong Peninsula: The kinetic process and tectonic implications: Acta Petrologica Sinica, v. 15, p. 21–36.

Ye, K., Yao, Y., Katayama, I., Cong, B.L., Wang, Q.C., and Maruyama, S., 2000, Large area extent of ultrahigh-pressure metamorphism in the Sulu ultrahigh-pressure terrane of East China: New implications from coesite and omphacite inclusions in zircon of granitic gneiss: Lithos, v. 52, p. 157–164, doi: 10.1016/S0024-4937(99)00089-4.

Zhang, R.Y., Hirajima, T., Banno, S., Cong, B., and Liou, J.G., 1995, Petrology of ultrahigh-pressure rocks from the southern Sulu region, eastern China: Journal of Metamorphic Geology, v. 13, p. 659–675.

Zhang, S., and Kang, W., 1989, The character of the blueschist belt and discussion of the formation age in central China: Journal of Changchun University of Earth Science, p. 1–9.

Manuscript Accepted by the Society 21 September 2005